

Aerodynamics and aeroelastic behaviour of ice-accreted bridge cables

Cristoforo Demartino



University of Naples Federico II
Department of Structures for Engineering and Architecture
Dottorato di Ricerca in Ingegneria delle Costruzioni - XXVI Ciclo
Coordinatore: Prof. Luciano Rosati
Tutor: Prof. Mario Pasquino
Co-tutor: Prof. Francesco Ricciardelli
PhD-thesis - 2014

University of Naples Federico II
Department of Structures for Engineering and Architecture
via Claudio, 21
80124 NAPOLI (Italy)
info.dist@unina.it
www.dist.unina.it

to my family (Aldo, Pilar, Massimiliano and Costanza)

Preface

This thesis is submitted in partial fulfillment of the requirements for the Italian Ph.D. degree. The work has been carried out at the Department of Structures for Engineering and Architecture at University of Naples Federico II and took place in the period between March 2011 to March 2014, with Full Professor Mario Pasquino as main supervisor and Associate Professor Francesco Ricciardelli as co-supervisor.

This dissertation investigates the effects of ice accretion on the aerodynamics and aeroelastic stability of bridge hangers and stay cables. First, a review of the state of art on the aerodynamics of nominally circular cylinders is given. Then, the aerodynamic behavior and accretion characteristics of ice accreted bridge cables were experimentally studied by climatic wind tunnel tests. The aerodynamic stability was investigated using the models proposed by different authors. Furthermore a novel 3D 3-DoFs quasi-steady aeroelastic model is proposed.

Napoli, the 31st March 2014

Cristoforo Demartino

Acknowledgements

Most people return small favors, acknowledge medium ones and repay greater ones - with ingratitude.

BENJAMIN FRANKLIN

The main thing that I learned from this Ph.D. is that after disappointments it always comes immense satisfaction and that life holds for us only the good things if we are willing to be dynamic. Anyway, this thesis would not be what it is without the supports of many people whom I would like to gratefully acknowledge.

I would like to express my very great appreciation to Professor Francesco Ricciardelli for his valuable and constructive suggestions during the planning and development of this research work. Without his guidance and persistent help this dissertation would not have been possible. I will remember for a lifetime the days spent together trying to understand better and better the amazing world of wind engineering.

I would like to offer my special thanks to Professor Mario Pasquino for his numerous advice and many discussions on the importance of education in the broadest sense in university.

I am deeply grateful to Professor Luciano Rosati for the interest showed in my research and for the important teachings and discussions on the mechanics of solids.

Also a special thank to Professor Christos T. Georgakis and to Professor Holger H. Koss of the Department of Civil Engineering at the Technical University of Denmark for sharing their experience within experimental wind tunnel testing and their useful and constructive recommendations on this project. In addition a great thank to them is due to the wonderful time spent in Denmark.

A special thank goes to the PhD student Giulia Matteoni, who contributed to the development of the novel aeroelastic model proposed.

I owe a deep thanks to Master student Mia Schou Møller Lund who contributed to the development of the spray bar system.

I would also like to thank Professor Francesco Marulo, for his great help in the development of the novel aeroelastic model and for the organization of the visit to the CIRA Icing Wind Tunnel.

I would also like to extend my thanks to the technicians of the laboratory of the Department of Civil Engineering at the Technical University of Denmark, in particular Erik Bjørn Kristiansen, for their help in offering me the resources in running the program.

I would like to thank the FORCE Technology for all the supports given.

I would also like to express my gratitude to University of Federico II° of Naples for its financial support.

Thanks to all other fellow and Ph.D. students part of the University of Naples Federico II, for sharing their knowledge, in particular Francesco Marmo, Ferdinando Toraldo, Salvatore Trotta, Enrico Ricciardi, Alfonso Pisciotta, Giuseppe La Manna Ambrosini and Vittorio Pasquino.

Thanks to all other fellow and Ph.D. students part of the Technical University of Denmark, in particular Antonio Acampora, Jan Winkler, Emanuele Mattiello, Mads Beedholm Eriksen, Iwona Budny, Rocco Custer, Nina Gall Jørgensen and Shouyung Zhan.

I am grateful for the loving support of Costanza for having always been close in the past three years and have shared many steps of my life.

Finally, I owe a deep thanks to my family for their support and encouragement throughout my study.

Abstract

This dissertation investigates the effects of ice accretion on the aerodynamics and the aeroelastic stability of bridge hangers and cable stays. First, a review of the state of art on the aerodynamics of nominally circular cylinders is given. Then, the aerodynamic behavior and ice characteristics of ice accreted bridge cables were experimentally studied by climatic wind tunnel tests. A novel 3D 3-DoFs quasi-steady aeroelastic model is proposed. The aerodynamic stability was investigated using the models proposed by different authors.

A systematic and comprehensive review of the state of art of research in the public domain addressing the aerodynamic of nominally circular cylinders is given. The review focuses on descriptions of the typical disturbance of the nominally circular cylinders that affects aerodynamics. The disturbances are classified in cylinder and flow irregularities and the former are further subdivided into surface irregularities, section irregularities and spanwise irregularities. The review clearly demonstrates the importance of assessing and estimating the effects of these disturbances in the entire design process. Furthermore, it was showed the lack of knowledge on the effects of ice accretion on the aerodynamics on bridge cables.

An extensive wind tunnel test campaign was then undertaken to understand the effects of in-cloud ice accretion on the aerodynamics of bridge hangers and stay cables, having a diameter of 160 mm and made of High Density PolyEthylene (HDPE) like a typical configuration of bridge cables. The tests were performed at the DTU/Force Technology collaborative Climatic Wind Tunnel (CWT) in Lyngby, Denmark. In order to investigate the aerodynamic behavior of ice accreted bridge hangers and stay cables, a particular setup was realized for reproducing the conditions of in-cloud icing. The setup consists of a spray bar system and two cable section models (a bridge hanger and a stay cable section models) placed in the CWT. The spray bar system was placed in the settling chamber downstream of the honeycomb grid, and the cable section model was placed in the centre of the test section. Different climatic conditions

were tested varying temperature, wind speed and cable orientation.

The time evolution of the ice accretion was investigated by means of a time-lapse technique. The final shape of accreted ice across the cable section determined by cutting the ice (in the direction perpendicular to the cable axis) with a heated metal plate and drawing the ice contour on a cardboard.

Aerodynamic forces of ice accreted bridge hangers and cable stays were measured at both ends of the model using two 6-DOFs force transducers. The drag, lift and moment coefficients were quantified. As the wind direction and the atmospheric conditions are variable in time, ice accretion can be generated in one particular condition whilst instability can occur in a different one; accordingly aerodynamic force coefficients were measured with varying angle of attack.

A novel 3D-3DoFs quasi-steady aeroelastic model is proposed. The model is able to predict the galloping and divergence instability of a cylinder with generic cross-section, the minimum required structural damping and stiffness to prevent instability, and to predict the cross-sectional response to a turbulent flow, considering both buffeting and self-excited contributions.

Finally, the aerodynamic stability of iced bridge cables was investigated by mean of analytical models proposed by different authors. In order to compare the background hypotheses, the models were classified into a general framework that highlights a common approach based on the quasi-steady theory. Not existing a benchmark, the comparison of the predictions of each model was not aimed at judging the quality of each approach, but rather at pointing out the differences they bring.

Sommario

Questa tesi si occupa dello studio degli effetti dell'accrescimento di ghiaccio sull'aerodinamica e la stabilità aeroelastica di pendini e stralli da ponte. In primo luogo, è stata eseguita un'indagine bibliografica sullo stato dell'arte dell'aerodinamica di cilindri nominalmente circolari. In seguito, sono state compiute indagini sperimentali in galleria del vento climatica con lo scopo di indagare le caratteristiche dell'accrescimento e il comportamento aerodinamico dei cavi da ponte ghiacciati. Con lo scopo di superare i limiti delle precedenti formulazioni, si propone un nuovo modello aeroelastico basato sulla teoria quasi-statica che considera la tridimensionalità del flusso e i tre gradi di libertà della sezione. Infine, è stata studiata la stabilità aeroelastica utilizzando i modelli presenti in letteratura.

L'indagine bibliografica ha riguardato lo studio, la correlazione e la valutazione dello stato dell'arte della ricerca di dominio pubblico riguardante l'aerodinamica di cilindri nominalmente circolari. Sono stati considerati studi sia di natura sperimentale che numerica. Si intende con il termine cilindro circolare perfetto il caso in cui il numero di Reynolds da solo è sufficiente a definire il comportamento aerodinamico. L'esigenza di considerare altri parametri allontana il comportamento da quello di cilindro circolare perfetto. In tal caso il cilindro è definito nominalmente circolare. Le possibili cause di deviazione dal comportamento teorico sono stati classificate in irregolarità del cilindro e del flusso. Le prime sono state a loro volta suddivise in irregolarità della superficie, irregolarità della sezione ed irregolarità lungo l'asse. L'indagine evidenzia l'importanza della valutazione e stima degli effetti di questi disturbi sull'aerodinamica di cilindri nominalmente circolari durante le fasi progettuali. Inoltre, viene rilevata la mancanza di conoscenza degli effetti sull'aerodinamica dell'accrescimento di ghiaccio su cavi da ponte.

È stata intrapresa una vasta indagine sperimentale al fine di comprendere gli effetti dell'accrescimento del ghiaccio in nuvola (*in-cloud icing*) sull'aerodinamica di pendini e stralli da ponte, aventi un diametro di 160 mm e realizzati in

polietilene ad alta densità (HDPE, dall'inglese *high-density polyethylene*) come in una configurazione reale da ponte. Le prove sono state condotte presso la galleria del vento climatica del DTU/Force a Lyngby, in Danimarca.

Un particolare apparato sperimentale è stato realizzato *ad hoc* per riprodurre le condizioni di accrescimento del ghiaccio in nuvola in galleria del vento. L'apparato sperimentale è costituito da un sistema di nebulizzazione installato in una barra (*spray bar*) e da un modello sezionale del cavo. Il sistema di nebulizzazione è stato collocato nella camera di calma a valle della griglia ad alveare mentre il modello sezionale del cavo è stato installato al centro della camera di prova. Le indagini sperimentali hanno riguardato la simulazione di differenti condizioni climatiche che sono state ottenute variando la temperatura, la velocità del vento e l'orientamento del cavo rispetto alla direzione del vento in camera di prova.

Particolare attenzione è stata rivolta allo studio dell'evoluzione nel tempo dell'accrescimento del ghiaccio attraverso l'utilizzo di una tecnica fotografica di tipo *timelapse*. La caratterizzazione della geometria finale dell'accrescimento è stata eseguita utilizzando una piastra metallica riscaldata per tagliare il ghiaccio in un piano perpendicolare all'asse del cavo e riportando il contorno su un foglio. Le immagini sono state in seguito digitalizzate e analizzate evidenziandone le caratteristiche.

Considerata la variabilità della direzione del vento e delle condizioni climatiche dei processi atmosferici, l'instabilità aeroelastica può verificarsi in una condizione diversa da quella che ha generato l'accrescimento; conseguentemente, i coefficienti di resistenza aerodinamica sono stati misurati variando l'angolo di attacco rispetto alla configurazione di accrescimento. La misurazione delle forze aerodinamiche è stata eseguita servendosi di due trasduttori di forza a 6 gradi di libertà installati su entrambe le estremità del modello.

Si propone un nuovo modello aeroelastico basato sulla teoria quasi-statica che considera la tridimensionalità del flusso e i tre gradi di libertà della sezione. Il modello considera un cilindro con generica sezione trasversale tendendo conto di tutte le derivate dei coefficienti aerodinamici e della possibilità di non coincidenza tra centro di rigidità e centro di massa. Il modello è in grado di predire le instabilità di tipo *galloping* e divergenza e il minimo smorzamento e rigidità strutturale richiesti per impedirle. In aggiunta, il modello consente la simulazione della risposta a un flusso turbolento tridimensionale, considerando sia i contributi di eccitazione derivanti dalla turbolenza stessa che quelli auto-eccitati.

Infine, la stabilità aeroelastica di cavi ghiacciati è stata valutata utilizzando i modelli presenti in letteratura. Al fine di confrontare le ipotesi di fondo, i vari modelli sono stati classificati in un quadro generale che ne evidenzia un approccio comune basato sulla teoria quasi-statica. Il confronto tra le previsioni dei vari modelli non è volto a giudicare la qualità di ciascun approccio, ma a mettere in luce le differenze nei risultati che questi producono.

Contents

1	Introduction	1
1.1	Problem statement	1
1.2	State of the art	5
1.3	Methodology	10
1.4	Main results	13
1.5	Thesis outline	13
2	Aerodynamics of nominally circular cylinders	21
2.1	Introduction	22
2.1.1	Parameters describing irregularities and classification	24
2.2	Basic characteristics of the aerodynamics of circular cylinders	27
2.3	Surface irregularities	32
2.3.1	Uniform roughness	35
2.3.1.1	Textures	35
2.3.1.2	Mean and fluctuating pressures and forces	41
2.3.1.3	Parameterization for design	49
2.3.1.4	Simulation of high values of Re in wind tunnels using roughness	51
2.3.1.5	Computational results	56
2.3.2	Non uniform and localized roughness	58
2.3.2.1	Non uniform roughness	58
2.3.2.2	Localized roughness	63
2.3.3	Wet cylinders	71
2.3.3.1	Wind tunnel tests	72
2.3.3.2	Numerical simulations	79
2.4	Section irregularities	81
2.4.1	Ovalysed sections	82
2.4.1.1	Experimental results	83

2.4.1.2	Numerical simulations	87
2.4.2	Polygonal sections	88
2.4.3	Ice accreted sections	96
2.4.3.1	Ice accretion phenomenon	96
2.4.3.2	Aerodynamics of ice accreted cylinders	97
2.5	Spanwise irregularities	102
2.5.1	End effects	102
2.5.2	Axis deviation	109
2.5.3	Variable diameter	113
2.5.3.1	Tapered cylinders	114
2.5.3.2	Discontinuous cylinders	116
2.5.3.3	Wavy cylinders	123
2.5.3.4	Hyperboloid cylinders	130
2.6	Aerodynamic devices	132
3	Atmospheric icing	153
3.1	Atmospheric environmental conditions	155
3.1.1	Cloud and fog characteristics	158
3.1.2	Precipitation characteristics	160
3.2	Ice accretion phenomenon	161
3.2.1	Hoar frost	165
3.2.2	In-cloud icing	165
3.2.3	Precipitation icing	168
3.2.4	Seawater spray icing	170
3.3	Effects of icing on structures	171
3.3.1	Ice shedding	172
4	Climatic wind tunnel testing	177
4.1	Icing simulation tools	177
4.1.1	Type of simulation	178
4.1.2	Climatic wind tunnels	179
4.1.3	CIRA – Icing Wind Tunnel	180
4.2	DTU/Force Technology Climatic Wind Tunnel	183
4.2.1	Temperature stability	184
4.3	Spray bar system	186
4.3.1	Preliminary design	186
4.3.2	Final design and construction	189
4.3.2.1	Spray nozzles	190
4.3.2.2	Aluminium bar	190
4.3.2.3	Aerodynamic devices	195
4.3.2.4	Tubing	196
4.3.2.5	Heating system	198
4.3.2.6	Monitoring system	200
4.3.2.7	Support system	200

4.3.2.8	Air and water suppliers	202
4.3.3	Droplet size control	202
4.3.4	LWC and cloud uniformity control	204
4.3.5	Turbulence	206
4.4	Section model, setup and instrumentation	208
4.4.1	Preliminary design	208
4.4.2	Temperature and hysteresis effects on force transducers	210
4.4.2.1	Hysteresis tests	212
4.4.2.2	Temperature dependency test	214
4.4.3	Bridge hanger model	220
4.4.4	Stay cable model	224
4.5	Test procedure and measurements	225
4.5.1	Preliminary checks	228
4.5.2	Ice accretion	229
4.5.2.1	Bridge hangers	230
4.5.2.2	Stay cables	230
4.5.3	Aerodynamic force measurement	231
4.5.4	Measurement of accreted sections	231
4.5.5	Test protocol	232
5	Characteristics of the ice accretion on bridge cables	235
5.1	Ice accretion on bridge cables	235
5.2	Bridge hangers	238
5.2.1	Final characteristics of the ice accretion	238
5.2.2	Time evolution of the ice accretion	241
5.3	Stay cables	244
5.3.1	Final characteristics of the ice accretion	244
5.3.2	Time evolution of the ice accretion	250
6	Aerodynamics of iced bridge cables	257
6.1	Bridge hangers	258
6.2	Stay cables	265
7	Quasi-steady model for self-excited and buffeting forces on cylinders	289
7.1	Basics of aeroelasticity	290
7.2	Derivation and linearization of the aeroelastic model	294
7.2.1	Flow around stationary inclined cylinders	294
7.2.2	Flow around moving inclined cylinders	296
7.2.3	Aerodynamic forces	300
7.2.3.1	General formulation for the derivation of the aerodynamic forces	302
7.2.4	Structural properties and equation of motion	304
7.3	State space representation	306

7.4	Eigenvalue problem and stability analysis	310
7.5	Three applications of the model	313
7.5.1	Ice accreted cable conductor in cross flow	314
7.5.1.1	Minimum damping	321
7.5.1.2	Galloping motion	322
7.5.2	Dry stay cable	326
7.5.2.1	Minimum damping	326
7.5.2.2	Galloping motion	327
7.5.3	Ice accreted stay cable	329
7.5.3.1	Minimum damping	329
7.5.3.2	Buffeting motion	330
8	Aerodynamic stability of ice accreted bridge cables	337
8.1	General framework for galloping stability models	338
8.2	Application of stability criteria to ice-accreted bridge cables . . .	342
8.2.1	Vertical bridge hangers	345
8.2.2	Stay cables	357
8.3	Case study	365
8.4	Some preliminary conclusions concerning the stability of ice-accreted bridge cables	368
9	Conclusions and perspectives	377
9.1	Conclusions	377
9.2	Future work	382
A	Derivatives of the aerodynamic coefficients	385
A.1	Ice accreted bridge hangers	385
A.2	Ice accreted stay cables	394
B	Fluctuating aerodynamic coefficients	425
B.1	Ice accreted bridge hangers	425
B.2	Ice accreted stay cables	430
C	Aerodynamic forces linearization	445
C.1	Linearization of the aerodynamic damping matrix	445
C.2	Linearization of the aerodynamic stiffness matrix	448
C.3	Linearization of the buffeting matrix	449
D	Terms of the characteristics polynomial	451

List of Figures

1.1	Scheme of a suspension bridge.	2
1.2	Scheme of a cable-stayed bridge.	2
1.3	Ice shedding on the Ravenel Bridge on 13 February 2014.	3
1.4	Damage on vehicle caused by falling ice on the Port Mann Bridge on December 19, 2012.	5
1.5	Atmospheric icing.	6
1.6	Ice formed on the cables of the Arthur Ravenel Bridge on 12 February 2014.	7
1.7	Sketch of the 1 DoF aerodynamic forces for a moving cylinder, after Den Hartog (1932).	9
1.8	Rendering of the Climatic Wind Tunnel.	11
1.9	Spray bar and cable section model during the accretion phase (a) and example of ice accreted on the cable model in the CWT (b).	12
2.1	Classification of irregularities.	23
2.2	Geometric definitions.	25
2.3	Flow definitions.	26
2.4	Region of disturbed flow.	31
2.5	Results from roughness measurements on regularly placed roughness elements. After (Schlichting, 1936).	34
2.6	Definition sketch of marine fouling, after Miller (1977).	36
2.7	Roughness pattern (a) and calibration of pyramidal roughness in terms of sand roughness (b). After Achenbach (1977).	37
2.8	Surface profiles and C_D in function of for different skewness number, after Fuss (2011).	41
2.9	$K_D = (1/2) C_D$ of a rough-surface cylinder for different roughness, after Fage & Warsap (1930).	42

2.10	Comparative measurements of drag and Strouhal number in terms of Re , after Achenbach & Heinecke (1981).	45
2.11	Definition of flow regimes in terms of the variation of the mean drag coefficient, after Basu (1985). The red lines represents the idealized concept of transitions and the black one the real C_D curve.	48
2.12	The drag C_D vs Re_K . (– Fage & Warsap (1930). Results obtained for roughened cylinders: \bigcirc , $K/D = 1.5 \times 10^{-4}$. \bullet , $K/D = 4 \times 10^{-4}$. \blacksquare , $K/D = 6.7 \times 10^{-4}$. \blacktriangle , $K/D = 1 \times 10^{-3}$. \diamond , $K/D = 8 \times 10^{-4}$. \triangle , $K/D = 8.4 \times 10^{-3}$. \square , $K/D = 1.7 \times 10^{-3}$. \diamond , $K/D = 2 \times 10^{-3}$. – \times –, smooth cylinder with Re_K calculated by assuming $K/D = 3.5 \times 10^{-5}$). After Szechenyi (1975).	52
2.13	Limits of flow regimes in a plane Re_K vs Re . \bullet sub critical to upper transition; +, upper transition to post critical; \bigcirc , smooth cylinder when assuming $K/D = 3.5 \times 10^{-5}$. After Szechenyi (1975).	53
2.14	Base pressure coefficient C_{pb} Vs. $(K/D)^m Re$. After Nakamura & Tomonari (1982).	55
2.15	Horizontal projection of the cable model radius, after Matteoni & Georgakis (2012b).	60
2.16	Effect on $K_D = (1/2) C_D$ of limited rough surface, after Fage & Warsap (1930).	61
2.17	Schematic diagram of V-groove circular cylinder, after Leung <i>et al.</i> (1992).	62
2.18	Effect on $K_D = (1/2) C_D$ of tripping wire at $\theta = \pm 65^\circ$, after Fage & Warsap (1930).	64
2.19	Schematic of the different flow regimes as a function of the perturbation angular position, after Nebres & Batill (1993).	65
2.20	Flow regimes as a function of angular position of the wire, after Ekmekci & Rockwell (2010).	66
2.21	Sketch of flow separation: (a) Regime A, (b) B, (c) C, (d) D, (e) E. After Alam <i>et al.</i> (2010).	68
2.22	Schematic of cross-section for various model for $d/D=0.09$, from Nigim & Batill (1997).	70
2.23	Rivulets definitions (a), variation of rivulets positions vs. wind speed for stationary cable (b). After Hikami & Shiraishi (1988).	72
2.24	Variation of rivulet position with wind speed and direction, after Bosdogianni & Olivari (1996).	73
2.25	Rivulets on the cylinder at a $U = 9\text{ m/s}$, and $Q = 8.0\text{ l/h}$: (a) Windward rivulet at $\theta \approx -160^\circ$; (b) leeward rivulet at $\theta \approx 30^\circ$, after Wang <i>et al.</i> (2005).	74
2.26	Comparison of aerodynamic coefficients of the cylinder with and without rivulet (a). Effect of rivulet size on aerodynamic coefficients (yaw angle equal to 35°) and shapes and dimensions in mm of artificial rivulet. After Xu <i>et al.</i> (2006).	76

2.27 Effect of running water rivulets (inclination equal to 55°) on C_D , C_D , C_L and St . ●, without water; ▲, with water. After Alam & Zhou (2007).	78
2.28 Mean and fluctuating wind force coefficients on the cylinder for different positions of an artificial rivulet, for $Re = 1.17 \times 10^5$. For a yaw angle of: (a) 25° ; (b) 35° ; (c) 45° . After Du <i>et al.</i> (2013).	80
2.29 Comparison of present numerical results with result of Lemaitre <i>et al.</i> (2007) for variation of film height where the incident wind acts from the left and Numerical prediction of temporal evolution in real time of film height under full loading conditions. After Robertson <i>et al.</i> (2010).	81
2.30 Ellipse and some of its mathematical properties.	82
2.31 Variation in C_D with Reynolds number for the elliptical cylinders, after Lindsey (1938)	84
2.32 Variation of total drag coefficient with axis ratio. After Khan <i>et al.</i> (2005).	88
2.33 Regular polygon and definition of corner radius r	89
2.34 Aerodynamic coefficients for octagonal, dodecagonal and hex-decagonal cylinders, after ASCE-74 (1991).	91
2.35 Drag coefficient values for round and multisided shapes, after NCHRP-494 (2003).	92
2.36 C_D for the dodecagonal cylinder in flat and corner orientation (a) and C_L and its derivative respect to the angle of attack for the dodecagonal cylinder (b), after Phares <i>et al.</i> (2007).	93
2.37 Flow velocity vectors around polygons with edges facing inlet wind and vertexes facing inlet wind, after Tang <i>et al.</i> (2013).	94
2.38 Drag coefficients of polygons with wind into a vertex and wind into an edge, after Tang <i>et al.</i> (2013).	95
2.39 Variation of the lift force with respect of the angle of attack, for an ice accreted conductor. After Rawlins <i>et al.</i> (1979).	97
2.40 C_D , C_L and C_M versus angle of attack from wind tunnel measurements on replicas of this ice shape, after Tunstall (1989).	98
2.41 Ice shapes (a) and aerodynamic coefficients for the sample 2 (b), after Nigol & Buchan (1981).	99
2.42 Cross section of the iced conductor and mean aerodynamic coefficients. After Shimizu <i>et al.</i> (2004).	100
2.43 Finite aspect ratio cylinders.	103
2.44 Drag coefficient from different authors in terms of aspect ratio. After Zdravkovich <i>et al.</i> (1989).	105
2.45 Sketch of flow around free ends. After Zdravkovich <i>et al.</i> (1989).	105
2.46 Measured drag coefficient in terms of aspect ratio: □, early tests; ○, second tests; ●, repeated tests; ▽, 60 cm disc. After Zdravkovich <i>et al.</i> (1998).	106

2.47	Tentative sketch of flow topology: IS —, primary separation; 2S —, secondary separation; SI —, separation islet; RA ···, re-attachment; — — —, separation bubble; $\sim \cdot \sim$, stream-wise vortex filaments. After Zdravkovich <i>et al.</i> (1998).	107
2.48	Cross-sectional view of flow around the cylinder free end in the plane orthogonal to the flow and to the cylinder axis. (a) flat tip; (b) bevelled tip; (c) radiussed tip; and (d) hemispherical tip. After Park & Lee (2004).	108
2.49	Curved cylinders and definition of local radius of curvature and orientation.	109
2.50	Three views of the flow pattern around a curved cylinder bowed away from the wind (a) and bowed into the wind (b). After Surry (1965).	111
2.51	Cylinders with variable diameter disturbances.	113
2.52	Variation of shedding frequency with local Reynolds number. After Gaster (1969).	115
2.53	Flow visualization at $Re = 76/57$ (based on D_2 / based on D_1) for the $D_2/D_1 = 1.34$ direct mode (a) and at $Re = 99/57$ for the $D_2/D_1 = 1.76$ (based on D_2 / based on D_1) direct mode (b). After Lewis & Gharib (1992).	119
2.54	Sketch illustrating the spanwise and streamwise vortices shed from a stepped cylinder with $D_2/D_1 = 0.51$, flow coming from left to right. After Dunn & Tavoularis (2006).	121
2.55	Brancusi tower. After Wikimedia Commons.	124
2.56	A time sequences of LIF results on spanwise vortical structure of the wavy cylinder, $Re = 600$. After Lam <i>et al.</i> (2004b).	127
2.57	Geometries of the wavy test cylinders. After New <i>et al.</i> (2013).	128
2.58	Flow pattern regimes of wavy cylinders with different spanwise wavelengths λ_w/D_m and wave amplitudes a/D_m at $Re = 100$. The symbol \circ represents each wavy cylinder case in the present simulations. After Lam & Lin (2008).	129
2.59	Pressure coefficients at different heights along the circumference of the cooling tower. After Harnach & Niemann (1980).	131
2.60	Goals, techniques and flow changes in flow control in civil engineering.	133
3.1	Ice accretion phenomenon: cause, effects and governing variables.	154
3.2	The water cycle, after Wikimedia Commons.	156
3.3	Type of atmospheric precipitation.	158
3.4	Cloud and fog types.	159
3.5	The heat balance over an ice surface. After Mazin <i>et al.</i> (2001).	164
3.6	Rime ice (a) and glaze ice (b) accretion phenomenon.	165

3.7	Rime ice accretion in April 1961 took up to 22 kV power line to the radio and television transmitter Lønahorgi (1410 MSL). Photo: Olav Wist.	166
3.8	Different type of ice accretion on an airplane wing. After CIRA website (http://extice.cira.it).	167
3.9	Icicles on electrical conductor. Photo: Crystal Murray.	168
3.10	Type of accreted ice as a function of wind speed and air temperature, after ISO 12494 - Atmospheric icing of structures.	169
3.11	Wires sagging after an freezing rain storm, Missouri 1949. After Wikimedia Commons.	169
3.12	Mist from the frosty waters of the north Atlantic engulfs a ship in a beautiful ice sculpture. Photo: Library and Archives Canada.	171
4.1	The visit in the CIRA – Icing Wind Tunnel. From left to right: Cristoforo Demartino, prof. Francesco Ricciardelli and prof. Francesco Marulo.	181
4.2	CIRA – Icing Wind Tunnel, Capua, Italy.	182
4.3	DTU/Force Technology Climatic Wind Tunnel.	184
4.4	Sketch of the experimental setup (bridge hanger simulation) including the spray bar.	185
4.5	Preliminary design sketch of the spray system.	188
4.6	Preliminary design sketch of the spray bar support system.	188
4.7	Different parts of spray nozzle.	191
4.8	Spray system of “Spraying Systems Co.”.	192
4.9	D_{30} as function of air pressure and liquid pressure. After technical specifications furnished by “Spraying Systems Co.”.	193
4.10	Spray bar during the assembly (a) and plexiglass cover installed (b).	194
4.11	Spray nozzle pieces for tight and straight fastening (a) and tight and straight orientation of spray nozzles (b).	195
4.12	Plexiglas half-circle nose(a) and wooden tail with a NACA 4-digit series profile (b).	196
4.13	Spray nozzle cover: front (a) and lateral (b) view and mounted on the nozzle (c).	197
4.14	Spray nozzle cover and protection cover streamlining the flow over the screw holes.	197
4.15	Scheme of water and air circuits.	198
4.16	Water (a) and air (b) connectors inside spray bar. Red wires are heating wires.	199
4.17	Heating wire wind 5 times around the spray nozzle (b) and fastened by tape to keep position (b).	199
4.18	Pressure transducer: Festo model SPTW-P10R-G14-VD-M12.	200
4.19	Spray bar control system.	201

4.20	Details of the suspension system: Traveller in ceiling (a), traveller at floor (b) and type of traveller employed (c).	201
4.21	Spray bar suspension system: sketch (a) and photo (b).	203
4.22	Air and water suppliers: first (a) and second (b) air compressor and water pump and electro-deionisation system (c).	204
4.23	Water-sensitive paper with impinged droplets (dark spots) (a). Example of DSD from the analysis with ImageJ (b); the MVD of $30\text{ }\mu\text{m}$ is shown with a green line.	205
4.24	Setup for measurement of LWC: measuring phase (a) and cylinder with cotton (b).	206
4.25	Grid installed in the CWT (a) and ice accrete on the bars of the grid (b).	207
4.26	Uniformity of spray at 11 m/s . Thickness of ice accretion is in $[\text{mm}]$. The white dash-lined rectangle indicates the region were the model would have been installed.	207
4.27	Non-dimensional power spectral density at 11 m/s in the center of the test section for the vertical configuration of the spray bar.	208
4.28	Turbulence intensity [%] at 11 m/s with the spray bar in the vertical configuration. The white dash-lined rectangle indicates the region were the model would have been installed.	209
4.29	Preliminary design sketch of the bridge hanger model.	209
4.30	Force transducer: AMTI model MC3A-500.	211
4.31	Experimental setup: Vötsch cooling chamber and control system.	212
4.32	Detail of the load system loaded in X direction and detail of the iced water in the cup inside the cooling chamber.	213
4.33	Time dependency of F_y with a load of 5.38 kg in Y direction at a temperature of 20°C	214
4.34	Time dependency of F_x , F_z , M_x , M_y , M_z with a load of 5.38 kg in Y direction at a temperature of 20°C	215
4.35	Temperature dependency of F_x with a load of 5.38 kg in X direction.	216
4.36	Temperature dependency of F_y , M_x , M_y and M_z (a) and of F_z (b) with a load of 5.38 kg in X direction.	217
4.37	Temperature dependency of F_y with a load of 5.38 kg in Y direction.	218
4.38	Temperature dependency of F_y , M_x , M_y and M_z (a) and of F_z (b) with a load of 5.38 kg in Y direction. + indicates a the test performed decreasing the temperature and – indicates a the test made increasing the temperature.	219
4.39	Temperature dependency of F_y with a load of 15.37 kg in Y direction.	220

4.40	Temperature dependency of F_y , M_x , M_y , and M_z (a) and of F_z (b) with a load of 15.37 kg in Y direction. + indicates a the test performed decreasing the temperature and – indicates a the test made increasing the temperature.	221
4.41	Temperature dependency of F_z with a load of 1.73 kg in Z direction.	222
4.42	Temperature dependency of F_x , F_y , M_x , M_y , M_z with a load of 1.73 kg in Z direction.	222
4.43	Bridge hanger model setup: sketch (a) and photo (b).	223
4.44	Detail of the bottom (a) and top (b) cable connection without dummy pieces: plates, thrust ball bearings, cardan joints and force transducers.	224
4.45	Cable section model setup ($\beta = 90^\circ$): sketch (a) and photo (b).	226
4.46	Cable geometry and force signs in the wind tunnel (a) and example of orientation of the spray bar and of the cable during the accretion phase (b).	227
4.47	Cleaning of the spray bar system (a) and spray bar system correctly working (b).	228
4.48	Ice on the cable at the end of the ice accretion phase: bridge hanger (a) and cable stay (b) simulations.	229
4.49	Ice cutting (a) and drawing of the ice contour (b).	232
5.1	Description of the zones of accretion.	237
5.2	Front and lateral view and contour tracing of the cable after ice accretion for CC V1.	239
5.3	Front and lateral view and contour tracing of the cable after ice accretion for CC V2.	240
5.4	Front and lateral view and contour tracing of the cable after ice accretion for CC V3.	240
5.5	Front and lateral view and contour tracing of the cable after ice accretion for CC V4.	241
5.6	Development of ice accretion with time for CCs from V1 to V4.	243
5.7	Front and lateral view, and contour tracing of the cable after ice accretion for CC I2 (a) and CC I3 (b).	245
5.8	Front and lateral view, and contour tracing of the cable after ice accretion for CC I4 (a) and CC I5 (b).	246
5.9	Front and lateral view, and contour tracing of the cable after ice accretion for CC I6 (a) and CC I7 (b).	248
5.10	Front and lateral view, and contour tracing of the cable after ice accretion for CC I8 (a) and CC I9 (b).	249
5.11	Front and lateral view, and contour tracing of the cable after ice accretion for CC I10 (a), CC I11 (b) and CC I2 (c).	251
5.12	Development of ice accretion with time for CCs from I2 to I7.	254
5.13	Development of ice accretion with time for CCs from I8 to I12.	255

6.1	Drag, lift and moment coefficients for the cable with ice accreted in CC V1.	259
6.2	Drag, lift and moment coefficients for the cable with ice accreted in CC V2.	260
6.3	Drag, lift and moment coefficients for the cable with ice accreted in CC V3.	262
6.4	Drag, lift and moment coefficients for the cable with ice accreted in CC V4.	264
6.5	Variation with the yaw angle of the mean aerodynamic coefficients for different wind speeds, in CC I1.	267
6.6	Time history of C_x and C_y with increasing U from 0 to approximately 30 m/s (a) and decreasing U from 30 to approximately 0 m/s (b) at $\beta = 90^\circ$, in CC I1.	268
6.7	Variation with the yaw angle of the mean aerodynamic coefficients for different wind speeds, in CC I2.	269
6.8	Variation with the yaw angle of the mean aerodynamic coefficients for different wind speeds, in CC I3.	270
6.9	Variation with the yaw angle of the mean aerodynamic coefficients for different wind speeds, in CC I4.	272
6.10	Variation with the yaw angle of the mean aerodynamic coefficients for different wind speeds, in CC I5.	273
6.11	Variation with the yaw angle of the mean aerodynamic coefficients for different wind speeds, in CC I6.	274
6.12	Variation with the yaw angle of the mean aerodynamic coefficients for different wind speeds, in CC I7a.	275
6.13	Variation with the yaw angle of the mean aerodynamic coefficients for different wind speeds, in CC I7b.	277
6.14	Variation with the yaw angle of the mean aerodynamic coefficients for different wind speeds, in CC I7c.	278
6.15	Variation with the yaw angle of the mean aerodynamic coefficients for different wind speeds, in CC I8.	279
6.16	Variation with the yaw angle of the mean aerodynamic coefficients for different wind speeds, in CC I9.	280
6.17	Variation with the yaw angle of the mean aerodynamic coefficients for different wind speeds, in CC I10.	282
6.18	Time history of the drag and lift coefficients at 100° and 22 m/s , in CC I10.	283
6.19	Variation with the yaw angle of the mean aerodynamic coefficients for different wind speeds, in CC I11.	284
6.20	Variation with the yaw angle of the mean aerodynamic coefficients for different wind speeds, in CC I12.	285
7.1	Collar's aeroelastic triangle.	291

7.2	3D geometry of the cylinder and flow and force coefficients definitions.	295
7.3	Plane normal to the cylinders's axis.	297
7.4	Mechanical model.	304
7.5	Definition of the mass center coordinates.	305
7.6	System description pre (a) and after (b) linearization.	309
7.7	Cable conductor model and ice silicon shape, after Chabart & Lilien (1998).	314
7.8	Aerodynamic force coefficients for an ice accreted cable conductor in cross flow for different angle of attack, after (Chabart & Lilien, 1998).	315
7.9	Regions of predicted instability. The red regions represent instability.	317
7.10	Comparison of the regions of predicted galloping instability with different models: Den Hartog (1956) (blue), Macdonald & Larose (2008a) (green), torsional galloping (grey), current model (red).	318
7.11	Effect of ξ_x and ξ_y on the galloping stability.	318
7.12	Effect of ξ_θ on the galloping stability.	319
7.13	Effect of ω_θ on the galloping (a,b,c) and static divergence (d,e,f) stability.	320
7.14	Effect of ω_x on the galloping stability.	321
7.15	Minimum requirement for the structural damping ratios, $\xi = \xi_x = \xi_y$ [%]. ($\omega_x = 6.25 \text{ rad/s}$, $\omega_y = 5.43 \text{ rad/s}$, $\omega_\theta = 54.35 \text{ rad/s}$, $\xi_\theta = 0.9\%$).	322
7.16	Minimum requirement for the structural rotational damping ratio, ξ_θ [%]. ($\omega_x = 6.25 \text{ rad/s}$, $\omega_y = 5.43 \text{ rad/s}$, $\omega_\theta = 54.35 \text{ rad/s}$, $\xi_x = 0.08\%$, $\xi_y = 0.08\%$).	323
7.17	Motion of the cylinder to an initial condition of displacement, $\mathbf{x}(0) = [0 \ 1 \ 0 \ 0 \ 0 \ 0]^T$ in the place $x - y$ and in term of time histories of each DoFs, $\xi(t)$, $\eta(t)$ and $\theta(t)$. ($Re = 2.7 \times 10^4$, $\alpha = 90^\circ$, $\omega_x = 6.25 \text{ rad/s}$, $\omega_y = 6.25 \text{ rad/s}$, $\omega_\theta = 54.35 \text{ rad/s}$, $\xi_x = -0.6\%$, $\xi_y = -0.6\%$, $\xi_\theta = 0.9\%$).	323
7.18	Motion of the cylinder to an initial condition of displacement, $\mathbf{x}(0) = [0 \ 1 \ 0 \ 0 \ 0 \ 0]^T$ in the place $x - y$ and in term of time histories of each DoFs, $\xi(t)$, $\eta(t)$ and $\theta(t)$. ($Re = 4.3 \times 10^4$, $\alpha = 30^\circ$, $\omega_x = 6.25 \text{ rad/s}$, $\omega_y = 6.25 \text{ rad/s}$, $\omega_\theta = 54.35 \text{ rad/s}$, $\xi_x = 2.42\%$, $\xi_y = 2.42\%$, $\xi_\theta = 0.9\%$).	325
7.19	Motion of the cylinder to an initial condition of displacement, $\mathbf{x}(0) = [0 \ 1 \ 0 \ 0 \ 0 \ 0]^T$ in the place $x - y$ and in term of time histories of each DoFs, $\xi(t)$, $\eta(t)$ and $\theta(t)$. ($Re = 4.3 \times 10^4$, $\alpha = 30^\circ$, $\omega_x = 6.25 \text{ rad/s}$, $\omega_y = 6.25 \text{ rad/s}$, $\omega_\theta = 54.35 \text{ rad/s}$, $\xi_x = 2.41\%$, $\xi_y = 2.42\%$, $\xi_\theta = 0.9\%$).	325

7.20	Galloping region instability type predicted regions. The red regions represent instability.	327
7.21	Minimum requirement for the structural damping ratios. ($\omega_x = 6.28 \text{ rad/s}$, $\omega_y = 6.28 \text{ rad/s}$, $\omega_\theta = 50.2 \text{ rad/s}$).	328
7.22	Motion of the cylinder to an initial condition of displacement, $\mathbf{x}(0) = [0 \ 1 \ 0 \ 0 \ 0]^T$ in the plane $x - y$ and in term of time histories of each DoFs, $\xi(t)$, $\eta(t)$ and $\theta(t)$. ($Re = 2.1 \times 10^5$, $\Phi = 150^\circ$, $\omega_x = 6.28 \text{ rad/s}$, $\omega_y = 6.28 \text{ rad/s}$, $\omega_\theta = 50.2 \text{ rad/s}$, $\xi_x = -0.07\%$, $\xi_y = -0.07\%$, $\xi_\theta = 0.02\%$).	329
7.23	Motion of the cylinder to an initial condition of displacement, $\mathbf{x}(0) = [0 \ 1 \ 0 \ 0 \ 0 \ 0]^T$ in the plane $x - y$ and in term of time histories of each DoFs, $\xi(t)$, $\eta(t)$ and $\theta(t)$. ($Re = 2.9 \times 10^5$, $\Phi = 107.2^\circ$, $\omega_x = 6.28 \text{ rad/s}$, $\omega_y = 6.28 \text{ rad/s}$, $\omega_\theta = 50.2 \text{ rad/s}$, $\xi_x = -0.06\%$, $\xi_y = -0.06\%$, $\xi_\theta = 0.02\%$).	330
7.24	Minimum requirement for the structural damping ratios $\xi = \xi_x = \xi_y$ [%]. ($\xi_\theta = 0.7\%$, $\omega_x = 6.28 \text{ rad/s}$, $\omega_y = 6.28 \text{ rad/s}$, $\omega_\theta = 50.2 \text{ rad/s}$).	331
7.25	Simulated wind time series of longitudinal turbulence component, $U'(t)/U$	331
7.26	Motion of the ice-accreted stay cable subject to turbulent flow, in the plane $x - y$ considering all the derivatives of the aerodynamic coefficients and neglecting those respect Φ , α , and Re , respectively. ($\Theta = 30^\circ$, $\beta = 140^\circ$, $f_x = 0.5 \text{ Hz}$, $f_y = 0.5 \text{ Hz}$, $\xi_x = \xi_x = 0.13$, $U = 28 \text{ m/s}$, $I_u = 13$).	333
7.27	Motion of the ice-accreted stay cable subject to turbulent flow, in the plane $x - y$ considering all the derivatives of the aerodynamic coefficients and neglecting those respect Φ , α , and Re , respectively. ($\Theta = 30^\circ$, $\beta = 130^\circ$, $f_x = 0.5 \text{ Hz}$, $f_y = 0.5 \text{ Hz}$, $\xi_x = \xi_x = 0.13$, $U = 28 \text{ m/s}$, $I_u = 13$).	334
7.28	Diagrams of the <i>RMS</i> of $\xi(t)$ (a) and $\eta(t)$ (b) [<i>m</i>] for different values of U and β	335
8.1	Schematic of the cylinder with flow direction and reference system definition.	339
8.2	DoFs and definition of R_δ and δ	340
8.3	Regions of potential instability for different values of α_s using the model of Macdonald & Larose (2006), considering (a) and neglecting (b) the dependency of the aerodynamic coefficients on Re . The contour lines are the instability thresholds. (CC: $U = 11 \text{ m/s}$, $T = -5^\circ\text{C}$).	347

8.4	Minimum non-dimensional structural damping Z_x needed to avoid instability for any α_s , using the model of Macdonald & Larose (2006) considering (a) and neglecting (b) the dependency of the aerodynamic coefficients on Re . The red contour lines are the instability thresholds. (CC: $U = 11\text{ m/s}$, $T = -5^\circ\text{C}$).	349
8.5	Comparison of the potential instability regions applying the 1-DoF and the tuned 2-DoF models (Den Hartog (1932), red; Martin <i>et al.</i> (1981), blue; Macdonald & Larose (2008a), green) (a). Minimum non-dimensional structural damping $Z_x = Z_y$ needed to avoid instability using the 2-DoF model of Macdonald & Larose (2008a) (b). (CC: $U = 11\text{ m/s}$, $T = -5^\circ\text{C}$).	350
8.6	Regions of potential instability for different values of $k_{y,x} = \omega_y/\omega_x$ using the 2-DoF model of Macdonald & Larose (2008a) (a). Minimum non-dimensional structural damping $Z_x = Z_y k_{y,x}$ needed to avoid instability using the 2-DoF model of Macdonald & Larose (2008a) for $k_{y,x} = 1.03$ (b). (CC: $U = 11\text{ m/s}$, $T = -5^\circ\text{C}$).	352
8.7	Regions of potential torsional instability, for different values of δ and for $R_\delta = 0.08\text{ m}$ using the model of Nigol & Buchan (1981b) (a), the contour lines are the instability thresholds. Minimum non-dimensional structural damping Z_θ needed to avoid torsional instability for $\delta = 90^\circ$ and for $R_\delta = 0.08\text{ m}$ (b), the red contour lines are the instability thresholds. (CC: $U = 11\text{ m/s}$, $T = -5^\circ\text{C}$).	354
8.8	Comparison of the potential instability regions among the 1-DoF and the 2-DoF tuned models (Den Hartog (1932), red; Nigol & Buchan (1981b), grey; Yu <i>et al.</i> (1992), green). (CC: $U = 11\text{ m/s}$, $T = -5^\circ\text{C}$).	355
8.9	Regions of potential instability for different values of $k_{y,\theta} = \omega_y/\omega_\theta$ using the 2-DoF model of Yu <i>et al.</i> (1992) (a). Comparison of the potential instability regions among the 1-DoF and the 3-DoF tuned models (b) (Den Hartog (1932), red; Martin <i>et al.</i> (1981), blue; Nigol & Buchan (1981b), grey; Gjelstrup & Georgakis (2011), green). (CC: $U = 11\text{ m/s}$, $T = -5^\circ\text{C}$).	356
8.10	Regions of potential instability for different values of $k_{\theta,x} = \omega_\theta/\omega_x = k_{\theta,y} = \omega_\theta/\omega_y$ (a) and of $k_{x,\theta} = \omega_x/\omega_\theta = k_{x,y} = \omega_x/\omega_y$ (b), using the 3-DoF model of Gjelstrup & Georgakis (2011). (CC: $U = 11\text{ m/s}$, $T = -5^\circ\text{C}$).	358
8.11	Regions of potential instability for different values of α_s using the model of Macdonald & Larose (2006), considering (a) and neglecting (b) the dependency of the aerodynamic coefficients on Re . The contour lines are the instability thresholds. (CC: $\beta = 90^\circ$, $U = 11\text{ m/s}$, $T = -5^\circ\text{C}$).	360

8.12	Minimum non-dimensional structural damping Z_x needed to avoid instability for any α_s , using the model of Macdonald & Larose (2006) considering (a) and neglecting the dependency of the aerodynamic coefficients on Re (b), on α (c) and on Φ (d). The red contour lines are the instability thresholds. (CC: $\beta = 90^\circ$, $U = 11 \text{ m/s}$, $T = -5^\circ\text{C}$).	362
8.13	Comparison of the potential instability regions applying the 1-DoF and the tuned 2-DoF models (Macdonald & Larose (2006) with $\alpha_s = 90^\circ$, red; Macdonald & Larose (2006) with $\alpha_s = 0^\circ$, blue; Macdonald & Larose (2008a), green) (a). Minimum non-dimensional structural damping $Z_x = Z_y$ needed to avoid instability using the 2-DoF model of Macdonald & Larose (2008a) (b). (CC: $\beta = 90^\circ$, $U = 11 \text{ m/s}$, $T = -5^\circ\text{C}$).	363
8.14	Regions of potential instability for different values of $k_{y,x} = \omega_y/\omega_x$ using the 2-DoF model of Macdonald & Larose (2008a) (a). Regions of potential torsional instability, for different values of δ and for $R_\delta = 0.08 \text{ m}$, using a 1-DoF torsional modified version of the model of Gjelstrup & Georgakis (2011) (b). The contour lines are the instability thresholds. (CC: $\beta = 90^\circ$, $U = 11 \text{ m/s}$, $T = -5^\circ\text{C}$).	364
8.15	Comparison of the potential instability regions between the 1-DoF and the 2-DoF tuned models (Macdonald & Larose (2006) with $\alpha_s = 90^\circ$, red; 1-DoF torsional modified version of the model of Gjelstrup & Georgakis (2011), grey; adapted 2-DoF model from the damping matrix derived by Gjelstrup & Georgakis (2011), green). (CC: $\beta = 90^\circ$, $U = 11 \text{ m/s}$, $T = -5^\circ\text{C}$).	366
8.16	Regions of potential instability for bridge hangers for CCs V1, V2, V3 and V4 evaluated using the 1-DoF model of Macdonald & Larose (2006) for any α_s (a) and using the 2-DoF model of Macdonald & Larose (2008a) for the tuned system (b). The contour lines are the instability thresholds.	371
8.17	Regions of potential instability for bridge hangers for CCs V1, V2, V3 and V4 evaluated using the 1-DoF models of Den Hartog (1932) (a) and of Martin <i>et al.</i> (1981) (b). The contour lines are the instability thresholds.	372
A.1	Variation with the angle of attack of the derivative of the mean aerodynamic coefficients with respect to α for different wind speeds, in CC V1.	386
A.2	Variation with the angle of attack of the derivative of the mean aerodynamic coefficients with respect to Re for different wind speeds, in CC V1.	387

A.3	Variation with the angle of attack of the derivative of the mean aerodynamic coefficients with respect to α for different wind speeds, in CC V2.	388
A.4	Variation with the angle of attack of the derivative of the mean aerodynamic coefficients with respect to Re for different wind speeds, in CC V2.	389
A.5	Variation with the angle of attack of the derivative of the mean aerodynamic coefficients with respect to α for different wind speeds, in CC V3.	390
A.6	Variation with the angle of attack of the derivative of the mean aerodynamic coefficients with respect to Re for different wind speeds, in CC V3.	391
A.7	Variation with the angle of attack of the derivative of the mean aerodynamic coefficients with respect to α for different wind speeds, in CC V4.	392
A.8	Variation with the angle of attack of the derivative of the mean aerodynamic coefficients with respect to Re for different wind speeds, in CC V4.	393
A.9	Variation with the yaw angle of the derivative of the mean aerodynamic coefficients with respect to Φ for different wind speeds, in CC I1.	395
A.10	Variation with the yaw angle of the derivative of the mean aerodynamic coefficients with respect to Re for different wind speeds, in CC I1. Plot scale is different from those of the other CCs. . .	396
A.11	Variation with the yaw angle of the derivative of the mean aerodynamic coefficients with respect to Φ for different wind speeds, in CC I2.	397
A.12	Variation with the yaw angle of the derivative of the mean aerodynamic coefficients with respect to Re for different wind speeds, in CC I2.	398
A.13	Variation with the yaw angle of the derivative of the mean aerodynamic coefficients with respect to Φ for different wind speeds, in CC I3.	399
A.14	Variation with the yaw angle of the derivative of the mean aerodynamic coefficients with respect to Re for different wind speeds, in CC I3.	400
A.15	Variation with the yaw angle of the derivative of the mean aerodynamic coefficients with respect to Φ for different wind speeds, in CC I4.	401
A.16	Variation with the yaw angle of the derivative of the mean aerodynamic coefficients with respect to Re for different wind speeds, in CC I4.	402

A.17 Variation with the yaw angle of the derivative of the mean aerodynamic coefficients with respect to Φ for different wind speeds, in CC I5.	403
A.18 Variation with the yaw angle of the derivative of the mean aerodynamic coefficients with respect to Re for different wind speeds, in CC I5.	404
A.19 Variation with the yaw angle of the derivative of the mean aerodynamic coefficients with respect to Φ for different wind speeds, in CC I6.	405
A.20 Variation with the yaw angle of the derivative of the mean aerodynamic coefficients with respect to Re for different wind speeds, in CC I6.	406
A.21 Variation with the yaw angle of the derivative of the mean aerodynamic coefficients with respect to Φ for different wind speeds, in CC I7a.	407
A.22 Variation with the yaw angle of the derivative of the mean aerodynamic coefficients with respect to Re for different wind speeds, in CC I7a.	408
A.23 Variation with the yaw angle of the derivative of the mean aerodynamic coefficients with respect to Φ for different wind speeds, in CC I7b.	409
A.24 Variation with the yaw angle of the derivative of the mean aerodynamic coefficients with respect to Re for different wind speeds, in CC I7b.	410
A.25 Variation with the yaw angle of the derivative of the mean aerodynamic coefficients with respect to Φ for different wind speeds, in CC I7c.	411
A.26 Variation with the yaw angle of the derivative of the mean aerodynamic coefficients with respect to Re for different wind speeds, in CC I7c.	412
A.27 Variation with the yaw angle of the derivative of the mean aerodynamic coefficients with respect to Φ for different wind speeds, in CC I8.	413
A.28 Variation with the yaw angle of the derivative of the mean aerodynamic coefficients with respect to Re for different wind speeds, in CC I8.	414
A.29 Variation with the yaw angle of the derivative of the mean aerodynamic coefficients with respect to Φ for different wind speeds, in CC I9.	415
A.30 Variation with the yaw angle of the derivative of the mean aerodynamic coefficients with respect to Re for different wind speeds, in CC I9.	416

A.31	Variation with the yaw angle of the derivative of the mean aerodynamic coefficients with respect to Φ for different wind speeds, in CC I10.	417
A.32	Variation with the yaw angle of the derivative of the mean aerodynamic coefficients with respect to Re for different wind speeds, in CC I10. Plot scale is different from those of the other CCs. . .	418
A.33	Variation with the yaw angle of the derivative of the mean aerodynamic coefficients with respect to Φ for different wind speeds, in CC I11.	419
A.34	Variation with the yaw angle of the derivative of the mean aerodynamic coefficients with respect to Re for different wind speeds, in CC I11.	420
A.35	Variation with the yaw angle of the derivative of the mean aerodynamic coefficients with respect to Φ for different wind speeds, in CC I12.	421
A.36	Variation with the yaw angle of the derivative of the mean aerodynamic coefficients with respect to Re for different wind speeds, in CC I12.	422
A.37	Variation with the yaw angle of the derivative of the mean aerodynamic coefficients with respect to α for different wind speeds, in CC I7.	423
B.1	Variation with the angle of attack of the fluctuating aerodynamic coefficients for different wind speeds, in CC V1.	426
B.2	Variation with the angle of attack of the fluctuating aerodynamic coefficients for different wind speeds, in CC V2.	427
B.3	Variation with the angle of attack of the fluctuating mean aerodynamic coefficients for different wind speeds, in CC V3.	428
B.4	Variation with the angle of attack of the fluctuating the mean aerodynamic coefficients for different wind speeds, in CC V4. . .	429
B.5	Variation with the yaw angle of the fluctuating aerodynamic coefficients for different wind speeds, in CC I1.	431
B.6	Variation with the yaw angle of the fluctuating aerodynamic coefficients for different wind speeds, in CC I2.	432
B.7	Variation with the yaw angle of the fluctuating aerodynamic coefficients for different wind speeds, in CC I3.	433
B.8	Variation with the yaw angle of the fluctuating aerodynamic coefficients for different wind speeds, in CC I4.	434
B.9	Variation with the yaw angle of the fluctuating aerodynamic coefficients for different wind speeds, in CC I5.	435
B.10	Variation with the yaw angle of the fluctuating aerodynamic coefficients for different wind speeds, in CC I6.	436
B.11	Variation with the yaw angle of the fluctuating aerodynamic coefficients for different wind speeds, in CC I7a.	437

B.12 Variation with the yaw angle of the fluctuating aerodynamic coefficients for different wind speeds, in CC I7b. 438

B.13 Variation with the yaw angle of the fluctuating aerodynamic coefficients for different wind speeds, in CC I7c. 439

B.14 Variation with the yaw angle of the fluctuating aerodynamic coefficients for different wind speeds, in CC I8. 440

B.15 Variation with the yaw angle of the fluctuating aerodynamic coefficients for different wind speeds, in CC I9. 441

B.16 Variation with the yaw angle of the fluctuating aerodynamic coefficients for different wind speeds, in CC I10. 442

B.17 Variation with the yaw angle of the fluctuating aerodynamic coefficients for different wind speeds, in CC I11. 443

B.18 Variation with the yaw angle of the fluctuating aerodynamic coefficients for different wind speeds, in CC I12. 444

List of Tables

2.1	Flow characteristics around a circular cylinder for regimes without interest for the civil engineering applications. Data from Wieselsberger (1922); Schewe (1983); Williamson (1989); Roshko (1961); Norberg (2003). U is expressed in m/s and the kinematic viscosity is the standard for the air at $20^{\circ}C$, $\nu = 1.50 \cdot 10^{-5} m^2/s$. The jagged line in the sketches denotes the flow in the turbulent state.	28
2.2	Flow characteristics around a circular cylinder for regimes of interest for the civil engineering applications. Data from Wieselsberger (1922); Schewe (1983); Williamson (1989); Roshko (1961); Norberg (2003). U is expressed in m/s and the kinematic viscosity is the standard for the air at $20^{\circ}C$, $\nu = 1.50 \cdot 10^{-5} m^2/s$. The jagged line in the sketches denotes the flow in the turbulent state.	29
2.3	Cable models, after Miyata <i>et al.</i> (1994).	38
2.4	Results of analysis of surface patterns, after Miyata <i>et al.</i> (1994).	38
2.5	Relative surface roughness of cylinders (tangential roughness K_{st} , axial roughness K_{sa}), after Adachi (1997).	40
2.6	Screen dimensions, after Shih <i>et al.</i> (1993).	48
2.7	Distribution of the sign of the lift C_L , when the critical regime is passed 28 times, after Schewe (1986).	59
2.8	Drag coefficients C_D for elliptic cylinders, after British Standard Institution (1972).	85
3.1	Water transformations and the latent heats. Positive values of the latent heat indicate release of energy, while negative values absorption.	157
3.2	LWC and mean droplet size for different types of low altitude clouds. After Mason (1957).	160

3.3	Meteorological parameters controlling atmospheric ice accretion, after ISO 12494 - Atmospheric icing of structures.	168
3.4	Meteorological parameters controlling precipitation ice accretion, after ISO 12494 - Atmospheric icing of structures.	170
4.1	Temperature stability tests.	185
4.2	Capacity of force transducers.	211
4.3	Technical specifications of AMTI MC3A force transducers.	211
4.4	Climatic conditions during ice accretion simulations of bridge hangers.	230
4.5	Climatic conditions during ice accretion simulations of stay cables.	231
5.1	Description of the ice accretion in the windward and lateral regions, mass accreted and maximum thickness of the accretion.	238
5.2	Description of the ice accretion in the frontal and lateral regions, mass accreted and maximum thickness of the accretion (I = Icicles, LS = Lower Side, BS = Both Sides).	244
6.1	Maximum and minimum values of the mean drag, lift and moment coefficients.	258
6.2	Maximum and minimum values of C_x , C_y and C_M	265
7.1	Structural and aerodynamic parameters of the ice accreted cable conductor tested by Chabart & Lilien (1998).	315
7.2	Comparison of the regions of predicted galloping instability, according to analytical models and dynamic wind tunnel tests.	316
7.3	Structural and aerodynamic parameters chosen to investigate the stability.	326
8.1	Galloping instability models and their characteristics. (C.F.= Cross Flow, I.F.=Inclined Flow, I.C. Inertial Coupling, D.D.=Detuned DoFs; for the DoFs refer to Figure 8.2)	343
8.2	Minimum required structural damping ratio [%] found for the ice-accreted bridge hanger with $m = 100$ kg/m and $\omega_x = 2\pi$, using different stability models.	368
8.3	Minimum required structural damping ratio [%] found for the ice-accreted stay cable with $m = 100$ kg/m and $\omega_x = 2\pi$, using different stability models *Adapted torsional model from the damping matrix derived by Gjelstrup & Georgakis (2011).	369

8.4 Minimum required non-dimensional structural damping predicted using the model of Macdonald & Larose (2006) for any α_s , the model of Den Hartog (1932), the model of Martin *et al.* (1981) and the model of Macdonald & Larose (2008a) with tuned frequency for different CCs. 373

CHAPTER 1

Introduction

Life is only a flicker of melted ice.

DEJAN STOJANOVIC, THE SUN WATCHES THE SUN

1.1 Problem statement

Climate change is a significant and lasting change in the statistical distribution of weather patterns over periods ranging from decades to millions of years. It may be a change in average weather conditions, or in the distribution of weather around the average conditions (i.e., more or fewer extreme weather events). Extreme weather events are becoming more frequent, with both peaks of heat and drought, and with peaks of cold and rain or snow.

At the same time, civil structures are becoming larger and lighter. Developments comprising this type of structures have been rapidly increasing in number worldwide in the last 40 years, requiring extensive expertise in occupancy comfort, wind engineering, and vibration performance to avoid the unnecessary use of dampers, material performance, and lastly but not least, over consumption of materials. In particular, bridge's span is increasing in the last 50 years.

The technology adopted for the bridges of medium to long size is the cable support system. Two type of bridge using structural cables are:

- Suspension bridges;
- Cable-stayed bridges.

A suspension bridge is a type of bridge in which the deck is hung below suspension cables on vertical suspenders (Figure 1.1). This type of bridge has cables suspended between towers, plus vertical suspender cables that carry the weight of the deck below, upon which traffic crosses. The longest suspension bridge in the world is the Akashi Kaikyō Bridge in Japan with a central span of 1.991 m . The longest designed suspension bridge is the Strait of Messina Bridge with a central span of 3.300 m .

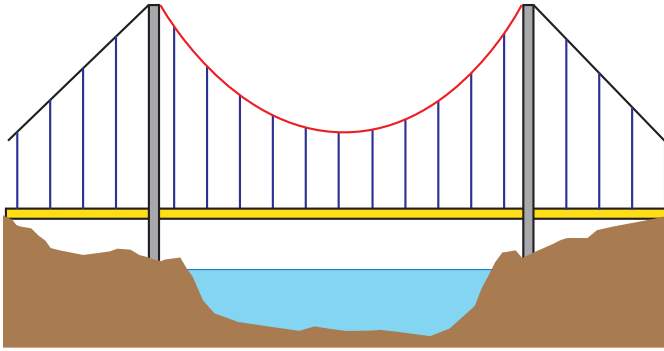


Figure 1.1: Scheme of a suspension bridge.

A cable-stayed bridge has one or more towers, from which cables support the bridge deck (Figure 1.2). There are two major classes of cable-stayed bridges: harp and fan. In the harp or parallel design, the cables are nearly parallel so that the height of their attachment to the tower is proportional to the distance from the tower to their mounting on the deck. In the fan design, the cables all connect to or pass over the top of the towers. The Russky bridge is the world's longest cable-stayed bridge, with a 1.104 m long central span.

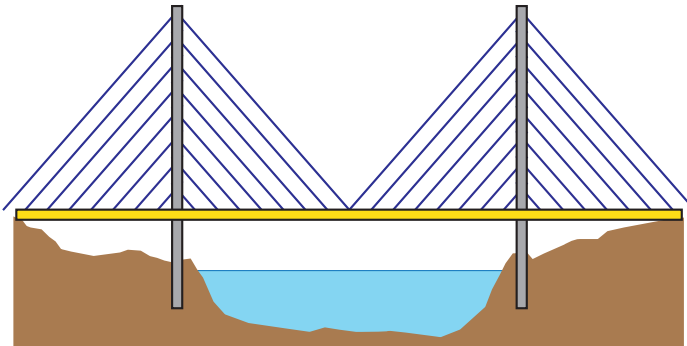


Figure 1.2: Scheme of a cable-stayed bridge.

Owing to the structural elegance and relative economy, more and more large-

span cable bridges have been built in recent years throughout the world. However, cables in bridges are prone to vibration induced by combination of wind and weather conditions due to their large flexibility, relatively small mass and low inherent damping.

There are a number of mechanisms that can potentially lead to vibrations of cables. Some of these types of excitation are more critical or probable than others, but all are listed here for completeness ([Kumarasena *et al.* , 2007](#)):

- CABLE-FLUID INTERACTION
 - Vortex excitation of an isolated cable or groups of cables
 - Rain/wind-induced vibrations of cables
 - Wake galloping of groups of cables
 - Galloping of single cables inclined to the wind
 - Galloping of cables with ice accumulations
 - Aerodynamic excitation of overall bridge modes of vibration involving cable motion
 - Motions caused by wind turbulence buffeting
- CABLE-SUPPORT INTERACTION
 - Motions caused by fluctuating cable tensions

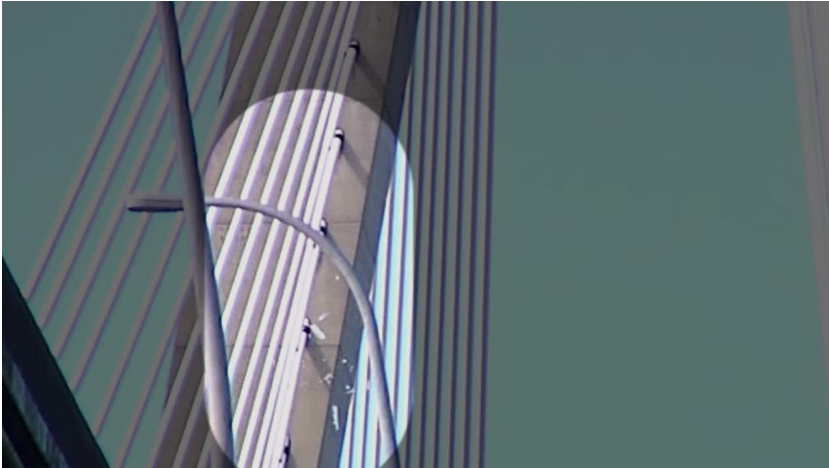


Figure 1.3: Ice shedding on the Ravenel Bridge on 13 February 2014.

Among this mechanism, galloping of cables with ice accumulations seems to be the least known. As a matter of fact, undesirable wind-induced vibrations

of bridge cables can occur when low-attitude atmospheric conditions are such to generate ice accretion. Large oscillations of long cables can cause premature fatigue failures at the anchor points. These oscillations can also trigger the phenomenon of ice shedding. Three types of cable ice shedding, or ice mass reduction, have been identified: ice melting, ice sublimation, and mechanical ice breaking (Druez *et al.*, 1995), the latter being influenced by the cable vibration. Falling ice becomes a safety issue for motorists and pedestrians crossing bridges, which need to be closed until the ice is gone. Gimsing & Georgakis (2011) report a series of closures occurred to bridges. For example, between 2004 and 2007, the Storebælt Bridge was closed an average of 14.3 hours a year, 12 of which were due to falling ice and snow. The Øresund Bridge had to be closed six times between 2000 and 2010 due to ice and snow. Many other bridges throughout the Northern Hemisphere have had similar closures, including the Uddevalla Bridge in Sweden, the Severn Bridge in the UK, the Zakim Bunker Hill Bridge in the USA and the Hukacho Bridge in Japan. On the 19th of December 2012 the Port Mann Bridge in Canada was closed between 1:30 pm and 6 pm. Before the closure, the vehicle insurance entity in British Columbia reported 60 separate claims of ice-damage. The claims were settled for about 400,000\$, according to Adam Grossman of ICBC. In January 2014, the Maine Department of Transportation closed the Penobscot Narrows Bridge due to large chunks of ice falling from the support cable onto the bridge deck for 24 hours. In February 2014, the Ravenel Bridge was closed for 43 hours because the risk of “ice bombs”. In addition, it must be considered that the closure of a bridge on a major route can produce severe consequences on industry, commerce and society as a whole.

Methods for accretion removal or prevention are available for use on bridges. Kleissl & Georgakis (2010) classified these methods in three categories: mechanical, based on the breaking of the ice; thermal, based on the melting of the ice and passive, based on natural forces. The majority of these methods derive from applications in the field of electrical distribution (Farzaneh *et al.*, 2008). A new solution is currently being installed on the Port Mann Bridge; a series of collars having sweepers are fastened around the cables and stored at the top of the bridge towers on remotely operated hangers. As required, the collars will be dropped down the cables one at a time to dislodge any accumulated snow or ice in their path. The collars are currently being reinstalled on 152 of the 288 bridge cables that cross the roadway.

Although, there have been reports of ice- and/or sleet-induced vibrations of bridge cables, little research has been undertaken to fully understand the causes of these or to find means for mitigating them. For cold climate regions, the effects of icing should be considered during the design process, including safety assessments and economical evaluations. The importance of understanding the phenomena that govern the ice accretion on bridge cables and the possible vibrations that may arise in iced configuration is crucial, given the significant number of closures of cable-stayed bridges occurred in recent years due to ice. Current



Figure 1.4: Damage on vehicle caused by falling ice on the Port Mann Bridge on December 19, 2012.

solutions used to solve the problems caused by ice accretion on stay cables are not sufficient to provide complete protection for motorists and pedestrians in all weather conditions. The general increase in the number and size of cable bridges around the world, especially in cold climate regions, makes the problem even more evident.

1.2 State of the art

Atmospheric icing is a general term for a number of processes where water either freezes in the atmosphere and sticks to objects exposed to the air, or freezes after getting in contact with cold surfaces. Ice accretion is a time-dependent modification of the shape of an object, occurring on a longer time scale compared with those of any possible structural dynamic behavior. Atmospheric icing occurs in different forms ([Farzaneh, 2008](#)):

- *Hoar frost*, which is caused by condensation of vapour;
- *In-cloud icing*, involving the freezing of supercooled water droplets in cloud or fog;
- *Precipitation icing*, resulting from freezing rain, drizzle, wet snow or dry snow.

The study of ice and wet-snow accretion on structures exposed to the atmosphere is of interest to engineers and scientists since ice/snow loads, in some cases combined with wind actions, can induce structural failures ([Poots, 1996](#)).

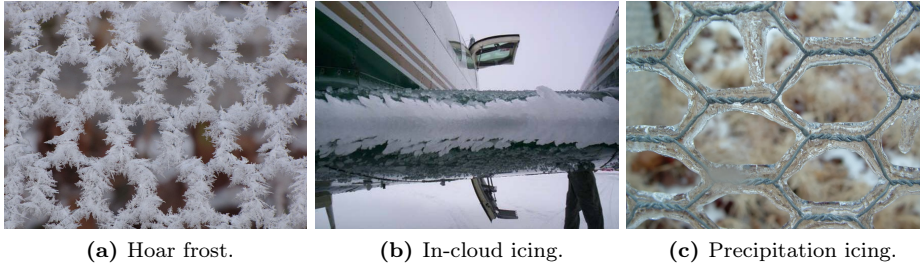


Figure 1.5: Atmospheric icing.

The influence of ice on aerodynamics has been studied mainly in the fields of electrical distribution ([Farzaneh, 2008](#)), of aviation ([Lynch & Khodadoust, 2001](#)) and of wind power ([Makkonen *et al.*, 2001](#)); less work is available in the area of bridge engineering. In many cases, however, bridge cables have experienced problems connected to the ice formation. There are many possible types of wind-induced vibrations of cables, among which [Kumarasena *et al.* \(2007\)](#) indicate the galloping of cables with ice accumulations. The accumulation of ice on a cable in an ice or freezing rain storm can lead to change in shape of the cable, making it aerodynamically unstable. This has caused large amplitude oscillations of long power conductor cables. On the other hand, [Kumarasena *et al.* \(2007\)](#) state that they are not aware of this being a common problem on bridges. [Tabatabai \(2005\)](#), citing [Zoli & McCabe \(2004\)](#), reports of ice formations on a major suspension bridge being periodically removed as a safety precaution. They concluded that the effects of icing on galloping vibrations of stay cables need to be studied. [Fujino *et al.* \(2012\)](#), explaining the problem of galloping of ice accreted cable, underlined that the theoretical analysis required reliable aerodynamic data for a range of realistic natural ice shapes formed under various weather conditions of interest.

Literature and general knowledge on ice accretion is still limited in the pursuit of a better understanding of ice accretion on structures. More information is needed which is clearly stated in the introduction to the International Standard, ISO 12494: “As more information about the nature of atmospheric icing becomes available during the coming years, the need for updating this International Standard is expected to be more urgent than usual.”.

The methods used for the investigation of the physics of ice accretion on structures and of its implications on the aerodynamics are ([Poots, 1996](#)):

1. Continuous field measurements of ice load and wind-on-ice load;
2. Simulations using climatic wind tunnels;
3. Use of mathematical and computational icing models.

Full-scale monitoring campaigns indicated that ice accretion from light precipitation at moderate low temperatures (i.e. between 0° and -5°C) may lead to large amplitude vibrations of bridge cables under wind action.



Figure 1.6: Ice formed on the cables of the Arthur Ravenel Bridge on 12 February 2014.

Research has been carried out in recent years with the purpose of understanding the behavior of ice accreted cylinders in cross flow conditions, both in vertical and horizontal configurations. The former is the case of overhead power lines and the latter is the case of bridge hangers. The typical diameters of the cylinder in the two cases are different; in the case of overhead power lines these are generally smaller than in the case of bridge hangers. The two conditions are not directly comparable, due to the different characteristics of the ice accretion. Vertical bridge hangers were studied by [Koss *et al.* \(2012\)](#). They investigated experimentally the shape of the ice accretion on circular cables with diameters of 0.0381 m and 0.089 m in vertical and horizontal configuration; the climatic conditions tested were among those in which large amplitude vibration of ice accreted bridge cables had been observed. [Gjelstrup *et al.* \(2012\)](#) performed static and dynamic wind tunnel tests on vertical cables, using simulated ice accretion reproduced using a rapid prototyping technique.

Inclined stay cables of cable-stayed bridges are prone to wind-induced oscillations due to their low structural damping, and research has been carried out with the purpose of understanding their aerodynamic behavior ([Matsumoto *et al.*, 1990](#)). The complicated inclined cable aerodynamics has been clarified

through wind tunnel tests and researches revealing the *dry inclined cable galloping* (Cheng *et al.* , 2008a,b; Matsumoto *et al.* , 2010). The existence of an axial flow and critical Reynolds number effects play a role in exciting vibrations. Less researchers have addressed the problem of ice accreted cylinders in inclined flow. Kollár & Farzaneh (2010) performed experiments on an inclined cylinder having a diameter of 0.038 m and a length of 0.92 m , in an icing wind tunnel. The diameter chosen is typical of overhead power lines. Kollár & Farzaneh (2010) varied the angle of the cylinder with respect to the oncoming flow and considered the two meteorological conditions of in-cloud icing and freezing rain icing. They concluded that the ice mass accreted on a unit length depends on the inclination of the flow with respect to the cylinder. They measured the mass, the shape and the profile of the ice accretion, but no aerodynamic force measurements were taken.

Some authors have tried to investigate numerically the problem of ice accretion (Poots, 1996; Launiainen, 1986; Lozowski *et al.* , 1983; Makkonen, 1984, 2000). Fu *et al.* (2006) developed a two-dimensional model of prediction the ice accretion process on a stationary transmission line. The shapes calculated under dry and wet icing conditions well compared with those obtained in experimental tests, but the surface roughness was not well predicted.

Several models have been developed with the aim of predicting cable aerodynamic instabilities, each of which considering different aspects of the dynamic behavior. In the 1930s, galloping of iced conductors has been a design and operating problem. Davison (1930) attributed the occurrence of galloping during freezing rain storms to the change in the aerodynamic lift when the wind blows across an iced conductor. Two years later, Den Hartog (1932) presented the mathematical description of the galloping mechanism. The model provides the critical condition, in terms of aerodynamic coefficients for the across-wind galloping of a cylinder placed in cross-flow, and accounts only for the dependence of the aerodynamic coefficients on the angle of attack. In the 1960s, Davenport (1962) proposed an expression for the aerodynamic damping in both across- and along-wind directions, of a cylinder in cross flow. Two decades later, the instability criterion, which today is widely referred to as drag crisis, was proposed by Martin *et al.* (1981). In the same year, Nigol & Buchan (1981b) investigated torsional galloping. They observed that when the center of mass does not coincide with the center of rotation (inertial coupling), as for eccentrically iced conductors, instability can occur, and they derived the critical condition. The inclined flow case was investigated by Macdonald & Larose (2006), who derived a general theoretical expression for the quasi-steady aerodynamic damping of a yawed and inclined cylinder, accounting for the dependence of the aerodynamic coefficients on the angle of attack, on the wind-cable angle and on the Reynolds number. The case of the cable at an angle with respect to the mean wind direction is of great practical importance, especially for stay-cables.

In the 1970s, the coupling between DoFs begun to be investigated. Until then galloping analyses have usually been based on the assumption that the

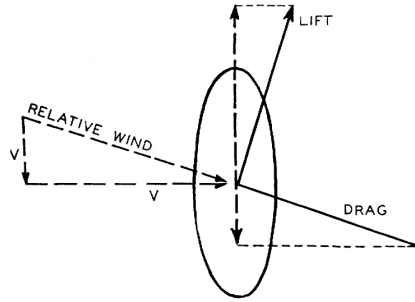


Figure 1.7: Sketch of the 1 DoF aerodynamic forces for a moving cylinder, after [Den Hartog \(1932\)](#).

structure vibrates in one DoF. For many structures, this is a restrictive assumption. [Blevins & Iwan \(1975\)](#) presented a model for the 2-DoFs galloping in the across-wind and torsional DoFs, of a cylinder in cross flow conditions; the model allows for different vibration frequencies in the two DoFs. In the 1990s, [Yu *et al.* \(1992\)](#) improved the model of [Blevins & Iwan \(1975\)](#), considering the inertial coupling and [Jones \(1992\)](#) derived a model for 2-DoFs galloping in the across and along wind directions. Both models are bound to cross flow conditions and to tuned systems (i.e. same frequency in all DoFs). [Luongo & Piccardo \(2005\)](#) improved the model of [Jones \(1992\)](#), considering the case of detuned systems. They used a perturbation approach to find an approximated analytical solution for the eigenvalue problem, which coincides with the exact solution for the tuned case, and which proves very accurate for the detuned case. The first 2-DoFs galloping criterion for cylinders in inclined flow is that of [Carassale *et al.* \(2004\)](#), who presented a model for the case of a detuned across- and along-wind vibration. In this model, the aerodynamic coefficients depend on the angle of attack and on the wind-cable angle. [Macdonald & Larose \(2008a,b\)](#) improved the model of [Carassale *et al.* \(2004\)](#) by including the dependence of the aerodynamic coefficients on the Reynolds number.

The first attempts to consider a 3-DoF behavior were made by [Yu *et al.* \(1993a,b\)](#). They developed a model to describe the galloping of a multi-span electrical transmission line, having an asymmetrical ice accretion. The model considers a cylinder in cross flow and accounts for inertial coupling and for the dependence of the aerodynamic coefficients on the angle of attack. [Wang & Lilien \(1998\)](#) improved the model by including the dependence of the aerodynamic coefficients on the Reynolds number. The case of an inclined flow was investigated by [Gjelstrup & Georgakis \(2011\)](#), who derived a quasi-steady 3-DoFs model for the evaluation of the aerodynamic stability. The model accounts for the dependence of the aerodynamic coefficients on the angle of attack, on the wind-cable angle and on the Reynolds number, and accounts for the inertial

coupling.

1.3 Methodology

In order to provide an exhaustive summary of current literature relevant to aerodynamics of nominally circular cylinders, a systematic and comprehensive review, correlation, and assessment of the state of art of research in the public domain, which address the aerodynamics of nominally circular cylinders to both theoretical and experimental research was produced. The review focuses on descriptions of the typical disturbance of the nominally circular cylinders that affects the aerodynamics. The disturbances are classified in cylinder and flow irregularities and the former are further subdivided into surface irregularities, section irregularities and spanwise irregularities. The review clearly demonstrates the importance of assess and estimate the effects of these disturbances on the aerodynamics of nominally circular cylinder in the entire design process. Furthermore, it was showed the lack of knowledge on the aerodynamic effects of ice accretion on bridge cables.

The necessity of a deeper understanding of the aerodynamics and aeroelastic behavior of ice accreted bridge cables, led in 2008 to the construction of a special Climatic Wind Tunnel (CWT) allowing tests simulating *low-altitude atmospheric icing* on full-scale section models under different climatic conditions (Georgakis *et al.* , 2009a). The Danish owners/operators Femern Bælt A/S, together with Storebælt A/S, were the lenders of this facility and of a large collaborative research project to examine the ways of reducing the risk of cable vibrations on a bridge solution connected to the newly proposed Femern fixed link between Denmark and Germany. During the last years, many efforts have been devoted to the development of the system for the simulation of the climatic condition of the in-cloud ice accretion on bridge cables. First results on ice accretion and static load coefficients using different preliminary version of the spray bar have been published in some MSc projects (Kordzadeh Kermani, 2012; Bajric & Holmen, 2011).

After the first attempts, an innovative spray bar creating the conditions for low-altitude atmospheric in-cloud icing of one-dimensional objects (i.e. bridge cables) has been constructed as a part of the author's project of research. First results on ice accretion and static load coefficients for an horizontal cable have been published by Koss & Lund (2013) in one MSc project in which the author of this thesis was involved. The set-up consists of a spray bar system and a cable section model placed in the CWT. The spray bar system was placed in the settling chamber downstream of the honeycomb grid, and the cable section model was placed in the center of the test section. The results from icing tests described in this thesis were obtained using this innovative spray bar, and are focused on the characterization of the in-cloud ice characteristics and aerodynamics of vertical bridge hangers and cable stays in different Climatic Conditions

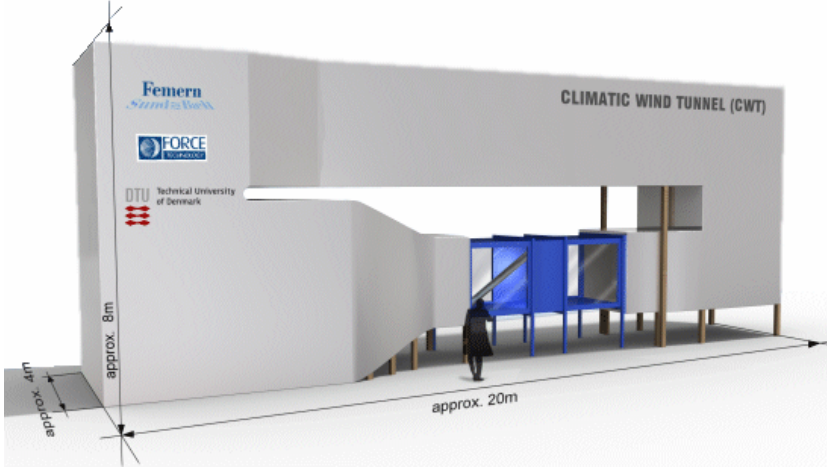


Figure 1.8: Rendering of the Climatic Wind Tunnel.

CCs. The plain cable adopted was made of High Density PolyEthylene (HDPE) with diameter of 160 mm like a typical configuration of bridge cable. Different climatic conditions are tested varying temperature, wind speed and cable orientation. In particular, experiments focused on the evaluation of the aerodynamic performances of the model in vertical configuration, simulating the behavior of bridge hangers, and in inclined configuration, simulating the behavior of cable stays.

The tests consisted of two phases: ice accretion and aerodynamic force measurement. During the ice accretion phase the pressure of air and water, the force transducers output, the temperature and the pitot tube were recorded. The characteristics of the ice accretion respect to the time were investigated using a time lapse technique in order to observe the effective evolution of the ice accretion. The final result of the accretion was recorded in plane perpendicular to the cable axis by cutting the ice section using a heated metal plate and drawing the ice contour on a cardboard. This was repeated for many sections to keep track also of the axial variability of the accretion. The cardboards were then scanned and digitized using a vector graphics editor.

Ice accretion can lead to instability phenomena. As the wind direction and the atmospheric conditions are variable in time, ice accretion can be generated in one particular condition whilst instability can occur in a different one; accordingly, in the measurement phase, the aerodynamic forces acting at different wind speeds and different angles of attack on the ice-accreted cable were measured. Aerodynamic forces were measured at both ends of the model using two 6-DOFs force transducers. For bridge hangers, force measurements were performed for angles of attack in the range of 0° to 180° at intervals of 10° and for wind speeds

in the range of 8 to 29 m/s , at intervals of approximately 2 m/s . For stay cables, force measurements were performed for the yaw angles in the range of 0° to 180° at intervals of 10° and for wind speeds equal to the bridge hanger case. For one specific accretion the aerodynamic coefficients were also characterized varying the angle of attack of $\pm 10^\circ$, i.e. rotating the cylinder around its axis.

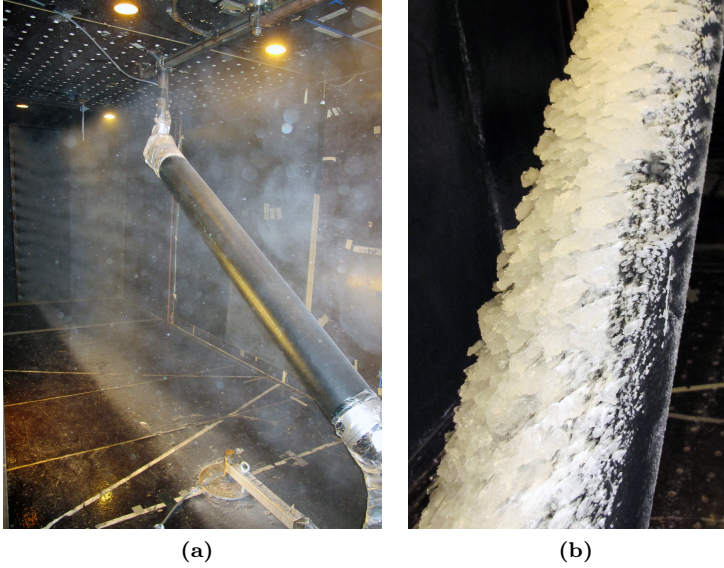


Figure 1.9: Spray bar and cable section model during the accretion phase (a) and example of ice accreted on the cable model in the CWT (b).

The instability of ice-accreted bridge cables was investigated by applying wind tunnel experimental data (i.e. drag, lift and moment coefficients) obtained during the tests in the CWT, to the quasi-steady sectional aerodynamic stability models available in literature. The aim of this comparison is to quantify the difference between the results obtained through the application of the different stability criteria in the case of ice-accreted bridge cables, and to investigate the limits of applicability of each of them. Not existing a benchmark, the comparison was not aimed at judging the quality of each approach, but rather at pointing out the differences they bring.

With the aim to overcome the previous limitations imposed by the models of instability used, a novel 3D/3DoFs quasi-steady aeroelastic model has been proposed. The model is able to predict the linear aerodynamic instability and the buffeting response of a cylinder with generic cross-section, immersed in a turbulent wind flow. 3D refers to the flow conditions and 3 DoFs refer to the two orthogonal displacements, perpendicular to the body's axis, plus the

rotation about the longitudinal body axis. The model incorporates the inertial coupling, i.e. the non-coincidence between the center of mass and the center of rotation between the degrees-of-freedom. It also accounts for variation of the force coefficients, i.e. drag, lift, and moment, with Reynolds number based on the flow velocity, with angle-of-attack, and cable-wind angle. Based on the analytical solution of the eigenvalue problem, by applying the Routh-Hurwitz criterion, an expression of the galloping- and static divergence-type instability condition is derived. A numerical solution of the minimum structural damping and structural stiffness required to prevent the same aerodynamic instabilities is given. The 3-D cross-sectional response to a turbulent flow is given considering both buffeting and self-excited contributions.

1.4 Main results

This study was not aimed at providing a definitive response to the problem of the ice-wind-bridge cables interaction, but rather at giving preliminary responses and triggering further research effort. The main findings are summarized below:

- Design and realization of an innovative spray system for the simulation of ice accretion on bridge hangers and cable stays;
- Characterization of the ice accretion characteristics in different climatic conditions for bridge hangers and cable stays;
- Aerodynamic characterization of ice accreted bridge hangers and stay cables in different climatic conditions for bridge hangers and cable stays;
- Comparison of the aerodynamic stability of ice accreted bridge cables predicted using different models available in literature;
- Definition of a novel 3D, 3DoFs quasi-steady aeroelastic;
- Prediction of the performances of the aerodynamic stability models.

1.5 Thesis outline

The present thesis is divided into 9 chapters. This introduction (Chapter 1) is followed by 8 chapters and 4 appendices.

- CHAPTER 2, [AERODYNAMICS OF NOMINALLY CIRCULAR CYLINDERS](#) gives a literature review on the aerodynamics of nominally circular cylinders. The review focuses on descriptions of the typical disturbance of the nominally circular cylinder that affects aerodynamics. The disturbances are classified in cylinder and flow irregularities and the former are further subdivided into surface irregularities, section irregularities and spanwise irregularities.

- CHAPTER 3, [ATMOSPHERIC ICING](#) describes the ice accretion phenomenon with particular focus on the ice accretion on civil engineering structures under conditions named as *low-altitude atmospheric icing*.
- CHAPTER 4, [CLIMATIC WIND TUNNEL TESTING](#) explains the design process and the characteristics of the testing facilities used in the tests. The tests performed in this study are all conducted in the CWT at FORCE Technology in Kgs. Lyngby, Denmark. A novel spray bar system was designed and realized specifically for these tests. Also a cable section model was designed and realized specifically for these tests. The spray bar system was realized in cooperation with the Master's project of Mia Lund (*Prediction and simulation of aerodynamic instability of iced bridge cable section*), in which the author of this dissertation was supervisor.
- CHAPTER 5, [CHARACTERISTICS OF THE ICE ACCRETION ON BRIDGE CABLES](#) reports the ice accretion process characteristics and final results. The description is given considering the strong relationship between the aerodynamic response and the ice accretion shape and uniformity.
- CHAPTER 6, [AERODYNAMICS OF ICED BRIDGE CABLES](#) shows results of static climatic wind tunnel tests undertaken in iced conditions. The mean drag, lift and moment coefficients are presented for different CC and varying the cable orientation and wind speed.
- CHAPTER 7, [QUASI-STEADY MODEL FOR SELF-EXCITED AND BUFFETING FORCES ON CYLINDERS](#) presents the sectional stiffness, damping and buffeting matrices derived taken into consideration the 3D flow condition and accounting for the dependence of the aerodynamic coefficients on the flow velocity, on the angle-of-attack, and on the cable-wind angle. The instability conditions for galloping and divergence are also derived. This part was developed together with Giulia Matteoni, Ph.D. candidate of the Department of Civil Engineering - Technical University of Denmark.
- CHAPTER 8, [AERODYNAMIC STABILITY OF ICE ACCRETED BRIDGE CABLES](#) gives a comparison among the galloping stability evaluation using the different existing models. Furthermore an application of the novel proposed model is given.
- CHAPTER 9, [CONCLUSIONS AND PERSPECTIVES](#) presents the overall conclusions of the dissertation as well as recommendations for future research.
- APPENDIX A, [DERIVATIVES OF THE AERODYNAMIC COEFFICIENTS](#) gives the derivatives of the aerodynamic coefficients of the bridge hangers and stay cables tests.
- APPENDIX B, [FLUCTUATING AERODYNAMIC COEFFICIENTS](#) gives the fluctuating aerodynamic coefficients of the bridge hangers and stay cables tests.

- APPENDIX C, [AERODYNAMIC FORCES LINEARIZATION](#) gives the expanded terms of the aerodynamic damping, stiffness and buffeting matrices presented in Chapter 7.
- APPENDIX D, [TERMS OF THE CHARACTERISTICS POLYNOMIAL](#) gives the expanded polynomial terms of the secular equation presented in Chapter 7.

References

- Bajric, A., & Holmen, C. 2011. *Simulation of Ice Accretion on Bridge Cable Section: An Experimental Study*. Master thesis - Technical University of Denmark.
- Blevins, R.D., & Iwan, W.D. 1975. The galloping response of a two-degree-of-freedom system. *Page 1975 of: American Society of Mechanical Engineers, Applied Mechanics Western Conference, University of Hawaii, Honolulu, Hawaii*.
- Carassale, L., Freda, A., & Piccardo, G. 2004. Quasi-static model for aerodynamic instability of yawed circular cylinder. *Pages 401–404 of: 5th International Colloquium Bluff Body Aerodynamics and Applications*.
- Cheng, S., Larose, G.L., Savage, M.G., Tanaka, H., & Irwin, P.A. 2008a. Experimental study on the wind-induced vibration of a dry inclined cable - Part I: Phenomena. *Journal of Wind Engineering and Industrial Aerodynamics*, **96**(12), 2231–2253.
- Cheng, S., Irwin, P.A., & Tanaka, H. 2008b. Experimental study on the wind-induced vibration of a dry inclined cable - Part II: Proposed mechanisms. *Journal of Wind Engineering and Industrial Aerodynamics*, **96**(12), 2254–2272.
- Davenport, A.G. 1962. Buffeting of a suspension bridge by storm winds. *ASCE Journal of Structural Division*, **88**(3), 233–268.
- Davison, A.E. 1930. Dancing conductors. *American Institute of Electrical Engineers, Transactions of the*, **49**(4), 1444–1449.
- Den Hartog, J.P. 1932. Transmission line vibration due to sleet. *Electrical Engineering*, **51**(6), 413–413.
- Druez, J., Louchez, S., & McComber, P. 1995. Ice shedding from cables. *Cold regions science and technology*, **23**(4), 377–388.
- Farzaneh, M. 2008. *Atmospheric icing of power networks*. Springer.
- Farzaneh, M., Volat, C., & Leblond, A. 2008. *Atmospheric icing of power networks*. Springer. Chap. Anti-icing and de-icing techniques for overhead lines.
- Fu, P., Farzaneh, M., & Bouchard, G. 2006. Two-dimensional modelling of the ice accretion process on transmission line wires and conductors. *Cold Regions Science and Technology*, **46**(2), 132–146.
- Fujino, Y., Kimura, K., & Tanaka, H. 2012. Wind Resistant Design Codes for Bridges in Japan. *In: Wind Resistant Design of Bridges in Japan*. Springer.

- Georgakis, C.T., Koss, H.H., & Ricciardelli, F. 2009a. Design specifications for a novel climatic wind tunnel for testing of structural cables. *In: 8th International Symposium on Cable Dynamics, Paris.*
- Gimsing, N.J., & Georgakis, C.T. 2011. *Cable supported bridges: concept and design.* Wiley.
- Gjelstrup, H., & Georgakis, C.T. 2011. A quasi-steady 3 degree-of-freedom model for the determination of the onset of bluff body galloping instability. *Journal of Fluids and Structures*, **27**(7), 1021–1034.
- Gjelstrup, H., Georgakis, C.T., & Larsen, C.T. 2012. An evaluation of iced bridge hanger vibrations through wind tunnel testing and quasi-steady theory. *Wind and Structures*, **15**(5), 385–407.
- Jones, K.F. 1992. Coupled vertical and horizontal galloping. *Journal of engineering mechanics*, **118**(1), 92–107.
- Kleissl, K., & Georgakis, C.T. 2010. Bridge ice accretion and de- and anti-icing systems: A review. *In: 7th International Cable Supported Bridge Owners Conference, Zhenjiang, China.*
- Kollár, L.E., & Farzaneh, M. 2010. Wind-tunnel investigation of icing of an inclined cylinder. *International Journal of Heat and Mass Transfer*, **53**(5), 849–861.
- Kordzadeh Kermani, A. 2012. *Development of Aerodynamic Loads on Bridge Cables under Icing.* Master thesis - Technical University of Denmark.
- Koss, H.H., & Lund, M.S.M. 2013. Experimental Investigation of Aerodynamic Instability of Iced Bridge Cable Sections. *In: 6th European and African Conference on Wind Engineering, Robinson College, Cambridge, UK.*
- Koss, H.H., Gjelstrup, H., & Georgakis, C.T. 2012. Experimental study of ice accretion on circular cylinders at moderate low temperatures. *Journal of Wind Engineering and Industrial Aerodynamics*, **104-106**, 540–546.
- Kumarasena, S., Jones, N.P., Irwin, P., & Taylor, P. 2007. *Wind-induced vibration of stay cables.* Tech. rept.
- Launiainen, J. 1986. Icing on a non-rotating cylinder under conditions of high liquid water content in the air: Form and size of ice deposits. *Journal of Glaciology*, **32**(110).
- Lozowski, E.P., Stallabrass, J.R., & Hearty, P.F. 1983. The Icing of an Unheated, Nonrotating Cylinder. Part I: A Simulation Model. *Journal of Applied Meteorology*, **22**, 2053–2062.

- Luongo, A., & Piccardo, G. 2005. Linear instability mechanisms for coupled translational galloping. *Journal of Sound and Vibration*, **288**, 1027–1047.
- Lynch, F.T., & Khodadoust, A. 2001. Effects of ice accretions on aircraft aerodynamics. *Progress in Aerospace Sciences*, **37**(8), 669–767.
- Macdonald, J.H.G., & Larose, G.L. 2006. A unified approach to aerodynamic damping and drag/lift instabilities, and its application to dry inclined cable galloping. *Journal of fluids and structures*, **22**(2), 229–252.
- Macdonald, J.H.G., & Larose, G.L. 2008a. Two-degree-of-freedom inclined cable gallopingpart 1: general formulation and solution for perfectly tuned system. *Journal of Wind Engineering and Industrial Aerodynamics*, **96**(3), 291–307.
- Macdonald, J.H.G., & Larose, G.L. 2008b. Two-degree-of-freedom inclined cable gallopingpart 2: analysis and prevention for arbitrary frequency ratio. *Journal of wind Engineering and industrial Aerodynamics*, **96**(3), 308–326.
- Makkonen, L. 1984. Modeling of ice accretion on wires. *Journal of Applied Meteorology*, **23**, 929–939.
- Makkonen, L. 2000. Models for the growth of rime, glaze, icicles and wet snow on structures. *Philosophical Transactions of the Royal Society of London. Series A: Mathematical, Physical and Engineering Sciences*, **358**(1776), 2913–2939.
- Makkonen, L., Laakso, T., Marjaniemi, M., & Finstad, K.J. 2001. Modelling and prevention of ice accretion on wind turbines. *Wind Engineering*, **25**(1), 3–21.
- Martin, W.W., Naudascher, E., & Currie, I.G. 1981. Streamwise oscillations of cylinders. *Journal of the Engineering Mechanics Division*, **107**(3), 589–607.
- Matsumoto, M., Shiraishi, N., Kitazawa, M., Knisely, C., Shirato, H., Kim, Y., & Tsujii, M. 1990. Aerodynamic behavior of inclined circular cylinders-cable aerodynamics. *Journal of Wind Engineering and Industrial Aerodynamics*, **33**(1), 63–72.
- Matsumoto, M., Yagi, T., Hatsuda, H., Shima, T., Tanaka, M., & Naito, H. 2010. Dry galloping characteristics and its mechanism of inclined/yawed cables. *Journal of Wind Engineering and Industrial Aerodynamics*, **98**(6), 317–327.
- Nigol, O., & Buchan, P.G. 1981b. Conductor galloping part II-Torsional mechanism. *Power Apparatus and Systems, IEEE Transactions on*, 708–720.
- Poots, G. 1996. *Ice and snow accretion on structures*. Vol. 338. Research Studies Press.

- Tabatabai, H. 2005. *Inspection and Maintenance of Bridge Stay Cable Systems: A Synthesis of Highway Practice*. Vol. 353. Transportation Research Board National Research.
- Wang, J., & Lilien, J.L. 1998. Overhead electrical transmission line galloping. A full multi-span 3-DOF model, some applications and design recommendations. *Power Delivery, IEEE Transactions on*, **13**(3), 909–916.
- Yu, P., Shah, A.H., & Popplewell, N. 1992. Inertially coupled galloping of iced conductors. *Journal of applied mechanics*, **59**, 140.
- Yu, P., Desai, Y.M., Shah, A.H., & Popplewell, N. 1993a. Three-degree-of-freedom model for galloping. Part I: Formulation. *Journal of Engineering Mechanics*, **119**(12), 2404–2425.
- Yu, P., Desai, Y.M., Popplewell, N., & Shah, A.H. 1993b. Three-degree-of-freedom model for galloping. Part II: Solutions. *Journal of engineering mechanics*, **119**(12), 2426–2448.
- Zoli, T., & McCabe, R. 2004. *Cable-Stayed Bridge Design*. Presented Presented at the High Performance Stay Cable Systems Seminar, sponsored by Freyssinet International Washington D.C.

CHAPTER 2

Aerodynamics of nominally circular cylinders

Bernard of Chartres used to say that we [the Moderns] are like dwarves perched on the shoulders of giants [the Ancients], and thus we are able to see more and farther than the latter. And this is not at all because of the acuteness of our sight or the stature of our body, but because we are carried aloft and elevated by the magnitude of the giants.

JOHN OF SALISBURY

Circular sections are widely used in the field of civil engineering due to their simplicity and structural and architectural value. On the other hand, when it comes to aero- or hydro-dynamics, simple geometry brings a complicated behavior, as the characteristics of the transition from laminar to turbulent flow depends strongly on the Reynolds number. Strong research efforts have been shifted towards the comprehension of the behavior of the aerodynamics of the perfect circular cylinders. Actually, the circular cylinders are not perfect in civil applications. In many cases, it was observed that the imperfection can affect the aerodynamics with important consequences. Due to this reasons, many researches performed experiments to understands how the aerodynamics of a nominally circular cylinder can change with respect to a perfect one. This chapter is a systematic correlation, and assessment of the state of art of research in the public domain which address the aerodynamics of nominally circular cylinders to both theoretical and experimental research. The review focuses

on descriptions of the typical disturbance of nominally circular cylinders that affects aerodynamics. The disturbances are classified in cylinder and flow irregularities and the former are further subdivided into surface irregularities, section irregularities and spanwise irregularities. The review clearly demonstrates the importance of assessing and estimating the effects of these disturbances in the entire design process.

2.1 Introduction

Because of their simple geometry, structural members with circular cross-section are widely used in many fields of Engineering; in particular, in Civil Engineering circular cross-sections are commonly used for chimneys, towers, bridge cables, bridge piers and towers, offshore piles, and so on. On the other hand, when it comes to aero- or hydrodynamics, simple geometry brings a complicated behavior, as the characteristics of the transition from laminar to turbulent flow depends strongly on the Reynolds number.

The diameter-based Reynolds number, Re , has been singled out as the governing parameter for the aerodynamics of perfect circular sections. In practical applications, Re ranges from less than one up to a hundred for tiny fibres in liquids up to hundreds of million for cooling towers and interplanetary rockets exposed to high cross wind. Indeed, for the unrealistic case of a perfectly smooth cylinders placed in a uniform cross flow, Re is the only parameter governing aerodynamics, and this is the case that may be defined as *perfect circular cylinder*. However, practical applications are more or less away from this theoretical situation and it can be defined *disturbance* any feature that causes deviation from it. This is case that may be defined as *nominally circular cylinder*.

With the aim of understanding the variability of the flow past circular cylinders, the conceptual division of parameters into *governing* and *influencing* is useful (Zdravkovich, 1997). In the case of nominally circular cylinders, all transition states can be defined by Re and by an appropriate set of influencing parameters which describe disturbances. When an influencing parameter exceeds a certain magnitude it can become the governing parameter in some transition states. However, when an influencing parameter becomes governing it cannot be precisely defined. Sarpkaya in a private communication (1983) to Zdravkovic pointed out that what may be an influencing parameter for a given set of governing parameters could be a governing parameter for another set of governing parameters. Detailed experimental data are required for a correct classification of these parameters.

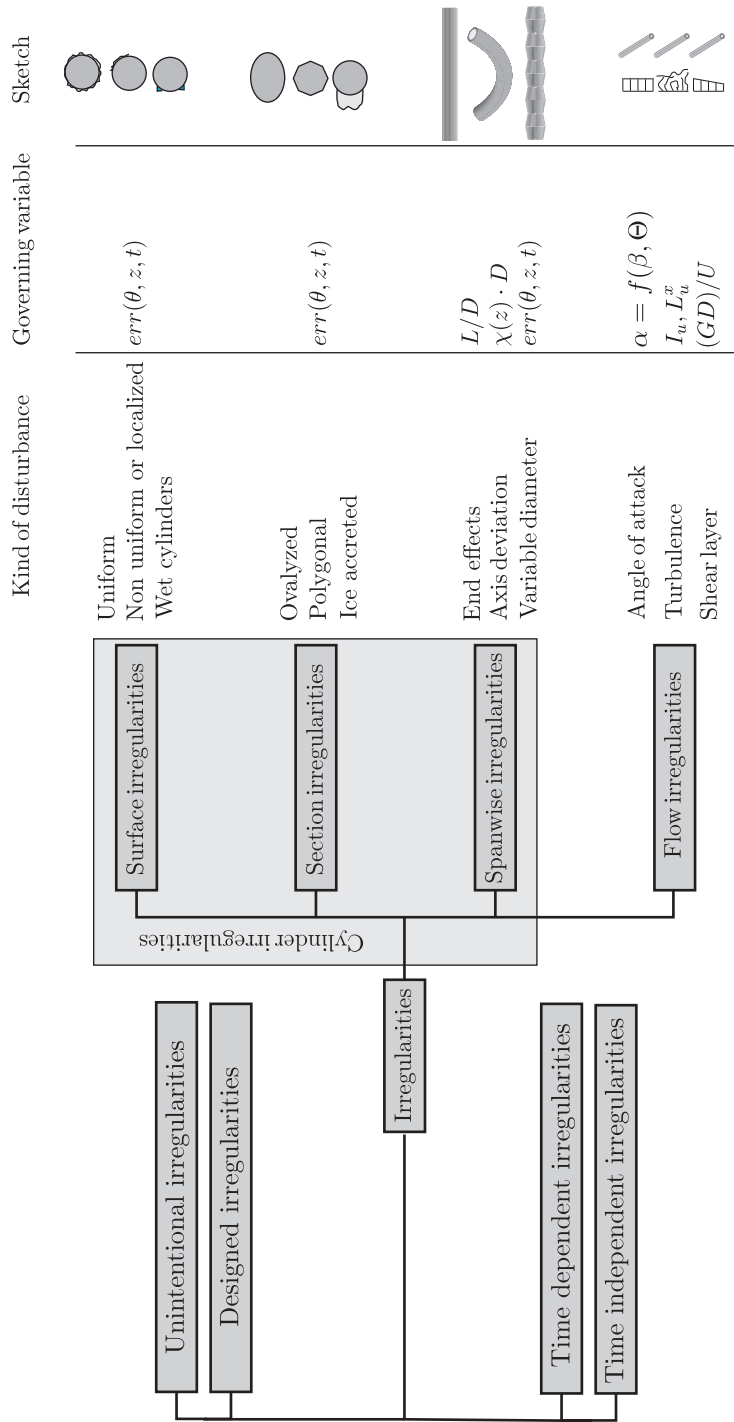


Figure 2.1: Classification of irregularities.

2.1.1 Parameters describing irregularities and classification

The effects brought by disturbances to the aerodynamics of circular cylinders are associated with the geometry of the *cylinder* or with the nature of the *flow*, and the former are further subdivided into *surface irregularities*, *section irregularities* and *spanwise irregularities* (Figure 2.1). The circular cylinder is always considered as stationary and accordingly no-aeroelastic effects are considered. Similarly, the presence of neighboring objects (i.e. aerodynamic interference) is not dealt with.

In the following, the term *cylinder* will be used to indicate an infinite-length, constant-section body with a straight axis, which is, therefore, completely defined by the cross sectional shape. The term *prism* will be used to indicate a finite-length, constant-section body with a straight axis which is, therefore, completely defined by the cross sectional shape and by the length. The term *elongated body* will be used to indicate any body in which one dimension is prevailing on the remaining two. The parameters defining the geometry and used to describe the cylinder disturbances are (Figure 2.2):

- *Axis length*, L ;
- *Local radius*, $R(\vartheta, z, t)$: the distance from the centre of the section, C , to a point on the body surface, which is a function of the angle θ in the body cross-section, of the position z along the cylinder axis and of time t ; the variability with time is meant to account for sectional shape variations associated with the presence of water rivulets or ice;
- *Curvature*, $\chi(z)$.

These parameters are expressed in a dimensionless form to make the comparison of data easier. As to the local radius, it is convenient to define a *surface primary form*, that for nominally circular cylinders is characterized by the nominal radius:

$$R = \frac{\int_0^L \int_0^{2\pi} R(\vartheta, z, t) d\vartheta dz}{2\pi L} \quad (2.1)$$

The dimensionless error between the local radius and the surface primary surface is:

$$err(\vartheta, z, t) = \frac{R(\vartheta, z, t) - R}{D} \quad (2.2)$$

where $D = 2R$ is the nominal diameter. If $err(\vartheta, z, t)$ is equal to 0 at each point, the cylinder is circular. The analysis of the function $err(\vartheta, z, t)$ can show

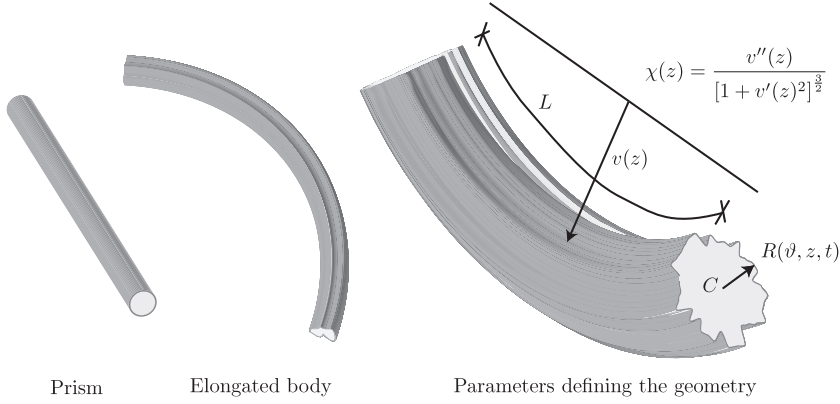


Figure 2.2: Geometric definitions.

irregularities of the surface and of the section, depending on dimension, as well as spanwise irregularities.

Surface irregularities comprise either uniform, non uniform or localized roughness, the presence of water films or rivulets (wet cylinders) and the presence of aerodynamic devices. Section irregularities comprise oval sections, polygonal section with a large number of faces and the presence of ice accretion. Spanwise irregularities comprise end effects in finite length bodies, axis deviation and variations in diameter. With the exceptions of end effects and axis deviations, all other cylinder irregularities can be analyzed using $err(\vartheta, z)$.

The end effect is related to the length of the prism, that is important to establish whether this effect is negligible or not. It can be taken into account through a non-dimensional slenderness parameter (aspect ratio):

$$\lambda = \frac{L}{D} \quad (2.3)$$

The axis deviation is related to the distance from the straight line joining the beginning and the end of prism and the axis, $v(z)$ (Figure 2.2). It can be expressed, in dimensionless differential form, as the curvature multiplied by the diameter:

$$\chi(z)D = \frac{v''(z)}{[1 + v'(z)^2]^{\frac{3}{2}}} D \quad (2.4)$$

where $v''(z)$ and $v'(z)$ are the first and the second derivative of $v(z)$. There is not temporal dependence in $\chi(z)$ because aeroelastic effects are neglected.

The *disturbances associated with the flow* are mainly due to the inclination of the mean flow (or of the cylinder axis), to the presence of turbulence, and to the existence of a shear flow.

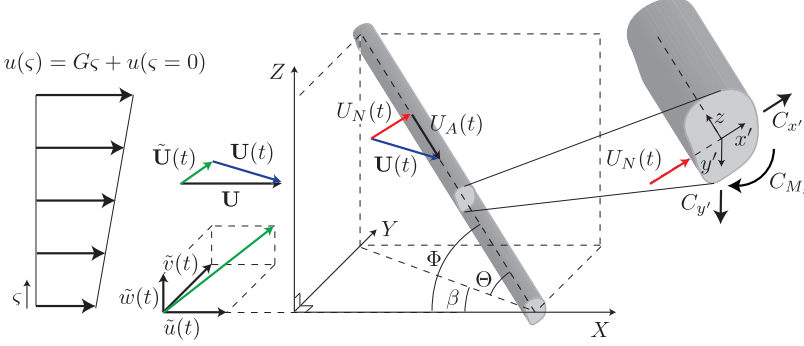


Figure 2.3: Flow definitions.

Inclination is quantified through the wind-axis angle of attack, Φ , i.e. the angle between the mean flow velocity and the cylinder axis (Figure 2.3). In the cross flow case, the angle of attack is equal to 90° . When gravity affects the behavior (e.g. in the case in which water rivulets form on the surface of the cylinder), two angles must be considered: the yaw angle, β , i.e. the angle between the projections of the mean flow velocity and the cylinder axis in the horizontal plane, and the inclination angle, Θ , i.e. the angle between the axis of the cylinder and the horizontal plane. The relationship between Φ , β and Θ is:

$$\Phi = \arccos(\cos \Theta \cos \beta) \quad (2.5)$$

In this case the flow can be decomposed into two components. The component of the wind velocity perpendicular to the cylinder axis, $U_N(t)$, and that parallel to it, named axial wind velocity, $U_A(t)$ (Figure 2.3).

Turbulence is quantified through its three intensities I_u , I_v , I_w , being the ratios of the root-mean-squares of the three velocity components $u(t)$, $v(t)$ and $w(t)$ to the mean value of velocity U (Figure 2.3), and through its nine integral length scales L_i^j , with $i = u, v, w$ being the turbulent component and $j = x, y, z$ being the direction of measurement of the scale.

Presence of a shear flow implies a variation of the flow velocity either in the direction of the cylinder axis, or across the cross section. The shear parameter is:

$$k = \frac{GD}{\bar{u}} \quad (2.6)$$

where G is the linear slope of variation of the wind velocity express as: $u(\zeta) = G\zeta + u(\zeta = 0)$, where ζ is the coordinate in the direction of the wind velocity variation (Figure 2.3). \bar{u} is the mean wind speed in the domain investigated. The effects of flow irregularities is not dealt with in this Chapter.

Irregularities can be further classified as either *designed irregularities* or *unintentional irregularities*. The former are made to improve some characteristics

(usually aerodynamics) of cylinders. The latter are the effect of manufacturing, and can be quantified but not modified nor eliminated. Designed irregularities are generated by the the installation of aerodynamic devices.

Finally, irregularities can be classified as *time dependent* or *time independent*. For time dependent irregularities, the time scale of the variation of the relevant parameter can be compared to the time scale(s) of the flow, thus giving rise to slowly varying irregularities (e.g. ice accretion or depositions phenomena) and rapidly varying irregularities (e.g wet cylinders).

2.2 Basic characteristics of the aerodynamics of circular cylinders

The flow around circular cylinders is characterized by the occurrence of transitions marked by abrupt changes in the flow and in the force parameters (Tables 2.1 and 2.2). The parameters usually adopted to describe the aerodynamics of a circular cylinders are local pressure, global forces and points of flow transition and separation.

Force parameters are expressed in terms of surface pressure, $p(\theta, z, t)$ and shear stress, $\tau_o(\theta, z, t)$. Friction is associated with the development of boundary layers, and it scales with Reynolds number. Surface pressure is expressed through pressure coefficients:

$$c_p(\theta, z, t) = \frac{p(\theta, z, t)}{\frac{1}{2}\rho U^2} \quad (2.7)$$

where ρ is the fluid density and U is the free stream velocity. Base pressure coefficient, c_{pb} , is defined as the average of the nearly constant pressure coefficients in the wake region; also of interest are the minimum pressure coefficient, c_{pm} , the location θ_m of the minimum pressure and the location of the beginning of the wake region, θ_w . The mean location of separation can be roughly expressed as a function of θ_w .

Integration of pressures around the circumference of the cylinder yields global forces per unit length. The along wind component of the mean resultant force per unit length due to pressure and friction are:

$$F_{p,x}(t) = \int_0^{2\pi} p(\theta, z, t) \cos(\theta) R d\theta \quad F_{\tau,x}(t) = \int_0^{2\pi} \tau_o(\theta, z, t) \sin(\theta) R d\theta \quad (2.8)$$

The total along-wind force per unit length, or *drag*, is the sum of these two forces:

$$F_D(t) = F_{p,x}(t) + F_{\tau,x}(t) \quad (2.9)$$

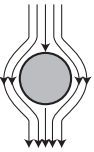



REGIME	NO SEPARATION	PAIR OF STATIONARY VORTEX	LAMINAR VORTEX SHEDDING	TURBULENT VORTEX SHEDDING
Re Range	$0 < Re < 5$	$5 < Re < 40$	$40 < Re < 200$	$200 < Re < 300$
$D = 10^{-1} \text{ m}$	$0 < U < 7.5 \cdot 10^{-4}$	$7.5 \cdot 10^{-4} < U < 6 \cdot 10^{-3}$	$6 \cdot 10^{-3} < U < 3 \cdot 10^{-2}$	$3 \cdot 10^{-2} < U < 4.5 \cdot 10^{-2}$
$D = 10^0 \text{ m}$	$0 < U < 7.5 \cdot 10^{-5}$	$7.5 \cdot 10^{-5} < U < 6 \cdot 10^{-4}$	$6 \cdot 10^{-4} < U < 3 \cdot 10^{-3}$	$3 \cdot 10^{-3} < U < 4.5 \cdot 10^{-3}$
$D = 10^1 \text{ m}$	$0 < U < 7.5 \cdot 10^{-6}$	$7.5 \cdot 10^{-6} < U < 6 \cdot 10^{-5}$	$6 \cdot 10^{-5} < U < 3 \cdot 10^{-4}$	$3 \cdot 10^{-4} < U < 4.5 \cdot 10^{-4}$
C_D	$\infty < C_D < 4$	$4 < C_D < 2.1$	$2.1 < C_D < 1.5$	$1.5 < C_D < 1.3$
C_L	0	0	0	0
St	/	/	$0.1 < St < 0.2$	$0.2 < St < 0.2$
$\tilde{C}_{L,rms}^2$	/	/	$0 < \tilde{C}_{L,rms}^2 < 0.4$	$0.4 < \tilde{C}_{L,rms}^2 < 0.5$
Spectrum of C_L	/	/	Single narrow peak	Single narrow peak
Sketch				

Table 2.1: Flow characteristics around a circular cylinder for regimes without interest for the civil engineering applications. Data from [Wieselsberger \(1922\)](#); [Schewe \(1983\)](#); [Williamson \(1989\)](#); [Roshko \(1961\)](#); [Norberg \(2003\)](#). U is expressed in m/s and the kinematic viscosity is the standard for the air at $20^\circ C$, $\nu = 1.50 \cdot 10^{-5} m^2/s$. The jagged line in the sketches denotes the flow in the turbulent state.





REGIME	SUB CRITICAL	CRITICAL	UPPER TRANSITION	POST CRITICAL
Re Range	$300 < Re < 3 \cdot 10^5$	$3 \cdot 10^5 < Re < 3.5 \cdot 10^5$	$3.5 \cdot 10^5 < Re < 4.5 \cdot 10^6$	$4.5 \cdot 10^6 < Re < \infty$
D = 10^{-1} m	$4.5 \cdot 10^{-2} < U < 4.5 \cdot 10^1$	$4.5 \cdot 10^1 < U < 5.25 \cdot 10^1$	$5.25 \cdot 10^1 < U < 6.75 \cdot 10^2$	$6.75 \cdot 10^2 < U < \infty$
D = 10^0 m	$4.5 \cdot 10^{-3} < U < 4.5 \cdot 10^0$	$4.5 \cdot 10^0 < U < 5.25 \cdot 10^0$	$5.25 \cdot 10^0 < U < 6.75 \cdot 10^1$	$6.75 \cdot 10^1 < U < \infty$
D = 10^1 m	$4.5 \cdot 10^{-4} < U < 4.5 \cdot 10^{-1}$	$4.5 \cdot 10^{-1} < U < 5.25 \cdot 10^{-1}$	$5.25 \cdot 10^{-1} < U < 6.75 \cdot 10^0$	$6.75 \cdot 10^0 < U < \infty$
C_D	$1.3 < C_D < 1.2$	$1.2 < C_D < 0.3$	$0.3 < C_D < 0.5$	$0.5 < C_D < ?$
C_L	0	$\cong 1.3$	0	0
St	$0.2 < St < 0.2$	$0.2 < St < 0.45$	$0.45 < St < 0.25$	$0.25 < St < ?$
$\tilde{C}_{L,rms}^2$	$0.5 < \tilde{C}_{L,rms}^2 < 0.09$	$0.09 < \tilde{C}_{L,rms}^2 < 0.04$	$0.04 < \tilde{C}_{L,rms}^2 < 0.02$	$0.02 < \tilde{C}_{L,rms}^2 < ?$
Spectrum of C_L	Single narrow peak	Random with 1 peak	Random with 2/1 peaks	Single narrow peak
Sketch				

Table 2.2: Flow characteristics around a circular cylinder for regimes of interest for the civil engineering applications. Data from [Wieselsberger \(1922\)](#); [Schewe \(1983\)](#); [Williamson \(1989\)](#); [Roshko \(1961\)](#); [Norberg \(2003\)](#). U is expressed in m/s and the kinematic viscosity is the standard for the air at $20^\circ C$, $\nu = 1.50 \cdot 10^{-5} m^2/s$. The jagged line in the sketches denotes the flow in the turbulent state.

Similarly, the across wind component of the mean resultant force per unit length due to pressure and friction are:

$$F_{p,y}(t) = \int_0^{2\pi} p(\theta, z, t) \sin(\theta) R d\theta \quad F_{\tau,y}(t) = \int_0^{2\pi} \tau_o(\theta, z, t) \cos(\theta) R d\theta \quad (2.10)$$

The total across wind force per unit length, or *lift*, is the sum of these two forces:

$$F_L(t) = F_{p,y}(t) + F_{\tau,y}(t) \quad (2.11)$$

The effects of shear stresses are small if compared to those of surface pressures, about $1\% \div 2\%$ of the total ([Achenbach, 1968](#)), and can be neglected in most of the cases. The aerodynamic force and moment coefficients are defined as follows:

$$C_D(t) = \frac{F_D(t)}{\frac{1}{2}\rho U^2 D} \quad C_L(t) = \frac{F_L(t)}{\frac{1}{2}\rho U^2 D} \quad (2.12)$$

The two aerodynamic coefficient can be split into time-averaged components, mean drag and lift coefficients, and fluctuating components:

$$C_D(t) = C_D + \widetilde{C}_D(t) \quad C_L(t) = C_L + \widetilde{C}_L(t) \quad (2.13)$$

The fluctuating parts are usually dealt with as stochastic processes. The mean lift coefficient zero in most of the cases, due to flow symmetry. However, instantaneous values can be non-zero and rather large. The Strouhal number is defined as:

$$St = \frac{f_v D}{U} \quad (2.14)$$

where f_v is the average frequency of vortex shedding.

Shear layer separation is defined by two angles, the angle of transition θ_T and the angle of separation θ_S .

The portion of the flow whose characteristics are affected by the presence of the cylinder is named *disturbed flow*. The disturbed flow region can be divided into four sub-regions (Figure 2.4), in which the local time-averaged velocity, v , can be greater than, equal to, or less than U ([Zdravkovich, 1997](#)):

- One narrow region of *retarded flow* ($v < U$);
- Two *boundary layer* regions attached to the surface of the cylinder ($v < U$);
- Two *sidewise regions* of displaced and accelerated flow ($v > U$);
- One wide down stream region of separated flow, the *wake* ($v < U$).

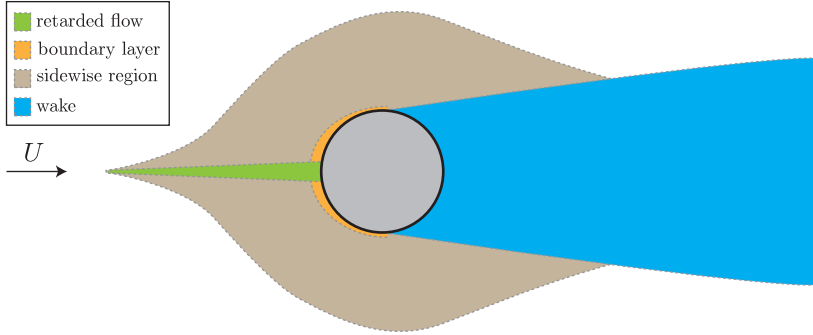


Figure 2.4: Region of disturbed flow.

The transitions in the disturbed flow region are governed by Re . Using the definition of the Reynolds number and three different characteristic linear dimensions ($10^{-1} m$ (size of a cable), $10^0 m$ (size of a chimney or a beam) and $10^1 m$ (size of a cooling tower)) it is possible to classify the regimes of interest for the civil engineering applications (Tables 2.1 and 2.2).

For very low values of Re no separation occurs, and separation first appears when Re is in the order of 5. For $5 < Re < 40$, a pair of stationary vortices forms in the wake of the cylinder, the length of which increases with Re . The wake becomes unstable when Re is further increased giving rise to the phenomenon of *vortex shedding*. The wake is characterized by a vortex street, which is laminar for $40 < Re < 200$ and becomes turbulent for $200 < Re < 300$; for $Re > 300$ the wake is completely turbulent. In this range, C_D is virtually ∞ at $Re = 0$ and decrease to 1.3 for $Re = 300$; C_L is zero. In this range, the most significant contribution to C_D comes from shear stresses. St has meaning in the range $40 < Re < 300$ where it is approximately 0.2.

Exceeded the value of $Re = 300$ the regimes begin to be of interest in civil engineering applications. Increasing Re over a very wide range, $300 < Re < 3 \cdot 10^5$, the boundary layer over the cylinder surface remains laminar and the wake becomes increasingly turbulent. This regime is known as the *sub critical regime*. In this regime C_D and St are approximately constant, and $C_L = 0$. In the range of $3 \cdot 10^5 < Re < 3.5 \cdot 10^5$, the boundary layer becomes turbulent at the separation point, but this occurs only at one side of the cylinder. This flow regime is called the *critical flow regime*. In this regime, separation is characterized by an unstable structure that is a two-dimensional separation-reattachment flow called *separation bubble*. In this structure separation is laminar and reattachment is turbulent. The flow asymmetry causes a non-zero value C_L . The separation bubble shifts the separation point towards the leeward region, thus reducing the size of the wake and the value of C_D . Increasing Re , separation bubbles form on both sides of the cylinder, bringing C_L back to zero and further reducing size of the wake and the value of C_D . The *critical Reynolds number*, Re_c , is defined as

that value at which C_D reaches a minimum value. In this range, St increases and the spectrum of C_L shows a more marked random behavior. Increasing Re the region of transition to turbulence propagates upstream over the cylinder surface towards the stagnation point inhibiting the separation bubble structure. The disappearance of the separation bubble and concurrent reappearance of strong vortex shedding indicates a regime change. In fact, in the wide range of $3.5 \cdot 10^5 < Re < 4.5 \cdot 10^6$, the boundary layer separation points are turbulent on both sides of the cylinder. However, transition to turbulence in the boundary layer has not been completed yet; the region of transition to turbulence is located somewhere between the stagnation point and the separation point. The boundary layer on one side becomes fully turbulent when Re reaches the value of about $1.5 \cdot 10^6$, and is partly turbulent on the other side. This type of flow regime, called the *upper-transition flow regime*; C_D slowly increases, C_L is zero and St decreases. When $Re > 4.5 \cdot 10^6$, the boundary layer over the cylinder surface is virtually turbulent everywhere. This flow regime is called the *post critical flow regime*; C_D and St are constant and C_L is zero. Knowledge of the aerodynamic behavior at larger Re is not fully available.

The typical values of the variables describing the flow and the aerodynamic forces around circular cylinders for all the regimes are given in Tables 2.1 and 2.2. A more detailed description of the aerodynamics of circular cylinder can be found in Zdravkovich (1997, 2003) and in Sumer & Fredsøe (2006).

2.3 Surface irregularities

Surface irregularities are usually named roughness, and are quantified by the deviation of a real surface from the surface primary form. In practice, there exists an extremely wide variety of surface roughness generated by superficial material defects, scratches, protrusions, contaminants and/or attachments such as deposits on underwater pipelines or water rivulets on bridge cables. Roughness plays an important role on how an object interacts with the environment, and attracted widespread interest in fields such as tribology, where it influences the friction coefficients between two surfaces. Many textbooks are available containing descriptions of roughness characteristics (Muralikrishnan & Raja, 2009; Whitehouse, 1994). From the aerodynamics viewpoint, surface imperfections modify the original flow around the obstacle, including the boundary layer and separation characteristics, the turbulence level and the structure of the wake. The fluid forces are also heavily affected.

In aerodynamics, the roughness of a surface is usually expressed as:

$$K(t) = \frac{\int_0^{2\pi} err(\vartheta, z, t) d\theta}{2\pi} \quad (2.15)$$

where $K(t)$ is the average height of excrescences. The dependence on t can be omitted in all cases where the imperfections do not change in time, or the

time scale of their variation is larger than the time scale(s) of the flow. The surface can be regarded as smooth when the excrescences are small enough not to affect, to any measurable extent, the aerodynamic characteristics (Fage & Warsap, 1930).

Nikuradse (1933) performed the first detailed experimental study of rough wall turbulent flow by gluing sand grains of different uniform sizes to the inside walls of pipes in the most dense arrangement possible. By measuring the pressure drop of water flow through the roughened pipes, he developed an empirical equation relating sand grain height, Re and pipe diameter to the flow resistance. For small Re , friction is the same for rough as for smooth pipes. With increasing Re , an increase in friction was observed for rough pipes, depending on the relative scale of roughness K/D as well as on Re . For high values of Re , friction becomes independent of Re and is a function of K/D . By measuring the flow resistance and velocity profiles, Nikuradse obtained a logarithmic velocity profile:

$$\frac{u}{U_f} = \frac{1}{k} \ln \frac{30y}{K} \quad (2.16)$$

in which u is the streamwise velocity, U_f is the wall shear-stress velocity, $k \cong 0.4$ is the von Karman constant, y is the distance from the wall and K is the mean diameter of the sand grains. The usual practice is to measure the velocity profile and then to determine K using the Eq. 2.16. Subsequently, Schlichting (1936) observed that the shape of the roughness elements and their distribution influence the boundary layer. Schlichting determined K for many roughness shapes (i.e. spheres, hemispherical caps, cones, etc.) in different arrangements. Some results are presented in Figure 2.5.

The first studies on the effect of roughness on the aerodynamics of circular cylinders were proposed in the 1930s by Fage & Warsap (1930). Their studies suggested that the surface roughness generates turbulence and affects the flow around the cylinder in an analogous manner as free stream turbulence. The difference is that the boundary layer is disturbed by the free stream turbulence from outside while the surface roughness turbulence acts from the inside. Fage & Warsap observed that the effects on the aerodynamics generated by roughness are related to relative roughness K/D , to shape of excrescences and to the distribution of the excrescences (regular, irregular, partial, etc.). The shape and distribution of the excrescences determine the *texture*. The roughness parameter K/D chosen by Fage & Warsap is a technical parameter with little physical meaning. Achenbach (1971) noted that from the physical point of view the boundary layer thickness δ must be introduced as the scaling length, so the roughness parameter takes the form K/δ . However, the boundary layer varies with angular position and Reynolds number. Therefore it is preferred to use the diameter D as scaling length. Thus, it must be expected that a small roughness height produces an important effect on the flow if the boundary layer is thin.

No.	Type	Dimension	D [cm]	d [cm]	k [cm]	k_s [cm]	Photo
1	Spheres		4	0.41	0.41	0.093	
2			2	0.41	0.41	0.344	
3			1	0.41	0.41	1.26	
4			0.6	0.41	0.41	1.56	
5			Tightest packing	0.41	0.41	0.257	
6			1	0.21	0.21	0.172	
7			0.5	0.21	0.21	0.759	
8	Hemispherical caps		4	0.8	0.26	0.031	
9			3	0.8	0.26	0.049	
10			2	0.8	0.26	0.149	
11			Tightest packing	0.8	0.26	0.365	
12	Cones		4	0.8	0.375	0.059	
13			3	0.8	0.375	0.164	
14			2	0.8	0.375	0.374	
15	"Short" angles		4	0.8	0.30	0.291	
16			3	0.8	0.30	0.618	
17			2	0.8	0.30	1.47	

Figure 2.5: Results from roughness measurements on regularly placed roughness elements. After (Schlichting, 1936).

Referring to these parameters, it is possible to classify the surface irregularities into:

- Uniform roughness;
- Non uniform or localized roughness;
- Presence of water rivulet.

The last case is defined considering the classification in time dependent irregularities. Only in the case of wet cylinders, time dependence has to be considered. In the following the three cases are analyzed.

2.3.1 Uniform roughness

The main characteristic of the uniform roughness is to have the pattern constant on the surface. Uniform is referred to a roughness characterized by a continuous and uniform pattern of elements that generate the function $err(\vartheta, z, t)$. In contrast, non-uniform is the case of conditions that vary on the surface. If the roughness is uniform, it can be expressed by one parameter, K , that represents the characteristic size of the superficial imperfections. The dimensionless form of this parameter is K/D .

2.3.1.1 Textures

A variety of roughness types has been used in experiments on flow over circular cylinders. In the following, the different approaches adopted to simulate surface roughness in different experiments are described.

The most used technique to simulate roughness on circular cylinders has been the provision on the surface of sandpaper. The first tests using this technique were performed by [Fage & Warsap \(1930\)](#). Similarly, [Batham \(1973\)](#) used machined aluminum casting cylinder manufactured with $D = 0.23\text{ m}$ and $L = 1.53\text{ m}$. The rough-model tests surface was painted with a thin adhesive varnish and a uniform layer of 0.5 mm diameter sand particles was applied giving $K/D = 0.22\%$.

The most common type of surface roughness in civil engineering is made by brick laying. Standard brick-laying is half staggered. [Ackeret \(1936\)](#) carried out wind tunnel tests using a brick chimney model fitted with two elliptical end plates. Three sets of measurements were carried out:

1. Joints between bricks 4 mm wide and 2 mm deep, and the brick surface smooth;
2. Joints between bricks 4 mm wide and 2 mm deep, and brick roughened by $1 - 2\text{ mm}$ sand grains;
3. Joints filled and model surface varnished.

He found that $C_{D\min}$ occurs at $Re = 3.5 \cdot 10^5$, $1.5 \cdot 10^5$ and $1 \cdot 10^5$ for smooth, grooved joints and rough bricks, respectively. The shape and sequence of the curves are similar to the other type of roughness.

Offshore structures are partly or wholly immersed in sea, and most structural members are circular cylinders. After deployment in the sea, these structures become roughened by corrosion and marine fouling. Forces exerted by waves and currents may be substantially altered by the increase in diameter and added surface roughness. [Miller \(1977\)](#) divided the accumulated marine fouling in two ways:

1. An average roughness height K is defined as the representative height of all excrescence from an imaginary smooth surface;

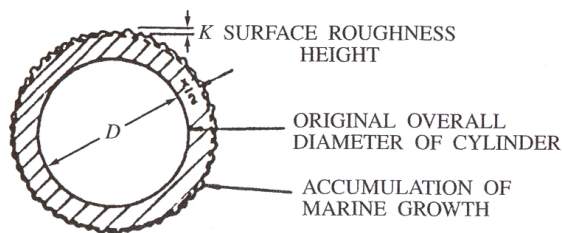


Figure 2.6: Definition sketch of marine fouling, after [Miller \(1977\)](#).

2. The thickness of the accumulated growth ΔD increases the cylinder diameter from D to $D + 2K/D$, Figure 2.6.

Surface roughness always increases heat transfer but it also increases drag. [Achenbach \(1977\)](#) studied the effect of surface roughness on the heat transfer on circular cylinders with the objective to increase the heat transfer without increasing C_D . The roughness was manufactured by knurling the surface of a copper cylinder. The roughness produced by this method were regular arrangements of pyramids, each having a rhomboidal base, as in Figure 2.7a.

[Achenbach \(1977\)](#) suggested a simple way of evaluating an equivalent sand roughness for the pyramidal roughness. [Fage & Warsap \(1930\)](#) and [Achenbach \(1974\)](#) Re values associated with C_{Dmin} are plotted in terms of the sand paper relative roughness K/D in Figure 2.7b. The three Re values for C_{Dmin} for pyramidal roughness are depicted with arrows, and the sand paper equivalent roughness obtained by referring to the vertical axis.

[Achenbach & Heinecke \(1981\)](#) noted that the roughness pattern is characterized not only by the height of the elements, but also by their local arrangements on the surface and by the statistical distribution on the different grain sizes: it seemed unsatisfactory to the authors to report only on the geometric size of the roughness.

[Buresti \(1981\)](#) demonstrated that a single dimensional parameter couldn't totally define surface roughness: in fact, the shape distribution of the particle can also influence the characteristics of the boundary layer and, consequently, the separation point and the flow regime around the cylinder.

In the experiments, [Nakamura & Tomonari \(1982\)](#) simulated the roughness by the use of polystyrene particles of approximately the same size that were glued by using two-side adhesive tape. The four different sizes of particle examined were 6.2, 3.2, 1.4 and 0.56 mm.

[Basu \(1985\)](#) observed that the most difficult group of experimental results to deal with are those obtained using nominally smooth cylinders. These include machined aluminium surfaces ([Bruun & Davies, 1975](#); [Batham, 1973](#)), phenoglaized surfaces ([Bearman, 1969](#)), sandblasted pipe ([Roshko, 1961](#)) and

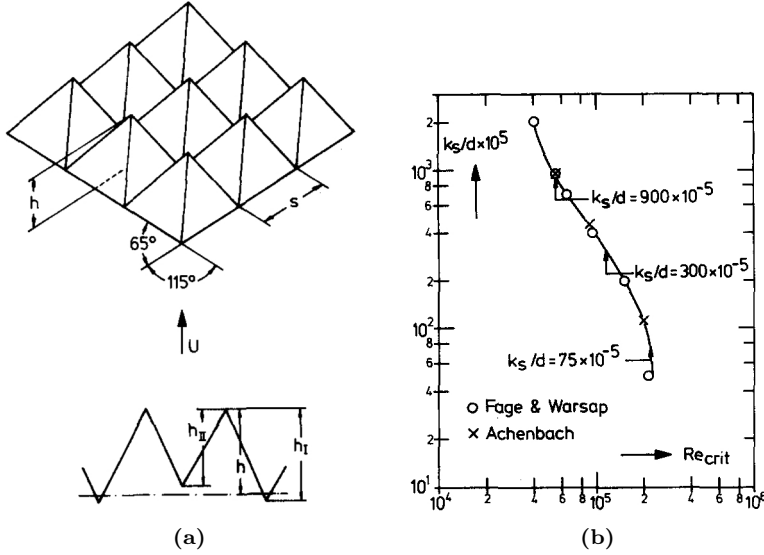


Figure 2.7: Roughness pattern (a) and calibration of pyramidal roughness in terms of sand roughness (b). After [Achenbach \(1977\)](#).

machined pipe ([James *et al.*, 1980](#)).

[Farell & Fedeniuk \(1988\)](#) used commercial stainless steel wire cloths as roughness, in two size, with wire diameter 0.165 mm and 0.254 mm on an aluminum cylinder having a diameter of 5.08 cm .

[Adachi *et al.* \(1989\)](#) showed that if the surface roughness is larger in the axial direction then in circumferential direction, there can be seen a retardation in the separation point along the cylindrical surface in the upper transition and post critical Reynolds number ranges.

[Zdravkovich \(1990\)](#) observed that the surface roughness could be characterized by at least two influencing parameter: the relative size of the roughness K and his texture. In his review, he noted that most of the research was carried out by the evenly roughened surface described by K/D .

[Farell & Arroyave \(1990\)](#) simulated the roughness using stainless steel wire cloth wrapped on the cylinder. The wire diameter was 0.114 cm and the roughness obtained was $K/D = 0.45\%$.

[Niemann & Holscher \(1990\)](#) classified the roughness textures in three groups:

- Uniform, densely packed roughness (emery papers, glass beads, knurled surface);
- Technical toughness with randomly varying size, form and distance of roughness elements (concrete surface);

Table 2.3: Cable models, after Miyata *et al.* (1994).

Model	D [m]	K [μm]	K/D	Kind of roughness
A ₁	0.1315	3	$2.3 \cdot 10^{-5}$	Smooth
A ₂	0.1220	30	$2.5 \cdot 10^{-5}$	Molten polyethylene particles
A ₃	0.1315	100	$7.6 \cdot 10^{-4}$	Molten polyethylene particles
A ₄	0.1235	200	$1.6 \cdot 10^{-3}$	Molten polyethylene particles
A ₅	0.1240	600	$4.8 \cdot 10^{-3}$	Molten polyethylene particles
A ₆	0.1275	1500	$1.2 \cdot 10^{-2}$	Molten polyethylene particles
B ₁	0.1465	200	$1.6 \cdot 10^{-3}$	Grid-like
B ₂	0.1465	600	$4.1 \cdot 10^{-3}$	Grid-like
B ₃	0.1490	1200	$8.1 \cdot 10^{-3}$	Grid-like
C ₁	0.1400	3	$2.1 \cdot 10^{-5}$	Smooth
C ₂	0.1400	1500	$1.1 \cdot 10^{-2}$	Concave discretely patterns
C ₃	0.1400	1500	$1.1 \cdot 10^{-2}$	Convex discretely patterns

Table 2.4: Results of analysis of surface patterns, after Miyata *et al.* (1994).

Model	R _a [mm]	Wavelength [mm]
A ₆	0.45	4.0
B ₃	0.41	11.1
C ₂	0.18	28.4

- Discrete ribs and wires parallel to the cylinder axis.

Duarte Ribeiro (1991a,b) noted that roughness density plays a critical role. Surfaces with the same roughness height but with different densities (e.g. sand paper with close-packed particles or dispersed particles) generally show different effects on regime transitions and flow parameters. The effect of the distribution density seems to be quite different for different roughness types. Moreover, it is certainly non linear.

Shih *et al.* (1993) used square-mesh wire screens to simulate roughness according to Table 2.6.

Miyata *et al.* (1994) studied the basic aerodynamic properties of cables with approximately uniform surface roughness using a wind tunnel and the description of roughness surfaces. A group of cylinder with different roughness were used in test, they are reported in Table 2.3. They did an accurate analysis of

cable surface patterns. In general, roughness is described in terms of the average peak-to-valley height, but this method fails to take the distribution of surface roughness into consideration. Since patterns can be regarded as irregular waveforms, they can be expressed mathematically as Fourier series. When expressing a surface wave form in terms of $f(x)$, the average arithmetic mean deviation of the roughness R_a , is give by the following equation:

$$R_a = \frac{1}{l} \int_0^l |f(x)| dx \quad (2.17)$$

In spectral analysis, the intensity of a waveform is often defined by the energy spectrum, $|x(f)|^2$. Table 2.4 shows the results of analyzing typical surface patterns. By considering R_a , it was possible to gain an understanding of the average height of the surface roughness on each side of the line while taking the concave and convex patterns into account. Where the surface roughness is uniformly distributed, the characteristics of the surface pattern can be expressed more precisely in terms of the average arithmetic mean deviation of the roughness than in term of the apparent relative surface roughness, K/D . The Fourier spectrum is dominated by a certain wavelength, L , which means that in the case of non-uniform distribution of surface roughness, the surface pattern is a repetition of certain patterns at certain intervals corresponding to the dominant wave number. The amount of spread in surface roughness can be considered small when the repeated dominant wave number is small. They concluded that this analytical method could not be correlated with the relationship between surface pattern and aerodynamic characteristics and further quantitative studies will be required preferably using wind tunnel tests and numerical analysis.

Adachi (1997) used rough cylinders (Table 2.5) in his tests. The value of relative roughness was measured by traversing a stylus along the surface using a roughness meter. The values of relative roughness were calculated by dividing the measured values of roughness based on JIS (Japanese Industrial Standard) B 0601 by the Diameter D . The values of the relative roughness were nearly uniform in the circumferential and axial direction with exception to that of cylinder B (Table 2.5). No information were given on the material and roughness type of the cylinder.

Okajima *et al.* (1999) studied the aeroelastic instability of a circular cylinder with surface roughness. The test models had a diameter of $D = 160 \text{ mm}$. They were made of acrylic acid resin. The models of a circular cylinder were covered with different surface roughness. Three kind of evenly roughened surface were adopted. Two of them by spherical glass bead particles of a diameter d of about 0.8 mm ($K/D = 5 \cdot 10^{-3}$) and 1.0 mm ($K/D = 6.2 \cdot 10^{-3}$), respectively, and the third roughness was made by attaching to the surface 64 stranded cables with a diameter of 6 mm .

Talley & Mungal (2002) studied the aerodynamics of the saguaro cactus and

Table 2.5: Relative surface roughness of cylinders (tangential roughness K_{st} , axial roughness K_{sa}), after [Adachi \(1997\)](#).

	$K_{st} \cdot 10^{-6}$	$K_{sa} \cdot 10^{-6}$	K_{st}/K_{sa}	$K_{st}/D \cdot 10^{-6}$
A	0.08 – 0.5	0.03 – 0.5	0.85	4.54
B	0.3 – 05	0.9 – 1.4	0.38	8.57
C	10 – 17	9 – 15	1.08	254
D	20 – 30	28 – 36	0.75	500
E	50 – 68	60 – 75	0.84	1160
F	70 – 90	78 – 94	0.89	1600
G	50 – 110	62 – 110	0.98	1810
H	130 – 150	119 – 126	1.03	2540

other tall arborescent (treelike) succulents that withstand high wind velocities in their natural habitat. These desert plants have a cylindrical shape, modified by complex surface geometry. They argued that bluff-bodied organisms reduce drag by surface roughness.

[Fuss \(2011\)](#) investigated the effect of surface skewness on C_D at constant relative roughness K/D , in order to isolate the specific skewness effect. The roughness elements were realized by a rapid prototype technique using a flexible polymeric rapid prototyping material. The length and diameter of the cylinder were 325 mm and 220 mm, respectively, resulting in an aspect ratio of 1.5. In order to reduce 3D effects, two endplates of three times the cylinder diameter was placed at both ends. The prototyped sheets were glued to the surface of the cylinder. He found that the larger the surface skewness, the “rougher” is the surface profile and the larger is the post critical C_D , and the smaller is Re_c . The surface profiles and the C_D found are shown in [Figure 2.8](#).

[Matteoni & Georgakis \(2012b\)](#) investigated the effects of surface roughness and cross-sectional distortions on the aerodynamic force coefficients of cross flow and inclined/yawed bridge cables made in HPDE. The roughness measurements were compared with the roughness measurement performed on three sample cables at the Øresund Bridge in October, 2010. The measured roughness of the cable model averaged in the wind flow direction was in the range $R_a = 1.5 - 2.5 \mu m$. Roughness measurements performed on cable sections at the Øresund bridge showed that the surface roughness was altered from its original state due to mechanical degradation and the measured roughness was in the range $R_a = 0.7 - 1 \mu m$.

[Chowdhury & Alam \(2013\)](#) experimentally studied the effect of surface roughness of textiles used in higher speed sports on C_D using finite circular cylinder

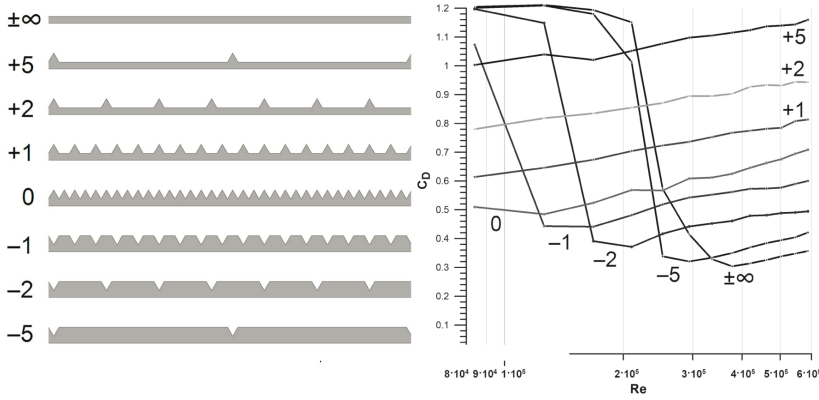


Figure 2.8: Surface profiles and C_D in function of for different skewness number, after [Fuss \(2011\)](#).

wrapped with the textiles. The Reynolds range was $1 \cdot 10^5 < Re < 2.4 \cdot 10^5$. K/D was in the range of $2.58 \cdot 10^{-4}$ to $7.38 \cdot 10^{-4}$. 10 textile samples mainly used in ski jumping, cycling, swimming, and other sports were tested. It was concluded that the textile with lower surface roughness could be used for larger diameter cylindrical objects to attain the minimum value of C_D , while the textile with higher surface roughness can be adopted for smaller diameter objects under the same fluid speed.

2.3.1.2 Mean and fluctuating pressures and forces

The first experiments on the effects of uniform surface roughness on the aerodynamics of circular cylinders in cross flow were performed by [Fage & Warsap \(1930\)](#). They determined C_D in the range of $2.5 \cdot 10^4 < Re < 2.5 \cdot 10^5$ (Figure 2.9), simulating the roughness by wrapping the cylinder with glass paper of five grades ($K/D = 2\%$, 0.9% , 0.4% , 0.2% and 0.05%). The turbulence during the tests was estimated later by [Baines & Peterson \(1951\)](#) to be about 1%. It was found that in the sub critical regime the roughness has a no influence on C_D , while in the upper transition regime C_D increases with increasing K/D . The most important changes are in the critical regime where the minimum value of C_D increases and Re_c decreases with increasing K/D . This result agree with the conclusion on the dependency of friction on K/D and on Re of [Nikuradse \(1933\)](#) on rough walls.

To better understand the effects of roughness on the boundary layer over a circular cylinder with uniform roughness, [Achenbach \(1971\)](#) measured the surface pressure, $p(\theta, z, t)$, and the shear stress, $\tau_o(\theta, z, t)$. The experiments were carried out in range of $4 \cdot 10^4 < Re < 3 \cdot 10^6$ using a pressurized wind tunnel

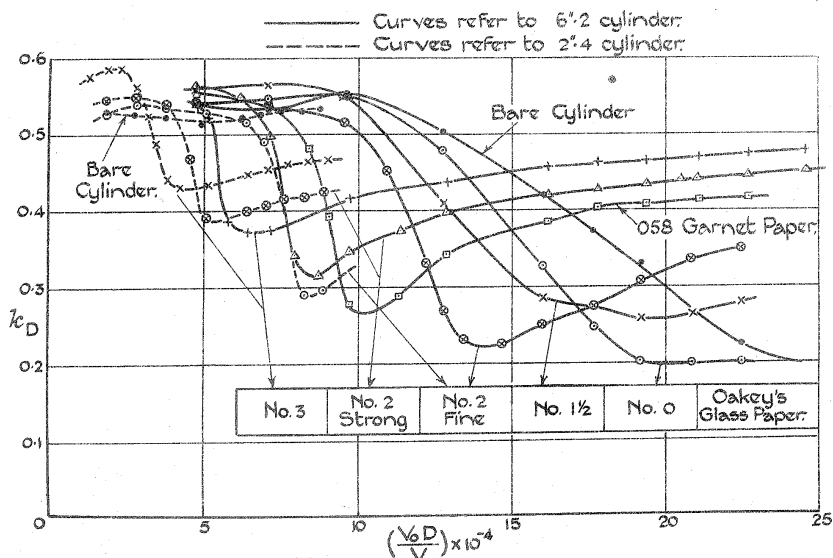


Figure 2.9: $K_D = (1/2) C_D$ of a rough-surface cylinder for different roughness, after Fage & Warsap (1930).

up to 40 bar, with $K/D = 0.9\%$, 0.45% and 0.11% . The values of C_D obtained through integration of pressures confirmed the trend found by Fage & Warsap (1930). The zero position of $\tau_o(\theta, z, t)$ indicates the separation point of boundary layer, θ_S (Achenbach, 1971, 1968). In the sub critical regime, the separation is laminar in the front portion of the cylinder as a consequence of friction forces. The disturbances produced by the rough surface support the boundary layer with energy from outside and cause a shifting of the separation point toward the leeward side producing a premature transition to the critical regime. At Re_c , roughness causes disturbances and therefore lead to a narrow flow range where the separation bubble phenomenon took place. In the Re range investigated, both for the rough and for the smooth surfaced cylinder, friction forces contributed only a few percent to the flow resistance. They found that in the case of the smooth cylinder in the post critical range, the percentage of friction diminishes with increasing Re and in the rough case it remains at a nearly constant level. Achenbach (1974) carried out similar experiments on spheres, confirming that also in that case increasing roughness produces a decrease in the critical Reynolds number.

Using the same approach, Batham (1973) observed that transition on a rough cylinder would be a more homogeneous process than is found on smooth cylinders and would not display the high values of $\tau_o(\theta, z, t)$. Thus the boundary layer on a rough surface would not be capable of withstanding such high mean

adverse pressure gradients as on a smooth surface. Tests were conducted in uniform and turbulent flow for smooth and rough cylinders at $Re = 1.11 \cdot 10^5$ and $2.35 \cdot 10^5$. It was found that the minimum value C_D of rough cylinders is always higher than that of smooth cylinders. The minimum of C_D increases with roughness until a very high no minimum is observed at all. Moreover, [Batham \(1973\)](#) observed that the spanwise correlation length is high for the smooth cylinder in uniform flow and very low for the turbulent flow. Rough cylinders show high spanwise correlation for both uniform and turbulent flow. On rough cylinders, the more homogeneous nature of the boundary layer would enable the transition boundary layer to exhibit vortex shedding which is not observed when the transition is promoted by free-stream turbulence on smooth cylinders.

[Miller \(1977\)](#) carried out tests with large artificial and natural marine roughness in the range of $1.5\% < K/D < 6.3\%$ and $2 \cdot 10^5 < Re < 4 \cdot 10^6$. He also found that for high values of Re , C_D increased with K/D . The rapid rise in C_D up to $K/D = 5\%$ is followed by a very small increase, indicating a significant change in the mechanism of roughness-generated turbulence. This result, however, has not attracted the attention of subsequent researches.

Using pyramidal elements as roughness (Figure 2.7a), [Achenbach \(1977\)](#) noted that for large roughness the separation bubble forms for only one value of Re , which is Re_c . The tests were carried out in two different wind tunnels of the same size, with three different types of roughness. The lower Reynolds number range ($3 \cdot 10^4 < Re < 3 \cdot 10^5$) was covered in the atmospheric tunnel, whereas the higher Reynolds numbers ($1 \cdot 10^5 < Re < 4 \cdot 10^6$) were obtained in a pressurize wind tunnel up to 40 bar. In the upper transition regime, the laminar-turbulent transition takes place on the windward part of the cylinder, with the exact position depending on Re and on K/D . The position of the separation point, however, is nearly independent of Re so that C_D is also constant.

The work was continued by [Achenbach & Heinecke \(1981\)](#). Using the data from [Fage & Warsap \(1930\)](#); [Achenbach \(1971\)](#); [Miller \(1977\)](#), they proposed that relationship between the dimensionless equivalent sand-grain roughness K/D and the critical Reynolds number is approximated as:

$$Re_{crit} = \frac{6000}{\sqrt{\frac{K}{D}}} \quad (2.18)$$

They also found that in the subcritical range, where the boundary layer is laminar roughness has no influence on drag (Figure 2.10). At the critical Reynolds number, laminar intermediate separation and turbulent reattachment occurs. The turbulent boundary layer transferring a higher amount of energy normal to the wall than the laminar boundary layer enables the flow to follow the contour of the cylinder far downstream. The value of Re_{crit} decreases with increasing roughness and at the same time the critical Reynolds range shrinks.

Achenbach & Heinecke (1981) also measured St (Figure 2.10) and find two types of behavior in the critical regime:

- Smooth and small $K_s/D < 0.075\%$: the extent of $C_{D\min}$ indicates the presence of the laminar separation bubble characterized by the high value of St ;
- $K_s/D > 0.3\%$: the laminar separation bubble is inhibited and the St curve is uninterrupted.

Güven *et al.* (1980) measured the mean pressure and the boundary layer development on rough cylinders in uniform flow. Five different sizes of sand paper roughness were used, with $7 \cdot 10^4 < Re < 5.5 \cdot 10^5$. They found that C_D , as well the pressure distribution parameters become independent of Re as Re is increased. Independence of the Reynolds number is reached at lower Re as the surface roughness increases. When independent of Re , C_D depends on the relative roughness. It is also shown that larger surface roughness leads to a thicker boundary layer with a larger momentum deficit; under those circumstances, the shear layer separates earlier, resulting in a smaller pressure rise ($C_{pb} - C_{pm}$) and a higher C_D . They noted that observations based on C_D alone can be in certain cases misleading, as this appears to be rather sensitive to factors such as tunnel blockage, aspect ratio of the model and side wall conditions. The non-dimensional pressure rise to separation, $C_{pb} - C_{pm}$, appears to be rather insensitive to such factors and is primarily a function of relative roughness, when independent of Re .

Buresti (1981) studied the influence of surface roughness, $0.09\% < K/D < 1.23\%$, in a open-jet wind tunnel using cylinders with $L/D = 22$ and 12 in a Reynolds range $2.6 \cdot 10^4 < Re < 2.8 \cdot 10^5$. He used four cylinders whose outer diameter were 118, 89, 60 and 33 mm. The results confirmed the striking influence of roughness on the flow regime; in particular he noted that the critical regime can be impressively reduced, and it may even disappear in the case of highly roughened cylinders. The measurement made by Buresti concern the Strouhal number and the mean pressure distribution from which the drag coefficient was obtained by integration. He defined the critical state as the regime in which there is the absence of regular vortex shedding, the upper transition regime in which vortex shedding is again detectable and post critical regime in which the Strouhal number and the drag are virtually independent on Re .

Nakamura & Tomonari (1982) made experimental investigation undertaken to understand the effects of surface roughness on the mean-pressure distribution and the Strouhal number. Cylinders with various types of surface roughness were examined over the Reynolds number range $4 \cdot 10^4 < Re < 1.7 \cdot 10^6$ in uniform flow. They used a PVC circular-cylinder mounted horizontally in the test section. Thirty-six pressure taps were drilled at every 10° along a meridian of the cylinder and its midspan. A hot-wire was set at a location of $1.5D$ downstream of the base of the cylinder and $1D$ down the tunnel centerline.

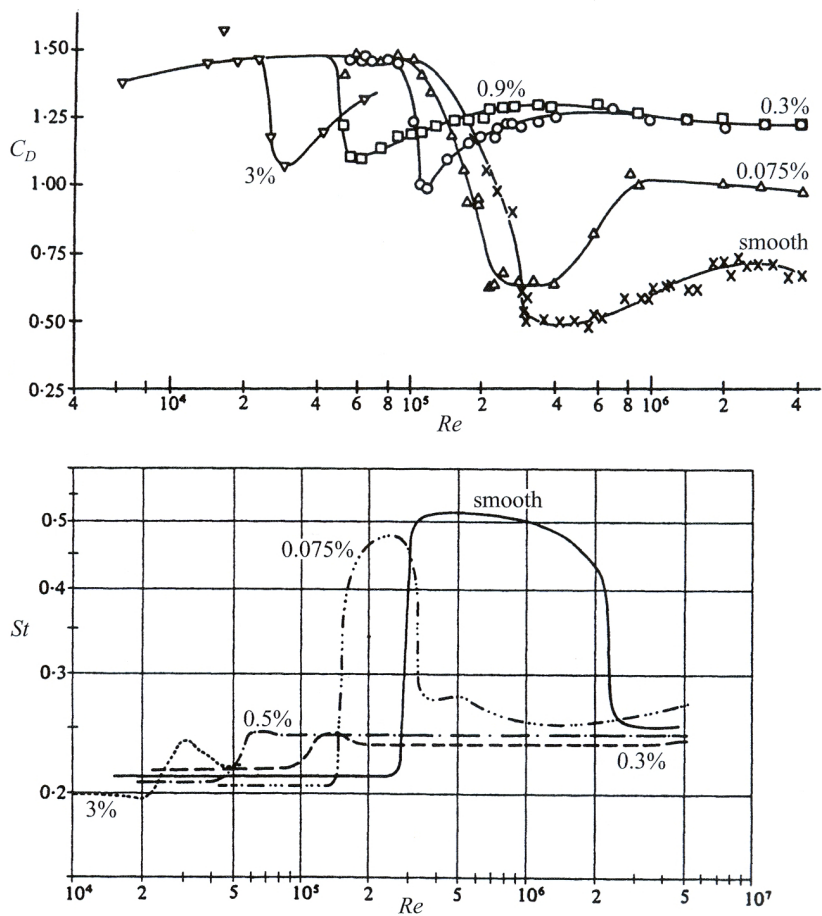


Figure 2.10: Comparative measurements of drag and Strouhal number in terms of Re , after [Achenbach & Heinecke \(1981\)](#).

The results given are the base pressure coefficient C_{pb} , the drag coefficient C_D and the Strouhal number St . They founded a good agreement with the results proposed by [Achenbach \(1971\)](#).

[Farell & Fedeniuk \(1988\)](#) carried out a series of measurements of mean and fluctuating pressures on a rough circular cylinder in uniform flow. The measurements were done with and without end plates, at critical and upper transition Reynolds numbers. The effect of the end plates was found to be very significant, of the order of 15 to 20 percent. The experiments were conducted in a open circuit wind tunnel with a test section 30.5 cm wide and 43.2 cm high, with and without end plates. An aluminum cylinder 5.08 cm in diameter was used as a model. The range of Reynolds number investigated was $0.42 \cdot 10^5 < Re < 2.2 \cdot 10^5$. The effect of end plates on vortex shedding frequencies was considerable. For the first roughness, the Strouhal number at the largest Re investigated was about 0.22 for the cylinder without end plates. With end plate, the asymptotic value was approximately 0.25. Similar difference was noted for the second roughness. They conclude that there is non-interaction between the end plates and the roughness. The end plates can be designed for all roughness.

[Zdravkovich \(1990\)](#) reviewed the scientific literature about the disturbance due to the free stream turbulence and to the surface roughness and described the effects of the roughness for each range of Reynolds numbers. He explained the effect of roughness is governed by the ratio between the boundary layer thickness and the size of roughness K , as proposed by [Achenbach \(1971\)](#). He noted that for low Reynolds numbers, the boundary layer is thick, and the roughness has negligible effect. The most powerful influence of the surface roughness occurs in the transition in the boundary layer state since the surface roughness can be regarded as a mechanism that produces local turbulence. The increase in surface roughness caused a progressive displacement of C_D towards the lower Reynolds numbers. In the case of perfect circular cylinders, the minimum value of C_D designates the two bubble regime. This regime is followed by the spanwise fragmentation of bubbles that causes inhibition of vortex shedding in the upper transition regime. The effects of surface roughness is to inhibit the formation of the separation bubble and hence to obliterate one and two bubble regime. When roughness is greater than $K/D = 0.01$ the vortex shedding persists and this means the sub critical regime is followed by the upper transition regime and the critical regime disappears. The post critical state of flow is strongly affected not only by the relative magnitude but also by the texture of surface roughness. He reported Karman observation for pipes: "All surface may considered rough when the Reynolds number is sufficiently high; for the frictional resistance of rough walls is made up essentially of the resistances of all excrescences and these become independent of friction at high values of Reynolds number". Typical value of the boundary layer momentum thickness at 90° in the post critical state say at $Re = 10^6$ is $0.002D$. Hence all excrescences protrude when $K/D > 0.002$ and over this threshold produce effect on the aerodynamics.

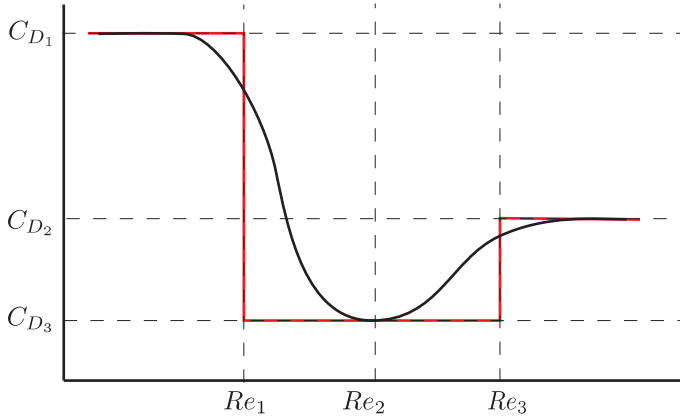
Farell & Arroyave (1990) investigated the transition Reynolds number range and the upper transition and post critical flow regimes for uniform flow around circular cylinders with large roughness using wind tunnel measurements of mean and fluctuating pressures. An aluminum cylinder with diameter $D = 5.08 \text{ cm}$ was used as a model. Stainless steel wire cloth was wrapped on the cylinder. They observed the existence of two critical transition subranges. The first is characterized by symmetric pressure distributions, an increasing lack of span-wise uniformity, and a gradual decrease in C_D . The second is characterized by pronounced flow instability, with oscillating, asymmetric pressure distributions and broad-band pressure spectra without well-defined, strong shedding peaks. For the roughness parameter adopted ($K/D = 4.5 \cdot 10^{-3}$ and $K/D = 9 \cdot 10^{-3}$), the first subrange was obtained approximately for $6.5 \cdot 10^4 < Re < 8 \cdot 10^4$ and the second for $8 \cdot 10^4 < Re < 8.6 \cdot 10^4$. The disappearance of the shedding in the second critical subrange is due to sporadic, asymmetric boundary layer reattachment on one or the other side of the cylinder, without preference for side. Bistable flow configurations were not detected. Farell & Arroyave (1990) noted a discrepancy between their results and the work of Buresti (1981) and Achenbach & Heinecke (1981) in the observation of the presence of regular vortex shedding in rough cylinders. This discrepancy may be due to the difference in the type of roughness adopted.

Shih *et al.* (1993) studied steady and unsteady surface pressures for evaluate lift and drag coefficient and Strouhal numbers for cylinders of several roughness at Reynolds numbers up to $8 \cdot 10^6$. The cylinder is 2.4 m long and 31.6 cm in diameter. The roughness was fixed by use of square-mesh wire screens according to the Table 2.6. The roughness scale K is taken as twice the wire diameter. The range of Reynolds numbers during the experiments was $3 \cdot 10^5 < Re < 8 \cdot 10^6$. The pressure rise $C_{pb} - C_{pm}$ showed that in the case of the smooth cylinder Reynolds-number independence was not evident in the range investigated. Instead, for the rough cylinders was confirmed Reynolds-number independence. Moreover, the asymptotic values of the pressure rise seem to decrease with increasing roughness. The asymptotic values of the separation angle are in the range from 85° to 90° except for the case of the smooth cylinder. The Strouhal number in the range of Re investigated is approximately constant and equal to 0.2. The shedding from the rough cylinders persisted throughout the Reynolds number regime tested, with the roughest cylinder producing the lowest Strouhal number.

Adachi (1997) studied the universality of the Strouhal number in the wake flow of a cylinder over a wide range of Reynolds number, $5 \cdot 10^4 < Re < 1 \cdot 10^7$. Strouhal number depends on the surface roughness value, especially in the post critical Reynolds number range. The dimension of a body D which is included in the Strouhal number $St = fD/U_\infty$ is not related to the vortex street. In order to have a uniform Strouhal number, some other length value relating to the vortex street and other than the diameter must be taken representative length. He used a cryogenic wind tunnel in which various Reynolds number is obtained

Table 2.6: Screen dimensions, after [Shih *et al.* \(1993\)](#).

Wire diameter (cm)	Mesh (per cm)	Percent	K/d
0.004	98	36.0	$3.0 \cdot 10^{-4}$
0.019	24	30.5	$1.20 \cdot 10^{-3}$
0.160	2.4	38.9	$1.01 \cdot 10^{-2}$

**Figure 2.11:** Definition of flow regimes in terms of the variation of the mean drag coefficient, after [Basu \(1985\)](#). The red lines represents the idealized concept of transitions and the black one the real C_D curve.

by circulating low temperature and high-pressure liquid nitrogen gas. He tested the different level of roughness in the range $K/D = 4.54 \times 10^{-6}$ to 2.54×10^{-3} . The strouhal numbers that are independent of the body shape, i.e., the universal strouhal numbers, which include dimensions of vortex streets of bluff bodies with various shapes, are discussed by Roshko, Bearmann, Simmons and Griffin. The idea lying behind the assumption of universality of Strouhal numbers is that same size vortex street may originate from different bluff body. They found that the Bearman's number was the most uniform universal Strouhal number among Roshko's number S_r , Bearman's number S_b , Griffin's number G and another non-dimensional number which took measured values of lateral vortex distance as reference length S' . A uniform Griffin number's can be obtained avoiding the data in the range which have separation bubbles.

[Zan & Matsuda \(2002\)](#) studied steady and unsteady loading in incompressible flow on a roughened circular cylinder in cross flow in the Reynolds number range $5 \cdot 10^4 < Re < 9 \cdot 10^5$. The experiments were conducted on a cylinder of 38 mm diameter with aspect ratio 10. Measurements were made in smooth flow

and in two levels of turbulence. Three aluminum models with the same surface roughness, $K/D = 10^{-4}$, were used for the investigation. The wind tunnel background turbulence level was measured to be about 0.5%. They shown that the return to coherent shedding, which had been reported on smooth cylinders in smooth flow at Reynolds numbers of several million, can occur in the former case at Reynolds as low as $4 \cdot 10^5$. The return to coherent shedding leads to larger forces in that Reynolds number range. Thus, engineering design limits based on smooth model smooth flow data are not necessarily conservative.

2.3.1.3 Parameterization for design

Parameterization is the process of defining the parameters necessary for a complete or relevant specification of a model. In aerodynamic problems, the definition of the flow and force characteristics are important in design. During the years, many authors tried to define parametric laws in order to characterize the influence of roughness.

ESDU 80025 (1980) gives C_D for different roughness. The idea of the ESDU 80025 is to give the drag coefficient as a function of an effective Reynolds number that is expressed as:

$$Re_e = \lambda_T \lambda_R Re \quad (2.19)$$

where λ_T is a factor depending of turbulence characteristics of the approaching flow and λ_R is a coefficient depending on the surface roughness ε/D . In general, the increasing of surface roughness has the effect of decreasing the value of the critical Reynolds number and λ_R is a parameter that characterizes this effect. The parameter ε/D is given in a graph as a function of the kind of material (brickwork, cast iron, etc.) and of the superficial condition (rough, smooth, etc.). Another graph gives the value of λ_R as a function of ε/D . For the evaluation of the drag coefficient the ESDU 80025 gives three graph for three Reynolds number range: $10^{-2} < Re < 10^2$, $10^2 < Re < 10^5$ and $10^5 < Re < 10^8$. In the first range there is no dependence of C_D form λ_R , in the second one the Reynolds number s expressed as Re_e and the drag coefficient is expressed as $C_D/(1 + 2(\varepsilon/D))$ and in the third one the axis of the graph are the same of the second but there are different function for different ε/D . ESDU 80025 also gives the mean pressure coefficient, the fluctuating pressure coefficient and velocity flow field away from surface. ESDU 80025 gives C_D for stranded wire cables as a function of Reynolds number and the ratio of strand to cable outside diameter (d/D). The d/D parameter considered are 0.07, 0.1, 0.15, 0.2 e 0.3. For $Re < 3.5 \cdot 10^4$ the value of C_D is given in a scatter band data. ESDU 80025 gives other technique for the evaluation of ε in function of the “centre-line-average”, k_a , or the maximum peak-to-valley height, k_p . Different relation of ε as function of k_a or k_b are given for different type of roughness like uniform sand grains, spheres, hemispheres, etc.

Basu (1985) review the data gathered from a number of experiments concerned with the flow around circular cylinders. He focused on the experiments conducted under two dimensional condition and in low turbulence streams and to the influence of the roughness of the surface of the cylinder on the magnitude of the mean drag coefficient, the Strouhal number and the RMS lift coefficient. He defined three regimes: subcritical, upper transition and post critical. For each regime he defined a coefficient of drag, C_{D1} , C_{D2} and C_{D3} , and a boundary value of the Reynolds number, Re_1 , Re_2 and Re_3 . This is showed in Figure 2.11. He fitted all the data, C_{D1} , C_{D2} , C_{D3} , Re_1 , Re_2 and Re_3 in function of K/D :

$$\begin{aligned}
 C_{D1} &= 1.17 \\
 C_{D2} &= 0.24 + 0.75 \exp \left(1.8 + \log \left(\frac{K}{D} \right) \right) \\
 C_{D3} &= 0.55 + 0.67 \exp \left(-\frac{(\log \left(\frac{K}{D} \right) + 1)^2}{6} \right) \\
 Re_1 &= 5.4 - 0.5 \exp \left(2.45 + \log \left(\frac{K}{D} \right) \right) \\
 Re_2 &= 5.9 - 1.15 \exp \left[0.7 \left(0.2 + \log \left(\frac{K}{D} \right) \right) \right] \\
 Re_3 &= 6.6 - 1.6 \exp \left[0.7 \left(0.2 + \log \left(\frac{K}{D} \right) \right) \right]
 \end{aligned} \tag{2.20}$$

The measurements of the St are not amenable to the procedure used for ordering the data on the mean drag coefficient as a function of K/D and Re . Basu (1985) used a different approach for St ; the measurements are grouped by roughness range and plotted versus Re . For smoother cylinders were found a lot of scatter. In the post critical regime, he noted a trend of increasing St with reducing roughness, poorly defined for smoother cylinders.

The RMS lift coefficient is also given in function of K/D :

$$\tilde{C}_L = 0.12 + 10 \left[\exp \left(1.36 \log \left(\frac{K}{D} \right) \right) \right] \tag{2.21}$$

However, the data available on the post critical RMS lift coefficient are very limited and the form proposed can be regarded only as a tentative.

Niemann & Holscher (1990) reviewed the effects of roughness on cylinders. He found that increasing roughness increases the critical and post critical drag with an asymptotic behavior for very large roughness. The values reported by Niemann & Holscher (1990) are similar to that one proposed by Basu (1985) and given in Eq. 2.20.

Uematsu & Yamada (1995) studied the effects of surface roughness and aspect ratio on cantilevered circular cylinders at high Reynolds numbers. The purpose of their study was to construct models of the aerodynamic coefficients

for full-scale application. Surface roughness was provided by gluing sand paper to the cylinder surface in order to obtain a post critical flow in the wind tunnel. The relative roughness K/D was in a range from $2.82 \cdot 10^{-3}$ to $1.070 \cdot 10^{-2}$. They verified that the aerodynamic forces on cantilevered cylinders in the post critical regime are mainly dependent on the roughness K/D of the cylinder. Using also data quote from [Basu \(1985\)](#) they found an equation between C_D and K/D in the post critical regime:

$$C_D = 0.51 + 0.67 \exp \left(- \frac{(\log (\frac{K}{D}) + 1)^2}{6} \right) \quad (2.22)$$

This equation is similar to Eq. 2.20 and it was obtained by using the least squares method. They also found a relation between the pressure rise $|C_{pb} - C_{pm}|$ and K/D in the post critical regime:

$$|C_{pb} - C_{pm}| = 1.28 - \exp \left(- \frac{(\log (\frac{K}{D}) + 1)^{2.5}}{10} \right) \quad (2.23)$$

indicating that the pressure rise decreases with increasing K/D . He found also the equation to describe the variation of these coefficients with the aspect ratio. These equations will be described in Sub Section 2.5.1.

[Chowdhury & Alam \(2013\)](#) experimentally studied the effect of surface roughness of textiles used in higher speed sports proposed two equations to determine the minimum drag coefficients and the critical Reynolds number as function of K/D :

$$\begin{aligned} C_{D_{min}} &= 0.043^{-1} \left(\frac{K}{D} - 0.23 \right) \\ Re_c &= -0.326^{-1} \left(\frac{K}{D} - 3.328 \right) 10^{-5} \end{aligned} \quad (2.24)$$

It was also observed that the relations proposed couldn't be evaluated with the same level of confidence for the knitted and woven textiles as the pattern of the roughness differs.

2.3.1.4 Simulation of high values of Re in wind tunnels using roughness

In wind-tunnel tests of circular cylinder, the Reynolds number is often limited to values that are very much smaller than those of the flow being simulated, in particular for very large structures as chimneys, cooling tower etc. In fact, the decrease in the size due to the scaling requires high wind velocities to obtain the same value of Re ; the velocity required can exceed those from the subsonic regime or the limit of the wind tunnels. Different researchers tried to simulate

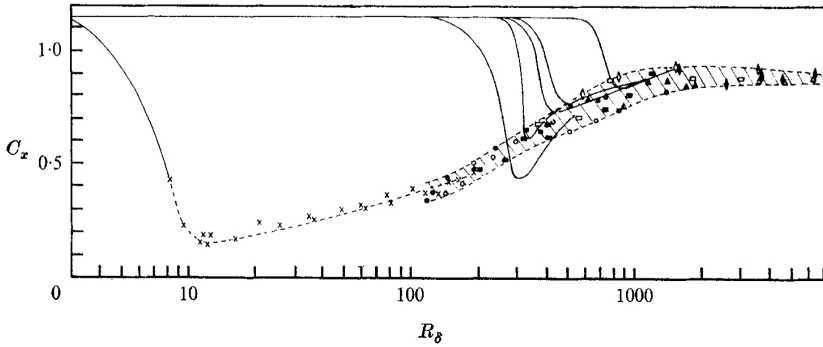


Figure 2.12: The drag C_D vs Re_K . (– Fage & Warsap (1930). Results obtained for roughened cylinders: \circ , $K/D = 1.5 \times 10^{-4}$. \bullet , $K/D = 4 \times 10^{-4}$. \blacksquare , $K/D = 6.7 \times 10^{-4}$. \blacktriangle , $K/D = 1 \times 10^{-3}$. \diamond , $K/D = 8 \times 10^{-4}$. \triangle , $K/D = 8.4 \times 10^{-3}$. \square , $K/D = 1.7 \times 10^{-3}$. \diamond , $K/D = 2 \times 10^{-3}$. – \times –, smooth cylinder with Re_K calculated by assuming $K/D = 3.5 \times 10^{-5}$). After Szechenyi (1975).

the pressure distribution in the post critical regime by means of surface roughness at lower values of Re in the same manner as increased diameter, speed or flow density would do.

The first attempt was done by Batham (1973). He concluded that the use of surface roughness to produce pressure distribution similar to those produced on high Reynolds numbers of $O(10^7)$ on smooth cylinders when the incident stream was turbulent is possible, but the pressure field was found to be completely different for uniform incident flow. Conclusions on the validity of the simulation of the amplitudes of the pressure fluctuations, associated with vortex shedding, by the use of roughness, cannot be drawn until high Reynolds number data are available.

Szechenyi (1975) observed that the cylinder surface condition has important effects on the value of the Reynolds number of transition. Szechenyi conducted tests in two different tunnel on cylinders roughened with calibrated spherical glass beads of seven different sizes, varying diameter from 0.04 to 0.7 mm. Experimental results reveals that for high values of K/D and of Re , C_D is no longer a function of D but only of K . He defined a dimensionless quantity $Re_K = UK/\nu$. At the higher values of Re_K , $C_D(Re_K)$ collapse onto a single curve within broad limits of experimental error (Figure 2.12). Szechenyi measured St across a wide range of $9.6 \cdot 10^4 < Re < 6.5 \cdot 10^6$ and a narrow range of $0.015\% < K/D < 0.2\%$ of a relatively small roughness. By using the spectrum of $\widehat{C}_L(t)$, the flow regimes were classified. The result show that the transition between the upper transition and post critical regime takes place at $Re_K = 200$

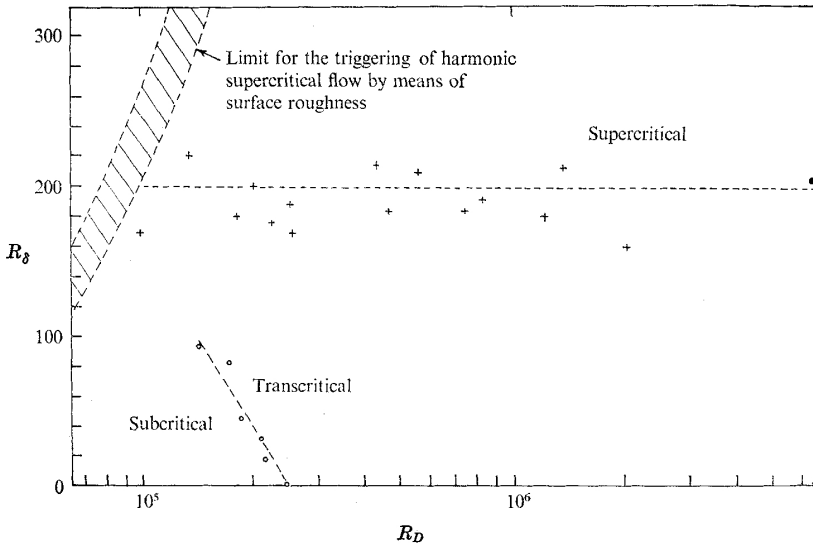


Figure 2.13: Limits of flow regimes in a plane Re_K vs Re . ● sub critical to upper transition; +, upper transition to post critical; ○, smooth cylinder when assuming $K/D = 3.5 \times 10^{-5}$. After [Szechenyi \(1975\)](#).

independently of D as in Figure 2.13. This criterion is valid only for his limited range of K/D values and can be used for simulating the post critical at low U using high values of K . The root mean square of $\widehat{C}_L(t)$ plotted against Re_K gives a coherent representation.

[Alemdaroğlu et al. \(1980\)](#) made an attempt to artificially increase the Reynolds number by means of surface roughness. Four circular cylinders with diameter of 20 mm, 32.4 mm, 41.4 mm and 59 mm were used. The surface was roughened with calibrated spherical glass beads of various sizes from 0.05 mm to 0.8 mm, or by simply covering them with calibrated abrasive paper. The acoustic far field pressures were measured with a capacitive microphone situated at a distance of 1122 mm above the cylinders. The simulation technique is evaluated by studying the influence of various grades of surface roughness on the far field vortex shedding noise and on the turbulent longitudinal velocity fluctuation spectra. The values of the coherence function corresponding to the critical Strouhal frequencies are intense in the sub critical regime, decrease sharply in the upper critical regime and then increase and stabilize in the post critical regime. They found that the critical Strouhal number and the coherence function values at these critical values showed decrease in the range of $Re_K = 100$ to 400. This Re_K range agrees adequately with the data published

by [Szechenyi \(1975\)](#). The high degree of agreement between these results and those of [Szechenyi \(1975\)](#) based upon pure aerodynamic measurements prove its power and accuracy in the range investigated.

[Güven *et al.* \(1980\)](#) used their and others data in the [Szechenyi's](#) correlation noting that the agreement is surprisingly good although the “broad limits of experimental error” ([Szechenyi, 1975](#)) become broader over the entire range of roughness Reynolds numbers of interest. This suggests that another parameter is needed to explain the scatter, which is not insignificant in magnitude. The two basic parameters proposed are Re and K/D . Re_K is no more than the product of these two parameters:

$$Re_K = Re \cdot \frac{K}{D} = \frac{UD}{\nu} \cdot \frac{K}{D} = \frac{UK}{\nu} \quad (2.25)$$

Their use separately is recommended by [Güven *et al.* \(1980\)](#) in order to re-establish Re as the primary measure of the overall influence of viscosity and to explain the scatter in the correlation of [Szechenyi](#).

[Buresti \(1981\)](#) confirmed that it is impossible to simulate high-Reynolds-number condition merely by requiring Re_K to be the same for model and prototype, as has been suggested by [Szechenyi \(1975\)](#). In fact, the pressure distribution, C_D and St are all functions of K/D , and of the type of surface roughness as well. A correct simulation should reproduce all the characteristics of the flow around the prototype and it should probably be possible, in principle, to find a suitable combination of Re and surface roughness to obtain the required characteristics, as previously stated by [Güven *et al.* \(1980\)](#).

[Achenbach & Heinecke \(1981\)](#) showed that the regularity of vortex shedding is not affected by increasing roughness in the whole range of roughness parameter examined. This was in contradiction to the results of [Szechenyi \(1975\)](#) that find the upper limit of K/D below which regular shedding occurred was $K/D = 120 \cdot 10^{-5}$ whereas for $K/D = 150 \cdot 10^{-5}$ no regular shedding was observed at a Reynolds number of $3.3 \cdot 10^6$.

[Nakamura & Tomonari \(1982\)](#) doubted about the validity of [Szechenyi \(1975\)](#) Reynolds number, Re_K . They observed that in the post critical range the base pressure coefficient is dependent on the roughness parameter, K/D , contrary to [Szechenyi \(1975\)](#). In this range, C_{pb} increase. [Nakamura & Tomonari \(1982\)](#) found a similarity parameter correlating the pressure distributions and C_D on circular cylinder with distributed roughness in the post critical range. The similarity parameter has the form:

$$(K/D)^m Re \quad (2.26)$$

They found that a similarity parameter with an exponent $m = 0.6$ can correlate the pressure distributions on the tested cylinders with distributed roughness. The results are presented in terms of base pressure coefficient C_p in [Figure 2.14](#). They correlated with the same approach the drag coefficients of spheres

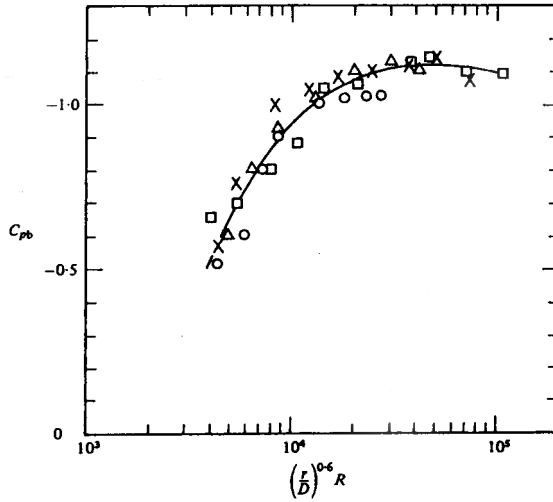


Figure 2.14: Base pressure coefficient C_{pb} Vs. $(K/D)^m Re$. After Nakamura & Tomonari (1982).

with different distributed roughness that Achenbach (1974) obtained in his measurements. Nakamura & Tomonari (1982) tried to explain the physical basis of this similar parameter. The most important physical parameter would be the height of roughness relative to the thickness of the viscous sublayer of the turbulent boundary layer, as observed by Nikuradse (1933) on the flow past rough pipes. The similarity parameter could be related to this ratio.

Lawson (1982) used a different approach. The ESDU Data Item 80025 (1980) A and B gives methods to evaluate the distribution of pressure around circular cylinders for all combinations of Re , K/D and I_u . All the parameters are described as a function of an equivalent Reynolds number, Re_e , given in Eq. 2.19. Lawson (1982) found that there is a minimum wind velocity below which it is impossible to reproduce high value of Re pressure distributions in smooth or simulated flow. He used the ESDU Data Item 80025 B to simulate shear flow condition at all location along a three-dimensional cylinder. Once a combination of K/D and wind velocity which gives good agreement is determined, the same combination will apply in a simulated shear flow, at all locations along a three-dimensional cylinder.

Duarte Ribeiro (1991a,b) tried to investigate which types of texture are more efficient in triggering a transition of the flow so as to simulate the mean and fluctuating pressures occurring at post critical Reynolds number on smooth cylinders at low wind velocity and if the flow field is the same. Experimental tests were performed on a cylinder machined from steel pipe. The first part of the experimental program (Duarte Ribeiro, 1991a) included measure-

ments of the mean force and pressure values for $5 \cdot 10^4 < Re < 4 \cdot 10^5$. Three types of texture were used: randomly distributed roughness made using sand paper ($K/D = 0.18\%$, 0.41% , 0.70% and 1.23%), two dimensional orderly distributed roughness made with wire mesh screen ($K/D = 0.23\%$, 0.41% , 0.70% and 1.22%) and one-dimensional orderly distributed roughness made using span-wise ribs ($K/D = 0.21\%$, 0.41% , 0.69% and 1.23%). The test were conducted in smooth flow, $I_u = 0.5\%$, for all the roughness types, and in turbulent flow, $I_u = 10.5\%$, for the ribs model. An increase in K/D , progressively distorts the mean pressure distribution results, in sense of deviating from what observed with smooth cylinders. The lines of minimum pressure and separation move a little to windward. With an increase in roughness, $|c_{pm}|$ decreases while $|c_{pb}|$ increases. The difference $c_{pb} - c_{pm}$ decreases steadily with an increase in roughness. This means that the mean pressure distribution becomes gradually distorted: the negative pressure peak diminishes, while the wake suctions increase. All these effect contribute to the increase of C_D . Duarte Ribeiro suggest to chose the smallest value of K/D sufficient to establish post critical conditions for simulation problems of cylindrical structures with circular cross-section and smooth surface. The comparison among the three types of textures showed that the sand paper was the least efficient in triggering regime transitions. The wire screen was more efficient but it had a relatively greater effect on the mean pressure and force coefficient. The ribs seems the most appropriate to be employed in simulation problems of cylindrical structures of circular section and smooth surface, because of its efficiency in establishing the post critical condition and because it does not interfere excessively with the mean forces and pressures. Duarte Ribeiro suggests using the ribs in simulation problems when the focus is restricted to a single flow direction, and distributed roughness around the entire surface when the focus is on the examination of several flow directions. The second part of the experimental program (Duarte Ribeiro, 1991b) included measurements of fluctuating forces and pressures. The results of models tested in smooth flow and fitted with all types of roughness revealed *RMS* and peak fluctuating values of $C_L(t)$ and of the pressure coefficients larger than those observed on smooth cylinders at high *Re* values. The results closest to those on smooth cylinders were obtained with the ribs model. The tests with the ribs revealed that the *rms* values of the force and pressure coefficient measured in smooth flow were practically identical with those measured in turbulent flow. The peak values, however, were 20 – 40% larger in the case of turbulent flow. In order to simulate the fluctuating pressures in cylindrical structures in smooth surface and circular cross section Duarte Ribeiro suggests using ribs model.

2.3.1.5 Computational results

Guven *et al.* (1977) noted that most of the available information about the effects of surface roughness on the flow past rounded structures, such as circular cylinders and hyperbolic cooling towers, has been obtained experimentally.

They presented a simple analytical model for two-dimensional mean flow at very large Reynolds numbers around a circular cylinder with distributed roughness. They compared the results of the theory with experimental data. The theory uses the wake-source potential-flow model of [Parkinson & Jandali \(1970\)](#) together with an extension to the case of rough-walled circular cylinder of the [Stratford \(1959\)-Townsend \(1961\)](#) theory for turbulent boundary-layer separation. In addition a semi-empirical relation between the base pressure coefficient and the location of separation is used. The results of the calculations definitely support the experimental observations. Of particular importance is the demonstration of the large influence of surface roughness on the pressure rise to separation, $C_{pb} - C_{pm}$, even at large Reynolds numbers.

[Kawamura *et al.* \(1986\)](#) carried out a series of computations on the flow around a cylinder with surface roughness. They didn't assume flow three-dimensionality and any explicit turbulence model. They used only a simple distortion of the grid cells. The height of the roughness considered was 0.5% of the diameter. The range of Reynolds numbers is $10^3 < Re < 10^5$. They developed a modified upwind scheme for the computation of high-Reynolds-number flows: the convectional second-order upwind is modified to eliminate the third error term. It was found that this scheme works very well at very high Reynolds number even with a limited number of mesh points such as 80×80 . They suggested that the reduction of drag is due to the small eddies generated on the surface near the separation points. A good agreement was found between the numerical results and the experimental results carried out by [Achenbach & Heinecke \(1981\)](#) in subcritical and critical range is reasonable. The flow in supercritical regime is not simulated well; the mesh employed are too coarse for the flow in the supercritical regime.

[Lakehal \(1999\)](#) studied the predictive capability of a computational modeling method for turbulent flows over rough-walled circular cylinders. The near-wall treatment procedure, based on a straight extension of the wall functions, was included in a Reynolds-averaged Navier-Stokes equation solver using the k/ε model. The surface effect is taken into account through the inclusion of a sink term in the momentum equations and a source term in the turbulent kinetic energy equation. The procedure employed to describe roughness effects on wall-bounded flows is based on an extension of the law of the wall that includes the roughness length z_0 for the determination of the velocity profile. The applicability of this model depends on the experimental correlation that relate z_0 to the relative roughness. The predicted results are found to agree well with the experimental data, including pressure and drag coefficient distributions.

[Mamou *et al.* \(2010\)](#) demonstrated the applicability of the $\kappa - \omega$ turbulence models for steady and unsteady flows with wall roughness effects for cases where the wake flow is expected to be highly unsteady. The performance of the Wilcox $\kappa - \omega$ turbulence models is explored in predicting the flow unsteadiness behavior past a fully rough circular cylinder at high Reynolds numbers. The computed drag and Strouhal number for a rough circular cylinder showed reasonably good

agreement with the experimental data.

Bimbato *et al.* (2013) carried out two-dimensional numerical simulations to study wake structures and flow dynamics past a circular cylinder. Based on a physical sense that roughness surfaces can promote turbulent flows a roughness surface model associated to the second-order velocity structure function model adapted to Lagrangian mesh-free Vortex Method is proposed. It was shown that the characteristics of high Reynolds number flows, like the drag crisis phenomenon, are well predicted by a two-dimensional roughness model. However, the comparisons between the numerical results and experimental ones were avoided due to the difficulty to determine exactly the roughness surface characteristics, especially the surface texture.

2.3.2 Non uniform and localized roughness

The non uniform and localized roughness are characterized by $err(\theta, z, t)$ that is non uniform or localized in ϑ . This condition leads to:

$$\frac{\partial |C_D|}{\partial \vartheta} \neq 0 \quad \frac{\partial |C_L|}{\partial \vartheta} \neq 0 \quad (2.27)$$

It means that the aerodynamic coefficients depend on the angle of attack. The aerodynamic variations observed are generated by the geometric imperfections that are not uniform on the surface. In the following, the non uniform and localized roughness are described.

2.3.2.1 Non uniform roughness

The non uniform roughness is a roughness non uniform in ϑ . In Section 2.3.1, except for some cases like the pyramidal surface roughness, the roughness simulated were of random nature. Many researchers tried to explain the effect of the roughness variability on the flow characteristics. Previous research can be classified in:

- Randomly varying roughness;
- Limited rough surface.

The first case are cylinders with a randomly varying roughness present on the entire surface. The latter leads to the case of localized roughness except for case of single roughness elements that will be treated in Section 2.3.2.2.

The first observation about the non uniformity of roughness was argued by Batham (1973). The cylinder tested was a machined aluminum without attempt to improve surface finish. He observed a strange peak at an angle of attack of 60° in the distribution of C'_p at the higher Reynolds number. This peak was

Table 2.7: Distribution of the sign of the lift C_L , when the critical regime is passed 28 times, after [Schewe \(1986\)](#).

	1	2	3	4	5	6	7	8	9	10	11	12	13	14
$Re \uparrow$	–	–	+	–	+	–	+	–	+	+	–	–	+	–
$Re \downarrow$	+	+	+	–	–	–	+	+	+	–	+	–	+	+

not due to the oscillating movement of the mean pressure distribution, but to a variation in the entire flow around the cylinder. This error was generated from the technique of acquisition of the data. As a matter of fact, they used a single pressure tips and they characterized the pressure on the entire surface by rotating the cylinder. He noted that the cylinder presented a different distribution of local surface roughness. He concluded that this variation in the roughness distribution caused the changes in the entire flow when the cylinder was rotated.

[Schewe \(1986\)](#) studied the influence of microscopic changes in the cylinder's surface on the entire structure of the flow. He tested a polished cylinder with a roughness of about $K = 1 \mu m$ ($K/D = 10^{-5}$). He set the flow speed at a critical Reynolds number in small steps. When the flow was approximately at the critical value, a natural perturbation provoked a transition jump in a few minutes. It was evaluated the characteristic time of transition that was approximately $\Delta t = 0.15 s$. The characteristic time is the time required for a transition from laminar to turbulent ($Re \uparrow$) or vice versa ($Re \downarrow$). He evaluated a statistic analysis of the sign of C_L (Table 2.7). The number of samples was small for a serious statistic study but a probability of occurrence of both sign nearly equal was found. He concluded that the sign of transition was generated by the presence of random imperfection on the surface. In order to better understand the effects of the small imperfections on the aerodynamics, he forced the transition by an artificial small perturbation. The perturbation was a little movable pin with diameter $d = 0.8 mm$. This pin was installed into the surface of the cylinder and allowed for the change of the angular position, ϕ , by rotating the cylinder, and the variation of the height of ejection from $0 mm$ to $3 mm$. The flow in the tunnel was set to a critical value and then the pin was made protrude from the surface into the flow. The transition occurred and the pin was totally retracted. The flow persisted in the new state for the aerodynamic hysteresis. In order to trip the transition the perturbation had to lie in the range $45^\circ < \phi < 60^\circ$. In this zone, τ_o and the deceleration of the fluid are higher ([Achenbach, 1968](#)). The characteristic time of transition with the pin was approximately $\Delta t = 0.1 s$.

[Miyata et al. \(1994\)](#) studied the effect of roughness geometry on the aerodynamic characteristics. They demonstrated the importance to consider not only the average surface roughness, but the distribution of surface roughness too. They concluded that the relationship between surface roughness pattern

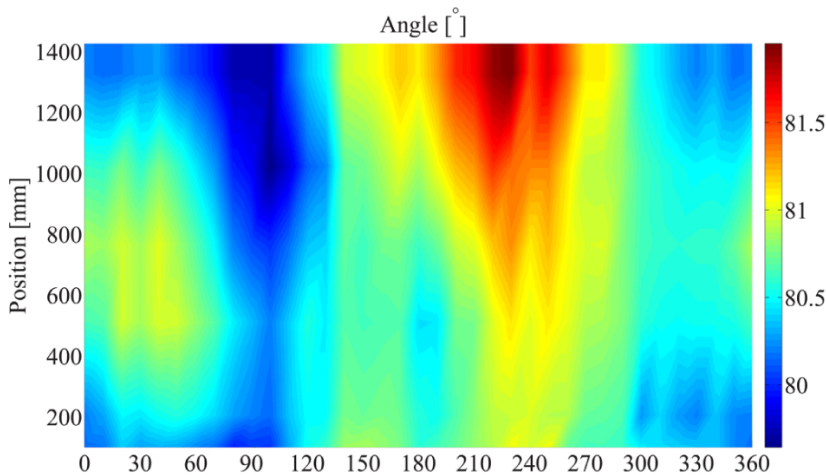


Figure 2.15: Horizontal projection of the cable model radius, after [Matteoni & Georgakis \(2012b\)](#).

and aerodynamic characteristics need to be further studied.

[Matteoni & Georgakis \(2012b\)](#), recently, investigated the effects of surface roughness and cross-sectional distortion of cable on the aerodynamic force coefficients of cross flow and inclined/yawed cylinder. Detailed measurement of roughness was performed for the characterization of the surface irregularities. The first, for the determination of the average roughness, was performed with a silicone replica and a 3D optical measurement device in different position on the cable in order to evidence the variability of the roughness average along the surface. The second, for the determination of the local radius, was performed with an analogue displacement transducer with a precision of 0.0014 mm . The spatial deviation of K was very high, from value of $0.7\text{ }\mu\text{m}$ to $3\text{ }\mu\text{m}$. The shape measurements showed a maximum diameter deviation of 1.25% (Figure 2.15). They performed test of cable varying the angle of attack. They found a perfect repeatability for the same angle of attack and variation of the aerodynamic coefficients when the cable is axially rotated. This observation indicates that roughness variation plays a determinant role in modifying the flow structure around the cable. These changes in the aerodynamic coefficients were generated by roughness alteration or distortions of the shape and were more evident on C_L . They concluded that for cables with a non-uniform distribution of surface roughness the average behavior cannot be predicted.

The effects of partially roughness on the aerodynamics of circular cylinders were reported in many works.

First tests were carried out by [Fage & Warsap \(1930\)](#). They investigated the effect of partially roughened surface of a circular cylinder with glass paper. They

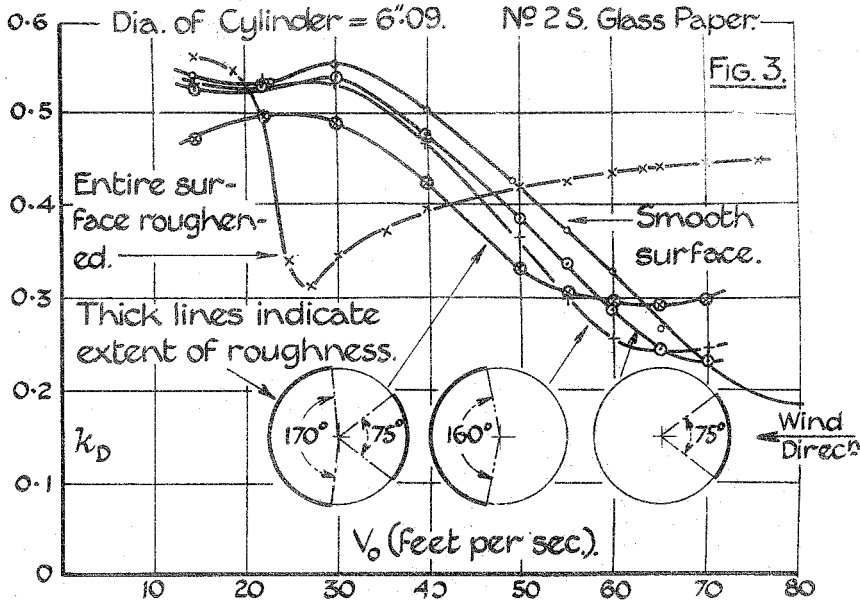


Figure 2.16: Effect on $K_D = (1/2) C_D$ of limited rough surface, after Fage & Warsap (1930).

tested three different symmetric conditions: the windward area $0^\circ < \theta < 37.5^\circ$, the windward area $0^\circ < \theta < 37.5^\circ$ and the leeward area $95^\circ < \theta < 180^\circ$ and the leeward area $100^\circ < \theta < 180^\circ$. The tests result is shown in Figure 2.16. They concluded that the flow is very sensitive to surface roughness in the symmetric regions $37.5^\circ < \theta < 100^\circ$ where the flow separates from the surface.

Okajima & Nakamura (1973) tested a short cylinder in the Reynolds range $4 \cdot 10^5 < Re < 2 \cdot 10^6$ for four different configurations fully and partly roughened cylinder. The symmetric configurations were: $50^\circ < \theta < 130^\circ$, $0^\circ < \theta < 180^\circ$, $0^\circ < \theta < 50^\circ$ and $\theta = 50^\circ$. They found similar results to Fage & Warsap (1930).

Nakamura & Tomonari (1982) studied the effects of the roughness symmetric strip about circular cylinder on the mean pressure distribution and the Strouhal number in the Reynolds range $4 \cdot 10^4 < Re < 1.7 \cdot 10^6$. They tested five different configurations; in all configuration there was a roughness strip of 2 cm with 3.2 mm roughness element placed symmetrical at $\theta = 50^\circ$, in the first configuration the cylinder was smooth, in the other four there was a distributed roughness over $50^\circ < \theta < 180^\circ$ with roughness particles of diameter 0.56 mm, 115 μm , 58 μm and 40 μm . They discovered that applying a strip of roughness at 50° rather than uniformly covering the entire model could produce Reynolds-number-independence.

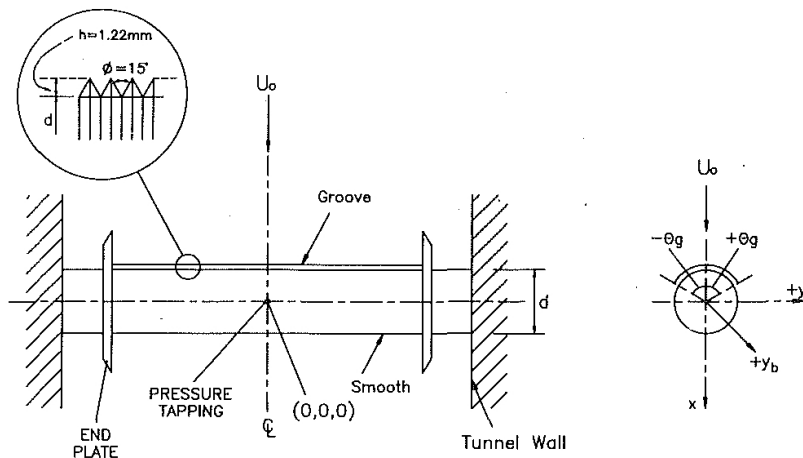


Figure 2.17: Schematic diagram of V-groove circular cylinder, after [Leung et al. \(1992\)](#).

[Leung et al. \(1992\)](#) performed measurement of the mean pressure distribution and Strouhal numbers on partially grooved cylinders with different groove subtend angles for a Reynolds range $2 \cdot 10^4 < Re < 1.3 \cdot 10^5$. They used a V-groove of height of 1.22 mm and with the angle of V of 15° (Figure 2.17). They tested a symmetric configuration with a subtend angle θ_g of grooves from $\pm 30^\circ$ to $\pm 165^\circ$ and two asymmetric configuration with $0^\circ < \theta_g < 180^\circ$ and $0^\circ < \theta_g < 75^\circ$. They observed, for the symmetric case, in the range from $\pm 30^\circ$ to $\pm 75^\circ$ a progressive shift of the flow regimes to lower Re with increasing groove subtend angle. At larger angle they didn't observe shift of the flow regime but only change in the drag coefficient and Strouhal number until $\pm 120^\circ$. They found the lowest value of Reynolds in the range of $\theta_g = \pm 75^\circ$. For the asymmetric case with $0^\circ < \theta_g < 75^\circ$ they found higher C_L and lower C_D . The increase in C_L is found to be associated with the different boundary layers developed at the smooth and groove halves, causing a downward shift of the wake and higher mean velocity on the smooth half side. Of the two vortex sheets the one sheds from the smooth half is much more dominant.

[Leung et al. \(1997\)](#) studied the transition characteristics of flow over an asymmetrically grooved circular cylinder. They used a V-groove of height of 1.22 mm and with the angle of V of 15° (Figure 2.17) in an asymmetric configuration with $0^\circ < \theta_g < 75^\circ$. Two flow configurations, subcritical-critical and subcritical-upper transition, respectively have been identified within the Reynolds number range $4.4 \cdot 10^4 < Re < 1.3 \cdot 10^5$. Within this Reynolds number range the flow over the smooth side of the cylinder lies within the sub-critical regime while that on the grooved side transits from the critical to the upper

transition regime at $Re = 7.2 \cdot 10^4$ and remains at this regime further increasing Re . The subcritical-critical flow is characterized by asymmetric pressure profiles, lower drag coefficient, higher Strouhal number, and the presence of a short separation bubble. The subcritical-upper transition flow is characterized by higher drag coefficient, lower lift coefficient and lower Strouhal number.

Matteoni & Georgakis (2012b) tested the effects of a commercial label distributed along the length of the HDPE tubing. The height of indentation was not constant but ranged in the interval of $50 \mu m$ to $100 \mu m$. They found that the role of labeling roughness is triggering flow transitions and they observed opposite sign of the lift coefficient for the two symmetric tested angles-of attack. Based on the development of the drag coefficient they assumed that the role of the indented labeling is similar to that of a tripping wire installed on the surface of a circular cylinder at a critical angular position.

2.3.2.2 Localized roughness

Many researchers have addressed the problem of the localized roughness. This kind of roughness is generated by rough elements named protrusions with smaller dimension compared with the cylinder diameter. According to the number of protrusions that create the roughness, the localized roughness can be classified in:

- Single discrete roughness element;
- Pairs or groups of discrete roughness element.

Prandtl (1914) was the first that explained the reduction in drag of a sphere after a certain Reynolds number that was due to the transition of flow in the boundary layer from laminar to turbulent. He demonstrated that a wire could initiate a transition from laminar to turbulent flow before. The first study on cylinder with localized roughness was performed by Fage & Warsap (1930). They attached two straight tripping wires of diameter d at $\theta = \pm 65^\circ$ and $\theta = \pm 25^\circ$ onto a smooth cylinder. A set of five wires, $0.02\% < d/D < 0.3\%$, was tested in the Reynolds range $90 \cdot 10^3 < Re < 26.2 \cdot 10^4$. The tests result is shown in Figure 2.18. They observed that if the wire diameter is greater than the thickness of the boundary layer, the flow would necessarily detach from the surface. The other parameter important is the position of the wire. The effect become less severe as the wires are removed away from the regions where the boundary layer separates from the surface. Also in the case $\theta = \pm 25^\circ$ (wires placed near the stagnation line) there were no effect on the pressure distribution. They demonstrated that the effect of free stream turbulence or surface roughness was similar to the disturbances created by symmetrically located tripping wires.

Many researchers studied the aerodynamics effects of one single protrusion on cylinders. The first study was performed by Lockwood & McKinney (1960). They studied the effect of the application of one flap attached normal to the

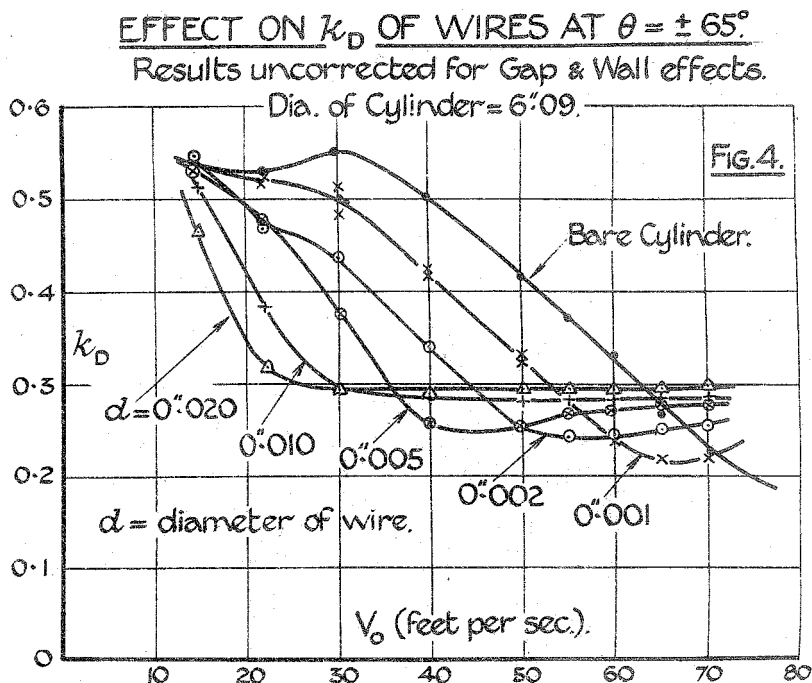


Figure 2.18: Effect on $K_D = (1/2) C_D$ of tripping wire at $\theta = \pm 65^\circ$, after Fage & Warsap (1930).

surface. All flaps were tested through a range of angular positions. The cylinder was constructed of mahogany and lacquered. A set of two flaps, with chords of 0.37% and 6% of the diameter, were tested in the range $1.35 \cdot 10^3 < Re < 1.58 \cdot 10^4$. The drag and lift coefficients were influenced by the flux velocity, angular position and flaps dimension.

James & Truong (1972) studied the steady state aerodynamic characteristics, in the transition range of Reynolds numbers, for a circular cylinder with a small spanwise protrusion and a step. The data showed that the two types of protuberance shapes are nearly identical in their effect on the aerodynamic characteristics, and their effect depends much more on location than on the size. The flow field was studied too by using hot wire anemometry. The changes of C_D and C_L and the changes in the boundary layer happened caused by the interaction of the protrusion with the fluid. They didn't measure the unsteady forces.

ESDU 80025 (1980) gives the drag coefficient, C_D , and lift coefficient, C_L , as a function of Re_e (Eq. 2.19) for a single span wise protrusion. The effect of the protrusion is twofold: it makes the C_D significantly greater than the

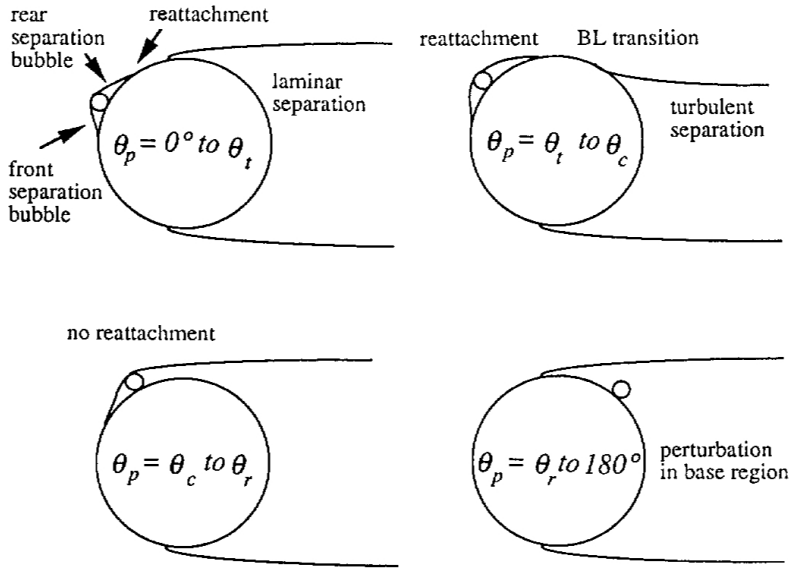


Figure 2.19: Schematic of the different flow regimes as a function of the perturbation angular position, after [Nebres & Batill \(1993\)](#).

plain cylinder and make the section asymmetrical with the result that a C_L is induced. The data are given for $d/D = 0.005, 0.03$ and 0.06 and $\vartheta = 30^\circ, 65^\circ$ and 90° . The data are given for different shape of protrusion like plate-ridge, cylindrical ridge and icing-droplet ridge. The idea is that C_D and C_L tend to be independent of the protrusion shape. The data can be used if a gap exist between the cylinder and the protrusion surface assuming for the protrusion height $d + h$ if the gap, h , is not too large (less than about $0.25D$). The data can also be used if roughness and turbulence are present.

After the first attempts, it was clear that the effects of one single protrusion were described by three governing parameters: the non-dimensional size of the protrusion d/D , the non-dimensional wind speed Re and the cylindrical position of the protrusion ϑ_p .

[Nebres & Batill \(1993\)](#) conducted experimental study of the flow around a cylinder with a single large scale straight perturbation. The size of the perturbation was varied from about the size of the boundary layer thickness, δ , to about 20δ . The boundary layer thickness for the circular cylinder was estimated using the Blasius method. The Reynolds number range was $1 \cdot 10^4 < Re < 4 \cdot 10^4$. They studied the variation of the Strouhal number with the position of the perturbation. They found three characteristic angular positions, θ_t , θ_c and θ_r that classify the flow in four patterns in function of the angular position. The three

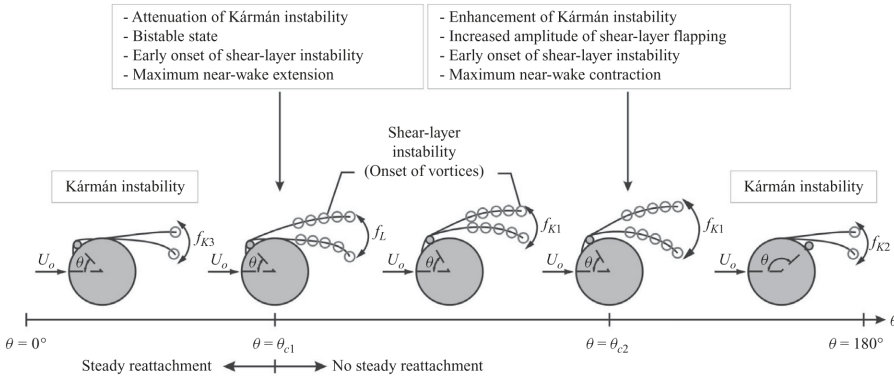


Figure 2.20: Flow regimes as a function of angular position of the wire, after [Ekmekci & Rockwell \(2010\)](#).

characteristic angular positions were expressed in function of different Re and different d/D . The four flow regimes are shown in Figure 2.19 in function of θ_P , the position of the protrusion. In the first regime, separation occurred at the same angle of a smooth cylinder. A small lift was generated due to the geometric asymmetry. In the second regime, the reattached boundary-layer delays the final separation and the Strouhal number increases to its maximum value; a separation bubble appeared. The lift as well as the base pressure increased, and the drag decreased. In the third regime, no reattachment was observed and the Strouhal number dropped to its minimum. The base pressure decreased and the drag increased. In the fourth regime, the perturbation is inside the base region and not affecting the flow and no lift was developed despite a geometric asymmetry.

[Ekmekci & Rockwell \(2010\)](#) studied the flow structures around a stationary cylinder with a single wire having a diameter approximately two orders of magnitude smaller than the cylinder at $Re = 1 \cdot 10^4$ with the PIV technique. They found that a single wire mounted spanwise along the surface of the cylinder, perturbs only the shear layers on the wire side of the cylinder. They identified two distinct critical angles. At one critical angle, θ_{c1} , substantial extension of the time-averaged near-wake bubble occurs, and at the other critical angle, θ_{c2} , significant contraction. The flow regimes as a function of the angular position of the wire are shown in Figure 2.20.

[Ekmekci & Rockwell \(2011\)](#) evaluated the effect of the scale of the spanwise wire on the global flow structures at $Re = 1 \cdot 10^4$ with the PIV technique. They found that the critical angles ([Ekmekci & Rockwell, 2010](#)) depends on the wire scale too; the smaller the wire, the larger the critical angle. They used three wires with $d/D = 0.029, 0.012$ and 0.005 . The two big wires induce bistable shear-layer oscillations when placed at their respective critical angles. These

oscillations have irregular time intervals that are much longer than the time scale associated with the classical Kármán instability. Moreover, the large-scale wire can either significantly attenuate or intensify the Kármán mode of vortex shedding at the critical states; the small-scale wires do not notably alter the strength of the Kármán instability.

Many researchers studied the aerodynamic effects of two single symmetric protrusions on cylinders. ESDU 80025 (1980) gives the drag and the lift coefficients for two plate protrusion symmetrically mounted 180° apart, with $d/D = 0.06$ for all the regime of flow with the correction for uniform distributed roughness and turbulence.

Aiba *et al.* (1979) affixed two spanwise wires ($d/D = 0.0046$), at locations $\theta = \pm 65^\circ$ from the forward stagnation point on the cylinder surface. The Reynolds number ranged from $12 \cdot 10^3 < Re < 52 \cdot 10^3$. Their study clarified the interactions between the heat transfer and the flow. Particularly, the heat transfer from cylinder to the flow is found to be closely related to the width of the near wake.

Lee & Kim (1997) studied the effects of three small wires ($d/D = 0.075$) wrapped helically with pitches of $5D$ and $10D$ in a Reynolds range of $5 \cdot 10^3 < Re < 5 \cdot 10^4$. They found that the surface protrusions make the near wake to have periodic structure along the spanwise direction. It is also observed that the surface protrusions elongate the vortex formation region, decrease the vortex shedding frequency and shrink the wake width. The flow visualization showed a periodic structure along the spanwise direction.

Hover *et al.* (2001) studied the flow around a circular cylinder oscillating and non oscillating with two symmetrical wires in a Reynolds range of $1.5 \cdot 10^4 < Re < 4.5 \cdot 10^4$. They used a cylinder with diameter of 7.62 cm and two wires of diameter $d = 0.23\text{ mm}$ located at $\pm 70^\circ$. They measured the drag coefficient, Strouhal number and lift coefficient and found that for $Re > 2 \cdot 10^4$ the two wires can reduce the lift and drag and increase the Strouhal number.

Similarly to the case of the single protrusion, the aerodynamic effects of two symmetric single protrusions were described by three governing parameters: the non-dimensional dimension of the protrusion d/D , the non-dimensional wind speed Re and the cylindrical position of the protrusion $\pm \theta_p$.

Fujita *et al.* (1985) investigated the effect of two-dimensional protuberances on the drag and heat transfer of circular cylinders in cross flow at $Re = 5 \cdot 10^4$, using a cylinder with $D = 50\text{ mm}$ to which two wires of the diameter, $0.1\text{ mm} < d < 2\text{ mm}$, were attached at two symmetrical positions of an angle θ from the frontal stagnation point. They classified, from the measure of pressure distribution, three patterns in function of the size of the wires and the position. The first pattern has the pressure distribution similar to a bare cylinder and the influence of the wire is observed only near the wire. The second pattern also shows a separation bubble behind the wire; however, the final separation angle from the cylinder surface is larger than that of a smooth cylinder. The third pattern is when flow separates at the wire with no reattachment to the cylinder

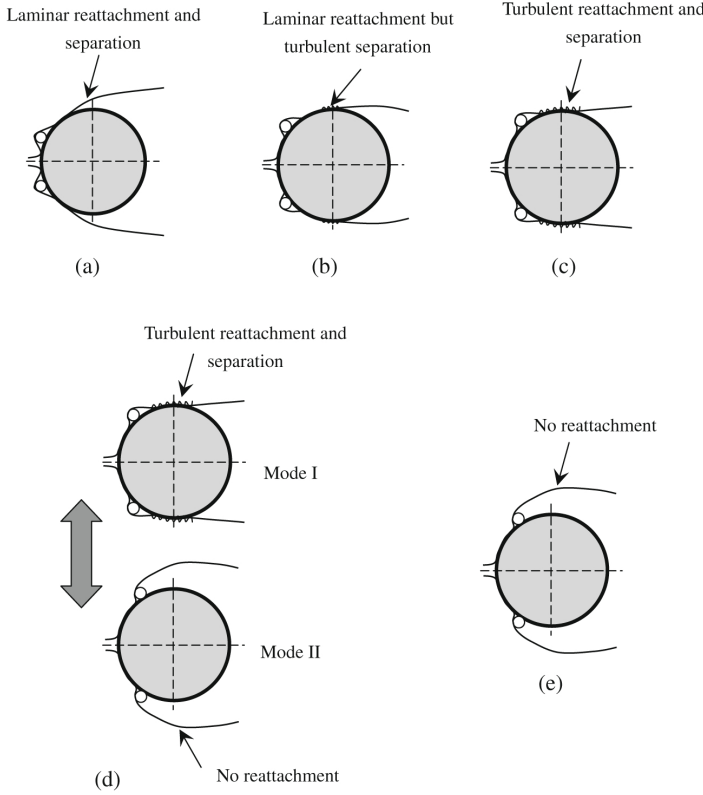


Figure 2.21: Sketch of flow separation: (a) Regime A, (b) B, (c) C, (d) D, (e) E. After Alam *et al.* (2010).

surface. In function of the pattern they found three different conditions of C_D and St :

$$\begin{aligned}
 \text{Pattern 1 : } C_D &= C_{D0} & St &= St_0 \\
 \text{Pattern 2 : } C_D &< C_{D0} & St &> St_0 \\
 \text{Pattern 3 : } C_D &> C_{D0} & St &< St_0
 \end{aligned} \tag{2.28}$$

where a subscript $_0$ represents the perfect cylinder case. They found some relation between the drag coefficient and the back pressure coefficient C_{pb} .

Igarashi (1986) studied the effect of tripping wires on the transition in a boundary layer on a circular cylinder in cross flow. Three circular cylinders of 34, 40 and 50 mm in acrylic resin were tested. The tripping wires are stainless steel tubes of $d_0 = 0.4, 0.6, 0.7, 0.8$ and 1 mm in diameter at angular position from front stagnation line of $\beta = 50^\circ$ and 60° . The Reynolds number range was $1.3 \cdot 10^3 < Re < 9.6 \cdot 10^4$. They measured the pressure distribution around the cylinder and by integration C_D, C_L, St . He found four patterns. In the first

pattern, A, the value of C_D and St is nearly equal to that of smooth cylinder. In the second pattern, B, the value of C_D decreases to 0.6 and the value of St increases with Re . In the third pattern, C, C_D is about 0.5 and the value of St is about $0.29 \div 0.30$. In the fourth pattern, D, C_D increases remarkably to 1.55 and St is about $0.17 \div 0.18$; this condition happens when the cable diameter is $d = 0.7 \div 1 \text{ mm}$. The flow condition for pattern A, B, C and D are similar to those found by Nebres & Batill (1993) in Figure 2.19. The pattern depends on the size and angular position of the protrusions and on the Reynolds number.

Alam *et al.* (2003) studied the effect of two symmetric tripping rods ($d/D = 8\%$, 10% and 12%) on flow characteristics and fluid forces at a Reynolds number of $5.5 \cdot 10^4$. They found that the optimum angular position for reduce the drag and lift coefficients was 30° . Using the oil visualization they found three different flow patterns in function of the angular position. In the first pattern ($\vartheta = 20^\circ - 40^\circ$), A, the boundary layers that separated from the tripping rods reattached on the cylinder surface behind the tripping rods, and finally laminar separation occurred from the cylinder surface and the fluid forces were reduced significantly and the Strouhal numbers were higher than one smooth cylinder. In the second pattern ($\vartheta = 45^\circ - 46^\circ$), B, the boundary layers separated from the cylinder surface at a position sufficiently upstream of the tripping rods, and the tripping rods forced the separated boundary layer to deflect outwards, causing a stronger vortex behind the cylinder. In the third flow pattern ($\vartheta = 41^\circ - 44^\circ$), C, flow patterns A and B intermittently appeared and switched from one to the other.

Alam *et al.* (2010) studied the flow around a circular cylinder with two symmetrical wires attached in a range angle $10^\circ < \theta < 70^\circ$ in a Reynolds range $2.5 \cdot 10^3 < Re < 6 \cdot 10^4$. The wires diameter were $0.045D$. They measured the force on the cylinder, the flow characteristics using a hotwire and perform PIV measurements and flow visualization. They classified the flow in five patterns in function of the wires position. In Regime A, $\vartheta < 20^\circ$, the forces, St and $St-Re$ relationship are similar of that in a smooth cylinder. In Regime B, $20^\circ < \theta < 35^\circ$, C_D decrease and St escalates with increasing θ . In Regime C, $35^\circ < \theta < 40^\circ$, C_D decreases rapidly. In Regime D, $40^\circ < \theta < 45^\circ$, the flow switches randomly in two distinct stable modes; the instantaneous drag and St display drastic up-and-down jumps. Regime E occurs at $45^\circ < \theta < 70^\circ$, where C_D are large and St is small. The flow classification is shown in Figure 2.21. The $Re-St$ relationship is distinct from one regime to another. In Regime A, St is insensitive to Re similarly to a plain cylinder wake. This is not unexpected because both cases are characterized by a laminar flow separation. St displays a significant variation with increasing Re in Regimes B and C, which are characterized by turbulent flow separation. In the two regimes, transition to turbulence occurs in the reattached boundary layer and shifts towards the tripwire with increasing Re , resulting in a postponed separation and subsequently an increase in St . In Regime E, laminar separation occurs, though earlier compared with a plain cylinder wake or Regime A.

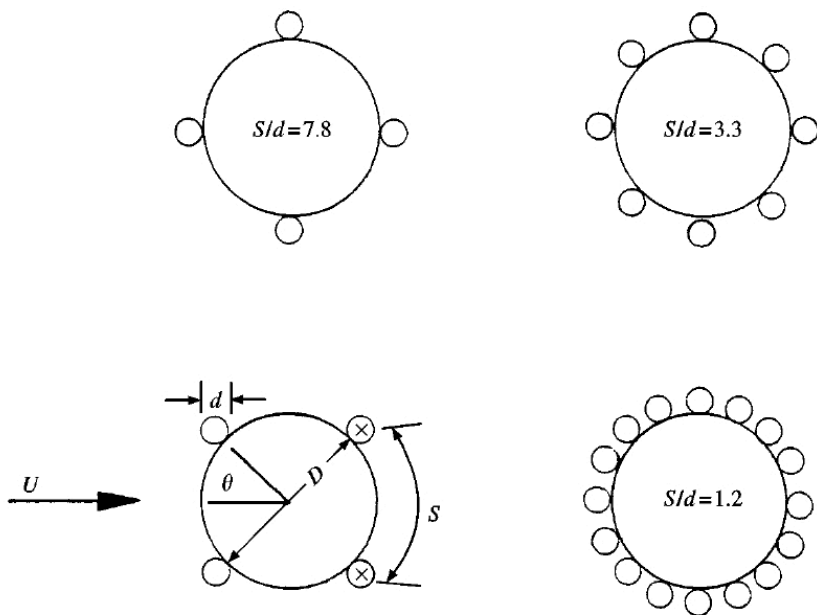


Figure 2.22: Schematic of cross-section for various model for $d/D=0.09$, from Nigim & Batill (1997).

The case of a group of protrusions was investigated by Nigim & Batill (1997). They performed some experiments for the characterization of the aerodynamics of a cylinder, $D = 44.5 \text{ mm}$, with two dimensional surface perturbations at a Reynolds number of $3 \cdot 10^4$. They tested three cylinders with four, eight and sixteen wires equally spaced. The parameter chosen to describe the configuration was S/D , where S is the distance between two wires. The tested configurations of cylinder are shown in Figure 2.22. They used the classification of surface perturbation proposed by Perry *et al.* (1969). They divided the surface perturbation in two categories in function of the spacing-to-height ratio. The k -type, with big ratio, has the vortices shed into the flow from the space between the perturbations, instead the d -type has the vortices are entirely in the cavities. Nigim & Batill found that $S/D = 3$ is the boundary between k and d -type perturbation. For $S/D > 3$, the perturbation are k -type and a small variation of the angle of attack can lead to significant variations in the drag coefficient and vortex-shedding frequency. It means that there is a big dependence with respect to the angle of attack. For $S/D < 3$, the perturbation are d -type and the drag coefficient is almost constant and less than that obtained for a smooth cylinder, and Strouhal number is almost constant and more than for a smooth cylinder. They found insensitivity to small variation of d/D .

Many researchers also tried to simulate high Reynolds at model scale using single spanwise protrusion, as in the case of uniform roughness explain in Section 2.3.1.4. Pearcey *et al.* (1982) concluded the diameter of tripping wires must be quite large to change a very low Reynolds flow to critical flow. Kareem & Cheng (1999) studied the flow on a circular finite height cylinder with two dimensional discrete surface roughness element. Among the various surface roughness types considered for simulating the high Reynolds number flow around cylindrical structures, the two-dimensional roughness elements of $d/D = 0.0067, 0.02$ at $\theta = \pm 65^\circ, \pm 115^\circ$ best simulated the post critical flow around the surface of a circular cylinder at a Reynolds number as low as $2.5 \cdot 10^4$. The surface pressure measured on the model with the optimal surface roughness elements has the characteristics of high Reynolds number flow.

2.3.3 Wet cylinders

Ever since being first observed over three decades ago (e.g., Wianecki (1979)), problematic vibrations of cables induced by the combination of wind and rain have been a concern to the bridge engineering community. Hikami & Shiraishi (1988) observed strong influences of the rain on cable vibrations during the construction period of the Meiko Nishi Bridge which is located at inlet of Nagoya Harbor in Japan. The cables, manifestly stable with respect to wind action under dry conditions, became very unstable with the rain. The vibrations are characterized by a much lower frequency than a vortex induced oscillation and by much higher amplitude. They explained the phenomenon attributing the rainwater rivulet formed along the upper windward surface of cable that makes the apparent cable cross-section aerodynamically unstable. They called this phenomenon *Rain-Wind Induced Vibration* (RWIV).

RWIV is a complex phenomenon that can occur when rain and wind acting simultaneously on bridge cables. Caused by wind and gravity the rainwater forms small rivulets, which flow down on the surface of the cable. The rivulets disturb the wind flow around the cross section and cause a modified unsymmetrical distribution of the surrounding wind pressure. Driven by the initial movement of the cable the rivulets oscillate on the cylinder's surface that entails to periodical exciting forces in the frequency of the cable. This can lead to an aero-elastic excitation and a continuous input of energy into the vibrating system. The vibrations can reach amplitudes as high as several diameters of the cable, and therefore pose a significant threat to the safety and serviceability of cable systems.

Excluding the aero-elastic effects (not dealt with in this review), the RWIV provoke a variation of the shape of the section due to the presence of rivulets similar to the case of the protrusions described in Section 2.3.2.2. The rivulets can move with temporal scale similar to the dynamic scale of the cable. For this reason, this disturbance is classified as temporal dependent.

In the years, many researchers tried to characterize the complex aerodynamic

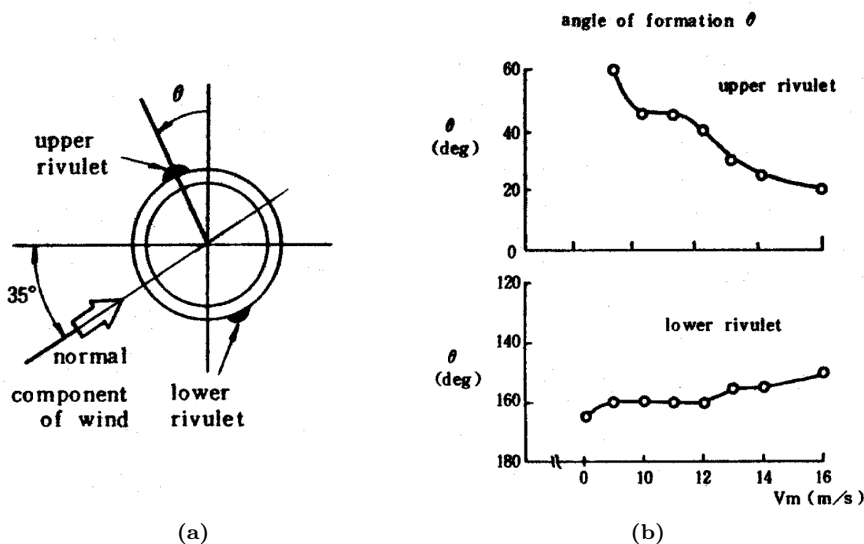


Figure 2.23: Rivulets definitions (a), variation of rivulets positions vs. wind speed for stationary cable (b). After Hikami & Shiraishi (1988).

behavior of the RWIV. In particular, researches was focused on:

- Evaluation of the aerodynamic properties of cylinders with artificial fixed protrusions;
- Evaluation of the aerodynamic properties of cylinders with real rivulets;
- Evaluation of the trajectories of the rivulets;
- Evaluation of the effect of the cylinder surface condition on the rivulets.

2.3.3.1 Wind tunnel tests

Hikami & Shiraishi (1988) investigated the role of upper rivulet by means of constructing the upper and lower rivulet separately (pouring the water directly on the cable surface) and by measuring the aerodynamic forces. They tested an inclined cylinder with the yaw angle equal to 45° and the inclination equal to 45° (declining). The definition of the angles of the upper and lower rivulets is shown in Figure 2.23a. When the wind speed is lower than a certain threshold, the rain drops slide down the surface. For higher velocity, the air forces on the raindrops overcome the gravity so that the water doesn't fall down but become the constituent of an upper rivulet. The variation of the upper and lower rivulet position for different wind speed is shown in Figure 2.23b.

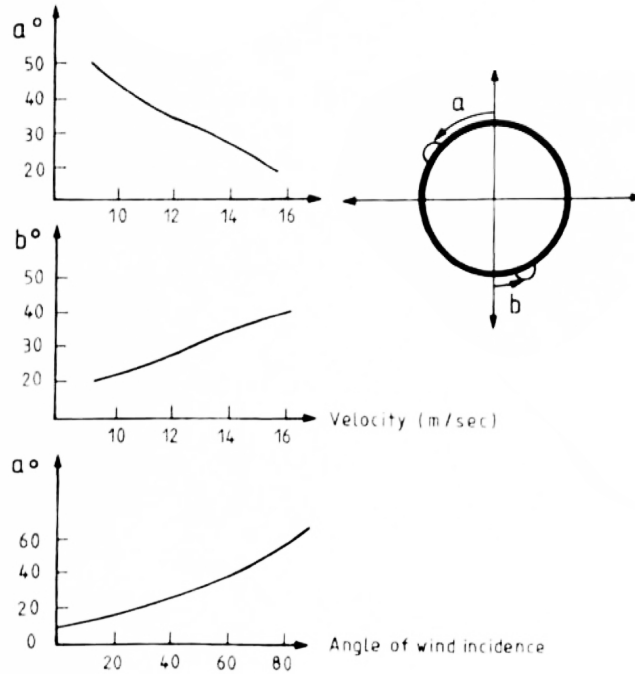


Figure 2.24: Variation of rivulet position with wind speed and direction, after Bosdogianni & Olivari (1996).

Flamand (1995) observed that RWIV depends on physical parameters such as cable size and shape, surface roughness and wettability. He carried out different tests with two kinds of materials, PE (polyethylene) and PP (polypropylene) smooth tubes. When the surface is coated with soot resulting from fuel-oil combustion, which is similar to atmospheric pollution, material surface is not water-repellent and the upper rivulet appears and oscillates.

Bosdogianni & Olivari (1996) experimentally investigated the rivulet position of a stationary cylinder in the Reynolds range $0 < Re < 4.2 \cdot 10^4$. The model was placed in the wind tunnel with an inclination of 45° . The experiments consisted in flow visualizations using thin oil mixed with white titanium dioxide flowing free on the cylinder surface and accumulating in a position expected to correspond to the actual position of the rain-associated rivulets. In Figure 2.24 is shown the position of the upper and lower rivulets for different wind speed for a yaw angle equal to 0° and the position of the upper rivulet for different yaw angles. They performed flow visualizations for different angles of the wind incidence and observed that there is no formation of the rivulet for all the negative yaw angles, and that the formation is more pronounced for the yaw

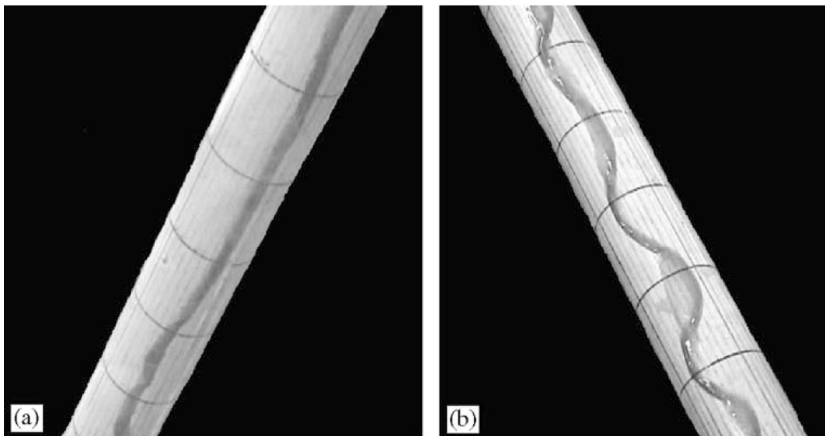


Figure 2.25: Rivulets on the cylinder at a $U = 9 \text{ m/s}$, and $Q = 8.0 \text{ l/h}$: (a) Windward rivulet at $\theta \approx -160^\circ$; (b) leeward rivulet at $\theta \approx 30^\circ$, after Wang *et al.* (2005).

angles between 0° and 45° . During the experiments dependence of rivulets formation on wind velocity was found. There is no formation of the rivulets for low wind velocities. For a velocity of 5.5 m/s the liquid tends to flow down the cylinder surface, and the rivulets began to form clearly at a wind velocity above 7.5 m/s and then they tend to climb up the cylinder surface as the wind velocity approaches 16 m/s . This tendency of both rivulets to climb up the cylinder surface as the wind velocity increases can be seen clearly from Figure 2.24. Moreover, from the third diagram of Figure 2.24 it is apparent that, as the angle of the wind incidence increase from 0° to 90° , the climbing tendency of the rivulets decreases for the whole range of the wind velocities.

Matsumoto *et al.* (2001) experimentally measured the total aerodynamic lift force of the cable model and the pressure distribution along the cable axis with an artificial water rivulet attached on the model varying the rivulet position from the stagnation point. He found that the existences of the axial flow and the upper water rivulet on the yawed cable have important roles on the occurrence of the vortex-induced vibration at high wind velocity. Furthermore, the combination of the axial flow, the water rivulet and the turbulence flow may enhance this aerodynamic instability.

Cosentino *et al.* (2003) carried out tests on cylinders on RWIV using devices specifically designed to measure pressures under rain and water thickness.

Wang *et al.* (2005) carried out wind tunnel tests on an inclined stationary cylinder with running water rivulets in order to characterize the fluid dynamics associated and the effects of water rivulets on the near-wake fluid dynamics. The maximum wind speed in the working section was 50 m/s . The cable was

modeled by a rigid polyethylene-lapped acryl glass tube of 0.6 m in length. Its surface conditions were similar to that associated with the real cables. The cable model used had an external diameter of 19 mm , with a vertical inclination and a yaw angle of 45° . Water was released at the upper end of the cylinder from a water tank. To maintain a steady flow rate, the liquid level H_0 in the tank was maintained to be constant throughout the experiments. Four flow rates were selected: $Q = 1.4, 3.0, 6.9$ and 8.0 l/h . The rivulets were marked by ink, and were recorded using a digital video camera. Figure 2.25 shows typical pattern of the rivulets trajectory along the cylinder axis. One windward (lower) and one leeward (upper) water rivulets were formed on the cylinder for $U = 8 - 15\text{ m/s}$. The rivulet position and behavior depend on the running water rate Q , wind speed, and cylinder yaw angle. Both water rivulets occur around the flow separation line. As the wind speed increases, the rivulets tend to climb up the cylinder surface, possibly due to the dependence of flow separation point on Re . Both water rivulets oscillate circumferentially, which is connected to the nature of the oscillating flow separation point associated with circular cross-section structures. The leeward rivulet appears to be pseudo-sinusoidal with an axial wavelength of about $2D$, which is probably linked to an axial vortex cell wavelength. It was found that the rivulets cause an increase in the normalized dominant frequencies in the near wake and further lead to a significant increase in C_D , which is consistent with the violent vibration associated with the rain-wind-structure interactions.

Xu *et al.* (2006) performed a series of wind tunnel tests to measure C_D and C_L of inclined circular cylinders with artificial rivulet. The Reynolds number for smooth circular cylinders in uniform flow ranged from 9.38×10^4 to 1.93×10^5 . Cable models were designed and manufactured as 1:1 scale stainless steel cylinders covered with high density polyethylene tube, which is the same material as used in the prototype stay cables of a real bridge, to ensure the Reynolds number similarity and the same surface condition for cable model and prototype. Three cylinders with smooth surface configuration were manufactured with a diameter of 140 mm , 160 mm , and 180 mm . The total length of the cylinder was about 3 m . They investigated the effects of artificial rivulet, its shape, and its size on aerodynamic coefficients. Furthermore, the influence of wind yaw angle, wind speed, and cable diameter was also estimated. The test results showed that with the artificial rivulet, C_D and C_L varied with the position of the rivulet significantly (Figure 2.26). The size and shape of artificial rivulet did affect the aerodynamic coefficients but did not have a significant effect on their variation patterns with rivulet angle (Figure 2.26). The wind yaw angle, wind speed, and cylinder diameter also affected the aerodynamic coefficients to some extent, but again they did not affect their variation patterns significantly.

Alam & Zhou (2007) measured C_D and C_L and the fluctuating drag and lift coefficients for a inclined 22.5 mm diameter cylinder over the Reynolds range of 0 to 2.2×10^4 . Two inclination angles, 80° and 55° , were examined. Water was released from the top of the cable by use of a funnel connected to a tank,

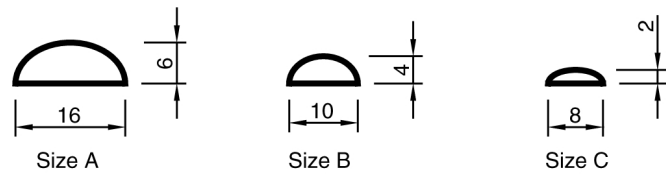
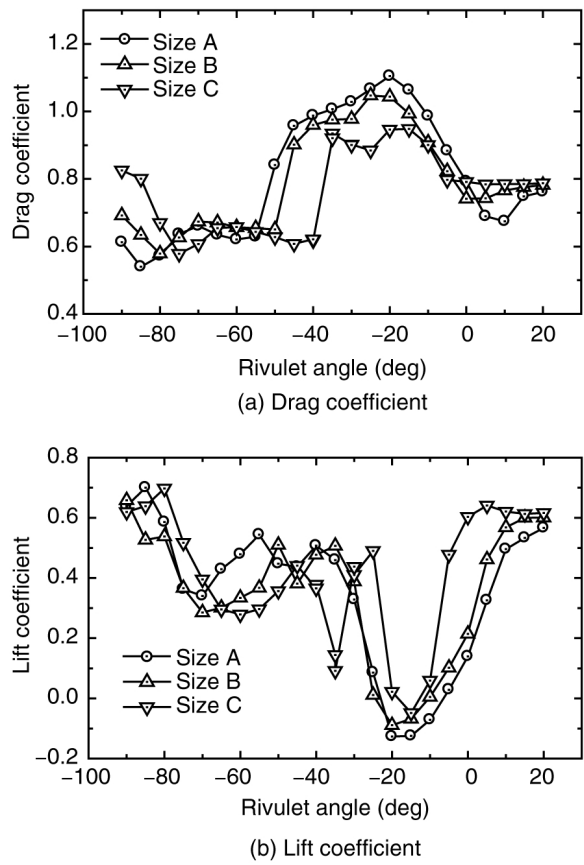


Figure 2.26: Comparison of aerodynamic coefficients of the cylinder with and without rivulet (a). Effect of rivulet size on aerodynamic coefficients (yaw angle equal to 35°) and shapes and dimensions in mm of artificial rivulet. After [Xu et al. \(2006\)](#).

uniformly at the upper end of the cylinder at a rate of $Q = 25 \text{ l/h}$. Five regimes were identified each associated with a specific range of Reynolds number, where the rivulet assumed a different angular position on the cable model. Category A refers to the case when only one water rivulet forms near the leading stagnation line. Re in this category is smaller than 1500 for an inclination of the cylinder of 80° and 3000 for 55° . In Category B, one or two rivulets occur intermittently, corresponding to $Re = 1500 - 2500$ at 80° and $3000 - 5200$ at 55° . In Category C, the two water rivulets occur symmetrically between the leading stagnation and separation lines. The rivulets should not have any significant effect on flow separation. The Re range is $2500 - 5300$ at $\alpha = 80^\circ$ and $5200 - 7400$ at 55° . In Category D, the two rivulets move further downstream and force the boundary layers to separate from them, earlier than in the absence of the rivulets. This category corresponds to $Re = 5300 - 8400$ for 80° and $Re = 7400 - 12000$ for 55° . In Category E, the rivulets move just beyond the separation line, with Re exceeding 8400 at 80° and 12000 at 55° . Using this classification the forces measured on the cylinder were compared to the rivulet position (Figure 2.27). In Categories A, B and C, the rivulets are steady, without oscillating appreciably, and have limited influence on the fluid forces and the near wake of the cylinder. Category D is distinct from the others. The circumferential oscillation of water rivulets is considerably more significant than in the other flow categories. The near wake is characterized by increased vortex strength, a relatively low Strouhal number, a short vortex formation length and narrow wake, highly correlated vortex shedding and fluctuating lift and an improved two-dimensionality of the flow around the cylinder. The maximum fluctuating aerodynamic coefficients were about 4.7 and 2.7 times, respectively, for 55° . In Category E, the significant oscillation of the rivulets disappears. This category is characterized by weakened vortex shedding and fluctuating velocities, smaller fluctuating aerodynamic coefficients, less correlated vortex shedding and lift force, and a longer vortex formation length.

Matteoni & Georgakis (2012a) evaluated the aerodynamic behavior from static wind tunnel tests on a plain cable in wet conditions are presented. The model is a section of a prototype HDPE tube, with a nominal outer diameter of 160 mm . The measured roughness average of the cable model is $Ra \ 1.8 \mu\text{m}$. Tests were performed for the two selected relative cable-wind angles $\Phi = 60^\circ$ and 55° . Rain was simulated using a spray system. They found that the upper and lower water rivulets form when the wind velocity reaches the value of $U = 8 \text{ m/s}$ ($Re = 0.80 \times 10^5$). Over this threshold, the rivulets follow a slightly sinusoidal trajectory along the cable length. As the wind velocity is increased, the rivulets trajectory changes to a straight line. When the wind velocity overcomes the value of $U = 18 \text{ m/s}$ ($Re = 1.8 \times 10^5$) the rivulets are disrupted, as all water is blown off of the cable. C_D was noticeably reduced, whilst C_L was near zero throughout the tested Re range. Furthermore, the fluctuating lift components are analyzed and it is found that cable Strouhal numbers increase in wet conditions. Based on the measured drag and lift coefficients, as well as

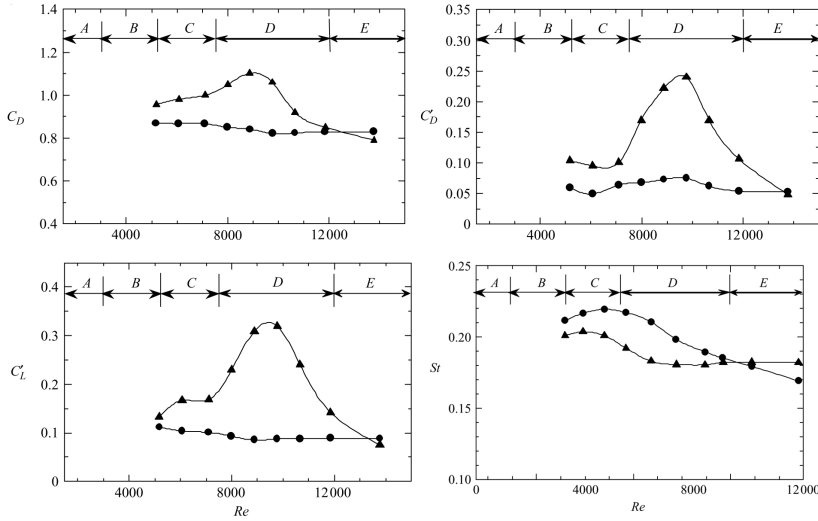


Figure 2.27: Effect of running water rivulets (inclination equal to 55°) on C_D , C_D' , C_L' and St . ●, without water; ▲, with water. After [Alam & Zhou \(2007\)](#).

the observed Strouhal number, it is conjectured that the running water rivulets plays a similar role on the flow structure around the cable as a stationary tripping wire at a critical angular position from the flow stagnation line. Finally, the rain rivulet seems to generate a form of enhanced vortex shedding, which may contribute in some way to the initiation of the RWIV vibrations.

[Du et al. \(2013\)](#) performed wind tunnel tests of an inclined and yawed circular cylinder with and without an artificial upper rivulet. The tested cable model has a diameter of 350 mm and a length of 3.5 m . The cylinder inclination was 30° and the yaw angles tested are 0° , 25° , 30° , 35° , 40° and 45° . The impacts of the artificial upper rivulets and axial flow on the aerodynamics of the cylinder were investigated. Two wind speeds were tested which correspond to the Reynolds numbers of 1.17×10^5 and 2.35×10^5 . Figure 2.28 shows the mean and fluctuating aerodynamic coefficients as functions of rivulet position θ_u for yaw angles of 25° , 35° and 45° . The variation patterns of the mean force coefficients for different wind angles are somewhat similar. There exists non-zero mean positive lift force associated with the decrease of C_D when θ_u is between 19° and 63° . This is likely the result of the reattachment of the separated flow on the upper side of the cylinder. When θ_u increases from 63° to 67° , a sharp decrease of C_L occurs along with a sudden increase of C_D at the same time. In the case of yaw angle equal to 45° , when θ_u is greater than 50° , C_L suffers a gradual increase because of the prominent negative value. The magnitude of the fluctuating lift coefficient is generally larger than that of the fluctuating drag

coefficient except for the case of yaw angle equal to 25° . Besides, the fluctuating wind forces show a prominent peak at the rivulet positions where the possible flow reattachment disappears and vortex shedding recovers. Also the forces acting on the artificial rivulets were measured. Moreover, results show that the upper rivulet can both enhance and depress Karman vortex shedding depending on the position of the rivulet.

2.3.3.2 Numerical simulations

Many efforts have also been made to evaluate the aerodynamics of cylinders under rainy conditions using computational methods. [Lemaitre *et al.* \(2006\)](#) derived a model for the evolution of a liquid film surrounding a cylinder swept by airflow. The model describes the evolution of a water film around a cylinder under the action of wind. The model was then used [Lemaitre *et al.* \(2007\)](#) to study the appearance of rivulets for a simplified configuration with a cylinder aligned with the wind direction. The model was able to predict the formation of two rivulets from the film, provided that the wind speed was large enough to overcome the effect of gravity. The position of the rivulets could also be determined. The results were compared successfully to experimental measurements. Solving the equations of this model numerically, [Lemaitre *et al.* \(2007\)](#) showed that a film of initially uniform thickness will develop rivulets in the neighborhood of the points where the air flow on a dry cylinder would separate; moreover, they concluded that shear and pressure forces are of similar importance in generating rivulets. [Lemaitre *et al.* \(2010\)](#) extend the model to the case of an arbitrary wind-cable configuration and evaluated the wind speed at which rivulets appear and their position are expressed. A maximum wind speed for the rivulets' existence is then estimated as the result of a balance between the drag force and the surface tension. A wind speed interval is consequently obtained for the rivulets' appearance and maintenance on a cylinder. The boundaries of this interval are expressed in term of Weber numbers, comparing the surface tension and wind effect. These predictions are successfully compared with all the measurements that have been published in the literature. The number of rivulets has been shown to depend on the relative magnitude of wind and gravity. At low Froude number, which is for dominant gravity, only one rivulet exists. At high Froude number, which is for dominant wind, two rivulets exist.

[Robertson *et al.* \(2010\)](#) developed a numerical method to undertake simulations of certain aspects of RWIV, in particular, rivulet formation and evolution. Specifically a two-dimensional model for the evolution of a thin film of water on the outer surface of a horizontal circular cylinder subject to the pressure and shear forces that result from the external flow field is presented. The governing evolution equation for the thickness of the film subject to normal and tangential stresses resulting from the aerodynamic field in addition to the forces of surface tension and gravity was derived. The bespoke pseudo-spectral solver was used to solve this equation. The temporal evolution of film thickness for all four loading

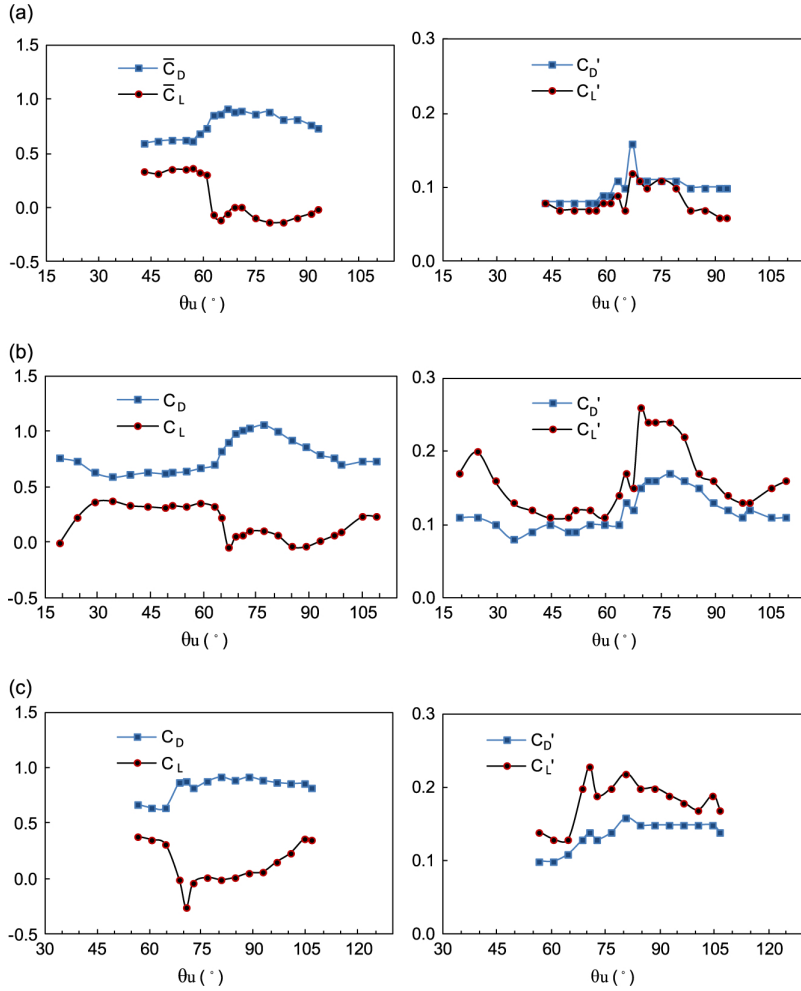


Figure 2.28: Mean and fluctuating wind force coefficients on the cylinder for different positions of an artificial rivulet, for $Re = 1.17 \times 10^5$. For a yaw angle of: (a) 25°; (b) 35°; (c) 45°. After [Du et al. \(2013\)](#).

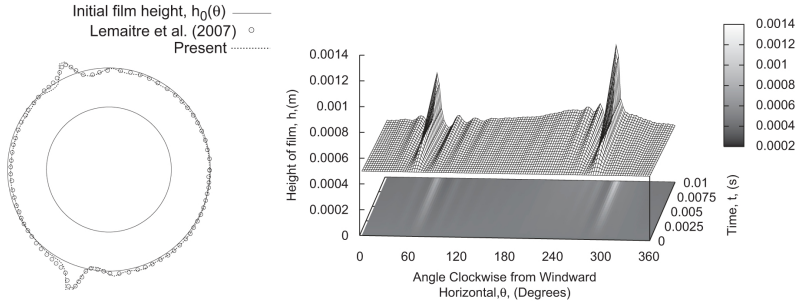


Figure 2.29: Comparison of present numerical results with result of [Lemaitre et al. \(2007\)](#) for variation of film height where the incident wind acts from the left and Numerical prediction of temporal evolution in real time of film height under full loading conditions. After [Robertson et al. \(2010\)](#).

conditions (pressure, shear, surface tension and gravity) acting simultaneously is shown in Figure 2.29. Two distinct rivulets can be seen to form. However, the symmetry about the axis of the incident wind is lost due to the effect of gravity. This gravitational loading results in the rivulets that evolve under full loading conditions being thicker on the lower surface and thinner on the upper surface, respect to the case in which gravity influence is neglected. The results were compared with those of [Lemaitre et al. \(2007\)](#) under the same loading conditions and the agreement is again excellent (Figure 2.29). They observed that as the two numerical solutions have been obtained independently and the results have been generated by two separate solvers, it allows a greater degree of confidence in both sets of results and the method used.

2.4 Section irregularities

Section irregularities are variations of the section with scale similar to the cylinder diameter. Sometimes, it is really difficult to classify irregularities in section and surface irregularities, due to the difficult to classify the scale of $err(\theta, z, t)$. In this review, section irregularities are to be understood as irregularities that visible modify the section shape. The shape is commonly used to refer to the geometric properties of an object or its external boundary. From a geometric viewpoint, when the section is not similar to the circular section, it is classified as section irregularities. Not similar means that the section and the perfect circular section are isotopic: one can be transformed into the other by a sequence of deformations that do not tear the object or put holes in it.

The section irregularities can be classified in three groups:

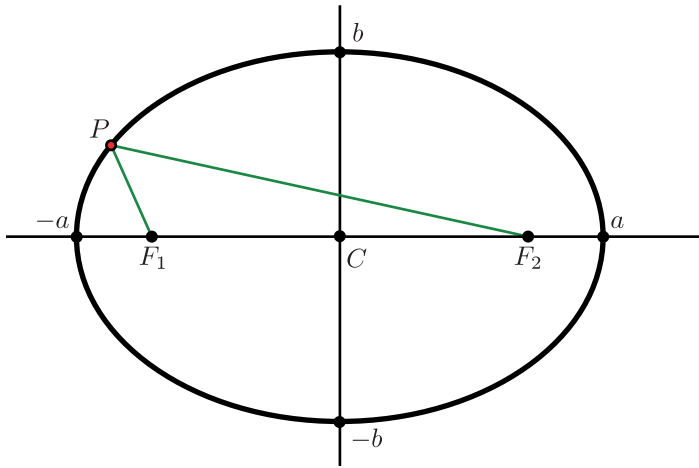


Figure 2.30: Ellipse and some of its mathematical properties.

- Ovalysed sections;
- Polygonal sections;
- Ice accreted sections.

2.4.1 Ovalysed sections

In mathematics, an ellipse is a plane curve that results from the intersection of a cone by a plane in a way that produces a closed curve (Figure 2.30). Circles are special cases of ellipses, obtained when the cutting plane is orthogonal to the cone's axis. The distance between antipodal points on the ellipse, or pairs of points whose midpoint is at the center of the ellipse, is maximum along the major axis or transverse diameter, and a minimum along the perpendicular minor axis or conjugate diameter. The semi-major axis, a , and the semi-minor axis, b , are one half of the major and minor axes, respectively. The foci of the ellipse are two special points F_1 and F_2 on the ellipse's major axis and are equidistant from the center point. The sum of the distances from any point P on the ellipse to those two foci is constant and equal to the major axis ($\overline{PF_1} + \overline{PF_2} = 2a$). The eccentricity of an ellipse, e , is the ratio of the distance between the two foci, to the length of the major axis or $e = 2f/2a = f/a$. Changing in eccentricity allow for shapes ranging from that of a circular cylinder ($e = 0$) to a flat plate ($e = \infty$).

2.4.1.1 Experimental results

The first work on elliptic cylinders was performed by Schubauer (1935, 1939). Schubauer (1935) studied the speed distribution in a laminar boundary layer on the surface of an elliptic cylinder, of major and minor axes 29.92 cm and 10.11 cm (1:3), respectively, oriented with his major axis parallel to the air stream of a wind tunnel, by means of a hot wire anemometer. Re was chosen to obtain a laminar boundary layer before separation. The air velocity was about 3.65 m/s. The pressure distribution around one side of the elliptic cylinder was measured. He tested the applicability of the Pohlhausen's solution for computing the speed distribution, the thickness of the layer and the point of separation and concluded that the method fails shortly before the separation point is reached and consequently cannot be used to locate this point. In the second work Schubauer (1939) used the same cylinder of his precedent work (Schubauer, 1935) for studying the conditions of air speed when the layer is partly laminar and partly turbulent. He measured the pressure distribution for different Re . He studied the separation for different air velocity using a mixture of kerosene and lampblack to the surface. At $Re = 1,39 \cdot 10^6$, the boundary layer separation was followed by a reattachment of the layer on the surface. The reattached layer was turbulent. He called this case "transition by separation", although such a designation would not mark the phenomenon as unique, since transition probably always occurs somewhere in the detached layer after a laminar separation. He also measured the main speed distribution and the speed fluctuation in the boundary layer.

In order to determine the effect of the shape and Reynolds number on drag, Lindsey (1938) performed tests in wind tunnel of elliptic cylinders with $b/a = 0.5, 0.25, 0.125$ in the Reynolds range $2.5 \cdot 10^4 < Re < 3 \cdot 10^6$. Results are shown in Figure 2.31. The model with the $b/a = 0.125$ indicates no pronounced change in C_D with Reynolds number. The other two elliptic cylinders, $b/a = 0.5, 0.25$, have a pronounced change of C_D .

Wiland (1968) studied in the Reynolds range $3 \cdot 10^4 < Re < 10^5$ for different angle of attack, $\alpha = 0^\circ, 90^\circ, 60^\circ, 30^\circ$ the variation of Strouhal number, the mean and fluctuating pressure distribution and the wake geometry for two elliptic models with eccentricities of 0.6 and 0.8. He found that the Strouhal law fits the experimental data and that the variation of Strouhal is less when based on projected height. The angle of attack increases the fluctuating pressure. He found a variation in the range $\alpha = 0^\circ \div 90^\circ$ of the $C_{P_{max}}$ increase from 0.1 to 0.8 for $e = 0.6$ and from 0.04 to 0.8 for $e = 0.8$. For $\alpha = 0^\circ$ the separation points for the boundary layer is approximately at $75^\circ \div 80^\circ$ for both eccentricities. He also evaluated C_D , C_L and C_M for different angle of attack.

The British Standard Institution (1972) give in his Code of Basic Data for the Design of Building a single value for C_D for both post and sub critical Reynolds number ranges in function of the product $U \cdot b$ and for different aspect ratio (Table 2.8). These are maximum values in both ranges because are given

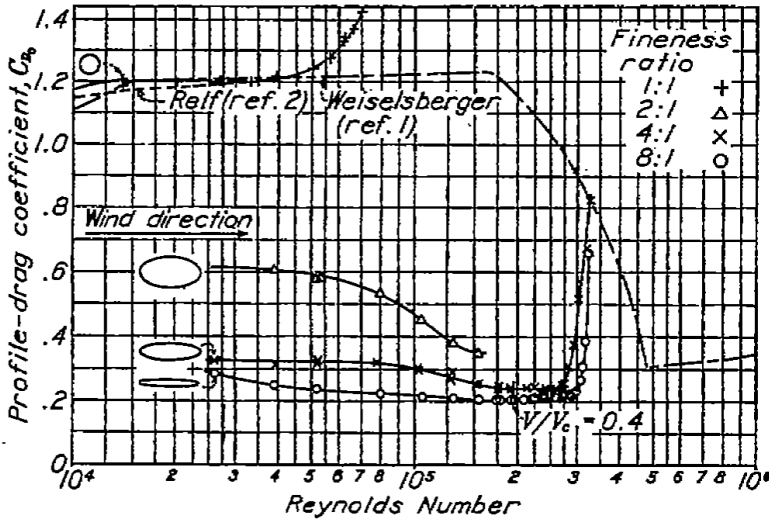


Figure 2.31: Variation in C_D with Reynolds number for the elliptical cylinders, after [Lindsey \(1938\)](#)

for a safe design.

The American Association of State Highway and Transportation Officials [A.A.S.H.T.O \(2009\)](#) give some equations for the evaluation of C_D for ellipse with $b/a = 0.5$ with wind on narrow-side and with wind on broad-side:

$$C_D = C_{Db} \left(1 - 0.7 \left(\frac{a}{b} - 1 \right)^{\frac{1}{4}} \right) \quad (2.29)$$

$$C_D = 1.7 \left(\frac{a}{b} \right) + C_{Da} \left(2 - \frac{a}{b} \right) \quad (2.30)$$

where C_{Da} and C_{Db} are the drag coefficient of a circular cylinder with diameter equal to a and b respectively. The equations are valid for $a/b \leq 2$. The equations were empirically derived to fit wind tunnel test data.

[Esdu 79026 \(1979\)](#) gives the force coefficient data as a function of Reynolds number and edge radius for elliptical sections and elliptical equal-sided polygons with 12 sides in the range Reynolds $5 \cdot 10^4 < Re < 3 \cdot 10^6$. The total mean force is expressed as:

$$\begin{aligned} \bar{F} &= C_F \cdot k_1 \cdot k_2 \cdot \frac{1}{2} \rho V \cdot a \cdot L \\ \bar{M} &= \bar{F} \cdot z_{cp} \end{aligned} \quad (2.31)$$

Table 2.8: Drag coefficients C_D for elliptic cylinders, after British Standard Institution (1972).

Plan position	$U \cdot b$	C_D for different b/a					
		1	2	5	10	20	∞
Flow parallel to the major axis	< 10	0.5	0.5	0.5	0.6	0.6	0.7
	≥ 10	0.2	0.2	0.2	0.2	0.2	0.2
Flow parallel to the minor axis	< 8	0.8	0.9	1.0	1.1	1.3	1.7
	≥ 8	0.8	0.9	1.0	1.1	1.3	1.5

where k_1 is a factor accounting for effect on C_D of aspect ratio, k_2 is accounting for effect of shear flow and taper, a is the major or the minor axis depending on how force coefficient is defined, $C_F = \sqrt{C_D^2 + C_L^2}$, z_{cp} is the centre of pressure along the cylinder through which total mean drag acts. The drag is reporter in a graph in function of the ratio b/a and Re multiplied for λ_T that is a factor used for evaluating turbulence effects. For the drag for any other angle of attack, different from 0° and 90° , is given this relation:

$$[C_D]_\alpha = [C_D]_{\alpha=0^\circ} + k_\alpha ([C_D]_{\alpha=90^\circ} - [C_D]_{\alpha=0^\circ}) \quad (2.32)$$

where k_α is a correction factor independent of b/c . k_α , C_L and z_{ep} are given in function of α . k_1 is given in function of a/L and k_2 is:

$$k_2 = \frac{a_0/a_H}{2\bar{\alpha} + 1} + \frac{(a_0/a_H) - 1}{2\bar{\alpha} + 2} \quad (2.33)$$

where a_0/a_H is the taper factor (the ratio between the major axis at the start and the end of the cylinder), $\bar{\alpha}$ is the coefficient of the velocity power law $V_z/V_H = (z/H)^{\bar{\alpha}}$ and is given in one Figure in function of the description of the roughness.

Ota *et al.* (1983, 1984) investigated the local and overall heat transfer characteristics from elliptic cylinders of axis ratio 1:2 and 1:3 varying the angle of attack from 0° to 90° in the Reynolds range $8 \cdot 10^3 < Re < 7.9 \cdot 10^4$. They observed that C_D at small angle of attack is lower than of a circular cylinder. The pressure distribution varies from with the angle of attack. The base pressure decreases with an increase of α . In the range $60^\circ < \alpha < 90^\circ$ the upstream separation point almost coincides with the leading edge and the pressure inside the separated flow region is very low. They also determined numerically C_D from the pressure distributions for different angle of attack, having for the case 1:3 a variation between 0.15 and 1.8.

Choi & Lee (2000) investigated experimentally an elliptic cylinder with an axis ratio of 2 located near a flat plate. A smooth flat plate 15 mm in thick-

ness and 4.8 m in length was installed 100 mm above the bottom surface of the test-section. A trip wire of 3.5 mm was attached on the plate surface at 100 mm downstream from the leading edge to generate a thick boundary layer. During the tests the Reynolds number was $1.4 \cdot 10^4$. They measured the pressure on the surface with pressure taps installed at regular intervals. C_D and C_L were evaluated by integration of the pressure. The smoke flow visualization was employed to visualize the flow. During the tests the distance between the cylinder and the plate was modified from 0 to twice of the minor axis. The power spectral of the record of a hot wire probe detect a variation of the Strouhal number up to about 20% with respect to the distance of the cylinder to the plate. Their results reveal that the ground effect suppressing the vortex shedding appears strongly for the elliptic cylinder, compared to the circular cylinder. They found the existence of a critical gap that separates distance of the cylinder from the plate when vortex shedding happens from where it doesn't happen. The deviation in surface pressure distribution on the elliptic cylinder is much smaller than for the circular cylinder. The drag coefficient of the elliptic cylinder is about half that of the circular cylinder for all gap ratios tested.

Choi & Lee (2001), with the same setup of Choi & Lee (2000), studied the flow characteristics around an elliptical cylinder located near a flat plate varying the attack of the cylinder. As the angle of attack varies, the location of the peak pressure on the windward cylinder surface moves towards the rear edge of the cylinder, while that of the leeward surface moves toward the front edge. With varying angles of attack, the vortex-shedding frequency gradually decreases and a critical angle of attack can be defined in terms of the distance between the cylinder and the plane. At negative angles of attack, the boundary layer near the wall becomes disturbed more than for positive angles of attack. This shows that the merging of the separated wall shear layer from the boundary layer and the lower shear layer of the cylinder wake becomes stronger at negative angles of attack than at positive ones.

Alonso *et al.* (2010) measured pressure distribution and drag and lift coefficients of elliptic cylinders with b/a with $a = 16$ and $b = 2, 3, \dots, 13$ in the Reynolds range $2.2 \cdot 10^3 < Re < 1.4 \cdot 10^5$ and angle of attack varied from 0° to 90° . The study is oriented to understand the characteristics of the galloping motion of elliptical cross-section bodies when subjected to a uniform flow using the well-known Den-Hartog stability criterion. The largest instability is found for $b/a = 11/16$ where the existence of a recirculation bubble. The influence of the boundary layer regime on the aerodynamic forces acting on the body was studied comparing the pressure distribution for an elliptic cylinder with $b/a = 0.5$ for two Reynolds number $Re = 2 \cdot 10^5$ and $Re = 4 \cdot 10^5$. In the first case the boundary layer on the cylinder was laminar, in the second case turbulent. In the laminar case for little angle of attack ($\alpha < 46^\circ$), a separation bubble is formed at the leading edge characterized by an intense suction peak. For bigger angle of attack, this peak disappears and the cylinder becomes stalled. In the turbulent case the boundary layer has more momentum and can maintain the

suction peak at higher values of the angle of attack than in the laminar case.

2.4.1.2 Numerical simulations

Rubin & Mummolo (1974) applied the slender-body theory for the evaluation of the three-dimensional surface velocities induced by a boundary layer on an elliptic cylinder. They studied the numerical solution for flow along spanwise direction when Reynolds number is sufficiently large so that the thin boundary approximation is valid.

Shintani *et al.* (1983) applied the Umemura's method of coordinate transformation through matching procedure in the analysis of the flow past an elliptic cylinder for low Reynolds number. They focused on shape effects due to the flattening of the cylinder and to inertial effects of the fluid.

Jackson (1987) used finite-elements simulation to examine the onset periodic flows about various body shapes. The method implemented a direct calculations of the eigenvalues of the Jacobian matrix of the flow equations crosses the imaginary axis that corresponds to a Hopf bifurcation that leads a periodic behavior. He made calculations for an ellipses oriented along the minor axis along the flow and ellipses with various angle of attack. He evaluated the Reynolds number at which the flow behavior becomes periodic and the associated Strouhal number for different eccentricity and angle of attack. His model provides a constant Strouhal number when the number is based on the cross section projection for different angle of attack.

Mittal & Balachandar (1995, 1996) gave results of two dimensional and three dimensional simulations of flow past elliptic cylinders using a Fourier-Chebyshev spectral collocation technique to simulate the full three dimensional incompressible flow over elliptic cylinders. They noted that the drag coefficient computed from two dimensional simulations is significantly higher than what is obtained from experiments. They found results with 3-D simulations that match better with experimental results, differently from the previous results of Lugt & Hausling (1974) which performed the flow over thin ellipse at 45° angle of attack using 2D simulation.

Khan *et al.* (2005) used an integral method of boundary layer to derive expression for the calculation of the total drag and average heat transfer for flow across an elliptical cylinder. They found a relation for the evaluation of the total drag:

$$C_D = \frac{1.353 + 4.43 \left(\frac{b}{a}\right)^{1.35}}{\sqrt{Re_{\mathcal{L}}}} + \left(1.1526 + \frac{1.26}{Re_{\mathcal{L}}}\right) \left(\frac{b}{a}\right)^{0.95} \quad (2.34)$$

where $Re_{\mathcal{L}}$ is the Reynolds number based on a characteristic length \mathcal{L} that is the equivalent diameter of a circular cylinder whose perimeter is the same as that of the elliptical cylinder. The first part of Eq. 2.34 is the friction drag

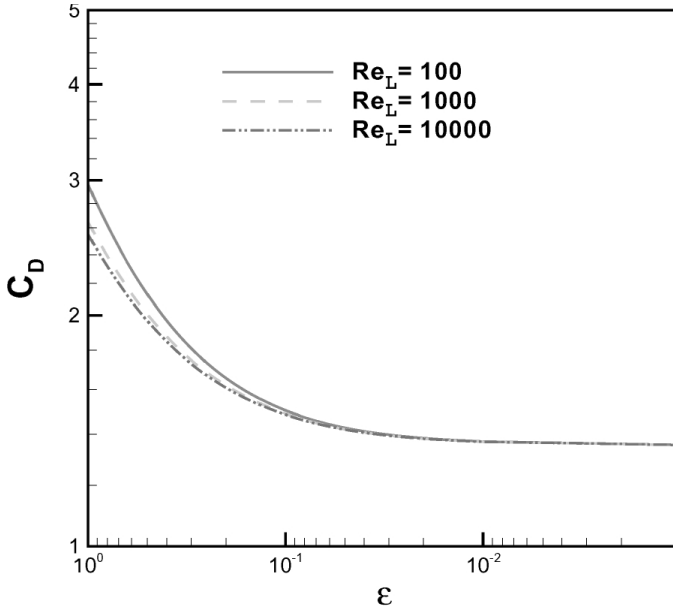


Figure 2.32: Variation of total drag coefficient with axis ratio. After [Khan *et al.* \(2005\)](#).

contribute and the second part, after the sum sign, is relative to the pressure-drag coefficients. Figure 2.32 shows the total drag versus Reynolds numbers for different $\varepsilon = b/a$ from Eq. 2.34 and from experimental data. The results are in good agreement with existing data and in the limiting case can be used for circular cylinders and finite plates. As expected, C_D is highest for the circular cylinder and lowest for the flat plate.

2.4.2 Polygonal sections

In geometry a polygon is traditionally a plane figure that is bounded by a finite chain of straight-line segments closing in a loop to form a closed chain or circuit. These segments are called its edges or sides, and the points where two edges meet are the polygon's vertices or corners. In this section only the case of regular convex polygon shape section will be analyzed. A polygon is convex if any line drawn through the polygon (and not tangent to an edge or corner) meets its boundary exactly twice (as a consequence, all its interior angles are less than 180°) and regular if all corners lie on a single circle, called the circumcircle and all edges are of the same length. If the number of sides of the polygon tends to infinity, the polygon becomes an approximation of the circumference.

From the aerodynamics viewpoint, the main important geometric parameters

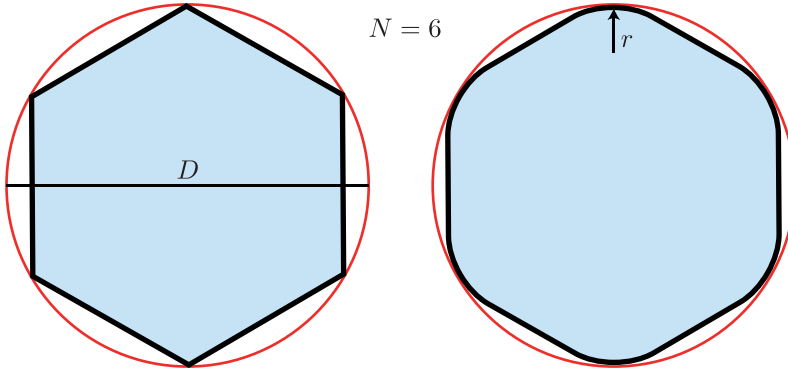


Figure 2.33: Regular polygon and definition of corner radius r .

are:

- The number of sides, N ;
- The ratio of the corner radius on the diameter, r/D .

Another important parameter is the angle of attack, because this imperfection introduces an asymmetry respect to the flow. For this reason, a lift force can be provoked by the flow for selected angle of attack.

James (1976) performed an extensive experimental work to characterize the aerodynamics of polygonal sections. He used wind tunnel tests to obtain C_D for octagonal, dodecagonal and hex-decagonal cylinders. It observed that the corner radius strongly influences the aerodynamic coefficients and that the maximum values of C_D were obtained for the angles of attack giving the flow directed towards a corner.

Esdu 79026 (1979) gives the force coefficient data as a function of Reynolds number and edge radius for equal-sided polygons with number of sides in the range of 4 to 20 for different turbulence and roughness. The procedure was explained in Section 2.4.1.1 for the case of elliptical cylinders.

Szalay (1989) carried out wind tunnel measurements to determine C_D of the 16-sided polygon and for comparison of 4 (square) and 12-sided polygons in the Reynolds range $3.5 \cdot 10^4 < Re < 1.4 \cdot 10^5$. In contrast with the expectancy, C_D of the 16 sided polygon were not in the range between coefficients of the 12 sided and the circular cross section. A possible explanation might be the different regime reached by each cylinder. Consequently, he concluded that the measurement of the complete drag curve for the wide Re range would be necessary to compare data.

Mehta *et al.* (1990) carried out tests in water tunnel on octagonal cylinder with characteristics similar to luminaire poles. They found differently from previous studies that C_D did not exhibit dependency on the Re ; C_D remained

in a range of 1.2 to 1.7 over the range $5 \cdot 10^4 < Re < 7 \cdot 10^5$. They observed that the drag coefficients found was 25% higher than the recommended one in the ASSHTO standard.

ASCE-74 (1991) gives the force coefficients for infinitely cylinders with aspect ratio greater than 40. The coefficients are given in form of Figure and are reported in Figure 2.34. It was also given a factor of conversion in order to consider cylinder with lower aspect ratio.

Gonçalves & Del Rio Vieira (1999) evaluated the Strouhal number for regular triangular, pentagonal, hexagon and octagonal cylinders for $Re < 600$. The vortex wakes generated by pentagon, hexagon and octagon cylinders show a structure similar to the circular cylinder structure, but the wake generated by the triangular cylinder shows a different structure. The vortices are generated in the triangular cylinder very close to the upper side of the body and the vortex formation is hardly influenced by the edges, implying in high values of Strouhal when compared with the Strouhal curve produced by a circular cylinder.

Bosch & Guterres (2001) experimentally characterized the aerodynamics of an octagonal cylinder shapes with varying taper ratio. Shedding frequency was increased by the introduction of taper for the circular cylinders. That behavior has not been confirmed for the octagonal cylinder cases yet. They also noted that the face orientation results in a significantly lower drag coefficient than the corner orientation for the octagonal cylinders.

NCHRP-494 (2003) furnishes the drag coefficient for transitions for multi-sided to round cross sections. Globally, multisided shapes have higher drag coefficients than round shapes. The drag coefficient is given as a function of the shape, the wind speed, the diameter and to the ratio to the radius of the corner radius of the inscribed circle r , in Figure 2.35.

Hu *et al.* (2006) carried out experimental water tunnel test in order to investigate the effects of the corner radius of a square prism on the near wake. They observed that the flow structure depends to a great extent on the corner radius of the cylinder. As r/D increases from 0 to 0.5, the maximum vorticity of the vortex attenuates, the circulation associated with vortices drops progressively by 50%; meanwhile, the Strouhal number climbs linearly by about 60%. The case $r/D = 0.5$ is the case of a circular cylinder. The flow visualizations show that in the case of square section the separation point is governed by the geometry while when r/D increases the detachment point is governed by Re . For this reason, from the aerodynamics viewpoint a square cylinder cannot be considered similar to a circular cylinder.

Portugaels *et al.* (2007) determined the aerodynamic forces induced by the wind on octagonal cylindrical elements with different diameters, different edge curvature radii and different roughness's have in a wind tunnel over the range $8 \cdot 10^4 < Re < 1.3 \cdot 10^6$. In total, 27 models, made in wood, have been tested, among which 6 present a circular cross-section and 21 have an octagonal cross-section with different edge radii. The different edge radii (0, 5, 10, 15, 20, 25 and 40 mm) have also been selected to provide a good knowledge of its effect

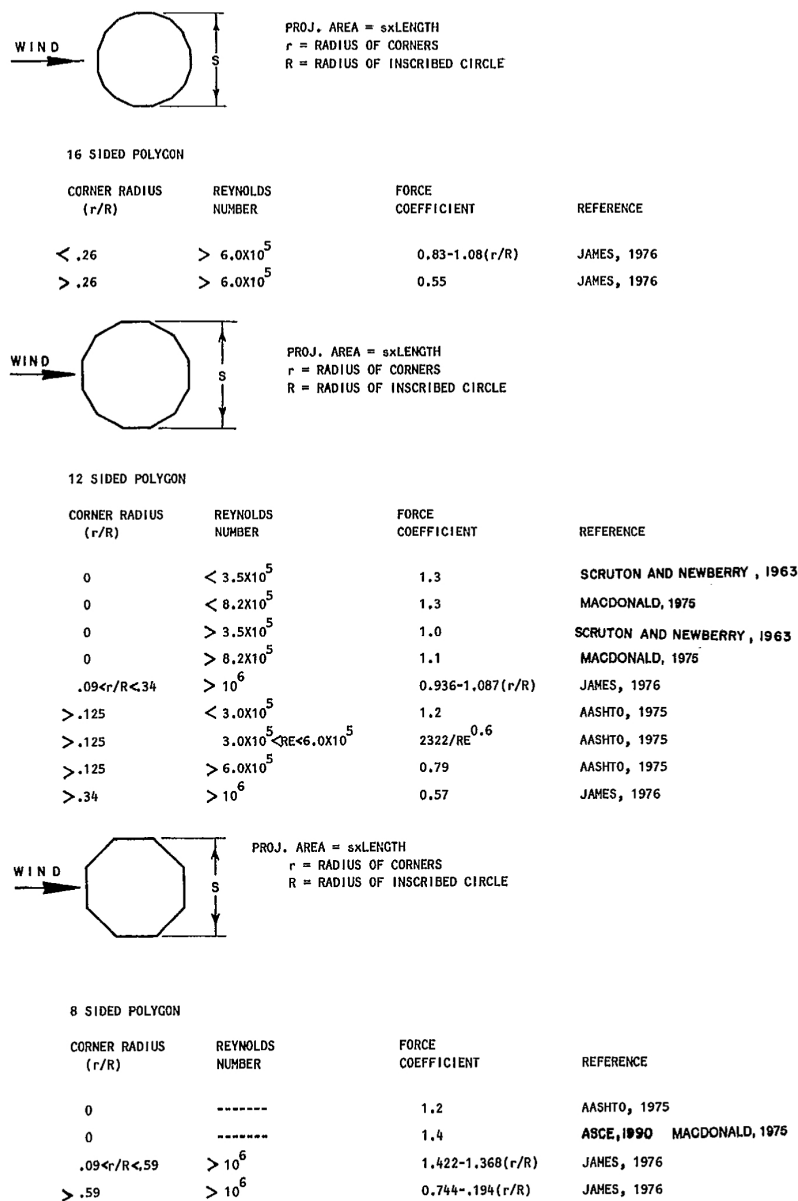
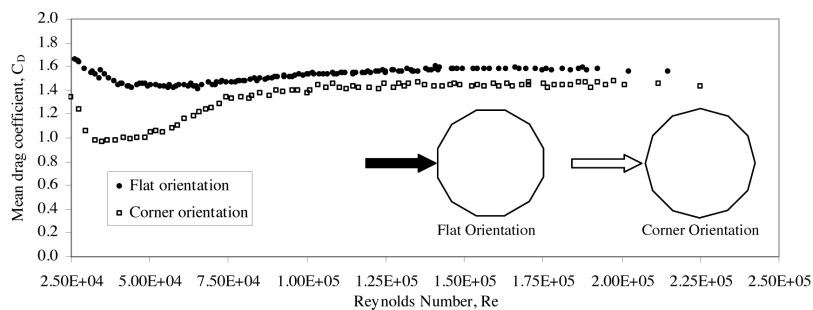


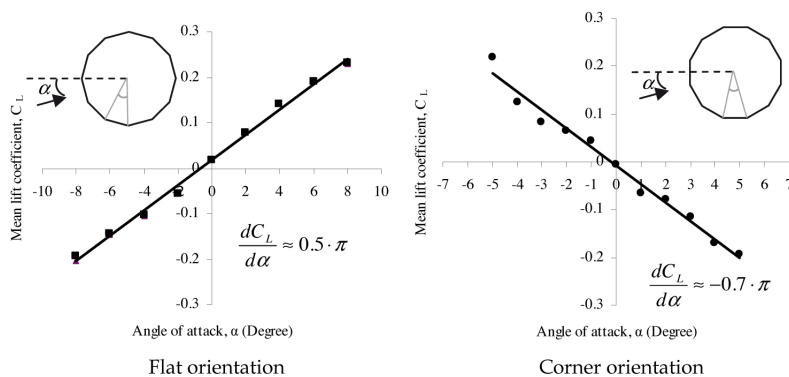
Figure 2.34: Aerodynamic coefficients for octagonal, dodecagonal and hex-decagonal cylinders, after ASCE-74 (1991).

	$C_v Vd \leq 5.33$ (39)	$5.33 (39) < C_v Vd < 10.66 (78)$	$C_v Vd \geq 10.66$ (78)
Hexdecagonal: $0 \leq r < 0.26$	1.10	$1.37 + 1.08r - \frac{C_v Vd}{19.8} - \frac{C_v Vdr}{4.94}$ (SI) $1.37 + 1.08r - \frac{C_v Vd}{145} - \frac{C_v Vdr}{36}$ (U.S. Cust.)	$0.83 - 1.08r$
Hexdecagonal: $r \geq 0.26$	1.10	$0.55 + \frac{(10.66 - C_v Vd)}{9.67}$ (SI) $0.55 + \frac{(78.2 - C_v Vd)}{71}$ (U.S. Cust.)	0.55
Dodecagonal (See Note 1)	1.20	$\frac{3.28}{(C_v Vd)^{0.6}}$ (SI) $\frac{10.8}{(C_v Vd)^{0.6}}$ (U.S. Cust.)	0.79
Octagonal	1.20	1.20	1.20
Cylindrical	1.10	$\frac{9.69}{(C_v Vd)^{1.3}}$ (SI) $\frac{129}{(C_v Vd)^{1.3}}$ (U.S. Cust.)	0.45
Notes: 1. Valid for members having a ratio of corner radius to distance between parallel faces equal to or greater than 0.125. 2. Units in top row are SI, with English Customary in parentheses. 3. Notation: C_v : velocity conversion factor V : basic wind velocity (m/s, mph) d : depth (diameter) of member (m, ft)			

Figure 2.35: Drag coefficient values for round and multisided shapes, after [NCHRP-494 \(2003\)](#).



(a)



(b)

Figure 2.36: C_D for the dodecagonal cylinder in flat and corner orientation (a) and C_L and its derivative respect to the angle of attack for the dodecagonal cylinder (b), after Phares *et al.* (2007).

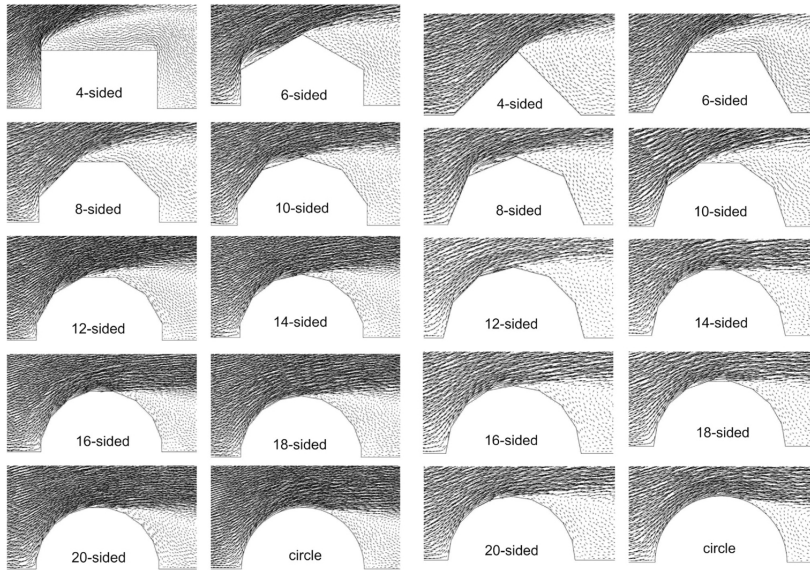


Figure 2.37: Flow velocity vectors around polygons with edges facing inlet wind and vertexes facing inlet wind, after [Tang et al. \(2013\)](#).

on the drag. The usual edge radius for the real luminaries columns is between 6 and 10 mm. Four surface roughnesses were considered. They were defined from absolute roughness measured on existing lighting columns. As for the circular cylinders, the roughness has no effect on C_D in the sub critical regime. For higher Reynolds number values, an increase of the roughness leads on one side to a reduction of C_D for the cylinders with sharp edges, but on the other side to a rise of C_D for the cylinders with rounded edges. The influence of the roughness is then highly dependent on the cross-section shape and on the edge radius. When the edge radius is higher, the cylinder behaves closer to a smooth circular cylinder. They observed that when the octagonal cylinder is oriented with a side of the model oriented towards the wind direction the flow is not symmetrical; if the cylinder is rotated respect to the flow direction, then a lateral force is added to the drag force. The amplitude of this force is more or less important depending on the angle of attack.

[Phares et al. \(2007\)](#) experimentally characterized C_D for a 12-sided polygon in the Reynolds number range $9.3 \cdot 10^4 < Re < 1.6 \cdot 10^5$. The results are shown in Figure 2.36a. C_L for various angles of attack is shown in Figure 2.36b. The ratio of C_L and angle of attack were calculated to be approximately $-0.7 \cdot \pi$ and $0.5 \cdot \pi$ for flat and corner orientation, respectively.

Numerical methods were also used to solve and analyze the problem of flow around polygonal sections. [Tian & Wu \(2009\)](#) studied the two-dimensional in-

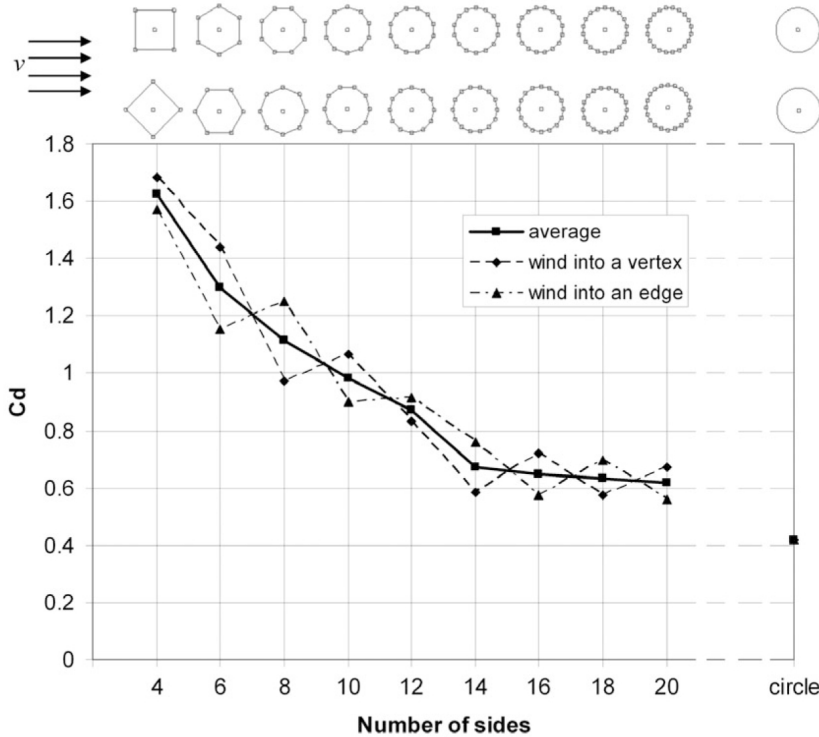


Figure 2.38: Drag coefficients of polygons with wind into a vertex and wind into an edge, after [Tang et al. \(2013\)](#).

viscid flow and low-Reynolds-number viscous flow past regular polygons, which have arbitrary but even numbers of edges and have one apex pointing to the incoming free stream. For the pure potential flow past polygons, an explicit formula exists for the pressure coefficient. Compared to the case of circular cylinders that only exhibits smooth flow, singularity around each apex was observed. The intensity of the singularity weakens when the number of sides increases, indicating that for large number of sides the aerodynamics of the polygon tend to the circular case. [Tian et al. \(2011\)](#) extend the results to the flow past polygons with an odd number of edges, and an arbitrary wind direction.

[Tang et al. \(2013\)](#) performed a systematic study of wind drags on both straight and twisted polygonal buildings using CFD techniques. Ten different cross-sectional shapes of regular towers have been investigated. The design of experiments showed that by increasing the number of polygon sides C_D decreases and eventually approaches to that of a circular cylinder. As a matter of fact, when a free stream flow passes a polygonal cylinder, the boundary layer

separates at a location after the front stagnation point due to adverse pressure gradient. When N increases, the surface turns to go smoother (Figure 2.37). This causes the separation to be delayed. This delay in the separation results in a narrowing in the wake flow, a lower pressure difference around the body and hence, a lower C_D . However, the width of wake flow does not change much after the case of 14-sided polygon (Figure 2.38). A parametric model has been created to investigate the drag coefficients of a square with different fillet radius on the rounded corners. Finally, the results demonstrated a substantial reduction in the wind drag while the radius is increased.

2.4.3 Ice accreted sections

The research on the aerodynamic behavior of ice accreted circular cylinders was mainly focused on two aspects:

- The ice accretion phenomenon:
 - Shape;
 - Evolution;
- The aerodynamic characteristics of iced cylinders.

In this review, it is mainly highlighted the aerodynamic behavior of ice accreted circular sections.

2.4.3.1 Ice accretion phenomenon

The ice accretion phenomenon is governed by the flow conditions, the cloud characteristics and the thermodynamic of the water phase transition. When atmospheric ice conditions are fulfilled, the air loads water droplets on the cylinder exposed to the flow. However, water droplets are much heavier than air particles and they do not pass round so easily. Some of them therefore impact on the cylinder. The cloud consists of supercooled droplets that are unstable, and supercooled liquid water freezes immediately or become runback water after the impact. Ice accretion results from the continuation of this process. The above process leads to an uneven distribution of water droplet impacts on the leading edge. It is easily conceivable that droplets, which are right in the middle, would not be deflected very much and would impact instead on the upper and lower sides of cylinders. This starts the double horn shape. But if the droplets are very heavy, as in the case of freezing rain, deflection is limited, and ice accretion takes place in an arc shape.

The impact mechanism and the freezing phase transition generate heat which generates a rise in temperature on the surface. When the temperature is high, water droplets do not freeze on impact, but explode into numerous little globules that are blown by the airflow along the cylinder lateral surfaces. It often

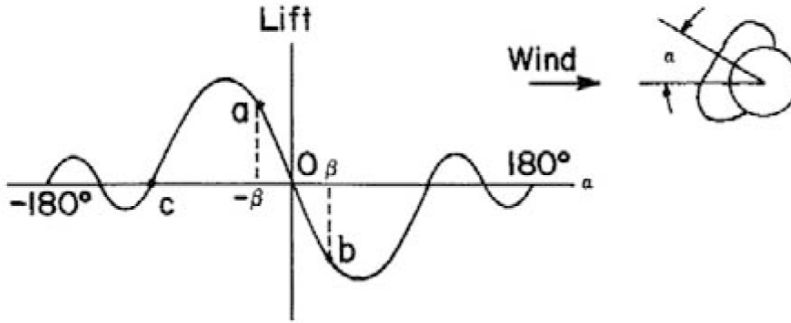


Figure 2.39: Variation of the lift force with respect of the angle of attack, for an ice accreted conductor. After [Rawlins et al. \(1979\)](#).

happens that the cooling is quicker than the blowing off and water freezes on the cylinder lateral surfaces and is not dragged off. This process is called *run-back ice*. Efficiency of runback ice process depends on the temperature, amount of water and wind speed in the cylinder boundary layer. Many authors investigated experimentally and numerically the accretion phenomenon on circular cylinders ([Koss et al. , 2012](#); [Fu et al. , 2006](#); [Lozowski et al. , 1983](#); [Makkonen, 1984b, 1985](#); [Kollár & Farzaneh, 2010](#)) and also some books were written on the topic ([Farzaneh, 2008](#); [Poots, 1996](#)).

The process here shortly explained generated a number of types of ice accreted sections depending on many parameters. The shape variation and local roughness strongly influence the aerodynamic behavior of the cylinder. It must be highlighted that due to thermodynamic issues, Reynolds scaling of geometry is not applicable in the presence of ice accretion; therefore any accreted geometry on a cylinder is referred to a specific diameter.

2.4.3.2 Aerodynamics of ice accreted cylinders

First indication on the variation of C_L acting on the conductor plus the shape of the ice accretion were given by [Rawlins et al. \(1979\)](#). He observed that when ice accretes on the conductor, the resulting shape might have varying aerodynamic coefficients as a function of the angle of attack. The results is shown in Figure 2.39.

[Tunstall \(1989\)](#) carried experimental test in order to characterize the aerodynamic coefficients of a conductor with a wet snow deposit using a replica of the ice shape. The aerodynamic coefficients are shown in Figure 2.40. Results evidence a strong dependence of the aerodynamic coefficients with respect of the angle of attack. In particular, C_D and C_M increase for angle of attack different of 0° and a negative lift characteristic was found in the ranges of angle of attack between -100° and -20° and between 20° and 90° .

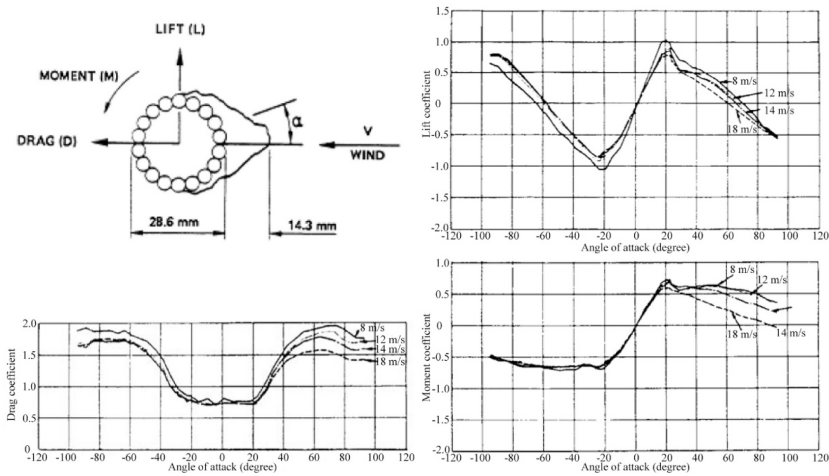


Figure 2.40: C_D , C_L and C_M versus angle of attack from wind tunnel measurements on replicas of this ice shape, after [Tunstall \(1989\)](#).

[Nigol & Buchan \(1981\)](#) measured aerodynamic force coefficients in wind tunnel, over a practical range of natural ice shapes and wind speeds. The ice accretion was realized putting section of conductor in a refrigerator. The conductors were suspended from their ends with music wire that was carefully adjusted in length and diameter to match the torsional stiffness in the centre region of a typical full scale span. The conductors were made as realistic as possible, both in diameter and distributed weight, by wrapping aluminum strands around a solid aluminum rod. The rotation of the conductors during the accretion was ensured suspending them from their ends with music wire that was carefully adjusted in length and diameter to match the torsional stiffness in the centre region of a typical full scale span. The conductors were sprayed at different angles with a wide variety of air-to-water mixtures to produce wet or slow freezing and dry or fast freezing ice build-up. The realistic ice shapes were used to make new plastic replicas which could be used in wind tunnel. A total of four different ice shapes on 2.8 cm diameter conductor were selected to cover the icing conditions observed during natural storms (Figure 2.41a). The aerodynamic coefficients found for the sample 2 are shown in Figure 2.41b. C_D is relatively constant with respect to the angle of attack as expected for samples having a relatively constant projected area. C_L is completely different for ice deposits of similar shape, as minor variations in surface texture seem to have large effects. C_M changes its sign for windward and leeward orientations of ice. This is not an unexpected result because a non-symmetric airfoil can produce a flow pattern which is different in the two orientations.

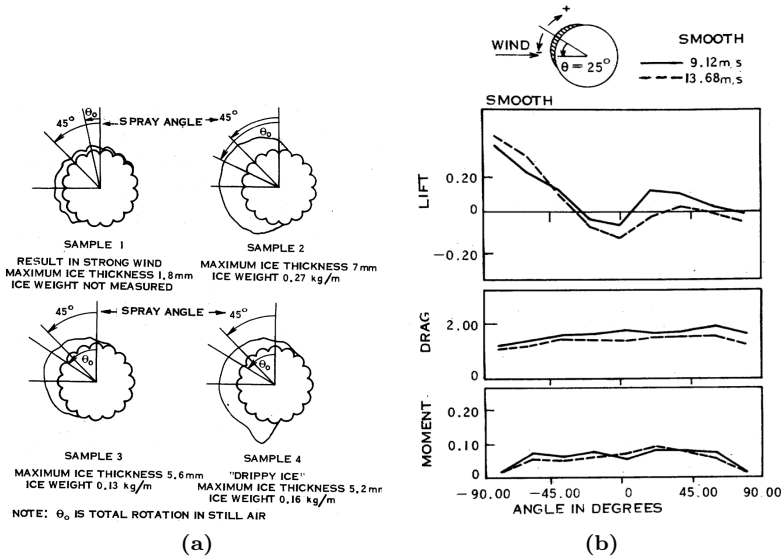


Figure 2.41: Ice shapes (a) and aerodynamic coefficients for the sample 2 (b), after [Nigol & Buchan \(1981\)](#).

[Chabart & Lilien 1998](#) carried out wind tunnel tests on a model of a cable sample on which the ice deposit was modeled with silicone. The cable was simulated by a sectional, rigid model. The pattern of the ice has been copied a sample of real ice accretion. The length of the artificial ice was 0.8 m and its eccentricity (the ratio between the ice thickness and the radius of the conductor) was 1.32. C_D , C_L and C_M were measured for different wind speed. They tested the cable at 4 wind speeds, 10, 12.5, 15, 17.5 and 20 m/s . They found that the effect of the wind speed on the aerodynamic coefficients was limited for the majority of the angle of attack.

[Shimizu *et al.* \(2004\)](#) conducted wind tunnel tests to measure the three aerodynamic coefficients of 4-conductor bundle as well as single conductor section models with artificial accreted ice. The cable model was made of aluminum and the simulated accreted ice of Japanese cypress. The two cross section tested and the aerodynamic coefficients are shown in [Figure 2.42](#). At an angle of attack of approximately 10° there is a strong variation of C_L and C_M that reach a peak. This phenomenon is correlated to an increase of C_D and looks similar to a stall.

[Oka & Ishihara \(2010\)](#) performed a numerical study on steady aerodynamic characteristics of ice accreted transmission lines using a LES turbulence model. They used the shape of ice accreted transmission line of [Shimizu *et al.* \(2004\)](#) ([Figure 2.42](#)). In addition a section with height $0.25D$ was employed in the sim-

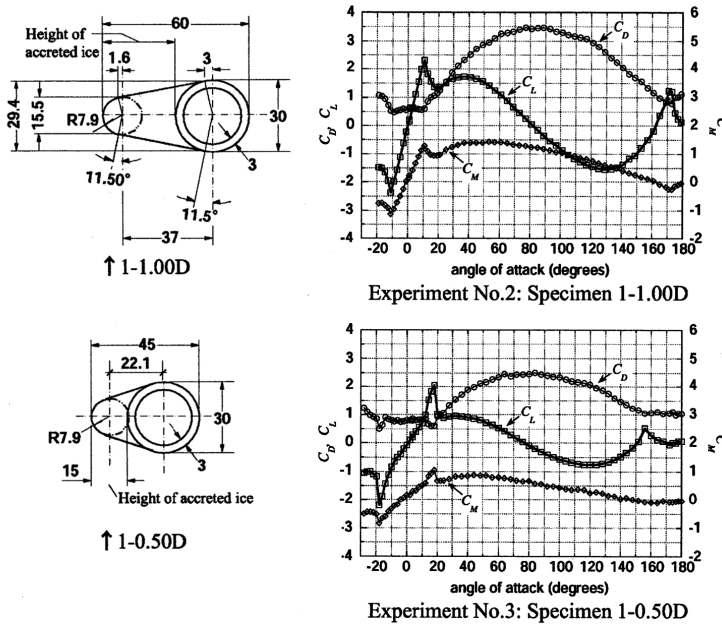


Figure 2.42: Cross section of the iced conductor and mean aerodynamic coefficients. After Shimizu *et al.* (2004).

ulation. The comparison of the aerodynamic coefficients numerically predicted by Oka & Ishihara (2010) with the experimental data of Shimizu *et al.* (2004) show good agreement with experiments, while C_L obtained by interpolations significantly overestimated the experiments in some angle of attack.

Gjelstrup *et al.* (2012) presented the results from a series of static wind tunnel tests on a circular cylinder representing a bridge hanger with simulated thin ice accretions. The experiments focus on ice accretions produced for wind perpendicular to the cylinder at velocities below 30 m/s and for temperatures between -5°C and -1°C . The cylinders tested in the wind tunnel were 960 mm long and the base cylindrical cross section was $D = 70\text{ mm}$. Ice accretion shapes were reproduced using a non-melting material and a rapid-prototyping (3-D printing) technique. The accretion was printed as additional pieces that could be glued on to the base cylinder longitudinally. The static wind tunnel tests on simulated iced cylinders reveal the significant effect of ice on the static force coefficients of the cylinder. Globally, a greater Reynolds number dependency for turbulent flow was observed. The difference in C_D is small for most wind angles-of-attack. The Reynolds number dependency of C_L is in angles less than -30° and greater than $+30^\circ$. No significant Reynolds number dependency is

found for C_M .

Recently, investigations have been performed on the aerodynamic coefficients of bridge cables in cross-flow conditions in both horizontal Koss & Lund (2013) and vertical (Demartino *et al.*, 2013a) and inclined/yawed (Demartino *et al.*, 2013b) configuration. Additionally, Koss *et al.* (2013) studied the influence of ice accretion on the aerodynamic forces of different bridge cables with surface modifications. In all this studies, the aerodynamic coefficients for varying Reynolds number and angles of attack were measured.

Koss & Lund (2013) tested two different climatic conditions characterized by wet and dry ice accretion. The wind speed during the accretion was 11 m/s and the mean temperature was -6°C and -3°C for the two climatic conditions tested. The exposure time was 1 hour. It was observed that the extension of the ice layer influences the flow separation and hence the aerodynamic performance. This becomes relevant when rotating the iced cable segment simulating a change of the wind direction after the icing incident. The effective body of the iced cable exhibits an aerodynamic drag behavior reflecting only a part of the dry cable behavior drag curve: either completely sub critical, i.e. constant C_D for all tested Re -numbers, or a drag drop over in the critical range. C_L exhibits similar characteristics. These transitions were more marked for the ice accreted at a temperature of -6°C .

Demartino *et al.* (2013a) measured the aerodynamic force coefficients of a cylinder vertically placed in the wind tunnel, simulating a vertical hanger of a suspension bridge, for 4 climatic conditions. The climatic conditions employed were: 1 hour exposure, flow velocity equal to 11 and 17 m/s and temperatures equal to -1° , -3° and -5° Celsius. The coefficients of the accreted cylinder showed considerable variations for each condition of ice accretion. This variation was due to the different features of each ice accretion. In particular, there were situations in which the aerodynamic coefficients did not depend on wind speed, and other situations in which they did. The values of the mean aerodynamic coefficients were mainly related to the position of separation point, which was determined by the size of the frontal accretion (hard rime or glaze ice type) and by the presence, dimension and density of iced rivulets on the lateral side. The soft rime accretion on the leeward side didn't influence the aerodynamic coefficient as it was removed by the wind at high velocities.

Demartino *et al.* (2013b) measured the aerodynamic force coefficients of an ice accreted cylinder with inclination of $\Theta = 30^\circ$ (the definition of Θ and β is given in Figure 2.3) simulating the inclined stays of a cable-stayed bridge, for different climatic conditions and yaw angles of accretion. The climatic conditions employed for the ice accretion were: 1 hour exposure, $U = 11\text{ m/s}$ and temperatures equal to -1° and -5° Celsius. For these parameters, accretions were generated for yaw angles of 0° , 90° and 180° . For all climatic conditions an increase of C_D was observed in the range of yaw angles of $\beta = 0^\circ$ to 90° , and a reduction in the range of $\beta = 90^\circ$ to 180° . The maximum of C_D was reached in all climatic conditions at approximately $\beta = 90^\circ$. The largest value

of C_D was found in the climatic conditions with position of accretion $\beta = 0^\circ$ and $\beta = 180^\circ$. The minimum of C_D was reached for approximately $\beta = 0^\circ$ and $\beta = 180^\circ$. In some case, C_L markedly depended on both the wind speed and on the yaw angle. The maximum of C_L were found when the icicles structures were more developed. Instead, the minimum of C_L was observed when lateral iced rivulets were more developed. The dependency of C_M on β was influenced by the yaw of accretion. Climatic conditions with the same yaw of accretion showed similar trend with respect to β and different values that depended on the dimension and shape of accretion.

Koss *et al.* (2013) studied the effect of ice accretion effects on the cable aerodynamics of horizontal cables in the case of a plain HDPE tube, a HDPE tube fitted with helical fillets and a HDPE tube with a pattern-indented surface. The climatic conditions employed for the ice accretion on each type of cables were: 1 hour exposure, $U = 11 \text{ m/s}$ and temperatures equal to -2° and -5° Celsius. It was found that the standard plain cable is most affected by ice accretion with respect to sensibility of drag to Reynolds number, to the magnitude of lift coefficient and to the sensibility of both force coefficients to surface roughness. Moreover, both helical fillet and pattern-indented cable are less susceptible to changes of the cable surface and ice accretion where the pattern-indented is least affected. For comparable icing conditions the pattern-indented cable has lower overall drag and lift coefficients compared to standard plain and helical fillet cable.

Huang & Li (2014) carried out icing wind tunnel tests on electrical conductor in order to characterize the aerodynamics. The test model was a section of real conductor. They found that the ice shape and ice thickness are both important factors that determine the aerodynamic characteristics of conductor. The sudden increase of lift coefficient, which is a kind of flow separation similar to the airfoil stalling, is likely to happen at low attack angle for conductor with thicker crescent ice shape.

2.5 Spanwise irregularities

Spanwise irregularities are variations of the cross section's shape along the cylinder axis, z . The spanwise irregularities can be classified in three groups:

- End effects (finite aspect ratio);
- Axis deviation;
- Variable diameter.

2.5.1 End effects

Practically, circular cylinders exist in many civil engineering applications such as offshore platforms, power lines, bridge supports, etc. Many of the previous

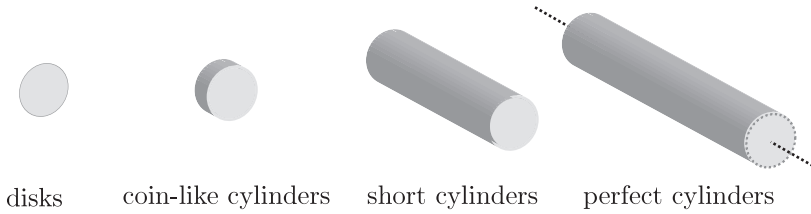


Figure 2.43: Finite aspect ratio cylinders.

studies have examined two-dimensional flow around a circular cylinder that is free of end effects. Practical circular cylinders are always finite. The variable describing the finite nature of the cylinder is the aspect ratio, $\lambda = L/D$. Different values of λ generate different aerodynamic behavior and different geometries (Figure 2.43). In particular, if λ is near to 0 the cylinder degenerates into disk. If λ assumes smaller values of D is a coin-like cylinder. If λ is larger than D is a short cylinder while if λ is greater than 10 the assumption of two-dimensional flow is satisfied. In this review only the case of both free ends will be considered, because the presence of near wall is not dealt with. However, in most practical applications there is at least one free end (chimney stacks, gas and oil storage reservoirs, etc.), and sometimes two free ends (ship radar aerials, submerged vehicles, fibres, projectiles carried by a tornado, etc.) (Zdravkovich *et al.*, 1989). The behavior of a finite circular cylinder with one end free and the other fixed on the ground is markedly different from that of two-dimensional bluff bodies and was studied by many authors (Etzold & Fiedler, 1976; Kawamura *et al.*, 1984; Okamoto & Sunabashiri, 1992; Uematsu & Yamada, 1995; Roh & Park, 2003; Sumner *et al.*, 2004; Sumner & Heseltine, 2008; Sumner, 2013).

When the cylinder has a free end exposed to the flow, the resulting aerodynamic behavior is much complex. In the past, there have been a number of measurements of the aerodynamic forces, surface pressures, wake periodicity and the wake velocity field downstream of the cylinder tip.

Wieselsberger (1922) was among the first to report drag measurements on a circular cylinder with two free ends having the aspect ratio $L/D = 5$. He covered an enormous range of Reynolds numbers from 400 to 8×10^5 . The drag coefficient curve varied with Re in a similar manner to that for the nominally two-dimensional cylinder but it was displaced towards lower C_D values. The plateau for the subcritical regime occurred for $C_D = 0.78$ instead of $C_D = 1.2$ for $L/D = \infty$. The drastic fall in C_D values in the critical regime took place at the same Reynolds number as for the nominally two-dimensional cylinder.

Williamson (1989) carried out wind tunnel tests to characterize the flow of a circular cylinder of finite span-length with end plates. He observed that, in the case of a long cylinder $L/D > 30$ at $Re > 64$, a cell of frequency f_L exists over the main body of the span, with two further cells of lower frequency f_e found near the ends and extending over a span-length of around 10 diameters. In the central

cell, oblique vortex shedding occurs, where the axes of the vortices are shed at some angle to the cylinder axis. Williamson (1989) also examined the effect of L/D on the cell structure of oblique vortex shedding for $16 \leq L/D \leq 240$ at $Re = 101$. He found that, if the length of the cylinder is reduced, the central cell contracts until this central cell suddenly vanishes at a certain critical value of $L/D = 28$. At the critical L/D , the end cells merge together, leaving the whole span shedding vortices at the one frequency, f_e .

Zdravkovich *et al.* (1989) measured the drag force across the range $6 \times 10^4 < Re < 2.6 \times 10^5$ for cylinders of aspect ratio between 1 and 10. The effect of hemispherical ends was also investigated. Figure 2.44 shows a considerable reduction in C_D when hemispherical ends were adopted, which is an indication that flat sides contribute to the overall drag. As the aspect ratio decreases, the cylindrical part of the cylinder shrinks and for $L/D = 1$ the cylinder with two hemispherical ends becomes a sphere. However, when the cylinder has two flat sides it is possible to reduce the aspect ratio down to $L/D = 0$, but the drag cannot tend to zero because of skin friction on both sides. Figure 2.45 shows the sketch of flow around free ends. The inflow consists of fluid near the x - z plane of symmetry that flows around the free ends. It takes some time for the inflow to turn and reach the near wake. The result is a low-pressure region near the free ends causing a high local drag coefficient. The separated shear layers from the sharp-edged circular ends form two counter-rotating swirling vortices, like those formed along the leading edge of the delta wing at an angle of incidence. The swirling vortices separate from the free ends and are carried downstream as a stream-wise vortex pair. The effect of the inflow on the near wake along the span does not merely increase the base pressure and widens the separated shear layers before roll-up into vortices. The former contributes additionally to the reduction of C_D .

Norberg (1994) experimentally examined the effect of L/D on the flow past a circular cylinder of finite span-length. Both cases of a cylinder with and without end plates were considered. Reynolds numbers were in the range of 50 to 4×10^4 . Different aspect ratios, at low blockage ratios, were achieved by varying the distance between circular end plates. It was not possible, by using these end plates in uniform flow, to produce parallel shedding all over the laminar shedding regime at very large aspect ratios. He presented also detailed results of the effect of L/D on vortex shedding. He didn't investigated condition of L/D smaller than the critical value 28 where the central cell disappears and end cells play dominant roles, although he noticed that the most dramatic effects of L/D at low Re occur for $L/D < 30$.

Zdravkovich *et al.* (1998) experimentally investigated the aspect ratio of short coin-like cylinders. Force and pressure measurements are extended down to $L/D = 0.025$. There is a systematic increase in the C_D up to 1.5 for $L/D = 0.06$. The apparent increase in the drag coefficient disappears when a new drag coefficient, scaled by the side area as the reference area, is used. As a matter of fact, the increase in drag coefficient for coin-like cylinders may be circumvented

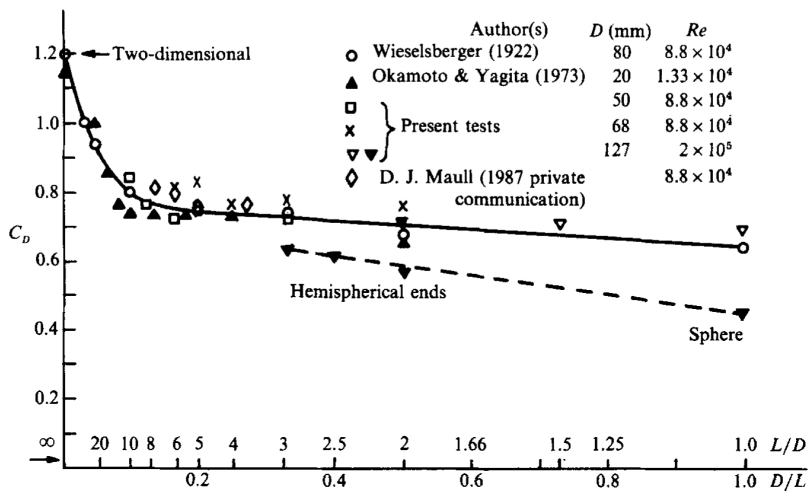


Figure 2.44: Drag coefficient from different authors in terms of aspect ratio. After Zdravkovich *et al.* (1989).

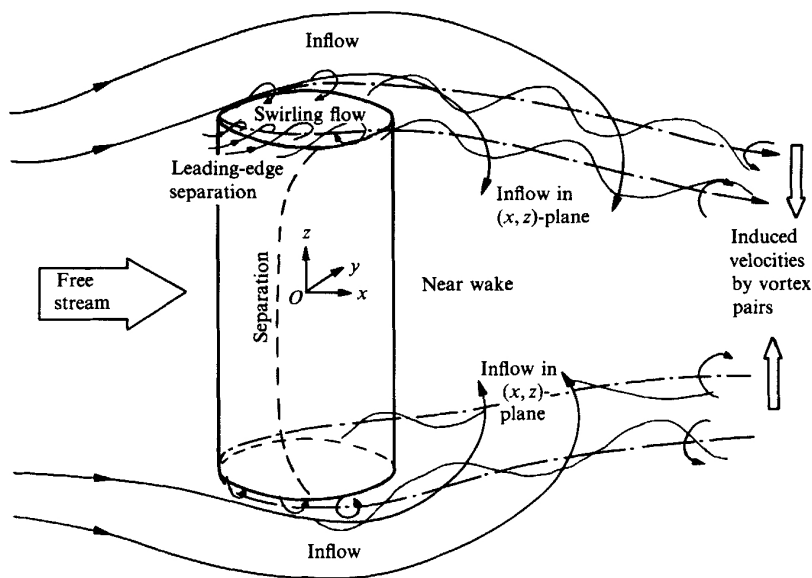


Figure 2.45: Sketch of flow around free ends. After Zdravkovich *et al.* (1989).

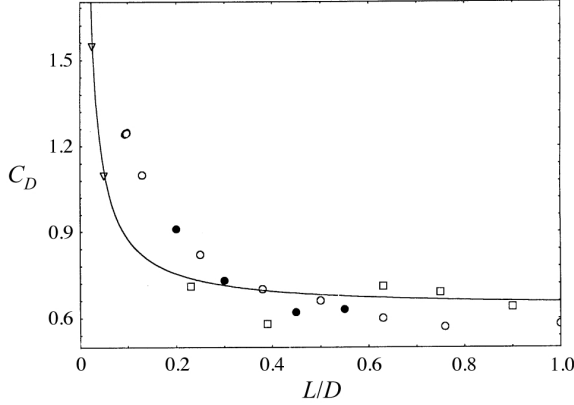


Figure 2.46: Measured drag coefficient in terms of aspect ratio: □, early tests; ○, second tests; ●, repeated tests; ▽, 60 cm disc. After [Zdravkovich *et al.* \(1998\)](#).

by replacing the projected area, LD , by the side area, $D^2 \cdot \pi/4$, as the reference area:

$$C_{DS} = C_D \frac{L}{D} \frac{4}{\pi} \quad (2.35)$$

Using their results, they found the best fit curve (Figure 2.46):

$$C_D = 0.24 \cdot L/D + 0.633 \quad (2.36)$$

The surface flow visualization on two flat sides reveals crescent-shaped areas between primary separation from the sharp edges and secondary separation of the reversed flow underneath the separation bubbles. The re-attachment region appears to be straight and perpendicular to the free stream. The surface flow visualization around the cylindrical section reveals the gradual disappearance of separation lines in the range $0.39 < L/D < 0.75$ and the appearance of separation ‘islets’ for $L/D > 0.39$. The change in separation is caused by the three-dimensional flow. A tentative topology of the flow around coin-like cylinders was proposed (Figure 2.47). It consisted of two horseshoe-shaped vortices attached onto the two flat sides. After their detachment at around $\pm 90^\circ$, the free vortices are coupled into two counter-rotating pairs on the lee side. Beyond the perimeter of the cylinder, two pairs of streamwise eddies are carried downstream. The geometry of these horseshoe eddies was visualized beyond a stationary frisbee in a wind tunnel by [Nakamura & Fukamachi \(1991\)](#). The position of the separation islet on the cylindrical segment coincides with the eddy pairs.

[Park & Lee \(2004\)](#) studied the flow structure around the free end of a finite circular cylinder by modifying the free-end corner shape. A finite cylinder with

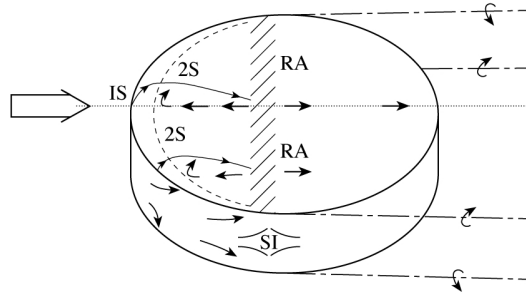


Figure 2.47: Tentative sketch of flow topology: IS —, primary separation; 2S —, secondary separation; SI —, separation islet; RA ···, reattachment; — — —, separation bubble; - · - ·, stream-wise vortex filaments. After [Zdravkovich *et al.* \(1998\)](#).

an aspect ratio of 6 was mounted vertically in the wind tunnel. In order to investigate the effects of the finite cylinder free-end corner shape on the wake structure, four different free-end shapes were tested (Figure 2.48):

- Flat tip;
- Bevelled tip;
- Radiussed tip;
- Hemispherical tips.

The size of the recirculation bubble formed above the flat-tip of the cylinder tip is largely reduced by shaping the corner of the tip smoothly. The shear layer separating from the plain tip expands as the flow goes downstream, compared to the other tips tested. The turbulence intensity around the tip decreased as the tip is modified to a more streamlined shape.

[Inoue & Sakuragi \(2008\)](#) numerically investigated the flow past a circular cylinder of finite span-length with two free ends based on direct numerical solutions of the three-dimensional unsteady incompressible Navier-Stokes equations. Results showed that the vortex shedding pattern changes drastically depending on both L/D and Re . Five basic patterns of vortex shedding were found to exist:

- Periodic oblique vortex shedding at relatively large L/D and at $Re > 70$;
- Quasi-periodic oblique vortex shedding also at relatively large L/D and at $Re < 60$;
- Periodic shedding of hairpin-shaped vortices which occurs when L/D is moderate;

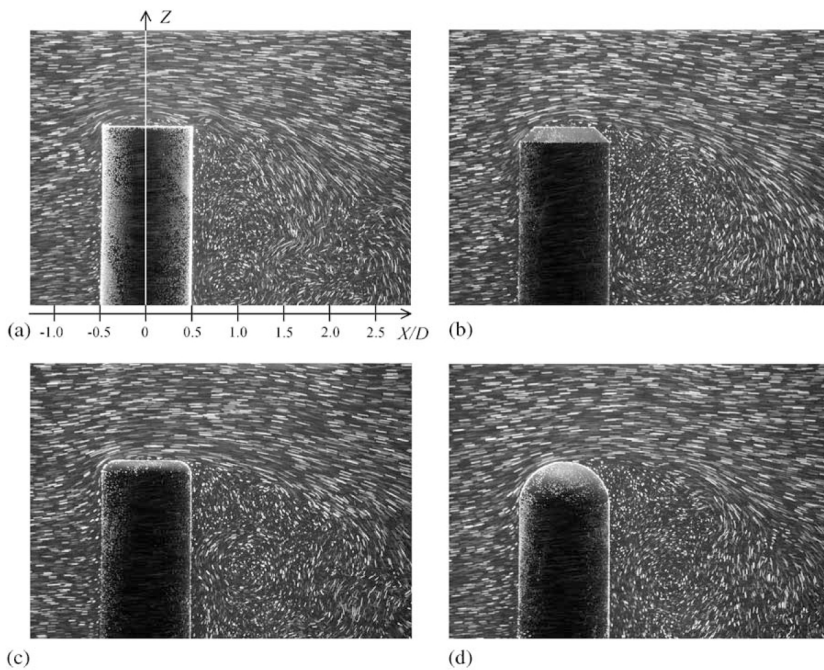


Figure 2.48: Cross-sectional view of flow around the cylinder free end in the plane orthogonal to the flow and to the cylinder axis. (a) flat tip; (b) bevelled tip; (c) radiussed tip; and (d) hemispherical tip. After [Park & Lee \(2004\)](#).

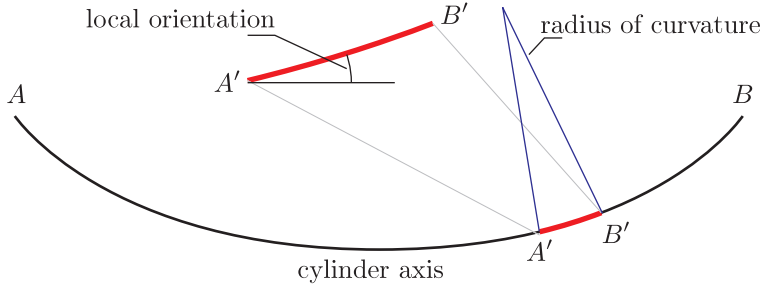


Figure 2.49: Curved cylinders and definition of local radius of curvature and orientation.

- Shedding of steady two counter- rotating vortex pairs which occurs when both L/D and Re are small;
- Alternate shedding of counter-rotating vortex pairs from two flat ends of the cylinder, which occurs when L/D is small and Re is high.

2.5.2 Axis deviation

In general, deformation is a change in the shape or size of an object due to an applied force or a change in temperature. In the case of one-dimensional bodies (beams or cables), the application of loads in directions parallel to the cross section produces the appearance of a curvature. In the case of beams, the curvature is generated by the bending moments. Differently, cables are usually characterized by having high axial tensile rigidity, and virtually no axial compressive rigidity. In addition, it is often reasonable to assume that the flexural rigidity of a cable is negligible. The flexural rigidity of a cable may be important, and must then be taken into account; the significance of the flexural rigidity of a cable depends on the cable tension and the radius of curvature of the cable centerline. In this case, the curvature is generated by the equilibrium reached in the deformed configuration.

From the aerodynamics viewpoint, curvature can impose additional strain on the flow that can vary along the entire length as the radius of curvature changes. The flow characteristics depend on the local orientation and curvature (Figure 2.49). Furthermore, the curvature produces three-dimensionality in the wake that can either attenuate or amplify the unsteady loads due to vortex shedding. The evaluation of the aerodynamic behavior of curved cylinders requires quantifying the variation due to the curvature of the flow-field around the cylinder. If the flow is not altered by the curvature (i.e. there is no interaction along the curved cylinder), the problem can be simply analyzed as a summation of single straight cylinders with different attitude to the wind (local orientation).

Surry (1965) investigated the flow and the associated forces of curved circular cylinders, at Reynolds Numbers between 10^4 and 10^6 . He defined a normal force coefficient expressed as:

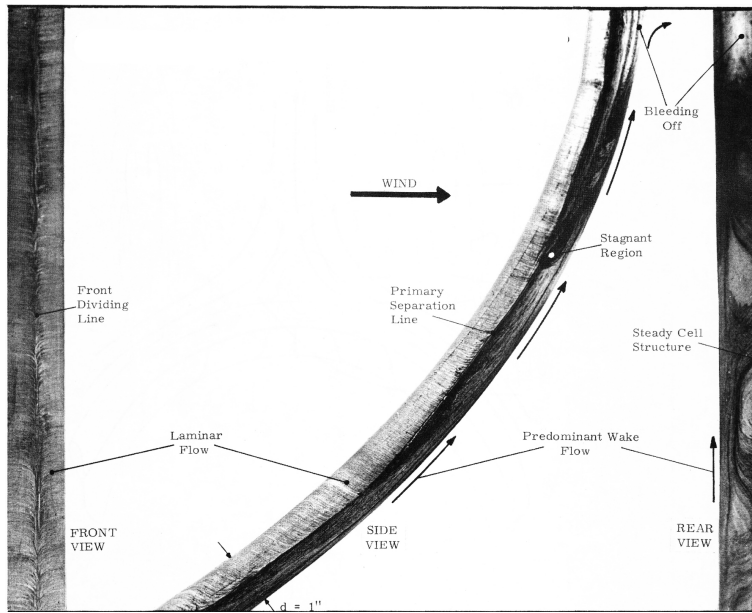
$$C_N = \frac{N}{\frac{1}{2}\rho U^2 D} \quad (2.37)$$

where N is the normal component of total aerodynamic force per unit length. The local normal force coefficient is very sensitive to the wake pressure hence C_N is not readily predictable for cylinders of appreciable curvature. However for large ratios of radius of curvature the effects of two dimensionality and wake flows becomes small, hence C_N is that given by the cross flow approximation. In this case, the local drag coefficients is estimated as:

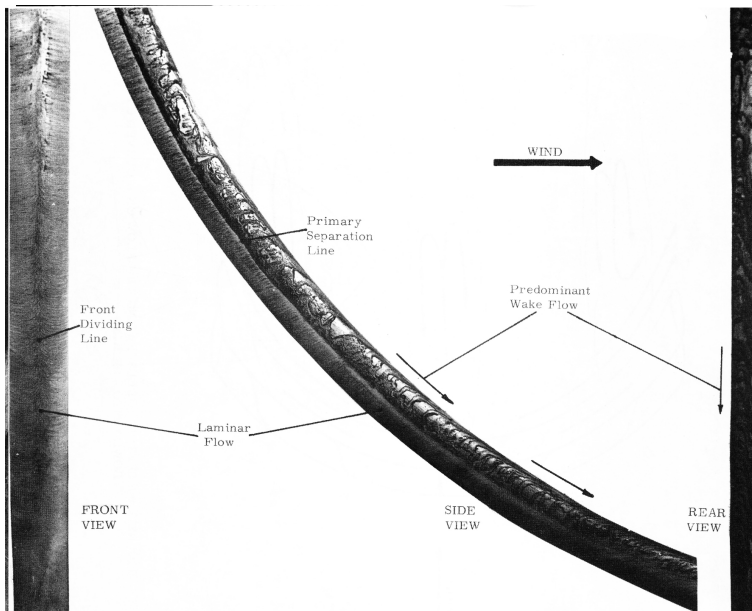
$$C_D = C_N \sin \phi \quad (2.38)$$

where ϕ is local angle of inclination of the cylinder axis to stream. He concluded that the curvature of a cylinder has a significant effect on the flow and pressure in the wake, and it should be considered in the prediction of the aerodynamic forces. He also performed flow visualization. Three views of the flow pattern around a curved cylinder bowed away from the wind and bowed into the wind are reported in Figure 2.50. In the case of the cylinder bowed away from the wind (Figure 2.50a), the tufts at the front lie on the cylinder surface quite steadily. Since the tufts were of the same length as the cylinder diameter they indicate a mean flow direction. The tufts are seen to be between the free-stream and the diametric directions. In the wake the tufts lie steadily along the axis toward the cylinder section that is normal to the flow. At the normal section the tufts in the wake appear unsteady with a mean downstream, horizontal, direction. In the case of curved cylinder bowed into the wind (Figure 2.50b), the flow seen from the detailed pattern is laminar at the front and shows a sharp separation line. The streamlines are parallel to the cylinder axis, forming a dividing line. The separation line is sharply defined but the angle of separation varies with the local angle of inclination of cylinder axis to stream.

Begak *et al.* (1985) investigated the vortex shedding phenomenon of a yawed and curved cylinders in wind tunnel. He tested a model with an axis of constant curvature (radius of curvature 4.3 m , maximum depth of arc 0.33 m) and a model with a curvilinear axis, which had two radii of curvature (1.56 m and 3.64 m , maximum depth of arc of the axis of the model equal to 0.66 m). The chords of the models were 3.3 m . The diameter of the cylinder was not specified. Each of the models was placed in the working part of the wind tunnel on a turntable, which made it possible to orient them in different ways in the flow. He obtained two main conclusions: reducing the radius of curvature of the cylinder induces a reduction in the Strouhal number, and the frequency of the vortex shedding along the model remains constant.



(a)



(b)

Figure 2.50: Three views of the flow pattern around a curved cylinder bowed away from the wind (a) and bowed into the wind (b). After [Surry \(1965\)](#).

Bartoli *et al.* (2006) performed wind tunnel tests, both in laminar and turbulent flow, on an experimental model that represents a whole cable supported at its ends to investigate the stochastic characteristics of its dynamic behavior. The experimental model of the cable was built using 48 cylinders, each one with a diameter of 40 mm and a length of 40 mm. The cylinders were connected by a 0.7 mm-diameter strand made of steel. The strand passed across holes coaxial to the axis of each cylinder, and joined to it with polyurethane foam. Each cylinder was placed at a distance of 8 mm from the next one to avoid contact during the motion of the cable: in this way, given the small diameter of the strand, the flexural stiffness of the cable could be assumed as not significant. The data logged by the load cells were elaborated to obtain the mean values of forces at increasing wind speed. With this procedure, they obtained an estimation of C_D of a cable supported at its ends. Moreover, the single cylinder elements producing the cable geometry, the model motion with regard to the flow, the porosity of the experimental model, due to the interspace between wood cylinders, affect the evolution of the drag force with increasing wind speed.

Recently, detailed investigations of the flow past curved cylinders have been carried out with the help of DNS. These studies have considered stationary geometries (Miliou *et al.* , 2003a,b, 2005, 2007). The curved cylinder in all these cases consisted of a quarter section of a ring. Miliou *et al.* (2003a) performed simulations at $Re = 100$. Different inflow velocity profiles and inflow directions were used in this study. They observed that when the flow acted normal to the plane of curvature, a shedding pattern similar to that corresponding to a uniform cylinder was produced, i.e. in-phase parallel shedding. When the flow was in the direction parallel to the plane of curvature of the cylinder, the shedding of vortices was found to be less energetic as the cylinder bends to become aligned with the main flow. Miliou *et al.* (2007) performed numerical simulations using three-dimensional spectral hypothesis at $Re = 100$ and 500 in order to study the shedding dynamics of curved cylinders. Fully three-dimensional wake dynamics were observed when the flow was directed towards the outer face of the bend (convex configuration), with the vortex shedding driven mainly from the vortices shed at the top of the cylinder. However, when they directed the free stream towards the inside of the bend (concave configuration), no vortex shedding was detected. An explanation suggested to this latter phenomenon was that the shedding was suppressed by the strong axial flow driven by the horizontal extension attached to the curved cylinder.

Globally, the study of the aerodynamics of curved or deformed cylinders has received much less attention, perhaps because of the higher degree of complexity involved in the three-dimensional geometry. From the state of the art research is not completely clear the limit of curvature at which the cylinder cannot be considered as straight from the aerodynamics viewpoint.

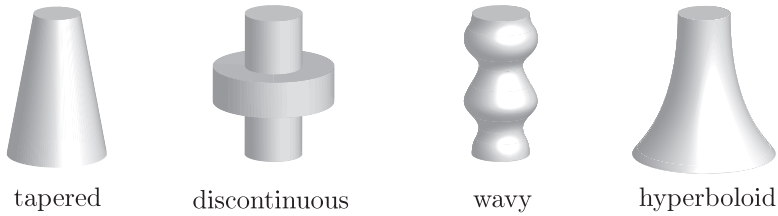


Figure 2.51: Cylinders with variable diameter disturbances.

2.5.3 Variable diameter

Some cylindrical structures in civil engineers applications have varying diameter along the cylinder axis (spanwise direction). The spanwise variation of the cross section can be may have different variation laws and generate different forms (Figure 2.51):

- Linear variation:
 - Cone;
 - Frustum of cone;
- Discontinuous variation:
 - Single step cylinders;
 - Dual step cylinders;
 - Multi-step cylinders;
- Sinusoidal:
 - Wavy cylinders;
- Non-linear variation:
 - Hyperboloid cylinders.

These variations in diameter can produce important effects on the aerodynamics: disruption of the vortical structures in the spanwise direction, of the spanwise correlation and of the organized Karman vortex street formation phenomenon. In this review, the case of faceted cylinders will not dealt in because they can't be considered nominally circular cylinders. As a matter of fact, the cylinders reported in Figure 2.51 have a circular section that it's scaled with different law of variation in spanwise direction. It must be emphasized that the majority of research on tapered cylinders and step cylinders has been done in the range of low Reynolds numbers, differently from the typical values for structures in civil engineering.

In the following, each of the variable diameter irregularities will be described.

2.5.3.1 Tapered cylinders

Tapered cylinders are characterized by a linear variation in cross sectional area along the spanwise direction. This variation produces a modification of the local values of Re that precludes eddy shedding at a constant Strouhal number. If the tapered cylinders are considered infinite they became cones. If they have limited length they are frustums of cone. The law of variation of the diameter in the spanwise direction, z , of the tapered cylinders is:

$$D(z) = az \quad (2.39)$$

where a is the taper ratio. To this equation the domain of z must be added to specify if it's a *cone* ($0 < z < \infty$) or a *frustum of cone* ($z_1 < z < z_2$).

Gaster (1969) pioneered with experiments on free-end cones with taper ratios of 36:1 and 18:1 and could show modulations in the velocity measurement signals at local Reynolds numbers from 50 to 200, indicating strong obliqueness in the vortex shedding. He did not notice any discontinuity in the frequency-Reynolds number relation. In Figure 2.52 show the comparison of the normalized shedding frequency in terms of local Re , i.e. based on the local diameter. The full line corresponds to Roshko's measurements for a perfect circular cylinder. Thus, it seems that the increased steepness of the Strouhal number curve is an intrinsic feature of tapered cylinders. Piccirillo & Van Atta (1993) defined the best-fit curve of the data to be:

$$St = 0.195 - 5 \cdot Re \quad (2.40)$$

Then, Gaster (1971) conducted experiments on a less tapered cylinder (120:1) and observed that the vortex wake structure consisted of a number of discrete cells having different shedding frequencies across the span. Four cells were observed along the span within which the signals were periodic and of constant amplitude except at the boundaries where modulation was observed. At higher flow velocities the vortex structure appeared to become similar to that observed on highly tapered cones (Gaster, 1969), with modulated signals over the entire span of the model. He observed a significantly lower frequency in the cell closest to the end-plate, as well as transitional regions along the span, which show an unstable affiliation to the neighboring cells. Moreover, Gaster (1971) adding small end-plate of 70 diameters observed that the discontinuity disappeared; he concluded that endplates limited the spanwise movement of the cells.

Piccirillo & Van Atta (1993) investigated the flow around tapered cylinders at low Reynolds numbers from 70 to 179. Four cylinders were used, with taper ratios varying from 50:1 to 100:1. They used a smoke-wire for flow visualization and a rake of four single-wired hot-wire probes for anemometry in the cylinder wake. It was observed that multiple spanwise vortex cells form in the wake, each associated with a distinct shedding frequency. The shedding frequency of each cell is lower than that expected for a uniform cylinder with the diameter

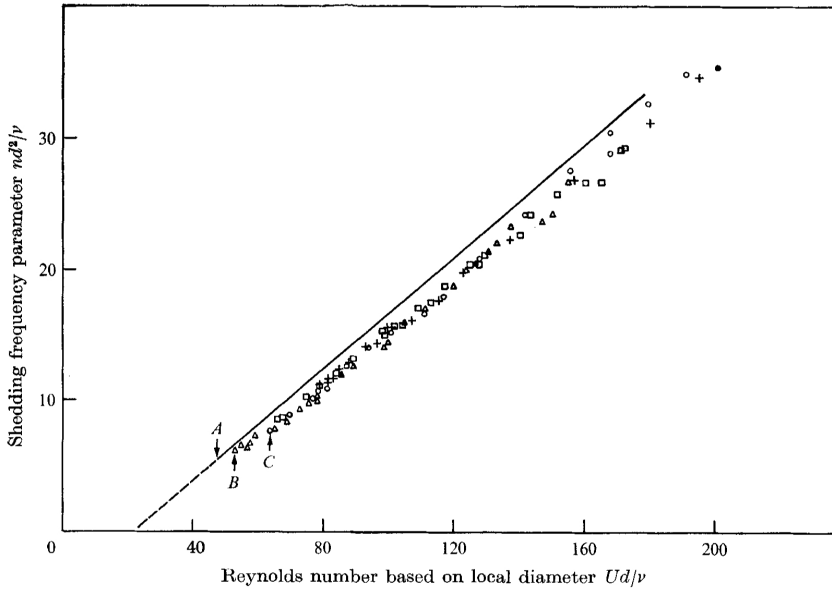


Figure 2.52: Variation of shedding frequency with local Reynolds number. After [Gaster \(1969\)](#).

equal to the local diameter of a tapered cylinder at the mid-span of the spanwise vortex cell. At the boundaries between adjacent cells, vortex interactions occur, involving vortex splitting and vortex dislocations.

[Papangelou \(1992\)](#) carried out wind-tunnel experiments on the flows created by a number of slightly tapered models of circular cross-section at Reynolds numbers of the order of 100. He found that the cell size decrease with local diameter. Individual cell size was found to be roughly self similar. Strouhal number and Reynolds number based on the diameter at cell centre showed a collapse for different taper ratios.

[Hsiao & Chiang \(1998\)](#) experimentally studied by hot-wire measurements in a wind tunnel in order to investigate the turbulent wake behind tapered cylinders experimentally. Their study covers 4 cylinders with taper ratios 24, 40, 51 and 75:1. The Reynolds number based on the cylinder's mean diameter ranges from 4×10^3 to 1.4×10^4 . They derived their results from hot-wire anemometry, using one X-wired probe and a rake of single wires to register the fluctuations of the velocity signal in the wake. They observed that two to three constant-frequency vortex cells of the shedding vortices along the spanwise direction. The corresponding Strouhal number based on the vortex shedding frequency and the cylinder's local diameter varies with respect to the taper ratio of the cylinder. They also found that most of the spanwise shedding vortices are well aligned

across the intersection region of the vortex cells except the vortex dislocation occurs to cause vortex lines discontinuous, in which the phase difference between the adjacent vortex cells jumps from π to $-\pi$.

Valles *et al.* (2002) conducted numerical simulations of flow behind tapered cylinders. They reproduced in the simulation the cellular structure of vortex shedding but other important parameters such as the variation of Strouhal number along the span were not well reproduced, showing a large discrepancy in the obtained results. In particular, the vortex splitting phenomenon described by Piccirillo & Van Atta (1993) was observed to occur in the wake of tapered cylinders.

Provansal & Monkewitz (2006) conducted experiments on tapered cylinders in a free surface water channel and studied the wake using hydrogen bubbles in the Reynolds number range between 40 and 180. Two cones made of polished brass with taper ratios 3.2×10^{-3} and 6.7×10^{-3} have been used. A technique called radon transform was used to analyze the vortex shedding angles in order to obtain time-series information. They reported from their analysis that the shedding frequency varies in a stepwise manner along the span of tapered cylinders.

Narasimhamurthy *et al.* (2009) have conducted a series of studies using Direct Numerical Simulations (DNS) of flow past tapered cylinders. They found that the Strouhal number versus local Reynolds number curves nearly collapse, thereby indicating that a change in the taper ratio by a factor of two does not affect the Strouhal number much. However, there still exists a significant contrast in the cellular shedding pattern.

Visser *et al.* (2011) experimentally investigated the time-dependent and three-dimensional flow behind different cylinders with taper ratio of 75:1 using a 3-component Stereo-PIV. Differently from the previous approach using hot-wire anemometry (Hsiao & Chiang, 1998; Piccirillo & Van Atta, 1993), the approach adopted provided not only long time-series of the individual velocity components, but also complete planar views of the instantaneous three-dimensional flow field. They suggested that the cellular shedding phenomenon and its dependence on Re and the cylinder aspect ratio could be presented based on analysis in the frequency domain. The shape and position of the vortex formation region was found to be in accordance with findings from uniform cylinders, while the local Strouhal numbers show some fundamental variation due to the locally varying diameter.

2.5.3.2 Discontinuous cylinders

Discontinuous cylinders are characterized by a discontinuous variation in the cross sectional area along the spanwise direction. This geometry is common in such engineering applications as heat exchangers and airport control towers. The law of variation of the diameter in the spanwise direction, z , of the tapered cylinders is:

$$D(z) = \begin{cases} D_1 & \text{if } z < z_1 \\ D_2 & \text{if } z_1 < z < z_2 \\ \vdots & \vdots \\ D_{n-1} & \text{if } z_{n-1} < z < z_n \\ D_n & \text{if } z < z_n \end{cases} \quad (2.41)$$

where n is the number of diameter variations and D_i are the diameter in each segment. Research was mainly focused on the definition of the characteristics of three geometries:

- Single step cylinders;
- Dual step cylinders;
- Multi-step cylinders.

In the following, each geometric case is analyzed.

A single step cylinder consists of a large cylinder (diameter D_1) and a small cylinder (diameter D_2) joined co-axially. A dual step cylinder consists of two small cylinders (diameter D_2) attached co-axially to the ends of a large cylinder (diameter D_1). A multi step cylinder consists of an alternating series of a small cylinders (diameter D_2) and a large cylinder (diameter D_1) attached co-axially to the ends. The last two geometries are also characterized by the extension of each sub-cylinder attached co-axially. In any case, there are one or many discontinuity at the edge of the large cylinder where a step change in diameter occurs. In the following, each case is presented.

Yagita *et al.* (1984) carried out pioneering experimental tests on the characterization of the flow around circular cylinder with a step in a uniform flow. They measured vortex shedding frequency over the Reynolds range $8 \times 10^2 > Re > 10^4$ for various diameter ratio D_2/D_1 in the range of 0 to 1 and length-diameter ratios L/D in the range of 10 to 27. They found that the vortex shedding frequency depends on Re and D_2/D_1 . In particular, for $D_2/D_1 \geq 0.8$, the Strouhal number of the step cylinder nearly agrees with that of the straight cylinder. Differently, for $D_2/D_1 < 0.8$, the Strouhal number of the step cylinder is much smaller of that of the straight cylinder.

Ko & Chan (1990) carried out wind tunnel tests to study the flow within the intermixing region behind circular cylinders with stepwise change of the diameter of diameter ratio $D_2/D_1 = 0.5$. Their measurements focus on a region within three diameters of the diameter discontinuity. Detailed measurements of the velocity fluctuations and of flow visualization within the intermixing region show the presence of the big and small vortex wakes. Both wakes were found under the dominant primary mode, which corresponds to the vortex shedding Strouhal number of two dimensional cylinder, and the less dominant secondary mode.

Lewis & Gharib (1992) investigated experimentally the wake caused by a local discontinuity in cylinder diameter. They found two distinct types of wake behavior governed by the diameter ratio: a direct mode and an indirect mode. The appearance of these different modes is a function of the diameter ratio and Re . The interaction region behavior can be divided into three categories, based on:

- $D_2/D_1 < 1.25$ - direct mode dominates;
- $1.25 < D_2/D_1 < 1.55$ -transitional (mode is a function of Re);
- $1.55 < D_2/D_1$ - indirect mode dominates.

In the direct mode, the vortex interaction region is relatively narrow, with vortex connections occurring between vortices shed from the large and the small cylinders and vortex dislocations involving connections between vortices in the same cell (Figure 2.53a). In the indirect mode, a distinct vortex shedding cell, different from the dominant vortex shedding cells in the wakes of the large and the small cylinders, forms within the interaction region (Figure 2.53b). The shedding frequency of this cell was found to be the lowest of the three cells. Complex vortex connections and vortex dislocations occur at the two cell boundaries, one located directly downstream of the step, and the other, offset to the large cylinder side.

Vallès *et al.* (2002) carried out computational flow analysis of wake phenomena caused by a discontinuity in cylinder diameter. The computer simulations support the experimental observations by Lewis & Gharib (1992) of the direct-mode interactions. The pressure and vorticity fields associated with the numerically generated flow field provide a distinct picture of the intricate vortex interactions downstream of the step and as such supplement the earlier smoke visualization by Lewis & Gharib (1992).

Dunn & Tavoularis (2006) investigated the interactions of vortices shed from two coaxially joined cylinders with a $D_2/D_1 = 0.51$ in a water channel, at Reynolds numbers, based on the large cylinder diameter, between 63 and 1100. Spectral and wavelet analyses of stream-wise velocity measurements have identified the formation of three distinct spanwise vortex-shedding cells away from the far ends of the two cylinders, including a low-frequency cell, which appeared in a cyclic manner near the step and behind the large cylinder. The three types of wake vortex shedding cells can be identified for indirect mode shedding in the wake of a step cylinder (Figure 2.54):

- The S-cell vortex shedding from the small cylinder;
- The L-cell vortex shedding from the large cylinder;
- The N-cell distinct vortex shedding in the region between the S-cell and the L-cell.

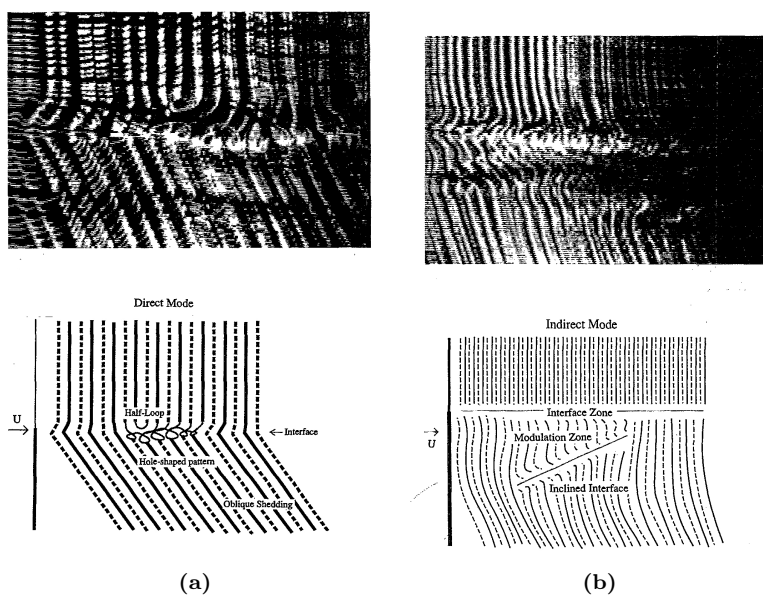


Figure 2.53: Flow visualization at $Re = 76/57$ (based on D_2 / based on D_1) for the $D_2/D_1 = 1.34$ direct mode (a) and at $Re = 99/57$ for the $D_2/D_1 = 1.76$ (based on D_2 / based on D_1) direct mode (b). After [Lewis & Gharib \(1992\)](#).

Based on flow visualization results, [Dunn & Tavoularis \(2006\)](#) suggest that the N-cell is a cyclic phenomenon; the formation of N-cell vortices interrupts periodically and then resumes after a few L-cell shedding cycles. However, the mechanism behind the N-cell formation and its cyclical nature remains unexplained. [Lewis & Gharib \(1992\)](#) have suggested that the frequency of occurrence of N-cell cycles is related to the growth rate of the N-cell, and the occurrence of a secondary instability, initiating the N-cell cycle. [Dunn & Tavoularis \(2006\)](#) suggest that the mechanism responsible for N-cell formation is related to that due to which the low frequency cell is believed to form near the end of a cantilevered cylinder. The formation of the N-cell near the step has been plausibly associated with downwash from the trailing edge of the step and the resulting recirculation that decreases the shedding frequency compared to parts away from the step.

[Morton & Yarusevych \(2010\)](#) investigated numerically the flow past a circular cylinder with a single stepwise discontinuity in diameter was for the diameter ratio $D_2/D_1 = 0.5$ and two Reynolds numbers based on the larger diameter, $Re = 150$ and 300 . The numerical results show that three distinct spanwise vortex shedding cells form in the step-cylinder wake, namely, the S-cell, N-cell, and L-cell. The N-cell, which forms in a region downstream of the step on the large cylinder side, has the lowest shedding frequency of the three cells. Due to the difference in shedding frequencies of the N-cell, L-cell, and S-cell, vortex dislocations occur at the boundaries between the adjacent cells. The numerical results provide new insight into vortex dynamics in the step-cylinder wake. In particular, complex vortex interactions, involving vortex dislocations and vortex splitting, occur within two regions located at the cell boundaries, referred to as transition regions, whose location and spanwise extent fluctuate with time. The formation of N-cell vortices was shown to be linked to downwash fluctuations near the step.

[Dunn & Tavoularis \(2011\)](#) studied the vortex-shedding patterns behind a step-cylinder in uniformly shear flow for Reynolds numbers between 152 and 674 using flow visualization and laser Doppler velocimetry. The effect of shearing on vortex shedding was found to be significant. Shearing affected both the spanwise length of the vortex cell and the difference between its frequency and that in the adjacent large-cylinder cell. The values of these parameters were found to depend on both Re and the orientation of the cylinder axis relative to the shear direction.

[Morton & Yarusevych \(2013\)](#) investigated experimentally the turbulent wake development of a circular cylinder with a single stepwise discontinuity in diameter using flow visualization and two-component Laser Doppler Velocimetry (LDV). The step cylinder model was made of stainless steel and aluminum. A solid smaller diameter cylinder ($D_2 = 6.35\text{ mm}$) is made of stainless steel, and a larger diameter cylinder ($D_1 = 12.71\text{ mm}$) was made of aluminum. The model was mounted between circular endplates and placed in a uniform region of the flow. The results show that turbulent vortex shedding from a single step cylin-

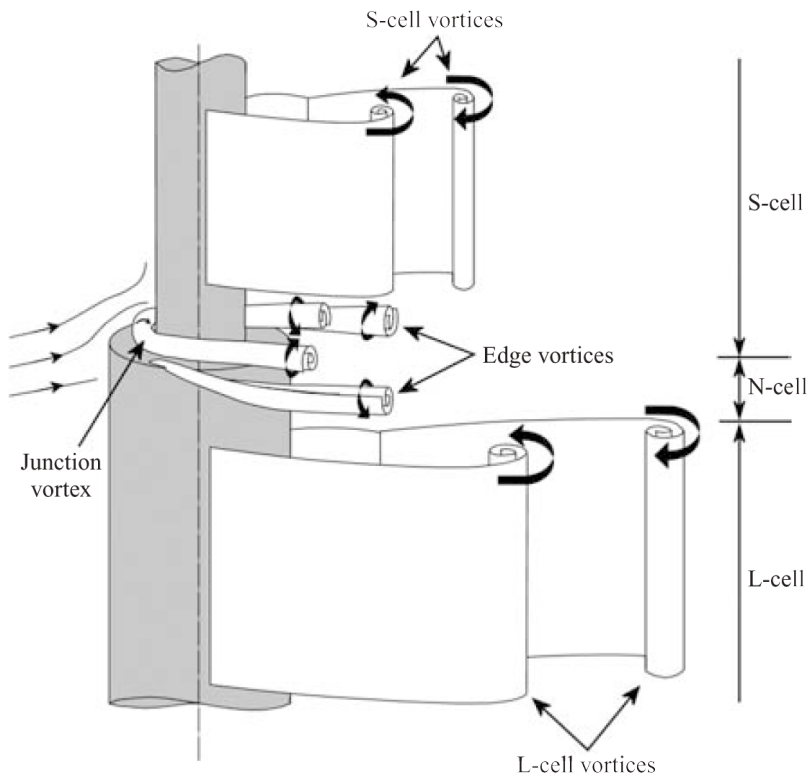


Figure 2.54: Sketch illustrating the spanwise and streamwise vortices shed from a stepped cylinder with $D_2/D_1 = 0.51$, flow coming from left to right. After [Dunn & Tavoularis \(2006\)](#).

der occurs in three distinct cells of constant shedding frequency. The differences in frequency and strengths between vortices in the cells lead to complex vortex interactions at the cell boundaries. The results demonstrate that vortex splitting, half-loop vortex connections, and direct cross-boundary vortex connections occur near the cell boundaries.

Williamson (1992) investigated the flow past dual step cylinders of small aspect ratio at Reynolds numbers pertaining to the laminar shedding regime. He used a dual step cylinder with $D_2/D_1 = 1.5$ and $L_c/D = 0.5$ to investigate the formation and development of vortex dislocations. L_c is the length of the diameter variation. The presence of the larger cylinder caused the formation of periodic vortex dislocations on both sides of the large cylinder. The dislocations were synchronized only when the flow conditions on either side of the large cylinder were carefully matched (i.e., the shedding frequencies of the small cylinders were nearly identical). He found that the frequency of dislocations and the influence of the dislocations on the wake development depend on the diameter ratio, D_2/D_1 .

Morton & Yarusevych (2012) studied the flow characteristics in the wake of a dual step cylinder using Laser Doppler Velocimetry and flow visualization. The experiments have been performed for $Re = 1050$, a diameter ratio $D_2/D_1 = 2$, and a range of large cylinder aspect ratios (L_c/D). The results show that the flow development is highly dependent on L_c/D . They found four distinct flow regimes based on the characteristics of the vortex dynamics in the wake of the large cylinder. For $L_c/D = 17$ five shedding cells were observed in the wake. At the middle span of the large cylinder, the familiar L-cell appeared in addition to two N-cells at the large cylinder ends. Behind the small cylinders a single cell shedding regular vortices was distinguished, similar to the S-cell. This behavior close to the steps is comparable to that of a single step cylinder. As the large cylinder aspect ratio was reduced, the N-cell's close to the steps vanished for aspect ratios in the range 7-14, resulting in a single vortex shedding cell across the large cylinder span. As the aspect ratio was reduced from 14 to 7, St reduced in a similar manner from 0.193 to 0.175 respectively. The shedding cells behind the small cylinders persisted, hence a total of three shedding cells were identified in the wake. Similarly, for aspect ratios between 2-7, a single vortex shedding cell across the large cylinder was identified. Large three-dimensional effects deformed the vortices shed behind the large cylinder into hairpin-like structures difficult to discern from flow visualization. However, a dominant vortex shedding frequency was detected in the L-cell and found to be decreasing as the aspect ratio decreased. Lastly, when the aspect ratio was reduced to $L/D = 1$, no distinct vortex shedding frequency was recognized in the large cylinder wake.

Many authors investigated the use of multi-step geometry to control the flow around circular cylinders. The first to propose the use of circular rings was Sallet & Berezow (1972), with the intension to avoid vortex shedding from suddenly occurring along the total length of the cylinder. In literature this geometry is usually called circular rings devices. A detailed investigation of the flow around

static cylinders with circular rings was done in [Lim & Lee \(2004\)](#). Four different cylinder models are tested: one plain smooth cylinder of diameter $D = 60\text{ mm}$ and three cylinders of the same diameter with O-rings of diameters $d = 0.0167D$, $0.05D$ and $0.067D$, respectively. O-rings are glued on the surfaces of smooth circular cylinders with pitches of $PPD = 2D, 1D, 0.5D, 0.25D, 0.165D, 0.083D$ and $0.0167D$. At $Re = 1.2 \times 10^5$, the cylinder fitted with O-rings of $d = 0.0167D$ in a pitch interval of $0.165D$ shows the maximum drag reduction of about 9%, compared with the smooth cylinder. Flow visualizations confirmed the presence of narrower wake and how the rings elongates vortex formation region. The simple attachment of O-rings controls the vortex shedding from the cylinder and elongates the vortex formation region, reducing drag force acting on the cylinder at high Reynolds numbers.

In an effort to reduce the overall drag force, [Nakamura & Igarashi \(2008\)](#) attached multiple cylinders (diameter D_2) to a uniform cylinder (diameter D_1). Each ring was separated by a fixed spanwise distance. It was varied the ring aspect ratio (L_c/D), the spanwise spacing between each ring, the diameter ratio (D_2/D_1), and Reynolds number (Re) to reduce the overall drag force. A range of parameters was determined for which the drag force was reduced by as much as 18% compared to a circular cylinder without rings. Furthermore, the flow visualization indicates that the flow separation on the ring surfaces is delayed when compared to a uniform circular cylinder. The delayed separation was associated with streamwise vortices that are generated at each of the step discontinuities in diameter.

[Lupi et al. \(2013\)](#) found the existence of a new type of bistable flow, induced around a single circular cylinder with a free-end by the presence of spanwise rings, through wind tunnel tests. The cylinder is a rigid body of 1 m in height and 15 cm in diameter. The model had the presence of a certain number of circular ring beams along the height (spanwise rings). In particular the investigated configuration has 10 ring beams, equally spaced along the height at a distance of 10 cm in the wind tunnel scale, i.e. $2/3$ of the diameter D .

2.5.3.3 Wavy cylinders

Wavy cylinders also known as sinusoidal or varicose cylinders are characterized by the diameter varying in a sinusoidal manner along its spanwise direction. This type of cylinders has been extensively studied for its ability in modify the aerodynamics. An example of the capability of this cylinder imperfection to reduce aerodynamic forces is the Brancusi Tower in Romania realized in 1938 (Figure 2.55). This tower is an interesting case study in bluff body aeroelasticity and its stability has been attributed to its unconventional shape ([Dragomirescu et al. , 2009](#)). The tower height is 29.35 m and its plane cross sections are square with 0.45–0.90 m sides. It is not a circular wavy cylinder because the base section is square and it's made of 17 rhomboidal modules. However, it has some aerodynamic characteristics similar with wavy cylinders.

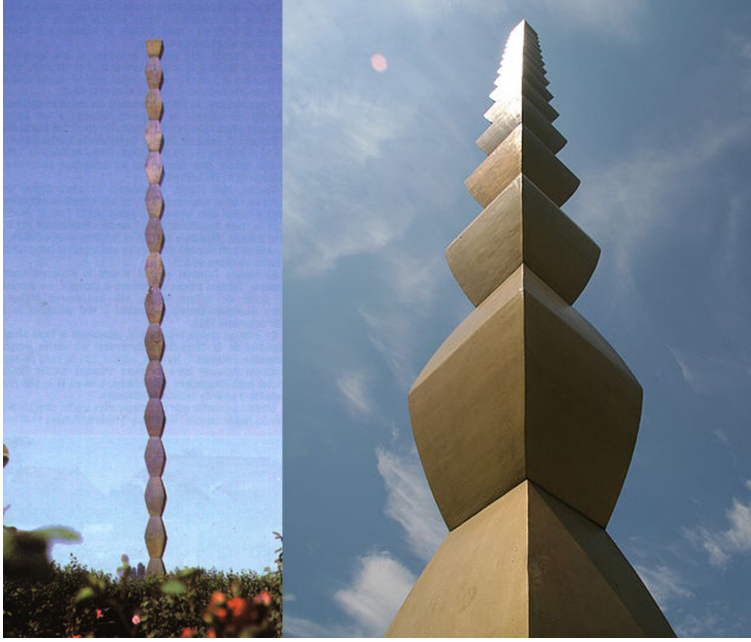


Figure 2.55: Brancusi tower. After Wikimedia Commons.

First study on wave cylinders were carried out by [Ahmed & Bays-Muchmore \(1992\)](#); [Ahmed et al. \(1993\)](#). They defined the law of variation of the diameter in the spanwise direction, z , of the wavy cylinders as:

$$D(z) = D_m - 2a \cos \left(\frac{2\pi z}{\lambda_w} \right) \quad (2.42)$$

where D_m is the nominal cylinder diameter, a is the amplitude of the surface curve and λ_w is the wavelength of the variation. Usually wavy cylinders can be described by two non-dimensional parameters: one is the normalized amplitude, a/D_m ; and the other is the normalized wavelength, λ_w/D_m . Moreover, the axial locations of maximum diameter are hereafter termed *geometric nodes* and the axial locations of minimum diameter are termed *geometric saddles*. [Ahmed & Bays-Muchmore \(1992\)](#) and [Ahmed et al. \(1993\)](#) investigated experimentally the pressure field and flow patterns over a wavy cylinder. [Ahmed & Bays-Muchmore \(1992\)](#) tested one right-circular cylinder and four wavy cylinder models in a wind-tunnel and in a water-tunnel. It was found that the flow appeared far more stable and symmetrical about the geometric saddle than the geometric node and that the base-pressure coefficient was slightly lower (more suction) at the geometric nodes than at the geometric saddles, suggesting a spanwise variation in the wake structure. They measured the mean drag force

acting on a wavy cylinder using surface pressure taps. Notwithstanding the large spanwise pressure variations, C_D for the wavy cylinders is not significantly different from that for a perfect circular cylinder. Ahmed *et al.* (1993) explored the effects of the three-dimensional separation line topology on the development of the wavy turbulent wake. They also presented and analyzed the mean velocity field and the Reynolds stresses. As a result, they found that the formation of trailing streamwise vortices behind nodal points of separation gave rise to a locally narrower wake, a rapid wake velocity recovery and a suppression of the turbulence development within the separated boundary layer. They further found that the Reynolds stress field in the immediate wake exhibited large spanwise variations.

Lam *et al.* (2004a) and Lam *et al.* (2004b) performed experiments to deal with the drag reduction and the relevant flow-induced vibration for different wavy cylinders. Lam *et al.* (2004a) experimentally investigated the effects wavy cylinders on mean drag and fluctuating lift reduction. The experiments were carried out in a low speed wind tunnel having a free-stream turbulence intensity less than 0.2%. The Reynolds numbers, based on the free-stream velocity and the nominal cylinder diameter, vary from about 2.0×10^4 to 5.0×10^4 . They measured mean and fluctuating forces induced by a cross-flow over three wavy cylinders and the circumferential pressure distributions at various spanwise positions. They defined a new normalized parameter that is used to express the degrees of cylinder obliqueness:

$$\frac{a^2}{\lambda_w D_m} \quad (2.43)$$

They tested three wavy cylinders with normalized obliqueness equal to 6.94×10^{-3} , 4.44×10^{-3} and 10.02×10^{-3} , respectively. The mean drag coefficients of the wavy cylinders are less than that of the circular cylinder. A drag reduction of up to 20% can be achieved depending on the degree of obliqueness. The pressure distributions indicated that the base pressure of the wavy cylinders at any spanwise location is higher than that of the circular cylinder at the same Re . The fluctuating force results show that the fluctuating lift coefficients of the wavy cylinders are lower than that of circular cylinders indicating that the fluctuating force characteristics of the wavy cylinders are more incoherent than for a circular cylinder. The Strouhal number is around 0.2, which equal to the values of circular cylinders. Lam *et al.* (2004b) carried out Laser Doppler Anemometry (LDA), Laser-Induced Fluorescence (LIF) and Digital Particle Image Velocimetry (DPIV) measurements in order to characterize the wake velocity field including the distributions of the mean velocity, the normal stresses and the shear stress as well as the flow patterns of a wavy cylinder. Figure 2.56 shows the spanwise vortical structures obtained using LIF. The formation length in the wake of the saddle plane is longer than that in the nodal plane, as indicated by the arrows. This 3-D phenomenon can be seen clearly after the Strouhal vortex has just been shed, for example, at $t/T = 0.25$ or 1.25 . In addition, a

rib-like structure was found in the cylinder wake joining neighboring vortices. The rib-like structure in the wake of a wavy cylinder seems to appear near the saddle planes. Therefore, the wavy shape caused the rib-like structure of the wake to be different from that behind a circular cylinder. The 3-D vortex sheet rolls up at a position further downstream (thus a longer formation length) with a weaker strength. Such vortices then interact and break down through a rib-like structure. As a result, the base pressure is increased and the fluctuation pressure is reduced. This, therefore, results in a reduction of the average mean drag coefficient and the fluctuating lift. The free shear layers shed from the points near the saddles extend along the spanwise direction, while the shear layers near the nodes contract. The turbulence correlations show that the vortex streets in the circular cylinder wake are more regular, while the wavy cylinder wake shows more incoherent turbulence due to enhanced turbulent mixing; a consequence of three-dimensional (3-D) effects.

Nguyen & Jee (2004) investigated flow characteristics of the near-wake behind two sinusoidal cylinders (model 1 with $\lambda_w/D_m = 1$ and model 2 with $\lambda_w/D_m = 2$) by measuring C_D , mean velocity and turbulence intensity profiles over Reynolds numbers ranging from 5.000 to 20.000. The sinusoidal cylinder with axial wavelength $\lambda/D_m = 2$ was found to reduce the drag coefficient by about 22% at $Re = 10.000$, compared with the corresponding smooth cylinder.

Zhang & Lee (2005) used the PIV technique to investigate the flow structures in the near wake of a wavy cylinder at $Re = 3.000$ and demonstrated well-organized stream-wise vortices in the spanwise direction. In particular, the pronounced spanwise variations of the flow structure in the near-wake behind the sinusoidal cylinder was attributed to the formation of counter-rotating stream-wise vortices at the two sides of each node and their interaction with the large-scale spanwise vortices. Well-organized stream-wise vortices with alternating positive and negative vorticity were observed along the span of the sinusoidal cylinder, of which the spanwise wavelength of approximately D_m was different from the instabilities of a smooth cylinder.

New *et al.* (2013) experimentally investigated the behavior of low aspect-ratio, $\lambda = 6$, wavy cylinders with different wavelengths and wave amplitudes enclosed by end-walls at a $Re = 2.700$. Wavelengths of $2D_m$ and $4D_m$, as well as wave amplitude of $0.1D_m$, $0.2D_m$ and $0.3D_m$ were tested in node and saddle configuration (Figure 2.57). The experiments were conducted in a recirculating water tunnel. They found that the flow behavior of shorter-wavelength $\lambda_w/D_m = 2$ cylinders is less sensitive to variations in the geometrical arrangement, aspect-ratio and the use of end-walls. This is primarily due to the regular formations of stream-wise vortices at their saddles under both node- and saddle-configured arrangements, which reduce external effects associated with cylinder-wall interferences. Conversely, the longer-wavelength $\lambda_w/D_m = 4$ cylinders are more susceptible to end-effects from cylinder-wall interferences. As a matter of fact, the longer-wavelength cylinders exhibited little or no formation of stream-wise vortices.

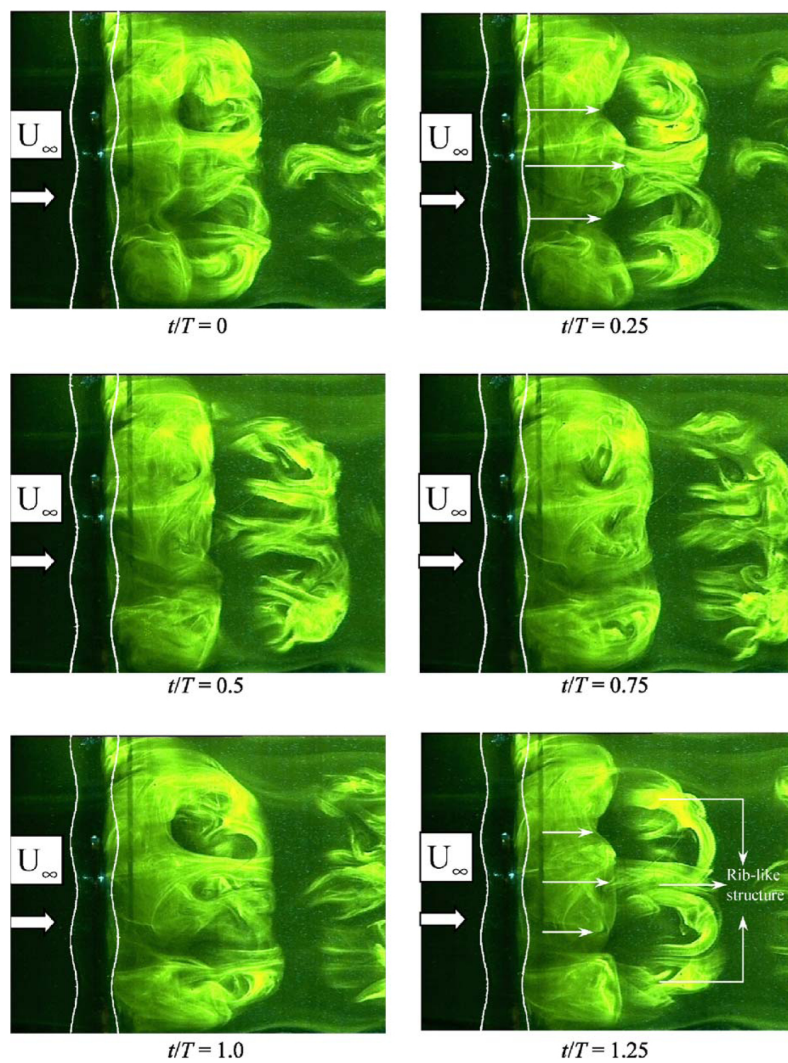


Figure 2.56: A time sequences of LIF results on spanwise vortical structure of the wavy cylinder, $Re = 600$. After [Lam *et al.* \(2004b\)](#).

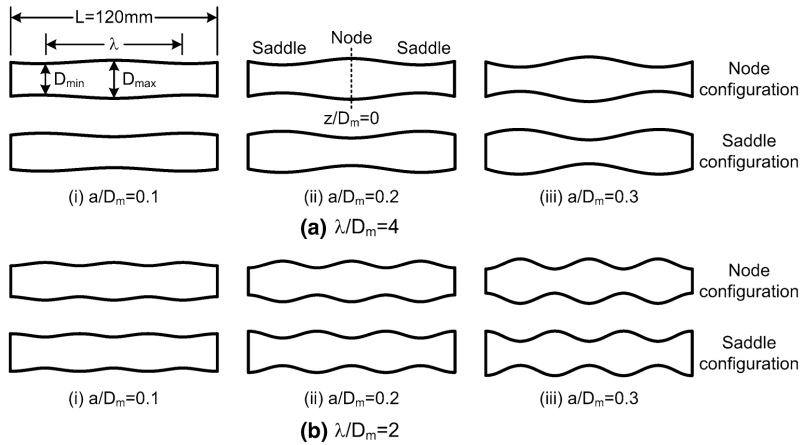


Figure 2.57: Geometries of the wavy test cylinders. After [New *et al.* \(2013\)](#).

Different authors tried to solve numerically the problem of characterization of the aerodynamic behavior of wavy cylinders. First analyses were performed by [Keser *et al.* \(2001\)](#) that used a three-dimensional discrete vortex method to simulate the separated flow around a circular cylinder with sinusoidal waviness along its span.

[Lam & Lin \(2008, 2009\)](#) studied numerically the turbulent and laminar flow over wavy cylinders using the large eddy simulation (LES). These studies revealed that the wavy surface can lead to the formation of a 3D shear layer, which is more stable than the 2D shear layer. [Lam & Lin \(2008\)](#) found that the Strouhal numbers for wavy cylinders are still approximately the same as that of a circular cylinder. C_D and the fluctuating lift force of wavy cylinders drop sharply with the increase of a/D_m at an optimal wavelength λ_w/D_m around 1.9. The vortices are well organized for a large value of a/D_m which has a strong effect on the fluctuating lift force. [Lam & Lin \(2009\)](#) investigated the three-dimensional near wake vortex structures of wavy cylinders at $Re = 100$. The wavy cylinders are classified into three wavelength regimes (I, II and III) with different flow patterns (A), (B) and (C). The definition of the regimes and pattern is shown in Figure 2.58. For flow pattern (A), the flow is unsteady and shows a quasi-two-dimensional unsteady wake structures similar to the straight circular cylinder. Flow pattern (B) is characterized by an increase of three-dimensional wake vortex distortion and vortex formation length with a progressive weakening of vortex shedding. In pattern (C), the flow pattern behind the wavy cylinder is very steady.

[Zou & Lin \(2009\)](#) studied the cross-flow past a wavy cylinder using LES at $Re = 3000$. They observed that the wake width expands in the region

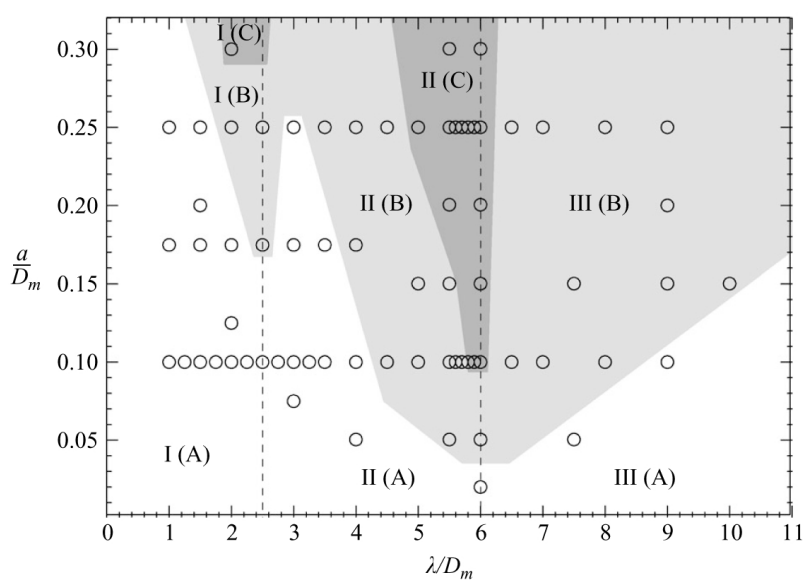


Figure 2.58: Flow pattern regimes of wavy cylinders with different spanwise wavelengths λ_w/D_m and wave amplitudes a/D_m at $Re = 100$. The symbol \circ represents each wavy cylinder case in the present simulations. After [Lam & Lin \(2008\)](#).

behind the saddles of cylinders and shrinks behind the nodes. As a result, the near wake vortex structures exhibit a periodic variation along the spanwise direction. Furthermore, the free shear layer is more difficult to roll up and develop to a mature vortex at a further downstream position by a longer vortex formation length. Hence, the effects of pressure and pressure fluctuation are less strongly felt by the cylinder. This observation justified the drag reduction of wavy cylinders. Furthermore they observed that the drag reduction is more consistent at higher values of Re .

Xu *et al.* (2010) performed numerical simulation of the compressible flow past a wavy cylinder using large-eddy simulation for a free-stream Mach number $M_\infty = 0.75$ and a Reynolds number based on the mean diameter $Re = 2 \times 10^5$. They found that C_D of the wavy cylinder is less than that of a corresponding circular cylinder with a drag reduction up to 26%. The fluctuating lift coefficient is nearly zero. They explained the drag reduction with a higher base pressure of the wavy cylinder. Moreover, the pressure fluctuation on the wavy cylinder is significantly suppressed in the base region, resulting in the fluctuating force reduction. The behavior of the compressible flow past the wavy cylinders overcomes the objective of this review.

2.5.3.4 Hyperboloid cylinders

Hyperboloid cylinders also known as hyperbolic cylinders are characterized by the diameter varying in a hyperboloid sinusoidal manner along its spanwise direction. In mathematics, a hyperboloid is a quadric described by the equation:

$$\frac{x^2}{a^2} + \frac{y^2}{b^2} - \frac{z^2}{c^2} = 1 \quad (2.44)$$

One-sheeted hyperboloids are used in construction, with the structures called *hyperboloid structures*. Examples include cooling towers, especially of power stations, and many other structures. A hyperboloid-cooling tower was patented by the Dutch engineers Frederik van Iterson and Gerard Kuypers in 1918. The first hyperboloid cooling towers were built in 1918 near Heerlen. Most of the research was focused on the aerodynamics of this structures.

Early wind tunnel tests of cooling towers were performed by Cowdrey & O'Neill (1956). They approximated the hyperboloid shape by the superposition of two truncated cones. Davenport & Isyumov (1966) performed pioneering tests on model of hyperbolic cooling tower in order to characterize the dynamic and static action of wind. Farell *et al.* (1976, 1977) evaluated the effect of wind tunnel walls on the mean pressure distributions on rough-walled circular cylinders and on cooling tower models fitted with longitudinal ribs in the range of Reynolds-number independence. For cooling towers, a correction procedure is proposed using the base pressure coefficient, C_{pb} , and the dimensionless pressure rise to separation, $C_{pb} - C_{pm}$, where C_{pm} is the minimum value of the pressure coefficient. The base pressure coefficient C_{pb} for cooling towers was found to be

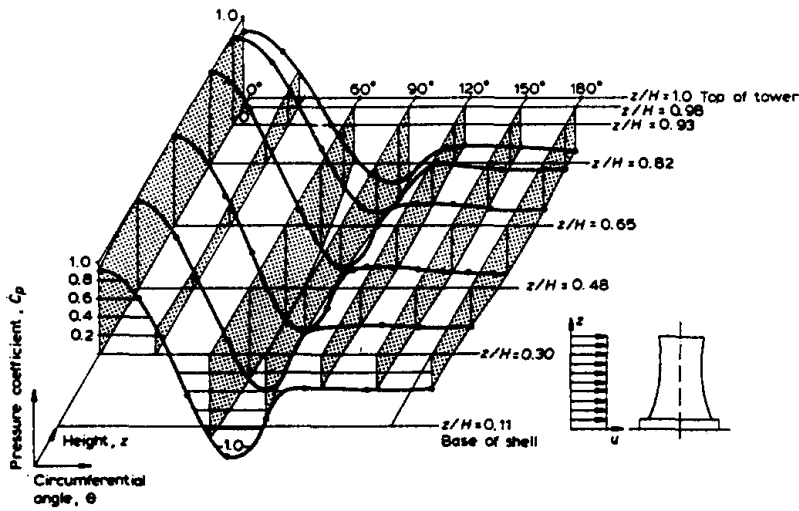


Figure 2.59: Pressure coefficients at different heights along the circumference of the cooling tower. After [Harnach & Niemann \(1980\)](#).

a function of the boundary geometry: model shape, tunnel type (open or closed jet) and blockage, and is independent of surface roughness. They tested three models of the Weisweiler hyperbolic cooling tower. Each model was fitted with 52 meridional ribs placed symmetrically with respect to the stream direction and spaced uniformly around the circumference. The three models had mean diameters of 12.7 cm , 21.0 cm and 26.3 cm , respectively, and a height-to-diameter ratio of 2. They found that the wind tunnel blockage has a pronounced effect on C_D as well as on the detailed mean pressure distribution.

[Harnach & Niemann \(1980\)](#) measured in wind tunnel in homogeneous flow conditions the pressure distribution on a hyperboloid-cooling tower. They used this data to verify that the common practice adopted in design to use a simplified height-constant pressure distribution is acceptable. Pressure coefficients measured are shown in Figure 2.59 over half of the shell surface at different levels z/H where H is the total height of the tower. They found that the simplified height-constant pressure distribution is sufficiently exact.

[Sun & Zhou \(1983\)](#) performed wind-tunnel tests and full-scale measurement on a 90 m high, ribless hyperbolic natural draft-cooling tower in Maomin Power Station, Guang-dong, China. Two models of 1:150 and 1:1000 scale of the prototype tower were used: the first has an height of 600 mm and the second of 90 mm . The tests were performed both in uniform and in ABL stream. They observed that Re and surface roughness have a great effect on the external pressure distribution. At same Re and same roughness for the same model, there is a difference of pressure distribution for uniform flow and ABL flow. The

magnitude of the difference depends upon the types of flow separation, which in turn depends on Re and roughness. They found a very large difference in some circumstance. Comparing the pressure distributions obtained in full-scale study and in wind tunnel test, they demonstrated that the pressure distribution at large Re may be achieved at a smaller Re in wind tunnel test if the surface roughness of model is increased appropriately.

2.6 Aerodynamic devices

Aerodynamic upgrades are named devices and come in many different forms and have evolved to obtain the best performance in the different fields of application. Devices are added on cylinders in order to change the flow around it. Devices are designed irregularities (Figure 2.1). A particular control fluid strategy is chosen based on the kind of flow and the control goal to be achieved. In civil problems, the reduction of fluid forces caused by motion of a fluid is a major issue. Many methods for reducing and suppressing fluid forces acting on a single structure have been proposed. All the methods used mechanism described in this section. Usually in civil engineer applications, the goal of these devices is to reduce the drag and the wind induced vibration effects. The principal application in civil engineering on circular sections is on bridge's cables, on chimneys or stacks and on mooring systems. The drag is a very important parameter for all the companies that produce cable systems for bridges. The classification used in this section is shown in Figure 2.60.

There are basically two methods of reducing the response of any fluid-elastic vibrating system (Every *et al.* , 1982):

- Alter the transfer function of the system fluid-elastic;
- Alter the magnitude and frequency of the input forcing function.

The first method is sometimes the more difficult and two approaches are available. The transfer function can be basically modified changing the structural damping or stiffness. Either the damping of the system must be increased or the natural frequency must be adjusted to cause mismatch between it and the dominant frequency of the input forces. In this review, these devices are not treated because the cylinder is fixed and no aeroelastic effects is considered. A good review of these methods is given by Walshe & Wootton (1970) and by Modi *et al.* (1995).

The second approach is based on an alteration of the external profile in order to affect the separation of the boundary layer, prevent the correlation of vortex shedding along the length of the structure or alter the formation of wake vortices and their interaction. This approach is also able to change the drag. The use of surface modifications to alter the loading and vibration of a circular cylinder has been pursued in a wide range of investigations, as summarized by Zdravkovich (1981) and Naudascher & Rockwell (1994).

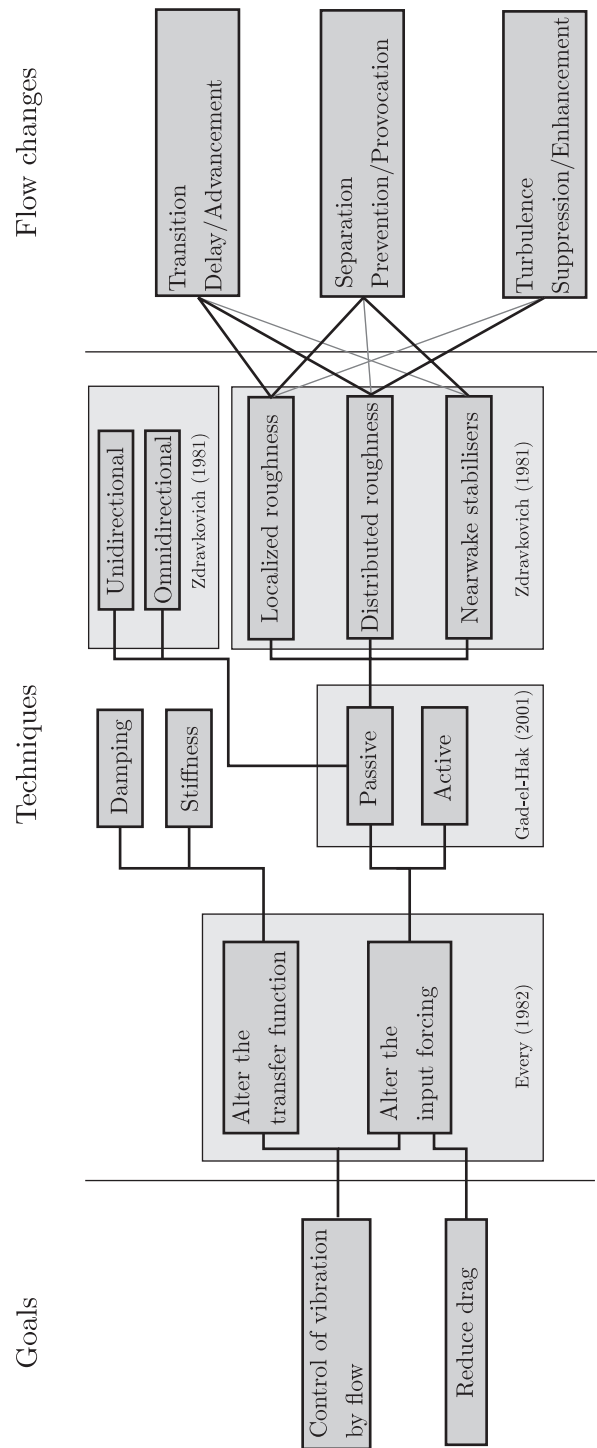


Figure 2.60: Goals, techniques and flow changes in flow control in civil engineering.

The best geometrical solution is by streamlining the body. Since this is not always possible, other approach must be considered. There are different classification schemes for flow control method. [Gad-el Hak \(2000\)](#) for classifying flow control method considers energy expenditure and the control loop involved. He considered passive control devices when they don't require auxiliary power and active when they requires energy expenditure. In this review, only passive methods are considered. As a matter of fact, passive devices are the most used in civil engineering applications.

[Gad-el Hak \(2000\)](#) describes the possible flow changes that are:

- Transition delay/advancement;
- Separation prevention provocation;
- Turbulence suppression/provocation.

The passive devices can be classified in three groups using the phenomenological mechanism ([Zdravkovich, 1981](#)):

- Localized roughness, which principally affects the boundary layer provoking separation or enhancing turbulence;
- Distributed roughness, which principally affect the boundary layer or enhancing turbulence;
- Nearwake stabilizer, which principally prevent separation.

The passive devices can be classified using the directional efficiency in omnidirectional and unidirectional ([Zdravkovich, 1981](#)). This classification is very important because in civil engineering applications wind has variable direction thereafter is important using omnidirectional devices. A lot of application requires unidimensional devices like horizontal pipelines, submarine periscope, heat exchanger tubes and piles subjected to tilde ([Zdravkovich, 1981](#)).

Finally, as observed by [Choi *et al.* \(2008\)](#), flow over a cylinder exhibits different regimes with increasing Re . Therefore, devices can have a successful control method in a certain Reynolds-number range than in others. A lot of application can require specific performances in specific Reynolds-number ranges.

Reviews on the aerodynamic control of bluff body have been given by [Walshe & Wootton \(1970\)](#), [Zdravkovich \(1981\)](#), [Gad-el Hak \(2000\)](#), [Choi *et al.* \(2008\)](#) and [Kleissl \(2013\)](#).

References

General

- Farzaneh, M. 2008. *Atmospheric icing of power networks*. Springer Verlag.
- Norberg, C. 2003. Fluctuating lift on a circular cylinder: review and new measurements. *Journal of Fluids and Structures*, **17**(1), 57–96.
- Roshko, A. 1961. Experiments on the flow past a circular cylinder at very high Reynolds number. *J. Fluid Mech*, **10**(3), 345–356.
- Schewe, G. 1983. On the force fluctuations acting on a circular cylinder in crossflow from subcritical up to transcritical Reynolds numbers. *Journal of Fluid Mechanics*, **133**(1), 265–285.
- Sumer, B.M., & Fredsøe, J. 2006. *Hydrodynamics around cylindrical structures*. Vol. 26. World Scientific Pub Co Inc.
- Wieselsberger, C. 1922. New data on the laws of fluid resistance.
- Williamson, C. H. K. 1989. Oblique and parallel modes of vortex shedding in the wake of a circular cylinder at low Reynolds numbers. *Journal of Fluid Mechanics*, **206**, 579–627.
- Zdravkovich, M.M. 1997. *Flow Around Circular Cylinders, vol. 1. Fundamentals*. Oxford University Press.
- Zdravkovich, M.M. 2003. *Flow Around Circular Cylinders, vol. 2. Applications*. Oxford University Press.

Surface irregularities

- Achenbach, E. 1968. Distribution of local pressure and skin friction around a circular cylinder in cross-flow up to $Re = 5 \cdot 10^6$. *Journal of Fluid Mechanics*, **34**(04), 625–639.
- Achenbach, E. 1971. Influence of surface roughness on the cross-flow around a circular cylinder. *Journal of Fluid Mechanics*, **46**(part 2), 321–335.
- Achenbach, E. 1974. The effects of surface roughness and tunnel blockage on the flow past spheres. *Journal of fluid mechanics*, **65**(1), 113–125.
- Achenbach, E. 1977. The effect of surface roughness on the heat transfer from a circular cylinder to the cross flow of air. *International Journal of Heat and Mass Transfer*, **20**(4), 359–369.

- Achenbach, E., & Heinecke, E. 1981. On vortex shedding from smooth and rough cylinders in the range of Reynolds numbers $6 \cdot 10^3$ to $5 \cdot 10^6$. *Journal of Fluid Mechanics*, **109**(1), 239–251.
- Ackeret, J. 1936. Wind load on brick stack of circular section. *Schweizerische bauzeitung*, **108**, 25–26.
- Adachi, T. 1997. Effects of surface roughness on the universal Strouhal number over the wide Reynolds number range. *Journal of wind engineering and industrial aerodynamics*, **69**, 399–412.
- Adachi, T., Ono, H., Matsuuchi, K., Kawai, T., & Cho, T. 1989. Flow around circular cylinder in the high Reynolds number range (effect of surface roughness). *Trans. Jpn. Soc. Mech. Eng. B 55 (in Japanese)*, 685–692.
- Aiba, S., Ota, T., & Tsuchida, H. 1979. Heat transfer and flow around a circular cylinder with tripping-wires. *Heat and Mass Transfer*, **12**(3), 221–231.
- Alam, M.D., & Zhou, Y. 2007. Turbulent wake of an inclined cylinder with water running. *Journal of Fluid Mechanics*, **589**, 261–303.
- Alam, M.M., Sakamoto, H., & Moriya, M. 2003. Reduction of fluid forces acting on a single circular cylinder and two circular cylinders by using tripping rods. *Journal of fluids and structures*, **18**(3), 347–366.
- Alam, M.M., Zhou, Y., Zhao, J.M., Flamand, O., & Boujard, O. 2010. Classification of the tripped cylinder wake and bi-stable phenomenon. *International Journal of Heat and Fluid Flow*, **31**(4), 545–560.
- Alemдарoğlu, N., Rebillat, J.C., & Goethals, R. 1980. An aeroacoustic coherence function method applied to circular cylinder flows. *Journal of Sound and Vibration*, **69**(3), 427–439.
- Baines, W. D., & Peterson, E.G. 1951. An Investigation of flow through screen. *Trans. ASME*, **73**, 476.
- Basu, R.I. 1985. Aerodynamic forces on structures of circular cross-section. Part 1. Model-scale data obtained under two-dimensional conditions in low-turbulence streams. *Journal of wind engineering and industrial aerodynamics*, **21**(3), 273–294.
- Batham, J.P. 1973. Pressure distributions on circular cylinders at critical Reynolds numbers. *Journal of Fluid mechanics*, **57**(pt 2), 209–228.
- Bearman, P.W. 1969. On vortex shedding from a circular cylinder in the critical Reynolds number regime. *Journal of Fluid Mechanics*, **37**(03), 577–585.
- Bimbato, A. M., Pereira, L.A.A., & Hirata, M.H. 2013. Numerical investigation of the drag crisis in flow past a rough circular cylinder.

- Bosdogianni, A., & Olivari, D. 1996. Wind-and rain-induced oscillations of cables of stayed bridges. *Journal of Wind Engineering and Industrial Aerodynamics*, **64**(2), 171–185.
- Bruun, H.H., & Davies, P. 1975. An experimental investigation of the unsteady pressure forces on a circular cylinder in a turbulent cross flow. *Journal of Sound and Vibration*, **40**(4), 535–559.
- Buresti, G. 1981. The effect of surface roughness on the flow regime around circular cylinders. *Journal of Wind Engineering and Industrial Aerodynamics*, **8**(1-2), 105–114.
- Chowdhury, H., & Alam, F. 2013. An experimental investigation on the aerodynamic drag coefficient and surface roughness properties of sport textiles. *Journal of The Textile Institute*, 414–422.
- Cosentino, N., Flamand, O., & Ceccoli, C. 2003. Rain-wind induced vibration of inclined stay cables. Part I: Experimental investigation and physical explanation. *Wind and Structures*, **6**(6), 471–484.
- Du, X., Gu, M., & Chen, S. 2013. Aerodynamic characteristics of an inclined and yawed circular cylinder with artificial rivulet. *Journal of Fluids and Structures*, **43**, 64–82.
- Duarte Ribeiro, J.È.L. 1991a. Effects of surface roughness on the two-dimensional flow past circular cylinders I: mean forces and pressures. *Journal of Wind Engineering and Industrial Aerodynamics*, **37**(3), 299–309.
- Duarte Ribeiro, J.È.L. 1991b. Effects of surface roughness on the two-dimensional flow past circular cylinders II: fluctuating forces and pressures. *Journal of Wind Engineering and industrial Aerodynamics*, **37**(3), 311–326.
- Ekmekci, A., & Rockwell, D. 2010. Effects of a geometrical surface disturbance on flow past a circular cylinder: a large-scale spanwise wire. *Journal of Fluid Mechanics*, **665**(1), 120–157.
- Ekmekci, A., & Rockwell, D. 2011. Control of flow past a circular cylinder via a spanwise surface wire: effect of the wire scale. *Experiments in fluids*, 1–17.
- Fage, A., & Warsap, J.H. 1930. *The effects of turbulence and surface roughness on the drag of a circular cylinder*. HMSO.
- Farell, C., & Arroyave, J. 1990. On uniform flow around rough circular cylinders at critical Reynolds numbers. *Journal of Wind Engineering and Industrial Aerodynamics*, **36**, 621–631.
- Farell, C., & Fedeniuk, S.K. 1988. Effect of end plates on the flow around rough cylinders. *Journal of Wind Engineering and Industrial Aerodynamics*, **28**(1-3), 219–230.

- Farell, C., Maisch, F., & Guven, O. 1976. Mean wind loading on rough-walled cooling towers. *Journal of the Engineering Mechanics Division*, **102**(6), 1059–1081.
- Flamand, O. 1995. Rain-wind induced vibration of cables. *Journal of Wind Engineering and Industrial Aerodynamics*, **57**(2), 353–362.
- Fujita, H., Takahama, H., & Kawai, T. 1985. Effects of tripping wires on heat transfer from a circular cylinder in cross flow (1st report, the pressure distribution around the cylinder and the drag coefficient). *Bulletin of the JSME*, **28**(235), 80–87.
- Fuss, F. K. 2011. The effect of surface skewness on the super/postcritical coefficient of drag of roughened cylinders. *Procedia Engineering*, **13**, 284–289.
- Guven, O., Patel, V.C., & Farell, C. 1977. A Model for High-Reynolds-Number Flow Past Rough-Walled Circular Cylinders. *Journal of Fluids Engineering*, **99**(3), 486–493.
- Güven, O., Farell, C., & Patel, V.C. 1980. Surface-roughness effects on the mean flow past circular cylinders. *Journal of Fluid mechanics*, **98**(04), 673–701.
- Hikami, Y., & Shiraishi, N. 1988. Rain-wind induced vibrations of cables stayed bridges. *Journal of Wind Engineering and Industrial Aerodynamics*, **29**(1), 409–418.
- Hover, F.S., Tvedt, H., & Triantafyllou, M.S. 2001. Vortex-induced vibrations of a cylinder with tripping wires. *Journal of Fluid Mechanics*, **448**, 175–196.
- Igarashi, T. 1986. Effect of tripping wires on the flow around a circular cylinder normal to an airstream. *JSME International Journal Series B*, **29**, 2917–2924.
- James, D.F., & Truong, Q.S. 1972. Wind load on cylinder with spanwise protrusion. *Journal of the Engineering Mechanics Division*, **98**(6), 1573–1589.
- James, W.D., Paris, S.W., & Malcolm, G.N. 1980. Study of viscous crossflow effects on circular cylinders at high Reynolds numbers. *AIAA Journal*, **18**(9), 1066–1072.
- Kareem, A., & Cheng, C.M. 1999. Pressure and force fluctuations on isolated roughened circular cylinders of finite height in boundary layer flows. *Journal of fluids and structures*, **13**(7), 907–933.
- Kawamura, T., Takami, H., & Kuwahara, K. 1986. Computation of high Reynolds number flow around a circular cylinder with surface roughness. *Fluid Dynamics Research*, **1**(2), 145–162.

- Lakehal, D. 1999. Computation of turbulent shear flows over rough-walled circular cylinders. *Journal of Wind Engineering and Industrial Aerodynamics*, **80**(1-2), 47–68.
- Lawson, T.V. 1982. The use of roughness to produce high reynolds number flows around circular cylinders at lower reynolds numbers. *Journal of Wind Engineering and Industrial Aerodynamics*, **10**(3), 381–387.
- Lee, S.J., & Kim, H.B. 1997. The effect of surface protrusions on the near wake of a circular cylinder. *Journal of wind engineering and industrial aerodynamics*, **69**, 351–361.
- Lemaitre, C., Mahmud Alam, M.D., Hémon, P., De Langre, E., & Zhou, Y. 2006. Rainwater rivulets on a cable subject to wind. *Comptes Rendus Mécanique*, **334**(3), 158–163.
- Lemaitre, C., Hémon, P., & De Langre, E. 2007. Thin water film around a cable subject to wind. *Journal of Wind Engineering and Industrial Aerodynamics*, **95**(9), 1259–1271.
- Lemaitre, C., De Langre, E., & Hémon, P. 2010. Rainwater rivulets running on a stay cable subject to wind. *European Journal of Mechanics-B/Fluids*, **29**(4), 251–258.
- Leung, Y.C., Ko, N.W.M., & Tang, K.M. 1992. Flow past circular cylinder with different surface configurations. *Journal of fluids engineering*, **114**(2), 170–177.
- Leung, Y.C., Wong, C.H., & Ko, N.W.M. 1997. Characteristics of flows over an asymmetrically grooved circular cylinder in the transitional regimes. *Journal of wind engineering and industrial aerodynamics*, **69**, 169–178.
- Lockwood, V.E., & McKinney, L.W. 1960. Effect of Reynolds Number on the Force and Pressure Distribution Characteristics of a Two-Dimensional Lifting Circular Cylinder. *NASA*.
- Mamou, M., Beyers, M., Dagdougui, H., Hasnaoui, M., *et al.* . 2010. Modeling of Unsteady Turbulent Flows past Roughened Circular Cylinders and Airfoils.
- Matsumoto, M., Yagi, T., Shigemura, Y., & Tsushima, D. 2001. Vortex-induced cable vibration of cable-stayed bridges at high reduced wind velocity. *Journal of Wind Engineering and Industrial Aerodynamics*, **89**(7), 633–647.
- Matteoni, G., & Georgakis, C.T. 2012a. Aerodynamic force coefficients of plain bridge cables in wet conditions. *In: The Seventh International Colloquium on Bluff Body Aerodynamics and Applications, Shanghai, China.*

- Matteoni, G., & Georgakis, C.T. 2012b. Effects of bridge cable surface roughness and cross-sectional distortion on aerodynamic force coefficients. *Journal of Wind Engineering and Industrial Aerodynamics*, **104-106**, 176–187.
- Miller, B.L.P. 1977. *The hydrodynamic drag of roughened circular cylinders*. National Maritime Institute.
- Miyata, T., Yamada, H., & Hojo, T. 1994. Experimental Study on Aerodynamic Characteristics of Cables with Patterned Surface. *Journal of Structural Engineering*. **40A**, 1065–1076.
- Modi, V.J., Welt, F., & Seto, M.L. 1995. Control of wind-induced instabilities through application of nutation dampers: a brief overview. *Engineering structures*, **17**(9), 626–638.
- Muralikrishnan, B., & Raja, J. 2009. *Computational surface and roundness metrology*. Springer.
- Nakamura, Y., & Tomonari, Y. 1982. The effects of surface roughness on the flow past circular cylinders at high Reynolds numbers. *Journal of Fluid Mechanics*, **123**(1), 363–378.
- Nebres, J., & Batill, S. 1993. Flow about a circular cylinder with a single large-scale surface perturbation. *Experiments in fluids*, **15**(6), 369–379.
- Niemann, H.J., & Holscher, N. 1990. A review of recent experiments on the flow past circular cylinders. *Journal of Wind Engineering and Industrial Aerodynamics*, **33**(1-2), 197–209.
- Nigim, H.H., & Batill, S.M. 1997. Flow about cylinders with surface perturbations. *Journal of fluids and Structures*, **11**(8), 893–907.
- Nikuradse, J. 1933. Stromungsgestze in rauhen Rohren.
- Okajima, A., & Nakamura, Y. 1973. Flow around rough-surfaced cylinder at high Reynolds numbers (in Japanese).
- Okajima, A., Nagamori, T., Matsunaga, F., & Kiwata, T. 1999. Some experiments on flow-induced vibration of a circular cylinder with surface roughness. *Journal of fluids and structures*, **13**(7), 853–864.
- Parkinson, G.V., & Jandali, T. 1970. A wake source model for bluff body potential flow. *J. Fluid Mech*, **40**(3), 577–594.
- Pearcey, H.H., Cash, R.F., & Salter, I.J. 1982. *Flow past circular cylinders: Simulation of full-scale flows at model scale*. US Department of Commerce, Technology Administration, National Technical Information Service.

- Perry, A.E., Schofield, W.H., & Joubert, P.N. 1969. Rough wall turbulent boundary layers. *Journal of Fluid Mechanics*, **37**(02), 383–413.
- Prandtl, L. 1914. Der luftwiderstand von Kugeln. *Nachrichten der Gesellschaft der Wissenschaften zu Göttingen, Mathematisch-physikalische Klasse*, **91**, 177–190.
- Robertson, A.C., Taylor, I.J., Wilson, S.K., Duffy, B.R., & Sullivan, J.M. 2010. Numerical simulation of rivulet evolution on a horizontal cable subject to an external aerodynamic field. *Journal of Fluids and Structures*, **26**(1), 50–73.
- Schewe, G. 1986. Sensitivity of transition phenomena to small perturbations in flow round a circular cylinder. *Journal of Fluid Mechanics*, **172**, 33–46.
- Schlichting, H. 1936. Experimentelle untersuchungen zum rauigkeitsproblem. *Archive of Applied Mechanics*, **7**(1), 1–34.
- Shih, W.C.L., Wang, C., Coles, D., & Roshko, A. 1993. Experiments on flow past rough circular cylinders at large Reynolds numbers. *Journal of Wind Engineering and Industrial Aerodynamics*, **49**(1-3), 351–368.
- Stratford, B.S. 1959. The prediction of separation of the turbulent boundary layer. *Journal of fluid mechanics*, **5**(01), 1–16.
- Szechenyi, E. 1975. Supercritical Reynolds number simulation for two-dimensional flow over circular cylinders. *Journal of Fluid Mechanics*, **70**(3), 529–542.
- Talley, S., & Mungal, G. 2002. Flow around cactus-shaped cylinders. *Annual Research Briefs, Center of Turbulence Research*, 363–376.
- Townsend, A.A. 1961. Equilibrium layers and wall turbulence. *J. Fluid Mech*, **11**(1), 97–120.
- Uematsu, Y., & Yamada, M. 1995. Effects of aspect ratio and surface roughness on the time-averaged aerodynamic forces on cantilevered circular cylinders at high Reynolds numbers. *Journal of wind engineering and industrial aerodynamics*, **54**, 301–312.
- Unit, Engineering Science Data. 1980. Mean forces and moment on cylindrical structures: Single cylinder with Two-dimensional flow. *ESDU data item 80025*.
- Wang, Z.J., Zhou, Y, Huang, J.F., & Xu, Y.L. 2005. Fluid dynamics around an inclined cylinder with running water rivulets. *Journal of fluids and structures*, **21**(1), 49–64.
- Whitehouse, D.J. 1994. *Handbook of surface metrology*. Taylor & Francis.

- Wianecki, J. 1979. Cables wind excited vibrations of cable-stayed bridges. *Pages 1381–1393 of: Proceedings of the 5th International Conference of Wind Engineering.*
- Xu, Y.L., Li, Y.L., Shum, K.M., Kwok, K.C.F., Kwok, K.C.S., & Hitchcock, P.A. 2006. Aerodynamic coefficients of inclined circular cylinders with artificial rivulet in smooth flow. *Advances in Structural Engineering*, **9**(2), 265–278.
- Zan, S.J., & Matsuda, K. 2002. Steady and unsteady loading on a roughened circular cylinder at Reynolds numbers up to 900,000. *Journal of Wind Engineering and Industrial Aerodynamics*, **90**(4), 567–581.
- Zdravkovich, M.M. 1990. Conceptual overview of laminar and turbulent flows past smooth and rough circular cylinders. *Journal of Wind Engineering and Industrial Aerodynamics*, **33**(1-2), 53–62.

Section irregularities

- A.A.S.H.T.O. 2009. *Standard Specifications for Structural Supports for Highway Signs, Luminaires, and Traffic Signals*. American Association of State Highway and Transportation Officials.
- Alonso, G., Meseguer, J., Sanz-Andrés, A., & Valero, E. 2010. On the galloping instability of two-dimensional bodies having elliptical cross-sections. *Journal of Wind Engineering and Industrial Aerodynamics*, **98**(8-9), 438–448.
- ASCE-74. 1991. *Guidelines for Electrical Transmission Line Structural Loading*. ASCE Publications.
- Bosch, H.R., & Guterres, R.M. 2001. Wind tunnel experimental investigation on tapered cylinders for highway support structures. *Journal of Wind Engineering and Industrial Aerodynamics*, **89**(14), 1311–1323.
- Chabart, O., & Lilien, J. L. 1998. Galloping of electrical lines in wind tunnel facilities. *Journal of Wind Engineering and Industrial Aerodynamics*, **74**, 967–976.
- Choi, J.H., & Lee, S.J. 2000. Ground effect of flow around an elliptic cylinder in a turbulent boundary layer. *Journal of Fluids and Structures*, **14**(5), 697–709.
- Choi, J.H., & Lee, S.J. 2001. Flow characteristics around an inclined elliptic cylinder in a turbulent boundary layer. *Journal of fluids and structures*, **15**(8), 1123–1135.
- Demartino, C., Koss, H.H., & Ricciardelli, F. 2013a. Experimental study of the effect of icing on the aerodynamics of circular cylinders - Part I: Cross flow. *In: 6th European and African Conference on Wind Engineering, Robinson College, Cambridge, UK.*

- Demartino, C., Georgakis, C.T., & Ricciardelli, F. 2013b. Experimental study of the effect of icing on the aerodynamics of circular cylinders - Part II: Inclined flow. *In: 6th European and African Conference on Wind Engineering, Robinson College, Cambridge, UK.*
- Farzaneh, M. 2008. *Atmospheric icing of power networks*. Springer Verlag.
- Fu, P., Farzaneh, M., & Bouchard, G. 2006. Two-dimensional modelling of the ice accretion process on transmission line wires and conductors. *Cold Regions Science and Technology*, **46**(2), 132–146.
- Gjelstrup, H., Georgakis, C. T., & Larsen, A. 2012. An evaluation of iced bridge hanger vibrations through wind tunnel testing and quasi-steady theory. *Wind & Structures*, **15**(5), 385–407.
- Gonçalves, H. C., & Del Rio Vieira, E. 1999. Strouhal Number Determination for Several Regular Polygon Cylinders for Reynolds Number up to 600. *In: Proceedings of the COBEM*, vol. 99.
- Hu, J.C., Zhou, Y., & Dalton, C. 2006. Effects of the corner radius on the near wake of a square prism. *Experiments in fluids*, **40**(1), 106–118.
- Huang, H. J., & Li, X. M. 2014. Experimental Research on Conductor's Ice Accretion and Aerodynamic Characteristics. *Advanced Materials Research*, **889**, 497–500.
- Institution, British Standards. 1972. *Code of basic data for the design of buildings: wind loads*. British standard code of practice, nos. Chapter 5, part 2. Council for Codes of Practice, British Standards Institution.
- Jackson, C.P. 1987. A finite-element study of the onset of vortex shedding in flow past variously shaped bodies. *Journal of Fluid Mechanics*, **182**(1), 23–45.
- James, W. D. 1976. *Effects of Reynolds number and corner radius on two-dimensional flow around octagonal, dodecagonal and hexdecagonal cylinders*[Ph. D. Thesis]. Ph.D. thesis, Iowa State University.
- Khan, W.A., Culham, J.R., & Yovanovich, M.M. 2005. Fluid flow around and heat transfer from elliptical cylinders: analytical approach. *Journal of thermophysics and heat transfer*, **19**(2), 178–185.
- Kollár, L. E., & Farzaneh, M. 2010. Wind-tunnel investigation of icing of an inclined cylinder. *International Journal of Heat and Mass Transfer*, **53**(5), 849–861.
- Koss, H.H., & Lund, M.S.M. 2013. Experimental Investigation of Aerodynamic Instability of Iced Bridge Cable Sections. *In: 6th European and African Conference on Wind Engineering, Robinson College, Cambridge, UK.*

- Koss, H.H., Gjelstrup, H., & Georgakis, C.T. 2012. Experimental study of ice accretion on circular cylinders at moderate low temperatures. *Journal of Wind Engineering and Industrial Aerodynamics*, **104**, 540–546.
- Koss, H.H., Henningsen, J.F., & Olsenn, I. 2013. Influence of icing on bridge cable aerodynamics. In: *15th International Workshop on Atmospheric Icing of Structures, St. John's, Newfoundland and Labrador, Canada, September 8-11*.
- Lindsey, W.F. 1938. *Drag of cylinders of simple shapes*. National Advisory Committee for Aeronautics.
- Lozowski, E.P., Stallabrass, J.R., & Hearty, P.F. 1983. The icing of an unheated, nonrotating cylinder. Part I: A simulation model. *Journal of Climate and Applied Meteorology*, **22**(12), 2053–2062.
- Lugt, H.J., & Haussling, H.J. 1974. Laminar flow past an abruptly accelerated elliptic cylinder at 45 incidence. *Journal of Fluid Mechanics*, **65**(04), 711–734.
- Makkonen, L. 1984b. Modeling of ice accretion on wires. *Journal of Climate and Applied Meteorology*, **23**(6), 929–939.
- Makkonen, L. 1985. Heat transfer and icing of a rough cylinder. *Cold Regions Science and Technology*, **10**(2), 105–116.
- Mehta, Kishorc, Ritchie, Davidl, & Oler, Walt. 1990. Wind drag coefficients for octagonal cylinders.
- Mittal, R., & Balachandar, S. 1995. Effect of three-dimensionality on the lift and drag of no two-dimensional cylinders. *Physics of Fluids*, **7**, 1841–1865.
- Mittal, R., & Balachandar, S. 1996. Direct numerical simulation of flow past elliptic cylinders. *Journal of Computational Physics*, **124**(2), 351–367.
- NCHRP-494. 2003. *Structural Supports for Highway Signs, Luminaires, and Traffic Signals*. National Cooperative Highway Research Program.
- Nigol, O., & Buchan, P.G. 1981. Conductor galloping part I-Den Hartog mechanism. *Power Apparatus and Systems, IEEE Transactions on*, 699–707.
- Oka, S., & Ishihara, T. 2010. Numerical study on steady aerodynamic characteristics of ice accreted transmission lines. *Pages 23–27 of: The Fifth International Symposium on Computational Wind Engineering (CWE2010), Chapel Hill, North Carolina, USA May*.
- Ota, T., Aiba, S., Tsuruta, T., & Kaga, M. 1983. Forced Convection Heat Transfer From on Elliptic Cylinder of Axis Ratio 1: 2. *Bulletin of JSME*, **26**(212), 262–267.

- Ota, T., Nishiyama, H.H., & Taoka, Y. 1984. Heat transfer and flow around an elliptic cylinder. *International Journal of Heat and Mass Transfer*, **27**(10), 1771–1779.
- Phares, B.M., Sarkar, P.P., Wipf, T.J., & Chang, B. 2007. *Development of fatigue design procedures for slender, tapered support structures for highway signs, luminaries, and traffic signals subjected to wind-induced excitation from vortex shedding and buffeting*. Tech. rept.
- Poots, G. 1996. *Ice and snow accretion on structures*. Research Studies Press.
- Portugaels, D., Anthoine, J., & Olivari, D. 2007. Determination of aerodynamic force coefficients of octagonal lighting columns from wind tunnel experiments. *Pages 81–89 of: 5th IASME/WSEAS International Conference on Fluid Mechanics and Aerodynamics, Athens, Greece*.
- Rawlins, C.B., Hard, A.R., Ikegami, R., & Doocy, E.S. 1979. Transmission line reference book: wind-induced conductor motion. *Electric Power Research Institute (EPRI), Palo Alto, California*.[\[Links\]](#).
- Rubin, S.G., & Mummolo, F.J. 1974. Boundary-layer-induced potential flow on an elliptic cylinder. *Journal of Fluid Mechanics*, **66**, 145–157.
- Schubauer, G.B. 1935. *Air flow in a separating laminar boundary layer*. Ph.D. thesis, Johns Hopkins University.
- Schubauer, G.B. 1939. *Air flow in the boundary layer of an elliptic cylinder*. Tech. rept. DTIC Document.
- Shimizu, M., Ishihara, T., & Phuc, P.V. 2004. A wind tunnel study on aerodynamic characteristics of ice accreted transmission lines. *Fifth International Colloquium on Bluff Body Aerodynamics and Applications, Summary Papers*, 369–372.
- Shintani, K., Umemura, A., & Takano, A. 1983. Low-Reynolds-number flow past an elliptic cylinder. *Journal of Fluid Mechanics*, **136**, 277–289.
- Szalay, Z. 1989. Drags on several polygon cylinders. *Journal of Wind Engineering and Industrial Aerodynamics*, **32**(1), 135–143.
- Tang, J.W., Xie, Y.M., Felicetti, P., Tu, J.Y., & Li, J.D. 2013. Numerical simulations of wind drags on straight and twisted polygonal buildings. *The Structural Design of Tall and Special Buildings*, **22**(1), 62–73.
- Tian, Z.W., & Wu, Z.N. 2009. A study of two-dimensional flow past regular polygons via conformal mapping. *Journal of Fluid Mechanics*, **628**, 121–154.

- Tian, Z.W., Niu, H.T., & Wu, Z.N. 2011. Flow past polygons with an odd number of edges. *Science China Physics, Mechanics and Astronomy*, **54**(4), 683–689.
- Tunstall, M. 1989. *Accretion of ice and aerodynamic coefficients. Study on galloping*. Ph.D. thesis, University of Liège.
- Unit, Engineering Science Data. 1979. Mean forces and moment on cylindrical structures: Polygonal sections with rounded corners including elliptical shapes. *ESDU data item 79026*.
- Wiland, E. 1968. *Unsteady aerodynamics of stationary elliptic cylinders in sub-critical flow*. Ph.D. thesis, University of British Columbia.

Spanwise irregularities

- Ahmed, A., & Bays-Muchmore, B. 1992. Transverse flow over a wavy cylinder. *Physics of Fluids A: Fluid Dynamics (1989-1993)*, **4**(9), 1959–1967.
- Ahmed, A., Khan, M.J., & Bays-Muchmore, B. 1993. Experimental investigation of a three-dimensional bluff-body wake. *AIAA journal*, **31**(3), 559–563.
- Bartoli, G., Cluni, F., Gusella, V., & Procino, L. 2006. Dynamics of cable under wind action: Wind tunnel experimental analysis. *Journal of wind engineering and industrial aerodynamics*, **94**(5), 259–273.
- Begak, M.V., Devnin, S.I., & Zavadovskaya, L.G. 1985. Investigation of vortex shedding from yawed and curved circular cylinders. *Fluid Dynamics*, **20**(2), 314–315.
- Cowdrey, C.F., & O'Neill, P.G.G. 1956. Report of Tests on a Model Cooling Tower for the CEA-Pressure Measurements at high Reynolds Numbers. *Unpublished report NPL/Aero/316a. National Physical Laboratory, Teddington, Middx.*
- Davenport, A.G., & Isyumov, N. 1966. *The dynamic and static action of wind on hyperbolic cooling towers I*. Boundary Layer Wind Tunnel Laboratory, Faculty of Engineering Science, the University of Western Ontario.
- Dragomirescu, E., Yamada, H., & Katsuchi, H. 2009. Experimental investigation of the aerodynamic stability of the Endless Column. *Journal of Wind Engineering and Industrial Aerodynamics*, **97**(9), 475–484.
- Dunn, W., & Tavoularis, S. 2006. Experimental studies of vortices shed from cylinders with a step-change in diameter. *Journal of Fluid Mechanics*, **555**, 409–437.

- Dunn, W., & Tavoularis, S. 2011. Vortex shedding from a step-cylinder in spanwise sheared flow. *Physics of Fluids (1994-present)*, **23**(3), 035109.
- Etzold, F., & Fiedler, H. 1976. The near-wake structure of a cantilevered cylinder in a cross-flow. *Zeitschrift fur Flugwissenschaften*, **24**, 77–82.
- Farell, C., Carrasquel, S., Guven, O., & Patel, V.C. 1977. Effect of wind-tunnel walls on the flow past circular cylinders and cooling tower models. *Journal of Fluids Engineering*, **99**(3), 470–479.
- Gaster, M. 1969. Vortex shedding from slender cones at low Reynolds numbers. *Journal of Fluid Mechanics*, **38**(03), 565–576.
- Gaster, M. 1971. Vortex shedding from circular cylinders at low Reynolds numbers. *Journal of Fluid Mechanics*, **46**(04), 749–756.
- Harnach, R., & Niemann, H.J. 1980. The influence of realistic mean wind loads on the static response and the design of high cooling towers. *Engineering Structures*, **2**(1), 27–34.
- Hsiao, F.B., & Chiang, C.H. 1998. Experimental study of cellular shedding vortices behind a tapered circular cylinder. *Experimental thermal and fluid science*, **17**(3), 179–188.
- Inoue, O., & Sakuragi, A. 2008. Vortex shedding from a circular cylinder of finite length at low Reynolds numbers. *Physics of Fluids (1994-present)*, **20**(3), 033601.
- Kawamura, T., Hiwada, M., Hibino, T., Mabuchi, I., & Kumada, M. 1984. Heat transfer from a finite circular cylinder on the flat plate. *Bulletin of the JSME*, **27**(233), 2430–2439.
- Keser, H.I., Unal, M.F., & Bearman, P.W. 2001. Simulation of wake from a circular cylinder with spanwise sinusoidal waviness. *Pages 131–137 of: Proceedings of the Second International Conference on Vortex Methods, Istanbul, Turkey*. DTIC Document.
- Ko, N.W.M., & Chan, A.S.K. 1990. In the intermixing region behind circular cylinders with stepwise change of the diameter. *Experiments in Fluids*, **9**(4), 213–221.
- Lam, K., & Lin, Y.F. 2008. Large eddy simulation of flow around wavy cylinders at a subcritical Reynolds number. *International Journal of Heat and Fluid Flow*, **29**(4), 1071–1088.
- Lam, K., & Lin, Y.F. 2009. Effects of wavelength and amplitude of a wavy cylinder in cross-flow at low Reynolds numbers. *Journal of Fluid Mechanics*, **620**, 195–220.

- Lam, K., Wang, F.H., Li, J.Y., & So, R.M.C. 2004a. Experimental investigation of the mean and fluctuating forces of wavy (varicose) cylinders in a cross-flow. *Journal of fluids and structures*, **19**(3), 321–334.
- Lam, K., Wang, F.H., & So, R.M.C. 2004b. Three-dimensional nature of vortices in the near wake of a wavy cylinder. *Journal of Fluids and Structures*, **19**(6), 815–833.
- Lewis, C.G., & Gharib, M. 1992. An exploration of the wake three dimensionalities caused by a local discontinuity in cylinder diameter. *Physics of Fluids A: Fluid Dynamics (1989-1993)*, **4**(1), 104–117.
- Lim, H.C., & Lee, S.J. 2004. Flow control of a circular cylinder with O-rings. *Fluid dynamics research*, **35**(2), 107–122.
- Lupi, F., Borri, C., Facchini, L., Niemann, H.J., & Peil, U. 2013. A new type of bistable flow around circular cylinders with spanwise stiffening rings. *Journal of Wind Engineering and Industrial Aerodynamics*, **123**, 281–290.
- Miliou, A., Sherwin, S.J. J, & Graham, J.M.R. 2003a. Fluid dynamic loading on curved riser pipes. *Journal of Offshore Mechanics and Arctic Engineering*, **125**(3), 176–182.
- Miliou, A., Sherwin, S.J., & Graham, J.M.R. 2003b. Wake topology of curved cylinders at low Reynolds numbers. *Flow, turbulence and combustion*, **71**(1-4), 147–160.
- Miliou, A., Mortazavi, I., & Sherwin, S.J. 2005. Cut-off analysis of coherent vortical structure identification in a three-dimensional external flow. *Comptes Rendus Mecanique*, **333**(3), 211–217.
- Miliou, A., De Vecchi, A., Sherwin, S.J., & Graham, J.M.R. 2007. Wake dynamics of external flow past a curved circular cylinder with the free stream aligned with the plane of curvature. *Journal of Fluid Mechanics*, **592**, 89–115.
- Morton, C., & Yarusevych, S. 2010. Vortex shedding in the wake of a step cylinder. *Physics of Fluids (1994-present)*, **22**(8), 083602.
- Morton, C., & Yarusevych, S. 2012. An experimental investigation of flow past a dual step cylinder. *Experiments in fluids*, **52**(1), 69–83.
- Morton, C., & Yarusevych, S. 2013. Vortex Dynamics in the Turbulent Wake of a Single Step Cylinder. *Journal of Fluids Engineering*.
- Nakamura, H., & Igarashi, T. 2008. Omnidirectional reductions in drag and fluctuating forces for a circular cylinder by attaching rings. *Journal of Wind Engineering and Industrial Aerodynamics*, **96**(6), 887–899.

- Nakamura, Y., & Fukamachi, N. 1991. Visualization of the flow past a frisbee. *Fluid Dynamics Research*, **7**(1), 31.
- Narasimhamurthy, V.D., Andersson, H.I., & Pettersen, B. 2009. Direct numerical simulation of vortex shedding behind a linearly tapered circular cylinder. *Pages 201–211 of: IUTAM Symposium on Unsteady Separated Flows and their Control*. Springer.
- New, T.H., Shi, S., & Liu, Y. 2013. Cylinder-wall interference effects on finite-length wavy cylinders at subcritical Reynolds number flows. *Experiments in fluids*, **54**(10), 1–24.
- Nguyen, A.T., & Jee, S.J. 2004. Experimental investigation on wake behind a sinusoidal cylinder. *Pages 17–21 of: Proceedings of the Tenth Asian Congress of Fluid Mechanics*.
- Norberg, C. 1994. An experimental investigation of the flow around a circular cylinder: influence of aspect ratio. *Journal of Fluid Mechanics*, **258**, 287–316.
- Okamoto, S., & Sunabashiri, Y. 1992. Vortex shedding from a circular cylinder of finite length placed on a ground plane. *Journal of fluids engineering*, **114**(4), 512–521.
- Papangelou, A. 1992. Vortex shedding from slender cones at low Reynolds numbers. *Journal of Fluid Mechanics*, **242**, 299–321.
- Park, C.W., & Lee, S.J. 2004. Effects of free-end corner shape on flow structure around a finite cylinder. *Journal of Fluids and Structures*, **19**(2), 141–158.
- Piccirillo, P.S., & Van Atta, C.W. 1993. An experimental study of vortex shedding behind linearly tapered cylinders at low Reynolds number. *Journal of Fluid Mechanics*, **246**, 163–195.
- Provansal, M., & Monkewitz, P. 2006. Vortex shedding dynamics in the laminar wake of cones. *arXiv preprint physics/0608310*.
- Roh, S., & Park, S.O. 2003. Vortical flow over the free end surface of a finite circular cylinder mounted on a flat plate. *Experiments in fluids*, **34**(1), 63–67.
- Sumner, D. 2013. Flow above the free end of a surface-mounted finite-height circular cylinder: A review. *Journal of Fluids and Structures*, **43**, 41–63.
- Sumner, D., & Heseltine, J.L. 2008. Tip vortex structure for a circular cylinder with a free end. *Journal of Wind Engineering and Industrial Aerodynamics*, **96**(6), 1185–1196.
- Sumner, D., Heseltine, J.L., & Dansereau, O.J.P. 2004. Wake structure of a finite circular cylinder of small aspect ratio. *Experiments in Fluids*, **37**(5), 720–730.

- Sun, T.F., & Zhou, L.M. 1983. Wind pressure distribution around a ribless hyperbolic cooling tower. *Journal of Wind Engineering and Industrial Aerodynamics*, **14**(1), 181–192.
- Surry, J. 1965. *Experimental investigation of the characteristics of flow about curved circular cylinders*. Tech. rept. DTIC Document.
- Vallès, B., Andersson, H.I., & Jenssen, C.B. 2002. Direct-mode interactions in the wake behind a stepped cylinder. *Physics of Fluids (1994-present)*, **14**(4), 1548–1551.
- Valles, B., Andersson, H.I., & Jenssen, C.B. 2002. Oblique vortex shedding behind tapered cylinders. *Journal of fluids and structures*, **16**(4), 453–463.
- Visscher, J., Pettersen, B., & Andersson, H.I. 2011. Experimental study on the wake behind tapered circular cylinders. *Journal of Fluids and Structures*, **27**(8), 1228–1237.
- Wieselsberger, C. 1922. *Further information on the laws of fluid resistance*. National Advisory Committee for Aeronautics.
- Williamson, C.H.K. 1989. Oblique and parallel modes of vortex shedding in the wake of a circular cylinder at low Reynolds numbers. *Journal of Fluid Mechanics*, **206**, 579–627.
- Williamson, C.H.K. 1992. The natural and forced formation of spot-like vortex dislocations' in the transition of a wake. *Journal of Fluid Mechanics*, **243**(1), 393–441.
- Xu, C.Y., Chen, L.W., & Lu, X.Y. 2010. Large-eddy simulation of the compressible flow past a wavy cylinder. *Journal of Fluid Mechanics*, **665**, 238–273.
- Yagita, M., Kojima, Y., & Matsuzaki, K. 1984. On the vortex shedding of circular cylinder with step. *Bulletin of JSME*, **27**, 426–431.
- Zdravkovich, M.M., Brand, V.P., Mathew, G., & Weston, A. 1989. Flow past short circular cylinders with two free ends. *Journal of fluid mechanics*, **203**, 557–575.
- Zdravkovich, M.M., Flaherty, A.J., Pahle, M.G., & Skelhorne, I.A. 1998. Some aerodynamic aspects of coin-like cylinders. *Journal of Fluid Mechanics*, **360**, 73–84.
- Zhang, W., & Lee, S. J. 2005. PIV measurements of the near-wake behind a sinusoidal cylinder. *Experiments in fluids*, **38**(6), 824–832.
- Zou, L., & Lin, Y.F. 2009. Force reduction of flow around a sinusoidal wavy cylinder. *Journal of Hydrodynamics, Ser. B*, **21**(3), 308–315.

Aerodynamic devices

- Choi, H., Jeon, W.P., & Kim, J. 2008. Control of flow over a bluff body. *Annu. Rev. Fluid Mech.*, **40**, 113–139.
- Every, M.J., King, R., & Weaver, D.S. 1982. Vortex-excited vibrations of cylinders and cables and their suppression. *Ocean Engineering*, **9**(2), 135–157.
- Gad-el Hak, M. 2000. *Flow control: passive, active, and reactive flow management*. Cambridge Univ Pr.
- Kleissl, K. 2013. *Cable Aerodynamic Control: Wind tunnel studies*. Ph.D. thesis, Technical University of Denmark - Section for Structural Engineering.
- Modi, V.J., Welt, F., & Seto, M.L. 1995. Control of wind-induced instabilities through application of nutation dampers: a brief overview. *Engineering structures*, **17**(9), 626–638.
- Naudascher, E., & Rockwell, D. 1994. *Flow-induced vibrations: an engineering guide*.
- Sallet, D.W., & Berezow, J. 1972. Suppression of flow-induced vibrations by means of body surface modifications. *Shock Vibration Bull.*, **42**, 215–228.
- Walshe, D.E., & Wootton, L.R. 1970. Preventing wind-induced oscillations of structures of circular section. *Pages 1–24 of: Proc. Inst. Civ. Eng.*, vol. 47.
- Zdravkovich, M.M. 1981. Review and classification of various aerodynamic and hydrodynamic means for suppressing vortex shedding. *Journal of Wind Engineering and Industrial Aerodynamics*, **7**(2), 145–189.

CHAPTER 3

Atmospheric icing

Some say the world will end in fire, some say in ice.

ROBERT FROST, FIRE AND ICE.

Atmospheric icing is a general term for a number of processes where water in various forms freezes in the atmosphere and sticks to objects exposed to the air or sticks and freezes directly to objects. Icing on circular cylinders is a time-dependent ice accretion process with a big temporal scale compared with any aerodynamic or dynamic characteristic time. This ice accretion generates a change in geometry of the circular cylinder section that can lead to instability phenomena. The problem is complex because the wind direction and atmospheric conditions are variable and the ice accretion can be generated in one direction whilst the instability phenomenon can occur in another direction. Ice accretion is often important in the design of structures because of the additional mechanical loads they may impose through their weight or increased wind loads, as well as the damage falling pieces of ice may cause during the melting phase or due to break-off by aerodynamic forces (List, 1977). The role of ice accretion on the aerodynamic instability of bridge cables has been recognized in the recent years. Nevertheless, a clear systematization of the knowledge on this form of instability doesn't exist, as neither field monitoring data nor static and dynamic wind tunnel test data have been collected.

Icing accretion on structures requires the simultaneous presence of water and temperatures below the freezing point. However, the ice accretion phenomenon on civil engineering structures and on aircrafts is different:

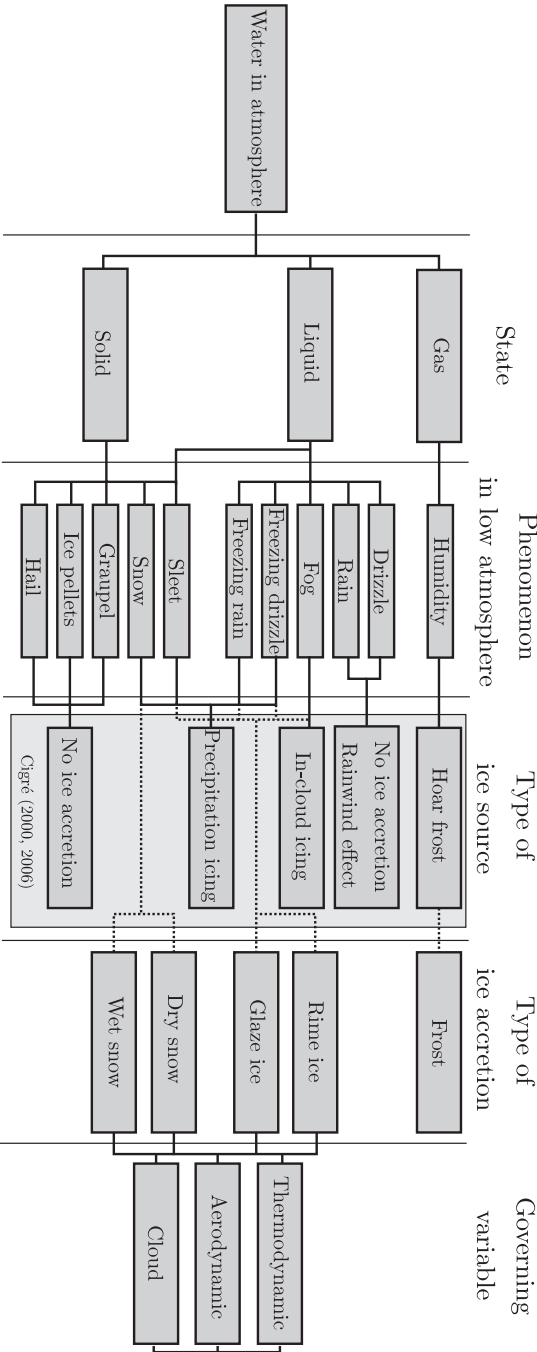


Figure 3.1: Ice accretion phenomenon: cause, effects and governing variables.

- Aircraft icing takes place at high air speed and small water droplets;
- Icing on low-altitude structures occurs in the presence of relatively low air velocity and largely varying droplet sizes.

In this chapter, the focus will be on the ice accretion phenomenon on civil engineering structures under conditions named as *low-altitude atmospheric icing*. The possible form of water in atmosphere and the process of icing will be described in the following.

3.1 Atmospheric environmental conditions

Water is a chemical compound with the chemical formula H_2O . A water molecule contains one oxygen and two hydrogen atoms that are connected by covalent bonds. Water is a liquid at standard ambient temperature and pressure, but it often co-exists on Earth with its solid state, named *ice*, and gaseous state, *water vapor*. Water covers 71% of the Earth's surface and is vital for all known forms of life and there are various theories about the origin of water on Earth. Water on Earth moves continually through the water cycle of evaporation and transpiration (evapotranspiration), condensation, precipitation, and runoff, usually reaching the sea (Figure 3.2).

Water moves perpetually through each of atmosphere, soil water, surface water, groundwater, and plants within the hydrosphere in the water cycle consisting of following transfer processes:

- *Evaporation* from oceans and other water bodies into the air and transpiration from land plants and animals into air;
- *Precipitation*, from water vapor condensing from the air and falling to earth or ocean;
- *Runoff* from the land usually reaching the sea;

Evaporation and transpiration contribute to the precipitation over land. Most water vapor over the oceans returns to the oceans, but winds carry water vapor over land at the same rate as runoff into the sea. Over land, evaporation and transpiration contribute. Precipitation has several forms: most commonly rain, snow, and hail, with some contribution from fog and dew (Gleick, 1993). Water runoff often collects over watersheds flowing into rivers. Some water is diverted to irrigation for agriculture. A flood occurs when an area of land, usually low-lying, is covered with water. It is when a river overflows its banks or flood comes from the sea.

Water can change the state from solid to liquid, liquid to gas, or solid to gas. During this transformations energy must be add. This energy, which is drawn in from the surroundings and stored within the water molecules, is called

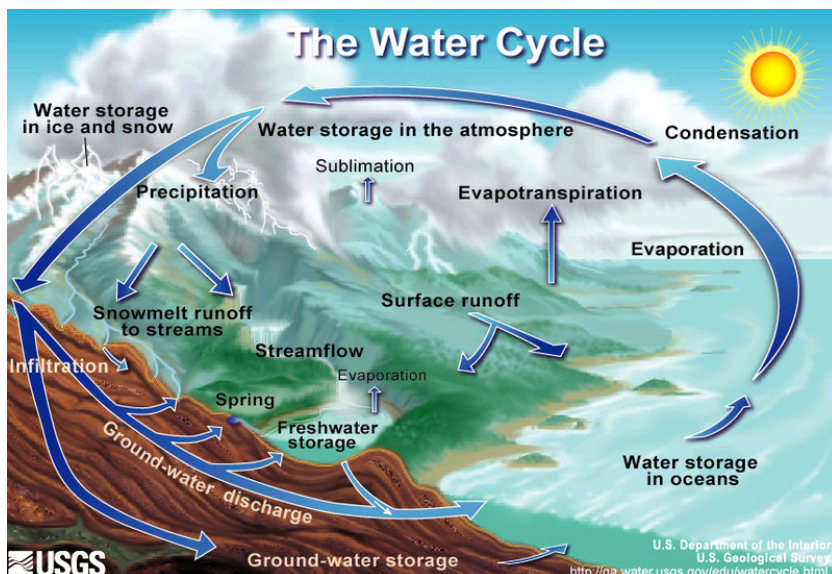


Figure 3.2: The water cycle, after Wikimedia Commons.

latent heat; in essence, it is the energy needed to break the molecular bonds that maintain the phase state. For instance when solid water (ice) melts, the water molecules absorb enough energy to break molecular bonds that maintain the ice crystals; the same process happens as water changes state from liquid to gas. Conversely, when water freezes, the water molecules release energy to the surroundings, lowering their internal energy. During this transformations energy must be removed. The water transformations and the latent heats are reported in Table 3.1.

Water is present in different forms in atmosphere (Figure 3.1). The typical atmosphere composition is 78.09% nitrogen, 20.95% oxygen, 0.93% argon, 0.039% carbon dioxide, and small amounts of other gases and a variable amount of water vapor, on average around 1%. The water and the gases in atmosphere form a *dispersion*. A dispersion is a system in which particles are dispersed in a continuous phase of a different composition. This dispersion is formed of air as continuous medium, and gas, liquid or solid water as dispersed phase, in function of thermodynamic parameters. This dispersion can be a *coarse dispersion* or a *colloid* as function of particle dispersed size. When water consists of non-associated molecules is vapor (gas) and in this case the system is a *gas mixture*. When water consists of associated molecules in the form of liquid droplet or solid crystals with diameter in the range $1\ \mu\text{m} \div 50\ \mu\text{m}$ the system is a *fog* or *clouds*. Fog is a collection of liquid water droplets or ice crystals suspended in the air at or near the level of the Earth's surface. Clouds are the same at high

Table 3.1: Water transformations and the latent heats. Positive values of the latent heat indicate release of energy, while negative values absorption.

From	To	Transformation name	Latent heat
Solid	Liquid	Melting	-330000 J/Kg
Liquid	Gas	Evaporation	-2500000 J/Kg
Solid	Gas	Sublimation	-2830000 J/Kg
Liquid	Solid	Freezing	$+330000 \text{ J/Kg}$
Gas	Liquid	Condensation	$+2500000 \text{ J/Kg}$
Gas	Solid	Deposition	$+2830000 \text{ J/Kg}$

altitude. When water consists of associated molecules in liquid droplet or solid crystals with diameter in the range $2 \cdot 10^2 \mu\text{m} \div 10^4 \mu\text{m}$ the system is a *rain* or *snow* depending on the temperature and state.

The rain is generated by the process of *collision-coalescence* or *ice-crystal model* (Bergeron process (Bergeron, 1933)). The difference between the two processes is fundamentally the temperature of the cloud. For the first process the temperature is above the freezing point of the water, instead for the second process is below.

For precipitation to form under the process of collision - coalescence there needs to be a variety of different size condensation nuclei. The smaller, lighter droplets are easily suspended in the updrafts of air, while the larger heavy collector droplets fall and collide with the smaller ones. Upon collision, the droplets coalesce into a bigger droplet. With enough collisions, the droplet achieves a size sufficient to fall all the way to the surface. The collision-coalescence model applies to warm clouds that form in the tropics.

When the clouds temperature is below the freezing point, water can exist in its liquid or solid form. Water that has a temperature below freezing but is still in a liquid state is called *super-cooled water*. Water normally freezes at 273.15 K (0°C) however it can also be supercooled at standard pressure down to its crystal homogeneous nucleation at almost 224.8 K (-48.3°) (Debenedetti, 2003). The process of supercooling requires that water be pure and free of nucleation sites. If water is cooled at a rate on the order of 10^6 K/s , the crystal nucleation can be avoided and water becomes a *glass*, however this is not the case of atmospheric processes. In atmosphere, water in extremely small amounts such as cloud droplets can exist in super-cooled state; droplets of supercooled water often exist in stratiform and cumulus clouds. Ice crystals co-exists with the super-cooled water in cold clouds. When this occurs, the ice crystals will grow at the expense of the water droplets. The droplet will dissipate in size while the ice crystal grows

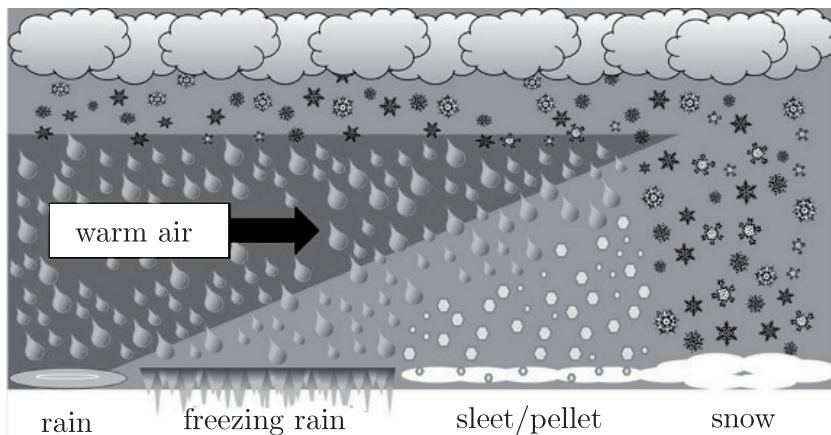


Figure 3.3: Type of atmospheric precipitation.

into a snow flake. The explanation of this phenomenon is that the saturation vapor pressure needed to maintain an ice crystal in equilibrium is considerably smaller than the corresponding value for a water droplet. Eventually this ice crystal will grow large enough to fall to the earth surface. The Bergeron Process often results in precipitation (Thériault *et al.*, 2006) (Figure 3.3). As the crystals grow and fall, they pass through the base of the cloud, which may be above freezing. This causes the crystals to melt and fall as rain. There also may be a layer of air below freezing below the cloud base, causing the precipitation to refreeze in the form of sleet or ice pellets. Similarly, the layer of air below freezing may be at the surface, causing the precipitation to fall as *freezing rain* that is super-cooled rain.

In summary, water in low altitude atmosphere that is in the interests of civil engineering applications, may be present in all three states. If it is present as gas is humidity. If it is present as a liquid is fog, drizzle, rain, freezing drizzle or freezing rain in function of the particle diameter and the temperature profile on the earth's surface. If it is present in solid form is snow, sleet (mixed solid-liquid), graupel, ice pellets or hail in function of the particle diameter and the temperature profile on the earth's surface.

3.1.1 Cloud and fog characteristics

In meteorology, a cloud is a visible mass of liquid droplets or frozen crystals made of water or various chemicals suspended in the atmosphere. According to the International Cloud Atlas published in 1957 by the World Meteorological Organization WMO (1956), clouds are classified according to appearance, form and height of their bases. The clouds may be divided as high clouds (above 6 km), middle clouds (2 km to 6 km), low clouds (below 2 km) and clouds of

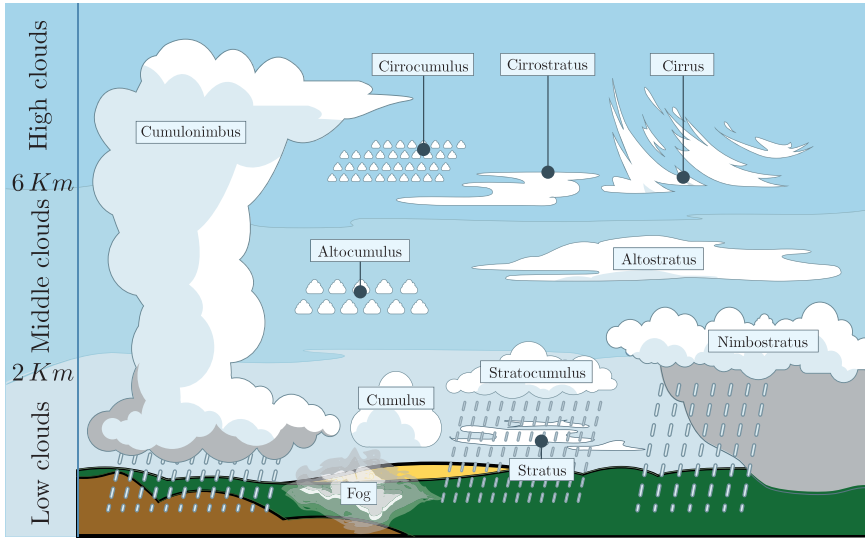


Figure 3.4: Cloud and fog types.

vertical development (Figure 3.4).

High clouds contain cirrus, cirrocumulus and cirrostratus clouds. The bases of high clouds are usually above 6 km . These types of clouds are composed of ice crystals. Middle clouds contain altostratus and altocumulus clouds. The bases of middle clouds range from 2 km to 6 km . These types of clouds are composed of water droplets and ice crystals. Low clouds contain nimbostratus, stratocumulus and stratus clouds, which are below 2 km . These types of clouds are composed of supercooled water droplets and sometimes ice crystals. Fog is distinguished from mist only by its density, as expressed in the resulting decrease in visibility: fog reduces visibility to less than 1 km , whereas mist reduces visibility to no less than 1 km . Fog forms when the difference between temperature and dew point is generally less than 2.5°C and occurs at a relative humidity near 100%.

Fog is a collection of liquid water droplets or ice crystals suspended in the air at or near the Earth's surface. The term fog is typically distinguished from the more generic term cloud in that fog is low-lying, and the moisture in the fog is often generated locally, such as from a nearby body of water, like a lake or the ocean, or from nearby moist ground or marshes.

Freezing fog occurs when liquid fog droplets freeze to surfaces. This is very common on mountaintops which are exposed to low clouds. Similarly this represents the meteorological conditions under which icing of cables can occur. Typically low-density clouds also have a low Liquid Water Content (LWC) whereas high density clouds have a high LWC. In Table 3.2 the typical LWC and mean droplet diameter for these types of clouds are seen.

Table 3.2: LWC and mean droplet size for different types of low altitude clouds. After [Mason \(1957\)](#).

Type of cloud	LWC [g/m^3]	D [μm]
Stratus	0.25-0.67	10.6-12
Cumulus (small)	$\ll 1$	18
Cumulus (congestus)	≈ 2	48
Stratoculumbus	≈ 0.3	8-16
Cumulonimbis	1-3	40
Fog	≈ 0.2	10-50

Droplet sizes of interests for icing in low atmosphere vary from 10 to 50 μm (diameter) up to 400 μm encountered in freezing rain. [Best \(1951\)](#) has analyzed experimental data for droplet size distribution in cloud and fog. The spectrum of droplet size and the liquid water content per unit volume is given by:

$$F(r < r_d(\mu m)) = 1 - \exp \left[(-2r_d/a)^k \right] \quad (3.1)$$

$$G = Aa^p$$

where F is the fraction of liquid water in the air comprised by droplets with radius $r < r_d(\mu m)$ and G is the liquid water content per unit volume of air expressed in g/m^3 . The distribution curve for cloud droplet is:

$$\frac{dF}{dr_d} = \frac{(2k/a)}{(2r_d/a)^{k-1}} \exp \left[(-2r_d/a)^k \right] \quad (3.2)$$

Recommended value for k , A and p are 3.27, $1.1 \cdot 10^{-3}$ and 1.79 ([Mason, 1957](#)). The typical value of the maximum amount of water in air at dew point is about $2g/m^3$ at -10° and $4g/m^3$ at 0° .

3.1.2 Precipitation characteristics

In meteorology, precipitation is any product of the condensation of atmospheric water vapour that falls under gravity. The main forms of precipitation include rain, freezing rain, sleet, drizzle, snow, snow pellets, ice pellets, and hail:

- **RAIN:** precipitation of water droplets with diameter ranging from 0.4 to 4.0 mm. The only difference between rain and drizzle is the size of water droplet. Rain drops are much larger than cloud droplets and therefore give a very high rate of catch. Its METAR code is RA.

- FREEZING RAIN: is composed of supercooled water droplets that freeze on impact with an object which is itself at a temperature below freezing. This is common ahead of warm front in winter. Its METAR code is FRRA.
- SLEET: precipitation composed of rain and partially melted snow. It is soft and translucent, but it contains some traces of ice crystals, due to partially fused snowflakes. In any one location, it usually occurs briefly as a transition phase from rain to snow or vice-versa. Its METAR code is RASN.
- DRIZZLE: precipitation in the form of very small water droplets which appear to float. At temperatures at or below the freezing level, drizzle will freeze on impact with objects and is known as freezing drizzle. Drizzle falls from stratus cloud with a high water content. Its METAR code is DZ.
- SNOW: precipitation of ice crystals. The water vapor in the air sublimates directly into ice crystals, without passing through any intermediate water stage. Snow flakes are formed of an agglomeration of ice crystals and are usually of a hexagonal or star like shape. Its METAR code is SN.
- SNOW PELLETS: precipitation of white, opaque, and spherical or conical grains of ice with diameter about 2-5 mm. Its METAR code is SG.
- ICE PELLETS: precipitation of transparent ice pellet, which are spherical or irregular with a diameter of 5 mm or less. The ice pellets usually bounce when they hit hard ground. Its METAR code is PL.
- HAIL: precipitation in the form of balls or lumps of ice with a diameter of 5 mm or more. Its METAR code is GR.

Usually meteorologists use a diameter of 200 μm as a demarcation between cloud droplets and raindrops.

3.2 Ice accretion phenomenon

Ice accretion is a process that happens when the water present in atmosphere freezes and adheres to objects exposed to the air. According to the ISO standard “the expression atmospheric icing comprises all processes where drifting or falling water droplets ... in the atmosphere freeze or stick to any object exposed to the weather”.

In general, ice accretion is linked to geographic conditions as for example distance to the coast, altitude above sea level and the local topography (Poots, 1996). Quantity measurements of ice and snow events are part of meteorological observations to derive probabilities of occurrence and to compare different

locations. This data is widely used to create risk maps of expected ice and snow quantities. Due to the complexity of icing processes their accuracy is limited.

The atmospheric icing accretion can be classified in three type of sources (Cigré, 2000, 2006):

- Hoar frost;
- In-cloud icing;
- Precipitation icing.

The factor that influencing the problem are mainly three (Figure 3.1): the *aerodynamic flow-field characteristics* on and around the body and growing ice accretion (aerodynamic), the establishment of the water particle (gas, liquid or solid) *trajectories with subsequent impingement characteristics and limits* (cloud), and, lastly, the *thermodynamics of the freezing/ice growth process* (thermodynamic) (Lynch & Khodadoust, 2001). This factors governs the type of ice accretion.

The aerodynamic flow characteristics are governed by the wind speed and by the shape of the section, that changes during the accretion process. The wind speed influences the type of ice accretion, the shape of the ice accretion as well as the adhesion of the ice. The droplet trajectories depends on the aerodynamic flow-field and on the droplet size. The ice accretion phenomenon took place because the droplets present in the air are moved from the flow on the object. The dynamics with which they are transported depends on the flow conditions and the droplets size.

The distribution density can be important in the description of the phenomena of interaction between the drops. The droplet diameter is the most common measure used to characterize a droplet (Ashgriz, 2011). Other variables used to describe the properties of a droplet are the temperature, the velocity and the composition. Different relevant diameters are used when describing the diameter of a droplet. Two commonly used are D_{10} and D_{30} . D_{10} describes the arithmetic median diameter, i.e. 50% of the liquid is made up of droplets having a diameter smaller or equal to this value. D_{30} describes the Volume Median Diameter, i.e. 50% of the total volume of the sprayed liquid is made up of droplets with a diameter equal to or less than D_{30} . Furthermore, D_{min} and D_{max} can be used to describe the minimum and maximum droplet diameter. The droplet size distribution is as important a parameter as the mean droplet size itself. The droplet size distribution expresses the droplet size as a function of the cumulative percent. Hence, the droplet size distribution shows the variety in the droplet sizes in a given liquid.

The trajectories of the smaller droplets are strongly influenced by the flow field and tend to follow the streamlines, impinging only close to the stagnation point, whereas the trajectories of the larger droplets are governed by inertia forces and tend to be straight, impinging on wider areas. The *tangent trajectories* are defined as the free-stream boundaries outside which a drop does not

collide with the body; according to the above these depend on the drop size. For a two-dimensional flow, there are two *impingement limits*, an upper and a lower. The *impingement limits* are the collision point of the tangent trajectories on the object.

The Liquid Water Content (LWC) describes the water mass per volume of air:

$$LWC = \frac{m_w}{V_{air}} \quad (3.3)$$

where m_w is the mass of water in the air and V_{air} is the volume of air considered. It is well known and understood that the *LWC* has a great influence on the shape of the ice accretion. Experimental studies have shown that an increase in LWC leads to an increased ice growth at a constant wind speed. As a matter of fact, the capacity of accretion depends on the heat balance of the accreting surface, whose main contributions come from the latent heat deriving from freezing of the impinging supercooled water droplets and the heat flux between the accretion and the airstream. The amount of latent heat depends on the amount of freezing water. An increase in LWC leads to an increase in the amount of heat released when the water freezes. At some LWC the heat of freezing will increase the surface temperature so much that it is not possible to freeze all the present water. At this given point a further increase in LWC will result in that a fraction of the supercooled water freezes and that the “extra” water is either shed away with the airflow or is running to the back of the cylinder where it freezes. Differently, the dissipating heat effect to the flow is the related to the boundary layer characteristics on the surface; these depend on the wind speed and on the superficial roughness.

Another important variable is the *exposure time*. The amount of ice accretion depends on the time that the surface is exposed to the watery air volume. The longer exposure time, the more ice accretion, not necessary in a linear fashion.

In summary, ice accretion phenomenon depends on:

- Liquid water content;
- Temperature;
- Droplet size distribution and density;
- Section material and geometry;
- Windspeed;
- Duration of exposure.

Other important variable regards heat balance of an icing surface. The pioneering work on heat balance of an icing surface goes back to the 1950s [Hardy \(1953\)](#); [Ludlam \(1951\)](#); [Messinger \(1953\)](#). [Mazin et al. \(2001\)](#) gives the

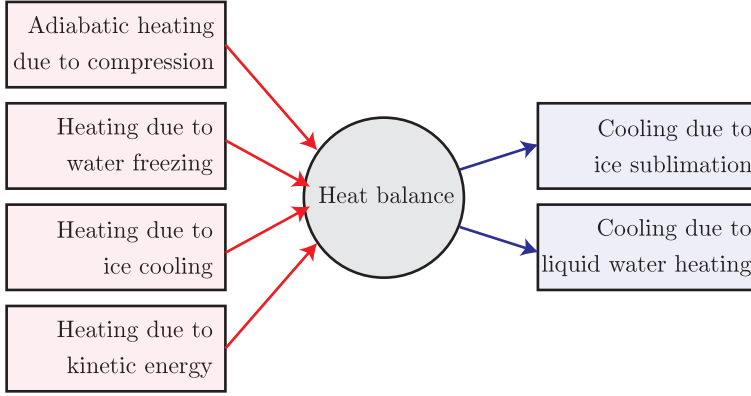


Figure 3.5: The heat balance over an ice surface. After [Mazin *et al.* \(2001\)](#).

heat balance of an icing surface. He considered a cylinder exposed to the flow of air with velocity U , temperature T , pressure P_a , and containing supercooled droplets and liquid water content LWC . It is assumed that the axis of the cylinder is perpendicular to the axis of the vector of the air velocity. The temperature of the droplets is considered to be the same as the temperature of the air. Because of dynamic heating and latent heat release from freezing droplets, the surface temperature will normally be higher than the ambient temperature. To derive the heat balance of an icing surface, he considered a steady-state heat balance at a local point on the surface of the cylinder. The surface temperature is defined by several processes: dynamic heating, freezing of droplets, ice sublimation, heat exchange between the droplets, and the cylinder's surface. The equation of the heat balance at a local point can be written as:

$$\sum q_i = 0 \quad (3.4)$$

where q_i are the densities of the heat fluxes resulting from different processes (Jm^2s^{-1}). The contribution are schematically shown in Figure 3.5. Each contribution of Eq. 3.4 is analyzed in [Mazin *et al.* \(2001\)](#).

It is evident that the process of scaling cannot occur as in the case of classical aerodynamic phenomena only taking into consideration in the Reynolds number; other variables, such as gravity, the description of cloud and thermodynamic phenomena, come into play. For this reason is preferable to make only full-scale experiments, due to the difficulties of scaling. For instance, it must be highlighted that ice forms first on the shortest radius of curvature meaning that a cylinder with small diameter experiments major accretion respect to one with larger diameter. For this reason, the ice accretion behavior of electrical conductors (small diameter) and bridge cables is different (large diameter).

In the following the different types of ice accretion are described.

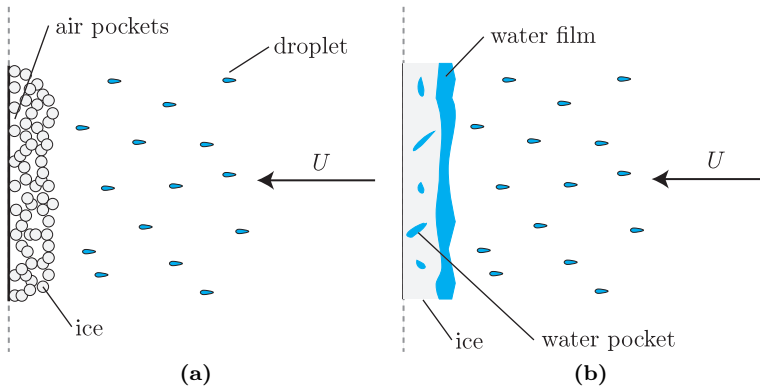


Figure 3.6: Rime ice (a) and glaze ice (b) accretion phenomenon.

3.2.1 Hoar frost

Hoar frost is a phenomenon in which water vapor is transformed directly to the solid phase (ice deposition) and forms light, nice-looking crystals (Farzaneh, 2008). It is formed when solid surfaces are cooled to below the dew point of the adjacent air as well as below the freezing point of water. Frost is also usually translucent in appearance. The density of hoar frost varies and will tend to be low and less than 100 kg/m^3 (Poots, 1996). Normally, hoar frost does not constitute a significant loading problem, however, it is a very good collector of supercooled liquid droplet and it can enhance the rime ice accretion process (Farzaneh, 2008; Makkonen, 1984a).

3.2.2 In-cloud icing

In-cloud icing is an ice accretion phenomenon that transforms the supercooled liquid water droplet in atmosphere on ice on a object. It is classified in:

- Rime ice;
- Glaze (or clear) ice;
- Mixed ice.

Rime ice has a rough, milky white appearance, and generally follows the contours of the surface closely. Rime ice is typically designated “dry growth” for the absence of a liquid layer between the structure and the surrounding cold air during the accretion process (Figure 3.6a). When supercooled droplets, typically in the size of $10 \mu\text{m}$, impact with a surface at a temperature below 0°C the droplets freeze instantaneously, hereby creating air pockets in between the rime grains.

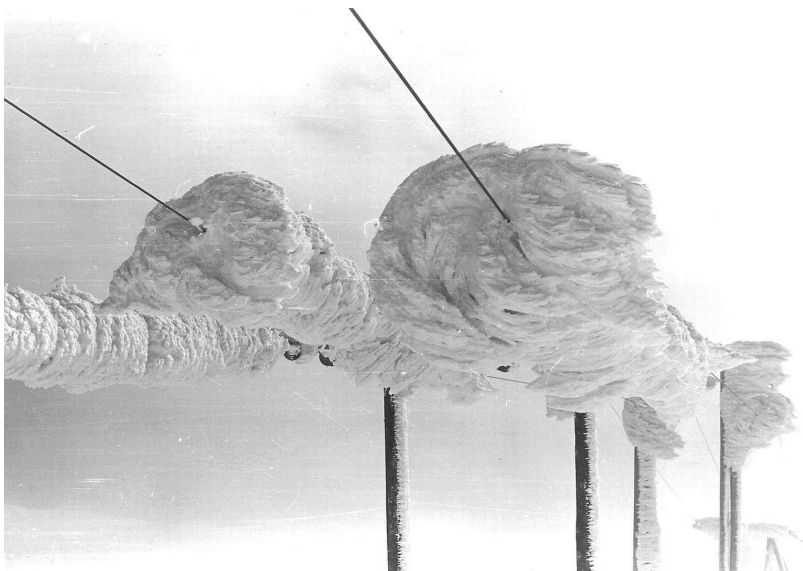


Figure 3.7: Rime ice accretion in April 1961 took up to 22 kV power line to the radio and television transmitter Lønahorgi (1410 MSL). Photo: Olav Wist.

Hence, the density of rime is considerably less than the density of pure bubble free ice. Dependent on how fast the freezing actually takes place, which among other things depends on the speed of the droplets and the temperature, more or less air is trapped between the frozen droplets. The higher the speed of the droplets and the bigger the droplets, the better the packing, hence the density of the formed ice increases. Typically *soft rime* is distinguished from *hard rime* in the sense that the density of soft rime is between $200 - 600 \text{ kg/m}^3$ while it is between $600 - 900 \text{ kg/m}^3$ for hard rime. Moreover, soft rime is typically formed at temperatures below -8°C . On the other hand hard rime is typically formed at temperatures varying between -8°C to -2°C . The adherence of hard rime to the surface is strong while it is low to medium for soft rime.

Glaze (or clear) ice is sometimes clear and smooth, but usually contains some air pockets that result in a lumpy translucent appearance. Glaze is typically designated “wet growth” because of the liquid layer on the accreting surface (Figure 3.6b). During wet growth accretion, the heat flux from the accretion is not enough to ensure that all supercooled droplets freeze and hereby are incorporated in the accretion immediately after they impact with the surface. This happens when the heat of fusion liberated by the freezing droplets exceeds the heat loss from the system meaning that the temperature becomes positive, hence a water film is formed. Since the surrounding air and the surface considered still

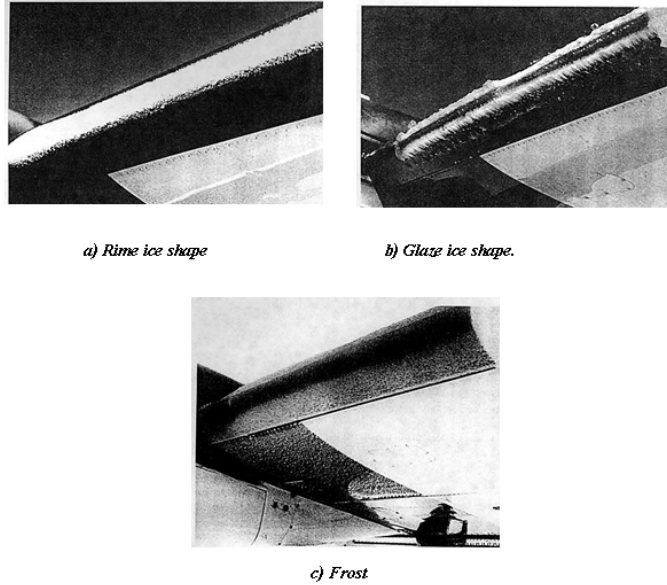


Figure 3.8: Different type of ice accretion on an airplane wing. After CIRA website (<http://extice.cira.it>).

have temperatures below 0°C freezing takes place underneath the liquid layer.

The liquid accretion is accompanied by the formation of *icicles* (Figure 3.9). Formation of icicles is often neglected when icing of structures is investigated. Even though they contribute significantly to the ice load and to the aerodynamic behavior. Icicles form under freezing precipitation or due to freeze and thaw cycles of larger ice deposits. The ice evolution is fed by a flux of supercooled water on the surface of the icicles. If sufficient water is present a liquid film of supercooled water develops. Gravity and wind drag drive the water towards the icicle tip, where it forms a pendant drop. The pendant drop at the tip grows as more water flows down. When it reaches a certain size it strips and a new drop can form. Experiments showed that under calm wind conditions the diameter of the pendant drop lay between 4.8 to 5.0 mm, regardless of the growing conditions (Maeno & Takahashi, 1984; Maeno *et al.*, 1994). The growth is proportional to the heat loss. Since icicles grow mainly in the longitudinal direction, the main heat loss must occur at the tip. To freeze the liquid water running down the icicle the latent heat released during freezing must be dissipated. This occurs mainly due to thermal convection and evaporation. The thin water film on the icicles surface is supercooled and therefore any changes in the film temperature can not contribute significantly to the heat transfer. Compared to that, the heat flux at the surface of the pendant drop is significant.



Figure 3.9: Icicles on electrical conductor. Photo: Crystal Murray.

Table 3.3: Meteorological parameters controlling atmospheric ice accretion, after ISO 12494 - Atmospheric icing of structures.

Type of ice	Temperature °C	Wind speed m/s	Droplet size	LWC	Typical event duration
Glaze	Fig. 3.10	Fig. 3.10	Medium	High	Hours
Hard rime	Fig. 3.10	Fig. 3.10	Medium	Medium	Days
Soft Rime	Fig. 3.10	Fig. 3.10	Small	Low	Days

Table 3.3 and Figure 3.10 summarizes the three different types of in-cloud icing as a function of wind speed and air temperature. The curves in Figure 3.10 shift to the left with increasing LWC and with decreasing object size.

Different moisture droplet sizes are commonly encountered in cloud, this variation produces a mixture of clear ice (from large drops) and rime (from small droplets.) Known as mixed ice most ice encounters take this form; it is a combination of rime and clear ice.

3.2.3 Precipitation icing

Precipitation icing forms from supercooled droplets and snow and sleet in atmosphere (Table 3.4). From the point of view of the supercooled droplets, precipitation icing distinguishes from in-cloud icing primarily with respect to the size of the droplets. The particles connected with in-cloud icing have the size of droplets of clouds or fogs. Differently, precipitation icing is formed from precipitation which means that the droplets have the size of rain.

Freezing rain is formed when a warm front (positive air temperatures) collides with air with temperatures below 0°C. In this case a warm air layer is pushed over the inclined surface of the warm front which means that a system

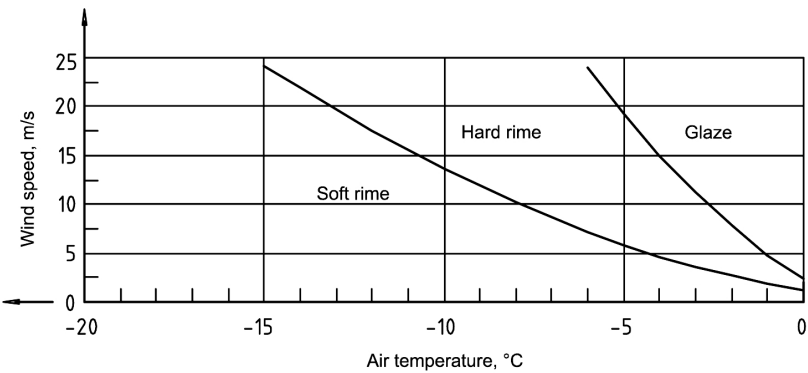


Figure 3.10: Type of accreted ice as a function of wind speed and air temperature, after ISO 12494 - Atmospheric icing of structures.



Figure 3.11: Wires sagging after an freezing rain storm, Missouri 1949. After Wikimedia Commons.

Table 3.4: Meteorological parameters controlling precipitation ice accretion, after ISO 12494 - Atmospheric icing of structures.

Type of ice	Temperature	Wind speed	Droplet size	LWC	Typical event duration
	$^{\circ}C$	m/s			
Freezing rain	$-10 \div 0$	Any	Large	Medium	Hours
Wet snow	$0 \div 3$	Any	Flakes	High	Hours

with warm air lying above cold air is formed. Snow crystals formed in a cold layer melt when they fall through the warm air layer where the temperatures are positive. Depending on the location of $0^{\circ}C$, i.e. the thickness of the warm air layer, the snow crystals transform more or less into rain droplets. As a rule of thumb it is known that if the thickness of the warm air layer is more than $500\,m$ all snow transforms into rain droplets. These droplets fall through the layer with negative temperatures below the warm front slope which means that they get supercooled. Finally, they freeze during their impact with a objects on earth’s surface. Freezing rain also results in the formation of glaze. The droplet sizes of freezing rain vary from $0.5-3\,mm$, hence they can be considerably larger than the droplets appearing in in-cloud icing.

Dry and wet snow ice accretion are ice accretion phenomenon that occur when snowflakes adhere to a circular cylinder. Dry snow accretion is characterized by the simple leaning of the snowflakes on objects. As a matter of fact, snowflakes usually don’t have any adhesion capability and can be simple dragged by the wind. Differently, wet snow accretion can either be formed in the same way as freezing rain or more simply as snow crystals falling through a warm layer close to the earth surface. Compared to freezing rain, the main difference is that the snow crystals do not melt completely when they fall through the warm air layer since the thickness of this layer is less than $500\,m$. Hence the snow crystals are only partly melted when they reach the surface which typically has a temperature around $-1^{\circ}C$ to $+2^{\circ}C$. When the air temperature decreases the liquid part in the wet snow freezes. Wet snow has a good adhesion with the surface when frozen but a weak adhesion when forming. High wind speeds can cause high densities of wet snow since it is compressed which means that the density can vary in the range $200-990\,kg/m^3$ (Poots, 1996).

3.2.4 Seawater spray icing

Freezing of seawater spray occurs when the temperature of air is below the freezing temperature of seawater (-2°). In this case, droplets can be generated from



Figure 3.12: Mist from the frosty waters of the north Atlantic engulfs a ship in a beautiful ice sculpture. Photo: Library and Archives Canada.

wave breaking and wind forces. The form of ice produced by freezing water spray varies from glaze ice to opaque ice as the air temperature drops. It is not common to have large amount of seawater spray at high levels of tall structures. However, the ice formation rate rises as the velocity of wind increases or seawater temperature decreases. Conditions affecting marine icing are considered to include environmental factors such as wave height, wind velocity, ambient air temperature, and seawater temperature, and some are closely related to the occurrence of sea spray. The most important aspects of the marine icing phenomena is the inclusion of salinity effects and their time dependence. The presence of salt within the water requires consideration of not only freezing temperature depression, but also salt rejection during freezing, which is accompanied with the inclusion of unfrozen brine pockets leading to spongy ice. This type of accretion is mainly studied in the marine industry (Figure 3.12).

3.3 Effects of icing on structures

The main effects of icing on structures are increased vertical loads on the structures as well as increased wind drag due to the larger area exposed to the wind. In the following, the most important effects of ice accretion are summarized:

- **STATIC ICE LOADS.** Different types of objects are affected in different ways by static ice loads. The sensitivity of an object is dependent on the type of structure as well as the varying aspects of icing.
- **WIND ACTION ON ICED STRUCTURES.** Structures are sensitive to increased

wind drag caused by icing. ISO 12494 shows how the drag coefficient varies with ice accretion and size of the object. A thicker ice coating on the object surface leads to increased drag coefficients and hence increased effects on the structure by wind drag. The drag coefficient depends on the properties of the icing event, such as ice type.

- **AERODYNAMIC INSTABILITY OF ICED STRUCTURES.** Flexible structures are sensitive to the variation of the wind forces caused by icing. Drag, lift and moment forces result varied with respect to the dry case and can enhance aerodynamic instability phenomenon. The instability can lead to the occurrence of severe vibrations that may increase effects of fatigue and lead structural damage.
- **DYNAMIC EFFECTS.** The resonance frequency of an object decreases with ice accretion due to the variation of mass. This may cause severe structural damage since the lower frequencies usually are the most critical ones. Shedding of ice from an object can cause severe dynamic effects and stresses in the structure.
- **ICE SHEDDING.** Ice shedding can be caused by ice melting, ice sublimation, and mechanical ice breaking. The fall of ice chunks can cause damage to objects and/or people who are hit.

3.3.1 Ice shedding

Sudden ice shedding generates high dynamic loads, which can cause severe damages on the transmission lines such as tower arm failure or even cascading failures of several towers (Farzaneh, 2008). Due to the recoil the conductor can hit another conductor, parts of the tower or the ground wire causing a flashover. The shedding ice may also threaten humans and passing vehicles or buildings in the places like bridge's decks and areas under electrical conductors. Druez *et al.* (1995) identified three types of cable ice shedding, or ice mass reduction:

- Ice melting;
- Ice sublimation;
- Mechanical ice breaking.

Each type of shedding can be characterized by specific atmospheric and load conditions.

In the case of ice shedding by melting, the principal characteristic is the air temperature, which has to be above 0°C . This kind of ice shedding is divided into two phases. The first phase corresponds to simple ice melting, characterized by a relatively low shedding rate, depending on air temperature, solar radiation and wind velocity. The second phase corresponds to the falling of ice chunks,

under the effect of wind and gravity forces, when melting occurs at the cable-ice interface.

In the case of ice sublimation, the most important atmospheric factors are relative humidity, temperature and wind velocity. The sublimation rate increases as temperature and wind velocity increase, and when relative humidity decreases. The phenomenon can be observed during several consecutive days, and the total ice mass reduction can be important, in the order of magnitude of a few kilograms per meter. It occurs at the ice-air interface, and consequently the sublimation rate should increase with the ice accretion external surface, and therefore with the ice load and the ice porosity.

Mechanical ice breaking is produced by adhesive or cohesive failure of the ice accretion due to stress/strain conditions beyond ice crystal rheological limits. Initiation and propagation of such failures are complex and can be induced by static loads or dynamic loads related to wind effects. Therefore, wind velocity, temperature, ice load and ice strength can be expected to influence ice shedding by mechanical breaking.

References

- Ashgriz, N. 2011. *Handbook of Atomization and Sprays*. Vol. 11. Springer.
- Bergeron, T. 1933. On the physics of clouds. *Memo. Met. Assoc., Intern. Union for Geodesy and Geophysics, Lisbon*.
- Best, A.C. 1951. Drop-size distribution in cloud and fog. *Quarterly Journal of the Royal Meteorological Society*, **77**(333), 418–426.
- Cigré. 2000. Guidelines for field measurements of ice loading on overhead power line conductors. *In: Technical Brochure 179*.
- Cigré. 2006. Guidelines for meteorological icing models, statistical methods and topographical effects. *In: Technical Brochure 291*.
- Debenedetti, P. G. 2003. Supercooled and glassy water. *Journal of Physics: Condensed Matter*, **15**(45), R1669.
- Druez, Jacques, Louchez, Sylvie, & McComber, Pierre. 1995. Ice shedding from cables. *Cold regions science and technology*, **23**(4), 377–388.
- Farzaneh, M. 2008. *Atmospheric icing of power networks*. Springer Verlag.
- Gleick, P. H. 1993. *Water in crisis: a guide to the world's fresh water resources*. Oxford University Press, Inc.
- Hardy, J.K. 1953. Kinetic temperature of wet surfaces: A method of calculating the amount of alcohol required to prevent ice, and the derivation of the psychrometric equation.
- List, R. 1977. Ice accretions on structures. *J. Glaciol*, **19**, 451–465.
- Ludlam, F.H. 1951. The heat economy of a rimed cylinder. *Quarterly Journal of the Royal Meteorological Society*, **77**(334), 663–666.
- Lynch, F.T., & Khodadoust, A. 2001. Effects of ice accretions on aircraft aerodynamics. *Progress in Aerospace Sciences*, **37**(8), 669–767.
- Maeno, N., & Takahashi, T. 1984. Studies on icicles. I. General aspects of the structure and growth of an icicle. *Low Temp Sci Ser A*, **43**(6), 125–138.
- Maeno, N., Makkonen, L., Nishimura, K., Kosugi, K., & Takahashi, T. 1994. Growth rates of icicles. *Journal of Glaciology*, **40**(13), 319–326.
- Makkonen, L. 1984a. *Atmospheric icing on sea structures*. Tech. rept. DTIC Document.
- Mason, B.J. 1957. *The Physics of Clouds*.

- Mazin, I.P., Korolev, A.V., Heymsfield, A., Isaac, G.A., & Cober, S.G. 2001. Thermodynamics of icing cylinder for measurements of liquid water content in supercooled clouds. *Journal of Atmospheric and Oceanic Technology*, **18**(4), 543–558.
- Messinger, B. L. 1953. Equilibrium temperature of an unheated icing surface as a function of air speed. *Journal of the Aeronautical Sciences (Institute of the Aeronautical Sciences)*, **20**(1).
- Poots, G. 1996. *Ice and snow accretion on structures*. Research Studies Press.
- Thériault, J.M., Stewart, R.E., Milbrandt, J.A., & Yau, M.K. 2006. On the simulation of winter precipitation types. *J. Geophys. Res*, **111**, D18202.
- WMO. 1956. International Cloud Atlas.

CHAPTER 4

Climatic wind tunnel testing

Every great advance in science has issued from a new audacity of imagination.

JOHN DEWEY, THE QUEST FOR CERTAINTY.

This chapter briefly describes the simulation techniques used to simulate the ice accretion phenomenon and to evaluate the aerodynamic behavior of ice accreted bridge cables. In particular, it describes the new spray bar system and the bridge hanger and cable stay sectional models. These were specially realized for this experimental campaign. At the same, it shows the results of all the tests carried out to characterize the experimental setup. A brief description of the climatic wind tunnel used is also given. Finally, the test procedures and the climatic conditions adopted in the simulations are given.

The spray bar system was developed as part of the Master's thesis work of Mia Lund ([Lund, 2013](#)) at the Department of Civil Engineering, Technical University of Denmark, for which the author of this dissertation acted as co-supervisor.

4.1 Icing simulation tools

The evaluation of the aerodynamics of ice accreted bridge cables with natural icing conditions is the most realistic means for checking effects of icing. However, natural icing of bridge cables is usually difficult to find in nature because the handling critical atmospheric conditions needed to control the adequacy of

the measurements. Even finding a reasonable encounter of the proper conditions for a short time period, can require many years. The boundary conditions are always very difficult to control. Nevertheless, the field observation demonstrated some form of interactions between the ice accretion phenomenon and the aerodynamics of bridge cables.

In order to overcome these difficulties, ground facilities are very valuable tools to analyze full scale components with respect to icing and to generate ice shapes. These facilities have been developed in different fields of application as the aircraft, naval and automotive industries. Furthermore large size wind tunnel, have been successfully used in certification process and results obtained have been accepted by the certification authorities worldwide. However, rather few special existing facilities are really able to generate realistic icing condition and contemporarily are large enough to accommodate full-scale components.

Experimental ice accretion simulations on the ground cover a wide range of test types. Some intend to simulate natural icing situations, and others only simulate certain aspects present in the complex ice accretion process. Compromises have to be accepted with respect to the similarity requirements as a possibility to obtain reliable data in repeatable and controlled environments. To perform tests in prescribed conditions, complex facilities are needed.

Last but not least, the area of computational prediction of ice accretion has progressed greatly during recent years and is now an important and quite reliable simulation tool, mostly in 2D. Yet, this topic is no further discussed in the present work.

4.1.1 Type of simulation

Experimental simulations of ice accretion are understood to cover a wide range of test types. In particular the tests can be classified in three groups:

- Dry air simulations;
- Warm climatic simulations;
- Cold climatic simulations.

In the first case the ice shape should be geometrically similar and objectives are either to measure global aerodynamic coefficients or to determine the characteristics of the flow field. The shape can be reproduced using the rapid prototyping technique. Studies of this type include thermal measurements, since the local heat transfer coefficient is one of the most critical values in the determination of the ice accretion process. Since some of the accreted ice surfaces are characterized by large and irregular roughness elements, the measurement of the local heat transfer coefficients becomes a complicated matter.

In the second case, it is used a two-phase flow, made up of water droplets and dry air. These simulations are used to study water droplet trajectories, local

impingement distributions, droplet splashing, surface runback water, thermal effects, etc. and include the presence of a liquid film that is deposited on the surface. The temperatures are above the freezing point and the experiments are aimed at understanding the role played by liquid water.

The third type of simulations aims at a complete similarity of all existing physical phenomena, maintaining air temperature below freezing values and including clouds of supercooled droplets. In many cases, the interest is only in the shape of the accreted ice, with its surface details and water phenomena, but there are also experiments undertaken to determine the flow field and the overall aerodynamic characteristics, as the ice accretion progresses with time. For these simulations, in which complete physical similarity is sought, direct measurements of important variables such as surface temperature distribution, droplet splashing and local convective heat transfer coefficients. These simulations require specialized instrumentation and measuring techniques in addition to the proper test facility.

4.1.2 Climatic wind tunnels

Experimental icing simulations are in many instances performed in specially designed ground facilities where icing conditions are to be reproduced. Such tests may be conducted with full-scale prototypes or sub-scale models. These tests are performed in cold airstreams, which contain icing clouds made up of supercooled droplets or ice particles.

Climatic wind tunnels have all the systems and are of similar configuration as conventional dry air wind tunnels, but they incorporate two additional features that make them special and unique:

- A refrigeration system that cools the air to well below freezing temperatures;
- A water spray system that injects water droplets into the air stream creating a supercooled cloud.

The typical configuration of a closed loop wind tunnel has the spray system located at the end of the settling chamber, before the tunnel contraction while the heat exchanger is in the leg upstream of the corner before the settling chamber. Some other deicing equipment is installed to remove ice from walls. Test section size usually ranges from intermediate dimensions of about $2\text{ m} \times 2\text{ m}$, to small ones of about $0.15\text{ m} \times 0.15\text{ m}$. The velocities usually cover only the low speed range ($M = 0$ to 0.4), especially for the largest facilities, but there are some small icing tunnels that can reach high subsonic values ($M = 0.8$). Most icing wind tunnels are atmospheric, low speed facilities with maximum velocities ranging from about 70 to 180 m/s and a temperature range of -35°C to 0°C . The water content of the air can be varied from about 0.2 to 3.0 g/m^3 , and with droplet size variation of 15 to $40\text{ }\mu\text{m}$. In addition to requirements for uniformity

of velocity and limits on flow angularity in the test section, temperature and droplet-cloud variables must have spatial uniformity. Also, the spray system must be capable of reproducing a wide range of values for liquid water content, droplet median volume diameter and droplet size spectra, in order to simulate nature. As these facilities include a two-phase flow in the test section, specialized instrumentation is needed to measure the flow variables, in particular for the liquid phase. The variable that usually are controlled are:

- Liquid water content;
- Temperature;
- Temperature uniformity;
- Flow velocity;
- Turbulence intensity distribution;
- Median volume diameter (MVD);
- Cloud uniformity;
- Model surface temperature.

Nowadays, climatic wind tunnels provide a controlled and repeatable icing environment for the generation of ice shapes on airfoils, wings, bodies, propulsion systems, and other components.

4.1.3 CIRA – Icing Wind Tunnel

During the period of April-May 2012, the author of this thesis has gone to visit a climatic wind tunnel with unique performance in the world (Figure 4.1). The visit to this gallery has been a huge source of inspiration to the later stages of design of the spray bar system. Despite being designed for completely different purposes, CIRA – Icing Wind Tunnel has characteristics similar to those that can serve for purposes of tests on bridge cables. A brief description of the facility visited is provided for sake of completeness.

The CIRA – Icing Wind Tunnel is managed by the Italian Aerospace Research Centre (Centro Italiano Ricerche Aerospaziali - CIRA) that is a consortium established in July 1984 to promote the growth and success of the aerospace industry in Italy (its head-office is in Capua). The majority of CIRA share capital is held by government organizations: the Italian Space Agency (ASI) and the National Research Council of Italy (Consiglio Nazionale delle Ricerche - CNR).

The CIRA Icing Wind Tunnel was officially inaugurated in September 2002. It has a number of features that make it unique in the world:

- The largest refrigerated wind tunnel in service;



Figure 4.1: The visit in the CIRA – Icing Wind Tunnel. From left to right: Cristoforo Demartino, prof. Francesco Ricciardelli and prof. Francesco Marulo.

- The highest speed icing wind tunnel ($M = 0.7$);
- The only facility combining altitude, humidity and temperature simulation;
- The largest number of different test configurations (4);
- The largest numbers of spray bar nozzles position (1000) and bars (20);
- The widest operating range for engine flow simulation (1.5-55 kg/s mass flow).

The IWT facility is a closed loop circuit, refrigerated wind tunnel, with three interchangeable test sections and one open jet configuration. As many conventional wind tunnels, the IWT is fan driven. Downstream the fan diffuser, a twin row heat-exchanger is located to provide low temperature operation capability. The facility settling chamber is fitted with a honeycomb module to reduce large scale eddies thus ensuring flow straightening. Downstream the honeycomb, an interchangeable section provides the possibility to install either:

- A spray bar module generating the cloud for icing tests;
- A screen module when lower turbulence airflow is necessary for high quality aerodynamic tests.



Figure 4.2: CIRA – Icing Wind Tunnel, Capua, Italy.

The facility is driven at the desired airspeed by a 24 blades, with variable blade pitch angle. The fan is located in the return circuit. The fan motor is located inside the fan nacelle. The motor is cooled through a dedicated air-cooling system. Upstream the fan, a grid avoids that major ice blocks could impinge on the blades. The fan power is 4 MW , however, a 35% power margin is available to compensate pressure losses increase due to ice build up inside the wind tunnel. Variable blade pitch angle allows an optimal setting for different aerodynamic load conditions. Fan blades have provisions for heating system.

Air flow refrigeration is obtained via a twin row heat exchangers. The cooling plant is made up of 4 compressor units (1700 kW motor power each), a single evaporator and a single condenser unit, the twin row heat exchanger, connecting pipes and specific auxiliaries (e.g. pumps and valves). Compressors, evaporator and condenser units are located in a separate building just facing the heat exchanger section. The minimum achievable temperature is -32°C . Temperature accuracy on the set-point is about $\pm 0.1^{\circ}\text{C}$. Temperature descent rate is up to $1^{\circ}\text{C}/\text{min}$. The Heat Exchanger is also capable to control the air Relative Humidity (RH) before the spray bar, by means of a hot air compressor and steam injection.

A 0.7 MW centrifugal compressor unit allows the pressure to be regulated between 0.39 bar (corresponding to an altitude of 7000 m) and 1.45 bar . Safety valves allow a fast tunnel evacuation and pressurization.

The IWT spray bar system is able to generate water droplets with diameters and liquid water content covering the overall envelope prescribed by the FAR 25/29 Appendix C for both continuous and intermittent cloud conditions. Furthermore, the system is capable to generate super-cooled large droplets, within the range of freezing drizzle conditions. Upstream the spray bar system section, a honeycomb section assures straight flow conditions at the cloud generation

section. The spray bar system has 20 bars having a low drag aerodynamic shaped section, whose main feature is a low sensitivity to flow separation. Each bar is removable and may be vertically adjusted for optimizing cloud coverage and uniformity, if necessary, during the calibration phase. Each bar is equipped with 50 spraying nozzle positions, for a maximum total of 1000 possible spraying positions over 20 bars. Each nozzle water supply line is equipped with a solenoid valve that can be remotely switched on and off. The number of operating nozzles may be changed during a run remotely. The spray bar system is fed by pressurized, dematerialized and conductivity-controlled water and dry compressed hot air at temperature.

4.2 DTU/Force Technology Climatic Wind Tunnel

The tests were performed at the DTU/Force Technology collaborative Climatic Wind Tunnel (CWT) in Lyngby, Denmark. The Climatic Wind Tunnel is established as a joint effort between Femern Bælt A/S, DTU-Byg and FORCE Technology. In order to be able to study cable vibrations under the influence of wind, rain and ice the wind tunnel has been designed and constructed with these features. The wind tunnel is closed circuit with test section dimensions: length \times width \times height = $5\text{ m} \times 2\text{ m} \times 2\text{ m}$. The walls of the testing section consist of eight movable panels, two of which are made of glass for visualization purposes. The technical specifications of the wind tunnel are reported by Georgakis *et al.* (2009). The maximum wind speed in the test section is 30 m/s and the minimum temperature is -5°C . The fan power is 210 kW . This shaft power is needed to circulate the air with $100\text{ m}^3/\text{s}$ at maximum drag configuration, i.e. all flow generating devices (turbulent flow) and model setup included. The cooling unit has a capacity of 250 kW to compensate for heat due to air friction and motor waste heat and to heat transmission from ambience. The control of the cooling unit is a on-off feedback control system, which induces a maximum variation with respect to the nominal temperature of $\pm 1.5^\circ\text{C}$ for a fixed wind speed below of 17 m/s ; such variation increases with speed. The wind tunnel is equipped with a pitot tube, a thermometer and a hygrometer for monitoring wind speed, temperature and humidity in the test chamber and in other points of the CWT.

In any of rain or ice simulation tests, there will be huge amount of water produced. CWT has a drainage system that is utilized at both ends of the testing section to evacuate the runoff water. Turning vanes are installed as parallel curved plates. The main role of turning vanes is guiding the flow at crossings and making a uniform flow at the mentioned parts. Due to possibility of ice accretion on vanes in icing tests, the vanes are equipped with heating systems. A safety grid is installed in the test section to protect the fan from probable incoming objects dragged by the wind from the chamber body. The

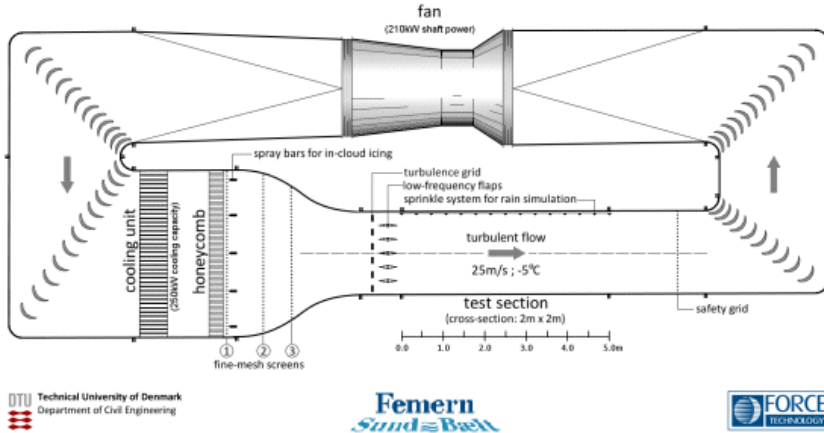


Figure 4.3: DTU/Force Technology Climatic Wind Tunnel.

performance of this grid is improved by adding a heating system to melt the ice that might detach from the cable and flow by the wind inside the testing section during an icing test.

The turbulence level of the empty CWT was evaluated by [Matteoni & Georgakis \(2012\)](#) in the geometrical center of the test chamber with values of $I_u = 0.4; 0.5; 0.6\%$ for $U = 10.33; 20.67; 31 \text{ m/s}$. They also found a uniform level of turbulence across the test section. They identified as $I_u = 0.5\%$ referring to the turbulence intensity measured at two-third of the maximum achievable wind velocity.

In order to investigate the aerodynamic behavior of ice accreted bridge cables, a particular set-up was realized in CWT for reproducing the conditions of in-cloud icing. The set-up consists of a spray bar system and a cable section model (bridge hanger or cable stay section models) placed in the CWT as shown in [Figure 4.4](#). The spray bar system was placed in the settling chamber downstream of the honeycomb grid, and the cable section model was placed in the center of the test section. In [Sections 4.3 and 4.4](#) the spray bar system and the cable section models are described.

4.2.1 Temperature stability

As already mentioned, the quality of the ice accretion is connected to the stability and control of the parameter in the wind tunnel. Temperature is one of the most important parameters because it strongly influences the thermodynamics of the ice accretion process. In order to characterize the temperature stability at different wind speeds, two different tests were performed as shown in [Table 4.1](#).

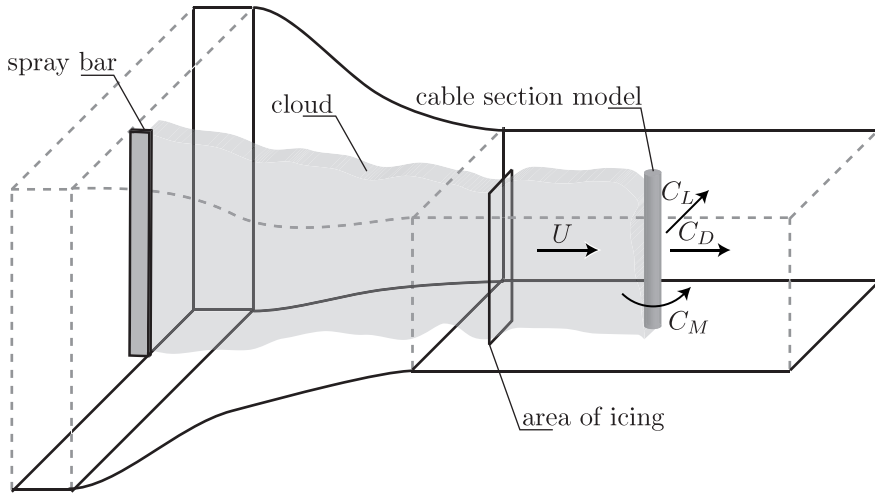


Figure 4.4: Sketch of the experimental setup (bridge hanger simulation) including the spray bar.

Table 4.1: Temperature stability tests.

Test	Wind speed [m/s]	T_{target} [°C]	T_{min} [°C]	T_{max} [°C]	\tilde{T} [°C]
T1	10	-5	-5.98	-4.26	$\approx 0.5^{\circ}C$
T2	24.5	-5	-4.89	-2.57	$\approx 1^{\circ}C$

The tests were performed by setting the temperature in the CWT to $-5^{\circ}C$, which is the target temperature in both tests. The test procedure is:

- The CWT was turned on at the minimum wind speed and the cooling unit is turned on at the target temperature;
- When the target temperature was reached the fan speed is set to the wind speed given in Table 4.1 for each test;
- The data is logged over a period of approximately 1.5 hours for both tests.

The thermometer used to measure the temperature was placed in the ceiling of the wind tunnel approximately in the center of the test section. It can be observed that in the test T1 the average temperature approximately coincides with the target temperature, T_{target} , while in T2 does not. This clearly indicates that the cooling unit is not able to balance the heat generated by the fan and by the external exchange. Moreover, increasing the wind speed the standard

deviation of the temperature increases; this happens because the temperature oscillates around a mean value. These oscillations are caused by the on-off feedback control system of the cooling unit. As a matter of fact, this control system is not able to modulate the heat transfer on the radiator but only to turn on and turn off the system. Globally, the temperature stability reached by the cooling system is not the greatest and is definitely unacceptable at high wind speeds. However, in the wind speed range investigated during the ice accretion phase (see Section 4.5.2) appears to be sufficiently stable to ensure an effective process of ice accretion on bridge cables.

4.3 Spray bar system

In this Section it is described the process of design and construction of the novel spray bar system. As a matter of fact, to obtain a more uniform ice accretion in the CWT it has been necessary to design and to realize this new spray bar system, giving more reliable results on the ice accretion phenomenon on bridge cables. This includes the design of the spray bar itself together with the design of a suspension system making it possible to adjust the spray bar to orientations varying between horizontal and vertical, allowing tests on inclined cables. In addition, a rigorous checking of the condition in the test chamber generated by the spray bar system was carried out.

4.3.1 Preliminary design

A preliminary design phase was carried out before the external stay in Denmark where the spray bar system was realized. A brief summary of those design ideas is reported in this section.

The main objective of icing simulations on bridge cables is to investigate the time-dependent ice accretion process, which occurs when cables are exposed to clouds containing super-cooled water droplets or freezing rain or drizzle. This ice accretion generates a change in geometry of the cable section that can lead to instability phenomena. The problem is complex because the wind direction is variable and the ice accretion can be generated in one direction whilst the instability phenomenon can occur in another direction.

The objective of the tests were established as:

- Understand the variables that govern the ice accretion;
- Measure the aerodynamic coefficients C_D , C_L and C_M for different angles of attack;
- Assess possible conditions of instability.

The most important variables governing the ice accretion process were defined as:

- Thermodynamics and flow regime:
 - Temperature;
 - Wind speed;
 - Turbulence.
- Exposure time:
 - Ice accretion time.
- Clouds characteristics:
 - LWC;
 - Drop size distribution;
- Cylinder direction:
 - Gravity;

All these variables must be checked before start with tests. The spray bar system (Figure 4.5) must comply with the following requirements:

- Allow control of the air and water pressure;
- Allow easy assembling and disassembling;
- Allow easy change in the location and density of nozzles;
- Allow easy rotation of the bar for tests on inclined cylinders;
- Induce lowest possible turbulence (profile must be as close as possible to a streamlined body);
- Contain a heating system to avoid freezing of the water in the pipes during the descent of the temperature to the target point;
- Produce uniform air and water pressure on each nozzle (it can be achieved using the same length for connection pipes in particular for water).

The perfect distance between nozzles, based on existing icing wind tunnels, were set to be about 20 *cm*. The tail pieces, if the distances between the nozzles are known, can be made using a rapid prototyping machine.

The best solution was set to be a system that can rotate for using it for yawed and inclined test. It can be realized using an external rings in which the bar can rotate (Figure 4.6). This solution was not adopted because a more efficient system described in the next section was adopted.

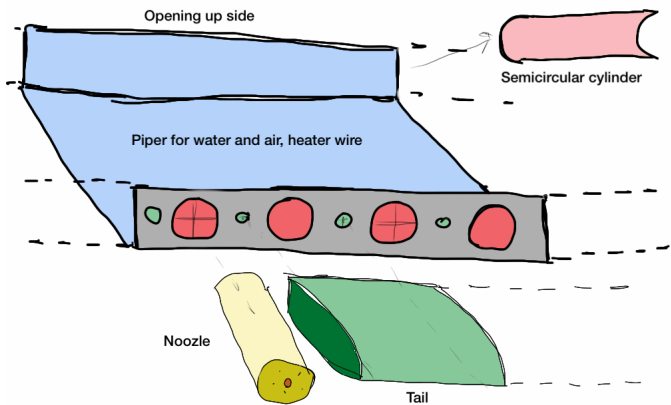


Figure 4.5: Preliminary design sketch of the spray system.

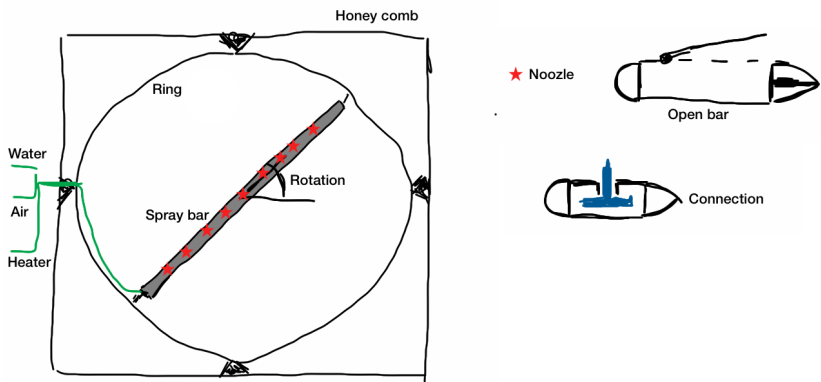


Figure 4.6: Preliminary design sketch of the spray bar support system.

The preliminary measurements that must be performed were:

- Clouds uniformity;
- Turbulence and turbulence uniformity with spray bar;
- Temperature uniformity;
- LWC and drop size distribution.

The LWC and drop size distribution is the critical point of the calibration. The LWC can be estimated using the icing blade method. The drop size distribution can be evaluated using the *phase doppler particle analyzer* (PDPA). Both of these instruments are very expensive. In the lack of the needed instrumentation, the possible solutions are:

- Rent or loan of instruments;
- Using the data of “Spraying Systems Co.” (Manufacturer of the nozzle in the spray bar) for drop size distribution as a function of air pressure and water pressure;
- The LWC can be measured using a cylinder with cotton.

4.3.2 Final design and construction

The innovative part of the experimental setup for simulating low altitude in-cloud icing is the rotatable spray bar (Figure 4.4).

The main components of the spray bar are:

- The spray nozzles;
- The aluminium bar;
- The aerodynamic devices;
- The tubing;
- The heating system;
- The monitoring system;
- The support system;
- The high-pressure air and water suppliers.

In the following each of this part is described.

4.3.2.1 Spray nozzles

To create in-cloud conditions of small super-cooled water droplets suspended in air, a spray system manufactured by “Spraying Systems Co.” was used, consisting of a nozzle body model 1/8J 316 SS, with a fluid cap model PF1050-316SS and a air cap model 67-6-20-70-316 SS. The spray is generated by internal mixing of water and air, and the configuration adopted enabled reproducing a cloud with a Median Volume Diameter (MVD) of the droplets in the range of 10 to $80\ \mu\text{m}$, by changing the water and air pressure (Schick, 2008). Shearing between high velocity gas and low velocity liquid disintegrates the liquid stream into droplets, producing a high velocity spray. This type of nozzle tends to use less atomizing gas than an external mix atomizer and is better suited to higher viscosity streams.

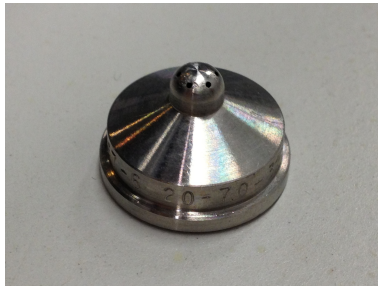
Each nozzle consists of different parts (Figure 4.7):

- Air cap (67-6-20-70-316SS);
- Fluid cap (PF1050-316SS);
- Retainer ring;
- Fluid cap and back seal gaskets;
- Inner and outer and extending tubes and helix;
- Spray nozzle body (1/8J 316SS).

The final assembly of a spray nozzle is seen in Figure 4.8a. The different parts are shown in Figure 4.8b. As declared by the manufacturer, the water pressure and the air pressure provided in the spray nozzle determines the droplet size. Figure 4.9 shows the correlation between the MVD ($=D_{30}$) and the air and liquid pressures.

4.3.2.2 Aluminium bar

The spray bar body is constructed from an aluminium chamber measuring $3.0\text{ m} \times 0.20\text{ m} \times 0.04\text{ m}$ with a thickness of 4 mm . The bar had three openings on one side ($0.798\text{ m} \times 0.148\text{ m}$), covered with removable Plexiglass sheets for visual inspection and maintenance. Hereby an easy accessibility is provided when assembling and mounting the pipes and spray nozzles and furthermore it is easier to see what actually happens in the spray bar during use and hereby correct any problems on the way. In order to keep a certain torsional rigidity of the aluminium chamber a complete opening of the top plate of the chamber was not chosen. All of the openings are covered by Plexiglas sheets with a thickness of 7 mm to minimize the influence on the flow over the spray bar. Each Plexiglas cover is supported by five circular steel blocks which are fixed to the bottom plate of the aluminium chamber with screws. The height of these steel blocks is



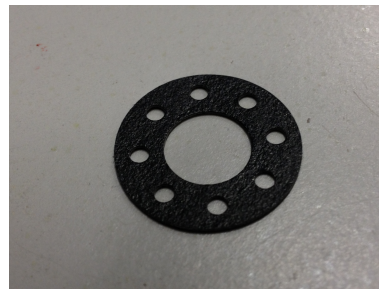
(a) Air cap.



(b) Fluid cap.



(c) Retainer ring.



(d) Gasket.



(e) Inner and outer extending tubes with helix.

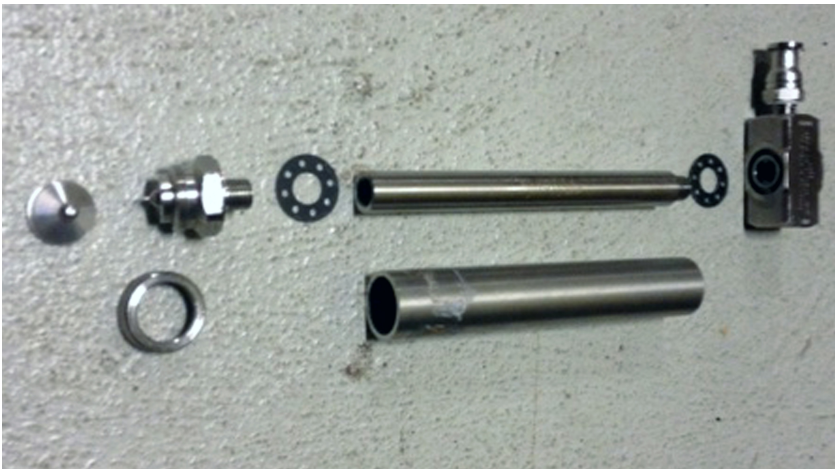


(f) Spray nozzle body.

Figure 4.7: Different parts of spray nozzle.



(a)



(b)

Figure 4.8: Spray system of “Spraying Systems Co.”.

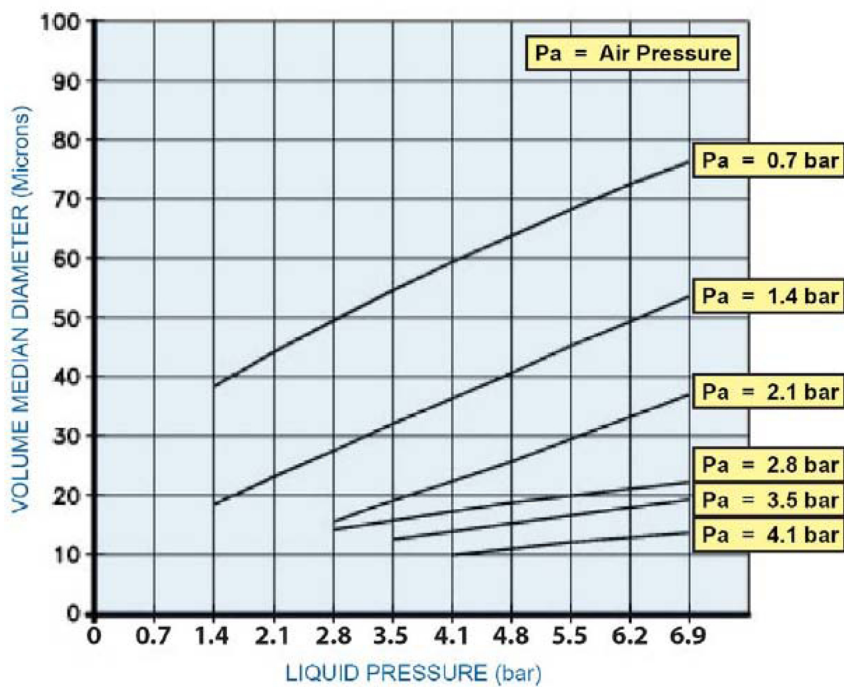


Figure 4.9: D_{50} as function of air pressure and liquid pressure. After technical specifications furnished by “Spraying Systems Co.”.

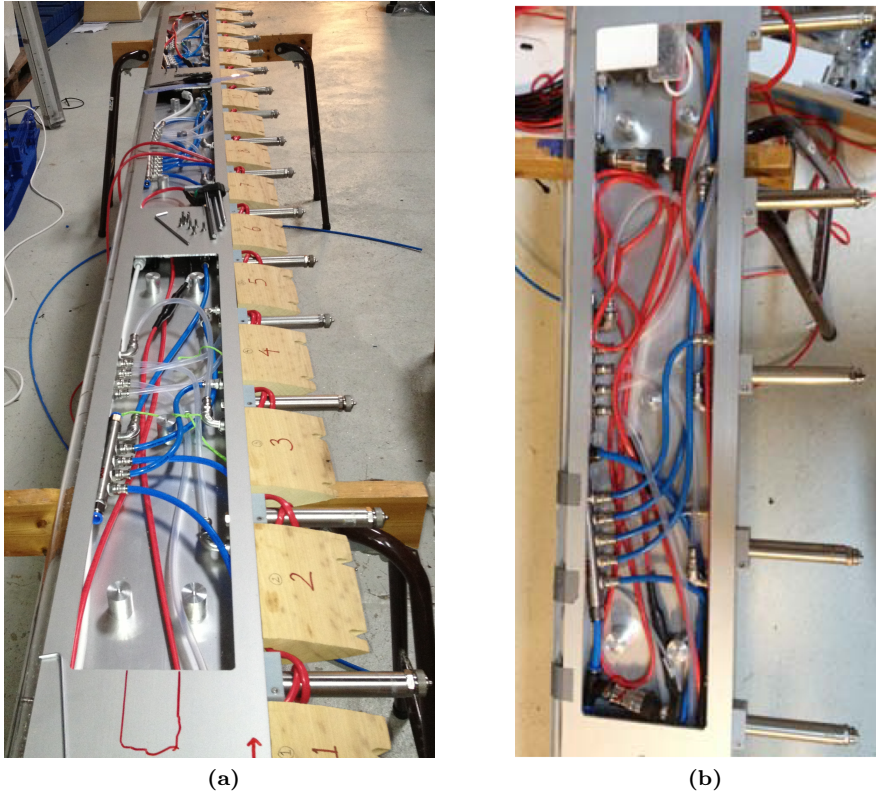


Figure 4.10: Spray bar during the assembly (a) and plexiglass cover installed (b).

chosen such that the top side of the Plexiglas lying on the blocks is in level with the top plate of the aluminium chamber. The Plexiglas covers are fastened with screws to the steel blocks. Figure 4.10a shows the bar during the assembling and Figure 4.10b shows the Plexiglas installed on the steel blocks.

15 holes with a diameter of 25 mm and a distance from center to center of 20 cm have been cut in the front panel of the aluminium chamber to fit the spray nozzles. As a matter of fact, the fifteen spray nozzles were mounted 20 cm apart.

The diameter of these holes in the spray bar body is not coincident with the diameter of the nozzle itself which means that the nozzle has some play. In order to obtain a spray as uniform as possible it is of great importance that

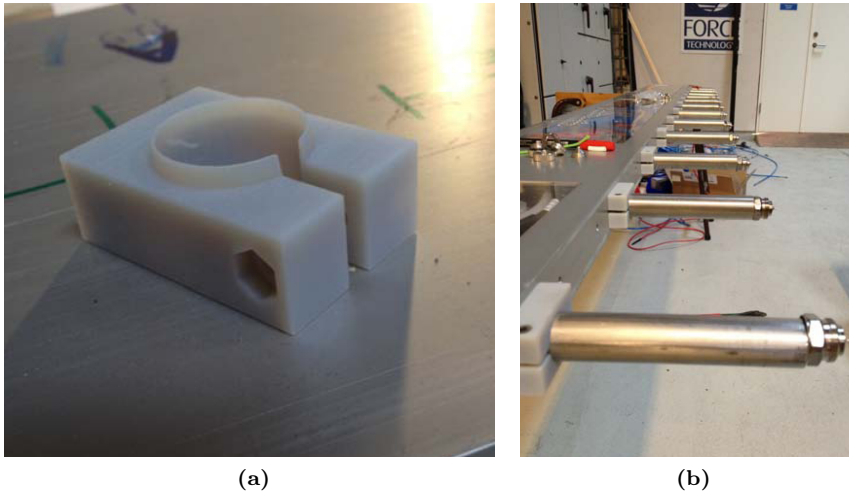


Figure 4.11: Spray nozzle pieces for tight and straight fastening (a) and tight and straight orientation of spray nozzles (b).

the orientation of all nozzles is aligned, hence the nozzles need to be fastened more tightly to the spray bar. Special devices were realized using a rapid 3D prototyping printer (Figure 4.11a). They measure $44\text{ mm} \times 30\text{ mm} \times 15\text{ mm}$ and have a circular part with an inner diameter equal to that of the spray nozzle and an outer diameter fitting exactly the hole in the spray bar. Hence, when mounting and tightening the device with a screw to the nozzle, as shown in Figure 4.11b, and hereafter installing the nozzle in the spray bar, it is prevented from movement in any direction.

4.3.2.3 Aerodynamic devices

In order to streamline the spray bar, and thus reduce turbulence generation, a Plexiglas half-circle nose with a diameter of 4 cm and a wooden tail with a NACA 4-digit series profile were added. Extending tubes were used to place the fluid and the air cap outside of the bar and produce the final spray at a specific distance from the bar. Moreover, aerodynamic covers manufactured on a rapid prototyping printer were installed on the extending tubes to reduce turbulence generation.

The rear end Plexiglas is simply a half circular cylinder with a thickness of 4 mm fastened to the spray bar with seven screws (Figure 4.12a). The front

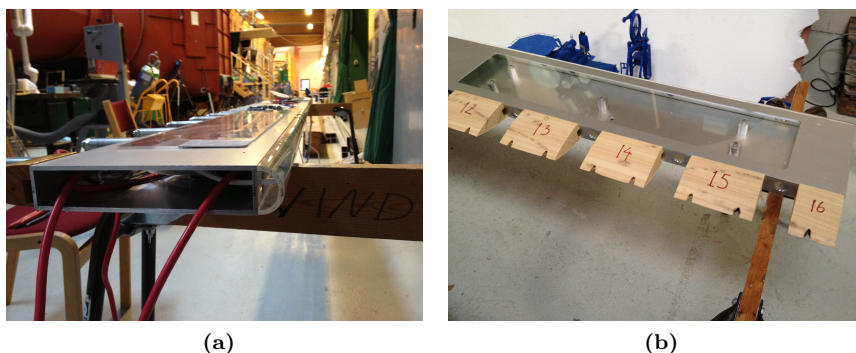


Figure 4.12: Plexiglas half-circle nose(a) and wooden tail with a NACA 4-digit series profile (b).

wood wing tail is a NACA profile with a maximum depth of 100 mm (Figure 4.12b). The wooden wing tail pieces were realized using a CNC controlled milling machine. Along the edge of the wing tail turned towards the spray bar body a groove has been cut where the heating wires fit into. In total 16 wing tail pieces exist (Figure 4.10a); one piece between every two nozzles and two shorter pieces at the ends. The 14 middle pieces are each fastened to the spray bar by two screws whereas the two outer pieces are only fastened by one screw each. A protection cover streamlining the flow over the screw holes has been prepared using a 3D printer. The wood was then finished with sanding by hand using a sanding block, and then the tung oil is applied in order to make wood resistant to water. When the wood tails are mounted a gap with a distance of approximately 75 mm exists between each piece. In each gap a spray nozzle is mounted. To make the flow over the nozzle streamlined as well and to protect the heating wire wind around each nozzle (described in Section 4.3.2.5), a special cover has been prepared using the 3D printer (Figure 4.13). The spray nozzle cover has the same shape as the wood wing tail but with an increased thickness around the spray nozzle itself. This has been necessary in order to fit the heating wire inside the cover.

4.3.2.4 Tubing

Figure 4.15 shows the water and air circuits inside the spray bar. In order to minimize the number of pipes outside the CWT and making the mounting of the spray bar easier it was chosen to have only one external water pipe and one external air pipe. These external pipes have a diameter of 16 mm . Inside the CWT each pipe is divided into two 10 mm pipes. These two pipes form together with three connectors a series connection. Each connector has five exits, giving a total of 15 exits which equals the number of spray nozzles. Hence, from each

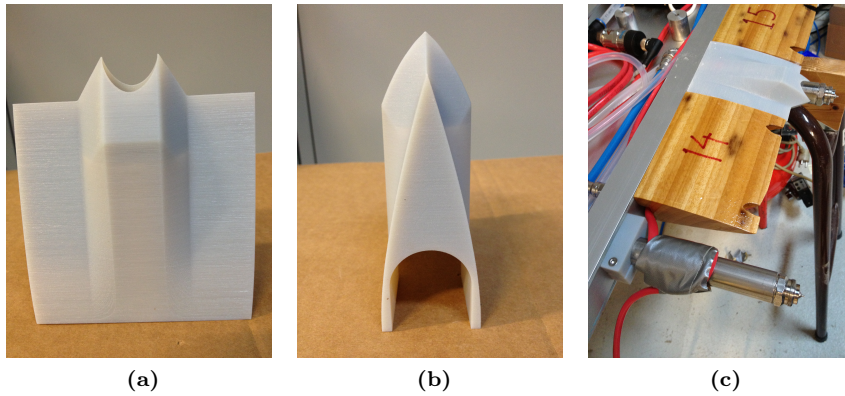


Figure 4.13: Spray nozzle cover: front (a) and lateral (b) view and mounted on the nozzle (c).



Figure 4.14: Spray nozzle cover and protection cover streamlining the flow over the screw holes.

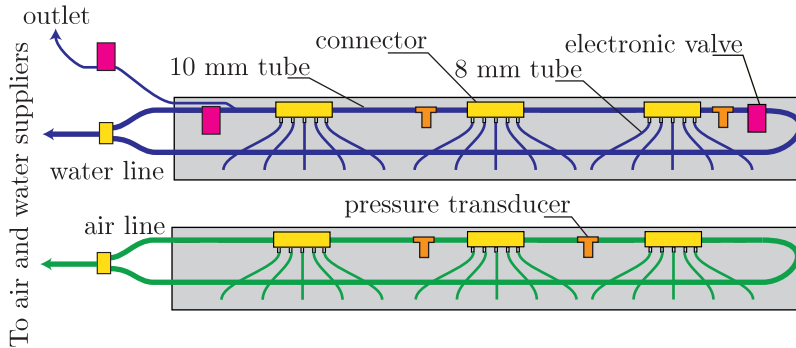


Figure 4.15: Scheme of water and air circuits.

connector exit a 8mm pipe was connected to a spray nozzle. This was done for water as well as for air. Blue pipes were used for air while transparent pipes were used for water (Figure 4.16). The nozzles were connected to the air and water supply using two ring circuits, which guaranteed a uniform pressure among the nozzles. Each nozzle was connected to the air and water circuit by two independent tubes. The air circuit is closed with a valve placed outside of the bar. The water ring circuit tubes were closed using two electrical valves placed in the two branches of the ring circuit, inside the spray bar as close as possible to the nozzles in order to reduce the delay between the actuation of the valves and the arrival of the fluid on the nozzles. In order to fit two electrical valves into the spray bar, it has been necessary to reduce the thick of the plexiglass that over the valves was reduced to approximately 4 mm. Finally a handle is installed at the water pipe and at the air pipe outside the CWT to close the suppliers manually. Moreover, a couple of pressure regulator and membrane-type manometer were placed on each circuit outside of the bar and the wind tunnel to set the pressures.

An adjunctive electrical valve connects the water ring circuit with the outlet for allowing the possibilities of leaving only the air circuit opened and avoids the siphon effect of the water contained in the closed water circuit (Figure 4.15). Using the valve connect to the outlet it is possible to close immediately the spray system to simulate fog patches. However, this operation was not used during the tests presented in this thesis.

4.3.2.5 Heating system

The heating system is made of heating wires. These converts electricity into heat through the process of resistive or Joule heating. Electric current passing through the wires encounters resistance, resulting in heating of the element. They were inserted for preventing the water from freezing when the spray system was inactive and the temperature below zero. Heating wires were placed close

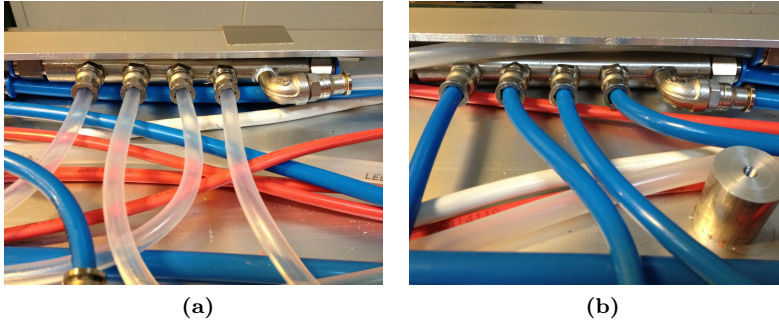


Figure 4.16: Water (a) and air (b) connectors inside spray bar. Red wires are heating wires.

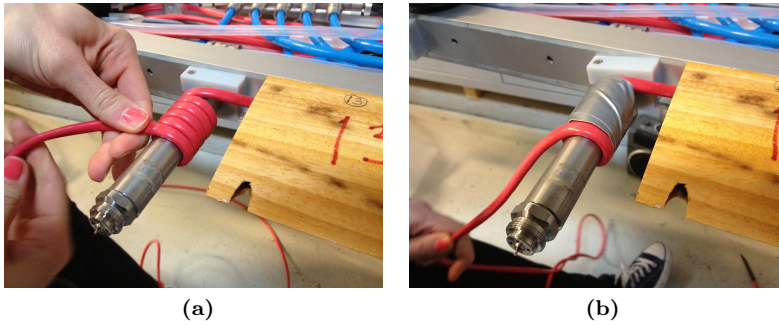


Figure 4.17: Heating wire wind 5 times around the spray nozzle (b) and fastened by tape to keep position (b).

to the water pipes inside the spray bar to prevent them from freezing when the temperature gets below the freezing point. Outside the spray bar but inside the CWT, heating wires were also winds around the water pipes. Moreover, heating wires were wind around the spray nozzles (Figure 4.17). The heating wire were winded around the nozzle as close to the fluid cap as possible to prevent any possible freezing. To keep the position of the heating wire when mounting the spray nozzle covers it has been necessary to fasten the heating wire with tape. The heating wire winded around the nozzle were placed the nozzle aerodynamic cover (Figure 4.13c).



Figure 4.18: Pressure transducer: Festo model SPTW-P10R-G14-VD-M12.

4.3.2.6 Monitoring system

The monitor system of the spray bar allows the control of the water and air pressure, of the heating systems and of the electro-valves. The control of the water and air pressure was achieved by installing pressure transmitters inside the spray bar. Four pressure digital sensors manufactured by Festo model SPTW-P10R-G14-VD-M12 (Figure 4.18) were installed on the water and air tubes for monitoring pressures along the two circuits. The pressure sensors were installed in the positions reported in Figure 4.15. A Virtual Instrument of Labview© control the spray bar and records all the informations.

Moreover a much easier handling of the spray bar supplies has been implemented with the installation of a *spray bar controller* (Figure 4.19). From this controller the water and air supply is immediately opened and closed together with the water outlet. The same is the case with the heating.

4.3.2.7 Support system

The spray bar was placed in the $4\text{ m} \times 4\text{ m}$ settling chamber directly downstream the honeycomb grid. Together with the spray bar a support system was designed to allow rotation of the bar in the range of 0° to 90° for use in horizontal, vertical and inclined tests.

The support was made of two rigid bars and two ropes respectively connected to four travelers which can move on two rails placed at the ceiling and at the floor of the settling chamber. The rails were fastened at the ceiling and the floor of the settling chamber for the all length of the chamber (4 m). The rigid bars were made in aluminum and the cross section was a NACA profile in order to reduce the turbulence generated. The travelers and the rails were of the same type used on sailing boats to secure the mainsail to the mast (Figure 4.20). The two ends of the bar were connected with the two travelers posts in the two rails by the two

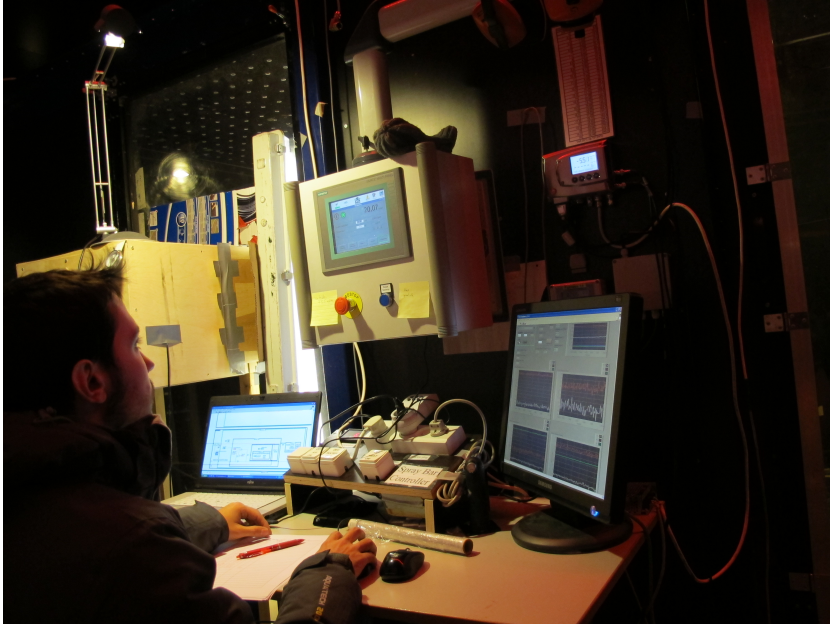
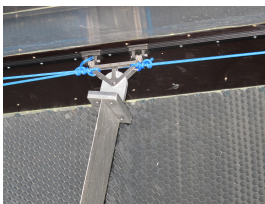


Figure 4.19: Spray bar control system.



(a)



(b)



(c)

Figure 4.20: Details of the suspension system: Traveller in ceiling (a), traveller at floor (b) and type of traveller employed (c).

rigid bars using hinges. Moreover both ends of the bar were connected to other two travelers posts in the two rails by a rope using two carabiners on the bar and two pulleys on the travelers. Each of the four travellers was maneuvered by two ropes, thus allowing changing the inclination of the spray bar (Figure 4.21). The length of all the ropes was changed pulling and fixed using the stoppers. All the supply pipes and the electrical wire were flexible to follow the displacement of the end of the bar. The spray bar suspension system is shown in Figure 4.21.

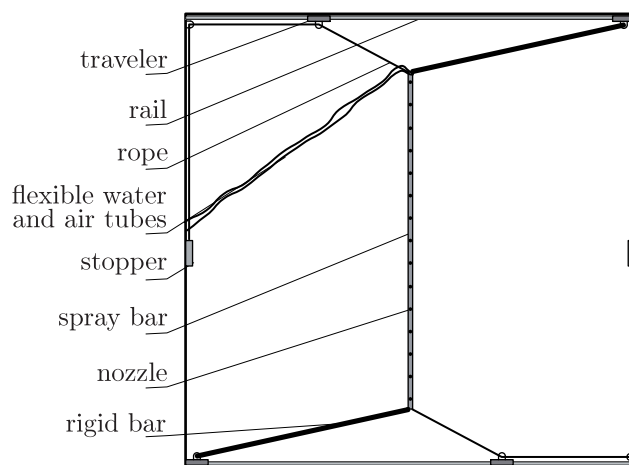
4.3.2.8 Air and water suppliers

Two oil-less air compressors with a total power of 7 kW were installed on the air circuit, with a refrigerant air dryer and an air filter connected to the air supply (Figures 4.22a and 4.22b). The oil-less system has more technical development, but is more expensive, louder and lasts for less time than oil-lubed pumps. The oil-less system delivers air of better quality essential for spray applications. The high pressure water was produced using a 1 kW water pump (Figure 4.22c). The water was desalinated using a reverse osmosis and electro-deionisation. Both water and air were preheated to a temperature of 20°C.

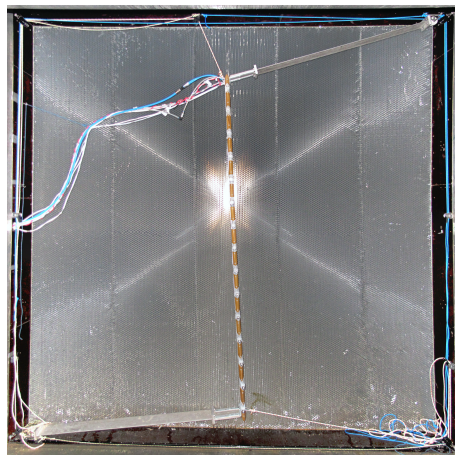
4.3.3 Droplet size control

The characteristics of a cloud are usually described through the Droplet Size Distribution (DSD) and the Liquid Water Content (LWC), and it is important that these be kept uniform across the test chamber. The relevant literature often characterizes the DSD through a single number, the MVD (Déchelette *et al.*, 2011). The problem of the characterization of a spray distribution is well known in agriculture for pesticide application. The distribution of a spray can be measured by collectors (e.g., water-sensitive paper or Kromekote® card) attached to selected target areas or leaves, and inspected after spraying (Figure 4.23a). Imaging or scanning devices are used to measure spots on the collectors and to calculate the size distribution. Zhu *et al.* (2011) develop a small and easy-to-use portable device using a pixel recognition scanning technique to measure spray quality under various working conditions. The technique used followed the same approach. A water-sensitive 7.5 cm × 2.5 cm paper produced by Q.Instruments was used as collector, which was exposed to the cloud for 1 s at a temperature of 20°C. After exposure, the collectors were digitized in images with a resolution of 9600 dpi using a photographic scanner. The images were processed using ImageJ, a public domain Java-based image-processing program, to count the number of spots in the user-defined areas and to measure the areas of the spots. The spot areas were corrected to the actual droplet diameters using the following equation:

$$D = 0.95D_s^{0.91} \quad (4.1)$$



(a)



(b)

Figure 4.21: Spray bar suspension system: sketch (a) and photo (b).

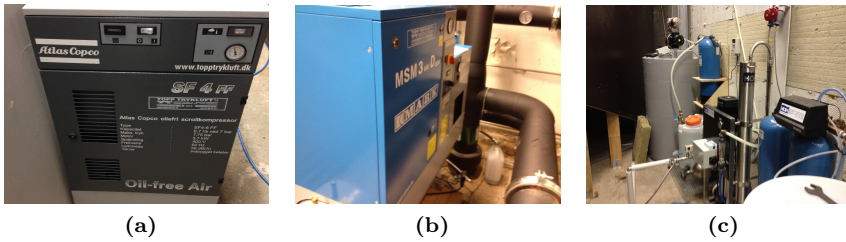


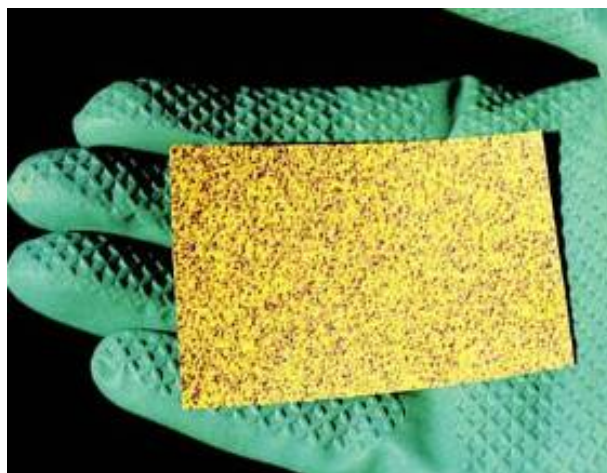
Figure 4.22: Air and water suppliers: first (a) and second (b) air compressor and water pump and electro-deionisation system (c).

where D is the diameter of the droplet and D_s is the diameter of spot on the paper. The test was repeat 3 times setting the water and air pressures to 4.1 bar and 2.5 bar , respectively. The result was an MVD of approximately $30 \mu\text{m}$, in agreement with the manufacturer's specifications. An example of the data obtained is shown in Figure 4.23b.

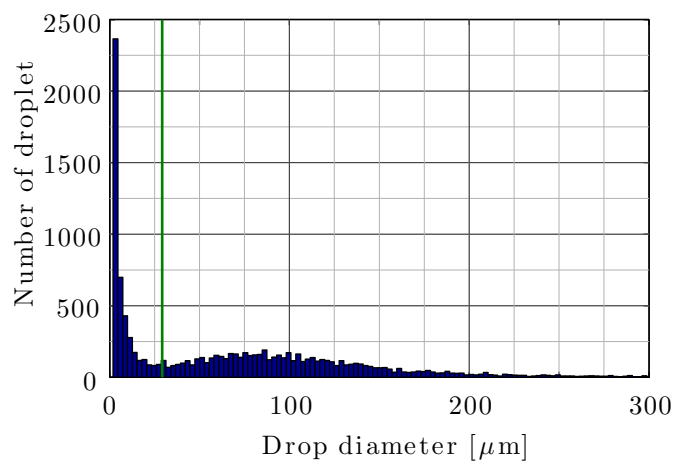
4.3.4 LWC and cloud uniformity control

LWC is defined as the amount of liquid water contained in a unit volume of cloud, usually as grams of water per cubic meter of air (g/m^3). The LWC was roughly estimated equal to $0.13 \text{ g}/\text{m}^3$, $0.24 \text{ g}/\text{m}^3$ and $0.32 \text{ g}/\text{m}^3$ at respectively $5 \text{ m}/\text{s}$, $11 \text{ m}/\text{s}$ and $13 \text{ m}/\text{s}$. The increase of the LCW with wind speed is explained as higher speeds generate a smaller extension of the cloud, with the same amount of water produced by the spray bar. Gates *et al.* (1988) described this phenomenon naming it the *focusing effect*, and described it as the convergence of the trajectories across the flow streamlines. The method used gave only a very rough indication of the LWC, yet the prediction of the trend of the LCW with wind speed was confirmed by the ice accretion tests. The main idea behind the method of measure is to capture droplets from the spray bar cloud in a cylinder filled with cotton. If the air is capable of penetrating through the cylinder only the water droplets are left. These are either absorbed by the cotton or adsorbed on the inside surface of the cylinder. The setup consists of cotton placed inside a cylinder with an inner diameter of 148 mm and a length of approximately 0.5 m . Small holes are drilled along the circumference at midspan of the cylinder and a thin metal wire is pulled through these holes to make a grid ensuring that the cotton cannot move through the cylinder when the CWT is running and the water droplets are collected. Figure 4.24 shows a moment of the measuring phase and cylinder with cotton used as setup. A number of tests were carried out repeating the above procedure to get a good estimate of the LWC. The cotton was exposed for 30 s to the cloud.

A simple test was performed to measure the extension and uniformity of the



(a)



(b)

Figure 4.23: Water-sensitive paper with impinged droplets (dark spots) (a). Example of DSD from the analysis with ImageJ (b); the MVD of $30\ \mu\text{m}$ is shown with a green line.

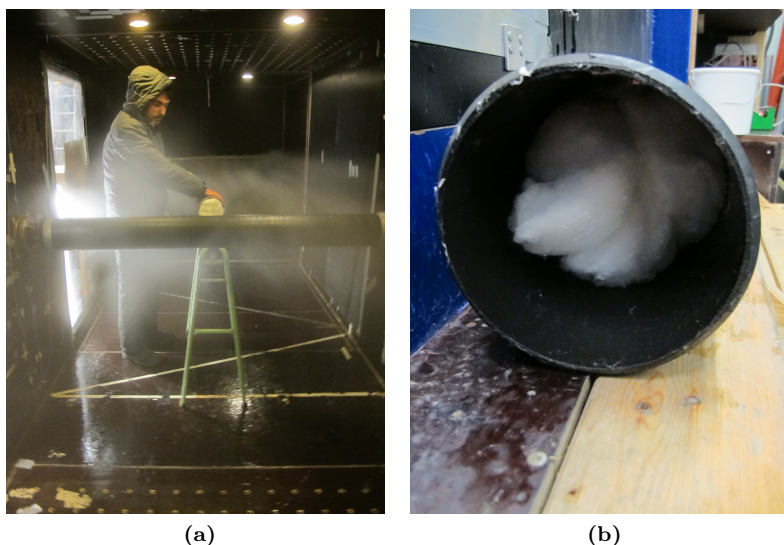


Figure 4.24: Setup for measurement of LWC: measuring phase (a) and cylinder with cotton (b).

cloud produced by the spray bar. A $15\text{ cm} \times 13\text{ cm}$ Plexiglass grid was placed in the test chamber. Sizes of each bar are $6 \times 10\text{ mm}$. The accretion condition was chosen in order to obtain a dry accretion without runback water: exposition time equal to 9 minutes at 11.0 m/s and -6°C (Figure 4.25). The icing grid is the standard calibration system used to measure cloud uniformity and coverage area. Digital calipers were used for fast thickness measurements of the accretion on the grid. The results are given in Figure 4.26, showing some small variations of the accretion in region where the model was to be placed. Tests carried out on the cable model confirmed a good uniformity of the ice accretion in the area where the model is located.

4.3.5 Turbulence

The characterization of the flow in the test chamber for the final spray bar configuration was carried out using a TFI Cobra probe. The spray bar was installed vertically, like in Figure 4.21. Measurements were made on a $50\text{ cm} \times 40\text{ cm}$ (horizontal and vertical distance) grid, at 11.0 m/s for 60 s at sampling frequency of 2048 Hz . The mean wind speed was uniform and showed only a small skew of the flow on one side. The turbulence intensity map is shown in Figure 4.28, indicating rather uniform values of less than 0.8% across the



Figure 4.25: Grid installed in the CWT (a) and ice accrete on the bars of the grid (b).

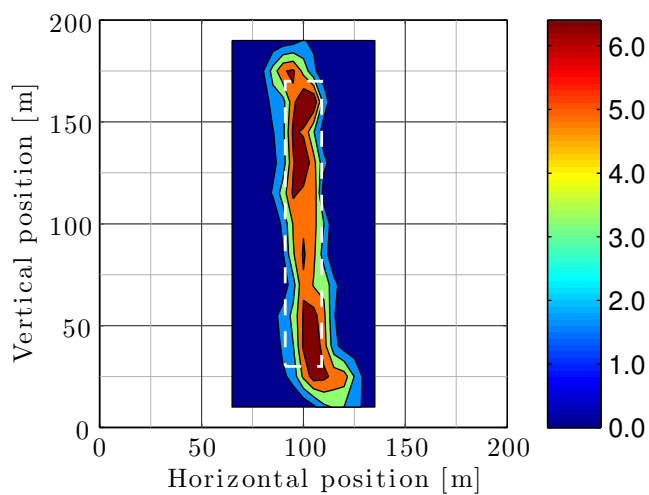


Figure 4.26: Uniformity of spray at 11 m/s . Thickness of ice accretion is in $[mm]$. The white dash-lined rectangle indicates the region where the model would have been installed.

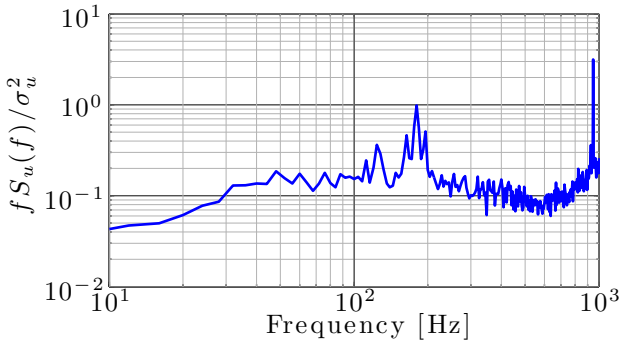


Figure 4.27: Non-dimensional power spectral density at 11 m/s in the center of the test section for the vertical configuration of the spray bar.

test section. An increase of the turbulence intensity was found towards the ceiling and the floor of the tunnel, probably due to the connections between the spray bar and the rigid bars. Notice that the measurements were done with the spray system off, therefore do not account for the modifications brought by the flow ejected from the nozzles. As a matter of fact, the free stream turbulence produced by the tunnel configuration may be enhanced by air jet used for atomizing the water in the nozzles and by the presence of the spray bar (Kollár & Farzaneh, 2009). The non-dimensional power-spectral density of the wind speed at 11 m/s in the center of the test section is shown in Figure 4.27. It was evaluated using a time window of 240 s and the sampling frequency of 2048 Hz.

4.4 Section model, setup and instrumentation

In this Section it is described the process of design and construction of the static section models. Two static section models were realized for this research; the first is a bridge hanger model and the latter is a cable stay model. During the design also the effects of temperature and time on the force transducers were investigated with the purpose to understand the applicability of this sensor for testing the aerodynamic effects of ice accretion on bridge cables.

4.4.1 Preliminary design

A preliminary design phase was carried out before the external stay in Denmark where the static section models were realized. A brief summary of those design ideas is reported in this section.

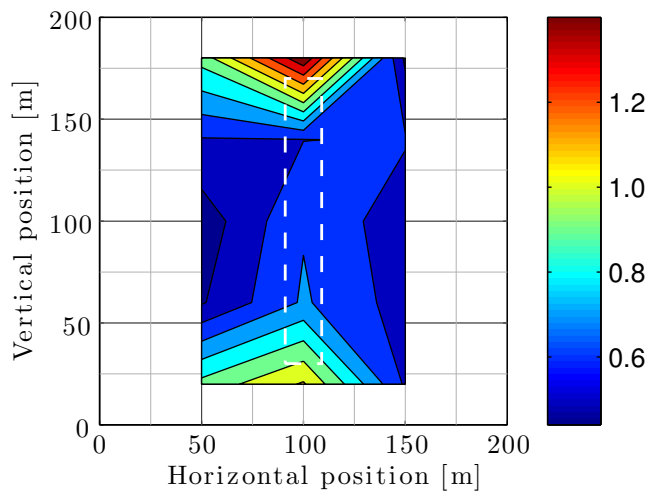


Figure 4.28: Turbulence intensity [%] at 11 m/s with the spray bar in the vertical configuration. The white dash-lined rectangle indicates the region were the model would have been installed.

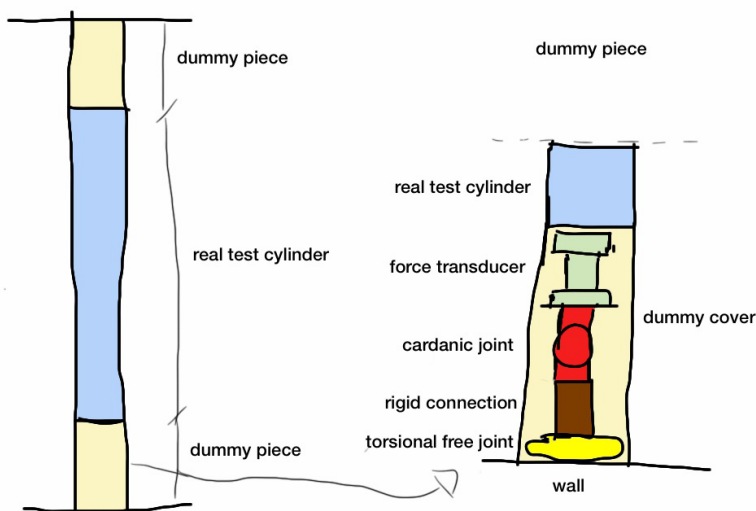


Figure 4.29: Preliminary design sketch of the bridge hanger model.

The cable section model is made of HDPE tube with an outer diameter of 160 mm placed on a inner aluminum tube. The model shall be composed by two parts in spanwise direction (Figure 4.29):

- A real test cylinder;
- Two dummy pieces.

The real test cylinder must be placed in a region within the area of uniform icing. The dummy cylinders are placed outside the real test cylinder for connecting it with the wall of the wind tunnel. The two dummy pieces are perfectly symmetric. Inside the dummy cylinders must be inserted a force transducers, a cardan joint, a torsional bearing and a connector to the wall. The dummy pieces must have same diameter as the real test cylinder. The torsional bearings are necessary to rotate the cylinder during the aerodynamics tests for measuring at different angles of attack. The importance of allowing a rotation of the cylinder without vibration is to avoid breaking of the ice. For inclined test a special support to be connected to the cardan joints is realized.

One main problem can be the rotation of the cylinder during the tests, due to the uncomfortable conditions. One possible solution would be to allow rotation of the cylinder from outside the tunnel. The idea is to make a hole in the tunnel floor and insert a shaft bars passing through the lower ball bearing. The shaft is connected with a steering wheel that allows rotation of the cylinder from outside the tunnel. This solution was not realized.

4.4.2 Temperature and hysteresis effects on force transducers

The effects of temperature and time on the force transducers were investigated with the aim to understand the applicability of this sensor for testing the aerodynamic effects of ice accretion on bridge cables.

The MC3A sensors are one of the smallest of AMTI's family of multi-component force transducers. These precision instruments feature high stiffness, high sensitivity, low crosstalk, excellent repeatability and long-term stability. The sensor is showed in figure 4.30. Force transducers of the type AMTI MC3A-500 are 6 DOFs: 3 translational and 3 rotational, F_x , F_y , F_z and M_x , M_y , M_z respectively. The force transducers employed are specified by their serial numbers: M5278M and M5283M.

The X , Y and Z axis conventions of the force transducers follows the standard right rule. The positive F_z axis always points vertically down in the transducers. The positive Y axis points in the direction of the transducer from the side of the transducer with the electrical connector. The X axis is rotated of 90° anti clockwise respect to Y . The location of the true X and Y plane is approximately the midpoint of the transducer, along the Z axis. The capacity



Figure 4.30: Force transducer: AMTI model MC3A-500.

Table 4.2: Capacity of force transducers.

Channel	F_x	F_y	F_z	M_x	M_y	M_z
Capacity	1112 N	1112 N	2224 N	56 Nm	56 N	28 N

of the force transducer is shown in Table 4.2. More technical specifications of the force transducers are shown in Table 4.3.

The temperature range of the force transducers covers -17.78°C to $+51.67^{\circ}\text{C}$ according to the manufacturer's specifications. However, previous tests have indicated that the expected temperature independency of the force transducers in this range might not be as prescribed. In the planned wind tunnel tests, it is important that the results of the force transducers are reliable at temperatures down to -10°C and that no hysteresis of the response occurs.

Tests were performed in a Vötsch cooling chamber (model VCV 7120-5) at DTU, Lyngby, Denmark. The series VCV of Vötsch testing systems is designed to simulate dynamic processes, i.e. mechanical as well as thermal loads, affecting components and equipment. The test chamber has a volume of 1150 l, temperature ranges from -70 to $+180^{\circ}\text{C}$ and temperature conditioning performances of 5 K/min .

The CWT provides a minimum temperature of approximately -10°C , at the

Table 4.3: Technical specifications of AMTI MC3A force transducers.

Dimensions	Weight	Excitation	Cross talk
$76 \times 76 \times 76\text{ mm}$	0.909 kg	$\leq 10\text{ V}$	$\leq 2\%$

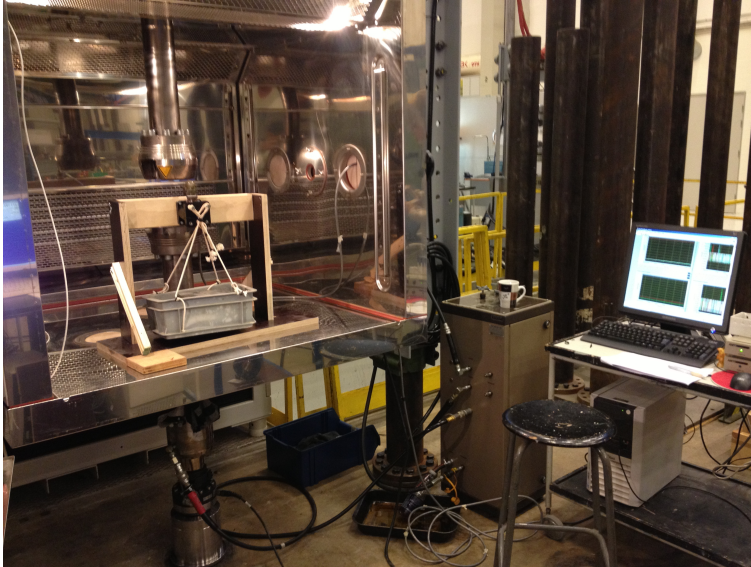


Figure 4.31: Experimental setup: Vötsch cooling chamber and control system.

lower wind speeds. The tests Vötsch cooling chamber were made principally in the range -10°C to $+20^{\circ}\text{C}$. Figure 4.31 shows the cooling chamber and the control system and Figures 4.32 shows the setup inside the cooling chamber. The force transducer was mounted on a wood arrangement with one of its principal axes aligned with the load direction. The load was applied by hanging a plastic box from two screws fastened to the top of the force transducer, attaching the wanted load to this box. The force transducer was connected to LabView© data acquisition system and the forces and moments at different temperatures were logged over a period of 20 s. The mean values at each temperature were determined.

4.4.2.1 Hysteresis tests

This test was performed with the aim of examining the hysteresis influence on the response of the force transducers. This was done by measuring the forces over a period of 75 minutes at 20°C keeping the weight constant. A load of 5.38 kg in Y direction was applied. A log of the data every 5 minutes was performed. The results are shown in Figures 4.33 and 4.34. From this test, the hysteresis is present only in the F_y and F_z components. In the F_y component, the curve seems to tend to a limit value at infinitive time. The hysteresis of the responses seems to be limited and compatible with the experimental tolerances. The maximum error in 75 minutes in the F_y component was:

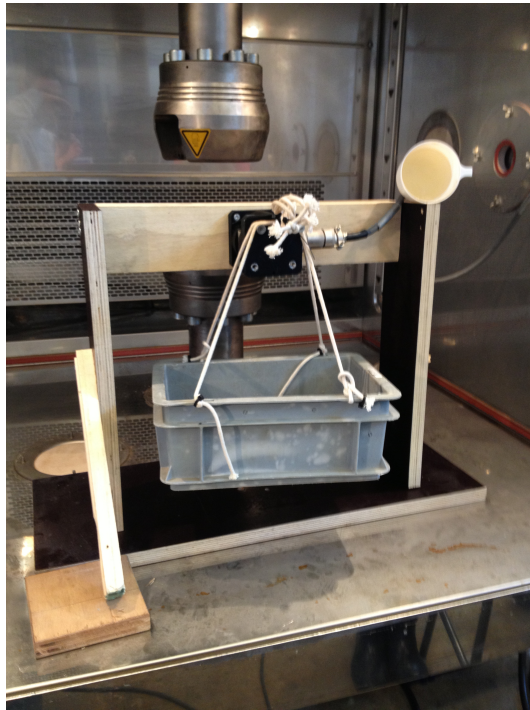


Figure 4.32: Detail of the load system loaded in X direction and detail of the iced water in the cup inside the cooling chamber.

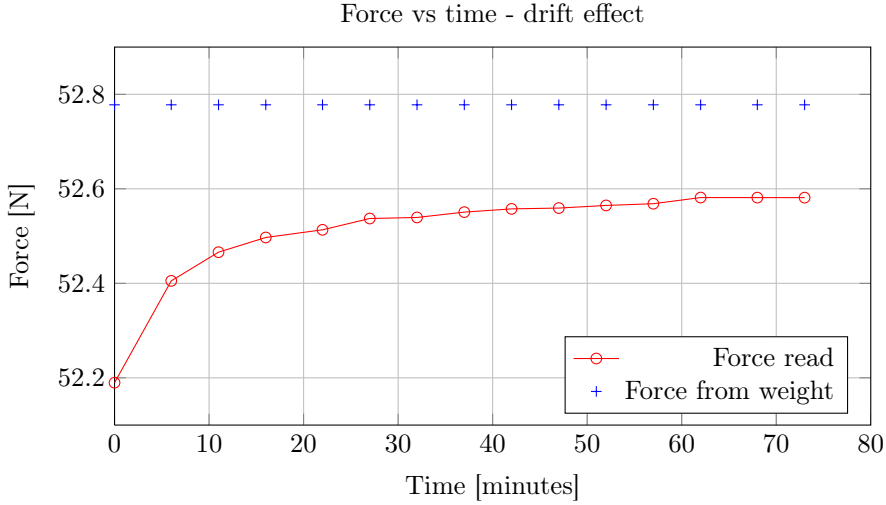


Figure 4.33: Time dependency of F_y with a load of 5.38 kg in Y direction at a temperature of 20°C .

$$err = \frac{52.6\text{ N} - 52.2\text{ N}}{52.2\text{ N}} = 0.007 \quad (4.2)$$

4.4.2.2 Temperature dependency test

These tests were performed with the aim of examining the temperature influence in the X , Y and Z directions. The following tests were performed:

- Load of 5.38 kg in X direction;
- Load of 5.38 kg in Y direction;
- Load of 15.5 kg in Y direction;
- Load of 1.7 kg in Z direction.

In the first test a load of 5.38 kg in X direction was applied to the force transducer and the forces were measured changing the temperature from 20°C to -10°C . Results are shown in Figures 4.35 and 4.36. From this test, the influence is evident only in the F_x and F_z components. F_x looks to decrease decreasing the temperature. Instead, F_z looks to increase decreasing the temperature. The temperature influence on F_x and F_y seems to be compatible with the experimental tolerances. The maximum error in 30°C of variation of the temperature in the F_x component was:

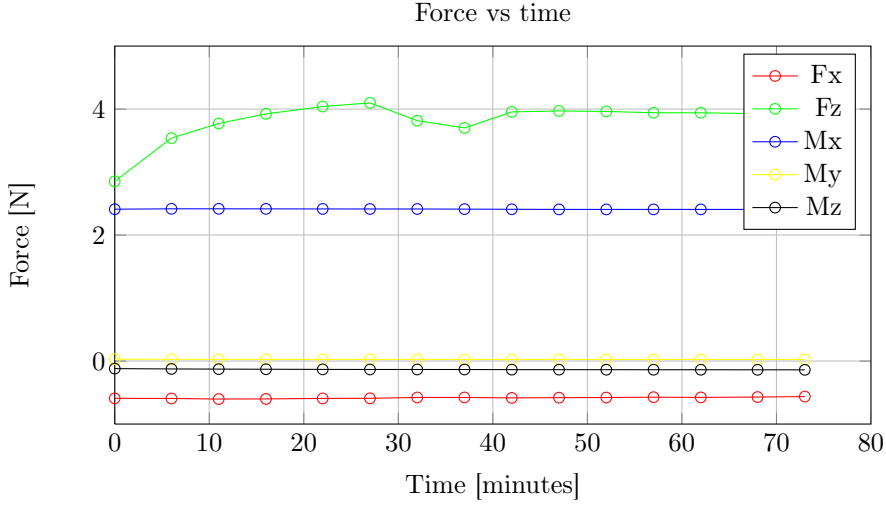


Figure 4.34: Time dependency of F_x , F_z , M_x , M_y , M_z with a load of 5.38 kg in Y direction at a temperature of 20°C .

$$err = \frac{52.25 \text{ N} - 50.6 \text{ N}}{52.25 \text{ N}} = 0.03 \quad (4.3)$$

Differently, the temperature influence seems to be a problem in the F_z component. The maximum error in 30°C of variation of the temperature in the F_z component was:

$$err = \frac{60 \text{ N} - 2 \text{ N}}{2 \text{ N}} = 29 \quad (4.4)$$

In the second test a load of 5.38 kg in Y direction was applied to the force transducer and the forces were measured changing the temperature from 25°C to -15°C . A log of the data every 1°C was performed when the temperature was decreased and with different steps when the temperature was increased. Results are shown in Figures 4.37 and 4.38. From this test, the influence of temperature on the response is evident only in the F_y and F_z components. F_y looks to increase decreasing the temperature. In the same manner, F_z looks to increase decreasing the temperature. The maximum error in 30°C of variation of the temperature in the F_y component was:

$$err = \frac{52.8 \text{ N} - 54.2 \text{ N}}{52.8 \text{ N}} = 0.02 \quad (4.5)$$

Differently, the maximum error in 30°C of variation of the temperature in the F_z component was:

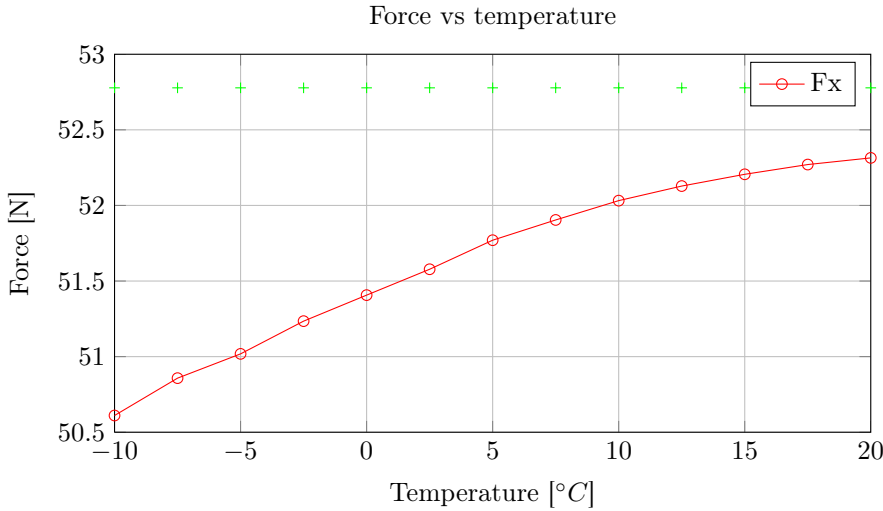


Figure 4.35: Temperature dependency of F_x with a load of 5.38 kg in X direction.

$$err = \frac{64\text{ N} - 1\text{ N}}{1\text{ N}} = 64 \quad (4.6)$$

This test, performed decreasing and increasing the temperature, guarantees that the variable influencing the response of the force transducer is the temperature and not only the time.

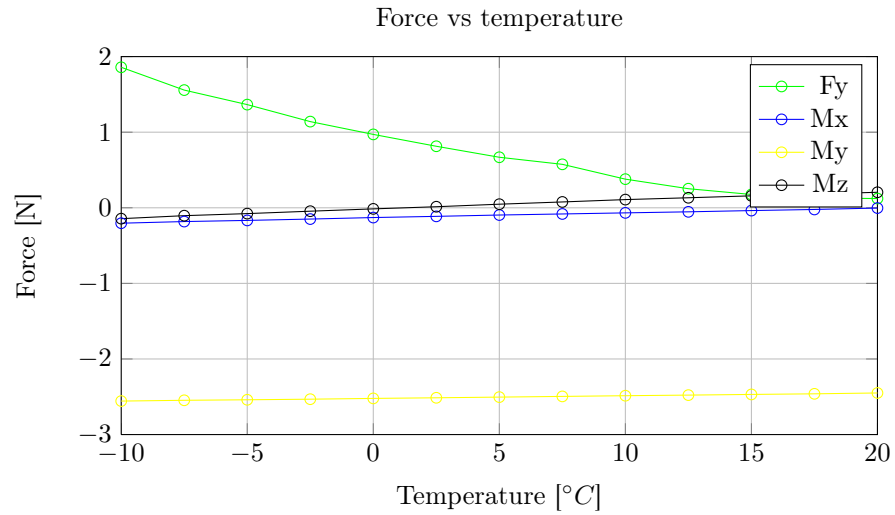
In the third test a load of 15.37 kg in Y direction was applied to the force transducer and the forces were measured changing the temperature from 20°C to -10°C . A log of the data with variable step was performed when the temperature was decreased and when was increased. Results are shown in Figures 4.39 and 4.40. From this test, the influence of temperature is evident only in the F_y and F_z components. F_y poorly increases decreasing the temperature. F_z looks to markedly increase decreasing the temperature.

The maximum error in 30°C of variation of the temperature in the F_y component was:

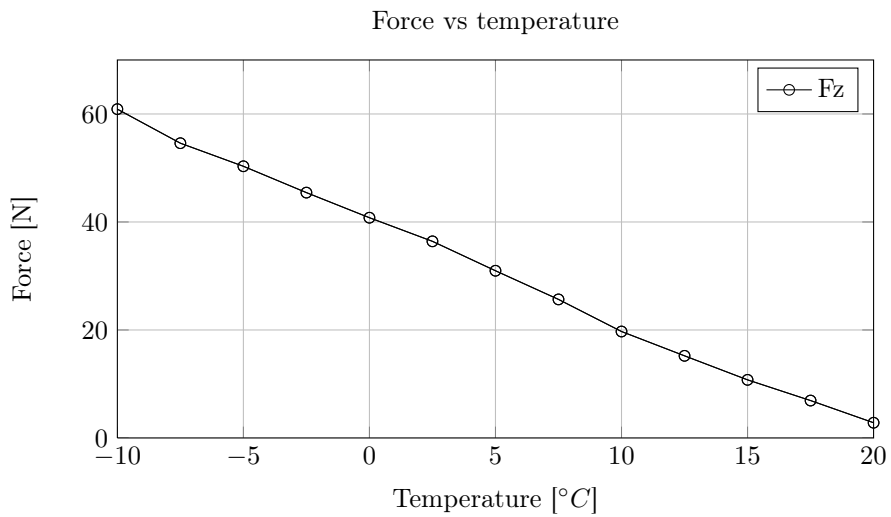
$$err = \frac{149.2\text{ N} - 149.7\text{ N}}{149.2\text{ N}} = 0.003 \quad (4.7)$$

The maximum error in 30°C of variation of the temperature in the F_z component was:

$$err = \frac{0.2\text{ N} - 1.5\text{ N}}{0.2\text{ N}} = 6.5 \quad (4.8)$$



(a)



(b)

Figure 4.36: Temperature dependency of F_y , M_x , M_y and M_z (a) and of F_z (b) with a load of 5.38 kg in X direction.

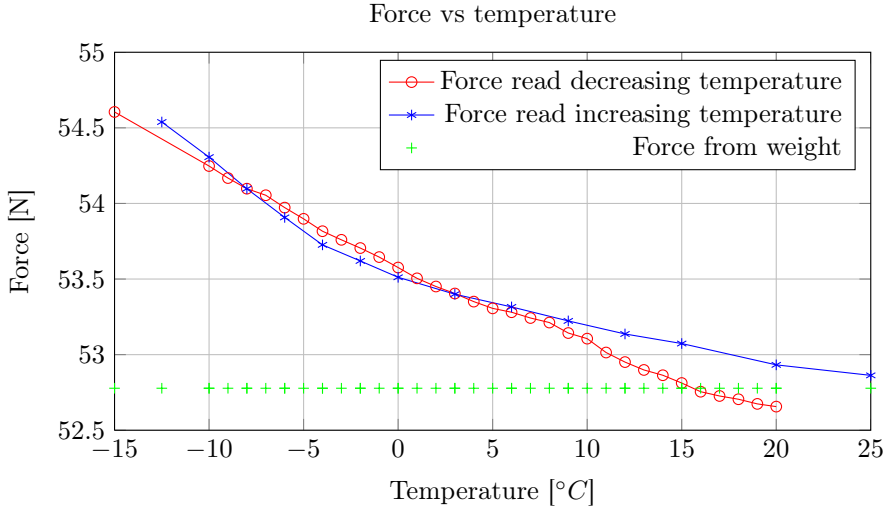


Figure 4.37: Temperature dependency of F_y with a load of 5.38 kg in Y direction.

This test, performed increasing the load, evidence that the error generated by the temperature decreases increasing of the load.

In the fourth test a load of 1.73 kg in Z direction was applied to the force transducer and the forces were measured changing the temperature from 14°C to -6°C . A log of the data with variable step was performed when the temperature was decreased. Results are shown in Figures 4.41 and 4.42. From this test, the influence of temperature is evident in all the components. F_z looks to increase with the decreasing of the temperature. In the same manner, F_y looks to increase decreasing the temperature. Instead, F_x looks to increase decreasing the temperature. The maximum error in 30°C of variation of the temperature in the F_z component was:

$$err = \frac{17\text{ N} - 43\text{ N}}{17\text{ N}} = 1.5 \quad (4.9)$$

The temperature influence in this condition seems to be a problem in the F_z component. This test, performed increasing the load, show that the error in all directions generated by the temperature decrease increasing of the load in the direction investigated and *vice versa*. Moreover, a suddenly variation of the response of the force transducer was found at 7°C ; no explanations were found.

Concluding, the maximum error found was small with the exception of the F_z component in which a significant error was found. This result is considered satisfactory, as the wind tunnel tests are carried out with a temperature fluctuation never exceeding 3°C and the loads on the transducers are larger with

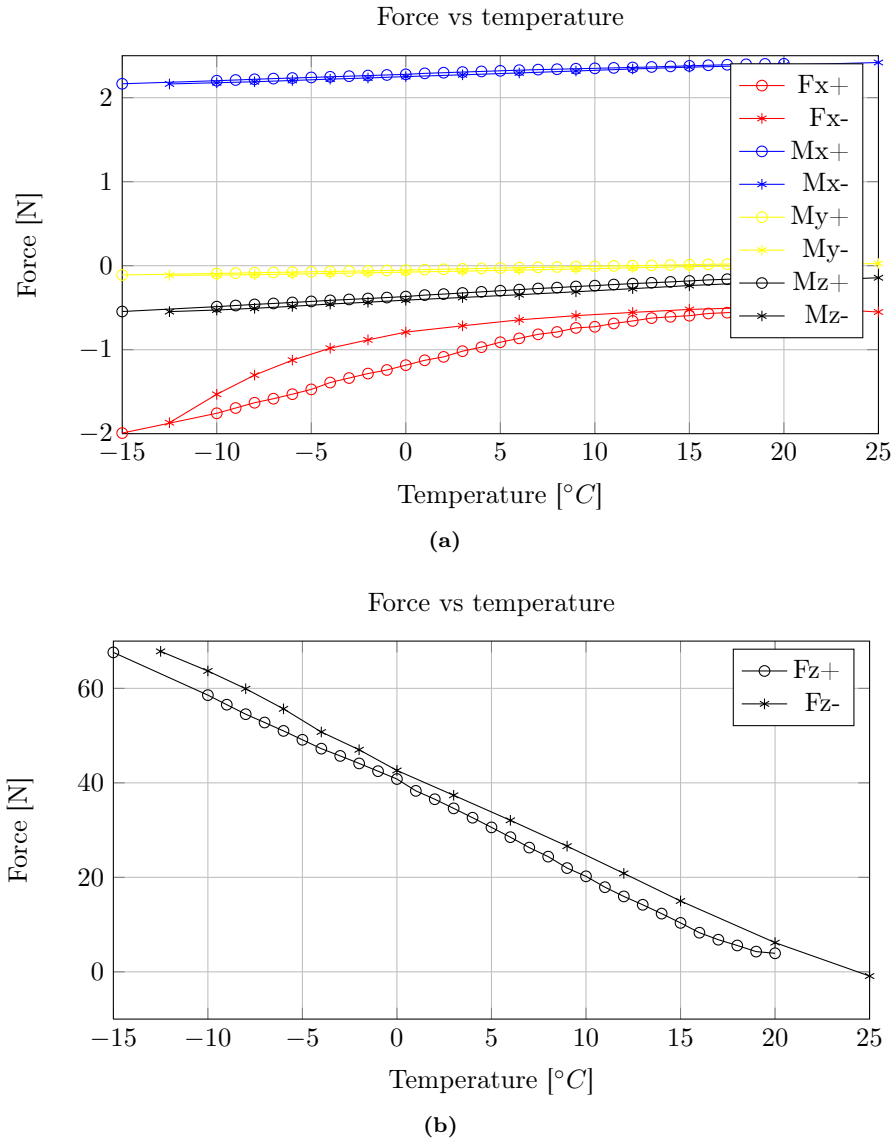


Figure 4.38: Temperature dependency of F_y , M_x , M_y and M_z (a) and of F_z (b) with a load of 5.38 kg in Y direction. + indicates a the test performed decreasing the temperature and - indicates a the test made increasing the temperature.

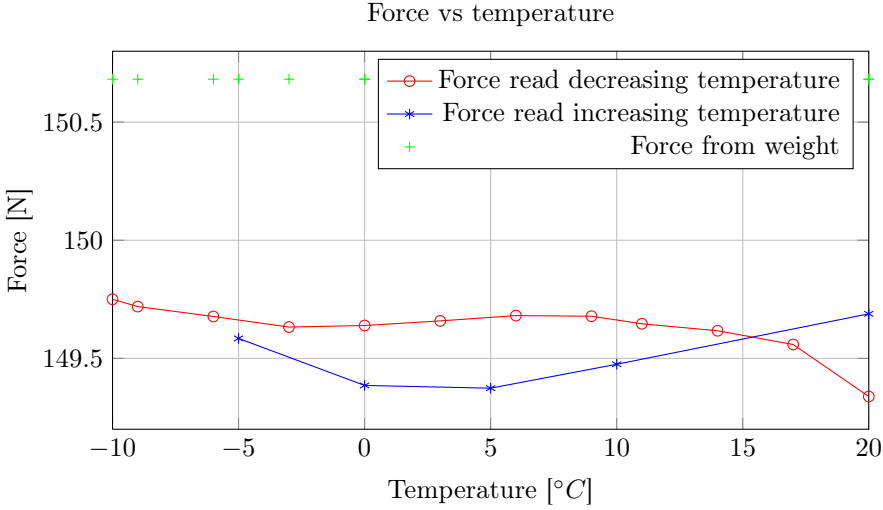


Figure 4.39: Temperature dependency of F_y with a load of 15.37 kg in Y direction.

respect to the tested loads. The great error found in F_z is not a problem for the measuring of the aerodynamic coefficients but for the evaluation of the ice accreted mass. This latter value is, therefore, given with high level of uncertainty. Therefore, it is concluded that the temperature and hysteresis dependence of the force transducers is so small that it can be neglected within the temperature and temporal range considered in the ice accretion tests.

4.4.3 Bridge hanger model

The bridge hanger model was made of a plain black HDPE tube, provided by bridge cable suppliers, with a nominal diameter of 160 mm , stiffened with a spacer-separated inner aluminum tube. The bridge hanger model setup is shown in Figure 4.43. The length of the model was 1.42 m . The blockage ratio was 8%. No end-plates were used. Aerodynamic forces were measured at both ends of the cable using two force transducers installed between the cable model and the supporting cardan joints. Two six DOF force transducers (AMTI MC3A-500) were employed for the measurements. F_x and F_y were associated with the drag and lift component, F_z was associated with the cable axis direction measuring the mass accretion and M_z with the torque component. M_x and M_y were associated to the bending moments and were not used in this work. The cardan joints were installed to reduce the bending moments on the transducers and to align the cable to the floor and to the ceiling (Figure 4.44). The force transducers and the cardan joints were covered by HDPE dummy pieces with

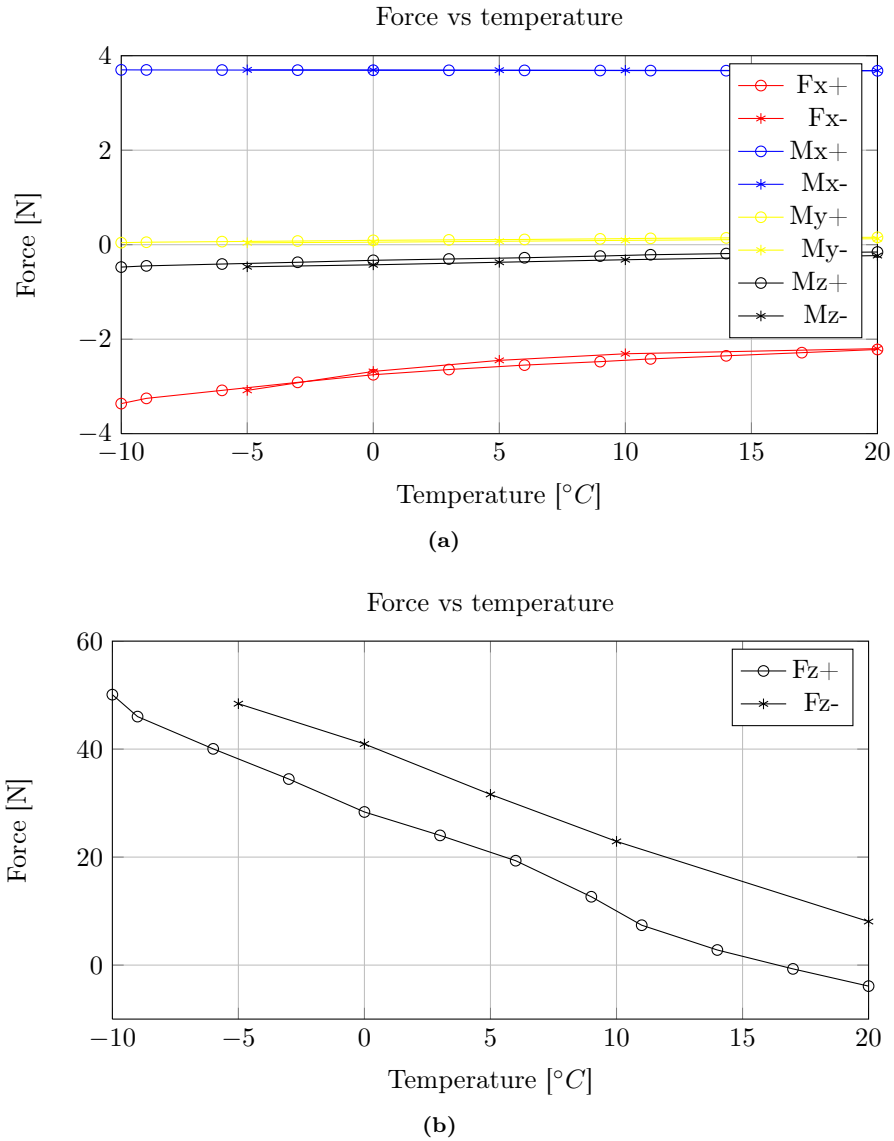


Figure 4.40: Temperature dependency of F_y , M_x , M_y , and M_z (a) and of F_z (b) with a load of 15.37 kg in Y direction. + indicates a the test performed decreasing the temperature and - indicates a the test made increasing the temperature.

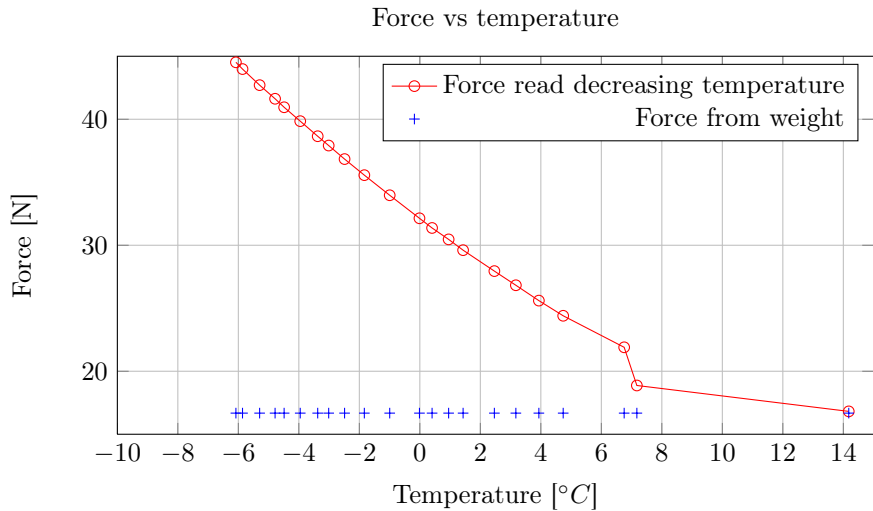


Figure 4.41: Temperature dependency of F_z with a load of 1.73 kg in Z direction.

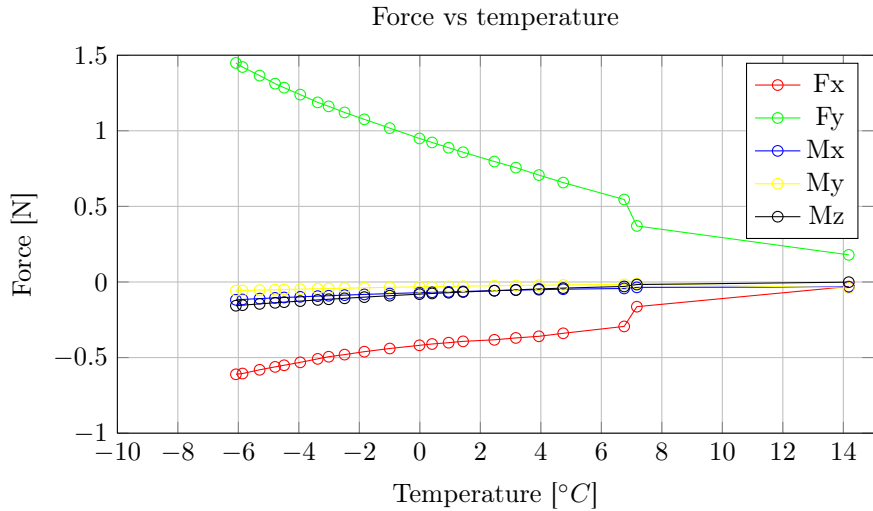


Figure 4.42: Temperature dependency of F_x , F_y , M_x , M_y , M_z with a load of 1.73 kg in Z direction.

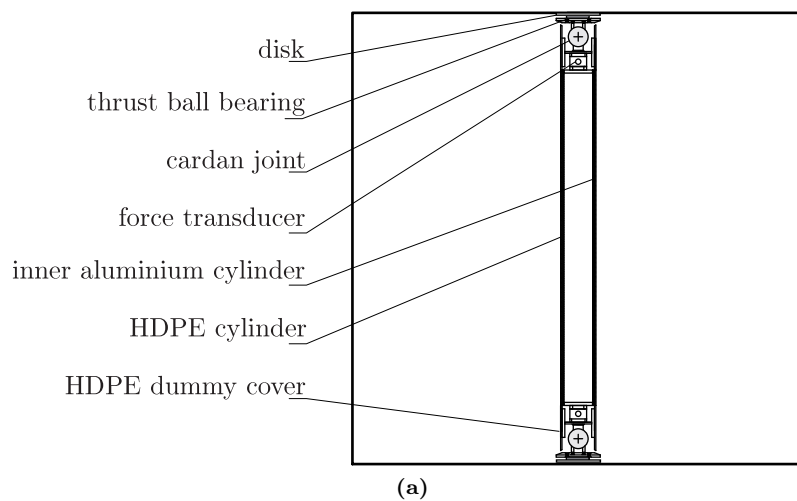


Figure 4.43: Bridge hanger model setup: sketch (a) and photo (b).

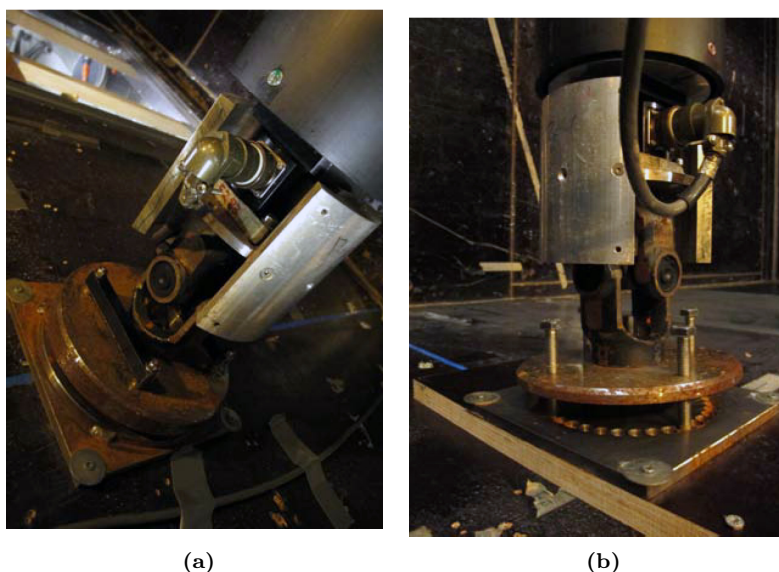


Figure 4.44: Detail of the bottom (a) and top (b) cable connection without dummy pieces: plates, thrust ball bearings, cardan joints and force transducers.

the same diameter as the cable. Two thrust ball bearings were installed at both ends to allow rotation of the cable around its axis. The bearings were installed between pairs of steel disks, one connected to the cardan joint and the other to the floor and the ceiling, respectively. The disks installed at the floor and at the ceiling had 36 threaded holes placed on a circumference, at 10° spacing. The disks installed on the cardan joints were provided with four screws which could fit in the holes to secure the model. This solution ensured a smooth rotation of the cable around its axis, such to prevent the accreted ice from being damaged.

4.4.4 Stay cable model

The tested cable section model was the same used for the bridge hanger model described in Section 4.4.3. To obtain the desired orientation in the space, the cardan joints connected to the model were mounted on two rigid links attached to two rotatable arms, each supported by a roller and a hinge (Figure 4.45). The definition of the angles of rotation of the cable is shown in Figure 4.46, where Θ is the inclination and β is the yaw. The inclination is the angle between the cable axis and the horizontal plane. In the wind tunnel tests the assumption was made that mean wind velocity U is horizontal; corrections would be needed to account for an inclined mean wind velocity, as it can occur for bridges located in

canyons. The inclination of the cable section model was modified by changing the length of the rigid links. The yaw angle is the angle between U and the projection of the cable axis on the horizontal plane. When the stays are in vertical planes parallel to the deck, β is also the angle between U and the bridge deck axis, otherwise β must be corrected. The yaw angle of the cable section model was modified by turning the arms, that were then secured in position using the base plate and the semi-circular arch on the ceiling. A series of holes on the plate and on the arch allowed variation of β in the range of 0° to 180° at intervals of 10° .

The aerodynamics of a perfect circular cylinder is usually described as a function of the cable-wind angle and of the yaw angle:

$$\Phi = \arccos(\cos \Theta \cos \beta) \quad (4.10)$$

In the case of ice accreted cables due to the non-symmetric cross section, the wind angle-of-attack must also be considered:

$$\alpha = \alpha_\beta + \alpha_r = \arctan\left(\frac{\tan \beta}{\sin \Theta}\right) + \alpha_r \quad (4.11)$$

The wind angle-of-attack represents the rotation of the cable section model about its axis, and is the sum of two contributions: the first, α_β , is the effect of the rotation around the section of the component U_N of U perpendicular to the cable axis associated with a variation of β ; the second is generated by the cable motion producing a relative wind angle-of-attack, α_r (Figure 4.46).

To account for α_r , the cable section model was designed such to allow axial rotation of the HDPE cable leaving the remaining components, force transducers included, in their original position. To this purpose, the HDPE cable was provided with a set of 3 holes at each end, whose centers were placed at an angular distance of 10° . The inner aluminium cylinder was provided with only one hole at each end. After releasing the bottom and top screws, the HDPE cable could be rotated and secured in a new position at -10° , 0° and $+10^\circ$ from the original, thus leading a change in the wind angle-of-attack. Larger variations of this angle were not considered, as for the application of linear stability criteria only small values of α are needed.

4.5 Test procedure and measurements

The tests consisted of four phases:

- Preliminary checks;
- Ice accretion;
- Aerodynamic force measurement;

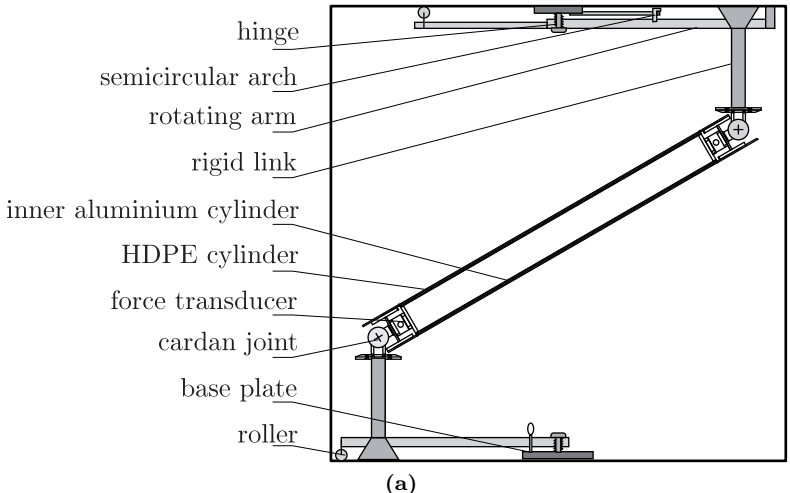


Figure 4.45: Cable section model setup ($\beta = 90^\circ$): sketch (a) and photo (b).

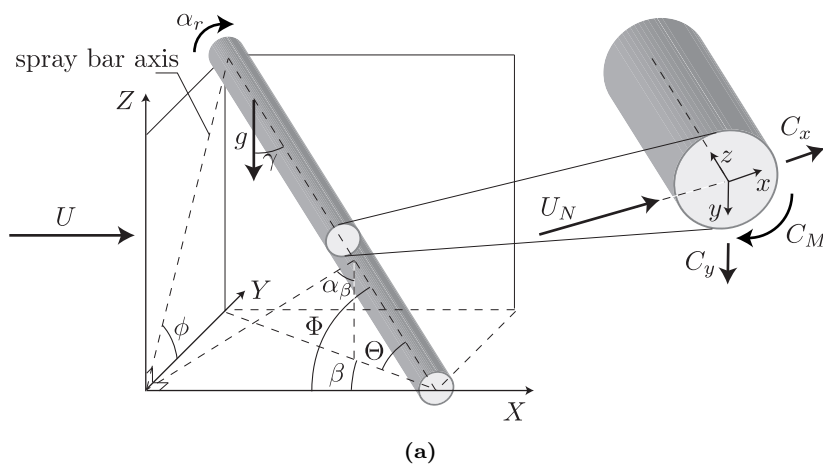


Figure 4.46: Cable geometry and force signs in the wind tunnel (a) and example of orientation of the spray bar and of the cable during the accretion phase (b).

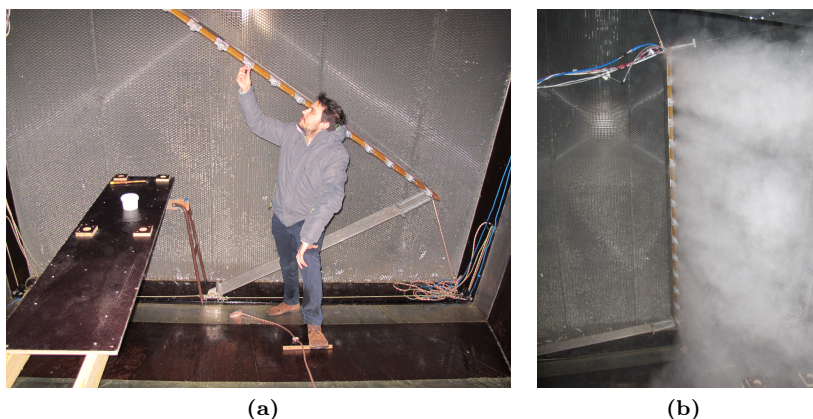


Figure 4.47: Cleaning of the spray bar system (a) and spray bar system correctly working (b).

- Cut of ice shape.

In the following, each phase of the test is described. In section 4.5.5 is reported the adopted protocol of the tests. On average, performing one complete test requires from 12 to 16 hours.

4.5.1 Preliminary checks

The performance of the spray bar is crucial for the result of the ice accretion. Therefore it was checked carefully that the spray bar was working optimal before each test. This included cleaning of all air caps with compressed air to ensure that they were not clogged up with dirt (Figure 4.47a). In some cases it was necessary to clean some of the fluid caps too. This was assessed after removing all air caps and turning on the water supply. The water jet from all nozzles should look identical. If not, the fluid cap concerned was removed and cleaned with compressed air. After reinstallation of all caps the water and air supply was turned on and the CWT started at a low wind speed to visually assess the appearance of the cloud proceeded (Figure 4.47b). If the results were satisfactory the water and air supplies and the CWT were turned on and the cable section dried with paper to guarantee that the surface was dry before the arrive of the cloud. Otherwise the air and fluid caps were cleaned again. Cellophane film was wrapped around the dummy pieces at each end of the cable and fastened with tape, so to protect the force transducers from icing.

Furthermore, the spray bar must be oriented in line with the position of the cable in the test chamber. In the bridge hangers tests, the spray bar was placed vertically. In the cable stays tests, the spray bar was placed with an inclination

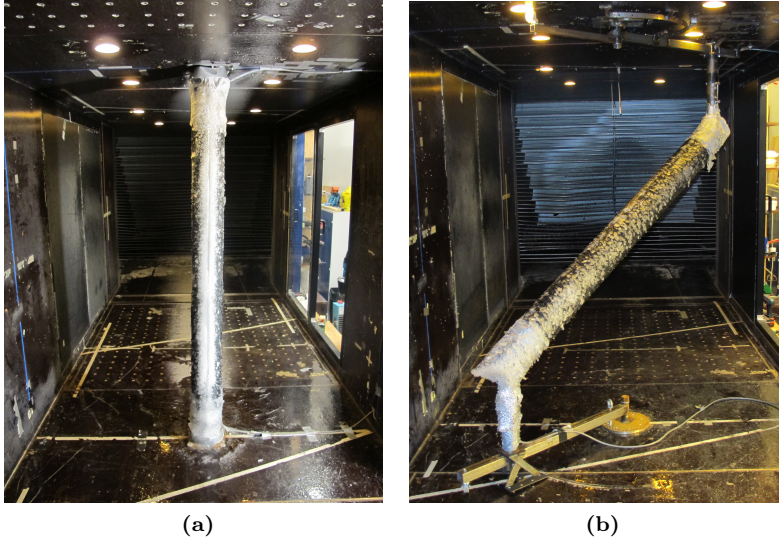


Figure 4.48: Ice on the cable at the end of the ice accretion phase: bridge hanger (a) and cable stay (b) simulations.

with respect to the horizontal plane:

$$\phi = \arctan \left(\frac{\tan \Theta}{\sin \beta} \right) \quad (4.12)$$

The definition of Θ , β and of the angle of rotation ϕ of the bar is shown in Figure 4.46. This configuration ensured that the projection of the cable axis on the plane of rotation of the spray bar had the same slope as the spray bar, and the centres of the cable and of the spray bar were aligned in the direction of the flow. This ensured that the cable was reached by a homogeneous cloud.

4.5.2 Ice accretion

The ice accretion phase started turning on the fan and setting the target temperature for the accretion. When temperature was reached, the wind tunnel was set to the wind speed requested and the spray bar supplies were opened on simultaneously and the ice accretion process was started. The water and air pressures were set to 4.1 bar and 2.5 bar, respectively, to obtain a MVD of $30 \mu m$, a typical value for in-cloud icing (Poots, 1996). During the ice accretion phase the pressure of air and water, the force transducers output, the temperature and the pitot tube were recorded with a sampling frequency of 100 Hz. Often the pitot tube got obstructed by ice during the accretion phase.

Table 4.4: Climatic conditions during ice accretion simulations of bridge hangers.

CC	U [m/s]	Temperature [$^{\circ}C$]	LWC [g/m^3]
V1	11	-5	0.2
V2	11	-3	0.2
V3	11	-1	0.2
V4	17	-5	0.3

A camera was installed so that the entire ice accretion process was photo captured. The first tests have highlighted the problem of condensation and of reflection on the glass of the windows of the CWT that prevented to take pictures. In order to solve the problem, it was designed a wood box in which place the camera. The wood box had one open side which was pointing towards one of the windows in the CWT. The box prevent any reflection from lights. Furthermore, the box was heated to prevent condensation. The camera was used to record the evolution of the accretion, with one frame every 5 seconds. After one hour of ice accretion 720 pictures had been captured making it possible to make a time lapse movie of the ice accretion process.

4.5.2.1 Bridge hangers

The control variables in the ice accretion phase were the wind speed and the temperature. The specific Climatic Conditions (CCs) employed in bridge hangers simulations were: 1 hour exposure, wind speed equal to 11 and 17 m/s and temperature equal to -1° , -3° and $-5^{\circ}C$. The angle of attack of the cable section model was fixed during each CC in the accretion phase simulating a static wind direction during the ice accretion process. A summary of the tests performed is given in Table 4.4.

4.5.2.2 Stay cables

The control variables in the ice accretion phase were the temperature and the yaw. Common to all CCs were 1 hour of exposure, $U = 11 m/s$ and $T = -1^{\circ}$ and -5° Celsius. In these CCs, accretions were generated for a cable inclination angle of 30° and yaw angles in the range of $\beta = 0^{\circ}$ to 180° at intervals of 45° . For $\beta = 180^{\circ}$, an additional CC with $T = -3^{\circ}$ was also tested. $\Theta = 30^{\circ}$ is the typical inclination of the longest stays of cable-stayed bridges of medium to large span. The yaw and inclination angles of the cable section model were fixed during each CC in the accretion phase. A summary of the tests performed is given in Table 4.5.

Table 4.5: Climatic conditions during ice accretion simulations of stay cables.

CC	β [°]	Temperature [°C]	α_r [°]	CC	β [°]	Temperature [°C]	α_r [°]
I1	-	-	0	I7b	90	-1	+10
I2	0	-5	0	I7c	90	-1	-10
I3	0	-1	0	I8	135	-5	0
I4	45	-5	0	I9	135	-1	0
I5	45	-1	0	I10	180	-5	0
I6	90	-5	0	I11	180	-3	0
I7a	90	-1	0	I12	180	-1	0

4.5.3 Aerodynamic force measurement

After the accretion phase, the temperature was set to a value of -5°C to prevent the ice accreted from melting. The force measurements were carried out for a number of cable positions. In the measurement phase, the aerodynamic forces acting at different wind speeds and different angles of attack on the ice-accreted cable were measured. Before starting the measurements, the ice accreted on the dummy pieces and the cellophane film were removed and the force transducers were accurately inspected to check for the presence of ice.

In the case of bridge hangers tests, force measurements were performed for angles of attack in the range of 0° to 180° at intervals of 10° and for wind speeds in the range of 8 to 29 m/s, at intervals of approximately 2 m/s. $\alpha = 0^\circ$ is the angle of attack of accretion. The value of α in the position of accretion is termed *angle of attack of accretion*. The sampling time was 30 s and the sampling frequency was 2048 Hz.

In the case of cable stays tests, the spray bar was left in the position of the accretion phase (Eq. 4.12). The aerodynamic forces exerted at different wind speeds and different yaws on the ice-accreted cable were measured. Force measurements were performed for $\Theta = 30^\circ$, for yaw angles in the range of 0° to 180° at intervals of 10° and for wind speeds in the range of 8 to 29 m/s, with steps of approximately 2 m/s. Limited to CC I7, measurements were made for $\alpha_r = -10^\circ$, 0° and $+10^\circ$, providing the results reported as I7a, I7b and I7c (Table 4.5). The value of α_β in the position of accretion is termed *angle of attack of accretion* and the value of β in the position of accretion is termed *yaw of accretion*. The acquisition time was 30 s and the sampling frequency was 2048 Hz.

4.5.4 Measurement of accreted sections

At the end of each measurement phase, the ice shape was recorded by cutting the ice with a metal plate heated with a gas burner and drawing the ice contour with

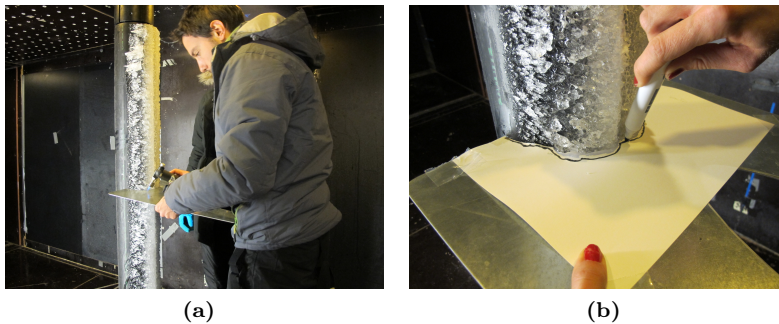


Figure 4.49: Ice cutting (a) and drawing of the ice contour (b).

a permanent marker on a piece of cardboard (Figure 4.49). This was repeated for many sections to keep track also of the axial variability of the accretion. The cardboards were then scanned and digitized using a vector graphics editor.

4.5.5 Test protocol

1. Take note of the atmospheric pressure
2. Open the air compressors and the water pump
3. Remove and clean the air caps
4. Check the fluid caps opening the water
5. Clean the dirty fluid caps
6. Reinstall everything on the spray bar
7. Check if the cloud produced it's ok
8. Close the spray bar supplies
9. Open the heating system
10. Dry the cylinder and install the cellophane around the dummy pieces
11. Place the cylinder in the $0^\circ C$ position
12. Remove everything from inside the wind tunnel
13. Turn on the wind tunnel to 500 rpm, turn on the cooling unit and set the temperature
14. Check if the temperature is stable

15. Turn off the wind tunnel
16. Reset the amplifiers
17. Set the fan speed to the accretion speed decided
18. Check if the air compressors and the water pump work and have the correct pressure
19. Start the time lapse photo shooting
20. Log the data with a time equal to the ice accretion time (100 Hz)
21. Open the water and the air in the same moment (air pressure < water pressure)
22. Close the water and the air in the same moment after time accretion time and open the outlet
23. Stop the time lapse photo shooting
24. After around one minute close the outlet and the heating system
25. Close the air compressors and the water pump
26. Set the fan speed to 100 rpm and the temperature to -5°C
27. Go inside the wind tunnel and remove all the mechanical connection between the cylinder and the dummy pieces
28. Make pictures of the cylinder from all the direction and some detail
29. Check if the temperature is stable
30. Turn off the wind tunnel
31. Reset the amplifiers
32. Log the data of the zero reading (30sec, 2048Hz)
33. Increase the speed of 100 rpm and log the data until the maximum speed (30sec, 2048Hz)
34. Set the fan speed to 100 rpm and the temperature to -5°C
35. Change the angle of attack of 10°
36. Repeat for all the angle of attack
37. Cut the ice and draw the shape
38. Close everything

References

- Déchelette, A., Babinsky, E., & Sojka, P.E. 2011. *Drop Size Distributions*. Springer. Chap. Handbook of atomization and sprays.
- Gates, E.M., Lam, W., & Lozowski, E.P. 1988. Spray evolution in icing wind tunnels. *Cold Regions Science and Technology*, **15**(1), 65–74.
- Georgakis, C.T., Koss, H.H., & Ricciardelli, F. 2009. Design specifications for a novel climatic wind tunnel for testing of structural cables. *In: 8th International Symposium on Cable Dynamics, Paris*.
- Kollár, L.E., & Farzaneh, M. 2009. Spray characteristics of artificial aerosol clouds in a low-speed icing wind tunnel. *Atomization and Sprays*, **19**(4), 389.
- Lund, M.S.M. 2013. *Prediction and Simulation of Aerodynamic Instability of Iced Bridge Cable Section*. Ph.D. thesis, Civil Engineering Structural Dynamics Group (CESDyn) - Technical University of Denmark.
- Matteoni, G., & Georgakis, C.T. 2012. Effects of bridge cable surface roughness and cross-sectional distortion on aerodynamic force coefficients. *Journal of Wind Engineering and Industrial Aerodynamics*, **104**, 176–187.
- Poots, G. 1996. *Ice and snow accretion on structures*. Vol. 338. Research Studies Press.
- Schick, R.J. 2008. *Understanding Drop Size*. Spraying Systems Co., Wheaton, IL, USA.
- Zhu, H., Salyani, M., & Fox, R.D. 2011. A portable scanning system for evaluation of spray deposit distribution. *Computers and electronics in agriculture*, **76**(1), 38–43.

CHAPTER 5

Characteristics of the ice accretion on bridge cables

I don't know anything, but I do know that everything is interesting if you go into it deeply enough.

RICHARD FEYNMAN.

This Chapter briefly describes the ice accretion phenomenon on bridge cables as a complementary part of Chapter 3. Subsequently, it is given a description of the ice accretion phenomenon at the end of the accretion phase in bridge hangers and cable stays tests. Moreover, a description of the time evolution during the accretion phase is given.

5.1 Ice accretion on bridge cables

The main factors affecting in-cloud ice accretion of bridge cables are: (i) the evolution of the aerodynamics of the ice accreted object, (ii) the trajectories of the droplets and of their impingement and (iii) the thermodynamics of the freezing/ice growth process (Lynch & Khodadoust, 2001).

During accretion, geometry and therefore aerodynamics vary. The trajectories of the smaller droplets are strongly influenced by the flow field and tend to follow the streamlines, impinging only close to the stagnation point, whereas the trajectories of the larger droplets are governed by inertia forces and tend to be straight, impinging on wider areas. The *tangent trajectories* are defined as

the free-stream boundaries outside which a drop does not collide with the cable; according to the above these depend on the drop size. For a two-dimensional flow, there are two *impingement limits*, an upper and a lower. The *impingement limits* are the collision point of the tangent trajectories on the object. The identification of the tangent trajectories and of the impingement limits allows the evaluation of the amount of impinging water, affecting accretion. The relevant parameter is the *collection efficiency*, defined as the ratio of the mass of droplets actually impinging on the cable to mass of droplets that would impinge if the trajectories remained straight. This parameter is function of the aerodynamics of the ice accreted cables. As an example, a large leading edge curvature radius (large diameter cables) collects less droplets than a smaller one, in particular small droplets. This is due to the fact that water droplets deviate more when radius of curvature is large, thus ice collected will be small.

The capacity of accretion also depends on the heat balance of the accreting surface, whose main contributions come from the latent heat deriving from freezing of the impinging supercooled water droplets and the heat flux between the accretion and the airstream. The amount of latent heat depends on the amount of freezing water. The heat flux between the accretion and the airstream depends on the flow field, on the area of the exposed surface and on the roughness (Achenbach, 1977). When the capacity of the airstream of absorbing heat from the accretion is large, then all the impinging droplet freeze on contact with the surface. In this case, droplets freeze at the point of impingement, and the result is the formation of *rime ice*. Rime ice tends to be white, due to the presence of air pockets inside the accretion. Rime ice can be hard or soft. Droplets with high momentum produce a *hard rime*, in which the frozen droplets pack close together in granules, making the ice similar to a sponge; if the momentum of the droplets is low a *soft rime* is produced, in which the frozen droplets grow as white ice needles and flakes. On the other hand, when the capacity of the airstream of absorbing heat is smaller than the latent heat that would be produced if all the impinging droplets froze, then only a portion of these can freeze on the contact with the surface and the remaining portion remain in the liquid state, forming *glaze ice*. This type of ice is a transparent, denser and more homogeneous than rime. The *freezing fraction* is the relative amount of water that freezes at contact to the surface of the object; this is equal to one for rime ice, while it is between zero and one if only part of the water freezes (glaze and mixed). The unfrozen portion of the impinging water is subject to aerodynamic forces, gravity and surface tension, giving rise to rivulets. The rivulet can, then, freeze forming a *runback*, an ice formation behind the impinging limits. Finally, some of the water can be dragged away from the object before freezing. Also intermediate conditions can take place, in which case the term *mixed ice* is used, and the accretion is classified as a rime or glaze dominant type ice.

In the case of the bridge hangers, the accretion can be divided into two parts, the windward accretion and the leeward accretion (Figure 5.1). The windward accretion is generated by the droplets that impact on the frontal surface of the

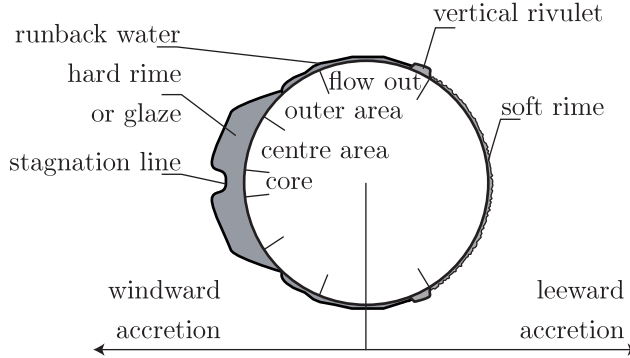


Figure 5.1: Description of the zones of accretion.

cable. In this area hard rime or glaze ice accretion was found. The area around the stagnation line is named *core* (Koss *et al.*, 2012), and is the first droplet-impinging zone; at the stagnation point a thinner accretion was found in all the CCs. In the *outer area* (Koss *et al.*, 2012) the impingement of droplets starts during the evolution of the accretion. There, a dominant hard rime or glaze ice accretion was found. Runback water starts from the outer area forming a *flow out* area (Koss *et al.*, 2012). The runback water flows out to the flow separation point forming a *vertical rivulet*. The flow separation point is the arrival point in the horizontal direction of the runback water; downstream that the aerodynamic forces acting on the water rivulets are considerably lower. The leeward accretion is generated by the droplets that impact on the leeward portion of the cable. The distribution in diameter of such droplets is different from that of the oncoming cloud, as only smaller droplets are entrained by the wake flow, while on larger ones inertia forces dominate.

Differently from the bridge hanger case, in the stay cables case the directions of g , of U_N and of the cable axis play a fundamental role. The angle between g and U_N is α_β (Figure 4.46), and it coincides with the angle between the vertical plane containing the cable axis and the plane containing U_N and the cable axis. The angle between g and the cable axis is the complementary angle γ of Θ (Figure 4.46). In cross flow, U and U_N coincide. In the horizontal case, g is perpendicular both to the cable axis and to U ($\alpha_\beta = 90^\circ$ and $\gamma = 90^\circ$). In this condition, the runback water flows mainly along the lower side of the cable, giving rise to the formation of *icicles* (Koss & Lund, 2013). An icicle is a spike of ice formed from the freezing of the water dripping or falling from an object. Over time, continued water runback causes the icicle to grow. The direction of accretion is governed by the aerodynamic and gravity forces. An icicle usually forms when the resultant of these two forces is able to push the runback water away of the stay cable. This phenomenon occurs, therefore, if the direction of the resultant force in the flow-out area is outgoing from the stay cable. In the

Table 5.1: Description of the ice accretion in the windward and lateral regions, mass accreted and maximum thickness of the accretion.

CC	Windward accretion	Rivulet presence	Mass accreted [kg/m]	Max accretion [cm]
V1	High	Absent	2.4	2.9
V2	Mid	Moderate	1.5	2.4
V3	Low	Massive	0.6	1.6
V4	Very High	Massive	3.0	3.5

vertical case, g is parallel to the cable axis and perpendicular to U ($\alpha_\beta = 90^\circ$ and $\gamma = 0^\circ$). In this condition, the runback water flows on both sides of the cable forming a vertical iced rivulet, located around the flow separation line. The formation of iced rivulet occurs if the direction of the resultant force in the flow-out area is ingoing from the stay cable.

In all cases, the occurrence of these phenomena depends on temperature, which governs the icing process. Other parameters, like wind speed and the MVD, also influence the presence of runback water, by changing the heat balance of the accreting surface.

5.2 Bridge hangers

In the following a description of the ice accretion at the end of the accretion phase is given for the four CCs tested. A description of the time evolution of the accretion follows. A description of the ice accretion in the windward and lateral regions, the amount of mass accreted and the maximum thickness of the accretion are given in Table 5.1.

5.2.1 Final characteristics of the ice accretion

In CC V1 the windward accretion was characterized by a hard rime with a narrow core and by the absence of lateral rivulets (Figure 5.2). The presence of granular structures of solidification was recognizable, producing a rough surface. In the outer area the growth was characterized by the evolution of structures with strongly unidirectional extension, eventually giving rise to a compact formation. At the end of the accretion phase, in the flow out area no iced rivulets were detected, with the exception of a few in the lower part of the model. The leeward accretion was a soft rime, which extended to the outer area.

In CC V2 the windward accretion was characterized by a hard rime combined with a moderate development of lateral rivulets (Figure 5.3). The core was a narrow structure like in CC V1, in which some soft rime detached from the

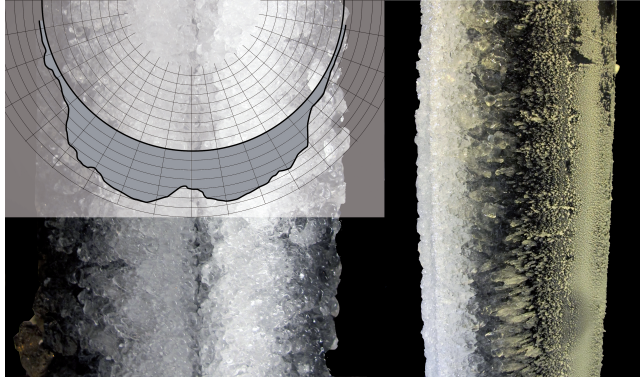


Figure 5.2: Front and lateral view and contour tracing of the cable after ice accretion for CC V1.

tunnel walls was visible. The structure of the centre area was similar to that of CC V1, while in the outer area the accretion was characterized by glaze. In the flow out area some rivulets were visible; the amount of liquid water was not sufficient to create a continuous vertical rivulet in which the rivulets of the flow out area could converge. In the lower portion of the model, an increase in the density of the rivulets in the flow out area generated a more defined continuous structure of the vertical rivulet. This effect, similarly to CC V1, was possibly due to the boundary conditions of the cable section model. In the lateral view, the point of separation of the flow is well recognizable; it approximately coincided with the vertical rivulet.

In CC V3 the windward accretion was dominated by glaze ice combined with a massive development of lateral rivulets (Figure 5.4). In this case the core is a wide structure. Compared to the other CCs, the amount of the accretion is smaller, probably due to the higher temperature. In the centre area the accretion was dominated by glaze ice. The structure of the ice was compact and transparent, with some granular structures. The outer area had a similar structure to that of CC V1, though it started closer to the core. In the flow out area a massive development of iced rivulets was recognizable. The density of the rivulets was so large to almost completely cover the cable in this area. The rivulets in the flow out area converged in a continuous, almost straight vertical iced rivulet, located approximately at the point of separation of the flow.

Finally, in CC V4 the windward accretion was again dominated by a hard rime combined with a massive development of lateral rivulets (Figure 5.5). Compared to the other CCs, the amount of the accretion is larger, probably due to the higher wind speed. The structure of the core, of the centre and of the outer area was similar to that of CCs V1 and V2. The structure of the flow out area was similar to that of CC V3, though the size of the iced rivulets was larger

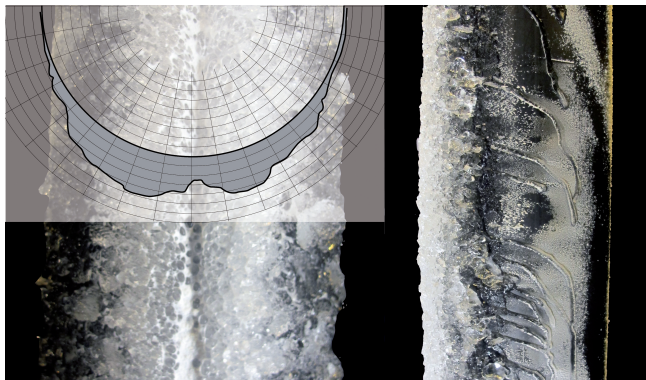


Figure 5.3: Front and lateral view and contour tracing of the cable after ice accretion for CC V2.

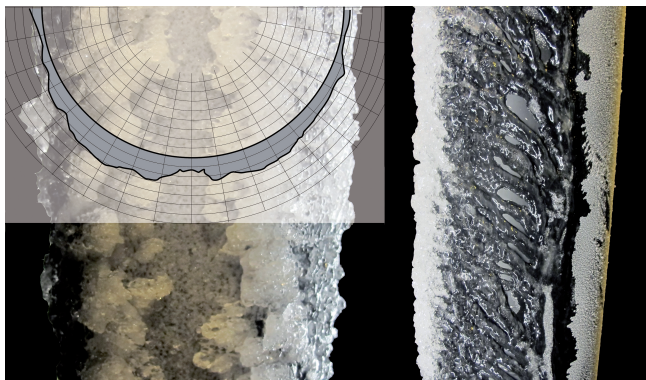


Figure 5.4: Front and lateral view and contour tracing of the cable after ice accretion for CC V3.

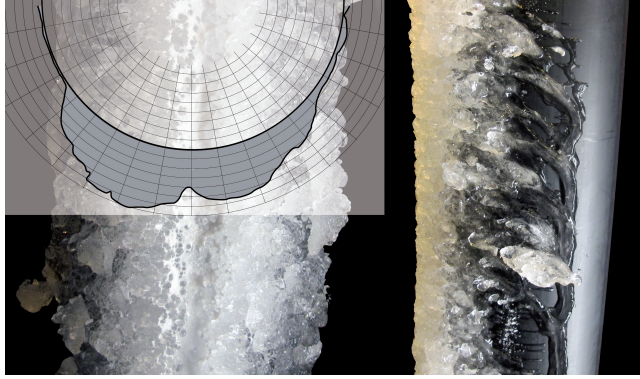


Figure 5.5: Front and lateral view and contour tracing of the cable after ice accretion for CC V4.

than for CC V3, and the density was lower. This result is related to the higher wind speed of this CC, which brought different aerodynamic forces on the liquid water during accretion. The rivulets converged in a continuous, almost straight iced vertical rivulet, as in CC V3. Phenomena of secondary ice accretion were detected in the flow out area, due to irregularities developed on the iced rivulets, which generated a suitable surface for the accretion.

5.2.2 Time evolution of the ice accretion

The development of the ice accretion with time is shown in Figure 5.6 for all the CCs. Picture taken with time-lapse technique are shown with a frequency of 1 frame every 10 minutes. The frame at time zero is not shown because the cylinder is always dry at the beginning of the accretion phase as explained in Section 4.5.

The first three CCs (V1,V1,V3) were characterized by the same wind speed of 11 m/s , but different temperatures, therefore the initial flow-field around the cable was the same. CC V4 was characterized by the same temperature as CC V1, but the wind speed was 17 m/s . The different wind speed caused a different flow-field, with an increase of LWC and of heat transfer between the accretion and the airstream.

In CC V1 after 5 minutes there was only a thin regular white accretion around the stagnation line. This area is named *accumulation area* (Koss *et al.*, 2012). The soft rime in the leeward region was visible almost instantly and it was kept until the end of the accretion phase; this feature is similar for all CCs. After 10 minutes an ice accretion in the centre area and a small layer of liquid water in the outer area were visible. After 20 minutes a second ice formation started to grow in the outer area, from mixed ice and liquid water. After

30 minutes the second formation has developed upstream, towards the centre area, on the superficial discontinuity generated by the iced layer of water. An important feature of the ice accretion phenomenon is that the accretion takes place at all points where there is a superficial discontinuity. The two accretions were separated by a small gap in the outer area, in which a thin layer of thin liquid water could flow. This region became narrower with time, and after 60 minutes the two accretions merged.

For the first 5 minutes, in CC V2 the accretion was similar to that of CC V1. After 10 minutes the water on the windward side was almost completely liquid, and part of it in the form of rivulets flowed to the separation line. After 20 minutes a mix of ice and water was visible on the surface. After 30 minutes an accretion of rime ice was visible in the centre area, which evolved following the same pattern as in CC V1, with more liquid water in the outer area and with the development of some rivulets in the flow out area.

In CC V3 after 5 minutes all the water on centre area was liquid and in the flow out area liquid rivulets flowed to the separation line. In this CC an accumulation area was not found due to the higher temperature. Between 10 and 30 minutes glaze ice formed in the outer region, with an intense development of rivulets in the flow out area. After 40 minutes the glaze type accretion developed towards the centre area and the rivulets on the flow out areas continued to grow. After 50 minutes a rime type accretion formed on the glaze type accretion, that could be recognized from its white color. Almost the entire lateral surface was covered with rivulets. At the end of the accretion a large amount of liquid water was still present on the surface of the cable. Before starting the aerodynamic force measurement, the temperature was decreased to better preserve the ice. During this transition all the liquid water on the surface froze. The different color of the ice between the last frame of CC V3 in Figure 5.6 and Figure 5.4 is due to this transition.

Finally, for CC V4 the difference with respect to CC V1 is due to the higher LWC and heat exchange. The combination of these two differences produced an increase in the amount of ice accreted. After 5 minutes the accumulation area was observed to be similar to those of CCs V1 and V2. After 10 minutes a small layer of liquid water covered the centre area. After 20 minutes a mix of ice and liquid water was observed in the centre and outer area. The accretion seemed to be similar to that of CC V2, though more wet. After 30 minutes large rivulets were visible in the flow out area. From 40 to 60 minutes the accretion in the centre area was similar to that of CC V1 and in the outer and flow out area was similar to that of CC V2. Opposite to CC V2, in the flow out area a massive development of iced rivulets was observed. Compared to CC V3, there were less rivulets, but these had a larger size. On the irregularities generated by the rivulets, phenomena of secondary growth were observed starting after 40 minutes.

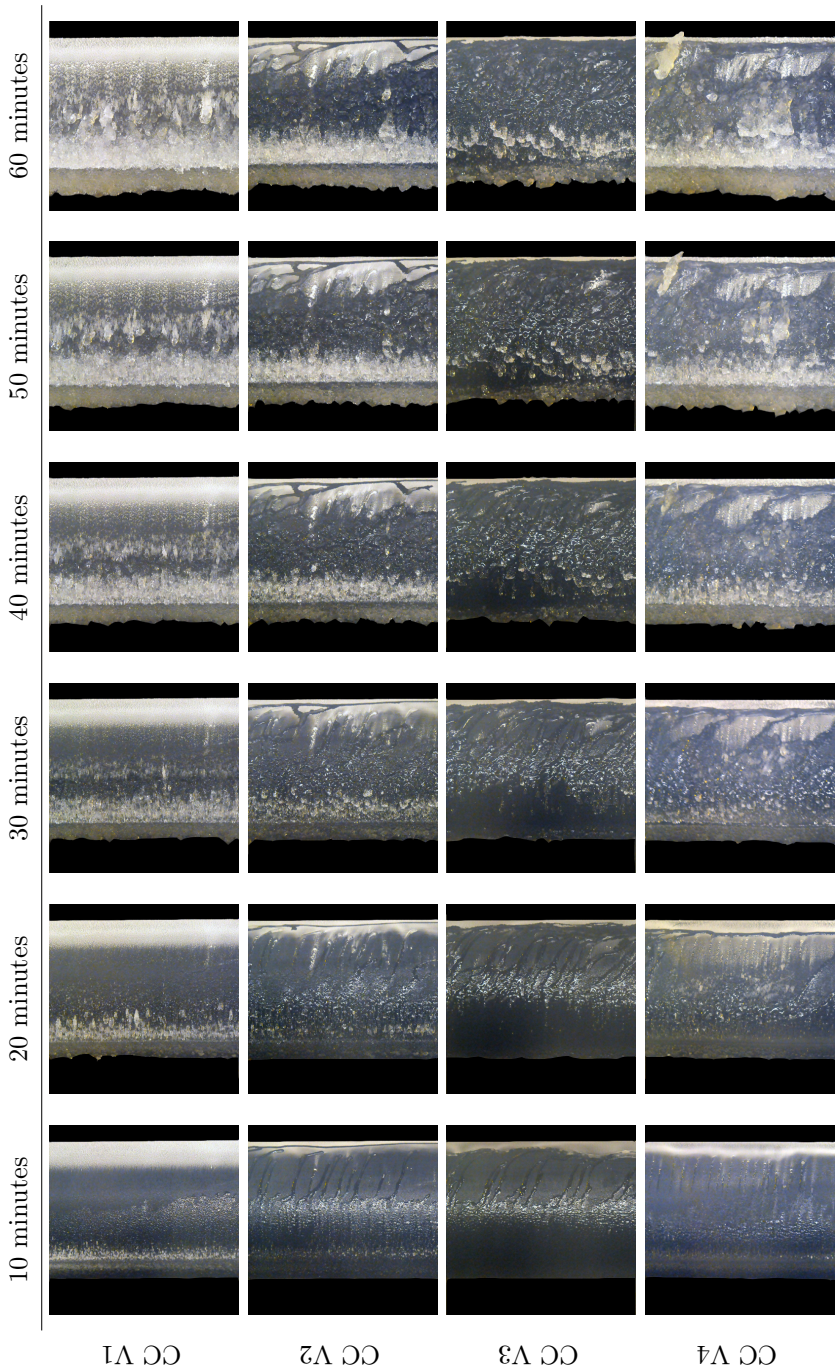


Figure 5.6: Development of ice accretion with time for CCs from V1 to V4.

Table 5.2: Description of the ice accretion in the frontal and lateral regions, mass accreted and maximum thickness of the accretion (I = Icicles, LS = Lower Side, BS = Both Sides).

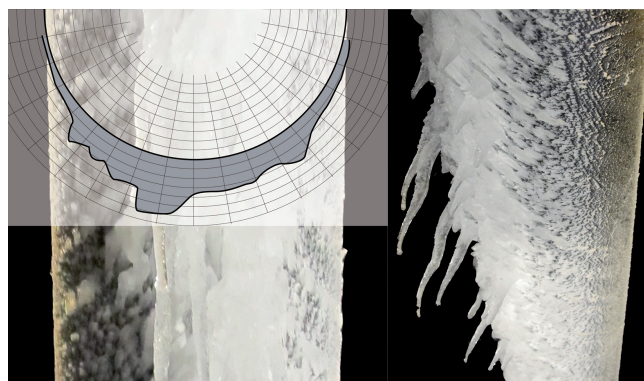
CC	Frontal accretion	Rivulet presence	Mass accreted [kg/m]	Max accretion [cm]
I1	-	Dry cable	-	-
I2	High	Moderate I	2.6	2.6
I3	Mid	Massive I	2.1	2.2
I4	High	Absent	2.3	2.7
I5	Mid	Massive LS	2.2	2.3
I6	Mid	Absent	2.1	2.2
I7a/b/c	Low	High LS	1.8	1.9
I8	High	Absent	2.8	3.3
I9	Mid	Massive LS	2.3	2.5
I10	High	Absent	3.0	3.4
I11	Mid	Absent	2.5	2.9
I12	Low	Massive BS	2.0	2.1

5.3 Stay cables

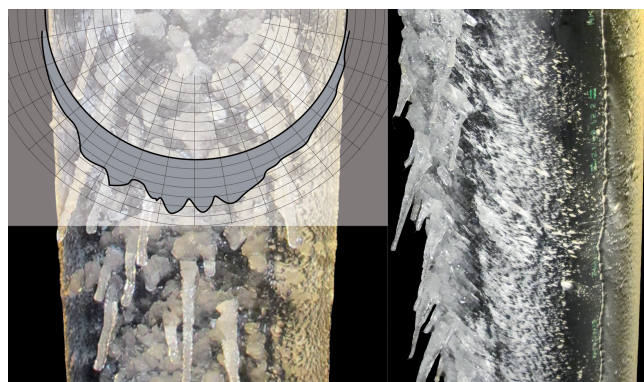
In the following a description of the ice accretion at the end of the accretion phase is given for all CCs tested. The description is given by associating CCs characterized by the same position of the cable during the ice accretion phase. A summary of the accretion result is shown in Table 4.5.

5.3.1 Final characteristics of the ice accretion

In CCs I2 and I3 the cable model was placed longitudinally, with declining slope. In these CCs, g was inclined to the cable axis and to U_N , but the three directions were coplanar, which gave rise to a roughly symmetric accretion. In CC I2 the windward accretion was dominated by a hard rime (Figure 5.7a). The direction of accretion of the structures of the centre and outer area (Koss *et al.*, 2012) was not inclined as U_N , but horizontal. At the core, in both CCs the accretion is thick and does not feature the thickness reduction observed in cross flow at the stagnation line. The water unable to freeze on contact with the surface generated icicles. These were concentrated mostly in the central area of the cable model and in smaller quantities near the ends, due to the limited length of the model. A moderate presence of icicles was detected also on the dummy pieces. In CC I2, the icicles were well spaced and characterized by large diameters, due to rime ice accretion occurred on them during their growth, and their shape was tapered (Figure 5.7a). The leeward accretion was a soft



(a)



(b)

Figure 5.7: Front and lateral view, and contour tracing of the cable after ice accretion for CC I2 (a) and CC I3 (b).

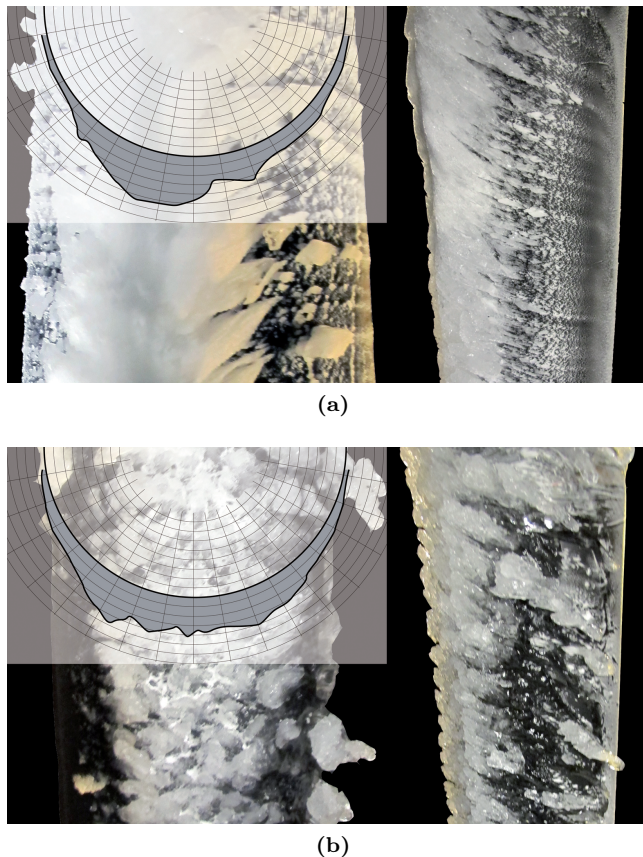


Figure 5.8: Front and lateral view, and contour tracing of the cable after ice accretion for CC I4 (a) and CC I5 (b).

rime, which extended to the outer area. On the other hand, due to the higher temperature in CC I3 the windward accretion was dominated by glaze, with a larger quantity of liquid water on the surface, generating a massive development of icicles (Figure 5.7b). In this CC, the icicles were dense and characterized by a smaller size, due to the inability to develop phenomena of rime ice accretion as it occurred in CC I2. With respect to CC I2, less windward accretion was also detected due to the higher temperature (Table 4.4).

In CCs I4 and I5, g was inclined to the cable axis and to U_N , and the three directions were not coplanar, bringing an asymmetry of the windward accretion. In CC I4 the windward accretion was dominated by hard rime (Figure 5.8a), which is recognized from the presence of air pockets inside the accretion, making the ice white. The windward accretion was concentrated in the centre area and

less accretion was found in the outer area, where only sparse elongated accretions were found. In the flow out area no runback water was observed. At the core, a thinner accretion was found in CC I4 and CC I5, as in the bridge hangers case. On the other hand, in CC I5 the windward accretion was dominated by glaze (Figure 5.8b). The accretion was concentrated at the centre area. The direction of the ice accretion was horizontal both in CC I4 and I5. Only on the lower lateral side of the cable runback water was observed in the flow out area. The runback water created some iced rivulets that converged in a continuous, almost straight iced rivulet parallel to the cable axis, located in the lower side of the cable at approximately the flow separation line. The leeward accretion was a soft rime in both CCs. Phenomena of secondary ice accretion were also detected in the flow out area, due to irregularities developed on the iced rivulets, that generated a surface suitable for further accretion. This secondary structures were similar to the icicles found in CC I3, and were spread all over the cable model, sparse and characterized by large diameters.

In CCs I6 and I7, g , the cable axis and U_N were not coplanar, and the conditions were those of cross flow, as $\Phi = 90^\circ$. The difference with respect to the horizontal ($\Theta = 0^\circ$) and vertical cases ($\Theta = 90^\circ$) is that the cable is inclined with $\Theta = 30^\circ$. In CC I6 the windward accretion was dominated by hard rime (Figure 5.9a). In the flow out area, the absence of lateral rivulets was observed, and some singularities in the accretion were found in the lower lateral side (Figure 5.9a). The presence of granular structures was recognized, producing a rough surface. An asymmetry of the windward accretion was also observed in this CC. In CC I7 the windward accretion was dominated by glaze (Figure 5.9b), and the smallest value of the maximum accretion thickness was found (Table 4.4). At the core, the line of lower accretion thickness was found like in CC I6, following the stagnation line; however, due to the effect of gravity, the windward accretion was clearly non-symmetric. Only on the lower lateral side of the cable, runback water in the flow out area was observed, creating a pattern of rivulets that converged into a continuous structure at the separation line, also observed in CC I5. On the upper lateral side, a small amount of runback water was seen, forming very sparse and small iced rivulets. Very small phenomena of secondary ice accretion were detected in the flow out area. In this CC, the iced rivulets in the flow out area were inclined downwards due to the effect of gravity, though the inclination was lower than the bridge hangers case. The leeward accretion was soft rime in both CCs I6 and I7.

In CCs I8 and I9, g , the cable axis and U_N were not coplanar. In CC I8 the windward accretion was dominated by hard rime (Figure 5.10a), and in the centre and outer area, granular structures were found. The direction of accretion of the ice structures was horizontal, and a small asymmetry of the windward accretion was found. In the flow out area, the absence of lateral rivulets was observed. In CC I9 the windward accretion was dominated by glaze (Figure 5.10b). In the centre and outer area, the ice was compact and transparent, with some granular structures, and an asymmetry of the windward accretion

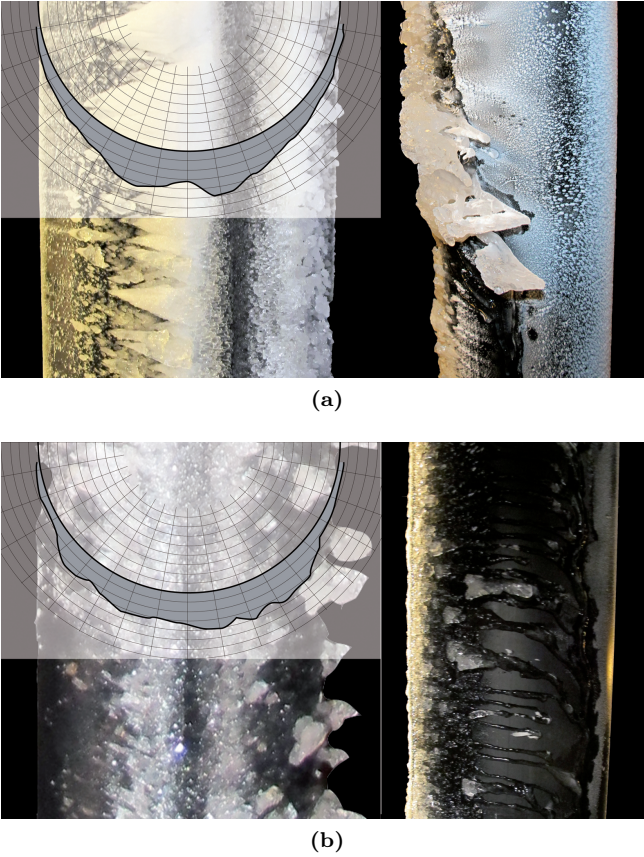


Figure 5.9: Front and lateral view, and contour tracing of the cable after ice accretion for CC I6 (a) and CC I7 (b).

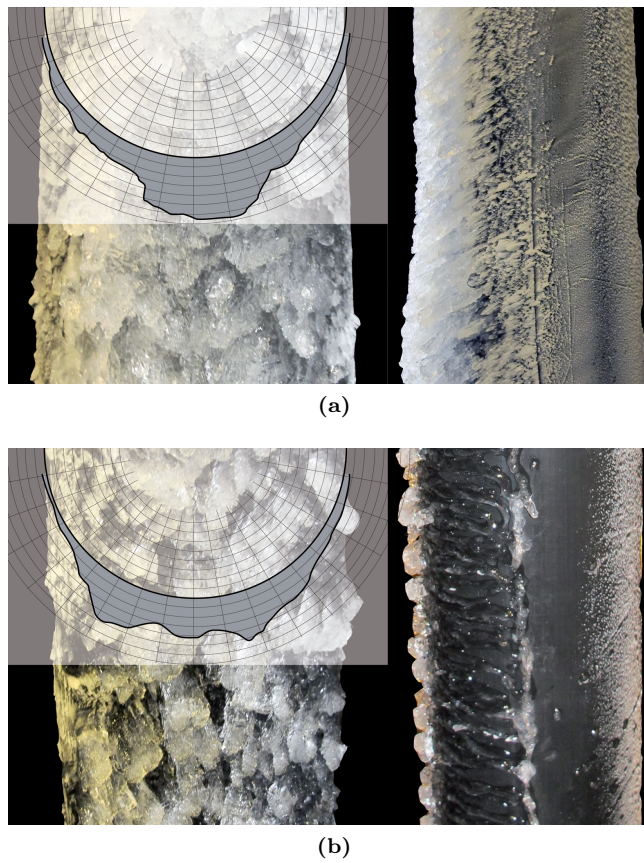


Figure 5.10: Front and lateral view, and contour tracing of the cable after ice accretion for CC I8 (a) and CC I9 (b).

was observed. In the flow out area, the runback water moved to the lower side of the cable, forming a series of iced rivulets which converged into a single one parallel to the cable axis and located on the lower side. The leeward accretion was soft rime both in CC I8 and I9.

Finally, in CCs I10, I11 and I12 the cable model was placed longitudinally, with ascending slope; g was inclined to the cable axis and to U_N , and the three directions were coplanar, generating a roughly symmetric accretion. In these CCs, the direction of accretion of the centre and outer area was horizontal. In CC I10 the windward accretion was dominated by hard rime (Figure 5.11a). In the centre and outer area, the ice was characterized by a compact structure and a dominant white color, indicating the presence of pockets of air. In the flow out area, no runback water were observed. The largest value of the maximum accretion thickness was found in this CC (Table 4.4). The thinner core accretion was not found in CCs I10, I11 and I12. In CC I11 the windward accretion was also dominated by hard rime (Figure 5.11b). In the centre and outer area, the characteristics of the ice accretion were similar to CC I10, but more wet and featuring less compact structures. In the flow out area, the presence of very parse iced rivulets was observed. These rivulets were inclined downwards due to gravity. In Figure 5.11b no leeward accretion appears; when the photo was taken this, of soft rime type, was removed by the wind in the measurements phase, differently from what it happened in CC I10 and I12 (Figures 5.11a e 5.11c, where the soft rime is well visible). In this CC, in the leeward region only some iced rivulets were recognized. In CC I12 the windward accretion was dominated by glaze (Figure 5.11c). In the centre and outer area, ice was wet and less compact. In the flow out region, the runback water flowed along both sides of the cable, forming sparse iced rivulets, not covering the entire lateral surface of the cable, and converging to a single continuous iced rivulet parallel to the cable axis (as for CCs I7 and I9). This rivulet was located on the lower side of the cable, with some small icicles starting from it.

5.3.2 Time evolution of the ice accretion

The development of the ice accretion with time is shown in Figure 5.12 for CCs from I2 to I7 and in Figure 5.13 for CCs from I8 to I12. Picture taken with time-lapse technique are shown with a frequency of 1 frame every 10 minutes. The frame at time zero is not shown because the cylinder is always dry at the beginning of the accretion phase as explained in Section 4.5.

In CCs I2 and I3 the cable model was placed longitudinally, with declining slope. CC I2 was characterized by temperature during the ice accretion phase of -5°C while CC I3 of -1°C . The temperatures difference causes an accretion of different type. In CC I2, up to 40 minutes the accretion occurs on the bottom side of the cylinder and is characterized by a bright white color typical of hard rime. Over 40 minutes, the excess of water on the surface generates rivulets that grow with a certain inclination relative to the vertical due to the aerodynamic

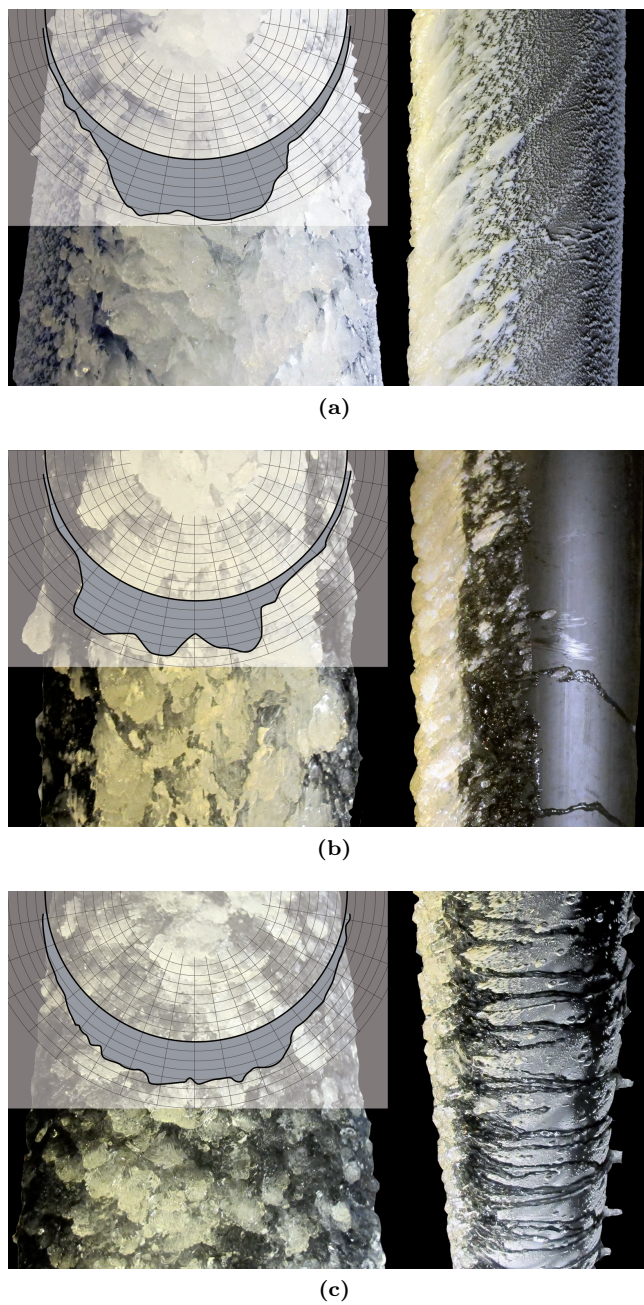


Figure 5.11: Front and lateral view, and contour tracing of the cable after ice accretion for CC I10 (a), CC I11 (b) and CC I2 (c).

force on the liquid. In CC I3, up to 30 minutes the accretion is characterized to be much wetter respect to CC I2 and with plenty of runback water. Over 40 minutes, the excess of water on the surface generates rivulets. In this case, the rivulets were smaller and spread onto the surface.

CCs I4 and I5 were characterized by temperature during the ice accretion phase of -5°C and -1°C , respectively. Also in this case, the temperature during the accretion phase influences the amount of runback water. No accretion was found on the bottom side of CC I4, except of soft rime strongly influenced by the flow coming from the frontal accretion. Differently in CC I5 the runback water produce iced rivulets on the bottom side. The rivulets start growing after 30 minutes.

CCs I6 and I7 were characterized by cross flow conditions. In both CCs at the beginning of the accretion process there was a thin regular white accretion around the stagnation line as for bridge hangers. This area is named *accumulation area* (Koss *et al.*, 2012). The inclination of the cable generates a different process of accretion respect to the bridge hanger case. CC I6 was characterized by a hard rime accretion except for an irregularity near the end of the cable model. At around 20 minutes, this irregularity generates some rivulets on the bottom side of the cable. After 30 minutes these rivulets become catalysts for a strong rime accretion on them. In CC I7, between 10 and 30 minutes glaze ice formed in the outer region, with development of rivulets in the bottom side of the cylinder. On the irregularities generated by the rivulets, phenomena of secondary growth were observed starting after 40 minutes.

CCs I8 and I9 were characterized by temperature during the ice accretion phase of -5°C and -1°C , respectively. In CC I8, the accretion occurs on the lateral side of the cylinder and is characterized by a bright white color typical of hard rime. Only near one end of the cable model the accretion seems to be more wet probably due to some end effect. However, this feature seems to disappear after 40 minutes, when the increase becomes approximately uniform. In CC I9, after 10 minutes all the water on centre area was liquid and in the bottom side liquid rivulets flowed to the separation line. Between 10 and 30 minutes glaze ice formed in the outer region, with an intense development of rivulets in the flow out area. After 50 minutes a rime type accretion formed on the glaze type accretion, which could be recognized from its white color. Almost the entire lateral surface was covered with rivulets and some small icicles appears.

Finally, in CCs I10, I11 and I12 the cable model was placed longitudinally, with ascending slope. CCs I10, I11 and I12 were characterized by temperature during the ice accretion phase of -5°C , -3°C and -1°C , respectively. In CC I10, after 10 minutes an ice accretion in the centre area were visible. The accretion was mainly localized in the centre area for all the time. No runback water was observed in the lateral sides. The accretion continues with a hard rime type accretion mainly located in the centre area and with the development of soft rime on the lateral sides. In CC V11 the accretion was similar to that of CC I10. After 10 minutes a small layer of liquid water in the frontal area

were visible. Up to 40 minutes, the accretion was dominated by the presence of liquid water on the surface. Over 40 minutes, a rime type accretion formed on the glaze type accretion, which could be recognized from its white color. Over 50 minutes, some rivulets forms on the lateral sides. In CC I10, after 10 minutes a small layer of liquid water covered the centre area. After 20 minutes a mix of ice and liquid water was observed in the centre and outer area. Between 10 and 30 minutes glaze ice formed in the outer region, with an intense development of rivulets in the flow out area. The rivulets converged in one rivulet located in the bottom side of the cable model.

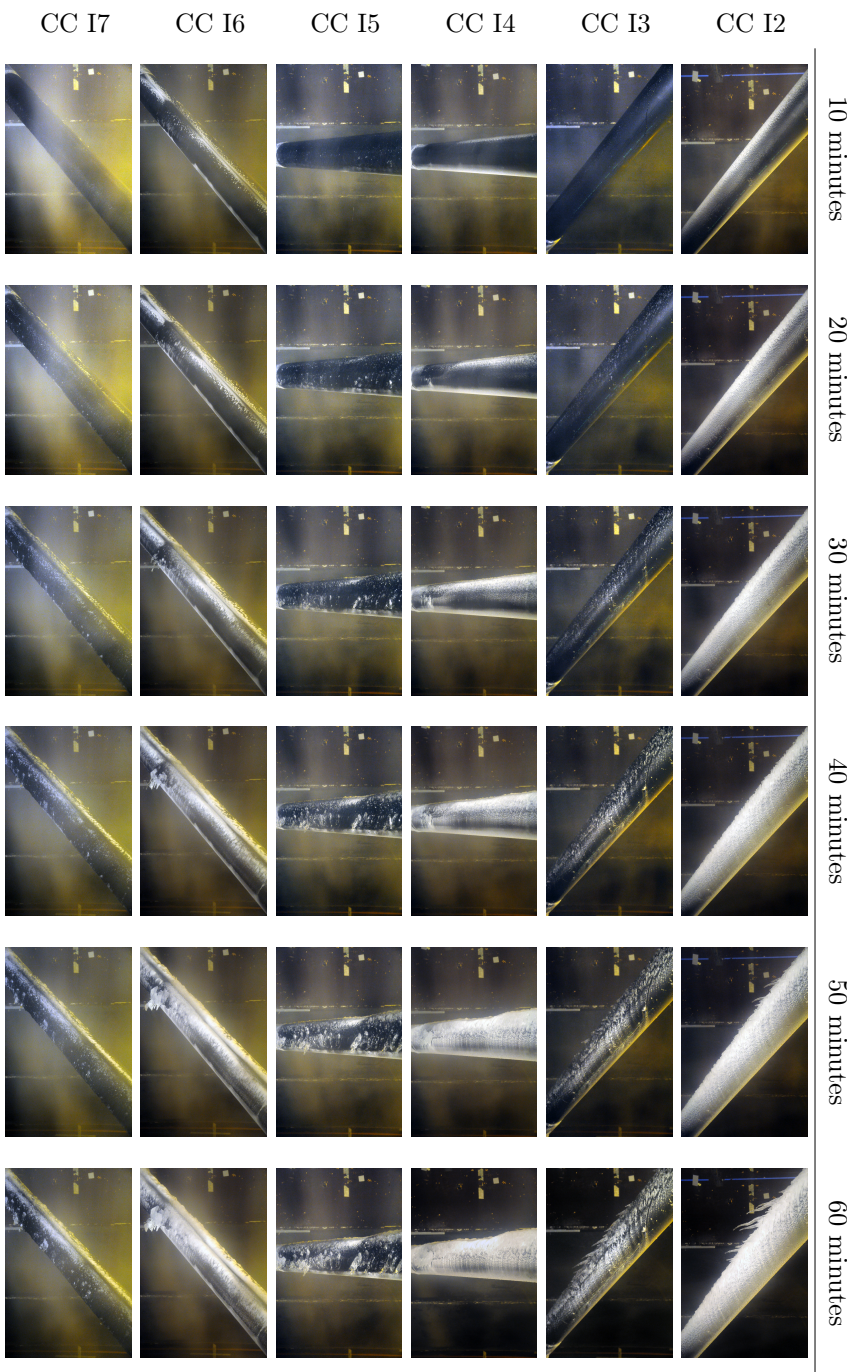


Figure 5.12: Development of ice accretion with time for CCs from I2 to I7.

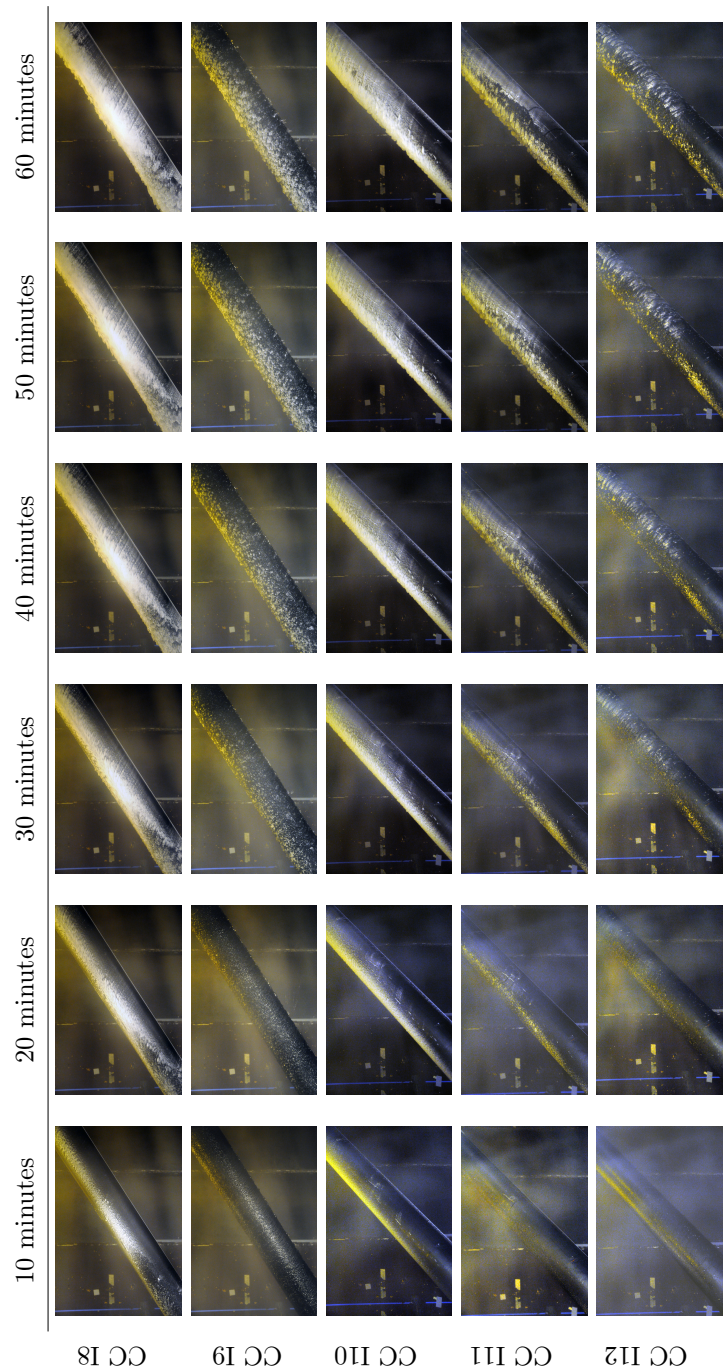


Figure 5.13: Development of ice accretion with time for CCs from I8 to I12.

References

- Achenbach, E. 1977. The effect of surface roughness on the heat transfer from a circular cylinder to the cross flow of air. *International Journal of Heat and Mass Transfer*, **20**(4), 359–369.
- Koss, H.H., & Lund, M.S.M. 2013. Experimental Investigation of Aerodynamic Instability of Iced Bridge Cable Sections. In: *6th European and African Conference on Wind Engineering, Robinson College, Cambridge, UK*.
- Koss, H.H., Gjelstrup, H., & Georgakis, C.T. 2012. Experimental study of ice accretion on circular cylinders at moderate low temperatures. *Journal of Wind Engineering and Industrial Aerodynamics*, **104-106**, 540–546.
- Lynch, F.T., & Khodadoust, A. 2001. Effects of ice accretions on aircraft aerodynamics. *Progress in Aerospace Sciences*, **37**(8), 669–767.

CHAPTER 6

Aerodynamics of iced bridge cables

All progress is experimental.

JOHN JAY CHAPMAN.

From the description given in Chapter 5, it is clear that the features of the ice accretion very much depend on the geometric and climatic conditions of accretion; therefore it is expected that the modifications brought to the aerodynamic forces also are, and that aerodynamic stability can vary from one case to another. In this Chapter are presented and described the mean aerodynamic force coefficients for each CCs in correlation with the geometry of the ice accretion.

Due to thermodynamic issues, Reynolds scaling of geometry is not applicable in the presence of ice accretion; therefore the results given are specific for plain HPDE cables with a nominal diameter of 16 cm. For this reason, the aerodynamic coefficients here presented are expressed as a function of the wind speed and not of the Reynolds number. Furthermore, the influence of gravity on growth makes the result of bridge hanger specific for the case of vertical cables in cross flow therefore the result is different from that of horizontal cables.

Additionally, the derivatives of the aerodynamic coefficients with respect to α and Re for bridge hangers tests are given in Appendix A.1. The derivatives of the aerodynamic coefficients to Φ and Re for stay cables are given in Appendix A.2. Only for CC I7, also the derivative with respect to α is given. The derivatives were evaluated in terms of Newton's difference quotient. The fluctuating aerodynamic coefficients for bridge hangers tests are given in Appendix B.1 and

Table 6.1: Maximum and minimum values of the mean drag, lift and moment coefficients.

CC	Maximum			Minimum		
	C_D	C_L	C_M	C_D	C_L	C_M
V1	1.07	0.33	0.09	0.41	-1.53	-0.20
V2	1.04	0.25	0.08	0.53	-1.42	-0.13
V3	0.97	0.22	0.08	0.43	-0.49	-0.08
V4	1.10	0.18	0.08	0.61	-1.33	-0.16

for stay cables in Appendix B.2.

6.1 Bridge hangers

The mean drag C_D , lift C_L and moment C_M coefficients (Figure 4.4) were calculated based on the mean along-wind and across-wind forces and torque normalized through the mean dynamic pressure and the reference area, i.e. the product of the nominal diameter and the length of the model. The variation of the reference area due to accretion was not considered. Drag coefficients were corrected for blockage following the Maskell III Method (Cooper *et al.*, 1999).

The mean aerodynamic coefficients measured for each CC are shown in Figures 6.1 through 6.4, as a function of the angle of attack, α , for different values of the wind speed. These were obtained rotating the cable about its axis. Grey areas indicate the range of angles of attack where the dependency with wind speed is more pronounced. There is a clear relationship between the ranges of each of the three coefficients, even though they do not perfectly overlap. However, these ranges are simply derived from observation of the trends of the aerodynamic coefficients and should therefore be construed as qualitative rather than quantitative. The minimum and maximum values of the coefficients for each CC are also given in Table 6.1.

Globally, the aerodynamic coefficients of the accreted cable show large variations with both CC and angle of attack, due to the different features of each accretion. In particular, there are situations in which the aerodynamic coefficients do not depend on wind speed, and others in which they do. The values of the aerodynamic coefficients depend on the position of the separation point, which is determined by the size of the windward accretion (hard rime or glaze ice type) and by the presence, dimensions and density of iced rivulets on the lateral sides. The position of the separation point, otherwise dependent on wind speed for a plain cable, can become independent of it when geometric perturbations are created by the accretion, hence determining separation points. The soft rime accretion on the leeward side did not influence the aerodynamic coefficient, as it was removed by the wind before the measurement phase.

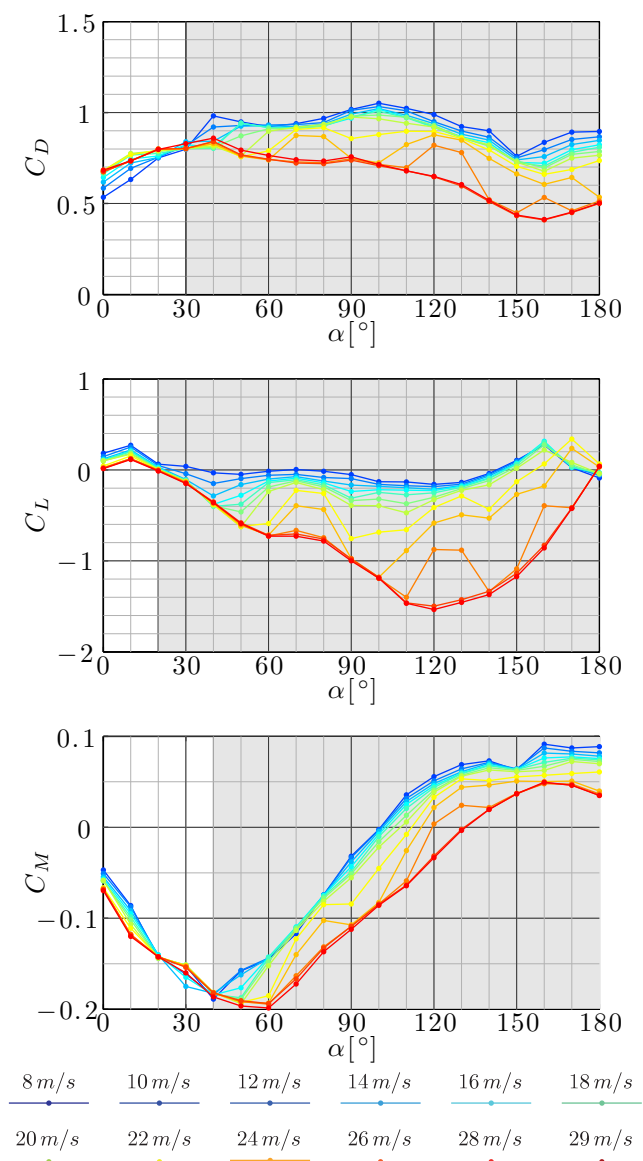


Figure 6.1: Drag, lift and moment coefficients for the cable with ice accreted in CC V1.

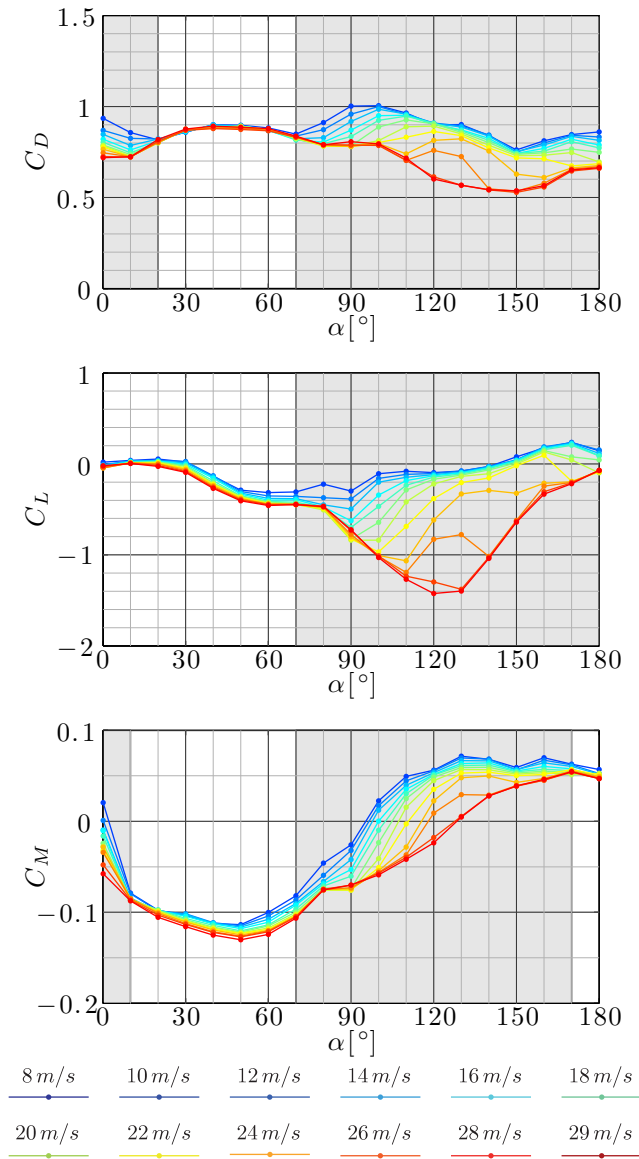


Figure 6.2: Drag, lift and moment coefficients for the cable with ice accreted in CC V2.

Common to all CCs is that the aerodynamic coefficients are only little dependent on wind speed for small angles of attack, whereas this dependency increases for larger angles. Another common feature is that the value of C_D decreases with increasing speed except for a very limited number of cases, as the effect of Reynolds critical behavior, and the maximum declining slope of C_L also does. Except for CC V3, the maximum declining slopes of C_L were observed for angles of attack in the range of 80° to 120° . Finally, in all the CCs, almost the same trend of C_M with respect to α was found. A more detailed description of the variation of the aerodynamic coefficients with angle of attack and wind speed follows, for the four CCs investigated.

In CC V1, C_D , C_L and C_M are slightly dependent on wind speed for angles of attack in the range of 0° to 30° , to 20° and to 40° , respectively. In this range, the shape of the windward accretion seems to determine separation from both sides of the cable. C_D increases from approximately 0.6 at 0° to approximately 0.8 at 30° . In this range, the maximum value of C_D is associated with the maximum wind speed, while for angles of attack in excess of 30° the maximum wind speed is associated to a minimum of C_D . C_L takes very small values, with a slight increase from 0° to 10° and a small decrease from 10° to 30° . C_M decreases from approximately -0.05 at 0° to approximately -0.15 at 30° . In the range of $\alpha = 20^\circ$ to 40° , the variation of C_M with the wind speed is reversed, a feature observed only in this CC. Outside these ranges, a pronounced dependency of the three aerodynamic coefficients on wind speed is observed. The maximum drag and the minimum lift are associated with the lowest wind speeds and the minimum drag and the maximum lift are associated with the highest wind speeds. Furthermore, independently of the angle of attack, C_D and C_L are almost independent of the wind speed below 22 m/s and above 28 m/s , whereas a strong variability of was observed in the range of 22 m/s to 26 m/s . This feature is common to all CCs. The transition is the effect of variations in the position of either one or both separation points, and it is observed that a reduction of C_D is accompanied by an increase in the negative value of C_L . This can be explained by a displacement of one of the separation points towards the clean side of the cable, thus reducing the width of the wake and increasing its asymmetry. In this CC the smallest values of the aerodynamic coefficients are found; the smallest C_L is found for $\alpha = 120^\circ$, and the smallest C_D is found for $\alpha = 160^\circ$. Moreover, the maximum C_D was found for $\alpha = 100^\circ$ at the smallest wind speed. At 100° the frontal area is maximum and for small values of the wind speed the wake is wider because the separation point is in the closest position to the stagnation point. In the range of 40° to 180° , C_M increases and becomes positive in the range of 100° to 130° , depending on wind speed. The maximum value of C_M is reached in the range of 160° to 180° . The maximum value of C_M , approximately the same for all CCs, is about 0.08. The smallest value of C_M is found in this CC for $\alpha = 60^\circ$ and is -0.20 .

In CC V2, the aerodynamic coefficients are almost independent of wind speed for α in the range of 0° to 70° . Only C_D and C_M show a moderate dependency

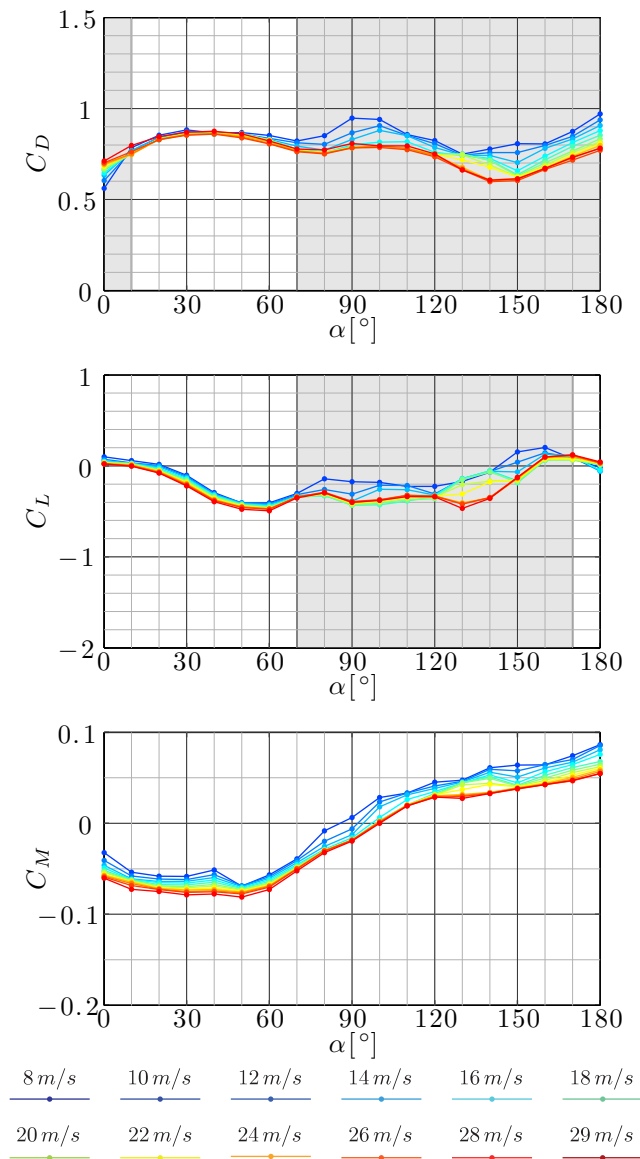


Figure 6.3: Drag, lift and moment coefficients for the cable with ice accreted in CC V3.

on wind speed in the range of 0° to 20° and to 10° , respectively, probably due to the shape of the ice accretion around the stagnation point. In particular, at $\alpha = 0^\circ$, C_M varies between -0.05 and 0.03 . In the range of 30° to 60° , C_D is almost constant around 0.9 , while C_L is almost constant around 0 in the range of 0° to 30° and decreases to approximately -0.3 from 30° to 70° . In the range of 10° to 50° , C_M slowly decreases to approximately -0.13 and in the range of 50° to 70° it increases back to 0.07 . In the range of 80° to 180° , a pronounced dependency of all the coefficients on wind speed was observed, with C_D and C_L having a similar behavior as in CC V1. The maximum C_D was found at 100° with a value of 1.04 , similar to CC V1. The minimum value of C_D and of C_L occurs approximately for the same angle of attack as in CC V1. Like in CC V1, a reduction of the largest values of C_D and C_M is observed for $\alpha = 150^\circ$. In the range of 80° to 150° , C_M strongly increases with wind speed, whereas in the range of 150° to 180° it is moderately dependent on wind speed and almost independent of the angle of attack. C_M becomes positive in the same range as in CC V1. The maximum and the minimum values of C_M are reached for the same wind speed and angle of attack as in CC V1. The minimum value of C_M is -0.13 , larger than in CC V1, probably due to the smaller windward accretion and to the presence of lateral iced rivulets.

In CC V3 the lowest dependence of the aerodynamic coefficients on wind speed was found. This is due to the different type of ice accretion (Figure 5.4). As in CC V2, C_D and C_L are nearly independent of wind speed in the range of $\alpha = 10^\circ$ to 70° and of $\alpha = 0^\circ$ to 70° , respectively. Differently, C_M is approximately independent on the wind speeds for all the values of α . In the range of $\alpha = 0^\circ$ to 70° , C_M has a similar variability to that found in CC V2, but smaller negative values. In the range of 70° to 180° , a moderate dependency of the three coefficients on wind speed was observed. In this range, C_D and C_L have a different behavior with respect to that found for CCs V1 and V2, as the effect of the different characteristics of the accretion in the windward and lateral areas, with respect to that found for CCs V1 and V2. The smallest value of the maximum of C_D is found in this CC, as the result of a small windward accretion. The maximum value of C_D in this CC is found at $\alpha = 90^\circ$, similarly to CCs V1 and V2. The largest minimum value of C_L was observed in this CC, the effect of massive lateral iced rivulets and a small windward accretion. In the range of 70° to 180° , C_M increases and becomes positive in the range of 90° to 100° , depending on wind speed. The maximum and the minimum values of C_M are reached for the same angles of attack as in CCs V1 and V2. The largest value of the minimum C_M was found in this CC, again the effect of the small windward accretion and of the massive presence of lateral iced rivulets.

Finally, in CC V4, the three aerodynamic coefficients are nearly independent of wind speed for α in the range of 0° to 80° . In the range of 0° to 40° , C_D increases from 0.8 to the largest value found in all CCs of 1.10 . This value is associated with the largest windward accretion of all CCs. In the range of 40° to 80° , C_D decreases to approximately 0.9 . C_L has the same behavior as in CCs V2

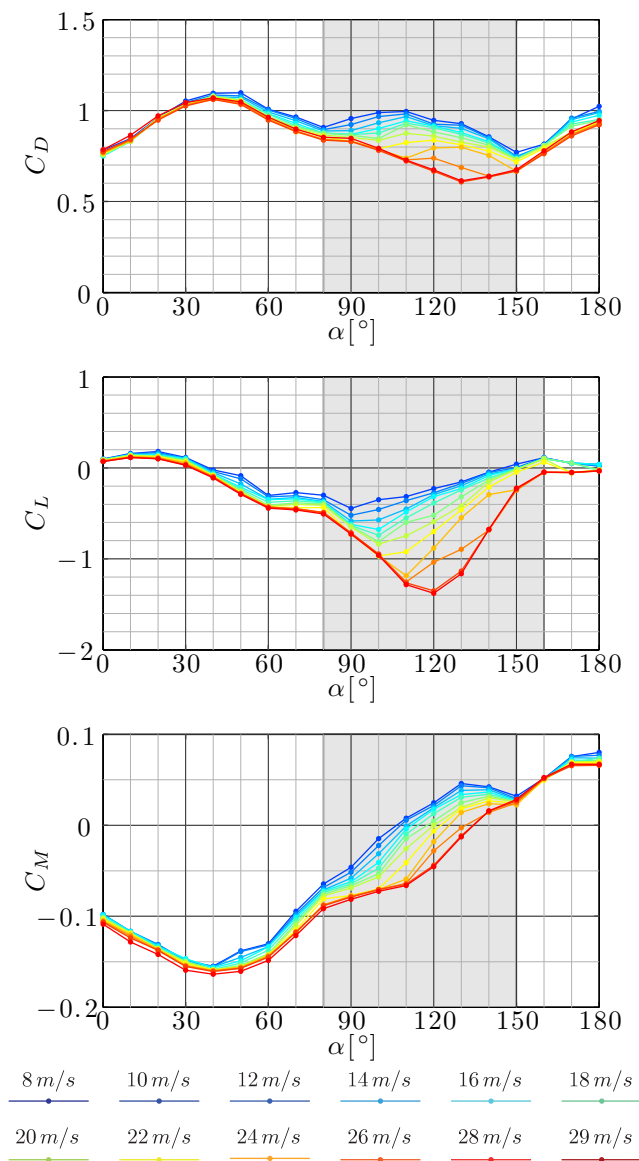


Figure 6.4: Drag, lift and moment coefficients for the cable with ice accreted in CC V4.

Table 6.2: Maximum and minimum values of C_x , C_y and C_M .

CC	Maximum			Minimum		
	C_x	C_y	C_M	C_x	C_y	C_M
I1	1.08	0.56	0.08	0.24	-0.66	-0.05
I2	1.36	0.36	0.20	0.19	-0.16	-0.03
I3	1.19	0.58	0.15	0.17	-0.18	-0.03
I4	1.17	0.58	0.25	0.29	-0.29	-0.06
I5	1.07	0.67	0.18	0.33	-0.21	-0.02
I6	0.79	0.29	0.11	0.36	-0.28	-0.04
I7a	0.92	0.35	0.10	0.30	-0.23	-0.02
I7b	0.89	0.35	0.08	0.30	-0.22	-0.01
I7c	0.95	0.46	0.12	0.29	-0.29	-0.02
I8	1.09	0.10	0.09	0.35	-0.77	-0.16
I9	1.24	0.31	0.04	0.36	-0.20	-0.02
I10	1.47	0.16	0.05	0.18	-1.65	-0.16
I11	1.19	0.04	0.03	0.18	-0.89	-0.12
I12	1.07	0.02	0.04	0.21	-0.52	-0.08

and V3, indicating that the presence of lateral iced rivulets influences the trend in this range. In the same range of angles of attack, C_M has the same behavior as in CCs V1 and V2, showing intermediate values between these two CCs. In the range of 90° to 150° , a dependency of the three coefficients on wind speed is observed, similar to that observed in CC V2. In particular, the same strong dependency on wind speed of C_D and C_L at $\alpha = 120^\circ$ and the reduction of the largest values of C_D and C_M for $\alpha = 150^\circ$ was observed. This two features are a common characteristic of the rime type dominant accretion (CCs V1, V2 and V3). In the range of 150° to 180° , the dependency of the three coefficients on wind speed reduces. In this range, the aerodynamic behavior is similar to that of CC V2, but with a lower dependence on wind speed. This effect can be due to the larger size of the lateral rivulets.

6.2 Stay cables

The mean aerodynamic force coefficients, C_x , C_y and C_M are normalized with respect to the mean wind tunnel speed, U , and to the diameter of the plain cable. The variation of the reference area due to the accretion and to the variation of β was not considered. No blockage correction was performed. C_x is the force coefficient associated with the force component parallel to U_N , C_y is the across-wind force coefficient perpendicular to C_x and C_M is the moment coefficient about z (Figure 4.46). The mean aerodynamic coefficients, measured for each CCs are shown in Figures 6.5 to 6.20, as a function of β for different values of

U . Grey hatched areas indicate the range of β where the dependency of the force coefficients with U is more pronounced. The vertical red line shows the yaw of accretion. The minimum and maximum values of the mean aerodynamic coefficients for each CC are also given in Table 6.2.

The aerodynamic behavior of the plain cable (CC I1) is shown as a reference case in Figure 6.5. The coefficients found are in agreement with the results from the literature (Larose *et al.*, 2005; Matteoni & Georgakis, 2012). An increase of C_x was observed in the range of $\beta = 0^\circ$ to 90° , and a reduction in the range of $\beta = 90^\circ$ to 180° . This variation is mainly due to a geometric effect, as the exposed area of the model increases in the range of $\beta = 0^\circ$ to 90° and decreases in the range of $\beta = 90^\circ$ to 180° . C_x is roughly symmetric with respect to $\beta = 90^\circ$, and its dependency on U is more pronounced for β around 90° . At $\beta = 90^\circ$, C_x decreased approximately from 1.1 to 0.5 with increasing U , whilst for $\beta = 0^\circ$ and $\beta = 180^\circ$ it decreased approximately from 0.4 to 0.2. This reduction is the effect of critical Reynolds conditions, where a single laminar bubble forms on one side of the cable creating a steady asymmetric pressure distribution. The reduction of C_x is accompanied by large (either positive or negative) values of C_y , otherwise small when β is close to 0° and 180° . As the yaw moves away from the two limiting cases, an increase in the values of C_y and of their dependency on U was observed, together with pronounced sign reversals. In a perfectly symmetric setup, the sign of C_y can be either positive or negative, depending on the side where the separation bubble forms; this is very sensitive to small perturbations (Schewe, 1986) and can therefore change in time. In an actual setup, perfect symmetry is never achieved, therefore when the model was rotated of 90° about its axis the variations of C_y in the critical regime changed completely, showing its dependency on the surface imperfections of the model (Matteoni & Georgakis, 2012). C_M was found to be in the narrow range of ± 0.05 and globally followed the trend of C_y , confirming that moment is the effect of a variable force with a fixed arm. To better understand the behavior in the critical regime, in Figure 6.6 time histories of C_x and C_y are shown, for the plain cable in CC I1 at $\beta = 90^\circ$, with increasing and decreasing wind velocity. In both cases, sudden jumps in the value of C_y , accompanied by sign reversals were observed, when the wind velocity was approximately 25 m/s, both when increasing and when decreasing; a similar result was found by (Larose *et al.*, 2005). These jumps were accompanied by smooth variation of C_x .

CCs I2 and I3 are characterized by the same yaw of accretion. The two CCs show trends of the aerodynamic coefficients, which are nearly independent of U (Figures 6.7 and 6.8). This independency was probably generated by the icicles (Figures 5.7a and 5.7b), that set geometric conditions for separation. C_x exhibited only a rough symmetry with respect to $\beta = 90^\circ$, as for CC I1. In the range of $\beta = 0^\circ$ to 90° , C_x increases approximately from 0.3 to 1.35 in CC I2 and to 1.2 in CC I3. The maximum value of C_x is reached at $\beta = 90^\circ$, when the core was rotated of 90° with respect to U_N and the exposed area was maximum. The large maximum value of C_x in CC I2 was therefore due to the large ice

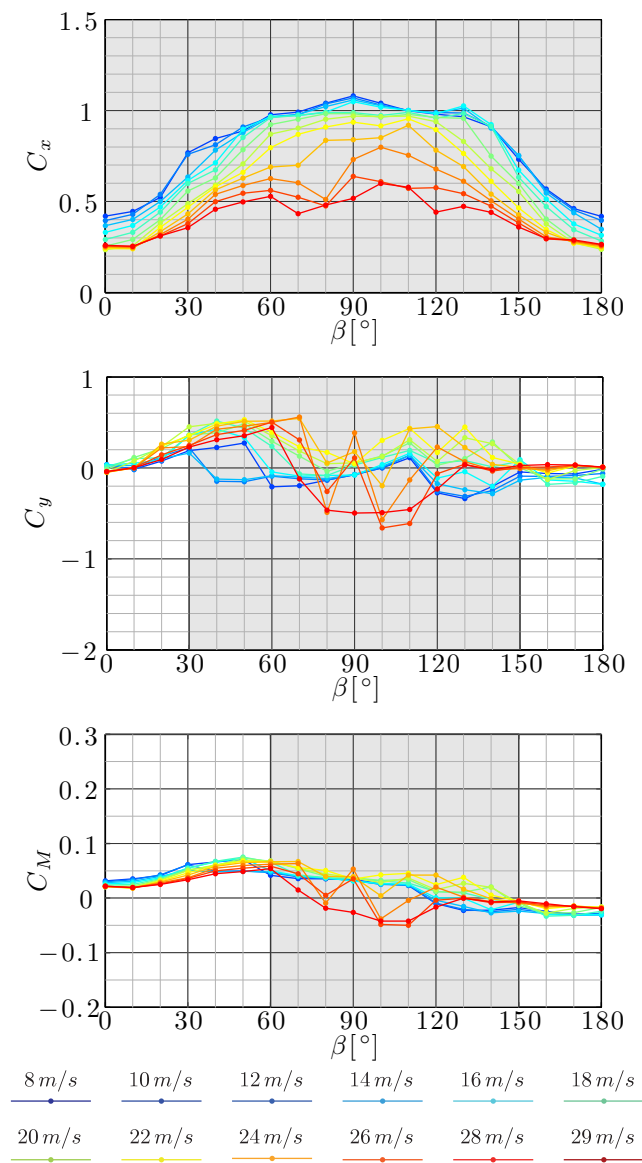
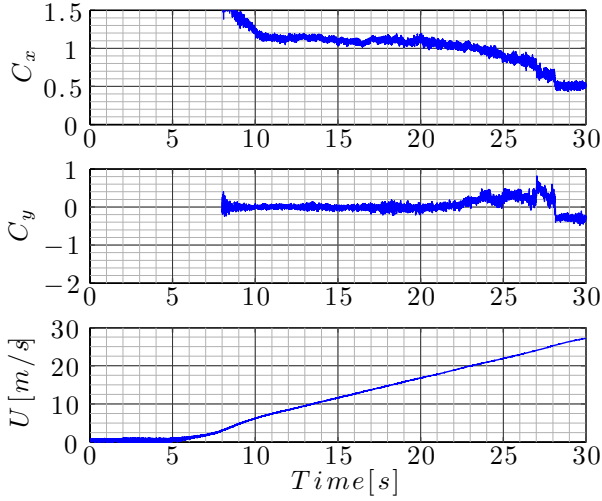
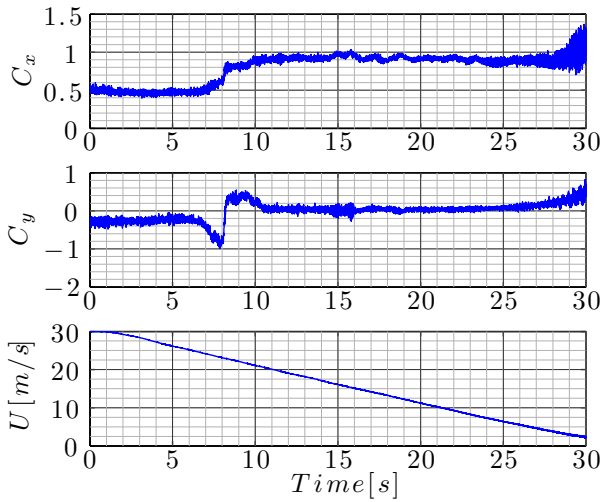


Figure 6.5: Variation with the yaw angle of the mean aerodynamic coefficients for different wind speeds, in CC I1.



(a)



(b)

Figure 6.6: Time history of C_x and C_y with increasing U from 0 to approximately 30 m/s (a) and decreasing U from 30 to approximately 0 m/s (b) at $\beta = 90^\circ$, in CC II.

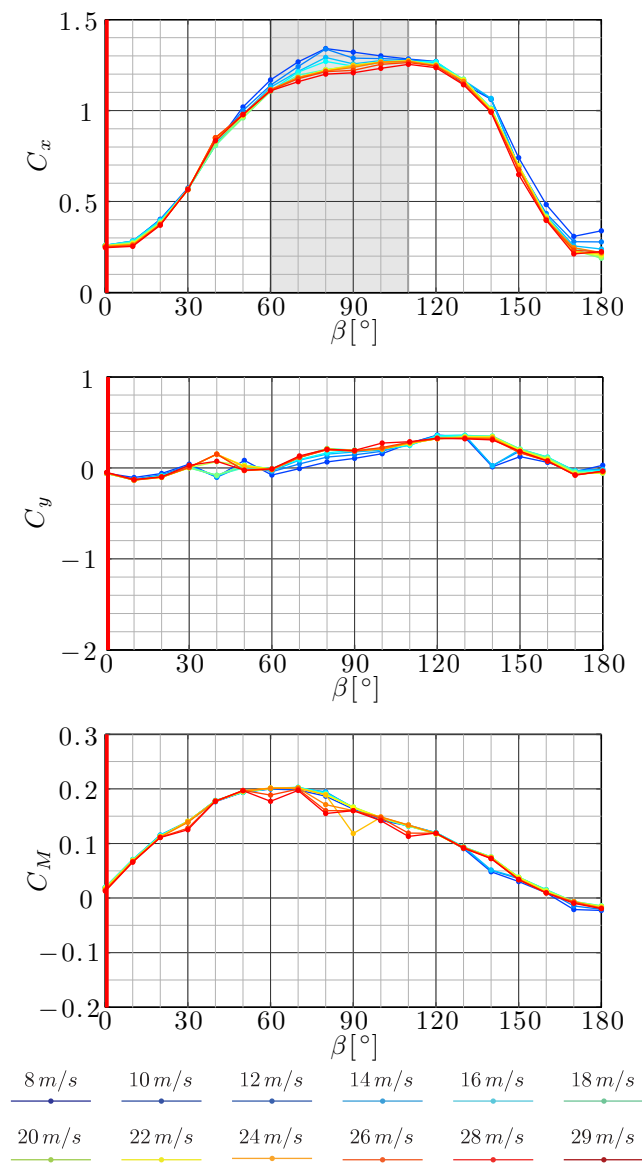


Figure 6.7: Variation with the yaw angle of the mean aerodynamic coefficients for different wind speeds, in CC I2.

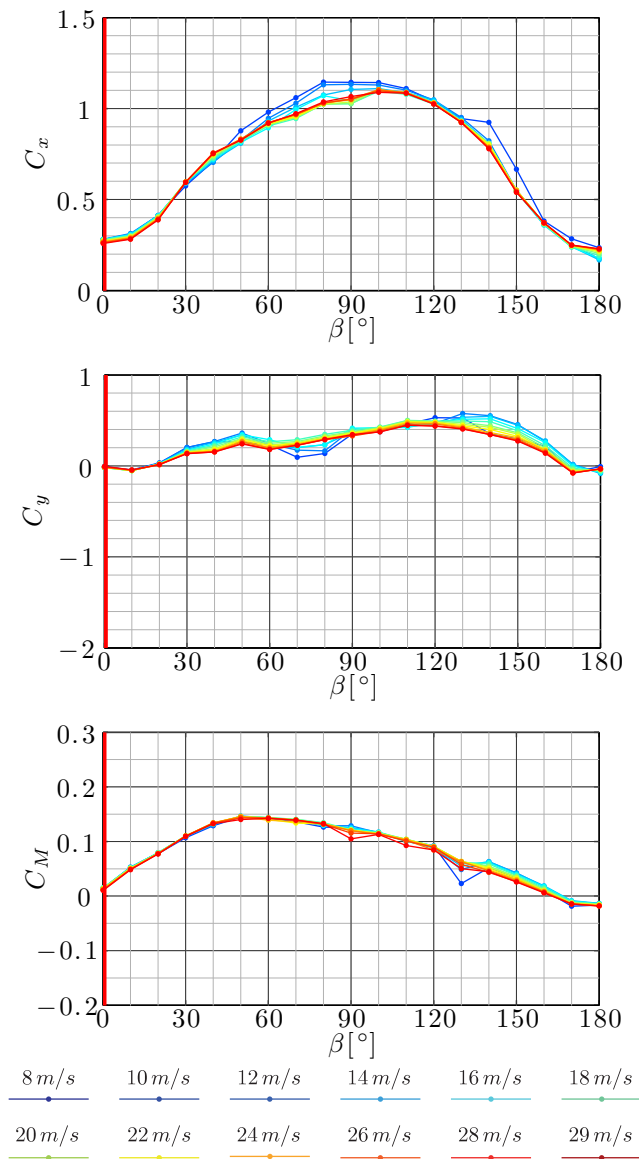


Figure 6.8: Variation with the yaw angle of the mean aerodynamic coefficients for different wind speeds, in CC I3.

accretion. In the range of $\beta = 90^\circ$ to 180° , C_x decreases to approximately 0.2. In CC I3 at $\beta = 180^\circ$, C_x takes its smallest value of 0.17 (Table 4.4). In the range of $\beta = 60^\circ$ to 100° , a minor dependency of C_x on U was observed. In the range of $\beta = 0^\circ$ to 130° , C_y grew from approximately 0 to 0.35 in CC I2 and to 0.58 in CC I3, to then decrease back to approximately 0 at $\beta = 180^\circ$. In both CCs, the maximum of C_y was found at approximately $\beta = 130^\circ$, and it is reasonable to think that this was due to the presence of icicle structures. As matter of fact, the larger value of C_y occurred in CC I3 where the icicles were more developed. In CCs I2 and I3, the maximum and minimum C_M occurred at approximately $\beta = 60^\circ$ and $\beta = 180^\circ$, respectively. At $\beta = 0^\circ$, C_M is 0 and increased up to 0.2 in CC I2 and up to 0.15 in CC I3 at $\beta = 60^\circ$, to decrease back to 0 at $\beta = 180^\circ$. The larger value of C_M was measured in CC I2, where the icicles were less developed and the centre ice is more accreted (Table 4.4).

In CCs I4 and I5, C_x was found to be about 0.4 for $\beta = 0^\circ$ and slightly decreasing for small values of β (Figures 6.9 and 6.10). In the range of $\beta = 20^\circ$ to 140° , C_x increased to maximum values of 1.17 in CC I4 and to 1.07 in CC I5. Above 70° and up to 180° in CC I4 and up to 150° in CC I5, a more pronounced dependency of C_x on U was observed up to 12 m/s , and a moderate dependency for larger values of U . In CC I5, C_x remains approximately constant between 0.8 and 1 for β in the range of 80° to 140° . In CC I4, a marked increase of C_x at the lowest values of U was observed at $\beta = 140^\circ$. In both CCs for $\beta > 140^\circ$, C_x decreases to approximately 0.5 at $\beta = 180^\circ$, and in CC I4 exhibited a small dependency on U , while in CC I5 it was almost independent of it. This independency was probably generated by the presence of iced rivulets, that imposed a geometric condition for separation. C_y was approximately 0 in the range of $\beta = 0^\circ$ to 60° in CC I4 and in the range of $\beta = 0^\circ$ to 30° in CC I5, in which it then increased up to 0.3 at $\beta = 60^\circ$. In CC I4, C_y becomes as large as 0.58 at $\beta = 120^\circ$ and decreases to approximately 0.3 at $\beta = 180^\circ$. In the range of $\beta = 70^\circ$ to 180° at $U = 8\text{ m/s}$, C_y showed a different trend with respect to the other wind speeds, indicating some aerodynamic transition at this wind speed. In particular, at $\beta = 140^\circ$, C_y underwent strong variations, consistently with the variations registered in C_x . In CC I5 in the range of $\beta = 60^\circ$ to 150° , C_y showed a more marked dependency on U with respect to CC I4. In the range of $\beta = 60^\circ$ to 90° , C_y slightly decreases to then increase again up to $\beta = 120^\circ$. In this configuration the ice accreted generated the maximum asymmetry of the section, driving a strongly asymmetric flow. As in CC I4, C_y decreased to approximately 0.3 at $\beta = 180^\circ$. At $\beta = 0^\circ$, C_M was -0.05 in CC I4 and 0 in CC I5 and then increased up to 0.25 for CC I4 and up to 0.18 for CC I5. The largest value of $C_M = 0.25$ was found in CC I4 (Table 4.4). Differently from CC I5, in CC I4 in the range of $\beta = 0^\circ$ to 40° C_M was negative. In both CCs, in the range of $\beta = 90^\circ$ to 180° , C_M decreased to 0.

In CCs I6 and I7a, the mean aerodynamic coefficients showed similar trends (Figures 6.11 and 6.12). In CC I6, the aerodynamic coefficients are almost independent of U . C_x is approximately 0.4 at $\beta = 0^\circ$, increases to 0.79 at

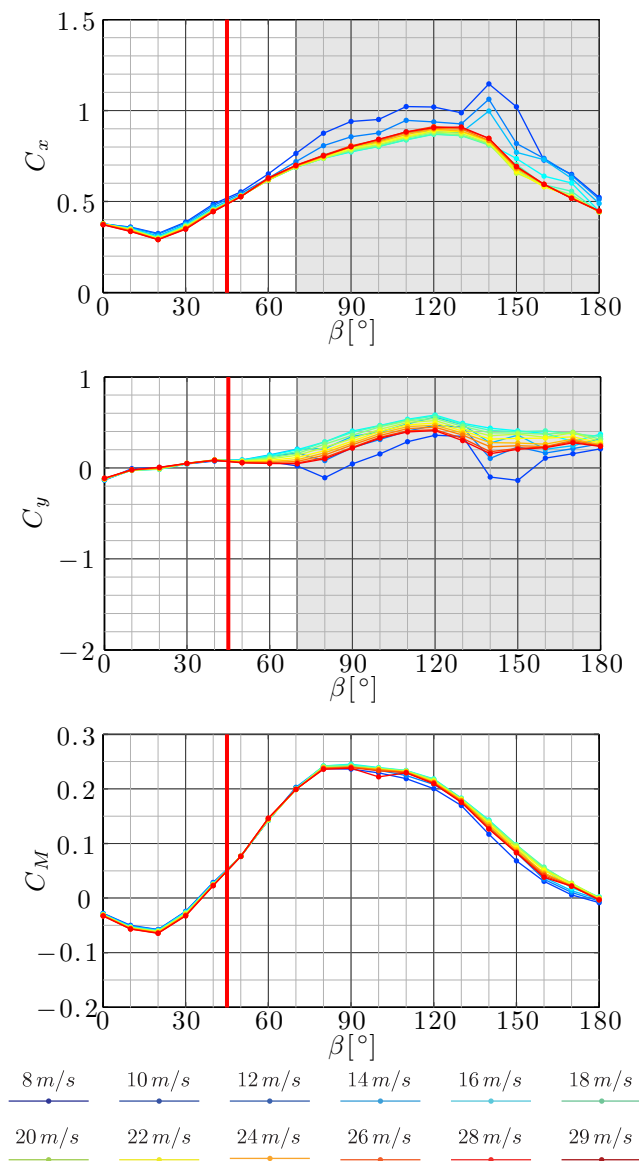


Figure 6.9: Variation with the yaw angle of the mean aerodynamic coefficients for different wind speeds, in CC I4.

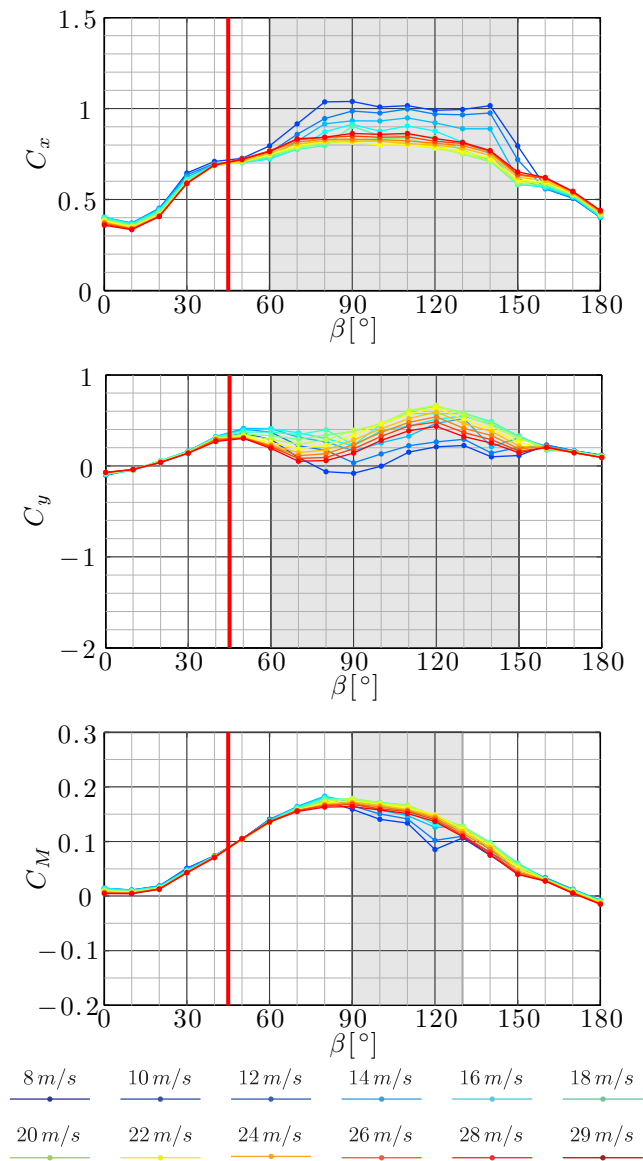


Figure 6.10: Variation with the yaw angle of the mean aerodynamic coefficients for different wind speeds, in CC I5.

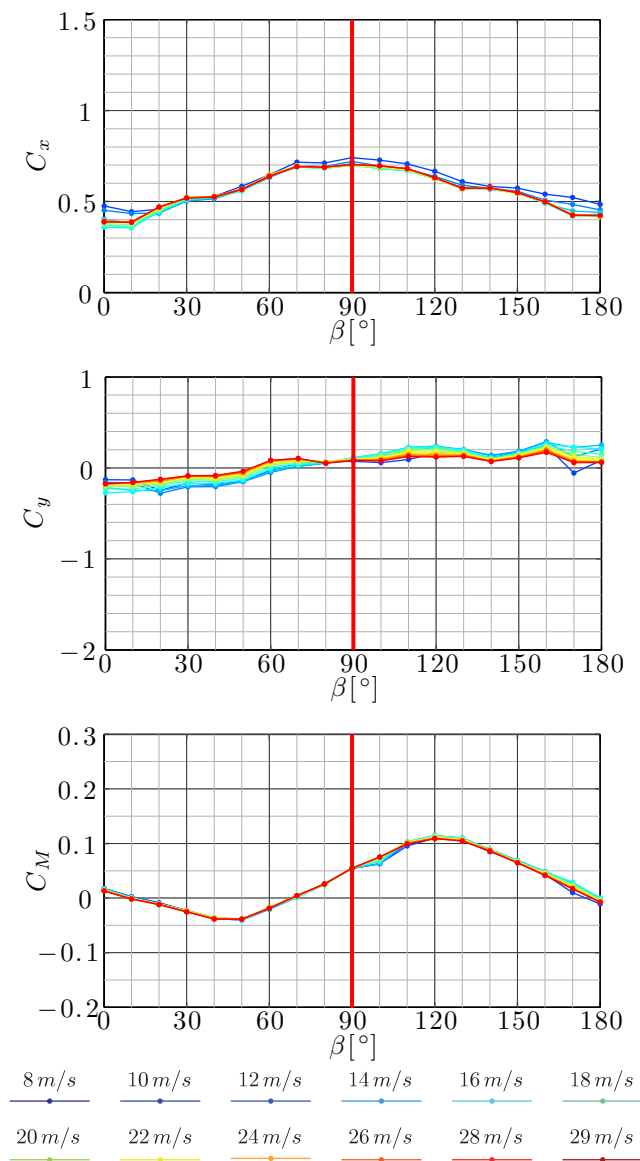


Figure 6.11: Variation with the yaw angle of the mean aerodynamic coefficients for different wind speeds, in CC I6.

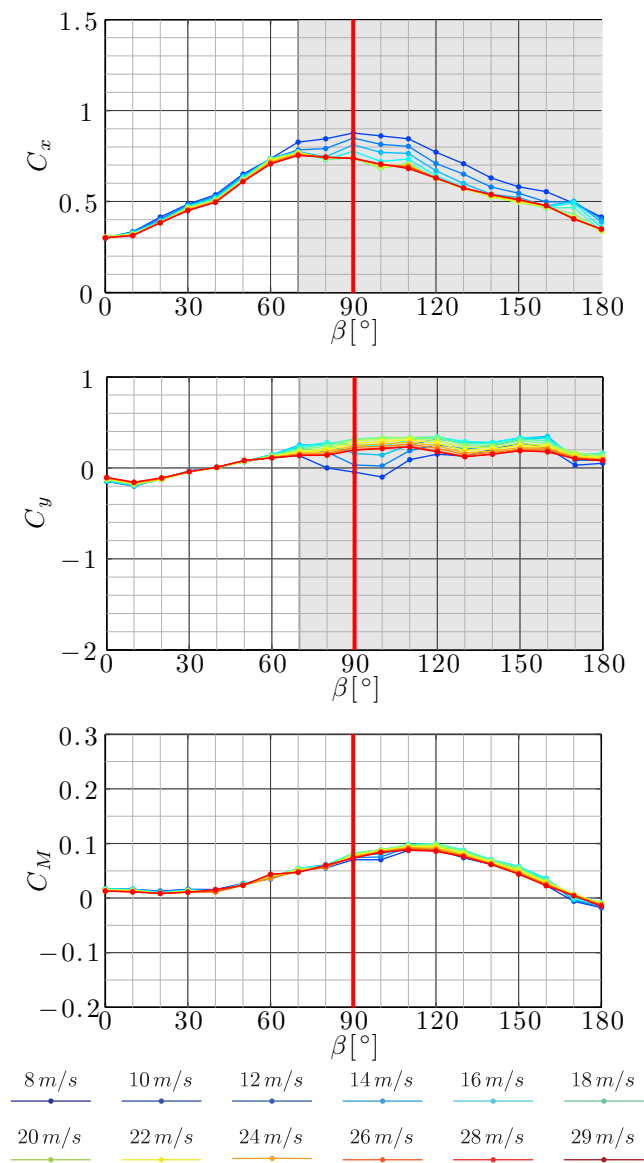


Figure 6.12: Variation with the yaw angle of the mean aerodynamic coefficients for different wind speeds, in CC I7a.

$\beta = 90^\circ$ and then decreased to approximately 0.4 at $\beta = 180^\circ$. The value reached by C_x at $\beta = 90^\circ$ is the smallest maximum value found in the tests, and is comparable with the results found with the model placed vertically at $\alpha = 0$ (Figures 6.1, 6.2, 6.3 and 6.4). C_y is approximately -0.2 at $\beta = 0^\circ$ and then grows to 0.2 at $\beta = 180^\circ$. In CC I7a, the trend of C_x is similar to that found in CC I6, with larger fluctuations with β and with a dependency on U in the range of $\beta = 60^\circ$ to 180° , limited to the lowest values of U . C_y has similar values to CC I6 and a dependency on U in the range of $\beta = 70^\circ$ to 180° . In both CCs, C_M is completely independent of U ; it is approximately 0 at $\beta = 0^\circ$, it decreases to -0.05 at $\beta = 50^\circ$, it grows back to 0.1 at $\beta = 120^\circ$ and finally it goes back to 0 at $\beta = 180^\circ$. Differently from CC I6, in CC I7a in the range of $\beta = 0^\circ$ to 50° C_M was nearly zero.

In CCs I7b and I7c, the aerodynamic coefficients are evaluated on the ice accreted cable rotated around its axis of $\alpha_r = +10^\circ$ and -10° , respectively (Figures 6.13 and 6.14). The rotation of the cable induced some variations in the aerodynamic coefficients. In particular, their dependency on U appeared to increase when decreasing α_r (CC I7c) and vice versa to decrease when increasing α_r (CC I7b). This effect is due to the increase, with increasing α_r , of the ice accreted surface exposed to the flow in the separation zone, which generates a geometric point of separation; the decrease of α_r produced an opposite effect. In CC I7c, this dependency is marked up to 16 m/s while in CC I7b up to 12 m/s . In CC I7c, C_y has a marked dependency on U in the range of $\beta = 70^\circ$ to 130° for U up to 14 m/s , whereas in CC I7a this dependency is less marked, and completely disappears in CC I7b. In CCs I7a, I7b and I7c, C_M showed similar trends and a general independency of U . Only in CCs I7c, a very moderate dependency of C_M on U was observed in the range of $\beta = 80^\circ$ to 110° . Comparison of CCs I7a, I7b and I7c shows how a variation of 10° of α_r produces clear modifications in the mean aerodynamic coefficients.

In CCs I8 and I9, the mean aerodynamic coefficients showed dependency and independency with respect to U , respectively (Figures 6.15 and 6.16). In both CCs at $\beta = 0^\circ$, C_x is approximately 0.4 and at $\beta = 80^\circ$ it increases up to 0.9 in CC I8 and up to 1.25 in CC I9, to then decrease to approximately 0.4 for $\beta = 180^\circ$. In CC I8, in the range of $\beta = 0^\circ$ to 110° at $U = 8\text{ m/s}$, C_x has a different trend, with larger values indicating an aerodynamic transition at this wind speed. In these CCs and in their symmetric cases (CCs I4 and I5), the maximum value of C_x is shifted by approximately -90° and $+90^\circ$ with respect to the yaw of accretion. In both CCs, C_y is approximately -0.2 at $\beta = 0^\circ$. In CC I8, C_y decreases to -0.7 and then increases again to 0 at $\beta = 110^\circ$, remaining then constant up to 180° . In CC I9, C_y showed a lower variation with respect of β . It remains constant up to $\beta = 50^\circ$ and then increases up to 0.3 at $\beta = 130^\circ$ and decreases down to 0 at $\beta = 140^\circ$ remaining constant up to 180° . In both CCs, C_M is approximately 0.025 at $\beta = 0^\circ$. In CC I8, C_M has pronounced variations with varying β , whereas in CC I9 it is almost 0 in the entire range of β . In CC I8, C_M decreases to -0.16 at $\beta = 90^\circ$, increased to

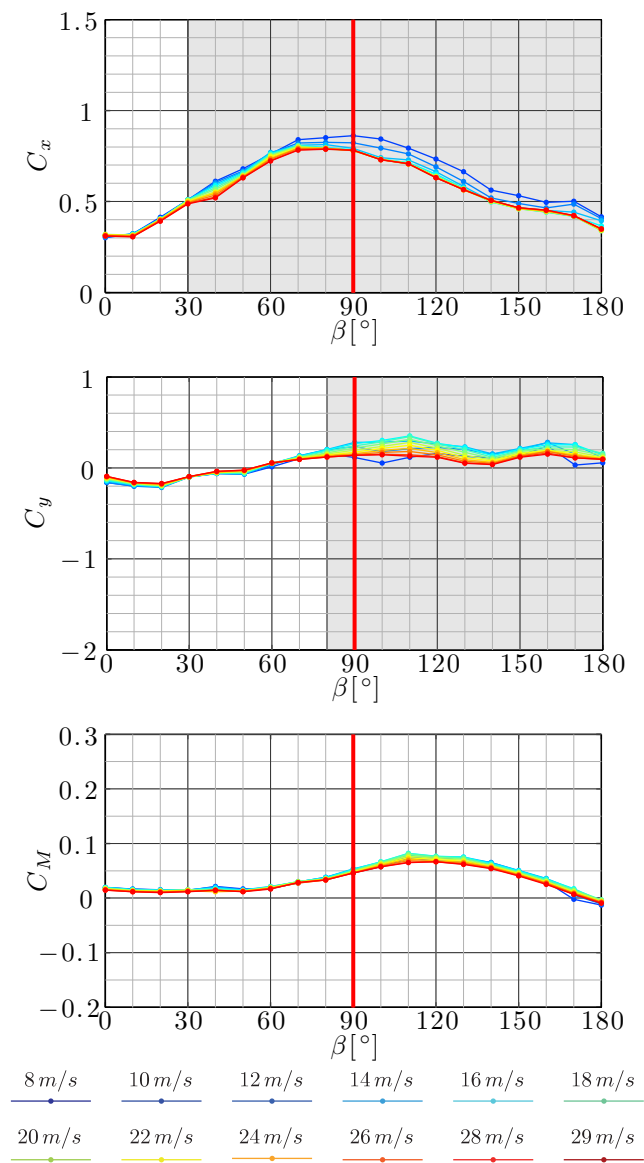


Figure 6.13: Variation with the yaw angle of the mean aerodynamic coefficients for different wind speeds, in CC I7b.

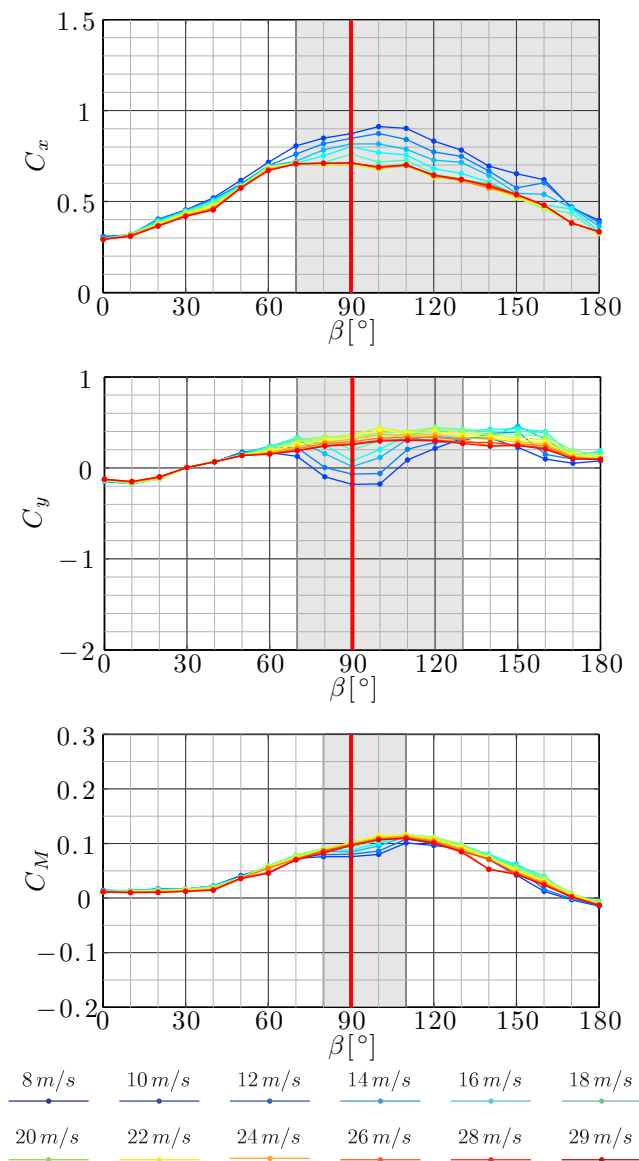


Figure 6.14: Variation with the yaw angle of the mean aerodynamic coefficients for different wind speeds, in CC I7c.

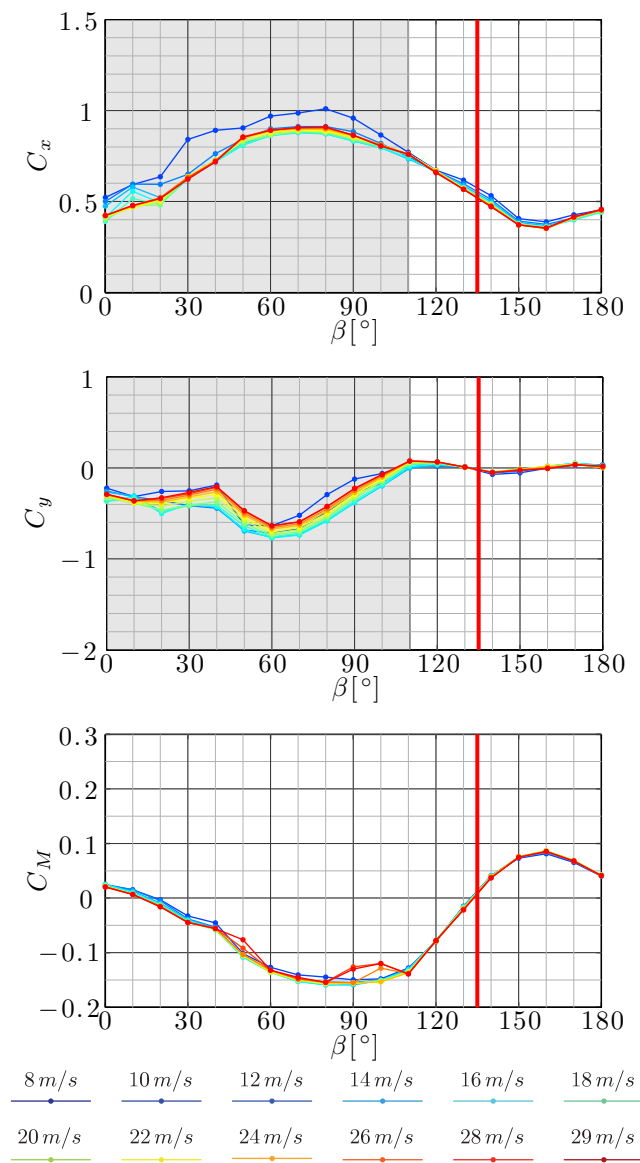


Figure 6.15: Variation with the yaw angle of the mean aerodynamic coefficients for different wind speeds, in CC I8.

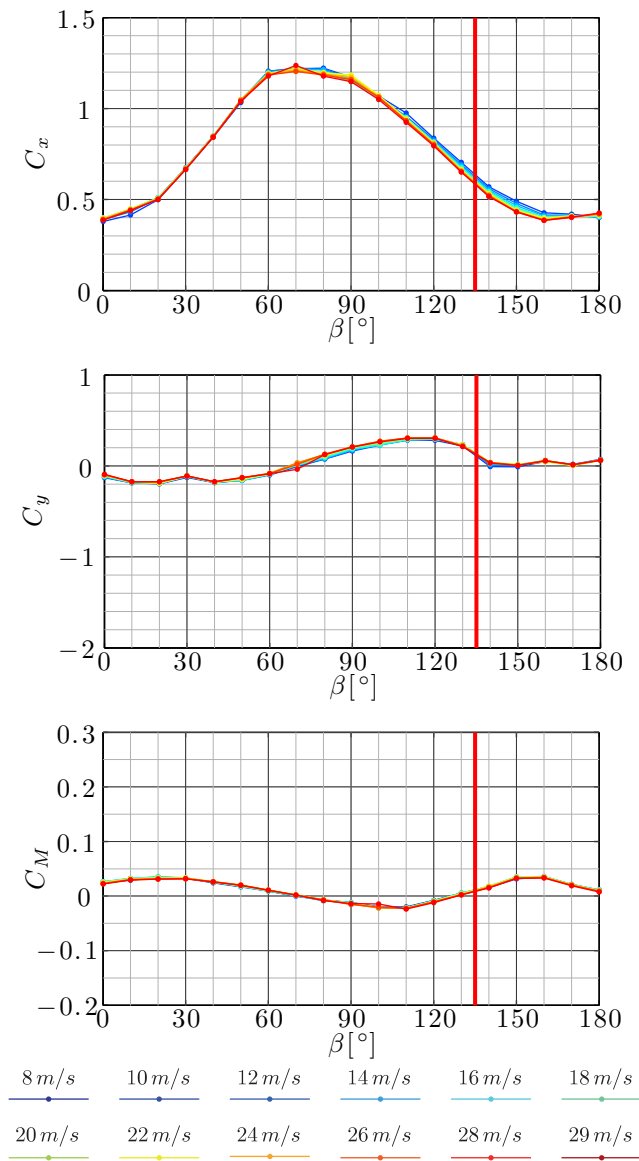


Figure 6.16: Variation with the yaw angle of the mean aerodynamic coefficients for different wind speeds, in CC I9.

0.09 at $\beta = 160^\circ$, and decreases to 0.05 at $\beta = 180^\circ$.

In CCs I10, I11 and I12, the mean aerodynamic coefficients show similar trends with β , nevertheless the values and the extension of the region of dependency on U are quite different from one case to another (Figures 6.17, 6.19 and 6.20). As found for the bridge hangers case (Section 6.1), decreasing the icing temperature increases the presence of iced rivulets on the lateral sides; as a consequence, the extension of the region of dependency of the aerodynamic coefficients on U reduces.

In CC I10 in the range of $\beta = 0^\circ$ to 30° , C_x has very similar values to those found in CC I1. In fact, in this range the core was rotated with respect to U_N of 180° , leaving the clean leeward part of the cable exposed to the flow, thus generating an aerodynamic condition similar to that of the plain cable. Above $\beta = 30^\circ$, the ice accreted modified, with respect to the plain case, the flow around the cable. The main effect was a general increase of C_x , more pronounced in the range of $\beta = 30^\circ$ to 150° , where the ice accreted was placed laterally with respect to U_N , thus increasing the exposed area. The largest value of C_x found in all the tests was found in this CC at the lowest value of U , at $\beta = 110^\circ$, where the largest maximum accretion was found (Table 4.4). In the range of $\beta = 150^\circ$ to 180° , the values of C_x are similar to the largest values found in CC I1, but the dependency on U is less pronounced, due to the presence of ice on the windward region, defining a geometric separation point. C_y has almost the same values as in CC I1 in the range of $\beta = 0^\circ$ to 20° . In the range of $\beta = 30^\circ$ to 150° , C_y is negative, with a pronounced dependency on U up to 24 m/s , as also for C_x . The ice accretion did not affect the dependency with U of C_y , but eliminated the sign reversals observed in the plain case (CC I1). The largest values of U tested gave rise to large negative values of C_y and small values of C_x , confirming the same behavior observed for the bridge hangers case (Section 6.1); in this case the flow separation point was free to move only on the clean lateral side of the cable, whereas it was fixed on the accreted side. The smallest value of C_y of all CCs was found in this CC at $\beta = 80^\circ$ equal to -1.65 . Similarly to C_x , in the range of $\beta = 150^\circ$ to 180° , C_y is independent of U . At $\beta = 100^\circ$ and $U = 22\text{ m/s}$ a tri-stable flow pattern was detected; sample time histories are shown in Figure 6.18. The first stable configuration was detected between 0 and 10 s. At approximately 10 s, a transition was observed, characterized by a reduction of C_x and an increase of C_y . This transition indicates a displacement of the separation line on the clean side of the cable, producing a reduction of the size of the wake and an increase in its asymmetry. At approximately 15 s, a second transition was observed, characterized by a minor adjustment of the aerodynamic coefficients towards the initial values. In CC I10, C_M like C_x has almost the same values as in CC I1 in the range of $\beta = 0^\circ$ to 30° . C_M is approximately 0 at $\beta = 0^\circ$ and remains constant up to $\beta = 40^\circ$. Above $\beta = 40^\circ$, C_M becomes strongly dependent on U , decreasing to -0.1 at the lowest value of U and to -0.18 at the largest value of U at $\beta = 130^\circ$. Above $\beta = 140^\circ$, C_M is again independent of U and increases to -0.03 at $\beta = 180^\circ$.

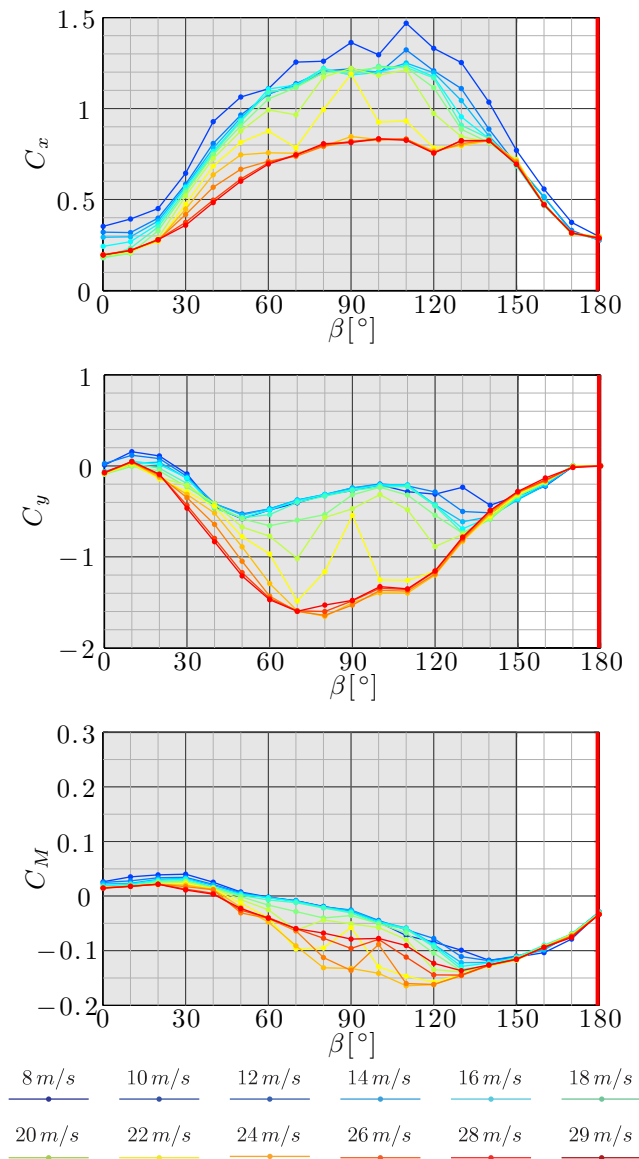


Figure 6.17: Variation with the yaw angle of the mean aerodynamic coefficients for different wind speeds, in CC I10.

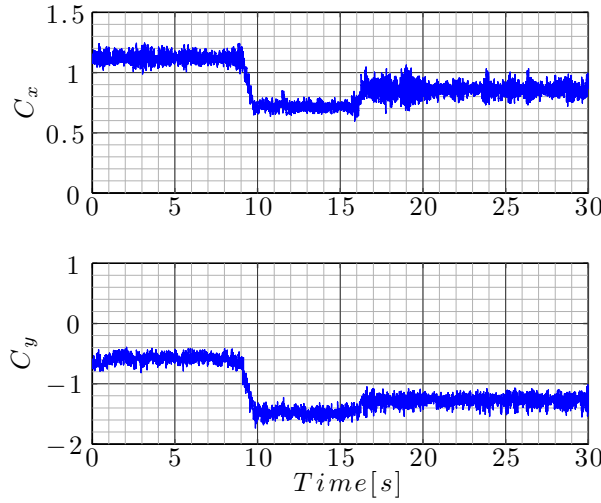


Figure 6.18: Time history of the drag and lift coefficients at 100° and 22 m/s , in CC I10.

In CCs I11 and I12, C_x , C_y and C_M have similar trends to those of CC I10; the main difference is in the extension of the region of dependency on wind velocity. In CC I11 this region is reduced to the range $\beta = 50^\circ$ to 120° and in CC I12 it vanishes. The values of C_x and C_y in CCs I11 and I12 are comprised in the range of the minimum to the maximum values found in CC I10; instead, C_M exceeds the maximum values of CC I10. In CCs I10, I11 and I12, the maximum of C_x and of $|C_y|$ and $|C_M|$ decreases with decreasing size of the accretion, indicating the relation between these parameters, as find for the vertical case.

In conclusion, the largest values of C_x were found at $\beta = 90^\circ$ for yaws of accretion of 0° and 180° . In these configurations the windward accretion was rotated of $\pm 90^\circ$ respect to U_N , thus maximizing the exposed area. The largest value of C_x among all CCs was found in CC I10, in which the maximum accretion was found. In all CCs, the minimum of C_x was reached for approximately $\beta = 0^\circ$ and $\beta = 180^\circ$, where the drag force is minimized, and the smallest values of C_x were found for yaws of accretion of 0° and 180° . The dependency of C_y and C_M on β was influenced by the yaw of accretion. CCs with the same yaw of accretion showed similar trends with respect to β and different values, which depend on the size and features of the accretion. The largest value of $|C_y|$ was found in CC I10. The largest value of C_x and $|C_y|$ were found for the same yaw and same CC, and for the largest and lowest wind speed, respectively. This mechanism is explained as the displacement of the separation line towards the clean side of the cable occurring with increasing the wind speed, which produces a reduction

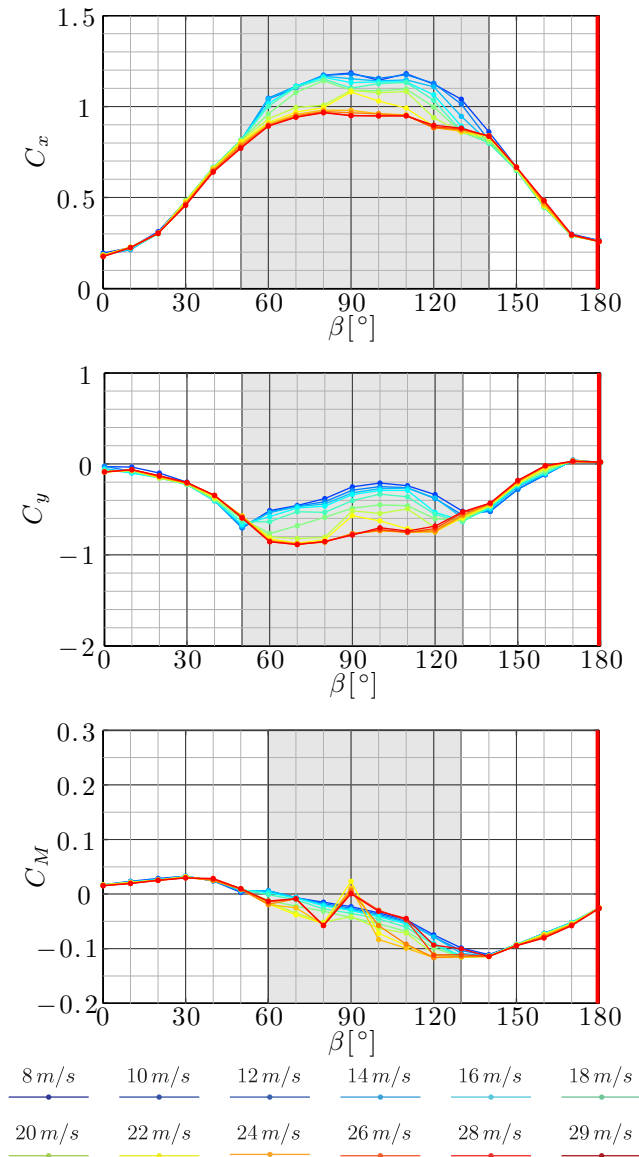


Figure 6.19: Variation with the yaw angle of the mean aerodynamic coefficients for different wind speeds, in CC I11.

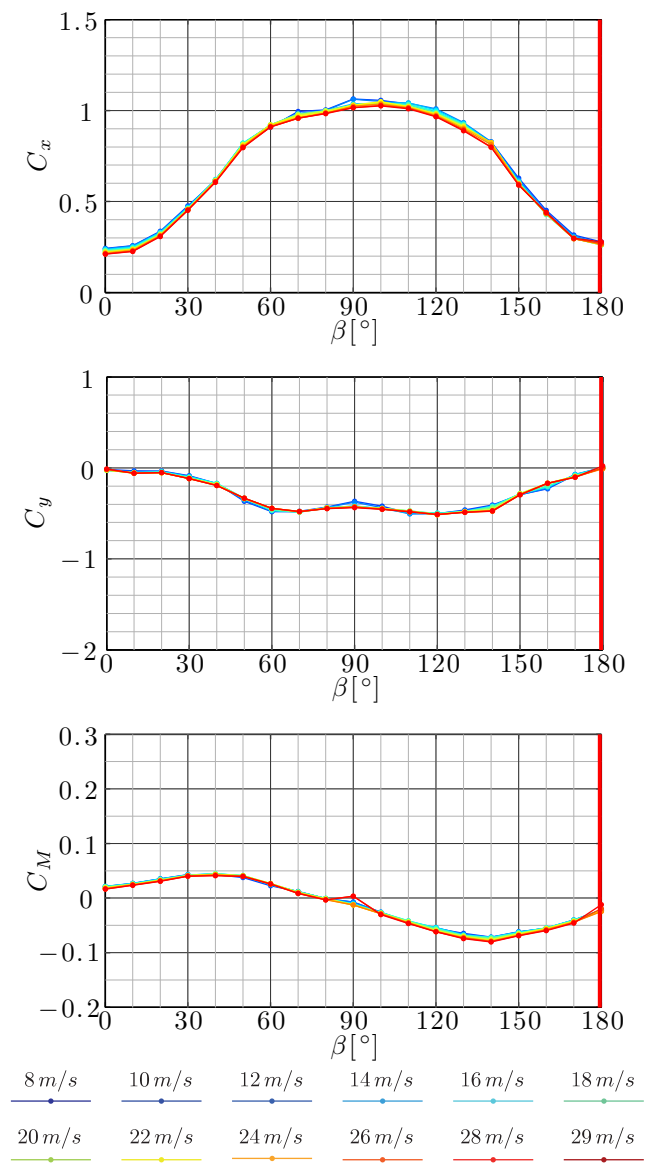


Figure 6.20: Variation with the yaw angle of the mean aerodynamic coefficients for different wind speeds, in CC I12.

of the size of the wake and an increase in its asymmetry. The largest value of $|C_M|$ was found in CCs I4. Only for CCs with yaws of accretion of 180° , the extension of the region of dependency on U showed a behavior similar to that found for bridge hangers case (Section 6.1). In these CCs, it was observed a dependency with U of the mean aerodynamic coefficients comparable with the plain case.

References

- Cooper, K.R., Mercker, E., & Wiedeman, J. 1999. Improved blockage corrections for bluff bodies in closed and open wind tunnels. *Wind engineering into the 21st century*, Larose and Livesey (eds).
- Larose, G.L., Zasso, A., & Giappino, S. 2005. *Experiments on a yawed stay cable in turbulent flow in the critical Reynolds number range*. 6th International Symposium on Cable Dynamics, Charleston.
- Matteoni, G., & Georgakis, C.T. 2012. Effects of bridge cable surface roughness and cross-sectional distortion on aerodynamic force coefficients. *Journal of Wind Engineering and Industrial Aerodynamics*, **104**, 176–187.
- Schewe, G. 1986. Sensitivity of transition phenomena to small perturbations in flow round a circular cylinder. *Journal of Fluid Mechanics*, **172**, 33–46.

CHAPTER 7

Quasi-steady model for self-excited and buffeting forces on cylinders

The purpose of models is not to fit the data but to sharpen the questions.

SAMUEL KARLIN.

In this Chapter a novel 3D/3DoFs quasi-steady aeroelastic model is proposed. The model is able to predict the linear aerodynamic instability and the buffeting response of a cylinder with generic cross-section, immersed in a turbulent wind flow. 3D refers to the flow conditions and 3 DoFs refer to the two orthogonal displacements, perpendicular to the body's axis, plus the rotation about the longitudinal body axis. The model incorporates the inertial coupling, i.e. the non-coincidence between the center of mass and the center of rotation between the DoFs. It also allows for variation of the force coefficients, i.e. drag, lift, and moment, with Reynolds number based on the flow velocity, with angle-of-attack, and cable-wind angle.

First, aerodynamic forces acting on the cylinder were modeled as non linear function of the cylinder's structural velocity along the 3 DoFs, of the structural rotation about the longitudinal axis, as well of the total wind velocity, which comprises a steady component and nil-mean fluctuating components. The forces are thus linearized about zero structural velocities, steady structural rotation

and about the steady component of the total wind velocity. The equations of motion were written by following the Euler-Lagrange method. Later, they are expressed in the state space representation.

Based on the analytical solution of the eigenvalue problem, by applying the Routh-Hurwitz criterion, an expression of the galloping- and static divergence-type instability condition is derived. A numerical solution of the minimum structural damping and structural stiffness required to prevent the same aerodynamic instabilities is given. The 3-D cross-sectional response to a turbulent flow is given considering both buffeting and self-excited contributions.

An application of the 3-DoFs analytical model was proposed to study the galloping and divergence stability of an ice-accreted cable conductor in cross flow, of a dry stay cable and of an ice-accreted stay cable.

This part is the result of a joint work carried out with Ph.D. candidate Giulia Matteoni of the Department of Civil Engineering - Technical University of Denmark.

7.1 Basics of aeroelasticity

Structures immersed in a flow, are subject to flow-induced forces and flow-induced vibration. These vibrations may be of small or large amplitude, and they may be inconsequential, or of moderate or even big concern. These phenomena are called *aeroelastics*, and the science that studies this interaction is called aeroelasticity.

A good example of aeroelasticity is on a regular plane wing. The wing is subjected to a flow, which results in lift generated. The lift deflects the wing and elastic forces will try to restore with an opposing force. Unless the forces are always balanced a net force is created and the wing will accelerate. From D'Alembert's principle one can establish that inertial forces will work to oppose this acceleration. As the wing moves the lift it generates changes. Aeroelasticity explodes when all three of these forces combine into a continuous feed back loop.

In 1947 Arthur Roderick Collar defined aeroelasticity as “*the study of the mutual interaction that takes place within the triangle of the inertial, elastic, and aerodynamic forces acting on structural members exposed to an airstream, and the influence of this study on design*” (Collar, 1978). The Collar's triangle is shown in Figure 7.1. Recently, in order to analyze aero-thermo-elastic problems, a new vertex is added to the triangle by becoming a pyramid. The fourth vertex represents the thermal effects.

In general, the behavior of a physical system in terms of its motion as a function of time is described by the equations of motions:

$$\mathbf{M}\ddot{\mathbf{x}} + \mathbf{C}\dot{\mathbf{x}} + \mathbf{K}\mathbf{x} = \mathbf{F}_m(\mathbf{U}) + \mathbf{F}_b(\mathbf{U}'(t)) + \mathbf{F}_a(\mathbf{U}, \dot{\mathbf{x}}, \mathbf{x}) + \mathbf{F}_s(St, Sc) \quad (7.1)$$

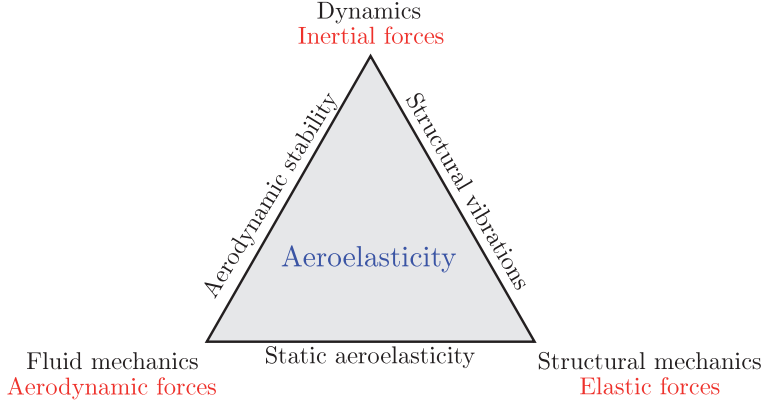


Figure 7.1: Collar's aeroelastic triangle.

where \mathbf{M} is the mass matrix, \mathbf{C} is the damping matrix, \mathbf{K} is the stiffness matrix, $\mathbf{F}_m(\mathbf{U})$ is the vector containing the mean forces, $\mathbf{F}_b(\mathbf{U}'(t))$ is the vector containing the (nil mean) forces induced by the fluctuating wind velocity, $\mathbf{F}_b(\mathbf{U}'(t))$ is the vector containing the (nil mean) forces induced by the fluctuating wind velocity, $\mathbf{F}_a(\dot{\mathbf{x}}, \mathbf{x})$ is the vector containing the aerodynamic forces and $\mathbf{F}_s(St, Sc)$ is the vector containing the (nil mean) fluctuating components of the wind loads associated with vortex shedding. $\ddot{\mathbf{x}}$, $\dot{\mathbf{x}}$ and \mathbf{x} are the vector containing the structural accelerations, velocity and displacements, respectively. \mathbf{U} is the vector containing the mean wind speed and $\mathbf{U}'(t)$ is the vector containing the (nil mean) fluctuating components of the wind speed. St is the Strouhal number defined as:

$$St = \frac{f_w D}{U} \quad (7.2)$$

where f_w is the vortex shedding frequency (or the Strouhal frequency) of a body at rest, D is the characteristic dimension of the body, and U is the mean velocity of the flow. Sc is the Scruton number defined as:

$$Sc = \frac{M\xi}{\rho D^2} \quad (7.3)$$

where M is the mass, ξ is the damping ration and ρ is the fluid density. In the case of M-DoFs systems M and ξ are related to the values of the dominant mode. Most types of wind-induced oscillation tend to be mitigated by increasing the Scruton number.

The interactions among forces and structure in Equation 7.1 generates aeroelastic phenomena. Some of the most important phenomena, among all, taken place on civil structures are:

- Vortex induced vibrations;
- Divergence;
- Flutter;
- Galloping;
- Buffeting.

In the following, each instability is described in qualitative terms.

Vortex-induced vibrations (VIV) are motions induced on bodies interacting with an external fluid flow, produced by periodical irregularities on this flow. It is related to the term $\mathbf{F}_s(St, Sc)$. The Strouhal number relates to the frequency of shedding while the Scruton number relates to the structural properties. The phenomenon of *lock-in* happens when the vortex shedding frequency becomes close to a natural frequency of vibration of the structure:

$$f_p \approx f_w \quad (7.4)$$

where f_p is the structure's oscillation frequency related to the values of the dominant mode. When this happens large and damaging vibrations can result.

There are two interpretations of aeroelastic forces where one can consider them to be an external force or be linearized to become a stiffness and damping terms. Considering the forces as the last case:

$$\mathbf{F}_a(\mathbf{U}, \dot{\mathbf{x}}, \mathbf{x}) = \mathbf{C}_a(\mathbf{U})\dot{\mathbf{x}} + \mathbf{K}_a(\mathbf{U})\mathbf{x} = \mathbf{C}_a(\omega_r)\dot{\mathbf{x}} + \mathbf{K}_a(\omega_r)\mathbf{x} \quad (7.5)$$

The aeroelastic forces are usually expressed as function of the reduced frequency that is the dimensionless number used in general for the case of unsteady aerodynamics and aeroelasticity and is equal to:

$$\omega_r = \frac{2\pi f_p D}{U} \quad (7.6)$$

The forces reported in Equation 7.5 can lead to three phenomena: divergence, flutter and galloping.

Divergence is a static instability occurring when a surface deflects under aerodynamic load so as to increase the applied load, or move the load so that the twisting effect on the structure is increased. The increased load deflects the structure further, which eventually brings the structure to the diverge point. This condition occurs when the stiffness of the aeroelastic effects overcome the natural stiffness in the system:

$$\mathbf{K} = \mathbf{K}_a(\omega_r) \quad (7.7)$$

Flutter and galloping are driven by the aeroelastic damping term, $\mathbf{C}_a(\mathbf{U})$. The damping term gives a good physical interpretation of aeroelastic phenomena. When the aeroelastic damping is positive the aeroelastic effects act to

dampen the vibrations; work is done by the system on the fluid. When the aeroelastic damping is negative the aeroelastic effects will draw energy from the fluid onto the structures; the result is a rapid growth in the vibrational amplitude. This is the birth of the flutter or galloping phenomenon. This condition occurs when the damping of the aeroelastic effects overcome the natural stiffness in the system:

$$\mathbf{C} = \mathbf{C}_a(\omega_r) \quad (7.8)$$

The difference between the galloping and flutter is that only in the first case the quasi-steady assumption is taken to apply. The quasi steady theory assumes the characteristic fluid-dynamic time scale of the velocity fluctuations in the wake of the cylinder is much faster than the characteristic time scale of the cylinder's oscillation. The assumption can be formulated as:

$$f_p \ll f_w = \frac{StU}{D} \quad (7.9)$$

The assumption implies that the wind sees the cylinder as a static object, and the aerodynamic forces can be evaluated using the mean aerodynamic force coefficients measured experimentally in static conditions, at the instantaneous cylinder's geometry and for the instantaneous velocity field. These conditions are met where no vortex shedding lock-in and/or flutter occur. Differently in the flutter analysis, aeroelastic forces are described through the dimensionless flutter derivatives, which are treated as cross sectional properties that are functions of the reduced frequency of motion. Using Equation 7.6, galloping aeroelastic damping term, $\mathbf{C}_{a,g}$, can be obtained as the damping forces of flutter in which the reduce frequency tends to 0:

$$\mathbf{C}_{a,g} = \lim_{\omega_r \rightarrow 0} \mathbf{C}_a(\omega_r) \quad (7.10)$$

The linearized quasi-steady model represents in fact the asymptotic aerodynamic behavior for the non dimensional frequency reducing to zero.

Finally, buffeting is related to the fluctuating components the (nil mean) forces induced by the fluctuating wind velocity. The wind turbulence is generally classified based on the space and time scale. The small-scale turbulence modifies the aerodynamic characteristics of such bodies where the position of the separation point can change, thus producing an effect on the aerodynamic force coefficients. The large-scale turbulence, which changes more slowly, generates a variation of the wind velocity and of the relative aerodynamic loading. The load variation can produce random forced vibration which can generate a type of instability named buffeting. Buffeting is defined as the unsteady loading of a structure by velocity fluctuations in the oncoming flow. It causes irregular motions in the bridge structure. Buffeting does not usually endanger the safety of the structure, but can result in discomfort for the users and lead to fatigue of structural elements.

7.2 Derivation and linearization of the aeroelastic model

In this Section the aerodynamic forces and the equations of motion are derived. The resulting equations of motion for the cylinder are non-linear. A typical approach to solve and analyze non-linear dynamic models is to approximate the non-linear equations characterizing the equilibrium point with linear ones. In the following, the non-linear equations describing the aerodynamic and mechanical model are derived. The terms related to the fluctuating components of the wind loads associated with vortex shedding are not considered, although their inclusion in the model is simple. These equations are then linearized by performing a first order Taylor approximation around the system's steady state, i.e. the equilibrium point.

7.2.1 Flow around stationary inclined cylinders

A cylinder of generic section is immersed in a conventional turbulent wind field. This is modeled by a mean wind velocity component U , and by fluctuating wind velocity components along three orthogonal directions, $u'(t)$, $v'(t)$, $w'(t)$. A global reference system (X, Y, Z) is defined, where the X , Y axes lay on a horizontal plane and are parallel to U , $u'(t)$ and $v'(t)$, respectively, while Z is vertical, and parallel to $w'(t)$, see Figure 7.2. The total wind velocity $\mathbf{U}(t)$ is given by:

$$\mathbf{U}(t) = \mathbf{U} + \mathbf{U}'(t) = [U \quad 0 \quad 0]^T + [u'(t) \quad v'(t) \quad w'(t)]^T \quad (7.11)$$

The attitude to the flow of a cylinder is described by the inclination Θ , i.e. the angle between the body's longitudinal axis and its projection in the horizontal plane, and the yaw angle β , i.e. the angle between the free-stream velocity U and the projection of the body's axis in the horizontal plane. In general, for civil engineering applications, the inclination is a physical/geometrical characteristic, while the yaw depends on the wind direction. A local reference system for the cylinder (x, y, z) is introduced, where x , y belong to its cross-sectional plane and z is parallel to the cylinder's longitudinal axis. If the cylinder is considered to be initially oriented parallel to the global Z axis, so that the local and global reference systems are coincident, the inclined/yawed configuration is obtained after a sequence of two elemental rotations, see Fig. 7.2. The first rotation, of entity $(\pi/2 - \Theta)$, is about the Y axis, while the second rotation, of entity $-\beta$, is about the Z axis.

The total wind vector in the rotated local reference system for the cylinder

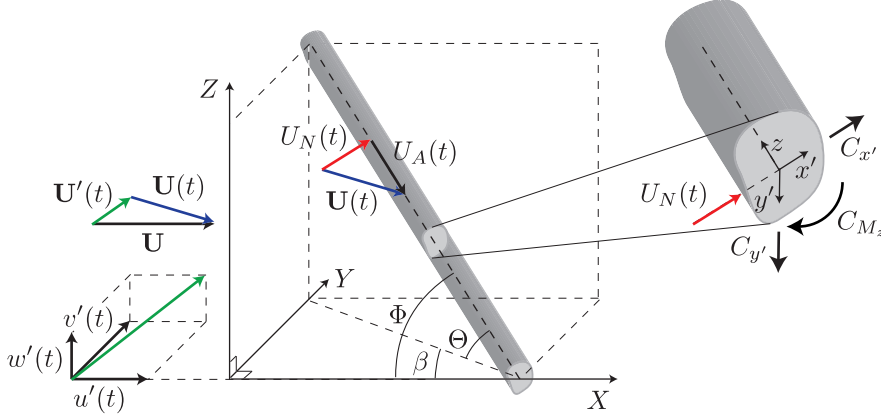


Figure 7.2: 3D geometry of the cylinder and flow and force coefficients definitions.

is given by:

$$\begin{aligned} \mathbf{U}_r(t) &= \mathbf{R}_Y(\pi/2 - \Theta) \mathbf{R}_Z(-\beta) \mathbf{U}(t) \\ &= \begin{bmatrix} \sin \Theta \cos \beta (U + u'(t)) + \sin \Theta \sin \beta v'(t) + \cos \Theta w'(t) \\ -\sin \beta (U + u'(t)) + \cos \beta v'(t) \\ -\cos \Theta \cos \beta (U + u'(t)) - \cos \Theta \sin \beta u'(t) + \sin \Theta w'(t) \end{bmatrix} \end{aligned} \quad (7.12)$$

where $\mathbf{R}_Y(\pi/2 - \Theta)$, $\mathbf{R}_Z(-\beta)$ are the rotation matrices around the axis Y and Z respectively.

The total component of the wind velocity in the cylinder's section, named normal flow velocity, $U_N(t)$, is given by:

$$\begin{aligned} U_N(t) &= \sqrt{(U_{r,1}(t))^2 + (U_{r,2}(t))^2} = \\ &= \sqrt{(\sin \Theta \cos \beta (U + u'(t)) + \sin \Theta \sin \beta v'(t) + \cos \Theta w'(t))^2 + \\ &\quad + (-\sin \beta (U + u'(t)) + \cos \beta v'(t))^2} \end{aligned} \quad (7.13)$$

The component of the wind velocity along the cylinder's longitudinal axis, known as axial wind velocity, is:

$$U_A(t) = U_{r,3}(t) = -\cos \Theta \cos \beta (U + u'(t)) - \cos \Theta \sin \beta v'(t) + \sin \Theta w'(t) \quad (7.14)$$

The angle $\Phi(t)$ between the cylinder's axis and the free-stream velocity \mathbf{U} is

given by:

$$\begin{aligned}\Phi(t) &= \arccos\left(\frac{|U_A(t)|}{U + u'(t)}\right) \\ &= \arccos\left(\frac{|-\cos\Theta \cos\beta (U + u'(t)) - \cos\Theta \sin\beta v'(t) + \sin\Theta w'(t)|}{U + u'(t)}\right)\end{aligned}\quad (7.15)$$

A second local reference system (x', y', z) is chosen for the cylinder, so that the local axis x' is parallel to the direction of the normal wind velocity $U_N(t)$ (Figures 7.2 and 7.3). The wind velocity vector in the (x', y', z) reference system is:

$$\mathbf{U}_{r'}(t) = \begin{bmatrix} U_N(t) & 0 & U_A(t) \end{bmatrix}^T \quad (7.16)$$

The angle between $U_N(t)$ and the plane containing the cylinder's longitudinal axis and its horizontal projection, i.e. the angle between x', y' and x, y , is:

$$\alpha_s(t) = \arctan\left(\frac{U_{R,2}}{U_{R,1}}\right) \quad (7.17)$$

7.2.2 Flow around moving inclined cylinders

For a single rigid body, the planar motion in two dimensions can be described in term of 3 DoFs defined at the shear centre (Takashi & Hughes, 1992), represented by the vector:

$$\mathbf{q}(t) = [\xi(t) \quad \eta(t) \quad \theta(t)]^T \quad (7.18)$$

where $\xi(t)$ and $\eta(t)$ are two orthogonal displacements with generic orientation belonging to the cylinder's cross section plane and $\theta(t)$ is the rotation about the cylinder's longitudinal axis. Most commonly, as in this analysis, the displacements $\xi(t)$ and $\eta(t)$, are assumed to be parallel to the vertical in-plane and out-of-plane directions, x and y , respectively. The structural velocity and acceleration are given by the first and second time derivatives of the displacement vector $\mathbf{q}(t)$, and are indicated as $\dot{\mathbf{q}}(t)$ and $\ddot{\mathbf{q}}(t)$, respectively.

The cross-radial tangential velocity varies in intensity and direction along the cylinder's cross-sectional boundary, due to the effect of $\dot{\theta}(t)$. In fact, its intensity is given by:

$$|\mathbf{R} \wedge \dot{\theta}(t)| \quad (7.19)$$

where \mathbf{R} is the position vector of a generic point located on the cylinder's section boundary in relation to the shear center (or center of rotation). The direction is tangent to the cylinder's cross-section at the specific point of evaluation. Following Blevins (1977), the velocity field on the cross section's boundary is thus approximated by choosing a reference point, at distance R_δ from the shear

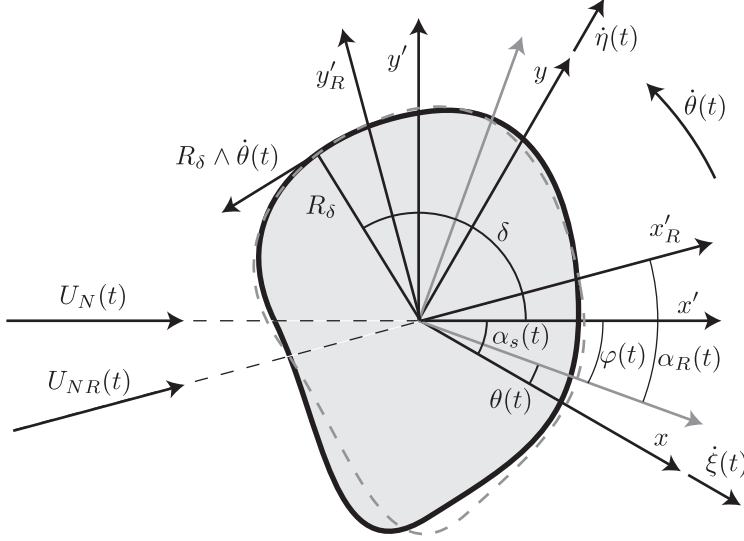


Figure 7.3: Plane normal to the cylinders's axis.

center and at angular distance δ from the x' local axis, which is representative of the net flow field. Normally this point is located at the leading edge. In the case of circular sections, R_δ is usually assumed as $D/2$ and δ as 90° . Alternative to this approach is to perform a full series of dynamic tests in order to characterize the forces on a rotating cross-section (Blevins, 1977).

The angle $\varphi(t)$, Figure 7.3, is defined as:

$$\begin{aligned} \varphi(t) &= \alpha_s(t) - \theta(t) \\ &= \arctan \left(\frac{-\sin \beta (U + u'(t)) + \cos \beta v'(t)}{\sin \Theta \cos \beta (U + u'(t)) + \sin \Theta \sin \beta v'(t) + \cos \Theta w'(t)} \right) \\ &\quad - \theta(t) \end{aligned} \quad (7.20)$$

The vector $\dot{\mathbf{q}}_R(t)$, defined as:

$$\begin{aligned} \dot{\mathbf{q}}_R(t) &= \mathbf{R}_z(-\varphi(t)) \dot{\mathbf{q}}(t) + \dot{\boldsymbol{\omega}}(t) \wedge \mathbf{R}_\delta = \\ &= \begin{bmatrix} \cos \varphi(t) & \sin \varphi(t) & 0 \\ -\sin \varphi(t) & \cos \varphi(t) & 0 \\ 0 & 0 & 1 \end{bmatrix} \begin{bmatrix} \dot{\xi}(t) \\ \dot{\eta}(t) \\ \dot{\theta}(t) \end{bmatrix} + \begin{bmatrix} 0 \\ 0 \\ \dot{\theta}(t) \end{bmatrix} \wedge \begin{bmatrix} R_\delta \cos \delta \\ R_\delta \sin \delta \\ 0 \end{bmatrix} \\ &= \begin{bmatrix} \dot{\xi}(t) \cos \varphi(t) + \dot{\eta}(t) \sin \varphi(t) - R_\delta \dot{\theta}(t) \sin \delta \\ -\dot{\xi}(t) \sin \varphi(t) + \dot{\eta}(t) \cos \varphi(t) - R_\delta \dot{\theta}(t) \cos \delta \\ \dot{\theta}(t) \end{bmatrix} \end{aligned} \quad (7.21)$$

represents the structural velocity in the (x', y', z) local reference system.

The structural motion of the cylinder affects the relative wind velocity in the cylinder's cross section (i.e. the plane of motion of the cylinder) leaving the axial velocity U_A unchanged. The relative wind velocity $\mathbf{U}_R(t)$ in the (x', y', z) local reference system is the difference between the total wind velocity $\mathbf{U}_{r'}(t)$ and the components of $\dot{\mathbf{q}}_R(t)$ in the cylinder's cross-section:

$$\begin{aligned} \mathbf{U}_R(t) &= \begin{bmatrix} U_N(t) & 0 & U_A(t) \end{bmatrix}^T - \begin{bmatrix} \dot{q}_{R,1} & \dot{q}_{R,2} & 0 \end{bmatrix}^T \\ &= \begin{bmatrix} U_N(t) - \dot{\xi}(t) \cos \varphi(t) - \dot{\eta}(t) \sin \varphi(t) + R_\delta \dot{\theta}(t) \sin \delta \\ \dot{\xi}(t) \sin \varphi(t) - \dot{\eta}(t) \cos \varphi(t) + R_\delta \dot{\theta}(t) \cos \delta \\ U_A(t) \end{bmatrix} \end{aligned} \quad (7.22)$$

The intensity $U_{NR}(t)$ of relative normal wind velocity is:

$$\begin{aligned} U_{NR}(t) &= \sqrt{(U_{R,1})^2 + (U_{R,2})^2} \\ &= \sqrt{\left(U_N(t) - \dot{\xi}(t) \cos \varphi(t) - \dot{\eta}(t) \sin \varphi(t) + R_\delta \dot{\theta}(t) \sin \delta \right)^2 + \left(\dot{\xi}(t) \sin \varphi(t) - \dot{\eta}(t) \cos \varphi(t) + R_\delta \dot{\theta}(t) \cos \delta \right)^2} \end{aligned} \quad (7.23)$$

The relative wind angle of attack, i.e. the angle between $U_{NR}(t)$ and the local x axis, is:

$$\begin{aligned} \alpha_R(t) &= \varphi(t) + \arctan \left(\frac{U_{R,2}}{U_{R,1}} \right) \\ &= \arctan \left(\frac{-\sin \beta (U + u'(t)) + \cos \beta v'(t)}{\sin \Theta \cos \beta (U + u'(t)) + \sin \Theta \sin \beta w'(t) + \cos \Theta w'(t)} \right) \\ &\quad - \theta(t) \\ &\quad + \arctan \left(\frac{\dot{\xi}(t) \sin \varphi(t) - \dot{\eta}(t) \cos \varphi(t) + R_\delta \dot{\theta}(t) \cos \delta}{U \sin \phi - \dot{\xi}(t) \cos \varphi(t) - \dot{\eta}(t) \sin \varphi(t) + R_\delta \dot{\theta}(t) \sin \delta} \right) \end{aligned} \quad (7.24)$$

Following Equation 7.15, the relative cylinder axis-wind angle $\Phi_R(t)$ is:

$$\begin{aligned} \Phi_R(t) &= \arccos \left(\frac{|U_A(t)|}{|\mathbf{U}_R(t)|} \right) \\ &= \arccos \left(\frac{|-\cos \Theta \cos \beta (U + u'(t)) - \cos \Theta \sin \beta v'(t) + \sin \Theta w'(t)|}{|\mathbf{U}_R(t)|} \right) \end{aligned} \quad (7.25)$$

The linearized expression of $U_R(t)$, $\Phi_R(t)$, $\alpha_R(t)$ are collected in a vector:

$$\mathbf{b}(\dot{\mathbf{q}}(t), \theta(t), \mathbf{U}(t)) = \begin{bmatrix} U_R(\dot{\mathbf{q}}(t), \theta(t), \mathbf{U}(t)) \\ \alpha_R(\dot{\mathbf{q}}(t), \theta(t), \mathbf{U}(t)) \\ \Phi_R(\dot{\mathbf{q}}(t), \theta(t), \mathbf{U}(t)) \end{bmatrix} \quad (7.26)$$

The vector $\mathbf{b}(\dot{\mathbf{q}}(t), \theta(t), \mathbf{U}(t))$ in Equation 7.26 is first order Taylor expanded about $\dot{\mathbf{q}}(t) = \mathbf{0}$, $\mathbf{q}(t) = \mathbf{0}$, $\mathbf{U}(t) = \mathbf{U}$ as:

$$\begin{aligned} \mathbf{b} &= \mathbf{b}|_{(\mathbf{0}, \mathbf{0}, \mathbf{U})} + \nabla_{\mathbf{U}(t)} \mathbf{b}|_{(\mathbf{0}, \mathbf{0}, \mathbf{U})} (\mathbf{U}(t) - \mathbf{U}) \\ &\quad + \nabla_{\dot{\mathbf{q}}(t)} \mathbf{b}|_{(\mathbf{0}, \mathbf{0}, \mathbf{U})} \dot{\mathbf{q}}(t) + \nabla_{\mathbf{q}(t)} \mathbf{b}|_{(\mathbf{0}, \mathbf{0}, \mathbf{U})} \mathbf{q}(t) \end{aligned} \quad (7.27)$$

where:

$$\mathbf{b}|_{(\mathbf{0}, \mathbf{0}, \mathbf{U})} = \begin{bmatrix} U \\ \bar{\varphi} \\ \Phi \end{bmatrix} \quad (7.28)$$

$$\nabla_{\mathbf{U}(t)} \mathbf{b}|_{(\mathbf{0}, \mathbf{0}, \mathbf{U})} = \begin{bmatrix} 1 & 0 & 0 \\ 0 & \frac{1}{U(\csc \Theta \sin^2 \beta + \cos^2 \beta \sin \Theta)} & \frac{1}{U(\cos \beta \sin \Theta + \csc \beta \sin \Theta \tan \Theta)} \\ 0 & -\frac{\cos \Theta \sin \beta}{U \sin \Phi} & \frac{\sin \Theta}{U \sin \Phi} \end{bmatrix} \quad (7.29)$$

$$\nabla_{\dot{\mathbf{q}}(t)} \mathbf{b}|_{(\mathbf{0}, \mathbf{0}, \mathbf{U})} = \begin{bmatrix} -\cos \bar{\varphi} \sin \Phi & -\sin \bar{\varphi} \sin \Phi & R_\delta \sin \delta \sin \Phi \\ \frac{\sin \bar{\varphi}}{U \sin \Phi} & -\frac{\cos \bar{\varphi}}{U \sin \Phi} & \frac{-R_\delta \cos \delta}{U \sin \Phi} \\ -\frac{\cos \bar{\varphi} \cos \Phi}{U} & -\frac{\sin \bar{\varphi} \cos \Phi}{U} & \frac{R_\delta \sin \delta \cos \Phi}{U} \end{bmatrix} \quad (7.30)$$

$$\nabla_{\mathbf{q}(t)} \mathbf{b}|_{(\mathbf{0}, \mathbf{0}, \mathbf{U})} = \begin{bmatrix} 0 & 0 & 0 \\ 0 & 0 & -1 \\ 0 & 0 & 0 \end{bmatrix} \quad (7.31)$$

where:

$$\bar{\varphi} = \alpha_R(t)|_{(\mathbf{0}, \mathbf{0}, \mathbf{U})} = - \left(\arctan \frac{\tan \beta}{\sin \Theta} + \bar{\theta} \right) \quad (7.32)$$

and:

$$\Phi = \Phi_R(t)|_{(\mathbf{0}, \mathbf{0}, \mathbf{U})} = \arccos(\cos \Theta \cos \beta) \quad (7.33)$$

and $\bar{\theta}$ represents the steady rotation of the section.

In order to express the vector $\mathbf{b}(\dot{\mathbf{q}}(t), \theta(t), \mathbf{U}(t))$ in term of Re instead of U , a new vector is defined: the vector $\mathbf{d}(\dot{\mathbf{q}}(t), \theta(t), \mathbf{U}(t))$ is obtained by applying the transformation to $\mathbf{b}(\dot{\mathbf{q}}(t), \theta(t), \mathbf{U}(t))$:

$$\begin{aligned}
 \mathbf{d} &= \mathbf{T}\mathbf{b}(\dot{\mathbf{q}}(t), \theta(t), \mathbf{U}(t)) \\
 &= \begin{bmatrix} Re_R(\dot{\mathbf{q}}(t), \theta(t), \mathbf{U}(t)) \\ \alpha_R(\dot{\mathbf{q}}(t), \theta(t), \mathbf{U}(t)) \\ \Phi_R(\dot{\mathbf{q}}(t), \theta(t), \mathbf{U}(t)) \end{bmatrix} \\
 &= \begin{bmatrix} Re \\ \bar{\varphi} \\ \Phi \end{bmatrix} + \\
 &+ \begin{bmatrix} \frac{D}{\nu} & 0 & 0 \\ 0 & \frac{D}{\nu Re(\csc \Theta \sin^2 \beta + \cos^2 \beta \sin \Theta)} & \frac{D}{\nu Re(\cos \Theta \sin \beta + \csc \beta \sin \Theta \tan \Theta)} \\ 0 & -\frac{D \cos \Theta \sin \beta}{\nu Re \sin \Phi} & \frac{D \sin \Theta}{\nu Re \sin \Phi} \end{bmatrix} \begin{bmatrix} u'(t) \\ v'(t) \\ w'(t) \end{bmatrix} \\
 &+ \begin{bmatrix} -\frac{D \cos \bar{\varphi} \sin \Phi}{\nu} & -\frac{D \sin \bar{\varphi} \sin \Phi}{\nu} & \frac{DR_\delta \sin \delta \sin \Phi}{\nu} \\ \frac{D \sin \bar{\varphi}}{\nu Re \sin \Phi} & -\frac{D \cos \bar{\varphi}}{\nu Re \sin \Phi} & -\frac{DR_\delta \cos \delta}{\nu Re \sin \Phi} \\ -\frac{D \cos \bar{\varphi} \cos \Phi}{\nu Re} & -\frac{D \sin \bar{\varphi} \cos \Phi}{\nu Re} & \frac{DR_\delta \sin \delta \cos \Phi}{\nu Re} \end{bmatrix} \begin{bmatrix} \dot{\xi}(t) \\ \dot{\eta}(t) \\ \dot{\theta}(t) \end{bmatrix} \\
 &+ \begin{bmatrix} 0 & 0 & 0 \\ 0 & 0 & -1 \\ 0 & 0 & 0 \end{bmatrix} \begin{bmatrix} \xi(t) \\ \eta(t) \\ \theta(t) \end{bmatrix}
 \end{aligned} \tag{7.34}$$

where \mathbf{T} is the transformation matrix:

$$\mathbf{T} = \begin{bmatrix} \frac{D}{\nu} & 0 & 0 \\ 0 & 1 & 0 \\ 0 & 0 & 1 \end{bmatrix} \tag{7.35}$$

and U is set equal to $Re\nu/D$.

7.2.3 Aerodynamic forces

The cylinder's aerodynamic force coefficients are thus expressed as non linear functions of the instantaneous flow-structure relative Reynolds number, Re_R , angle-of-attack, α_R , and angle between the cylinder's axis axis and the mean wind velocity component, Φ_R . This dependency can be expressed as:

$$\mathbf{C}(\mathbf{d}(\dot{\mathbf{q}}(t), \theta(t), \mathbf{U}(t))) = [C_{x'}(\mathbf{d}) \quad C_{y'}(\mathbf{d}) \quad DC_{Mz}(\mathbf{d})]^T \tag{7.36}$$

and $\mathbf{d}(\dot{\mathbf{q}}(t), \theta(t), \mathbf{U}(t))$ is a vector reported in Equation 7.34.

The aerodynamic forces \mathbf{F}_a per unit length along the x'_R , y'_R axes, and the moment about the z axes are:

$$\begin{aligned}
\mathbf{F}_a(\dot{\mathbf{q}}(t), \theta(t), \mathbf{U}(t)) &= \begin{bmatrix} F_x(\dot{\mathbf{q}}(t), \theta(t), \mathbf{U}(t)) \\ F_y(\dot{\mathbf{q}}(t), \theta(t), \mathbf{U}(t)) \\ M_z(\dot{\mathbf{q}}(t), \theta(t), \mathbf{U}(t)) \end{bmatrix} \\
&= \frac{1}{2} \rho D U_R^2(\dot{\mathbf{q}}(t), \mathbf{U}(t)) \mathbf{R}_z(\alpha_R(\dot{\mathbf{q}}(t), \theta(t), \mathbf{U}(t))) \mathbf{C}(\mathbf{d}) \\
&= \frac{\rho \nu^2}{2D} Re_R^2(\dot{\mathbf{q}}(t), \mathbf{U}(t)) \mathbf{R}_z(\alpha_R(\dot{\mathbf{q}}(t), \theta(t), \mathbf{U}(t))) \mathbf{C}(\mathbf{d})
\end{aligned} \tag{7.37}$$

where $\mathbf{R}_z(d_2)$ is the rotation matrix about the z axis.

The aerodynamic forces are non linear functions of $\dot{\mathbf{q}}(t)$, $\theta(t)$, $\mathbf{U}(t)$. A first order Taylor expansion of the aerodynamic forces about $\dot{\mathbf{q}}(t) = \mathbf{0}$, $\mathbf{q}(t) = \mathbf{0}$, $\mathbf{U}(t) = \mathbf{U}$ is performed:

$$\begin{aligned}
\mathbf{F}_a(\dot{\mathbf{q}}(t), \theta(t), \mathbf{U}(t)) &= \mathbf{F}_a|_{(\mathbf{0}, \mathbf{0}, \mathbf{U})} + \nabla_{\dot{\mathbf{q}}(t)} \mathbf{F}_a|_{(\mathbf{0}, \mathbf{0}, \mathbf{U})} \dot{\mathbf{q}}(t) \\
&\quad + \nabla_{\mathbf{q}(t)} \mathbf{F}_a|_{(\mathbf{0}, \mathbf{0}, \mathbf{U})} \mathbf{q}(t) \\
&\quad + \nabla_{\mathbf{U}(t)} \mathbf{F}_a|_{(\mathbf{0}, \mathbf{0}, \mathbf{U})} (\mathbf{U}(t) - \mathbf{U})
\end{aligned} \tag{7.38}$$

The first term of equation 7.38, i.e.:

$$\mathbf{F}_{a(\mathbf{0}, \mathbf{0}, \mathbf{U})} = \frac{\rho Re^2 \nu^2}{2D} \begin{bmatrix} C_{x'} \cos \bar{\varphi} - C_{y'} \sin \bar{\varphi} \\ C_{x'} \sin \bar{\varphi} + C_{y'} \cos \bar{\varphi} \\ DC_M \end{bmatrix} \tag{7.39}$$

contains the steady components of the aerodynamic forces per unit length. The detailed derivation of the last three terms of Equation 7.38 is reported in Section 7.2.3.1.

The second and third terms of Equation 7.38 can be rearranged as:

$$\begin{aligned}
\nabla_{\dot{\mathbf{q}}(t)} \mathbf{F}_a|_{(\mathbf{0}, \mathbf{0}, \mathbf{U})} \dot{\mathbf{q}}(t) &= \mathbf{C}_a \dot{\mathbf{q}}(t) = \mathbf{T}_{C\xi} \circ \boldsymbol{\xi}_a \dot{\mathbf{q}}(t) \\
&= \begin{bmatrix} 2m\omega_x & 2m\omega_x & 2m\omega_x \\ 2m\omega_y & 2m\omega_y & 2m\omega_y \\ 2J\omega_\theta & 2J\omega_\theta & 2J\omega_\theta \end{bmatrix} \circ \boldsymbol{\xi}_a \dot{\mathbf{q}}(t)
\end{aligned} \tag{7.40}$$

and

$$\begin{aligned}
\nabla_{\mathbf{q}(t)} \mathbf{F}_a|_{(\mathbf{0}, \mathbf{0}, \mathbf{U})} \mathbf{q}(t) &= \mathbf{K}_a \mathbf{q}(t) = \mathbf{T}_{K\omega} \circ \boldsymbol{\omega}_a^2 \mathbf{q}(t) \\
&= \begin{bmatrix} m & m & m \\ m & m & m \\ J & J & J \end{bmatrix} \circ \boldsymbol{\omega}_a^2 \mathbf{q}(t)
\end{aligned} \tag{7.41}$$

where m is the cylinder's mass per unit length, J is the rotational inertia, ω_i are the angular frequencies along the i DoF. $\mathbf{C}_a \dot{\mathbf{q}}(t)$ and $\mathbf{K}_a \mathbf{q}(t)$ represent the aerodynamic damping and stiffness forces per unit length. $\boldsymbol{\xi}_a$ and $\boldsymbol{\omega}_a^2$ are the

aerodynamic damping ratio and frequency matrices, respectively. $\mathbf{T}_{C\xi}$ is the tensor transforming ξ in \mathbf{C} and $\mathbf{T}_{K\omega}$ is the tensor transforming ω^2 in \mathbf{K} . \circ is the Hadamard product, i.e. $(\mathbf{A} \circ \mathbf{B})_{ij} = A_{ij}B_{ij}$.

In order to express the aerodynamic damping and stiffness matrices in Equation 7.40-7.41 in terms of aerodynamic damping ratio, ξ_a , and angular frequency, ω_a^2 , the following transformation can be applied:

$$\xi_a = \mathbf{T}_{\xi C} \circ \mathbf{C}_a \quad \omega_a^2 = \mathbf{T}_{\omega K} \circ \mathbf{K}_a \quad (7.42)$$

where $\mathbf{T}_{\xi C}$ is the tensor transforming \mathbf{C} in ξ and $\mathbf{T}_{\omega K}$ is the tensor transforming \mathbf{K} in ω^2 . The inverse transformation, i.e. from damping and stiffness to damping ratio and frequency are obtained by inverting each element of $\mathbf{T}_{C\xi}$ and $\mathbf{T}_{K\omega}$, i.e. $T_{\xi C i,j} = T_{C\xi i,j}^{-1}$ and $T_{\omega K i,j} = T_{K\omega i,j}^{-1}$, (Equations 7.40, 7.41). The transformation matrices $\mathbf{T}_{C\xi}$, $\mathbf{T}_{K\omega}$, $\mathbf{T}_{\xi C}$ and $\mathbf{T}_{\omega K}$ are valid for both structural and aerodynamic parameters.

The fourth term of equation 7.38, i.e.:

$$\nabla_{\mathbf{U}(t)} \mathbf{F}_a|_{(\mathbf{0}, \mathbf{0}, \mathbf{U})} (\mathbf{U}(t) - \mathbf{U}) = \mathbf{B} (\mathbf{U}(t) - \mathbf{U}) \quad (7.43)$$

represents the buffeting forces, i.e. given by the product of the buffeting matrix \mathbf{B} to the fluctuating velocity vector $(\mathbf{U}(t) - \mathbf{U})$.

7.2.3.1 General formulation for the derivation of the aerodynamic forces

In the following, detailed derivation of the linearized expression of the aerodynamic forces, based on equation 7.38, is reported. Generally, the gradient of the aerodynamic force per unit length, $F_a(\dot{\mathbf{q}}(t), \theta(t), \mathbf{U}(t))$, with respect to a generic vector time function, $\mathbf{f}(t)$, can be written as:

$$\begin{aligned} \nabla_{\mathbf{f}(t)} \mathbf{F}_a|_{(\mathbf{0}, \mathbf{0}, \mathbf{U})} = \frac{\rho \nu^2}{2D} \left\{ \left[(\mathbf{R}_z(\alpha_R) \mathbf{C}) \otimes (\nabla_{\mathbf{f}(t)} Re_R^2) \right] \right. \\ \left. + Re_R^2 \left[(\nabla_{\mathbf{f}(t)} \mathbf{R}_z(\alpha_R) \mathbf{C}) \right. \right. \\ \left. \left. + \mathbf{R}_z(\alpha_R) (\nabla_{\mathbf{f}(t)} \mathbf{C}) \right] \right\} \Big|_{(\mathbf{0}, \mathbf{0}, \mathbf{U})} \end{aligned} \quad (7.44)$$

where $\mathbf{f}(t) \in \{\dot{\mathbf{q}}(t), \mathbf{q}(t), \mathbf{U}(t)\}$.

Equation 7.44 is made of three terms obtained by applying the product rule to Equation 7.37. Each term with some mathematical manipulation can be further simplified. In particular the first one can be rearranged as:

$$\nabla_{\mathbf{f}(t)} Re_R^2 = 2Re_R \nabla_{\mathbf{f}(t)} Re_R = 2Re_R \nabla_{\mathbf{f}(t)} T_{11} b_1 = 2Re_R \frac{D}{\nu} \nabla_{\mathbf{f}(t)} U_R \quad (7.45)$$

The second term is a third order tensor obtained from the derivation of the rotation matrix with respect $\mathbf{f}(t)$. This tensor can be reduced in the tensorial product of two vectors considering the properties:

$$\frac{\partial \cos f(x)}{\partial x} = -\frac{\partial f(x)}{\partial x} \sin x \quad \frac{\partial \sin f(x)}{\partial x} = \frac{\partial f(x)}{\partial x} \cos x \quad (7.46)$$

that are the term contained in the rotation matrix expressed respect a generic function $f(x)$. After simple manipulation it is obtained:

$$\nabla_{\mathbf{f}(t)} \mathbf{R}_z(\alpha_R) \mathbf{C} = \mathbf{F} \mathbf{C} \otimes \nabla_{\mathbf{f}(t)} \alpha_R \quad (7.47)$$

where:

$$\mathbf{F} = \nabla_x \mathbf{R}_z(x)|_{x=\bar{\varphi}} = \begin{bmatrix} -\sin(\bar{\varphi}) & -\cos(\bar{\varphi}) & 0 \\ \cos(\bar{\varphi}) & -\sin(\bar{\varphi}) & 0 \\ 0 & 0 & 0 \end{bmatrix} \quad (7.48)$$

The third term contains the derivative of the vector $\mathbf{C}(\mathbf{d})$ with respect to $\mathbf{f}(\mathbf{t})$. As the vector of the aerodynamic coefficients \mathbf{C} depends on $\mathbf{f}(\mathbf{t})$, towards \mathbf{d} , the chain rule need to be implemented. This is given by:

$$\nabla_{\mathbf{f}(t)} \mathbf{C}|_{(0,0,\mathbf{U})} = [(\nabla_{\mathbf{d}} \mathbf{C}) (\nabla_{\mathbf{f}(t)} \mathbf{d})]|_{(0,0,\mathbf{U})} \quad (7.49)$$

Equation 7.44 may thus be re-written as:

$$\begin{aligned} \nabla_{\mathbf{f}(t)} \mathbf{F}_a|_{(0,0,\mathbf{U})} = \frac{\rho \nu^2}{2D} \left\{ \left[(\mathbf{R}_z(\alpha_R) \mathbf{C}) \otimes \left(\left(2Re \frac{D}{\nu} \right) \nabla_{\mathbf{f}(t)} U_R \right) \right] \right. \\ \left. + Re_R^2 [(\mathbf{F} \mathbf{C} \otimes \nabla_{\mathbf{f}(t)} \alpha_R) \right. \\ \left. + \mathbf{R}_z(\alpha_R) [(\nabla_{\mathbf{d}} \mathbf{C}) (\nabla_{\mathbf{f}(t)} \mathbf{d})]] \right\} \Big|_{(0,0,\mathbf{U})} \end{aligned} \quad (7.50)$$

The structural velocity and displacement proportional terms of equation 7.38 are obtained by setting $\mathbf{f}(t) = \dot{\mathbf{q}}(t)$ and $\mathbf{f}(t) = \mathbf{q}(t)$ in equation 7.50, respectively. The fluctuating wind velocity proportional, i.e. buffeting terms, are similarly obtained upon substitution of $\mathbf{f}(t) = \mathbf{U}(t)$ in equation 7.50

The results of Equations 7.40, 7.41 and 7.43 are reported in Appendix C. The terms of the aerodynamic damping matrix relative to the translational DoFs agree with the equivalent terms in the formulation of Macdonald & Larose (2008a). The terms of the complete of the aerodynamic damping matrix agree with the equivalent terms in the formulation of Gjelstrup & Georgakis (2011). The terms of the buffeting matrix relative to the translational DoFs evaluated for $\alpha_R = 0^\circ$ and $\beta = 0^\circ$, and neglecting the derivatives of the aerodynamic coefficients with respect to Re and Φ is the same used in buffeting analyses by Piccardo & Solari (2000).

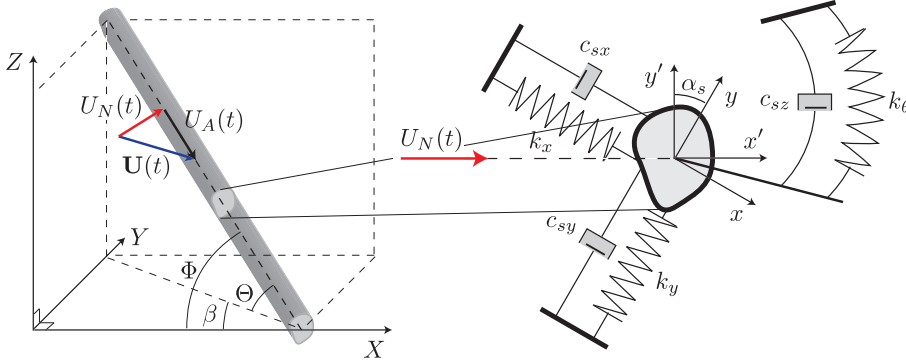


Figure 7.4: Mechanical model.

7.2.4 Structural properties and equation of motion

The cylinder is modeled as a spring-damped rigid body of indefinite length, i.e. a sectional model, see Figure 7.4. The mechanical properties are assumed to be linear and time invariant. A more sophisticated model can consider the mechanics as nonlinear. In this case the equation of motion should be linearized about the stationary steady state, i.e. the equilibrium point of the steady forces.

The derivation of the equations of motion is made following the Euler-Lagrange method. Figure 7.5 shows the definition of the mass center coordinates. The Center of Mass CM is located at distance L_0 from the origin of the local body's reference system (x, y, z) and at angular distance γ_0 from the x axis.

The rigid rotation and translation of the section about the Shear Center (SC) is evaluated for the CM as:

$$\mathbf{r}_g(t) = \mathbf{q}(t) + \boldsymbol{\omega}(t) \wedge \mathbf{L}_0 \quad (7.51)$$

The kinetic energy is evaluated as:

$$T = \frac{1}{2} (|\dot{\mathbf{r}}_g(t)|^2) \quad (7.52)$$

The potential energy is evaluated as:

$$V = \frac{1}{2} (|\mathbf{K}_s \dot{\mathbf{r}}_g(t)|^2) \quad (7.53)$$

The dissipative terms are:

$$\mathbf{F}_D = \mathbf{C}_s \dot{\mathbf{q}}(t) \quad (7.54)$$

where:

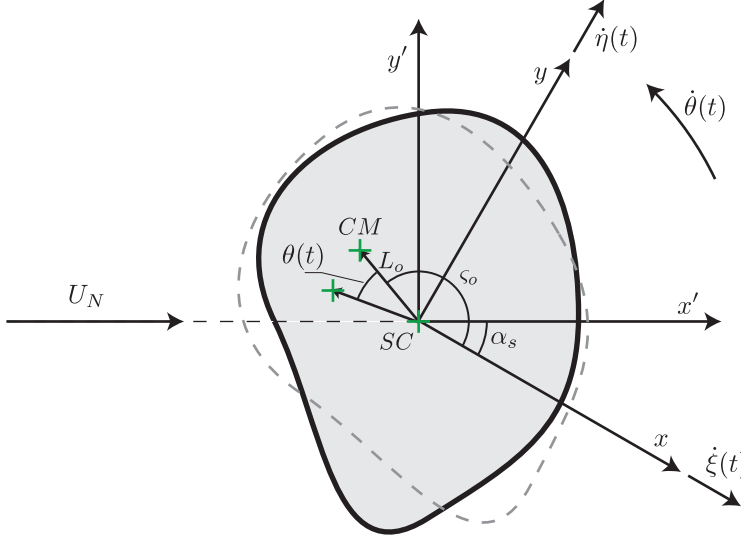


Figure 7.5: Definition of the mass center coordinates.

$$\mathbf{I} = \begin{bmatrix} m & 0 & 0 \\ 0 & m & 0 \\ 0 & 0 & J \end{bmatrix} \quad (7.55)$$

$$\mathbf{C}_s = \begin{bmatrix} c_{sx} & 0 & 0 \\ 0 & c_{sy} & 0 \\ 0 & 0 & c_{s\theta} \end{bmatrix} = 2 \begin{bmatrix} m\xi_x\omega_x & 0 & 0 \\ 0 & m\xi_y\omega_y & 0 \\ 0 & 0 & J\xi_\theta\omega_\theta \end{bmatrix} \quad (7.56)$$

$$\mathbf{K}_s = \begin{bmatrix} k_{sx} & 0 & 0 \\ 0 & k_{sy} & 0 \\ 0 & 0 & k_{s\theta} \end{bmatrix} = \begin{bmatrix} m\omega_x^2 & 0 & 0 \\ 0 & m\omega_y^2 & 0 \\ 0 & 0 & J\omega_\theta^2 \end{bmatrix} \quad (7.57)$$

where m and J are the mass and the mass moment of inertia per unit length of the cylinder respectively. k_{si} and c_{si} with $i \in \{x, y, \theta\}$ are the diagonal terms of the structural stiffness and damping matrices respectively. ξ_i and ω_i with $i \in \{x, y, \theta\}$ are the damping ratio and the natural angular frequency respectively.

The Equation of Motion (EOM) is:

$$\nabla_t (\nabla_{\dot{\mathbf{q}}(t)}(T - V)) - \nabla_{\mathbf{q}(t)}(T - V) + \mathbf{F}_D = \mathbf{F}_m + \mathbf{F}_a(\dot{\mathbf{q}}(t), \theta(t), \mathbf{U}(t)) \quad (7.58)$$

where \mathbf{F}_m represents the gravitational contribution and $\mathbf{F}_a(\dot{\mathbf{q}}(t), \theta(t), \mathbf{U}(t))$ represents the aerodynamic forces (see Equation 7.37).

The final result of the EOM is:

$$\mathbf{M}_s \ddot{\mathbf{q}}(t) + \mathbf{C}_s \dot{\mathbf{q}}(t) + \mathbf{K}_s \mathbf{q}(t) = \mathbf{F}_m + \mathbf{F}_a(\dot{\mathbf{q}}(t), \theta(t), \mathbf{U}(t)) \quad (7.59)$$

where:

$$\mathbf{M}_s = \begin{bmatrix} m & 0 & -mL_0 \sin \varsigma_0 \\ 0 & m & mL_0 \cos \varsigma_0 \\ -mL_0 \sin \varsigma_0 & mL_0 \cos \varsigma_0 & J + mL_0^2 \end{bmatrix} \quad (7.60)$$

\mathbf{C}_s , \mathbf{K}_s are the structural mass, damping and stiffness matrices, respectively, and \mathbf{F}_m is the product of the mass matrix, \mathbf{M}_s , by the vector \mathbf{g}'_s :

$$\mathbf{F}_m = \mathbf{M}_s \mathbf{g}'_s = \begin{bmatrix} m & 0 & -mL_0 \sin \varsigma_0 \\ 0 & m & mL_0 \cos \varsigma_0 \\ -mL_0 \sin \varsigma_0 & mL_0 \cos \varsigma_0 & J + mL_0^2 \end{bmatrix} \begin{bmatrix} g'_1 \\ 0 \\ 0 \end{bmatrix} \quad (7.61)$$

where \mathbf{g}'_s is the vector containing only the first component of the gravity vector in the (x, y, z) local system:

$$\mathbf{g}' = \mathbf{R}_Y(\pi/2 - \Theta) \mathbf{R}_Z(-\beta) \begin{bmatrix} 0 & 0 & g \end{bmatrix}^T \quad (7.62)$$

In the following, it will be assumed that \mathbf{M}_s , \mathbf{C}_s , \mathbf{K}_s are symmetric. Additionally, \mathbf{M}_s is positive definite, and \mathbf{C}_s and \mathbf{K}_s are non-negative definite. When the shear center of the cylinder's cross-section is not coincident with the center of mass, a sectional rotation can induced by gravitational forces \mathbf{F}_m . For instance, this phenomenon can take place on ice accreted sections. In this case the rotation of the section can change the parameter $\bar{\theta}$, which represents the steady rotation of the section.

7.3 State space representation

The system's representation in the state space form before and after linearization (Section 7.2) is presented here below.

The state space approach is a mathematical model of a physical system as a set of input, output and state variables related by first-order differential equations. In the state space representation, the three differential equations of order two governing the system are transformed into six first-order differential equations.

The non linear system is described in Figure 7.6a. The state of the system is fully described by the state vector $\mathbf{x}(t)$, given by:

$$\mathbf{x}(t) = \begin{bmatrix} \mathbf{q}(t) & \dot{\mathbf{q}}(t) \end{bmatrix} \quad (7.63)$$

The inputs are the total wind velocity described by the vector $\mathbf{U}(t)$ and the gravity described by the vector \mathbf{g}'_s . The inputs are transformed into accelerations

by applying the input matrix, which in this case is decomposed in $\mathbf{B}_a(\mathbf{x}(t), \mathbf{U}(t))$ and \mathbf{B}_g . $\mathbf{B}_a(\mathbf{x}(t), \mathbf{U}(t))$ is a nonlinear vector which depends on the state vector $\mathbf{x}(t)$ and on the instantaneous wind speed vector $\mathbf{U}(t)$:

$$\mathbf{B}_a(\mathbf{x}(t), \mathbf{U}(t)) = \mathbf{M}_s^{-1} \begin{bmatrix} \mathbf{0} \\ \mathbf{F}_a(\dot{\mathbf{q}}(t), \theta(t), \mathbf{U}(t)) \end{bmatrix} \quad (7.64)$$

where $\mathbf{F}_a(\dot{\mathbf{q}}(t), \theta(t), \mathbf{U}(t))$ is derived from Equation 7.37. \mathbf{B}_g is equal to the identity matrix \mathbf{I} . The mechanical properties of the system are assumed to be linear and time invariant and are represented by the state structural matrix, \mathbf{A}_s .

If the dynamical system is linear and time invariant, the differential and algebraic equations may be written in matrix form. The system's trajectories and the stability are evaluated by performing a linearization about the equilibrium points. The system is at equilibrium when the velocity and acceleration are equal to zero:

$$\dot{\mathbf{x}}(t) = \mathbf{0} \quad (7.65)$$

The equilibrium points are evaluated in the non linear configuration of the system using the static parts of the input parameters. Figure 7.6b describes the system after linearization. The linearization is described in Paragraph 7.2.3. In this case, the system's input is represented by the gravity vector, \mathbf{g}'_s , the mean wind vector, \mathbf{U} , and by the turbulence vector, $\mathbf{U}'(t)$. The two latter can be summed in one vector which represents the instantaneous wind speed $\mathbf{U}(t)$, see Equation 7.11. After linearization, $\mathbf{F}_a(\dot{\mathbf{q}}(t), \theta(t), \mathbf{U}(t))$ is decomposed into four force components (Equation 7.38). The first one is a constant term which depends on \mathbf{U} , and is referred to as mean or steady aerodynamic forces. The mean aerodynamic forces are given by the product of the input matrix $\mathbf{B}_s = \mathbf{F}_a|_{(0,0,\mathbf{U})}$ and the scalar U . The second and third terms depend on the structural velocities and displacements, $\mathbf{x}(t)$, respectively and on the mean wind speed, U , and are referred to as self-excited or aeroelastic forces. The aeroelastic contribution is given by the product of the matrix \mathbf{A}_a times the state vector $\mathbf{x}(t)$. From a state space description the aeroelastic matrix \mathbf{A}_a can be considered as a state feedback that can be summed to the state structural matrix \mathbf{A}_s . The state matrix, $\mathbf{A}_s + \mathbf{A}_a$, obtained considering these two parameters is time invariant for a given wind velocity, as the mean wind velocity is time invariant. The fourth term depends on $\mathbf{U}'(t)$ and is referred to as buffeting. The buffeting contribution is given by the product of the input matrix $\mathbf{B}_b = \nabla_{\mathbf{U}(t)} \mathbf{F}_a|_{(0,0,\mathbf{U})}$ times the vector vector $\mathbf{U}'(t)$.

The so obtained system is *Linear Time Invariant* (LTI). The defining properties of any LTI system are linearity and time invariance. Linearity means that the relationship between the input and the output of the system is a linear map. Time invariance means that whether is applied an input to the system now or with a delay from now, the output will be identical except for a time delay.

Any LTI system can be characterized entirely by a single function called the system's impulse response. The output of the system is simply the convolution of the input to the system with the system's impulse response. For all LTI systems, the eigenfunctions, and the basis functions of the transforms, are complex exponentials.

The state space representation consists of two systems of equations, i.e. the state and output equations. The state equations are:

$$\begin{aligned}
 \dot{\mathbf{x}}(t) &= (\mathbf{A}_s + \mathbf{A}_a) \mathbf{x}(t) + \mathbf{B}_s U + \mathbf{B}_b \tilde{\mathbf{U}}(t) + \mathbf{B}_g \mathbf{g}'_s \\
 \begin{bmatrix} \dot{\mathbf{q}}(t) \\ \ddot{\mathbf{q}}(t) \end{bmatrix} &= \left(\begin{bmatrix} \mathbf{0} & \mathbf{I} \\ -\mathbf{M}_s^{-1} \mathbf{K}_s & -\mathbf{M}_s^{-1} \mathbf{C}_s \end{bmatrix} \right. \\
 &\quad \left. + \begin{bmatrix} \mathbf{0} & \mathbf{0} \\ \mathbf{M}_s^{-1} \nabla_{\mathbf{q}(t)} \mathbf{F}_a|_{(0,0,U)} & \mathbf{M}_s^{-1} \nabla_{\dot{\mathbf{q}}(t)} \mathbf{F}_a|_{(0,0,U)} \end{bmatrix} \right) \begin{bmatrix} \mathbf{q}(t) \\ \dot{\mathbf{q}}(t) \end{bmatrix} \\
 &\quad + \begin{bmatrix} \mathbf{0} \\ \mathbf{M}_s^{-1} \mathbf{F}_a|_{(0,0,U)} U^{-1} \end{bmatrix} U \\
 &\quad + \begin{bmatrix} \mathbf{0} \\ \mathbf{M}_s^{-1} \nabla_{\mathbf{U}(t)} \mathbf{F}_a|_{(0,0,U)} \end{bmatrix} \tilde{\mathbf{U}}(t) + \begin{bmatrix} \mathbf{0} \\ \mathbf{I} \end{bmatrix} \mathbf{g}'_s
 \end{aligned} \tag{7.66}$$

The output equation, giving the displacement, is:

$$\mathbf{y}(t) = \mathbf{c} \mathbf{x}(t) + \mathbf{d} U = \begin{bmatrix} \mathbf{I} & \mathbf{0} \end{bmatrix} \begin{bmatrix} \mathbf{q}(t) \\ \dot{\mathbf{q}}(t) \end{bmatrix} \tag{7.67}$$

where \mathbf{d} is the feedforward matrix that is non-existent in this case.

The general solution of the state space problem is:

$$\begin{aligned}
 \mathbf{y}(t) &= \mathbf{c} e^{(\mathbf{A}_s + \mathbf{A}_a)t} \mathbf{x}(0) + \int_0^t \mathbf{c} e^{(\mathbf{A}_s + \mathbf{A}_a)(t-\tau)} \left[\mathbf{B}_s U + \mathbf{B}_b \tilde{\mathbf{U}}(\tau) + \mathbf{B}_g \mathbf{g}'_s \right] d\tau \\
 &= \mathbf{\Phi}(t) \mathbf{x}(0) + \int_0^t \mathbf{c} e^{(\mathbf{A}_s + \mathbf{A}_a)(t-\tau)} \left[\mathbf{B}_s U + \mathbf{B}_b \tilde{\mathbf{U}}(\tau) + \mathbf{B}_g \mathbf{g}'_s \right] d\tau
 \end{aligned} \tag{7.68}$$

As in the classical solution method for ordinary differential equations with constant coefficients, the total system state response $\mathbf{y}(t)$ is considered as summation of two parts, a homogeneous solution, $\mathbf{\Phi}(t) \mathbf{x}(0)$, which describes the response of the system to an arbitrary set of initial conditions $\mathbf{x}(0)$, and a particular solution which satisfies the state equations for the given input. The two components are then combined to form the total response. $\mathbf{\Phi}(t) = \mathbf{c} e^{(\mathbf{A}_s + \mathbf{A}_a)t}$ is defined to be the state transition matrix.

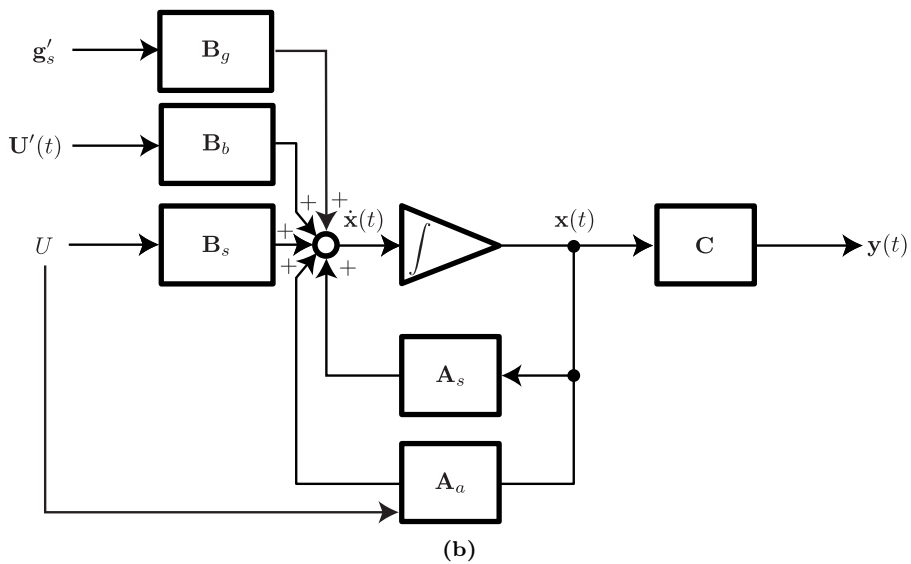
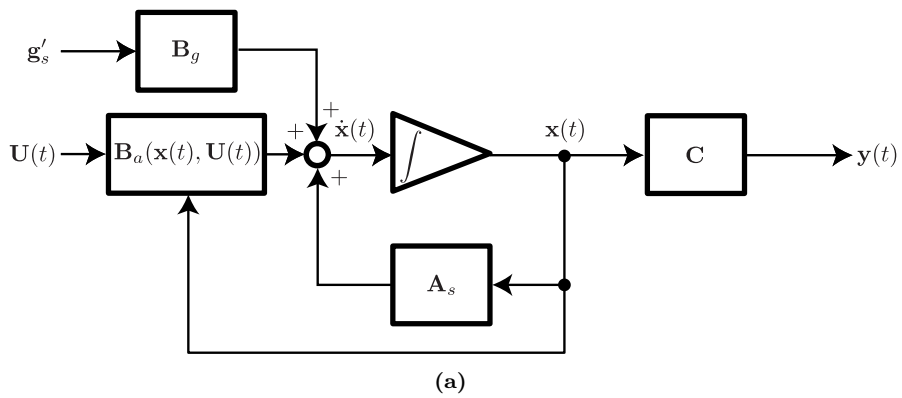


Figure 7.6: System description pre (a) and after (b) linearization.

In state-space terminology, a system is said to be asymptotically stable if the homogeneous response of the state vector $\mathbf{x}(t)$ returns to the origin of the state-space from any arbitrary set of initial conditions $\mathbf{x}(0)$ as time $t \rightarrow \infty$. This definition of stability is equivalent to stating that the homogeneous response of all state variables must decay to zero in the absence of any input to the system, or:

$$\lim_{t \rightarrow \infty} \Phi(t)\mathbf{x}(0) = \mathbf{0} \quad (7.69)$$

A LTI system, described by state equations $\dot{\mathbf{x}}(t) = \mathbf{A}\mathbf{x}(t) + \mathbf{B}U$, is asymptotically stable if and only if all eigenvalues of the matrix \mathbf{A} have negative real parts. In the following the solution of the eigenvalue problem and the determination of the condition of the linear instability will be analyzed.

7.4 Eigenvalue problem and stability analysis

In order to find the eigenvalues, the characteristic equation is solved:

$$\det(\mathbf{A}_s + \mathbf{A}_a - \lambda \mathbf{I}) = 0 \quad (7.70)$$

where $\mathbf{A}_s + \mathbf{A}_a$ is the state-space matrix, \mathbf{A} , \mathbf{I} is the identity matrix and λ are the eigenvalues. Equation 7.70 is a monic polynomial of 6th degree, of the form:

$$p(\lambda) = p_0\lambda^6 + p_1\lambda^5 + p_2\lambda^4 + p_3\lambda^3 + p_4\lambda^2 + p_5\lambda + p_6 = 0 \quad (7.71)$$

where $p_0 = 1$, and p_1 - p_6 are reported in Appendix D. The eigenvalues found using the Equation 7.71 are either real values or complex conjugate pairs. The system is stable if the real parts of all eigenvalues are negative. The Abel-Ruffini theorem states that there is no general algebraic solution to polynomial equations of 5th degree or higher degree. In these cases, the eigenvalue problem is normally solved numerically. The solution of the problem can be used to verify the stability of the system, inputting the structural values of damping and stiffness, or in order to find the values of the structural damping/stiffness at the boundary of instability, namely the minimum ones that guarantee stability.

On the other hand, the Routh-Hurwitz criterion (Hurwitz, 1895) allows to check the stability of the system without solving the characteristic equation. The criterion establishes that a system is stable, i.e. all roots of the characteristic polynomial have negative real parts, if and only if all the leading principal minors of the Hurwitz matrix \mathbf{H} , i.e. the so called Hurwitz determinants, are positive. The Hurwitz matrix is defined by:

$$\mathbf{H} = \begin{bmatrix} p_1 & 1 & 0 & 0 & 0 & 0 \\ p_3 & p_2 & p_1 & 1 & 0 & 0 \\ p_5 & p_4 & p_3 & p_2 & p_1 & 1 \\ 0 & p_6 & p_5 & p_4 & p_3 & p_2 \\ 0 & 0 & 0 & p_6 & p_5 & p_4 \\ 0 & 0 & 0 & 0 & 0 & p_6 \end{bmatrix} \quad (7.72)$$

The principal diagonal minors of the Hurwitz matrix are:

$$\Delta_1 = p_1 \quad (7.73)$$

$$\Delta_2 = p_1 p_2 - p_3 \quad (7.74)$$

$$\Delta_3 = p_3 \Delta_2 - p_1 \Delta_0 \quad (7.75)$$

$$\Delta_4 = p_4 \Delta_3 + (p_1 p_6 - p_2 p_5) \Delta_2 + p_5 \Delta_0 \quad (7.76)$$

$$\Delta_5 = p_5 \Delta_4 - p_6 [p_3 \Delta_3 - p_1 (p_5 \Delta_2 - p_1^2 p_6)] \quad (7.77)$$

$$\Delta_6 = p_6 \Delta_5 \quad (7.78)$$

where:

$$\Delta_0 = (p_1 p_4 - p_5) \quad (7.79)$$

If $\Delta_1 - \Delta_5$ are positive, the stability condition on Δ_6 reduces to imposing $p_6 > 0$. The condition $\Delta_6 = 0$ represents a boundary of stability, then there are two options:

- $p_6 = 0$. This condition corresponds to the case when one of the eigenvalues is zero without imaginary part. The system is on the boundary of the aperiodic stability. In fact, $p_6 = 0$ corresponds to the condition $-\omega_{a\theta\theta}^2 + \omega_\theta^2 = 0$, i.e. the aerodynamic and structural stiffness are the same. This is the critical condition for static divergence;
- $\Delta_5 = 0$. In this case a complex conjugate pair of the eigenvalues of \mathbf{A} at a fixed point becomes purely imaginary. This is the critical condition for galloping. A single Hopf bifurcation occurs.

If $\Delta_1 - \Delta_5$ are not positive, in the 3-DoFs system the Hopf bifurcation can be single, double or triple in function of:

- $p_6 = 0$ and $\Delta_i = 0$, $i = 4, 5$. In this case, a complex conjugate pairs of the eigenvalues of \mathbf{A} at a fixed point becomes purely imaginary and one of the eigenvalues is zero without imaginary part;

- $\Delta_i = 0$, $i = 3, 4, 5$. In this case, two complex conjugate pairs of the eigenvalues become purely imaginary. This is the critical condition for complex galloping. A double Hopf bifurcation occurs;
- $p_6 = 0$ and $\Delta_i = 0$, $i = 2, 3, 4, 5$. In this case, two complex conjugate pairs of the eigenvalues become purely imaginary and one of the eigenvalues is zero without imaginary part;
- $\Delta_i = 0$, $i = 1, 2, \dots, 5$. In this case, three complex conjugate pairs becomes purely imaginary. A triple Hopf bifurcation occurs.

In order to simplify the computational problem of the stability analysis, the Liénard & Chipart (1914) criterion can be used. The criterion has the advantage of providing a test for the system instability by means of a lower number of determinants to be computed. In fact, the determinants tend to be substantially more complicate than original coefficients as the polynomial order gets large. According to the criterion the system is stable if:

$$p_2, p_4, p_6 > 0 \text{ and } \Delta_1 = p_1, \Delta_3, \Delta_5 > 0 \quad (7.80)$$

The eigenvectors of \mathbf{A} represent the cylinder's trajectories. When the values of the eigenvectors are real the response is planar. Instead when the eigenvectors are a complex conjugate pair and the motion is then the sum of two modes of different frequencies following the same elliptical trajectory in opposite directions (Macdonald & Larose, 2008a). In the latter case, the displacement time histories presents a characteristic beat shape, called complex galloping in Jones (1992). The characteristic of complex galloping is the existence of two or more couples of critical eigenvalues (i.e. double Hopf bifurcation), whereas the usual galloping critical condition is a simple Hopf bifurcation (Luongo & Piccardo, 2005). The double Hopf bifurcation is a bifurcation of an equilibrium point in a two-parameter family of autonomous ODEs at which the critical equilibrium has two pairs of purely imaginary eigenvalues. This new type of critical condition can be responsible for possible bi/tri-modal galloping and quasi-periodic motions.

In order to determine the minimum structural damping needed to prevent galloping vibrations, i.e. the design structural damping, the principal diagonal minors of the Hurwitz matrix $\Delta_1 - \Delta_5$ are written as function of the structural damping (one or more of the term of the matrix), and are imposed equal to zero. By checking the sign of the derivative of $\Delta_1 - \Delta_5$ with respect to the structural damping parameter in the zeroing position it is possible to establish whether the system passes from unstable to stable condition (positive derivative) and vice versa (negative derivative). Similarly, by imposing p_6 to be equal to zero, the design (or minimum) structural stiffness to prevent static divergence is determined.

7.5 Three applications of the model

The 3-DoFs model allows one to:

- Verify the stability of a system against galloping and static divergence;
- Design the minimum structural damping and stiffness in order to avoid the occurrence of the instability;
- Derive the trajectories of the motion to an initial condition of $\mathbf{x}(t)$;
- Evaluate the 3-D cross-sectional response to a turbulent flow considering both buffeting and self-excited contributions.

The stability of the system can be verified once its geometrical and structural properties are assigned, i.e. the cable diameter D , the mass per unit length, m , mass moment of inertia per unit length, J , the angle offset and distance of the mass center to the shear center of the cable section, ς_0 and L_e , as well as the vibration angular frequencies ω_x , ω_y , ω_θ , and the damping ratios ξ_x , ξ_y , ξ_θ in the x , y , and θ directions. The aerodynamic properties of the cylinder, i.e. in terms of drag, lift and moment coefficients for varying Re , α , Φ , as well as the angle between the wind direction and the cylinder's axis, Φ , must also be specified. The stability is verified by applying the Liénard-Chipart criterion as illustrated in paragraph 7.4. In particular, the galloping-type instability is associated with the sign of the first five principal diagonal minors of the Hurwitz matrix $\Delta_1 - \Delta_5$ (Equations 7.73-7.77), while the static divergence-type instability is associated with the sign of p_6 (Equation 7.78).

An application of the 3-DoFs model is proposed in order to study the galloping and static divergence stability conditions of:

- Ice-accreted conductor in cross flow;
- Dry stay cable (CC I1);
- Ice accreted stay cable (CC I7).

The *ice accreted cable in cross-flow* case refer to a series of static and dynamic wind tunnel tests undertaken by Chabart & Lilien (1998) for an ice accreted cable conductor. The *dry inclined cable* case refers to the aerodynamic data of CC I1 (Chapter 6). The *ice accreted inclined cable* case refers to the aerodynamic data of CC I7 (Chapter 6). Furthermore, for the ice accreted stay cable case, the response of the system to a turbulent flow in conditions of incipient instability is analyzed.

The three examples of the model presented in this Section are given with the aim of show the prediction capabilities of the model.

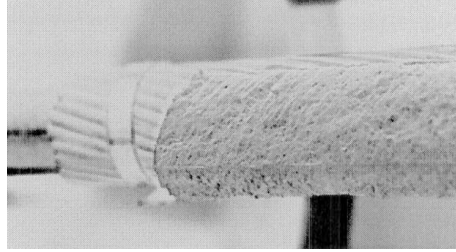


Figure 7.7: Cable conductor model and ice silicon shape, after Chabart & Lilien (1998).

7.5.1 Ice accreted cable conductor in cross flow

Quasi-steady drag and lift coefficients were measured by means of static wind tunnel tests by Chabart & Lilien (1998) for a model of a cable conductor, made of a circular cylinder covered by a silicon shape (Figure 7.7), reproducing a real ice accretion. Tests were performed for wind velocities in the range of 12.5 to 20 m/s and angles-of-attack, α , in the range of 0° to 180° . The mean force coefficients were found as independent of the wind velocity (i.e. Reynolds number). In all tests, the conductor model was oriented perpendicular to the mean flow, so that $\Phi = 90^\circ$, i.e. cross flow condition. The aerodynamic force coefficients. Figure 7.8 shows the aerodynamic force coefficients for different angle of attack.

The same model of conductor was later suspended in the wind tunnel with a system of springs which allowed the vertical, horizontal and rotational motion. This in order to obtain a system which resembled as much as possible the dynamic behavior of a real overhead line. Dynamic wind tunnel tests were performed in order to derive the regions of galloping instability in terms of angle-of-attack, α . The tests showed that the ice accreted cable conductor experiences galloping for α in the range of 20° to 180° (Chabart & Lilien, 1998).

In Table 7.1 are summarized the structural and aerodynamic parameters of the ice accreted cable conductor tested by Chabart & Lilien (1998).

In Figures 7.9a and 7.9b are reported the maps of static divergence and galloping instability as function of Re and α , respectively. In particular, in Figure 7.9a, the grey areas represent the regions of predicted stability against static divergence, associated with $p_6 > 0$, i.e. where the structural rotational angular frequency is greater than the aerodynamic rotational angular frequency, $\omega_\theta^2 > \omega_{a\theta\theta}^2$. The red areas represent the region of predicted instability against static divergence, which is associated to minimum value of the derivative of C_M with respect of α is minimum (Figure 7.37). Using the proposed approach, the divergence instability is predicted for all the values of the tested Re and in the ranges of $\alpha = 20^\circ$ to 40° and $\alpha = 60^\circ$ to 130° . In Figure 7.9b, the galloping instability is predicted for approximately all the tested Re values and in the

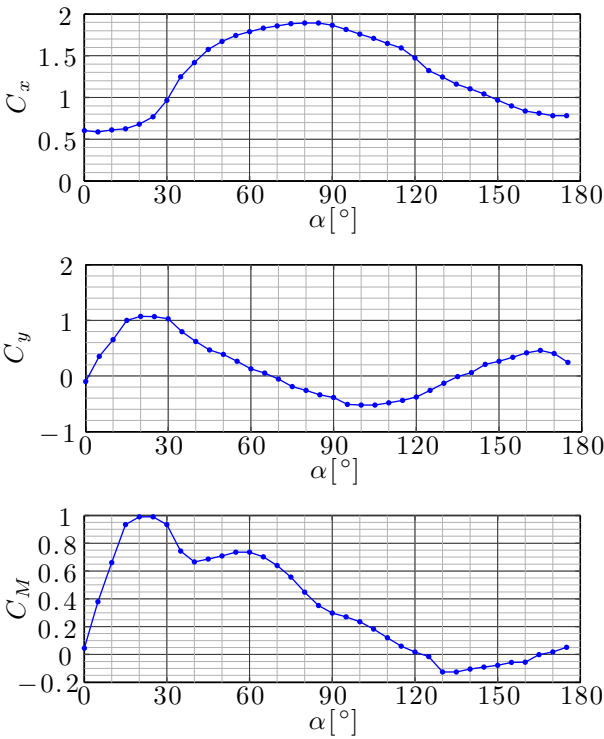


Figure 7.8: Aerodynamic force coefficients for an ice accreted cable conductor in cross flow for different angle of attack, after (Chabart & Lilien, 1998).

Table 7.1: Structural and aerodynamic parameters of the ice accreted cable conductor tested by Chabart & Lilien (1998).

Parameter	Value	Parameter	Value	Parameter	Value
m [kg/m]	2.99	ς_0 [°]	0	ω_θ [rad/s]	5.43
D [m]	0.0325	Φ [°]	90	ξ_x [%]	0.08
J [kg m]	$4.9689 \cdot 10^{-4}$	ω_x [rad/s]	6.25	ξ_y [%]	0.08
L_o [m]	0.0025	ω_y [rad/s]	5.31	ξ_θ [%]	0.3

Table 7.2: Comparison of the regions of predicted galloping instability, according to analytical models and dynamic wind tunnel tests.

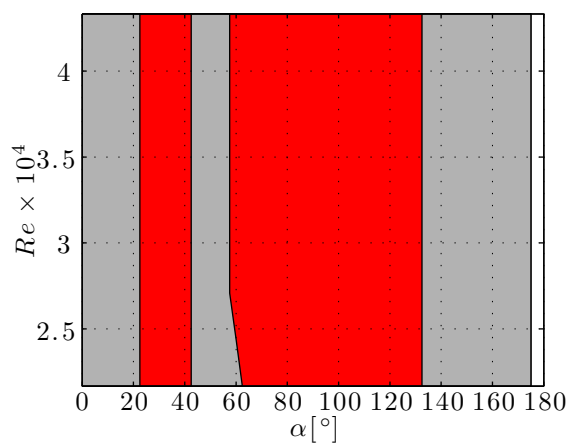
Model used	DoFs	α_{instab} [°]
Den Hartog (1956)	1	30°-42°&165°-180°
Macdonald & Larose (2008a)	2	27.5°-45°&168°-180°
Chabart & Lilien (1998)	3	20°-180°
Gjelstrup & Georgakis (2011)	3	25°-45°&70°-135°&170°-180°
Current	3	20°-150°&170°-180°

range of $\alpha = 20^\circ$ to 150° and for values of α larger than 170° . Additional regions of instability are found in the range of $\alpha = 10^\circ$ to 20° for Re over 3.7×10^4 and in the range of $\alpha = 150^\circ$ to 160° for Re up to 3×10^4 . These results show good agreement with predictions of dynamic wind tunnel tests performed by Chabart & Lilien (1998), where the ice accreted cable conductor experiences galloping for wind angles of attack in the range of $\alpha = 20^\circ$ to 175° .

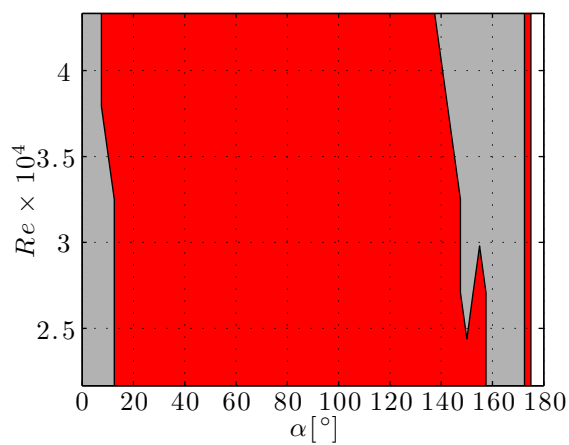
Figure 7.10 and Table 7.2 show a comparison of the galloping instability regions for the cable conductor evaluated according to several analytical models and dynamic wind tunnel tests carried out by Chabart & Lilien (1998). Macdonald & Larose (2008a) and Den Hartog (1956) predicted almost the same range of instability for all the Re and at around $\alpha = 30^\circ$. The quasi-steady 3-DoFs analytical model developed by Gjelstrup & Georgakis (2011) didn't allow the prediction of static divergence instability, as it didn't include aerodynamic stiffness proportional terms. It is observed that the current model significantly improves the prediction of the instability, compared with respect of the results of the dynamic tests.

In Figure 7.11 are shown the maps of galloping instability as function of Re and α , for varying ξ_x and ξ_y . As it is well known, an increase in the structural damping produces a reduction of the regions of instability. Accordingly, the increase in the structural damping (ξ_x and ξ_y) from 0.24% to $\xi_x = \xi_y = 0.32\%$ produces the disappearance of the instability in the range of $\alpha = 150^\circ$ to 160° for Re up to 3×10^4 , and in the range of $\alpha = 50^\circ$ to 60° for $Re = 2.5 \times 10^4$ to 4×10^4 .

In Figure 7.12 are shown the maps of galloping instability as function of Re and α for varying ξ_θ . In particular, this range of variation of ξ_θ produces the disappearance of the instability in the range of $\alpha = 170^\circ$ to 175° for Re up to 4.5×10^4 , in the range of $\alpha = 90^\circ$ to 100° for Re up to 2.5×10^4 , and in the range of $\alpha = 50^\circ$ to 60° for Re over 3×10^4 .



(a) Static divergence instability type predicted regions.



(b) Galloping region instability type predicted regions.

Figure 7.9: Regions of predicted instability. The red regions represent instability.

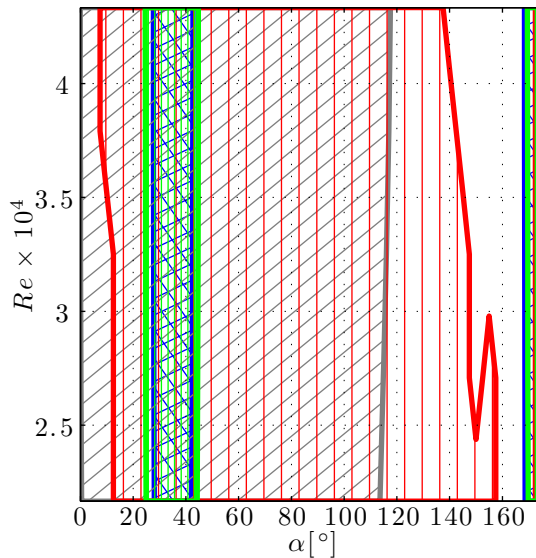


Figure 7.10: Comparison of the regions of predicted galloping instability with different models: [Den Hartog \(1956\)](#) (blue), [Macdonald & Larose \(2008a\)](#) (green), torsional galloping (grey), current model (red).

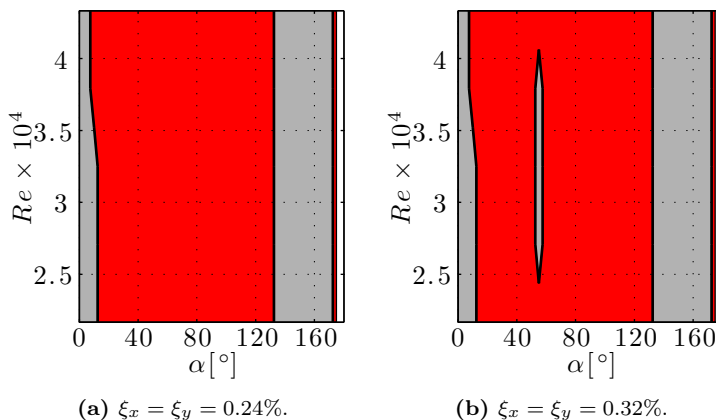


Figure 7.11: Effect of ξ_x and ξ_y on the galloping stability.

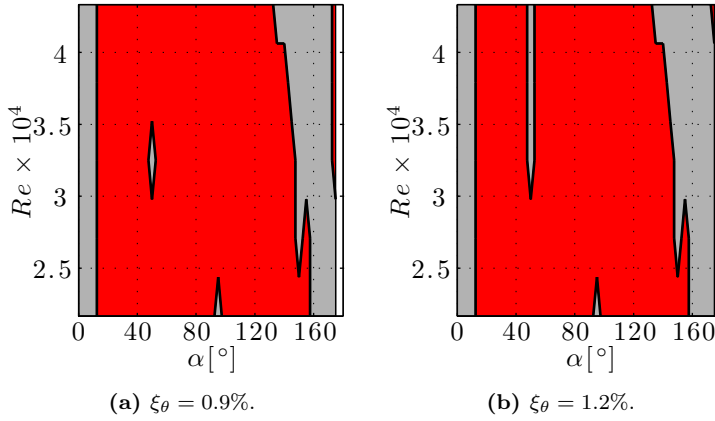


Figure 7.12: Effect of ξ_θ on the galloping stability.

A further increase in ξ_x , ξ_y and ξ_θ , produces further narrowing of the range of instability. The map of the static divergence instability is not reported as the variation of the structural damping does not alter the prediction of the static divergence.

In Figure 7.13 are shown the maps of galloping and static divergence instability as function of Re and α for varying levels of structural rotational stiffness, ω_θ . An increase in the structural rotational stiffness alters both the regions of both galloping and the static divergence instability. By increasing ω_θ from 10.86 to 21.72 rad/s, the galloping instability disappears in the range of $\alpha = 80^\circ$ to 130° for Re up to 3×10^4 , and for specific values of α over this Re threshold. Moreover, this range of variation of ω_θ produces the disappearance of the static divergence instability in almost all the entire evaluated domain, with exception of $\alpha = 30^\circ$ to 40° and $\alpha = 70^\circ$ to 80° , for Re up to 3.5×10^4 . A further increase in ω_θ results in the total disappearance of the static divergence phenomenon, but not of the galloping instability; in fact, when the structural rotational stiffness increases beyond the value which produces stabilization against structural divergence, decoupling of the DoFs occurs, and no stabilizing effect on the other DoFs occurs.

In Figure 7.14 are shown the maps of galloping instability as function of Re and α for varying levels of the structural stiffness, ω_x . The map of the static divergence instability is not reported, as the variation of ω_x does not alter the prediction of this type of instability. A change in the structural frequencies, in order to obtain non-coincident values along separate DoFs, is called in literature de-tuning. De-tuning or increasing the structural damping is a typical technique adopted in order to limit the structural response of a system (de Sá Caetano, 2007). Macdonald & Larose (2008b) demonstrated that for a 2-DoFs system

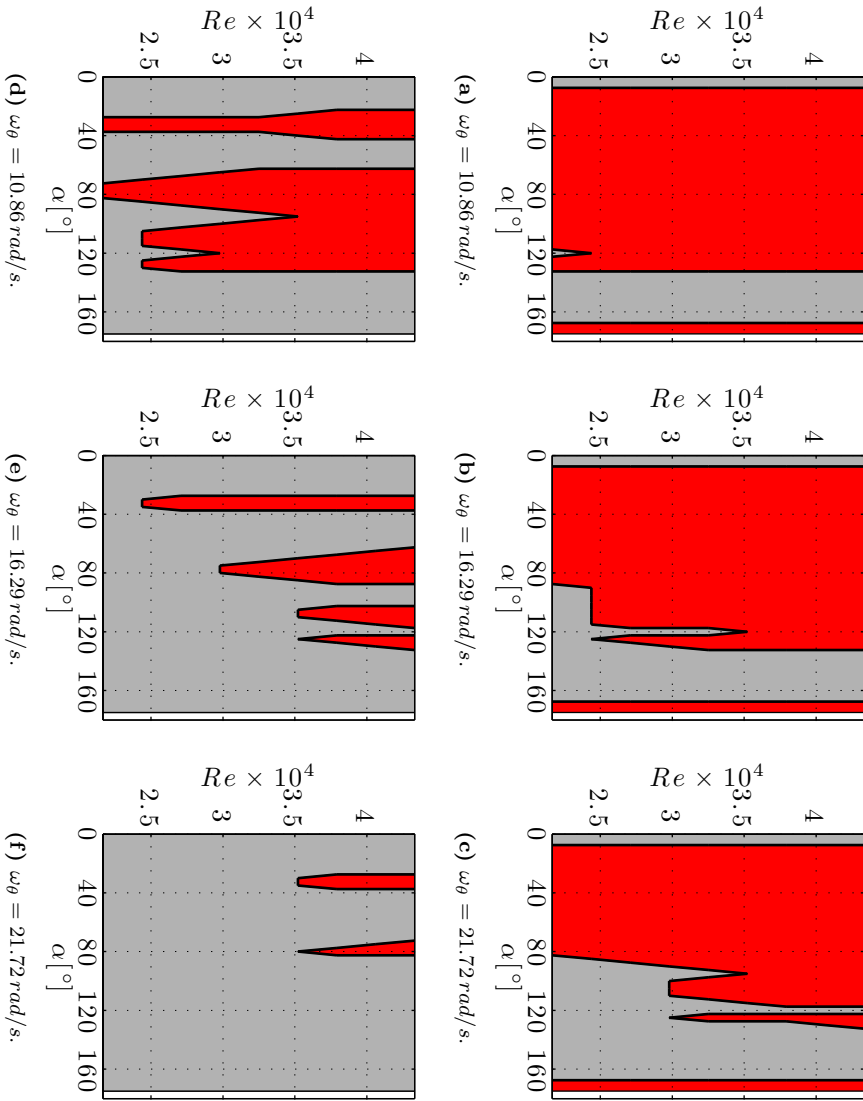


Figure 7.13: Effect of ω_θ on the galloping (a,b,c) and static divergence (d,e,f) stability.

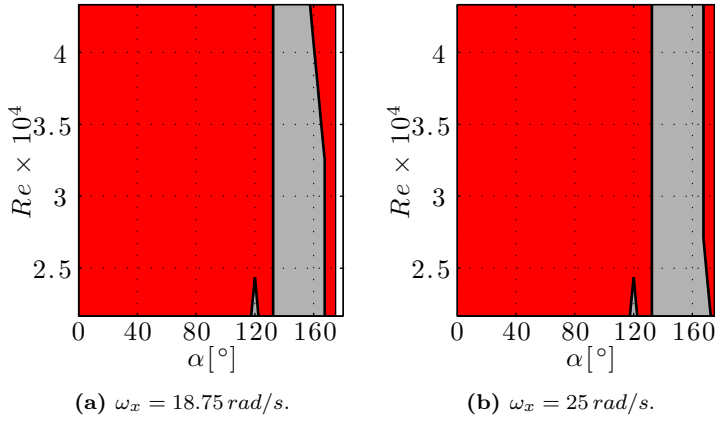


Figure 7.14: Effect of ω_x on the galloping stability.

characterized by low levels of structural damping, de-tuning makes the solutions to approach those of an uncoupled 1-DoF system and that the 2-DoFs coupling is only significant for systems with very close natural frequencies in the two planes. At $\omega_x = 12.5 \text{ rad/s}$ (not shown in the Figure) the galloping instability occurs over almost all of the investigated domain, with exception of the range of $\alpha = 130^\circ$ to 160° for Re up to 3×10^4 , and over this Re threshold for specific values of α . At $\omega_x = 18.75 \text{ rad/s}$, in the range of $\alpha = 130^\circ$ to 160° , the system is unstable for all Re of the domain. A further increase of ω_x beyond 18.75 rad/s , seems to have no effect on the stability of the system. In fact, for larger values of ω_x , the two DoFs are totally uncoupled and the frequency can't alter the solution.

7.5.1.1 Minimum damping

In Figure 7.15 are reported the minimum structural damping ratio maps ($\xi = \xi_x = \xi_y$) as function of Re and α , for $\omega_x = 6.25 \text{ rad/s}$, $\omega_y = 5.43 \text{ rad/s}$, $\omega_\theta = 54.35 \text{ rad/s}$ and $\xi_\theta = 0.9\%$. The value of the structural rotational stiffness, ω_θ , has been chosen so to prevent the occurrence of the static divergence, i.e. $p_6 > 0$, throughout all the investigated domain. The contour lines along which ξ has a zero value are shown in red. A positive value of the minimum ξ indicates susceptibility to the galloping instability. Regions of galloping instability are observed in the range of $\alpha = 30^\circ$ to 50° and $\alpha = 165^\circ$ to 175° for all the values of Re . In these regions, the galloping instability occurs in the out-of-plane direction, i.e. it is a Den Hartog-type, associated with the occurrence of the condition $C_x + (\partial C_y / \partial \alpha) < 0$. In fact, in these regions, the negative derivatives of C_y are maximum in absolute value and the values of C_x are relatively low

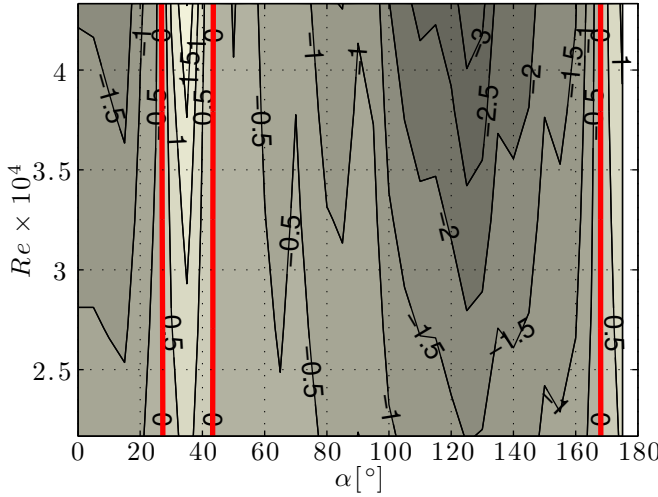


Figure 7.15: Minimum requirement for the structural damping ratios, $\xi = \xi_x = \xi_y$ [%]. ($\omega_x = 6.25 \text{ rad/s}$, $\omega_y = 5.43 \text{ rad/s}$, $\omega_\theta = 54.35 \text{ rad/s}$, $\xi_\theta = 0.9\%$).

(Figure 7.8).

In Figure 7.16 are reported the minimum structural rotational damping ratio maps, ξ_θ , as function of Re and α , for $\omega_x = 6.25 \text{ rad/s}$, $\omega_y = 5.43 \text{ rad/s}$, $\omega_\theta = 54.35 \text{ rad/s}$, $\xi_x = 0.08\%$, $\xi_y = 0.08\%$. In white are represented the regions where no real values of ξ_θ were found such as to satisfy the stability conditions given by Equations 7.80. Note that these regions approximately coincide with the region of galloping instability (see Figure 7.15), which are governed by the parameters ξ_x and ξ_y . The regions are approximately coincident because the value used for ξ_x and ξ_y is low. This solution shows that, if the instability is in a DoF different (y) from that in which it is modified the structural damping value (θ), it will not be possible to find a value of the latter such as to make the system stable.

7.5.1.2 Galloping motion

A system is said to be at the stability boundary condition when it possesses a minimum structural damping (or stiffness), evaluated as in paragraph 7.5.1.1. The motion of the system, governed by Equation 7.68, at the stability boundary is here analyzed. The validity of the response is obviously confined to a small interval of time, as, when the amplitude of motion increases, the mechanical and aerodynamic non linearities, here neglected, govern the problem. The system's motion is described in terms of trajectories of the shear centre in the plane $x - y$ and in terms of the time histories of each DoFs, $\xi(t)$, $\eta(t)$ and $\theta(t)$.

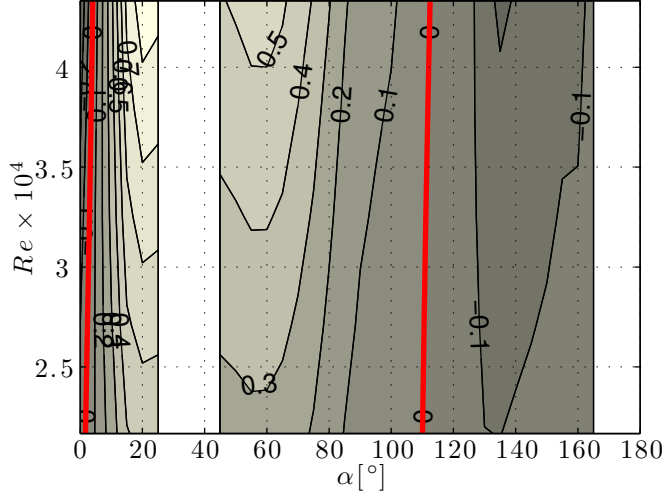


Figure 7.16: Minimum requirement for the structural rotational damping ratio, ξ_θ [%]. ($\omega_x = 6.25 \text{ rad/s}$, $\omega_y = 5.43 \text{ rad/s}$, $\omega_\theta = 54.35 \text{ rad/s}$, $\xi_x = 0.08\%$, $\xi_y = 0.08\%$).

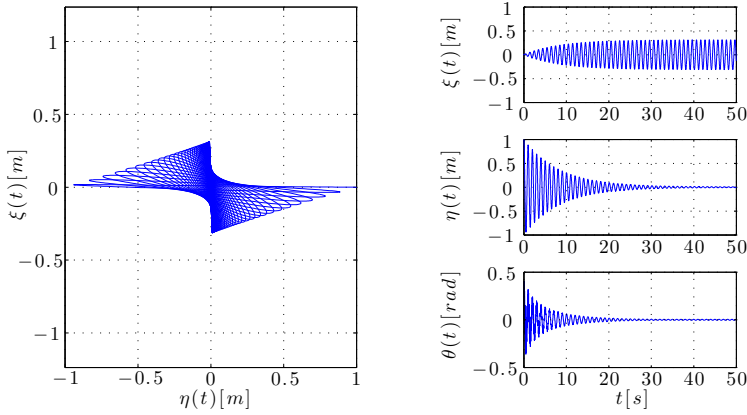


Figure 7.17: Motion of the cylinder to an initial condition of displacement, $\mathbf{x}(0) = [0 \ 1 \ 0 \ 0 \ 0 \ 0]^T$ in the plane $x-y$ and in term of time histories of each DoFs, $\xi(t)$, $\eta(t)$ and $\theta(t)$. ($Re = 2.7 \times 10^4$, $\alpha = 90^\circ$, $\omega_x = 6.25 \text{ rad/s}$, $\omega_y = 6.25 \text{ rad/s}$, $\omega_\theta = 54.35 \text{ rad/s}$, $\xi_x = -0.6\%$, $\xi_y = -0.6\%$, $\xi_\theta = 0.9\%$).

In Figure 7.17 it is shown the motion of the cylinder at the boundary of stability condition for $Re = 2.7 \times 10^4$, $\alpha = 90^\circ$, after imposing an initial displacement $\mathbf{x}(0) = [0 \ 1 \ 0 \ 0 \ 0 \ 0]^T$. In this case the condition of boundary stability corresponds to a negative value of the structural damping (see Figure 7.15). Clearly, the negative value of the structural damping has no physical meaning, but represents only the critical value beyond which the instability can occur. Here, the stability boundary condition is associated with $\xi(t)$. In fact, the motion along $\eta(t)$ decays exponentially but there is an energy transfer among the DoFs due to the off-diagonal terms of the aerodynamic stiffness and damping matrices which produces coupling. This energy transfer causes a motion with an exponentially decaying amplitude in $\theta(t)$ and a motion with a growing amplitude in $\xi(t)$. The growth takes place as long as there is movement along the other DoFs. When the motion ceases along the other DoFs an harmonic oscillation along $\xi(t)$ occurs. This type of oscillation is typical of the undamped system and corresponds to a single Hopf bifurcation giving galloping.

In Figure 7.18 it is shown the motion of the cylinder at the stability boundary condition, for $Re = 4.3 \times 10^4$ and $\alpha = 30^\circ$, after imposing an initial displacement $\mathbf{x}(0) = [0 \ 1 \ 0 \ 0 \ 0 \ 0]^T$. In this case the stability boundary condition corresponds to a positive value of the structural damping (Figure 7.15). According to the initial condition, the movement starts along $\eta(t)$ and it's characterized by an initial decaying amplitude. This decay is accompanied by an energy transfer among the DoFs due to the off-diagonal terms of the aerodynamic stiffness and damping matrices. This energy transfer causes a motion with a growing amplitude in $\xi(t)$. For the first 10s the system motion grows. After 10s the motion along DoFs is an harmonic oscillation. This type of oscillation is typical of undamped systems and corresponds to a multiple Hopf bifurcation. In fact, in this condition all the DoFs are characterized by pair of purely imaginary eigenvalues. The motion of the system keeps to be stable, but a small reduction of the structural damping can create instability along all the DoFs.

In Figure 7.18 it is shown the motion of the cylinder at the stability boundary condition reducing the value of ξ_x of 0.01%, for $Re = 4.3 \times 10^4$ and $\alpha = 30^\circ$, after imposing an initial displacement $\mathbf{x}(0) = [0 \ 1 \ 0 \ 0 \ 0 \ 0]^T$. Reducing the value of the structural damping ξ_x of 0.01% the system is beyond the limit of stability. Accordingly, the movement of the transitional phase has a behavior similar to the previous case (Figure 7.18), while after 10s the motion in the $\eta(t)$ and $\theta(t)$ DoFs is an harmonic oscillation and the motion in $\xi(t)$ is a growing oscillation. The growing oscillation is characterized by a positive real part of the eigenvalues and occurs just in the DoF in which the structural damping has been decreased compared to the minimum required to avoid instability.

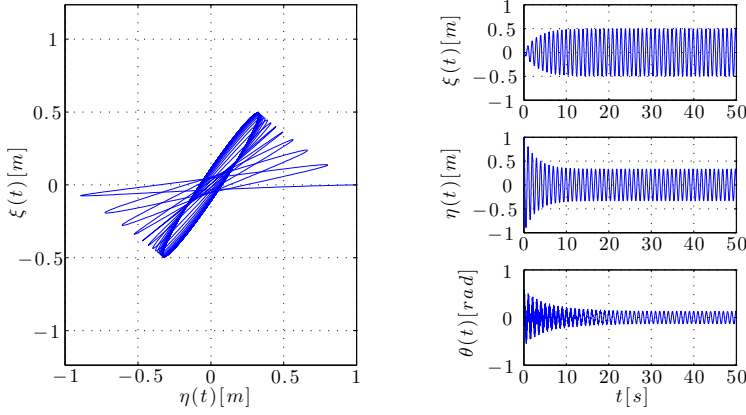


Figure 7.18: Motion of the cylinder to an initial condition of displacement, $\mathbf{x}(0) = [0 \ 1 \ 0 \ 0 \ 0 \ 0]^T$ in the plane $x-y$ and in term of time histories of each DoFs, $\xi(t)$, $\eta(t)$ and $\theta(t)$. ($Re = 4.3 \times 10^4$, $\alpha = 30^\circ$, $\omega_x = 6.25 \text{ rad/s}$, $\omega_y = 6.25 \text{ rad/s}$, $\omega_\theta = 54.35 \text{ rad/s}$, $\xi_x = 2.42\%$, $\xi_y = 2.42\%$, $\xi_\theta = 0.9\%$).

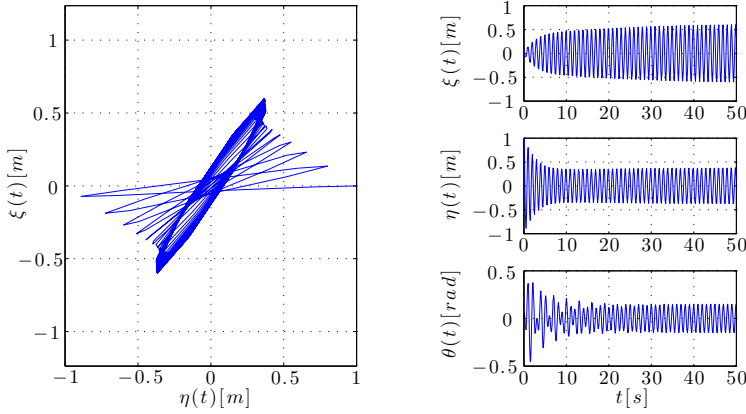


Figure 7.19: Motion of the cylinder to an initial condition of displacement, $\mathbf{x}(0) = [0 \ 1 \ 0 \ 0 \ 0 \ 0]^T$ in the plane $x-y$ and in term of time histories of each DoFs, $\xi(t)$, $\eta(t)$ and $\theta(t)$. ($Re = 4.3 \times 10^4$, $\alpha = 30^\circ$, $\omega_x = 6.25 \text{ rad/s}$, $\omega_y = 6.25 \text{ rad/s}$, $\omega_\theta = 54.35 \text{ rad/s}$, $\xi_x = 2.41\%$, $\xi_y = 2.42\%$, $\xi_\theta = 0.9\%$).

Table 7.3: Structural and aerodynamic parameters chosen to investigate the stability.

Parameter	Value	Parameter	Value	Parameter	Value
m [kg/m]	100	ς_0 [°]	0	ω_θ [rad/s]	50.2
D [m]	0.16	Θ [°]	30	ξ_x [%]	0.02
J [kg m]	0.32	ω_x [rad/s]	6.28	ξ_y [%]	0.02
L_o [m]	0	ω_y [rad/s]	6.28	ξ_θ [%]	0.02

7.5.2 Dry stay cable

Quasi-steady drag, lift and moment coefficients were measured by means of static wind tunnel tests, for a model of a full-scale bridge stay cable, made of a plain-surfaced HDPE tube, provided by bridge cable suppliers, with a nominal diameter of 160 mm. The aerodynamic force coefficient are shown in Figure 6.5. Note that the values of C_M are ten times smaller than for the ice-accreted cable (Chabart & Lilien, 1998). Table 7.3 illustrates the geometrical and structural properties of the cable model adopted in the analysis. The parameters were chosen in order to simulate typical characteristics of a stay cable.

In Figure 7.20 is shown the map of the galloping instability as function of Re and Φ . The static divergence map is not reported, as this type of instability is fully verified in the investigated domain. The grey areas represent the region of predicted stability and the red areas represent the region of predicted instability. The galloping instability is predicted for $Re > 2.5 \times 10^5$ and in the range of $\Phi = 60^\circ$ to 120° . This is in good agreement with predictions of Macdonald & Larose (2006).

Differently from the ice accreted conductor case, the parametric study is not reported, as the effect of an increase in the structural damping/stiffness is similar.

7.5.2.1 Minimum damping

In Figure 7.21a are shown the minimum structural damping ratio maps, ($\xi = \xi_x = \xi_y$), as function of Re and Φ , and for $\xi_\theta = 0.02\%$. The contour lines along which ξ has a zero value are represented in red. The areas of instability are the same as in Figure 7.20. This is due to the fact that the damping ratios are very low. In these regions the values of the negative derivative of C_y are maximum in absolute value (Figure 6.5).

In Figure 7.21b are shown the maps of minimum structural rotational damping ratio, ξ_θ , as function of Re and Φ , for constant values of the damping ratios, ξ_x and ξ_y . The white areas represent the regions where it was not possible to find real values of ξ_θ such as to satisfy the conditions of stability (Equations 7.80).

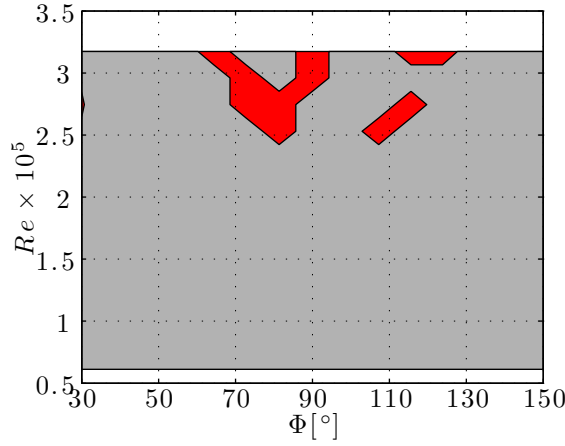


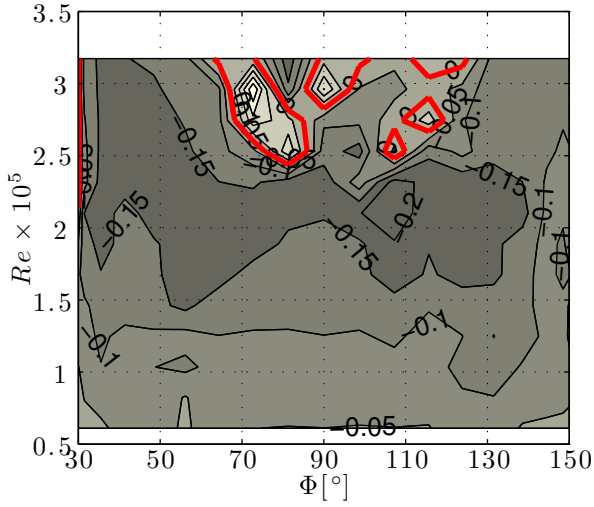
Figure 7.20: Galloping region instability type predicted regions. The red regions represent instability.

Note that these areas approximately coincide with the region of susceptibility to the instability of Figure 7.21a. The regions are approximately coincident because the value used for ξ_x and ξ_y is low.

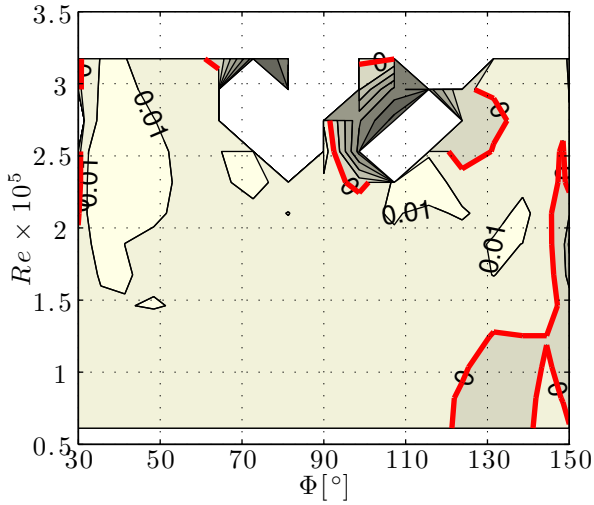
7.5.2.2 Galloping motion

In Figure 7.22 is shown the motion of the cylinder, i.e. in terms of trajectories and time histories along the three DoFs, in the condition of stability boundary, for $Re = 2.1 \times 10^5$ and $\phi = 150^\circ$. In this case the condition of stability boundary corresponds to a negative value of the structural damping (Figure 7.21a). Clearly, the negative value of the structural damping has no physical meaning, but represents only the critical value beyond which the instability can occur. In this condition, the boundary of stability is in $\eta(t)$. As imposed by the initial condition, the movement starts along $\eta(t)$ and it's characterized by an harmonic oscillation. During the motion, there is a very small energy transfer among the DoFs due to the off-diagonal terms of the aerodynamic stiffness and damping matrices which produce negligible movements along the other DoFs. The oscillation along $\eta(t)$ is typical of the undamped system and corresponds to a single Hopf bifurcation giving galloping.

In Figure 7.23 is shown the motion of the cylinder, i.e. in terms of trajectories and time histories along the three DoFs, for the condition of boundary of stability for $Re = 2.9 \times 10^5$ and $\phi = 107.2^\circ$. As in the previous case, this condition corresponds to a negative value of the structural damping (Figure 7.21a). The movement starts along $\eta(t)$ and it's characterized by an initial decaying amplitude. This decay is accompanied by an energy transfer among the DoFs



(a) $\xi = \xi_x = \xi_y$, $\xi_\theta = 0.02\%$



(b) ξ_θ , $\xi_x = \xi_y = 0.02\%$.

Figure 7.21: Minimum requirement for the structural damping ratios. ($\omega_x = 6.28 \text{ rad/s}$, $\omega_y = 6.28 \text{ rad/s}$, $\omega_\theta = 50.2 \text{ rad/s}$).

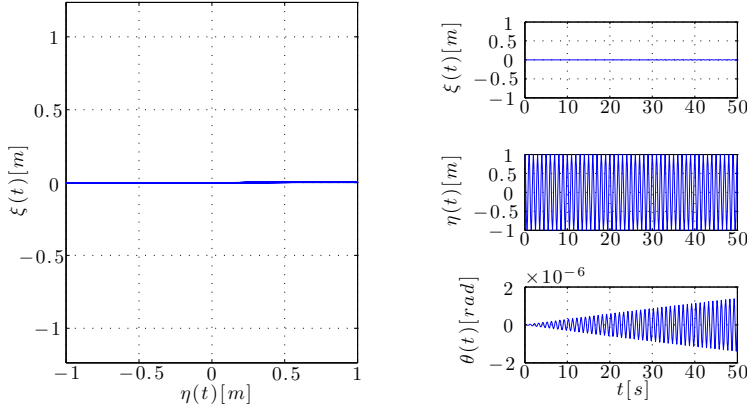


Figure 7.22: Motion of the cylinder to an initial condition of displacement, $\mathbf{x}(0) = [0 \ 1 \ 0 \ 0 \ 0 \ 0]^T$ in the plane $x-y$ and in term of time histories of each DoFs, $\xi(t)$, $\eta(t)$ and $\theta(t)$. ($Re = 2.1 \times 10^5$, $\Phi = 150^\circ$, $\omega_x = 6.28 \text{ rad/s}$, $\omega_y = 6.28 \text{ rad/s}$, $\omega_\theta = 50.2 \text{ rad/s}$, $\xi_x = -0.07\%$, $\xi_y = -0.07\%$, $\xi_\theta = 0.02\%$).

due to the off-diagonal terms of the aerodynamic stiffness and damping matrices. This transfer of energy induces an oscillation with a growing amplitude along $\xi(t)$. The growth takes place for about 70s. After that the oscillation starts to decrease whereas $\eta(t)$ resumes growing. $\theta(t)$ has a similar trend as $\eta(t)$ but with a shift in phase. This behavior is cyclic and produces a quasi-periodic motion. The motion is the sum of three modes of different frequencies. In this case the contributions of the two planar modes is equal giving near-planar motion with the orientation of the plane gradually rotating, as described by Jones (1992) and found by Macdonald & Larose (2008a).

7.5.3 Ice accreted stay cable

Quasi-steady drag, lift and moment coefficients were measured by means of climatic static wind tunnel tests, as described in Chapter 6. The aerodynamic force coefficient are shown in Figures 6.12, 6.13 and 6.14. As for the case of dry stay cable, Table 7.3 illustrates the geometrical and structural properties of the cable model adopted in the analysis.

7.5.3.1 Minimum damping

In Figure 7.24 are shown the minimum structural damping ratio maps, ($\xi = \xi_x = \xi_y$), as function of Re and Φ , and for $\xi_\theta = 0.7\%$. The value of the structural rotational stiffness, ω_θ , has been chosen so to prevent the occurrence

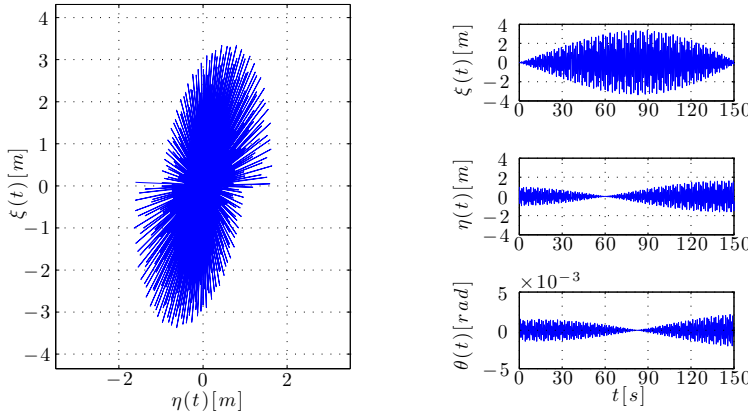


Figure 7.23: Motion of the cylinder to an initial condition of displacement, $\mathbf{x}(0) = [0 \ 1 \ 0 \ 0 \ 0 \ 0]^T$ in the place $x - y$ and in term of time histories of each DoFs, $\xi(t)$, $\eta(t)$ and $\theta(t)$. ($Re = 2.9 \times 10^5$, $\Phi = 107.2^\circ$, $\omega_x = 6.28 \text{ rad/s}$, $\omega_y = 6.28 \text{ rad/s}$, $\omega_\theta = 50.2 \text{ rad/s}$, $\xi_x = -0.06\%$, $\xi_y = -0.06\%$, $\xi_\theta = 0.02\%$).

of the static divergence, i.e. $p_6 > 0$, throughout all the investigated domain. The contour lines along which ξ has a zero value are represented in red. The areas of instability and the values of the minimum required structural damping are similar to that found applying the 1-DoF models reported in Figure 8.12a. As it will be shown in Chapter 8, this instability is related to the derivatives of aerodynamic coefficients with respect to α .

7.5.3.2 Buffeting motion

Time simulation of longitudinal turbulence component $U'(t)/U$ is given in Figure 7.25. The mean wind speed is $U = 30 \text{ m/s}$ and the turbulence intensity is 13%. The wind time series is scaled in order to obtain the same mean wind speed at which the aerodynamic coefficients are referred maintaining constant the turbulence intensity.

Numerical analyses were performed with the aim of assessing the response of the system to a turbulent flow in conditions of incipient instability. Only the translational DoFs were considered. The condition of incipient instability was evaluated using the 2DoFs model of Macdonald & Larose (2008a) that give the minimum required structural damping. The structural damping was set equal to the value required to avoid instability in all the domain $\Phi - Re$ investigated.

In Figure 7.26, the motion of the ice-accreted stay cable subject to turbulent flow in the in the $x - y$ plane is shown. The yaw of the cable was $\beta = 140^\circ$, the frequencies were equal to $f_x = 0.5 \text{ Hz}$, $f_y = 0.5 \text{ Hz}$, the structural damping

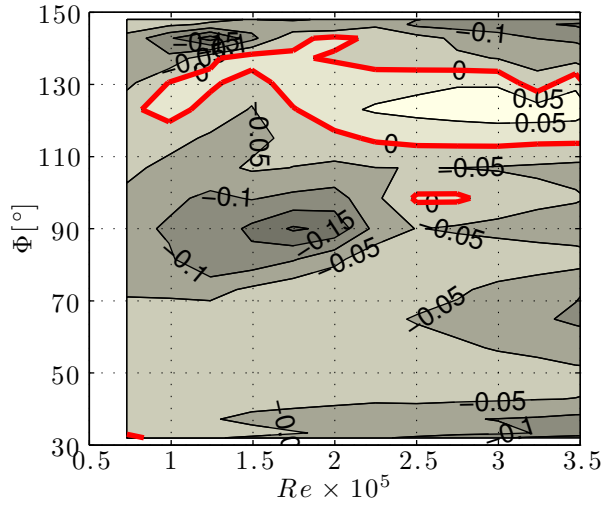


Figure 7.24: Minimum requirement for the structural damping ratios $\xi = \xi_x = \xi_y$ [%]. ($\xi_\theta = 0.7\%$, $\omega_x = 6.28 \text{ rad/s}$, $\omega_y = 6.28 \text{ rad/s}$, $\omega_\theta = 50.2 \text{ rad/s}$).

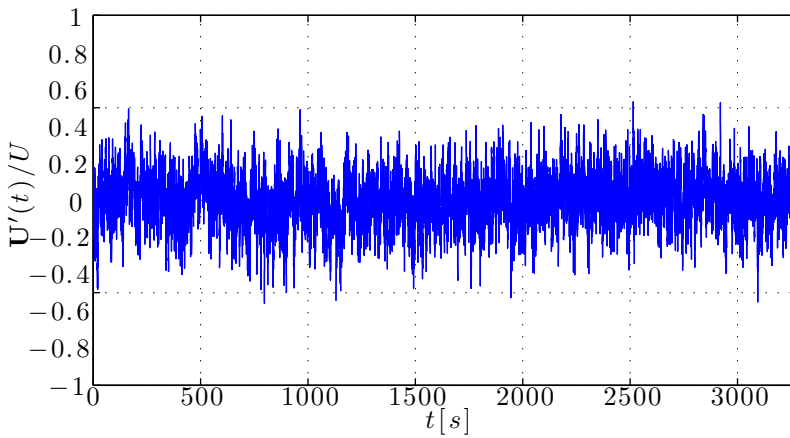


Figure 7.25: Simulated wind time series of longitudinal turbulence component, $U'(t)/U$.

were equal to $\xi_x = \xi_x = 0.13\%$ and the wind speed was $U = 28 \text{ m/s}$. It can be observed that neglecting the derivatives of the aerodynamic coefficients on α considerably underestimates the response. In Figure 7.27, the motion of the ice-accreted stay cable subject to turbulent flow in the $x - y$ plane is shown. The yaw of the cable was $\beta = 130^\circ$ and other parameters were equal to the previous case. In this case, it can be observed that neglecting the derivatives of the aerodynamic coefficients on Re considerably overestimates the response. These results confirm the importance of considering derivatives of aerodynamic coefficients in the evaluation of buffeting response. As a matter of fact, quasi-steady aerodynamics is governed by three parameters, the wind-cable angle Φ , the angle of attack α , and the Reynolds number Re , on which the aerodynamic coefficients depend.

In Figure 7.28 the *RMS* of $\xi(t)$ (a) and $\eta(t)$ is shown for different values of U and of β . From Figure 7.28a, it is observed that the maximum ξ -response is found for $\beta = 130^\circ$, which corresponds to the potentially unstable behavior (red line) shown in Figure 7.24. Large value of ξ_{rms} were also obtained for approximately $\beta = 0^\circ$ and $\beta = 180^\circ$ and large values of η_{rms} are obtained for $\beta = 90^\circ$. Further work is required to investigate in detail the buffeting response of ice accreted bridge cables. The author of this thesis is currently working on this topic.

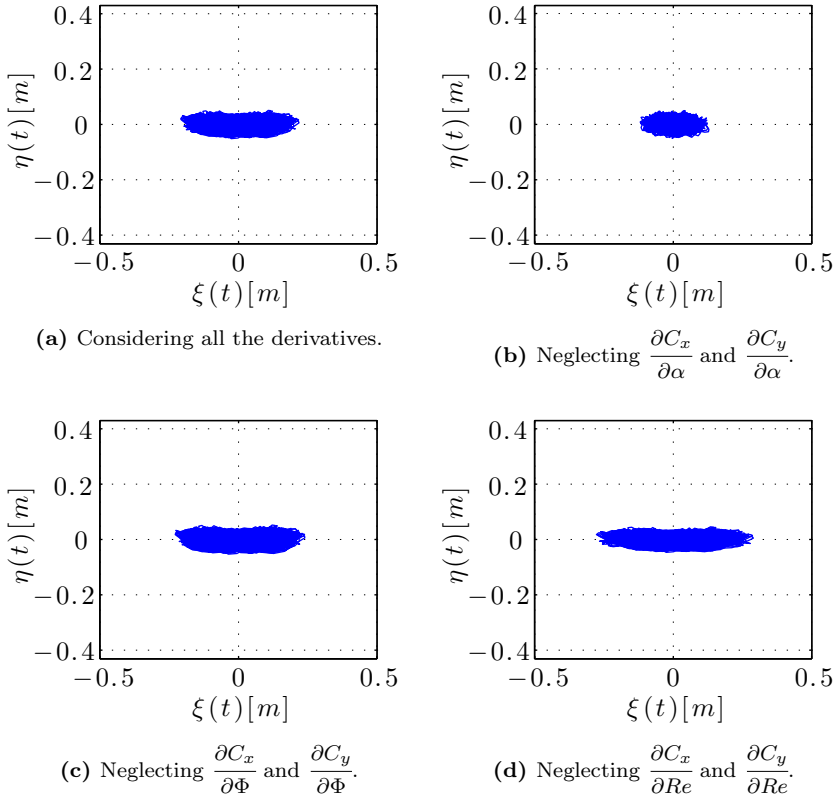


Figure 7.26: Motion of the ice-accreted stay cable subject to turbulent flow, in the plane $x - y$ considering all the derivatives of the aerodynamic coefficients and neglecting those respect Φ , α , and Re , respectively. ($\Theta = 30^\circ$, $\beta = 140^\circ$, $f_x = 0.5 \text{ Hz}$, $f_y = 0.5 \text{ Hz}$, $\xi_x = \xi_x = 0.13$, $U = 28 \text{ m/s}$, $I_u = 13$).

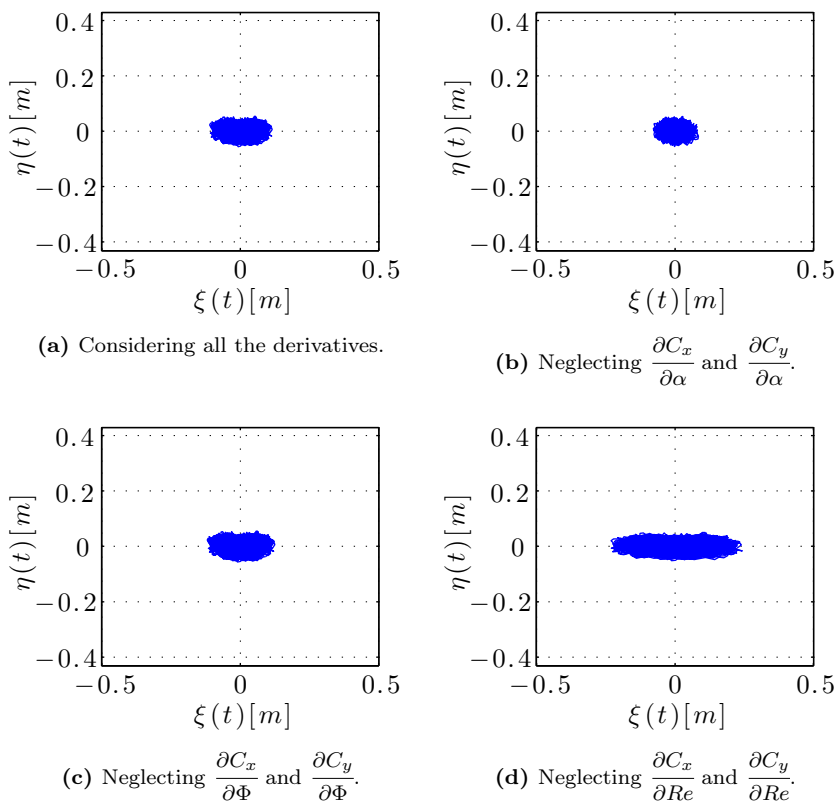
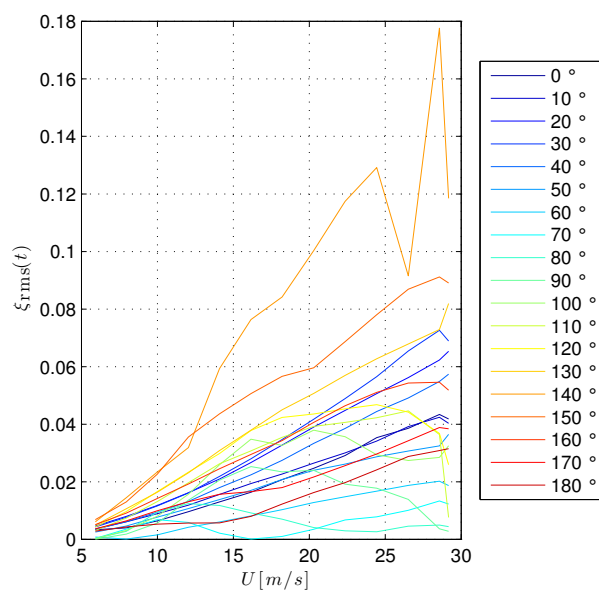
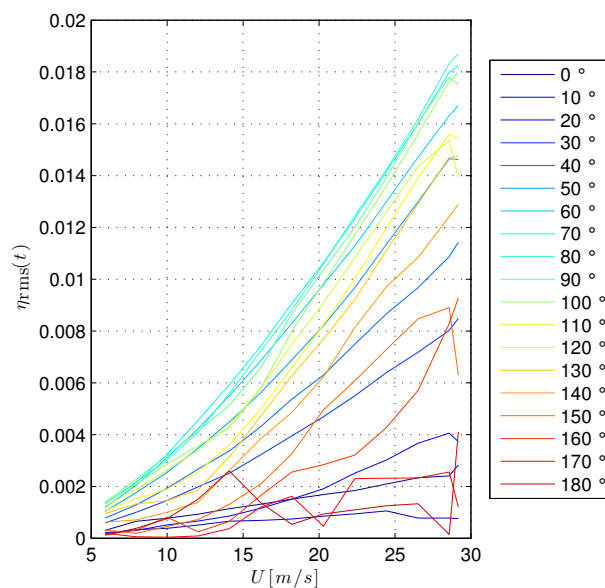


Figure 7.27: Motion of the ice-accreted stay cable subject to turbulent flow, in the plane $x - y$ considering all the derivatives of the aerodynamic coefficients and neglecting those respect Φ , α , and Re , respectively. ($\Theta = 30^\circ$, $\beta = 130^\circ$, $f_x = 0.5 Hz$, $f_y = 0.5 Hz$, $\xi_x = \xi_x = 0.13$, $U = 28 m/s$, $I_u = 13$).



(a)



(b)

Figure 7.28: Diagrams of the *RMS* of $\xi(t)$ (a) and $\eta(t)$ (b) [m] for different values of U and β .

References

- Blevins, R.D. 1977. Flow-induced vibration. *New York, Van Nostrand Reinhold Co., 1977. 377, 1.*
- Chabart, O., & Lilien, J.L. 1998. Galloping of electrical lines in wind tunnel facilities. *Journal of Wind Engineering and Industrial Aerodynamics*, **74-76**, 967–976.
- Collar, A.R. 1978. The first fifty years of aeroelasticity. *Aerospace*, **5**(2), 12–20.
- de Sá Caetano, E. 2007. *Cable vibrations in cable-stayed bridges*. Vol. 9. IABSE.
- Den Hartog, J.P. 1956. *Mechanical vibrations*. Courier Dover Publications.
- Gjelstrup, H., & Georgakis, C.T. 2011. A quasi-steady 3 degree-of-freedom model for the determination of the onset of bluff body galloping instability. *Journal of Fluids and Structures*, **27**(7), 1021–1034.
- Hurwitz, A. 1895. Ueber die Bedingungen, unter welchen eine Gleichung nur Wurzeln mit negativen reellen Theilen besitzt. *Mathematische Annalen*, **46**, 273–284.
- Jones, K.F. 1992. Coupled vertical and horizontal galloping. *Journal of engineering mechanics*, **118**(1), 92–107.
- Liénard, A., & Chipart, M.H. 1914. Sur le signe de la partie réelle des racines d'une équation algébrique. *J. Math. Pures Appl*, **10**(4), 291–346.
- Luongo, A., & Piccardo, G. 2005. Linear instability mechanisms for coupled translational galloping. *Journal of Sound and Vibration*, **288**, 1027–1047.
- Macdonald, J.H.G., & Larose, G.L. 2006. A unified approach to aerodynamic damping and drag/lift instabilities, and its application to dry inclined cable galloping. *Journal of fluids and structures*, **22**(2), 229–252.
- Macdonald, J.H.G., & Larose, G.L. 2008a. Two-degree-of-freedom inclined cable gallopingpart 1: general formulation and solution for perfectly tuned system. *Journal of Wind Engineering and Industrial Aerodynamics*, **96**(3), 291–307.
- Macdonald, J.H.G., & Larose, G.L. 2008b. Two-degree-of-freedom inclined cable gallopingpart 2: analysis and prevention for arbitrary frequency ratio. *Journal of wind Engineering and industrial Aerodynamics*, **96**(3), 308–326.
- Piccardo, G., & Solari, G. 2000. 3D wind-excited response of slender structures: Closed-form solution. *Journal of Structural Engineering*, **126**(8), 936–943.
- Takashi, N., & Hughes, T.J.R. 1992. An arbitrary Lagrangian-Eulerian finite element method for interaction of fluid and a rigid body. *Computer methods in applied mechanics and engineering*, **95**(1), 115–138.

CHAPTER 8

Aerodynamic stability of ice accreted bridge cables

Remember, the storm is a good opportunity for the pine and the cypress to show their strength and their stability.

HO CHI MINH

Gallopings are a low-frequency, self-excited oscillation of elongated, flexible structures exposed to a wind field. Its prediction is based on a quasi-steady approach, in which instantaneous wind forces are derived from the aerodynamic force coefficients obtained in static wind tunnel tests. Several galloping models exist, that differ for the Degrees of Freedom and for the geometric and aerodynamic characteristics considered. The aim of this Chapter is twofold; first, it compares the background hypotheses of the different galloping models, and the results they produce. This is done through an application to ice-accreted bridge cables, the analysis of the stability of which is the second aim of the paper. Wind tunnel data obtained by the authors for bridge hangers and stay cables are used in the calculations. As to the comparison among the different models, not existing a benchmark, the research is not aimed at judging the quality of each of them, but rather at pointing out the differences they bring and at discussing their most appropriate application.

8.1 General framework for galloping stability models

A cylinder of arbitrary cross section (Figure 8.1) is considered, exposed to a uniform flow $\mathbf{U} = [U \ 0 \ 0]^T$, in the global reference system (X, Y, Z) . The attitude of the cylinder to the flow is described through the *inclination*, Θ , i.e. the angle between the cylinder axis z and its projection on the horizontal plane, and the *yaw*, β , i.e. the angle between \mathbf{U} and the projection of the cylinder axis on the horizontal plane. These two angles can be condensed in a single parameter, the *wind-cable angle*, Φ . In this context \mathbf{U} is decomposed into two components: one perpendicular to the cylinder axis, named *normal flow*, U_N , and one parallel to the cylinder axis, named *axial flow*, U_A (Figure 8.1). If $\Phi = 90^\circ$ cylinder is said to be in *cross flow*, and $U_N = U$ and $U_A = 0$; otherwise it is said to be in *inclined flow*.

In a quasi-steady approach, the cylinder is considered stationary, and the instantaneous aerodynamic forces are evaluated using mean aerodynamic force coefficients measured in static wind tunnel tests. The in-plane motion of the cylinder cross section is described in terms of the three DoFs defined at the shear centre (Takashi & Hughes, 1992), represented by the vector $\mathbf{q}(t) = [\xi(t) \ \eta(t) \ \theta(t)]^T$. ξ and η are two mutually orthogonal displacements of the section, and θ is the rotation about the cylinder axis. The displacements ξ and η are defined in the (x, y) reference system, rotated of $-\alpha_s$ with respect to the (x', y') reference system. The choice of x and y is arbitrary for bridge hangers, as the polar symmetry of the stiffness matrix makes the natural frequencies the same in all directions; for stay cables x is in the vertical plane containing the cable, and y is perpendicular to it. The angle α_s between x' and x is called the *structural angle*. The different stability models consider all three DoFs or some of them, and are therefore classified as 1-DoF, 2-DoF or 3-DoF.

The instantaneous relative velocity, $\mathbf{U}_R(t)$, is evaluated as the sum of \mathbf{U} and the opposite of the cylinder velocity vector. To this aim, the ξ and η , and the θ components of the velocity vector are accounted for differently. The relative velocity in the x' and y' directions is given as the difference between the x' - and y' -components of $\dot{\xi}(t)$ and $\dot{\eta}(t)$ and \mathbf{U} . The relative velocity associated with θ is evaluated using the approach of Blevins (1977). The problem with the rotational DoF is that no exactly equivalent static situation can be defined, as for each point of the cross section a different velocity vector is defined, and hence a different local relative angle of attack. In the approach of Blevins (1977), the velocity field on the cross section boundary is approximated by choosing a reference point P , located at a distance R_δ from the shear center and at an angular distance δ from the direction $-x'$. This approach is derived from the three-quarter chord rule in airfoil flutter (Bisplinghoff & Ashley, 1962), though there is no theoretical justification for its use in the case of separated flow. On the other hand, this technique has been extensively used for many geometries.

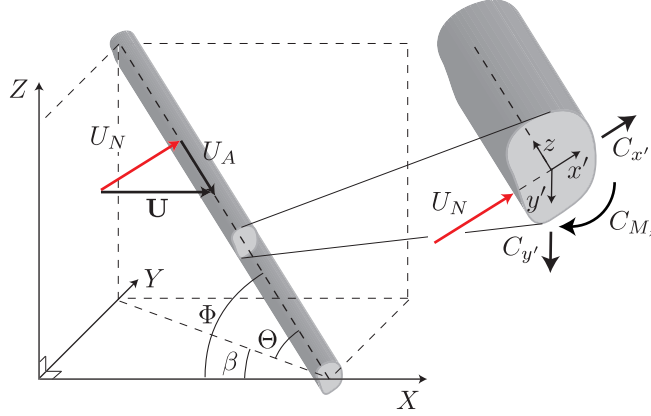


Figure 8.1: Schematic of the cylinder with flow direction and reference system definition.

P is usually located at the leading edge.

$\mathbf{U}_R(t)$ has components $U_{RN}(t)$ perpendicular to the cylinder axis (named *relative normal flow*), and $U_{RA}(t)$ parallel to the cylinder axis (named *relative axial flow*). The angle between the directions of $U_{RN}(t)$ and of U_N is the *relative angle of attack*, α_R , and the angle between the directions of $U_{RN}(t)$ and of $U_{RA}(t)$ is the *relative wind-cable angle of attack*, Φ_R . These are all instantaneous values.

Let us consider simply supported cables of length L , mass density m , torsion constant J_t , shear modulus G , viscous damping per unit length c , tension T , subjected to a load in the in plane and out of plane directions, $p(s, t)$ and $q(s, t)$ and to a torsional load $m_t(s, t)$. The Equations of Motion (EOMs) of the cable has the form (Irvine, 1981):

$$\begin{aligned}
 m \frac{\partial^2 \xi(s, t)}{\partial t^2} + c \frac{\partial \xi(s, t)}{\partial t} - \frac{\partial}{\partial s} \left\{ (T + \tau) \left(\left(\frac{dv}{ds} + \frac{\partial \xi(s, t)}{\partial s} \right) \right) \right\} &= p(s, t) + mg \\
 m \frac{\partial^2 \eta(s, t)}{\partial t^2} + c \frac{\partial \eta(s, t)}{\partial t} - \frac{\partial}{\partial s} \left\{ (T + \tau) \left(\left(\frac{dw}{ds} + \frac{\partial \eta(s, t)}{\partial s} \right) \right) \right\} &= q(s, t) \\
 G J_t \theta(s, t) &= m_t(s, t)
 \end{aligned} \tag{8.1}$$

where v and w are the coordinates of the static configuration and s is the curvilinear abscissa of the cable. In order to apply it to the analysis of a complete system, the modal co-ordinates of the undamped modes are considered. The

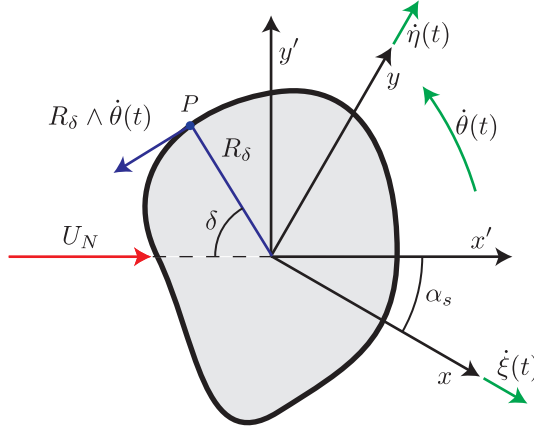


Figure 8.2: DoFs and definition of R_δ and δ .

displacement of the system can be expressed as the superposition of modal contributions. The mass, damping and stiffness per unit length are post-multiplied by the mode shape matrix and pre-multiplied by its transpose, integrated over the domain of the cable and divided by L obtaining the corresponding modal characteristics. The modal force per unit length is obtained pre-multiplying by the transpose of the mode shape matrix, integrating over the domain of the cable and dividing by L . Usually only the first mode for each directions (two translational and one rotational) are considered dominant and used in the analysis.

The governing equation of motion is:

$$\mathbf{M}_s \ddot{\mathbf{q}}(t) + \mathbf{C}_s \dot{\mathbf{q}}(t) + \mathbf{K}_s \mathbf{q}(t) = \mathbf{F}_a(\dot{\mathbf{q}}(t)) \quad (8.2)$$

where \mathbf{M}_s , \mathbf{C}_s , \mathbf{K}_s are the $n \times n$ structural mass, damping and stiffness modal matrices, respectively. $n = 1, 2, 3$ is the number of DoFs considered. In all the models, the stiffness and the damping matrices are diagonal. The majority of the existing models consider also \mathbf{M}_s as a diagonal matrix, therefore do not allow for inertial coupling. A few allow for inertial coupling, i.e. for the non-coincidence of the shear centre with the centre of mass. $\mathbf{F}_a(\dot{\mathbf{q}}(t))$ is the vector of the aerodynamic forces:

$$\mathbf{F}_a(\dot{\mathbf{q}}(t)) = \frac{1}{2} \rho D |\mathbf{U}_R(\dot{\mathbf{q}}(t))|^2 \mathbf{R}_z(\dot{\mathbf{q}}(t)) \mathbf{C}(\dot{\mathbf{q}}(t)) \quad (8.3)$$

where ρ is the fluid density, D is a characteristic dimension of the section, $|\mathbf{U}_R(\dot{\mathbf{q}}(t))|^2$ is the square of the norm of the instantaneous relative velocity

vector, $\mathbf{R}_z(\dot{\mathbf{q}}(t))$ is the rotation matrix between the aerodynamic force directions and the DoFs considered, and $\mathbf{C}(\dot{\mathbf{q}}(t))$ is the vector containing the aerodynamic force coefficients.

To investigate stability, the aerodynamic forces are expanded in Taylor series for $\dot{\mathbf{q}}(t)$ at the equilibrium point $\dot{\mathbf{q}}_0 = \mathbf{0}$:

$$\mathbf{F}_a(\dot{\mathbf{q}}(t)) = \mathbf{F}_a(\dot{\mathbf{q}}_0) + J_{\dot{\mathbf{q}}(t)} \mathbf{F}_a(\dot{\mathbf{q}}(t)) \big|_{\dot{\mathbf{q}}_0} \cdot \dot{\mathbf{q}}(t) = \mathbf{F}_a(\dot{\mathbf{q}}_0) - \mathbf{C}_a \dot{\mathbf{q}}(t) \quad (8.4)$$

To this aim, the aerodynamic force coefficients measured in the wind tunnel for different values of $Re = UD/\nu$, α and Φ must be expressed as a function of $\dot{\mathbf{q}}(t)$; this is done applying the derivation chain rule. ν is the kinematic viscosity.

The first term of the expansion represents the steady forces, while the second term is the Jacobian matrix of the aerodynamic forces, and coincides with the opposite of the aerodynamic damping matrix, $\mathbf{C}_a = -J_{\dot{\mathbf{q}}(t)} \mathbf{F}_a(\dot{\mathbf{q}}(t)) \big|_{\dot{\mathbf{q}}_0}$. Substituting Eq. 8.4 in Eq. 8.2 and neglecting the steady forces, a linearized version of the homogeneous equation of motion is obtained:

$$\mathbf{M}_s \ddot{\mathbf{q}}(t) + (\mathbf{C}_s + \mathbf{C}_a) \dot{\mathbf{q}}(t) + \mathbf{K}_s \mathbf{q}(t) = \mathbf{0} \quad (8.5)$$

In 1-DoF models, susceptibility to galloping is assessed, independently of the mechanical properties, by looking at the diagonal terms of \mathbf{C}_a : a negative value indicates an unstable behavior. Instability manifests itself when any diagonal term of \mathbf{C}_a is opposite to the corresponding term of \mathbf{C}_s .

When coupled DoFs are considered, susceptibility to galloping is assessed solving an eigenvalue problem. The solution of Eq. 8.5 is in the form $\mathbf{q}(t) = \mathbf{w} \exp(\lambda t)$, giving rise to the algebraic equation:

$$[\lambda^2 \mathbf{M}_s + \lambda (\mathbf{C}_s + \mathbf{C}_a) + \mathbf{K}_s] \mathbf{w} = \mathbf{0} \quad (8.6)$$

By setting the determinant of the matrix in Eq. 8.6 equal to zero, the characteristic (or secular) polynomial equation $f(\lambda) = 0$ is found, whose solutions are the eigenvalues λ of the matrix in Eq. 8.6. $f(\lambda)$ is in the form:

$$\begin{aligned} f(\lambda) &= \det [\lambda^2 \mathbf{M}_s + \lambda (\mathbf{C}_s + \mathbf{C}_a) + \mathbf{K}_s] \\ &= \lambda^{2 \cdot n} + a_1 \lambda^{2 \cdot n - 1} + \dots + a_{2 \cdot n - 1} \lambda^1 + a_{2 \cdot n} \end{aligned} \quad (8.7)$$

Stability is investigated using Lyapunov theorem, i.e. analyzing the sign of $\text{Re}(\lambda)$. Stability boundaries are found by setting $\lambda = \pm i\omega$, corresponding to the case of purely imaginary eigenvalues. In the case of 1-DoF systems, Eq. 8.7 can be solved in closed form, giving the same condition discussed above concerning the sign of the diagonal aerodynamic damping coefficients. In general, 2-DoF systems require numerical solution, except for the particular case in which structural damping coefficients and natural frequencies of the two DoFs are the same; in that case Eq. 8.7 degenerates into a biquadratic equation. For

3-DoF systems, a numerical solution is always required. \mathbf{w} in Eq. (8.6) is the eigenvector representing the cable trajectories.

Another approach to stability, not requiring solution of the eigenvalue problem, is the application of the Routh-Hurwitz theorem. The Hurwitz matrix corresponding to the polynomial $f(\lambda)$ is defined as:

$$\mathbf{H} = \begin{bmatrix} a_1 & a_3 & a_5 & a_7 & \dots & 0 \\ 1 & a_2 & a_4 & a_6 & \dots & 0 \\ 0 & a_1 & a_3 & a_5 & \dots & 0 \\ 0 & 1 & a_2 & a_4 & \dots & 0 \\ 0 & 0 & a_1 & a_3 & \dots & 0 \\ \vdots & \vdots & \vdots & \vdots & \ddots & \vdots \\ 0 & 0 & 0 & 0 & \dots & a_{2 \cdot n} \end{bmatrix} \quad (8.8)$$

and the system is stable, if and only if all the leading principal minors (the Hurwitz determinants) of \mathbf{H} are positive:

$$\begin{aligned} \Delta_1(f(\lambda)) &= |a_1| = a_1 > 0 \\ \Delta_2(f(\lambda)) &= \begin{vmatrix} a_1 & a_3 \\ 1 & a_2 \end{vmatrix} = a_2 a_1 - a_3 > 0 \\ \Delta_3(f(\lambda)) &= \begin{vmatrix} a_1 & a_3 & a_5 \\ 1 & a_2 & a_4 \\ 0 & a_1 & a_3 \end{vmatrix} = a_3 \Delta_2 - a_1(a_1 a_4 - a_5) > 0 \\ &\dots = \dots \end{aligned} \quad (8.9)$$

Among the models discussed in this thesis, this approach was used only by [Yu *et al.* \(1993a,b\)](#) and [Gjelstrup & Georgakis \(2011\)](#).

The main characteristics of the models described in Section 1.2 are summarized in Table 8.1.

8.2 Application of stability criteria to ice-accreted bridge cables

In this section, the galloping models available in the literature and reported in Table 8.1 are compared, with specific reference to bridge cables through application with the aerodynamic data coming from the experimental campaign reported in Chapter 6. For vertical hangers, data coming from the CC giving rise to the most pronounced unstable behavior are used for the analyses; this is CC V1. For stay cables, the only CC is used in which the aerodynamic coefficients were available with varying angle of attack α ; this is CC I7. Sectional 1-DoF,

2-DoF and 3-DoF stability models are used. Inertial coupling was neglected, as a result of the low mass of the ice accretion (Tables 5.1 and 5.2).

All models were applied numerically; closed form solutions available for some of the models were not used. This was done with the only aim of understanding the characteristics of the solution, while any issue related to computational efficiency is beyond the scope of this research. Nevertheless, consistency of the numerical results with the closed form solution has always been checked, where applicable.

The models were applied using the reference input parameters presented in the following. The diameter $D = 0.16$ m is the same as that of the wind tunnel model, and typical of medium- to long-span bridge cables. The reference value of the detuning parameter $k_{i,j} = \omega_i/\omega_j$, with $i, j = x, y, \theta$ and ω_i being the circular natural frequency in the DoF i , is taken equal to 1, which is the case of perfectly tuned DoFs. This applies only to bridge hangers for $i, j = x, y$, whereas when the torsional DoF is considered in bridge hangers, and for all DoFs for stay cables, detuning is always different from 1 (Irvine, 1981). In particular, the torsional natural frequency is much larger than the remaining frequencies, thus making $k_{\theta,y} \gg 1$ and $k_{\theta,x} \gg 1$. With the only purpose of investigating the effects on stability, $k_{\theta,y}$ and $k_{\theta,x}$ are here also first set equal to 1. Values of $R_\delta = D/2 = 0.08$ m and of $\delta = 90^\circ$ were chosen, typical of circular sections. Some of the parameters were then varied with respect to the reference value, to understand their influence on the predictions of each model.

In all applications of the 2-DoF and 3-DoF models, the solution was sought assuming that the structural damping was the same in all DoFs, $\xi_x = \xi_y = \xi_\theta$. With the aim of expressing the minimum required structural damping, independently of the cable dynamic properties (natural frequency and mass), the non-dimensional damping parameters proposed by Macdonald & Larose (2006) are used:

$$\begin{cases} Z_x = \frac{\xi_x \omega_x m}{2\nu \rho \pi} \\ Z_y = \frac{\xi_y \omega_y m}{2\nu \rho \pi} \\ Z_\theta = \frac{\xi_\theta \omega_\theta}{2\nu \rho \pi} J = \frac{\xi_\theta \omega_\theta}{2\nu \rho \pi} \frac{m D^2}{8} \end{cases} \quad (8.10)$$

where m and J are the mass and the polar mass moment of inertia per unit length. Z_i can be related to the Scruton number as:

$$Sc_i = Z_i \frac{Re}{U_{r,i}} \quad (8.11)$$

where $U_{r,i} = 2\pi U_N / \omega_i D$ is the reduced velocity and:

$$Sc_i = \begin{cases} \frac{m\xi_i}{\rho D} & \text{for } i = x, y \\ \frac{J\xi_i}{\rho D} = \frac{mD\xi_i}{8\rho} & \text{for } i = \theta \end{cases} \quad (8.12)$$

is the Scruton number. Z_i depends on $k_{y,x}$, $k_{\theta,x}$, $k_{\theta,y}$, δ , R_δ , D and on the aerodynamic coefficients and on their derivatives with respect to α , Φ and Re . Z_i can be expressed as a function of Z_j as:

$$Z_i = \begin{cases} Z_j k_{i,j} & \text{for } i, j = x, y \quad i \neq j \\ Z_j k_{i,j} \frac{D^2}{8} & \text{for } i = \theta \quad j = x, y \\ Z_j k_{i,j} \left(\frac{D^2}{8} \right)^{-1} & \text{for } i = x, y \quad j = \theta \end{cases} \quad (8.13)$$

It can be observed that when $k_{x,y} = 1$, then the corresponding non-dimensional damping parameters coincide, $Z_x = Z_y$; differently when $k_{\theta,y} = 1$ or $k_{\theta,x} = 1$, the corresponding non-dimensional damping parameters differ by a constant amount, $Z_\theta = Z_y (D^2/8)$ and $Z_\theta = Z_x (D^2/8)$, respectively. Finally, if the system is detuned, then the non-dimensional damping parameters are always different from each other, even when $\xi_x = \xi_y = \xi_\theta$.

8.2.1 Vertical bridge hangers

For vertical hangers, data coming from CC V1 (Figure 6.1). First, the stability of bridge hangers in 1-DoF was investigated applying the cross-wind and along-wind models derived by Den Hartog (1956) and Martin *et al.* (1981), respectively, as well as with the model of Macdonald & Larose (2006) with varying structural angle α_s , considering and neglecting the dependency of the aerodynamic coefficients on Re . Then, torsional stability was investigated applying the model of Nigol & Buchan (1981b), with varying δ . Stability in the coupled x and y DoFs was investigated using the model of Macdonald & Larose (2008a), considering both cases of tuning and of detuning of the DoFs. Stability in the coupled y and θ DoFs was investigated using the model of Yu *et al.* (1992), considering both cases of tuning and of detuning of the DoFs. Finally, stability of the coupled 3-DoF tuned and detuned system was investigated using the model of Gjelstrup & Georgakis (2011).

To start with, in Figure 8.3 the regions of the $Re - \alpha$ plane of potential instability are shown, as evaluated using the model of Macdonald & Larose (2006) for six values of α_s . In Figure 8.3a the results obtained accounting for the dependency of the aerodynamic coefficients on Re are shown, while in Figure 8.3b the results obtained neglecting such dependency are shown. α is the rotation of the cable with respect to the angle of attack of accretion, i.e. $\alpha = 0$ is the angle of attack of accretion. The condition $\alpha_s = 90^\circ$ corresponds

to across-wind vibrations, which is the case of the Den Hartog (1932) criterion; the condition $\alpha_s = 0^\circ$ corresponds to along-wind vibrations, which is the case of drag crisis (Martin *et al.*, 1981). Results for $\alpha_s = 180^\circ$ are not reported as they coincide with those found for $\alpha_s = 0$.

Three different regions of instability were found. The first region is found for $Re > 10^5$ and for $\alpha = 20^\circ$ to 50° ; it has its largest extension for $\alpha_s = 90^\circ$, it becomes smaller for $\alpha_s = 120^\circ$ and disappears for the other values of α_s , and is not affected by the derivatives of the aerodynamic coefficients with respect to Re , as it has exactly the same shape in Figure 8.3a and in Figure 8.3b; this is a Den Hartog instability. The second region is found for $Re > 2.5 \times 10^5$ and for $\alpha = 70^\circ$ to 180° , and represents a combination of Den Hartog and drag crisis instabilities; it has its largest extension for $\alpha_s = 120^\circ$ and $\alpha_s = 150^\circ$, and becomes smaller for other values of α_s ; in particular, for $\alpha_s = 90^\circ$ a Den Hartog type instability is observed, for $Re > 2.5 \times 10^5$ and $\alpha = 80^\circ$ to 100° , which manifests itself in Figure 8.3a and Figure 8.3b; for $\alpha_s = 0^\circ$, a drag crisis instability is observed for $Re = 3.0 \times 10^5$ to 3.5×10^5 and $\alpha = 120^\circ$ to 180° , which disappears when the contribution of the derivatives of the aerodynamic coefficients with respect to Re is neglected. A third region is found for $Re = 10^5$ to 2.5×10^5 and around $\alpha = 170^\circ$, which exists only for $\alpha_s = 90^\circ$, and represents a Den Hartog type instability.

In Figure 8.4 the minimum structural damping Z_x required to avoid instability for any α_s is shown. The results reported in Figure 8.4 are the envelope of the maxima of Z_x obtained with varying α_s , using the model of Macdonald & Larose (2006). Negative values of the required damping indicate that the system is always stable. In Figure 8.4a the results obtained accounting for the dependency of the aerodynamic coefficients on Re are shown, while in Figure 8.4b the results obtained neglecting such dependency are shown. Considering or neglecting the dependency of the aerodynamic coefficients on Re strongly modifies the structural damping required for stability; when the derivatives of the aerodynamic coefficients are taken into account, the maximum value of Z_x is approximately 6×10^4 , whereas when they are neglected this drops to approximately 1.5×10^4 . This indicates that drag crisis instability is more violent than Den Hartog type instability. A more careful observation of the strong value taken by Z_x using the model of Macdonald & Larose (2006) for any α_s shows that this value is related to the strong peak of the derivative of C_y with respect to Re (Figure 6.1) observed at $\alpha = 120^\circ$ and $Re = 3.19 \times 10^5$. Differently, in the models of Den Hartog (1932) and Martin *et al.* (1981), the prediction is not affected by this term. The prediction of the model of Macdonald & Larose (2008a) considers both DoFs simultaneously and does not depend on the value of α_s . As a matter of fact, the variation of the aerodynamic damping with respect to α_s is the rotation of the aerodynamic damping matrix in Euclidean space. As

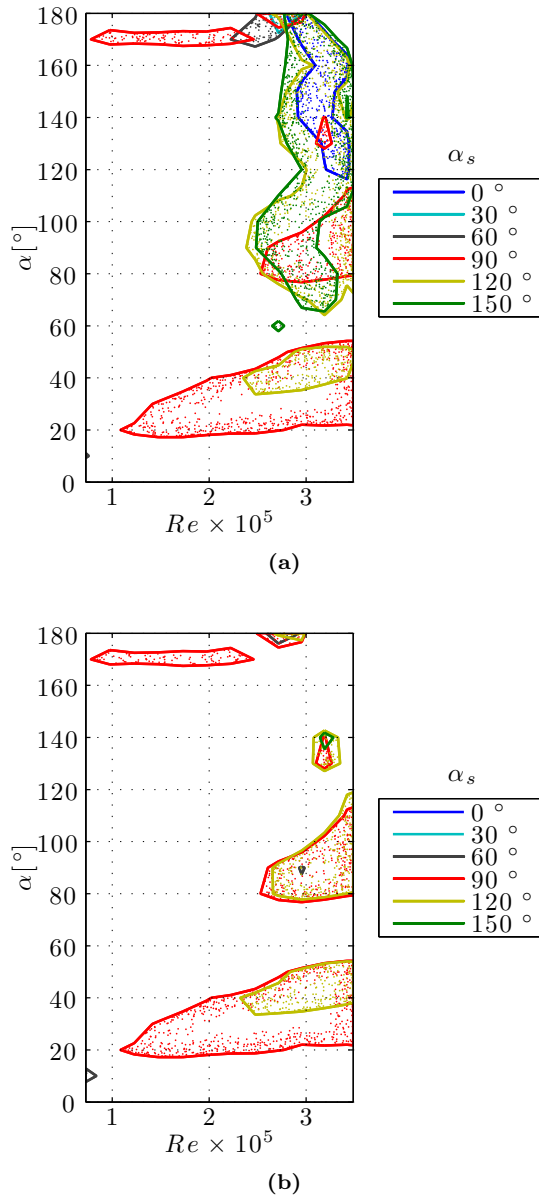


Figure 8.3: Regions of potential instability for different values of α_s using the model of [Macdonald & Larose \(2006\)](#), considering (a) and neglecting (b) the dependency of the aerodynamic coefficients on Re . The contour lines are the instability thresholds. (CC: $U = 11 \text{ m/s}$, $T = -5^\circ\text{C}$).

explained above, the 1-DoF model of Macdonald & Larose (2006) considers only the diagonal term of \mathbf{C}_a while the 2-DoF model of Macdonald & Larose (2008a) considers all the terms of \mathbf{C}_a . This justifies the strong difference in the prediction among the models. Anyway, the maximum between the prediction of the 1-DoF models of Den Hartog (1932) and Martin *et al.* (1981) is always greater than that of the 2-DoF model of Macdonald & Larose (2008a). Therefore, it can be concluded that in the tuned case the use of the maximum predicted value of the 1-DoF model furnishes predictions on the safety side respect to the model of Macdonald & Larose (2008a). This was also verified for the other CCs.

The models of Den Hartog (1932) and Martin *et al.* (1981) describe two particular situations among those included in the model of Macdonald & Larose (2006), therefore it is expected that they produce the same result as the latter, when this is applied for $\alpha_s = 90^\circ$ and for $\alpha_s = 0^\circ$, respectively. Indeed this result was found, and can be seen from comparison of Figure 8.3a and Figure 8.5a, where the potential instability regions found applying the 1-DoF models of Den Hartog (1932) (red lines, as in figure 8.3a) and Martin *et al.* (1981) (blue lines, as in 8.3a) are shown. In Figure 8.5a the result obtained through the application of the model of Macdonald & Larose (2008a) to the x and y tuned 2-DoF system is also shown (green lines). It can be observed that, following the classification given for Figure 8.3, the first and the third regions of potential instability, i.e. those associated with Den Hartog type instability, are the same when the models of Den Hartog (1932) and of Macdonald & Larose (2008a) are used, and coincide with those of Figure 8.3 for $\alpha_s = 90^\circ$. On the other hand, the second region of potential instability is differently predicted by the different models; in particular when it comes to the comparison of the results of the application of the 1-DoF model of Macdonald & Larose (2006) and of the 2-DoF model of Macdonald & Larose (2008a), these bring rather different results. The extension of the regions of potential instability found on the 2-DoF system are smaller than those found on the 1-DoF system, indicating that coupling of the perfectly tuned DoFs can be beneficial to stability, confirming the results of Macdonald & Larose (2008b,a). This conclusion is also corroborated by the results of Figure 8.5b, in which the minimum non-dimensional structural damping required to avoid instability of the tuned 2-DoF system, is shown. The maximum value found of $Z_x = Z_y = 10^4$ is quite lower than that found for the 1-DoF instability of $Z_x = 6 \times 10^4$ (Figure 8.4a).

Finally, in Figure 8.6a the effect of the detuning $k_{y,x} = \omega_y/\omega_x$ on the regions of potential instability evaluated using the model of Macdonald & Larose (2008b), is shown. The instability regions are plotted for values of the detuning in the range of $k_{y,x} = 1$ to 1.03; larger values give the same result as that found

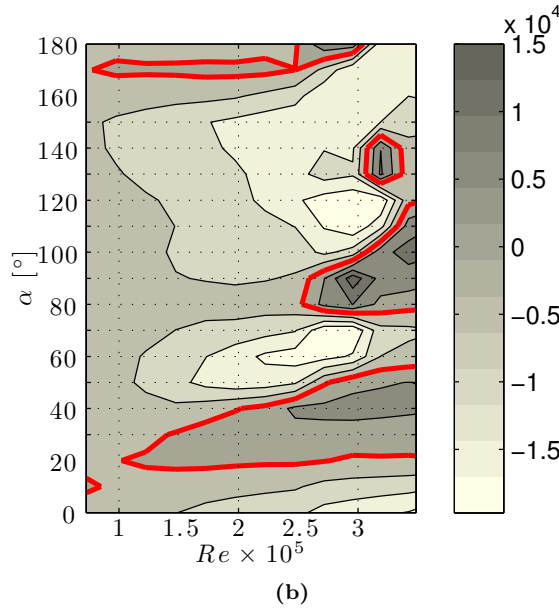
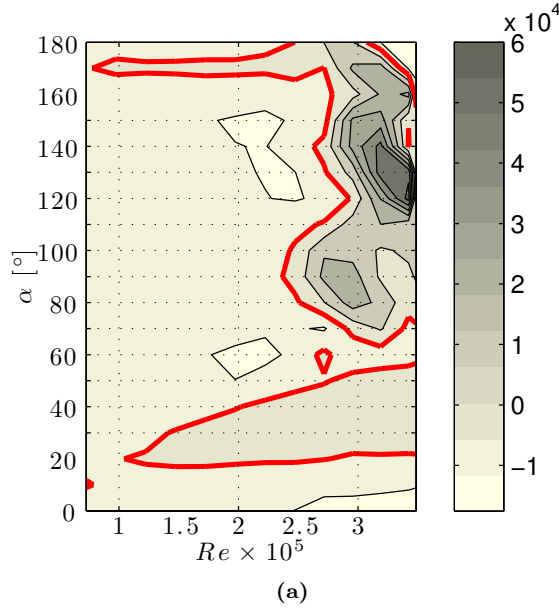


Figure 8.4: Minimum non-dimensional structural damping Z_x needed to avoid instability for any α_s , using the model of [Macdonald & Larose \(2006\)](#) considering (a) and neglecting (b) the dependency of the aerodynamic coefficients on Re . The red contour lines are the instability thresholds. (CC: $U = 11 \text{ m/s}$, $T = -5^\circ\text{C}$).

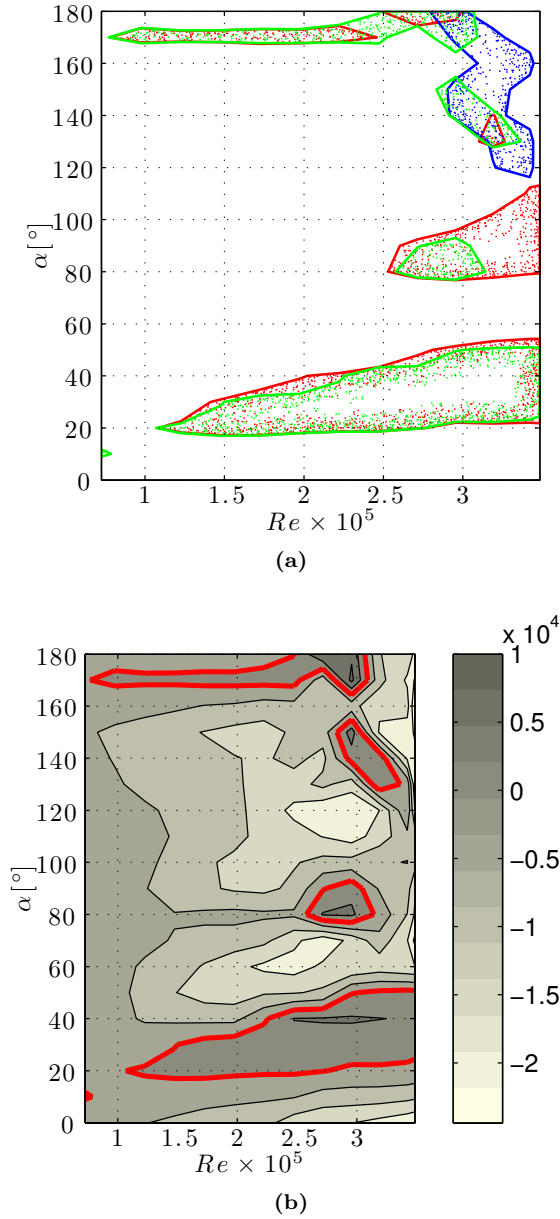
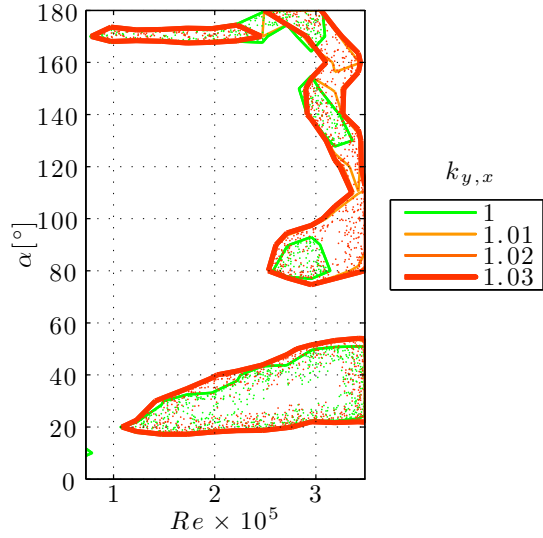


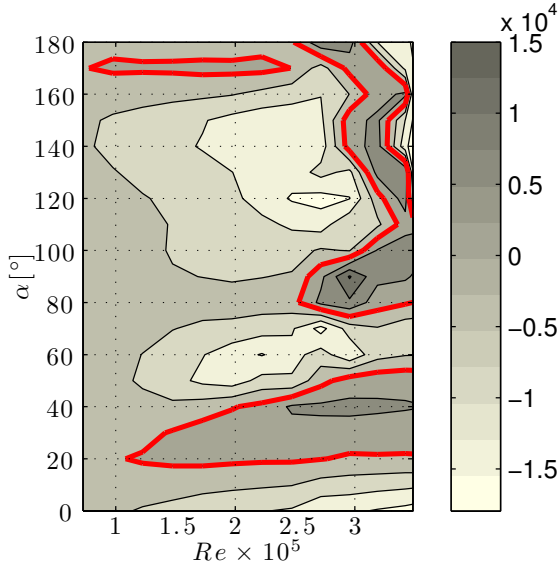
Figure 8.5: Comparison of the potential instability regions applying the 1-DoF and the tuned 2-DoF models (Den Hartog (1932), red; Martin *et al.* (1981), blue; Macdonald & Larose (2008a), green) (a). Minimum non-dimensional structural damping $Z_x = Z_y$ needed to avoid instability using the 2-DoF model of Macdonald & Larose (2008a) (b). (CC: $U = 11 \text{ m/s}$, $T = -5^\circ\text{C}$).

for $k_{y,x} = 1.03$, and it is therefore concluded that even very small values the detuning make the system behave as it were uncoupled in the x - and y -directions, with effective aerodynamic damping values given by the diagonal terms of \mathbf{C}_a . Hence, for iced-accreted bridge hangers, 2-DoF coupling occurs only when the natural frequencies in the two planes are very close to each other, confirming the result of Macdonald & Larose (2008b). On the other hand, the off-diagonal terms in \mathbf{C}_a are non-zero, and cause mode shapes to be slightly elliptical. In the range of $k_{y,x} = 1$ to 1.03, beneficial effects of tuning on the extension of the potential instability region were predicted by the model of Macdonald & Larose (2008b). This result was found also for the case in which the dependency of the aerodynamic coefficients on Re is neglected (not shown in the figures). In Figure 8.6b the minimum non-dimensional structural damping, $Z_x = Z_y k_{y,x}$, required to avoid instability for $k_{y,x} = 1.03$, is shown. The values predicted corresponds to those predicted by the model of Macdonald & Larose (2006) for $\alpha_s = 0^\circ$ and 90° . In general, 2-DoF models for small detuned systems predict the required structural damping of the 1-DoFs models evaluated in the DoFs in which the 2-DoF models are expressed. The comparison between Figures 8.6b and 8.5b confirms the beneficial effect for stability of the tuning between the DoFs: the maximum value of $Z_x = Z_y k_{x,y}$ for $k_{x,y} = 1$ is approximately 10^4 (Figure 8.5b), whereas it is approximately 1.5×10^4 for $k_{x,y} = 1.03$ (Figure 8.6b).

Torsional vibrations are not an issue for bridge cables, nevertheless, the availability of wind tunnel data allows implementation of torsional and coupled-torsional stability models, which apply to any elongated structural element; this, therefore, is done with the only aim of a general comparison among the models and the results they produce; the results obtained are of no interest for practical application to bridge cables. In Figure 8.7a the regions of potential torsional instability for different values of δ in the range of 50° to 100° , characterizing the separation point on plain circular cross sections, and for $R_\delta = 0.08$ m, are shown, as evaluated applying the model of Nigol & Buchan (1981b). For all the values of δ considered, one region of torsional instability was found, approximately in the range of $\alpha = 80^\circ$ to 180° and for $Re < 3 \times 10^5$ and in the range of $\alpha = 140^\circ$ to 170° for $Re > 3 \times 10^5$. For $Re < 3 \times 10^5$, the lowest value of α at which instability can occur depends on δ , and varies between $\alpha = 80^\circ$ and 110° ; for larger values of Re the instability condition is independent of δ . As to the effect of R_δ , this is to vary the predicted value of Z_θ , not modifying the extension of the regions of potential instability. A proper choice of R_δ and δ requires knowledge of the separation point; this is function of Re for circular cylinders, whereas for ice-accreted bridge hangers it is also function of the angle of attack α . To the authors' best knowledge, data allowing a different choice of R_δ are not available. In Figure 8.7b the minimum required non-dimensional structural damping, Z_θ , is shown, for $\delta = 90^\circ$ and $R_\delta = 0.08$ m. Under these



(a)



(b)

Figure 8.6: Regions of potential instability for different values of $k_{y,x} = \omega_y/\omega_x$ using the 2-DoF model of [Macdonald & Larose \(2008a\)](#) (a). Minimum non-dimensional structural damping $Z_x = Z_y k_{y,x}$ needed to avoid instability using the 2-DoF model of [Macdonald & Larose \(2008a\)](#) for $k_{y,x} = 1.03$ (b). (CC: $U = 11 \text{ m/s}$, $T = -5^\circ\text{C}$).

circumstances, susceptibility to torsional instability is predicted in the range of approximately $\alpha = 100^\circ$ to 180° and for $Re < 2.5 \times 10^5$ and in the range of $\alpha = 140^\circ$ to 170° for $Re > 2.5 \times 10^5$. The structural damping required to avoid instability (i.e. the maximum value found in Figure 8.7b) is apparently low ($Z_\theta = 20$), with respect to the values found for Z_x ; however, when Eq. 8.13 is applied, this value is converted into $Z_x = 6.25 \times 10^3$, smaller but comparable with the values shown in Figures 8.4a, 8.5 and 8.6b.

Though not realistic for bridge cables, coupling can occur for other structural situations between the torsional and the heaving degrees of freedom. In Figure 8.8 comparison of the potential instability regions in the y and θ DoFs is shown, as evaluated using the 1-DoF (Den Hartog (1932), Nigol & Buchan (1981b)) and the tuned 2-DoF (Yu *et al.* (1992)) models. The regions of potential instability predicted applying the 2-DoF model are broad than the sum of those predicted using the 1-DoF models. In particular for low values of α and for all Re investigated, the same region of potential instability in the y direction is found using the models of Den Hartog (1932) and of Yu *et al.* (1992)); however, for larger values of α in excess of 60° and for all Re investigated, a broad region of potential coupled instability is found, including also combinations of α and Re for which 1-DoF instability does not take place.

The 2-DoF instability found in Figure 8.8 for large values of α using the model of (Yu *et al.* (1992)) is related to the perfectly tuning of the DoFs, and disappears when detuning is introduced. In Figure 8.9a, the effect of the detuning $k_{\theta,y} = \omega_\theta/\omega_y$ on the potential instability regions evaluated using the 2-DoF model of Yu *et al.* (1992), is shown. As already observed for the x and y DoFs case, very small values of the detuning $k_{\theta,y}$ make the system behave as it were uncoupled in the θ - and y -DoFs. Also here, for values of $k_{\theta,y}$ in excess of 1.03, the predicted potential instability regions do not depend on $k_{\theta,y}$, and superimpose to those predicted using the 1-DoF models. The same result was found also when the dependency of the aerodynamic coefficients on Re is neglected (not shown in the figures). This is the actual behavior of bridge hangers, featuring a much larger torsional frequency than the heave and sway frequencies ($k_{\theta,y} \gg 1$).

Finally, in Figure 8.9b comparison of the potential instability regions evaluated using the 1-DoF and the tuned 3-DoF models (Den Hartog (1956), Martin *et al.* (1981), Nigol & Buchan (1981b) and Gjelstrup & Georgakis (2011)), is shown. This also is an unrealistic case, for the same reason above. From the

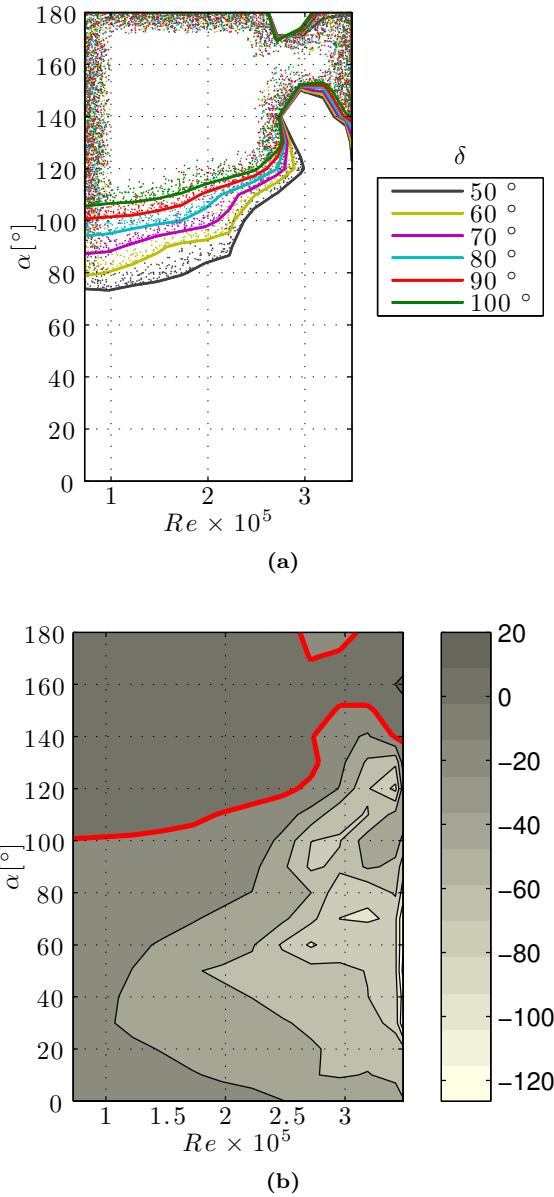


Figure 8.7: Regions of potential torsional instability, for different values of δ and for $R_\delta = 0.08 m$ using the model of [Nigol & Buchan \(1981b\)](#) (a), the contour lines are the instability thresholds. Minimum non-dimensional structural damping Z_θ needed to avoid torsional instability for $\delta = 90^\circ$ and for $R_\delta = 0.08 m$ (b), the red contour lines are the instability thresholds. (CC: $U = 11 m/s$, $T = -5^\circ C$).

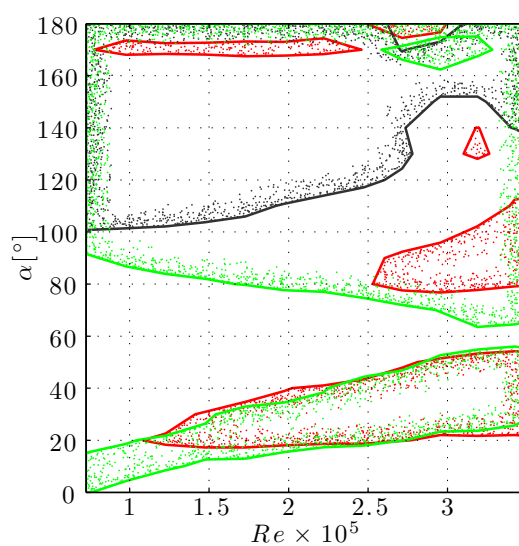


Figure 8.8: Comparison of the potential instability regions among the 1-DoF and the 2-DoF tuned models (Den Hartog (1932), red; Nigol & Buchan (1981b), grey; Yu *et al.* (1992), green). (CC: $U = 11 \text{ m/s}$, $T = -5^\circ\text{C}$).

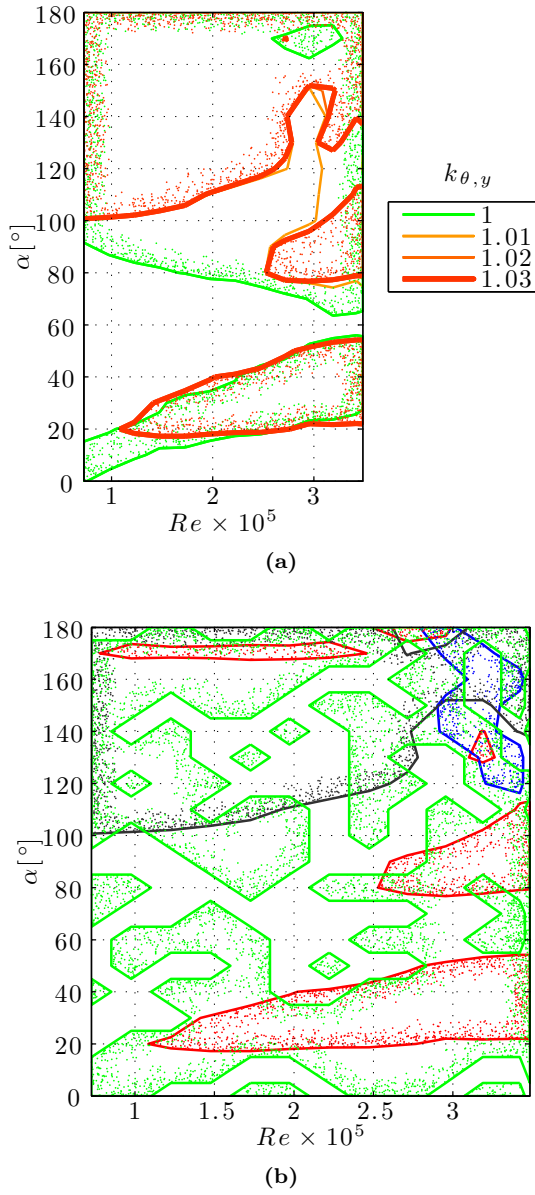


Figure 8.9: Regions of potential instability for different values of $k_{y,\theta} = \omega_y/\omega_\theta$ using the 2-DoF model of Yu *et al.* (1992) (a). Comparison of the potential instability regions among the 1-DoF and the 3-DoF tuned models (b) (Den Hartog (1932), red; Martin *et al.* (1981), blue; Nigol & Buchan (1981b), grey; Gjelstrup & Georgakis (2011), green). (CC: $U = 11 \text{ m/s}$, $T = -5^\circ\text{C}$).

figure no apparent correlation appears between the instability prediction of the 3-DoF model and those of the 1-DoF models; in addition, instability regions evaluated with the 3-DoF model are quite scattered in the $Re - \alpha$ plane. The model of Gjelstrup & Georgakis (2011) provides information about the onset of instability, but does not allow evaluating the amount of structural damping required to stabilize the unstable system; to understand the result of Figure 8.9b, a modified version of the model of Macdonald & Larose (2008a) was used to evaluate the amount of structural damping required to stabilize the tuned 2-DoF $x - \theta$ system. The modified version of the model was obtained using the aerodynamic damping terms derived by Gjelstrup & Georgakis (2011) in the 2-DoF stability model of Macdonald & Larose (2008a,b) written in this case in the y and θ DoFs. The result in the $Re - \alpha$ plane (not shown here) is as scattered as that of Figure 8.9b, with values of the required non-dimensional structural damping never larger than $Z_\theta = \pm 5 \times 10^{-3}$, except for larger values in the order of 1.5×10^4 for $Re > 3 \times 10^5$ and $\alpha > 140^\circ$, i.e. in the region where a drag crisis type instability occurs. This justifies the scatter of the instability regions in Figure 8.9b, which are the result of the system being in a condition of onset x and θ 2-DoF instability for almost all values of α and Re considered. This validates the apparently confusing results obtained through application of the model of Gjelstrup & Georgakis (2011).

On the other hand, when the torsional frequency is detuned with respect to the y and the x frequencies, the same result of the model of Macdonald & Larose (2008a) is obtained. This is presented in Figure 8.10a, where the effect of torsional detuning ($k_{\theta,x} = \omega_\theta/\omega_x = k_{\theta,y} = \omega_\theta/\omega_y$) on the potential instability regions evaluated using the model of Gjelstrup & Georgakis (2011), is shown. The result obtained is the superposition of the result shown in Figure 8.5b concerning the tuned $x - y$ system, and the region of torsional instability predicted through the model of Nigol & Buchan (1981b) (Figure 8.7b). For completeness, in Figure 8.10b the results obtained using the model of Gjelstrup & Georgakis (2011), with a detuning between the x frequency and the y and θ frequencies ($k_{x,\theta} = \omega_x/\omega_\theta = k_{x,y} = \omega_x/\omega_y$), is shown. The predicted potential instability regions appear to be the superposition of the result shown in Figure 8.8 concerning the tuned $y - \theta$ system, and the region of potential instability in the x DoF predicted by the model of Den Hartog (1956). In conclusion it appears that when one DoF is detuned with respect to the remaining two, the potential instability regions are the superposition of those pertaining to the 1-DoF and to the tuned 2-DoF systems taken separately.

8.2.2 Stay cables

For stay cables, data coming from CC I7 (Figures 6.12, 6.13 and 6.14). First, lateral stability of stay cables in 1-DoF was investigated using the model of Mac-

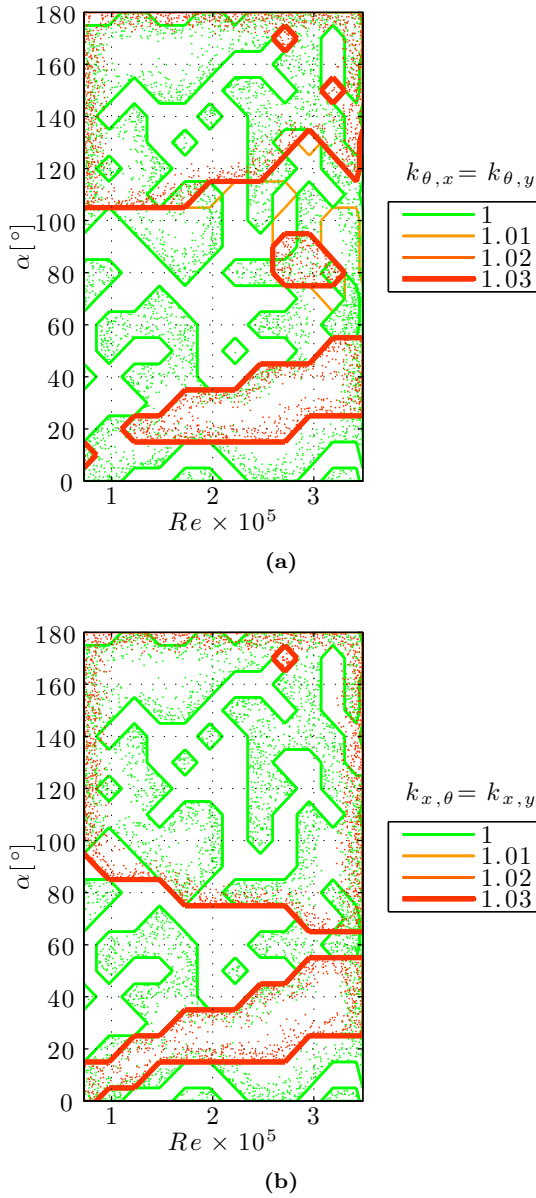
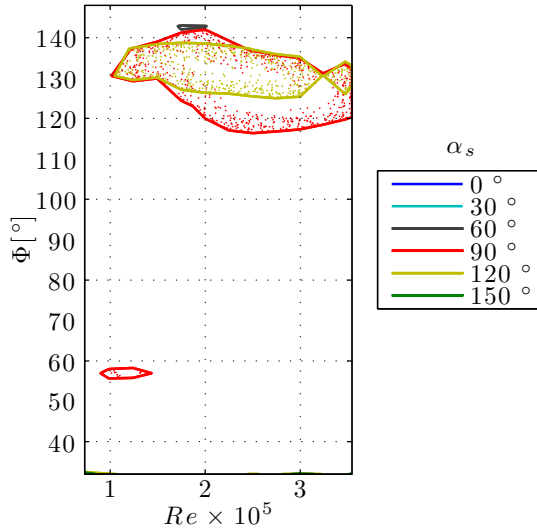


Figure 8.10: Regions of potential instability for different values of $k_{\theta,x} = \omega_{\theta}/\omega_x = k_{\theta,y} = \omega_{\theta}/\omega_y$ (a) and of $k_{x,\theta} = \omega_x/\omega_{\theta} = k_{x,y} = \omega_x/\omega_y$ (b), using the 3-DoF model of Gjelstrup & Georgakis (2011). (CC: $U = 11 \text{ m/s}$, $T = -5^\circ\text{C}$).

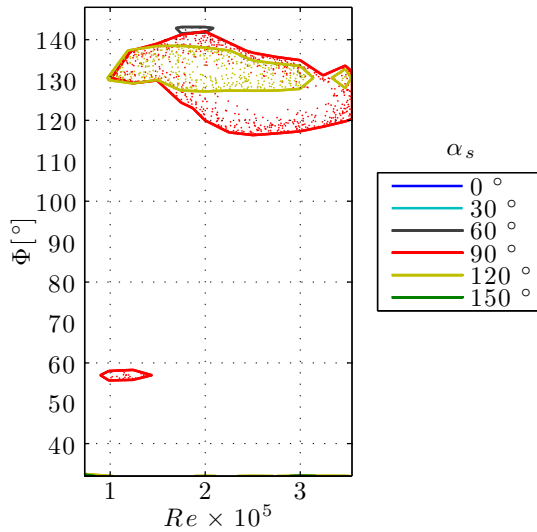
donald & Larose (2006) for different values of α_s , considering and neglecting the dependency of the aerodynamic coefficients on Re and on α . Then, torsional stability was investigated using the aerodynamic torsional damping terms derived by Gjelstrup & Georgakis (2011) for different values of δ . Stability in the coupled x and y tuned and detuned DoF was investigated using the model of Macdonald & Larose (2008a,b). Stability in the coupled y and θ tuned and detuned DoFs was investigated using the aerodynamic damping terms derived by Gjelstrup & Georgakis (2011) in a modified version of the 2-DoF stability condition of Macdonald & Larose (2008a,b). Finally, stability of the coupled 3-DoF tuned and detuned system was investigated using the model of Gjelstrup & Georgakis (2011).

In Figure 8.11 the regions of potential instability for different values of α_s evaluated using model of Macdonald & Larose (2006), are shown in the plane $Re - \Phi$. The contour lines indicate the instability threshold. In Figure 8.11a the regions of potential instability evaluated considering the dependency of the aerodynamic coefficients on α , Φ and Re , are shown, while, in Figure 8.11b the regions obtained neglecting the dependency on Re are shown. Calculations were repeated also neglecting the dependency on α , which made the unstable behavior completely disappear (the result is not shown). One major region of instability is found for any values of α_s . This region is visible for $Re > 10^5$ and in the range of $\Phi = 120^\circ$ to 140° , and is broader for $\alpha_s = 90^\circ$, it becomes smaller for $\alpha_s = 120$ and completely disappears for other values of α_s . The regions of instability are approximately the same considering and neglecting the dependency of the aerodynamic coefficients on Re . A second, narrow region of instability is found, only for $\alpha_s = 90^\circ$, located approximately in the range of $Re = 10^5$ to 1.5×10^5 and $\Phi = 50^\circ$ to 60° . In this case it is clear that only one type of instability exists, related to the variation of the aerodynamic coefficients with α_s .

The minimum non-dimensional structural damping, Z_x , needed to avoid instability for any α_s , is shown in Figure 8.12 in the plane $Re - \Phi$. In Figure 8.12a the result considering all the derivatives of the aerodynamic coefficients is shown, and in Figures 8.12b, 8.12c and 8.12d the results obtained neglecting the derivatives with respect to Re , to α and to Φ are shown, respectively. The regions reported in Figure 8.12 are the envelope of the maxima of Z_x obtained with varying α_s . Again, negative values indicate that the system is stable. When all the derivatives are considered, the maximum value of the structural damping required to stabilize the cable is in the order of $Z_x = 2 \times 10^3$. Comparison of Figures 8.12a and 8.12b suggests that it is not a variation of the aerodynamic coefficients on Re to be responsible a possible instability. Comparison of Figures 8.12a and 8.12c, on the other hand, suggests that a key role to stability is played by the dependency of the aerodynamic coefficients on α ; when this is neglected



(a)



(b)

Figure 8.11: Regions of potential instability for different values of α_s using the model of [Macdonald & Larose \(2006\)](#), considering (a) and neglecting (b) the dependency of the aerodynamic coefficients on Re . The contour lines are the instability thresholds. (CC: $\beta = 90^\circ$, $U = 11 \text{ m/s}$, $T = -5^\circ \text{C}$).

the unstable behavior disappears and the aerodynamic behavior is roughly proportional to Re , which is the case for linear aerodynamics. Comparison of Figures 8.12a and 8.12d indicates that when the variation of the aerodynamic coefficients on Φ is neglected the unstable behavior is overestimated. The results evidenced that neglecting some dependence of the aerodynamic coefficients can give rise to a wrong assessment of aerodynamic stability with both beneficial and detrimental effects, differently from what concluded in the bridge hanger case.

As for the bridge hanger case, a comparison can be made between the results obtained through the application of 1-DoF models and on coupled 2-DoF. For the stay cable, however, two observations are in order; the first is that in inclined flow no specific models exist for particular directions of oscillation, as it happens in cross flow, therefore reference must always be made to the model of Macdonald & Larose (2006); the second is that for stay cables the perfectly tuning is not realistic, as the vertical sag makes the in-plane and the out-of-plane natural frequencies different (Irvine, 1981). The case of perfectly tuning is considered here with the only purpose of comparison. In Figure 8.13a a comparison of the potential instability regions found applying the 1-DoF model of (Macdonald & Larose (2006) for $\alpha_s = 0^\circ$ and 90° and the tuned 2-DoF model of Macdonald & Larose (2008a)), is shown. The regions of instability found using the different models are similar. In particular, a wider region is found in the range of $Re = 10^5$ to 3.5×10^5 and $\Phi = 120^\circ$ to 140° when the 1-DoF model is used, which becomes smaller when the 2-DoF model is used. A second, smaller region is found in the range of $Re = 10^5$ to 1.5×10^5 and $\Phi = 50^\circ$ to 60° , which is wider when the 2-DoF model is used. In Figure 8.13b the minimum non-dimensional structural damping, $Z_x = Z_y$, needed to avoid instability is shown, as evaluated using the 2-DoF model of Macdonald & Larose (2008a); comparison with Figure 8.12a is very good. Therefore it is concluded that coupled stability in the tuned x and y DoFs is the same as that of the two DoFs taken separately. Nevertheless, as already pointed out, this is an unrealistic case.

Therefore, in Figure 8.14a the effects of detuning ($k_{y,x} = \omega_y/\omega_x$) evaluated using the model of Macdonald & Larose (2008b), are shown. As for the cross flow case, small values of $k_{y,x}$ make the system behave as it were uncoupled in the x and y directions, and in this case the transition between the coupled and the uncoupled behavior is even more abrupt than in cross flow. As a matter of fact, for values of $k_{y,x}$ in excess of 1.01 the predicted potential instability regions already become independent of $k_{y,x}$, and overlap to those predicted using the 1-DoF models (Figure 8.11a). This excludes any possible 2-DoF instability of stay cables.

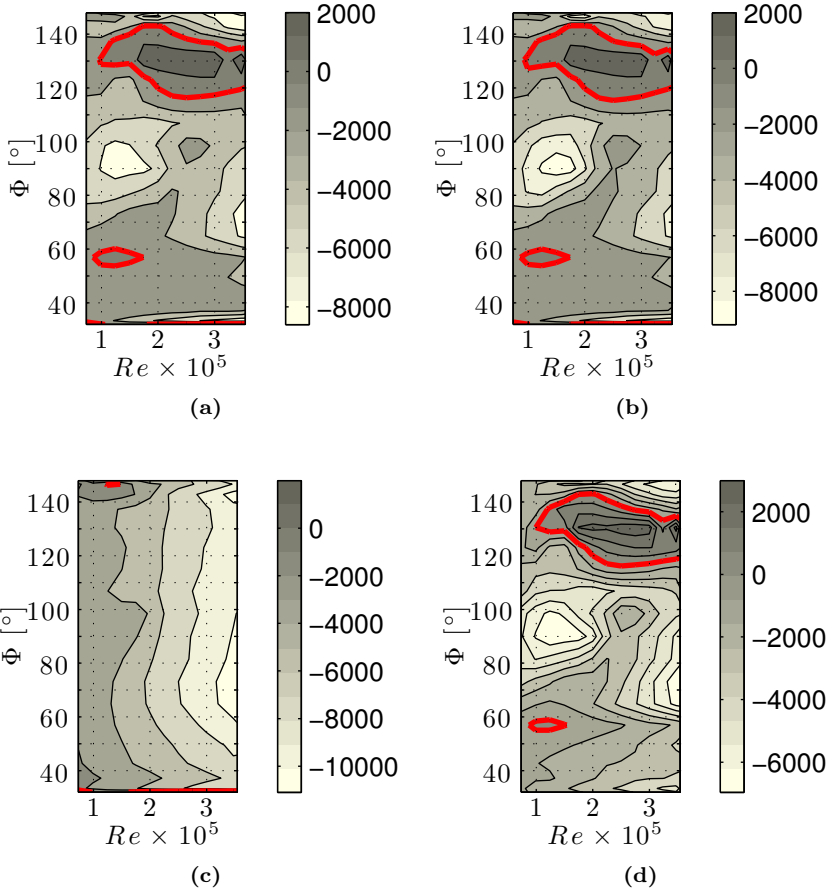


Figure 8.12: Minimum non-dimensional structural damping Z_x needed to avoid instability for any α_s , using the model of [Macdonald & Larose \(2006\)](#) considering (a) and neglecting the dependency of the aerodynamic coefficients on Re (b), on α (c) and on Φ (d). The red contour lines are the instability thresholds. (CC: $\beta = 90^\circ$, $U = 11 \text{ m/s}$, $T = -5^\circ \text{C}$).

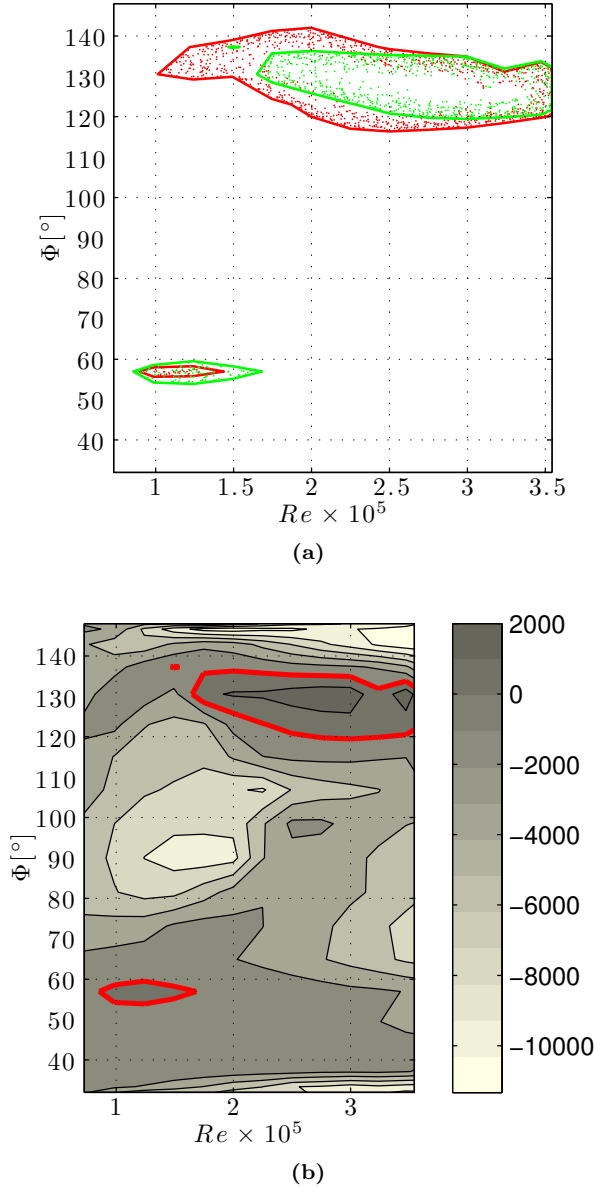


Figure 8.13: Comparison of the potential instability regions applying the 1-DoF and the tuned 2-DoF models (Macdonald & Larose (2006) with $\alpha_s = 90^\circ$, red; Macdonald & Larose (2006) with $\alpha_s = 0^\circ$, blue; Macdonald & Larose (2008a), green) (a). Minimum non-dimensional structural damping $Z_x = Z_y$ needed to avoid instability using the 2-DoF model of Macdonald & Larose (2008a) (b). (CC: $\beta = 90^\circ$, $U = 11 \text{ m/s}$, $T = -5^\circ\text{C}$).

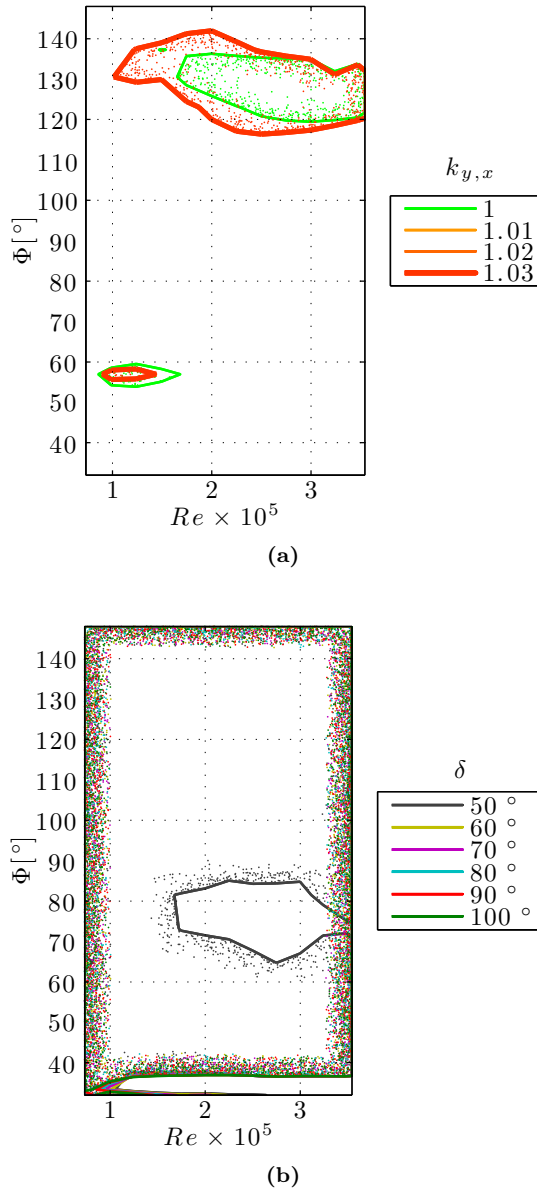


Figure 8.14: Regions of potential instability for different values of $k_{y,x} = \omega_y/\omega_x$ using the 2-DoF model of [Macdonald & Larose \(2008a\)](#) (a). Regions of potential torsional instability, for different values of δ and for $R_\delta = 0.08$ m, using a 1-DoF torsional modified version of the model of [Gjelstrup & Georgakis \(2011\)](#) (b). The contour lines are the instability thresholds. (CC: $\beta = 90^\circ$, $U = 11$ m/s, $T = -5^\circ\text{C}$).

As already pointed out for bridge hangers, torsional vibrations are not an issue for bridge cables. Only for completeness, in Figure 8.14b the regions of potential torsional instability for different values of δ in the range of 50° to 100° and for $R_\delta = 0.08$ m, are shown, evaluated using the torsional aerodynamic terms derived by Gjelstrup & Georgakis (2011). The system appears to be prone to instability almost in the entire range investigated, except when $\Phi < 40^\circ$. Limited to $\delta = 50^\circ$, a region of stability appears in the range of $\Phi = 70^\circ$ to 90° and for $Re = 1.5 \times 10^5$ to 3.5×10^5 . As for the cross flow case, the effect of R_δ is to change the predicted value of Z_θ , without altering the regions of potential instability.

In Figure 8.15 the effects of the coupling of the y and θ DoFs is analyzed, through comparison of the potential instability regions found applying the 1-DoF model of Macdonald & Larose (2006) for $\alpha_s = 90^\circ$, the 1-DoF torsional modified version of the model of Gjelstrup & Georgakis (2011) and the adapted tuned 2-DoF model from the damping matrix derived by Gjelstrup & Georgakis (2011). Again, this is an unrealistic case. Also here, as already pointed out for the 1-DoF torsional case, the system is prone to instability in the entire range of parameters investigated, except for values of $\Phi < 40^\circ$.

Finally, stability in the 3 DoF was evaluated using the model of Gjelstrup & Georgakis (2011). In this case, as for the hanger case, it is not possible to identify a correlation between the predictions obtained with 1-DoF models and those obtained with 3-DoF models. As for the case of bridge hangers, this is due to the very low values of the required structural damping. Also in this case, small deviations from 1 of $k_{\theta,y}$ and of $k_{y,x}$ make the potential instability regions tend to the superposition of those pertaining to the 1-DoF and to the tuned 2-DoF systems, taken separately.

8.3 Case study

The results presented in Sections 8.2.1 and 8.2.2 come from specific aerodynamic data, but are not related to any specific structural situation. In this section they are applied to values of the natural frequencies, mass and torsional mass moment of inertia per unit length typical of hangers and stay cables of long span bridges. In particular, values of $\omega_x = \omega_y = 2\pi$ were considered, associated with the first in-plane and out-of-plane modes. The mass of the 0.16 m diameter cable was assumed to be 100 kg/m. The minimum required structural damping ratio found applying the different models for the iced hanger and stay cable are reported in Table 8.2 and 8.3, respectively. Negative values reported in the Tables indicate a stable behavior in the entire domain investigated, and the

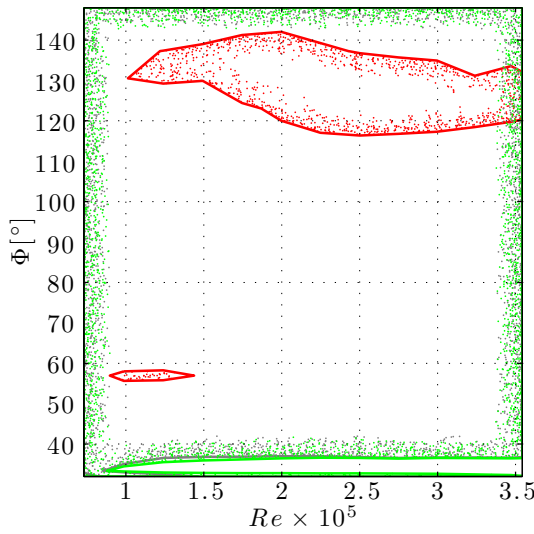


Figure 8.15: Comparison of the potential instability regions between the 1-DoF and the 2-DoF tuned models (Macdonald & Larose (2006) with $\alpha_s = 90^\circ$, red; 1-DoF torsional modified version of the model of Gjelstrup & Georgakis (2011), grey; adapted 2-DoF model from the damping matrix derived by Gjelstrup & Georgakis (2011), green). (CC: $\beta = 90^\circ$, $U = 11 \text{ m/s}$, $T = -5^\circ\text{C}$).

magnitude of the negative minimum required structural damping is a measure of the level of stability.

For the bridge hanger, the model of [Macdonald & Larose \(2006\)](#) for any α_s predicts a very large value of the minimum required structural damping of 1.27%. This value is primarily associated with the derivative of C_L with Re . As a matter of fact, considering only the dependency of the aerodynamic coefficients on α , the minimum required structural damping ratio drops to 0.35%. The models of [Martin *et al.* \(1981\)](#) and of [Den Hartog \(1956\)](#) predict a minimum required structural damping of 0.23% and 0.32%, respectively. The torsional model of [Nigol & Buchan \(1981b\)](#) evaluated for $\delta = 90^\circ$ and $R_\delta = 0.08$ m predicts a minimum required structural damping of 0.14%; this value doesn't change when the dependency of the aerodynamic coefficients on α is neglected, and drops to 0.11% when the dependency on Re is neglected. When applied to the tuned 2-DoF system, the model of [Macdonald & Larose \(2008a\)](#) predicts much smaller values of the required damping, then those predicted with the model of [Macdonald & Larose \(2006\)](#) for any α_s and smaller than those predicted with the models of [Martin *et al.* \(1981\)](#) and [Den Hartog \(1956\)](#). When the same model is applied to the detuned system with $k_{y,x} = 1.03$, the minimum required structural damping is equal to the maximum between the values predicted by the 1-DoF models of [Martin *et al.* \(1981\)](#) and [Den Hartog \(1956\)](#). When applied to the tuned 2-DoF system, the model of [Yu *et al.* \(1992\)](#) predicts larger values of the required damping than those predicted with the models of [Den Hartog \(1932\)](#) and of [Nigol & Buchan \(1981b\)](#). When the same model is applied to the detuned system with $k_{y,\theta} = 1.03$, the minimum required structural damping is equal to the maximum between the values predicted by the 1-DoF models of [Den Hartog \(1932\)](#) and of [Nigol & Buchan \(1981b\)](#).

For the stay cable, the model of [Macdonald & Larose \(2006\)](#) for any α_s predicts a minimum required structural damping of 0.08%. This value is almost the same neglecting the dependency of the aerodynamic coefficients on either Φ , α or Re ; this is a symptom of a combined instability. When the same model is applied for $\alpha_s = 0^\circ$, it predicts stability in the entire domain investigated; when applied for $\alpha_s = 90^\circ$ it predicts a minimum required structural damping of 0.07%, not far from that predicted for any α_s . In the latter case, when the dependency of the aerodynamic coefficients on α is neglected, a false stable behavior is found. When the adapted torsional model from the damping matrix derived by [Gjelstrup & Georgakis \(2011\)](#) is applied with $\delta = 90^\circ$ and $R_\delta = 0.08$ m it predicts a minimum required structural damping ratio that is equal to 0.7%, larger than the values found for the translational DoFs. This value is approximately the same when the dependency of the aerodynamic coefficients on either α or Re is neglected, and drops to 0.26% when the dependency on Φ is neglected. Application of the model of [Macdonald & Larose \(2008a\)](#) to the tuned 2-DoF system predicts the same value of the minimum required structural damping than that predicted with the model of [Macdonald & Larose \(2006\)](#) for $\alpha_s = 90^\circ$, and slightly deviates from that when not all the derivatives of

Table 8.2: Minimum required structural damping ratio [%] found for the ice-accreted bridge hanger with $m = 100$ kg/m and $\omega_x = 2\pi$, using different stability models.

Model	DoFs	α_s	Tuned	Dependency		
				$\alpha - Re$	Re	α
Macdonald & Larose (2006)	x	any	n/a	1.27	1.25	0.35
Martin <i>et al.</i> (1981)	x	0°	n/a	0.23	0.23	n/a
Den Hartog (1932)	y	0°	n/a	0.32	n/a	0.32
Nigol & Buchan (1981b)	θ	0°	n/a	0.14	0.14	0.11
Macdonald & Larose (2008a)	$x - y$	0°	\checkmark	0.22	0.18	0.22
Macdonald & Larose (2008b)	$x - y$	0°	$k_{y,x} = 1.03$	0.32	0.22	0.32
Yu <i>et al.</i> (1992)	$y - \theta$	0°	\checkmark	0.4	0.14	0.36
Yu <i>et al.</i> (1992)	$y - \theta$	0°	$k_{y,\theta} = 1.03$	0.32	0.14	0.32

the aerodynamic coefficients are incorporated. When the same model is applied with a detuning $k_{y,x} = 1.03$, the minimum required structural damping coincides with the maximum between the values predicted with the model of Macdonald & Larose (2006) for $\alpha_s = 0^\circ$ and $\alpha_s = 90^\circ$. When the model of Yu *et al.* (1992) is applied to the tuned 2-DoF system, it predicts the same values as the maxima between the values predicted with the models of Macdonald & Larose (2006) for $\alpha_s = 90^\circ$ and of adapted torsional model from the damping matrix derived by Gjelstrup & Georgakis (2011). This applies regardless of what derivatives of the aerodynamic coefficients are included in the calculations. Finally, when the same model is applied with a detuning $k_{y,\theta} = 1.03$, the minimum required structural damping is approximately equal to that found in the case of perfectly tuning, and the dominant instability is in torsion.

8.4 Some preliminary conclusions concerning the stability of ice-accreted bridge cables

In Sections 8.2 and 8.3, the stability of bridge hangers and stay cables was investigated using different models reported in literature applied to one particular CC, with the purpose of comparison. This was done considering also unrealistic cases. For bridge hangers, aerodynamic data are available for 4 different CCs, and can be used to investigate the actual stability. It must be clear that for a comprehensive analysis, data coming from a much broader variety of CCs would be needed; nevertheless, it seems that in the lack of a larger database, the avail-

Table 8.3: Minimum required structural damping ratio [%] found for the ice-accreted stay cable with $m = 100$ kg/m and $\omega_x = 2\pi$, using different stability models * Adapted torsional model from the damping matrix derived by Gjelstrup & Georgakis (2011).

Model	DoFs	α_s	Tuned	Dependency				
				$\Phi - \alpha - Re$	$\alpha - Re$	$\Phi - Re$	$\Phi - \alpha$	
Macdonald & Larose (2006)	x	any	n/a	0.08	0.07	0.07	0.07	
Macdonald & Larose (2006)	x	0°	n/a	-0.03	-0.02	-0.03	-0.03	
Macdonald & Larose (2006)	x	90°	n/a	0.07	0.07	-0.03	0.07	
Adapted torsional model*	θ	0°	n/a	0.70	0.26	0.70	0.74	
Macdonald & Larose (2008a)	$x - y$	0°	✓	0.07	0.05	-0.01	0.05	
Macdonald & Larose (2008b)	$x - y$	0°	$k_{y,x} = 1.03$	0.07	0.07	-0.03	0.07	
Yu <i>et al.</i> (1992)	$y - \theta$	0°	✓	0.70	0.27	0.71	0.75	
Yu <i>et al.</i> (1992)	$y - \theta$	0°	$k_{y,\theta} = 1.03$	0.70	0.26	0.70	0.73	

able data cover at least the conditions in which a more pronounced unstable behavior is expected. Differently, in the case of stay cables, despite the larger number of CCs investigated, it was not possible to reach general findings about the conditions of instability. As a matter of fact, only in one CC the aerodynamic coefficients were measured also by varying the angle α , and when such dependency is neglected, the prediction of stability can prove quite misleading.

A summary of the regions of instability predicted for bridge hangers in different CCs are shown in Figures 8.16 and 8.17. The regions of potential instability predicted using the model of Macdonald & Larose (2006) for any α_s are shown in Figure 8.16a. The figure indicates three main regions of instability, similar to what was observed for Figure 8.3a in Section 8.2.1 concerning one single CC. The first instability region is for $\alpha = 20^\circ$ to 50° and for all values of Re investigated. This region is broader for CC V1, is smaller for CCs V2 and V3 and disappears for CC V4. The second instability region is located in for $Re > 2 \times 10^5$ and $\alpha = 80^\circ$ to 180° . In this range, the instability regions of CCs V1, V2 and V4 appear similar, whereas in CC V3 the hanger is stable. The third region of instability exists only for CC V1 and is in the range of $Re = 10^5$ to 2.5×10^5 and at approximately $\alpha = 170^\circ$.

The regions of potential instability predicted using the 2-DoF model of Macdonald & Larose (2008a) for the tuned system are shown in Figure 8.16b. The instability regions of CCs V2, V3 and V4 almost disappear. In particular, in the first region, the instability of CC V1 is almost the same, while the instability regions of the other CCs disappears. The second region shirks in two sub-regions. The first sub-region is at approximately $\alpha = 90^\circ$ and exists for CCs V1, V2 and V4 while the second exists only for CCs V1 and V2. The third region of instability is approximately unchanged whereas the system is tuned.

The regions of potential instability predicted using the model of Den Hartog (1932) are shown in Figure 8.17a. The figure indicates three main regions of instability, as in Figure 8.17a. The first instability region is similar to the prediction of the model of Macdonald & Larose (2006) for any α_s . The second region shirks in two sub-regions. The first sub-region is at approximately $\alpha = 90^\circ$ and exists for CCs V1, V2 and V4 while the second exists only for CCs V1. The third region of instability exists only for CC V1 and is similar to the prediction of the model of Macdonald & Larose (2006) for any α_s .

The regions of potential instability predicted using the model of Martin *et al.* (1981) are shown in Figure 8.17. The figure indicates one main regions of instability associated to a drag crisis instability is observed for $Re = 3.0 \times 10^5$ to 3.5×10^5 and $\alpha = 120^\circ$ to 180° for CC V1 and $\alpha = 120^\circ$ to 140° for CC V2. This region disappears in CC V3 and V4.

The minimum required non-dimensional structural damping for different CCs predicted using the 1-DoF model of Macdonald & Larose (2006) for any α_s , of Den Hartog (1932) and of Martin *et al.* (1981) and the 2-DoF model of Macdonald & Larose (2008a) of the tuned system are reported in Table 8.4. The maximum values of Z_x is predicted for CCs V1 and V2 in the second re-

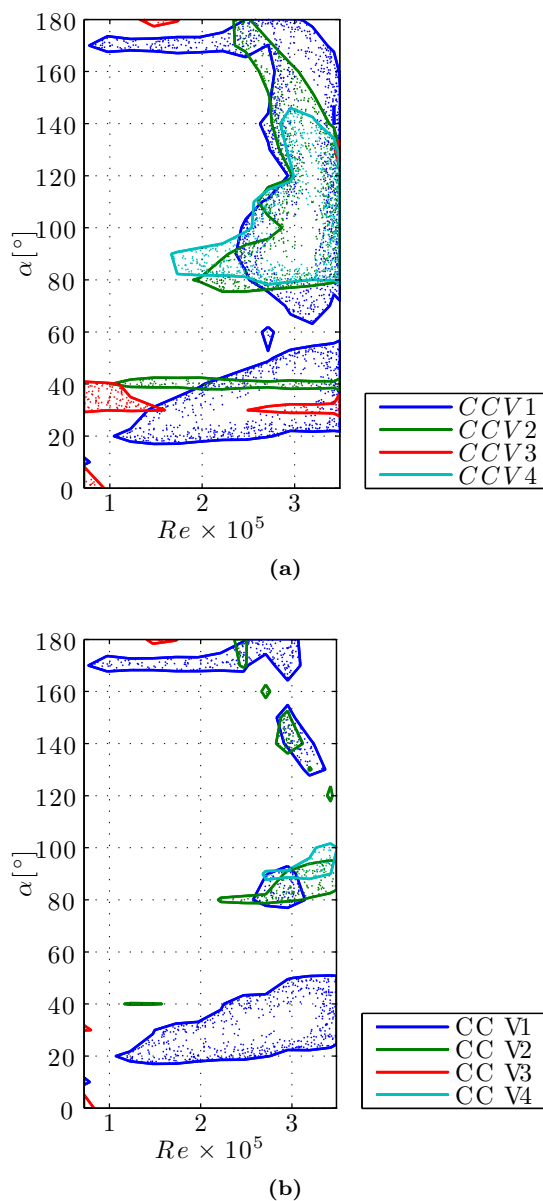


Figure 8.16: Regions of potential instability for bridge hangers for CCs V1, V2, V3 and V4 evaluated using the 1-DoF model of [Macdonald & Larose \(2006\)](#) for any α_s (a) and using the 2-DoF model of [Macdonald & Larose \(2008a\)](#) for the tuned system (b). The contour lines are the instability thresholds.

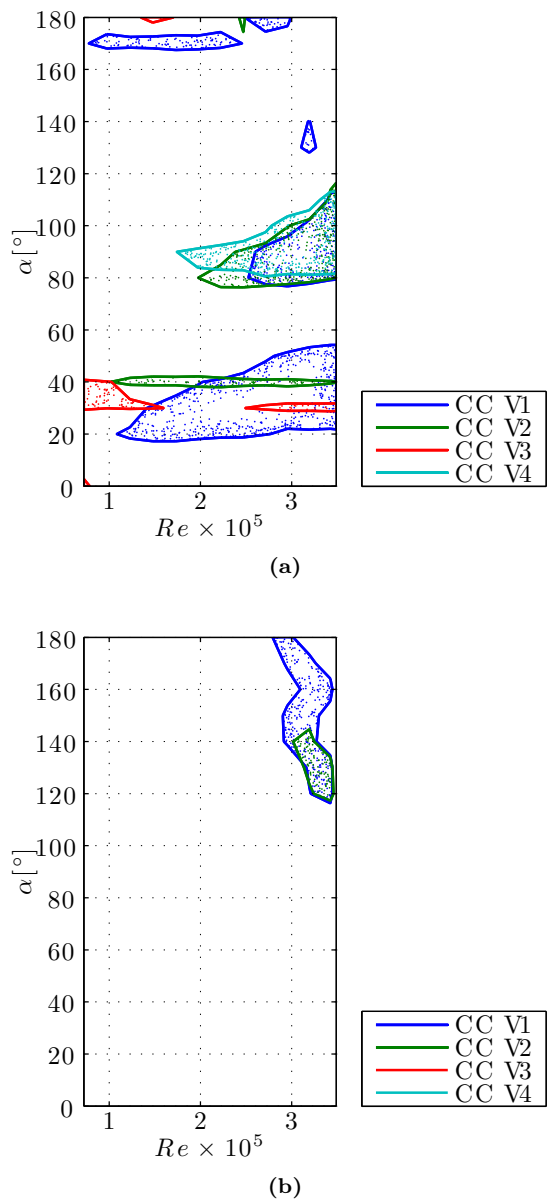


Figure 8.17: Regions of potential instability for bridge hangers for CCs V1, V2, V3 and V4 evaluated using the 1-DoF models of Den Hartog (1932) (a) and of Martin *et al.* (1981) (b). The contour lines are the instability thresholds.

Table 8.4: Minimum required non-dimensional structural damping predicted using the model of [Macdonald & Larose \(2006\)](#) for any α_s , the model of [Den Hartog \(1932\)](#), the model of [Martin *et al.* \(1981\)](#) and the model of [Macdonald & Larose \(2008a\)](#) with tuned frequency for different CCs.

	CC V1	CC V2	CC V3	CC V4
1-DoF any α_s	6.41×10^4	6.06×10^4	1.04×10^4	2.73×10^4
Den Hartog (1932)	1.63×10^4	1.10×10^4	0.14×10^4	1.1×10^4
Martin <i>et al.</i> (1981)	1.14×10^4	0.92×10^4	-0.35×10^4	-0.09×10^4
2-DoF tuned	1.13×10^4	0.98×10^4	0.09×10^4	0.13×10^4

gion of instability. A smaller value is predicted for CC V3 in the same region. In CC V3, the smallest value of the minimum required non-dimensional structural damping is predicted. Considering the system as tuned, the ranking of the values of the minimum required non-dimensional structural damping does not change, although they are considerably lower. However, the decrease is not proportional among the CCs. As already mentioned, it must be highlighted that the tuned solution tends to the 1-DoF solutions of [Martin *et al.* \(1981\)](#) and [Den Hartog \(1956\)](#) for very small values of the detuning.

References

- Bisplinghoff, R.L., & Ashley, H. 1962. *Principles of aeroelasticity*. Dover Publications.
- Blevins, R.D. 1977. Flow-induced vibration. *New York, Van Nostrand Reinhold Co., 1977. 377, 1.*
- Blevins, R.D., & Iwan, W.D. 1975. The galloping response of a two-degree-of-freedom system. *In: American Society of Mechanical Engineers, Applied Mechanics Western Conference, University of Hawaii, Honolulu, Hawaii.*
- Carassale, L., Freda, A., & Piccardo, G. 2004. Quasi-static model for aerodynamic instability of yawed circular cylinder. *Pages 401–404 of: 5th International Colloquium Bluff Body Aerodynamics and Applications.*
- Den Hartog, J.P. 1932. Transmission line vibration due to sleet. *Electrical Engineering*, **51**(6), 413–413.
- Den Hartog, J.P. 1956. *Mechanical vibrations*. Courier Dover Publications.
- Gjelstrup, H., & Georgakis, C.T. 2011. A quasi-steady 3 degree-of-freedom model for the determination of the onset of bluff body galloping instability. *Journal of Fluids and Structures*, **27**(7), 1021–1034.
- Irvine, H.M. 1981. *Cable structures*. Dover Publications New York.
- Jones, K.F. 1992. Coupled vertical and horizontal galloping. *Journal of engineering mechanics*, **118**(1), 92–107.
- Luongo, A., & Piccardo, G. 2005. Linear instability mechanisms for coupled translational galloping. *Journal of Sound and Vibration*, **288**, 1027–1047.
- Macdonald, J.H.G., & Larose, G.L. 2006. A unified approach to aerodynamic damping and drag/lift instabilities, and its application to dry inclined cable galloping. *Journal of fluids and structures*, **22**(2), 229–252.
- Macdonald, J.H.G., & Larose, G.L. 2008a. Two-degree-of-freedom inclined cable gallopingpart 1: general formulation and solution for perfectly tuned system. *Journal of Wind Engineering and Industrial Aerodynamics*, **96**(3), 291–307.
- Macdonald, J.H.G., & Larose, G.L. 2008b. Two-degree-of-freedom inclined cable gallopingpart 2: analysis and prevention for arbitrary frequency ratio. *Journal of wind Engineering and industrial Aerodynamics*, **96**(3), 308–326.
- Martin, W.W., Naudascher, E., & Currie, I.G. 1981. Streamwise oscillations of cylinders. *Journal of the Engineering Mechanics Division*, **107**(3), 589–607.

- Nigol, O., & Buchan, P.G. 1981b. Conductor galloping part II-Torsional mechanism. *Power Apparatus and Systems, IEEE Transactions on*, 708–720.
- Takashi, N., & Hughes, T.J.R. 1992. An arbitrary Lagrangian-Eulerian finite element method for interaction of fluid and a rigid body. *Computer methods in applied mechanics and engineering*, **95**(1), 115–138.
- Wang, J., & Lilien, J.L. 1998. Overhead electrical transmission line galloping. A full multi-span 3-DOF model, some applications and design recommendations. *Power Delivery, IEEE Transactions on*, **13**(3), 909–916.
- Yu, P., Shah, A.H., & Popplewell, N. 1992. Inertially coupled galloping of iced conductors. *Journal of applied mechanics*, **59**, 140.
- Yu, P., Desai, Y.M., Shah, A.H., & Popplewell, N. 1993a. Three-degree-of-freedom model for galloping. Part I: Formulation. *Journal of Engineering Mechanics*, **119**(12), 2404–2425.
- Yu, P., Desai, Y.M., Popplewell, N., & Shah, A.H. 1993b. Three-degree-of-freedom model for galloping. Part II: Solutions. *Journal of engineering mechanics*, **119**(12), 2426–2448.

Conclusions and perspectives

Mathematics is the science which draws necessary conclusions.

BENJAMIN PEIRCE.

9.1 Conclusions

In this dissertation the effects of ice accretion on the aerodynamics and the aeroelastic stability of bridge hangers and stay cables were analyzed. First, a review of the state of art on the aerodynamics of nominally circular cylinders was given. Then, the aerodynamic behavior and the characteristics of ice accretion on bridge cables were experimentally studied by climatic wind tunnel tests. The aerodynamic stability was investigated using the models proposed by different authors. Furthermore a novel 3D 3-DoFs quasi-steady aeroelastic model was proposed.

There are a number of mechanisms that can potentially lead to vibrations of cables. Among this mechanism, galloping of cables with ice accumulations seems to be the least known. For this reason, this research was undertaken. Large oscillations of long cables can cause premature fatigue failures at the anchor points. These oscillations can also trigger the phenomenon of ice shedding. Falling ice becomes a safety issue for motorists and pedestrians crossing bridges, which eventually need to be closed until the ice is gone. Scientific literature and

news report a series of closures occurred to bridges due to ice accretion on bridge cables. The importance of understanding the phenomena that govern the ice accretion on bridge cables and the possible vibrations that may arise in iced configuration is crucial. Current solutions used to solve the problems caused by ice accretion on stay cables are not sufficient to provide complete protection for motorists and pedestrians in all weather conditions. The general increase in the number and size of cable supported bridges around the world, especially in cold climate regions, makes the problem even more pronounced.

In the following, a summary of the main conclusions from this study is given.

Aerodynamics of nominally circular cylinders Circular sections are widely used in the field of civil engineering due to their simplicity and structural and architectural value. On the other hand, when it comes to aero- or hydro-dynamics, simple geometry brings a complicated behavior, as the characteristics of the transition from laminar to turbulent flow depends strongly on the Reynolds number. Actually, circular cylinders are not perfect in civil applications. In many cases, it was observed that the imperfection can affect the aerodynamics with important consequences. The review presented in the thesis focuses on descriptions of the typical disturbance of the nominally circular cylinder that affects aerodynamics. The disturbances are classified in two categories, i.e. those due to geometrical irregularities of the cylinder and those due to the non uniformity of the flow. The former are further subdivided into: surface irregularities, section irregularities and spanwise irregularities. The importance of identifying and quantifying these disturbances and estimating their effects on aerodynamics was pointed out. It was also observed a lack of knowledge on the aerodynamic effects of ice accretion on bridge cables. The contribution advanced in this review is rather conceptual than factual.

Characteristics of ice accretion and aerodynamic behavior of ice accreted bridge cables The aerodynamics and aeroelastic behavior of ice accreted bridge cables have been investigated by climatic wind tunnel testing of a full-scale bridge cable model. Different climatic conditions, i.e. combinations of temperature and wind speed, were reproduced in the wind tunnel, giving rise to different types of accretion on a HPDE cable, simulating the vertical bridge hangers of a suspension bridge and the inclined stay cable of a cable-stayed bridge.

In order to investigate the aerodynamic behavior of ice accreted bridge cables, a particular set-up was obtained in a CWT for reproducing the conditions of in-cloud icing. The set-up consists of a spray bar system and a cable section model. The spray bar system was placed in the settling chamber downstream of the honeycomb grid, and the cable section model was placed in the center of the test section. The entire setup were specially designed for this experimental campaign.

For the vertical model, representing a bridge hanger, the aerodynamic force coefficients measured for different wind speeds and angles of attack showed considerable variations with varying CC. If the temperature is low and the wind speed large, the runback water in the flow out area can form iced rivulets converging in two symmetric vertical rivulets located at the separation point. There are situations in which the mean aerodynamic coefficients do not depend on wind speed, and other situations in which they do. This dependency is due to the different features of each ice accretion, in particular the type and the dimension of the accretion in the windward region (either rime or glaze), and the presence, size and density of iced rivulets on the lateral sides. In particular, the size of the frontal accretion influences the maximum value of the coefficients, whereas the presence of the iced rivulets on the lateral sides inhibits the variation of the aerodynamic coefficients with respect to wind speed.

For the inclined model, representing a stay cable, the direction of gravity, that of the cable axis and that of the normal flow play a fundamental role. It was observed that if these three directions are coplanar, then the accretion is symmetric, otherwise it is asymmetric. For the inclined model, the runback water can form different structures (e.g. icicles and iced rivulets), depending on the yaw angle of accretion and on temperature. Generally, the aerodynamic force coefficients showed different trends, depending on the CC. A general independence of the aerodynamic coefficients of wind speed was observed, with the exception of CCs with yaw of accretion of 180° , in which a dependency was found, similar to that detected when the model was placed vertically. As a matter of fact, in these CCs the accretion showed features similar to the vertical case.

Both for vertical and for inclined cables, and differently from what happens for dry cables, the moment coefficient can take large non-zero values. The mass accreted was in all CCs never larger than 3.0 kg/m , i.e. much smaller than the typical weight of the cable tested (which is in the order of 100 kg/m), indicating that there is no need to account for inertial coupling. This would not be the case for cables of smaller diameter, such as electrical overhead lines, in which the contribution of the inertial coupling is marked and cannot be neglected.

Compared to previous researches available in the literature, generally performed on cables of smaller diameter, these tests have shown the different behavior of ice accretion of cables with diameter comparable to those of bridge hangers or stay cables.

3D, 3DoF stability and buffeting model A novel 3D-3DoFs quasi-steady aeroelastic model has been proposed. The model is able to predict the galloping and divergence instability of a cylinder with generic cross-section, the minimum required structural damping and stiffness to prevent instability, and to predict the cross-sectional response to a turbulent flow, considering both buffeting and self-excited contributions. In its present form does not incorporate

effects of vortex shedding. The model accounts for inertial coupling between the DoFs, and allows for variation of the force coefficients with Reynolds number, angle-of-attack and relative cable-wind angle. The aerodynamic forces acting on the cylinder were linearized about zero structural velocities, steady structural rotation and about the steady component of the total wind velocity. The representation of the aerodynamic forces in tensor is suitable for software application. The equations of motion were written following the Euler-Lagrange method. Later, they are expressed in a state space representation. Based on the analytical solution of the eigenvalue problem, by applying the Routh-Hurwitz criterion, an expression of the galloping- and static divergence-type instability condition, is derived. Additionally, a numerical solution of the minimum structural damping and structural stiffness required to prevent the instabilities is given.

An application of the 3-DoFs analytical model was proposed to study the galloping and divergence stability of an ice-accreted cable conductor in cross flow, of a dry stay cable and of an ice-accreted stay cable.

For the ice accreted cable conductor in cross flow a comparison of the regions of galloping instability derived analytically, revealed that the present model provides an improved prediction of the regions of galloping instability in comparison to existing models. It was found that for selected ranges of angle-of-attack and Reynolds number, the ice accreted conductor in cross-flow can undergo both galloping and static divergence. An increase in the structural damping in all DoFs helps reducing the extension of the regions of galloping instability. A reduction of the structural rotational stiffness reduces the extension of both the regions of galloping and divergence. The dry stay cable and the ice-accreted stay cable exhibit galloping instability but not static divergence, for a selected range of Reynolds number and cable-wind angles. Results are in agreement with those coming from existing models. Maps of minimum damping ratios were derived for all cases.

The trajectories of the shear centre and time histories of the displacements in the three DoFs were analyzed at the stability limit. The stationary trajectories of the shear centre tend to be elliptical. This behavior was dominated by the detuning and by the cross terms of the aerodynamic damping and stiffness matrix. In particular, for small detuning of the translational DoFs, the motion of the system is described by wider orbits; a larger detuning narrower orbits.

Aerodynamic stability of ice accreted bridge cables The need to evaluate the aerodynamic galloping stability of elongated flexible structures and in particular cables, both in cross- and inclined-flow conditions, led to the development of a number of quasi-steady sectional aerodynamic stability models. These mainly differ in the DoFs of possible instability and in the variables considered in the Taylor expansion of the aerodynamic coefficients. In order to compare the background hypotheses, the models were classified into a general framework

that highlights a common approach based on the quasi-steady theory. Consequently, the models are classified according to the flow conditions, to the DoFs and to terms of the Taylor expansion retained.

The mean aerodynamic coefficients measured experimentally in wind tunnel tests of ice accreted vertical bridge hangers and inclined stay-cables, have been used to compare the results obtained with the different models. All models were applied numerically; closed-form solutions available for some of them were not used. Not existing a benchmark, the research was not aimed at judging the quality of each approach, but rather at pointing out the differences they bring. In particular, two CCs were analyzed. For vertical hangers, the CC giving rise to the strongest susceptibility to instability is used for the analysis. For inclined cable-stays, it is used the only CC in which the aerodynamic coefficients were available with varying angle of attack α .

For vertical bridge hangers, the 1-DoF models in the transactional directions predict the same regions of potential instability regardless of whether the Re dependency of the aerodynamic coefficients is considered or not. However, neglecting the contribution of these terms means neglecting the drag crisis type instability, and predicting smaller values of the required structural damping. Instead, the predictions of the 1-DoF torsional model depends on R_δ and δ . In the absence of real data, indicative values of these parameters are used to perform a parametric analysis. In particular, changing δ modifies the extension of the region of instability, while changing R_δ alters only the value of the predicted required damping. The tuned 2-DoF models predicts less extended regions of instability and lower value of the required structural damping, indicating that tuning can have a beneficial effect. However, a detuning as low as 3% is sufficient to make the 1-DoF and the 2-DoFs predictions coincident. For bridge hangers, equal frequencies in the x and y directions can be a fairly assumption. Differently, equal frequencies in the translational and torsional DoFs are clearly unrealistic. Finally, the application of the 3-DoFs model reveals a prediction that is different respect to the results of the 1-DoF models only for the perfectly tuned case. However, when one DoF is small detuned with respect to the remaining two, the potential instability regions are the superposition of those pertaining to the 1-DoF and to the tuned 2-DoF systems taken separately.

Globally, for inclined stay-cables, similar conclusions to those found for vertical hangers were found. One difference is that, neglecting the Re dependency of the aerodynamic coefficients the models predict larger values of the required structural damping, indicating that these terms can also be beneficial. Another difference is that neglecting the derivative with respect to α , the models erroneously predict stability in the entire domain investigated, indicating the importance of these terms. The 1-DoF torsional model predicts larger values respect to 1-DoF models in the translational directions, differently from the bridge hangers case. Finally it is noticed that for inclined stay-cables, equal frequencies in the in-plane and out-of-plane directions is a unrealistic assumption due to sag effects.

Concluding, it was observed that the use of the 1-DoF models is generally conservative, and that the use of M-DoFs models is justified only in the case of perfectly tuned frequencies. On the other hand, it was also shown that neglecting the derivatives of the aerodynamic coefficients modifies the solution. This has to sound like a warning when applying stability models with only partial availability of data. The use of the models requires an accurate knowledge of the same and of the limits of applicability. Also the wind tunnel test must be performed with the aim of produce data applicable to the models.

9.2 Future work

The results presented in this thesis provides basis for future research in different areas. These areas include:

Performing a large number of tests in different CCs In this thesis a total of 16 CCs were tested. It must be clear that for a comprehensive analysis, data coming from a much broader variety of CCs would be needed. In particular, other important parameters as the time of accretion must be investigated. For the stay cable case, only in one CC the aerodynamic coefficients were measured also by varying the angle α . It was demonstrated that when such dependency is neglected, the prediction of stability could prove quite misleading. For this reason, the aerodynamic measurements need to be performed also by varying the angle α .

Passive dynamic wind tunnel tests of ice accreted bridge cables In order to verify the aeroelastic behavior of ice accreted bridge cables passive-dynamic wind tunnel tests would be required with different mass, frequency and damping, varying Reynolds number, yaw angle and wind angles-of-attack. Preliminary dynamic test performed during a Master's project highlights all the difficulties related to the implementation of a dynamic rig that could operate in the climatic conditions of the test chamber. In particular, the dynamic rig must allow keeping the temperature stable inside the test chamber in order to preserve the ice and therefore it is not possible to create openings thought the tunnel walls. This type of testing would also allows one to validate the results from the application of the aeroelastic models.

Identification of the ice shedding governing variables Ice shedding is a complex phenomenon, leading to the separation of ice from cables. Falling ice becomes a safety issue for motorists and pedestrians crossing bridges, which need to be closed until the ice is gone. Three types of cable ice shedding have been identified: ice melting, ice sublimation, and mechanical ice breaking. Experimental campaigns would be required to understand the variables governing

the phenomenon. Parallel to this activity, it would be necessary to develop efficient protection systems motorists and pedestrians crossing bridges.

Classification of the aerodynamic dissipative mechanisms and development of design methods The results coming from the application of aeroelastic models based on the quasi steady approach highlights the need for a deeper understanding of the energy balance, including the mechanisms of transfer among the degrees of freedom. Moreover, it seems that it is not entirely clear how to convert the structural damping or stiffness required by the sectional aeroelastic models to real characteristics of the dampers.

Development of an aeroelastic model the whole cable Finally, although important for section models, variations of the mean aerodynamic coefficients may not ultimately be important when averaged over the full length of a bridge cable. Another factor that may be accounted is the hysteresis of the transitions of the force coefficients in the critical Re region. To the writer knowledge, no models exists that reliably bring into account the spanwise variation of the aerodynamic behavior and the effects of the turbulence.

Accurate investigation of the buffeting response of ice accreted bridge cables Buffeting of ice accreted bridge cables has never been studied. An approach could be that of carrying out numerical simulations of the 3-D cross-sectional response in the time domain with a quasi steady approach. The final goal would be that of producing relationships between the mean wind velocity and direction and the statistics of the cable displacements, identifying critical conditions.

Development of a probabilistic fatigue model for bridge cables Bridge hangers and stay cables are flexible structural elements, with very low damping and therefore prone to vibrations. These are mainly caused by traffic and by wind, with the latter becoming dominant as bridge spans increases. Wind induced vibrations can occur under three different surface states of the cable, i.e. dry, wet and ice-accreted. A general framework for the evaluation of the fatigue life would to account for all this phenomena. The model would need to incorporate, with a fully probabilistic approach, the climatic conditions at the site and the conditions of the cable surface (dry, wet or iced) and the evaluation of the dynamic response. Finally, a model of fatigue (e.g. rain-flow method) must be considered for the evaluation of the fatigue life.

APPENDIX A

Derivatives of the aerodynamic coefficients

A.1 Ice accreted bridge hangers

In this Section, the derivatives of the aerodynamic coefficients with respect to α and Re are given for the climatic conditions:

- CC V1
- CC V2
- CC V3
- CC V4

The derivatives were evaluated in terms of Newton's difference quotient.

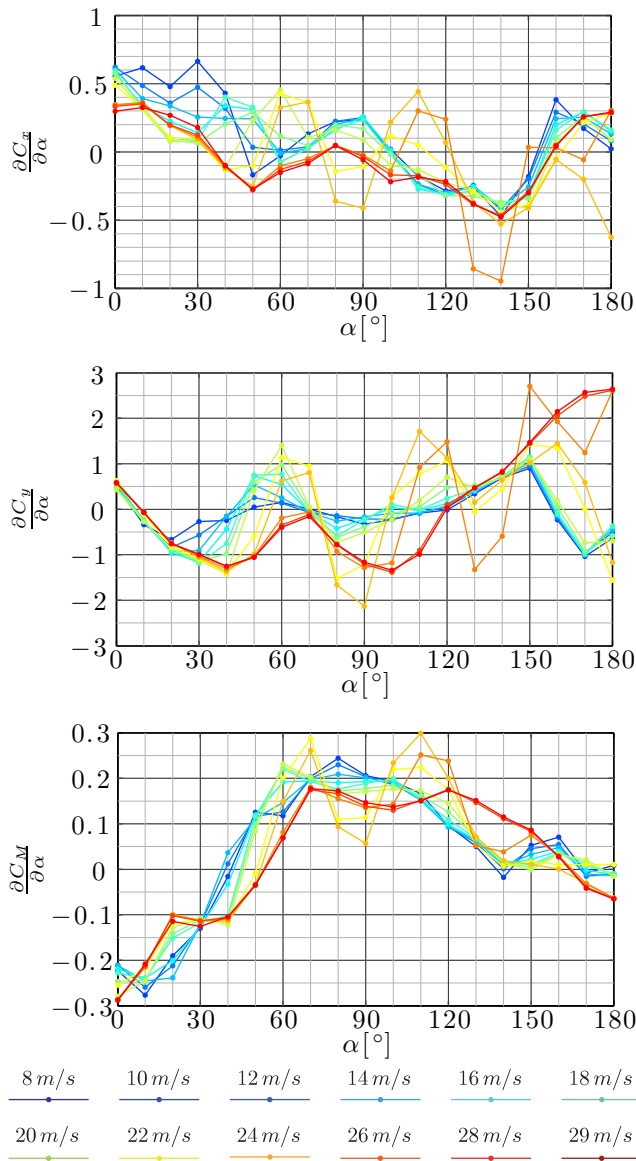


Figure A.1: Variation with the angle of attack of the derivative of the mean aerodynamic coefficients with respect to α for different wind speeds, in CC V1.

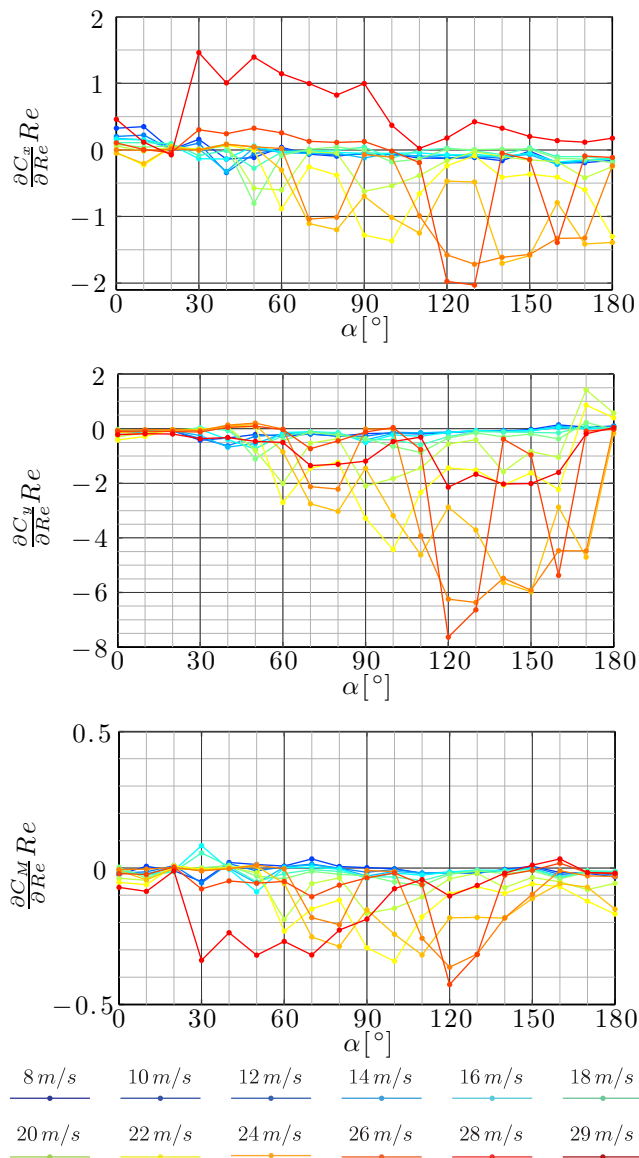


Figure A.2: Variation with the angle of attack of the derivative of the mean aerodynamic coefficients with respect to Re for different wind speeds, in CC V1.

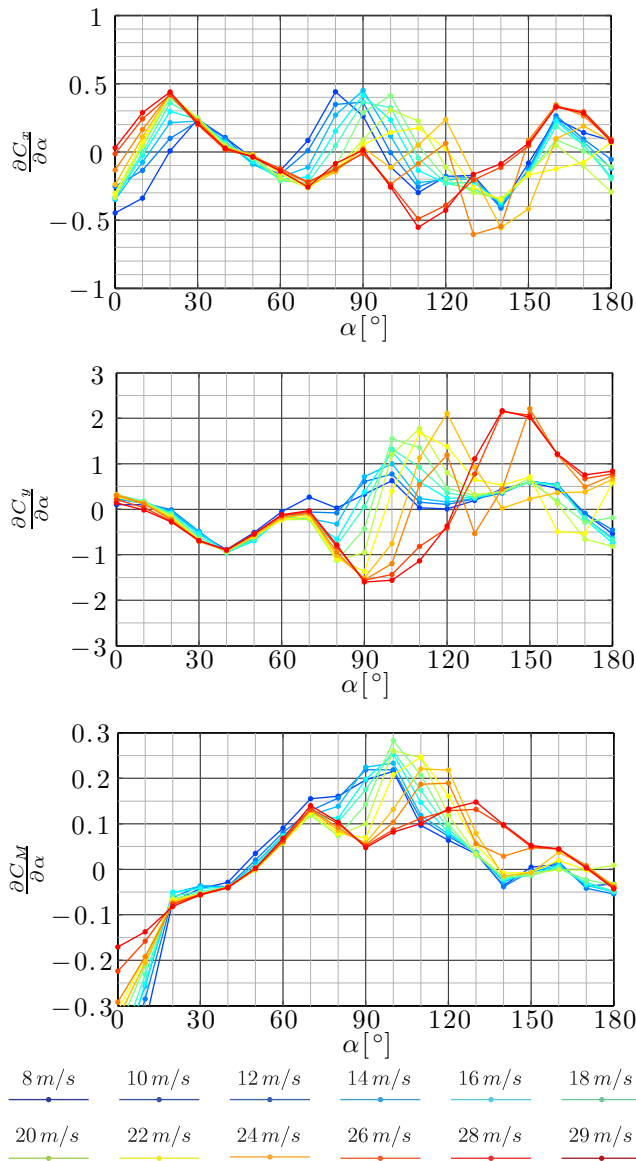


Figure A.3: Variation with the angle of attack of the derivative of the mean aerodynamic coefficients with respect to α for different wind speeds, in CC V2.

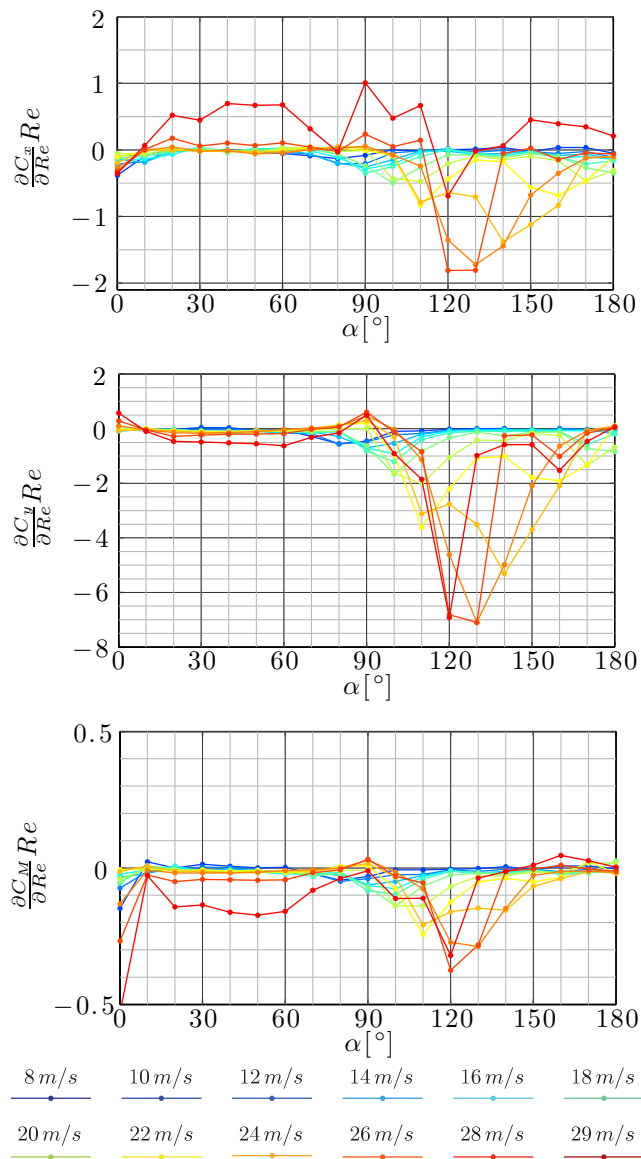


Figure A.4: Variation with the angle of attack of the derivative of the mean aerodynamic coefficients with respect to Re for different wind speeds, in CC V2.

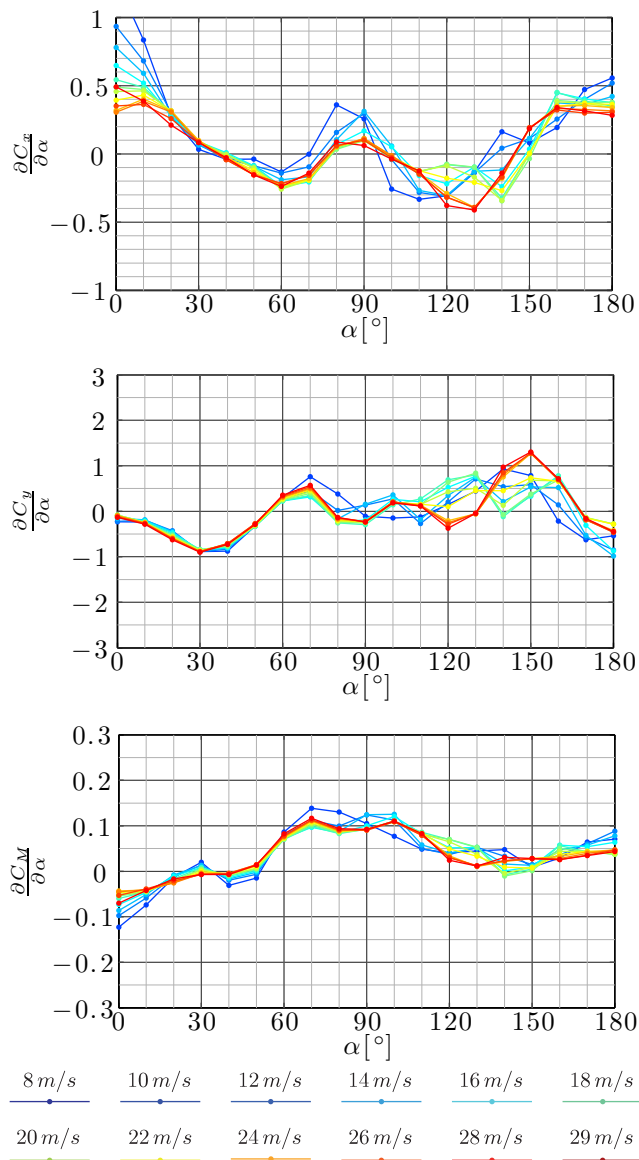


Figure A.5: Variation with the angle of attack of the derivative of the mean aerodynamic coefficients with respect to α for different wind speeds, in CC V3.

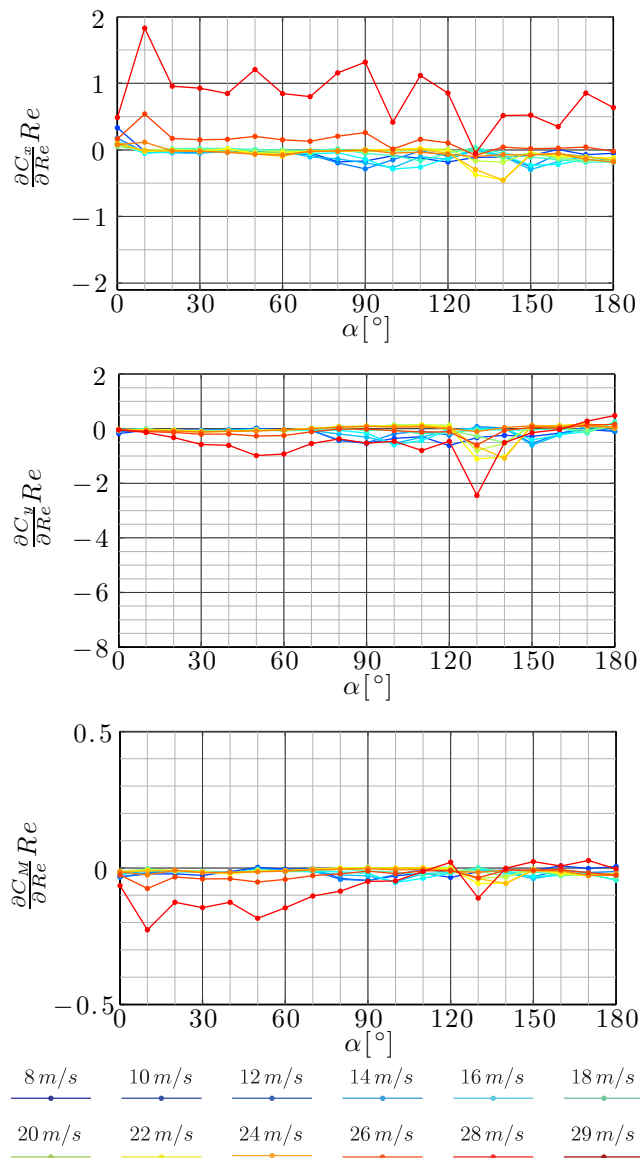


Figure A.6: Variation with the angle of attack of the derivative of the mean aerodynamic coefficients with respect to Re for different wind speeds, in CC V3.

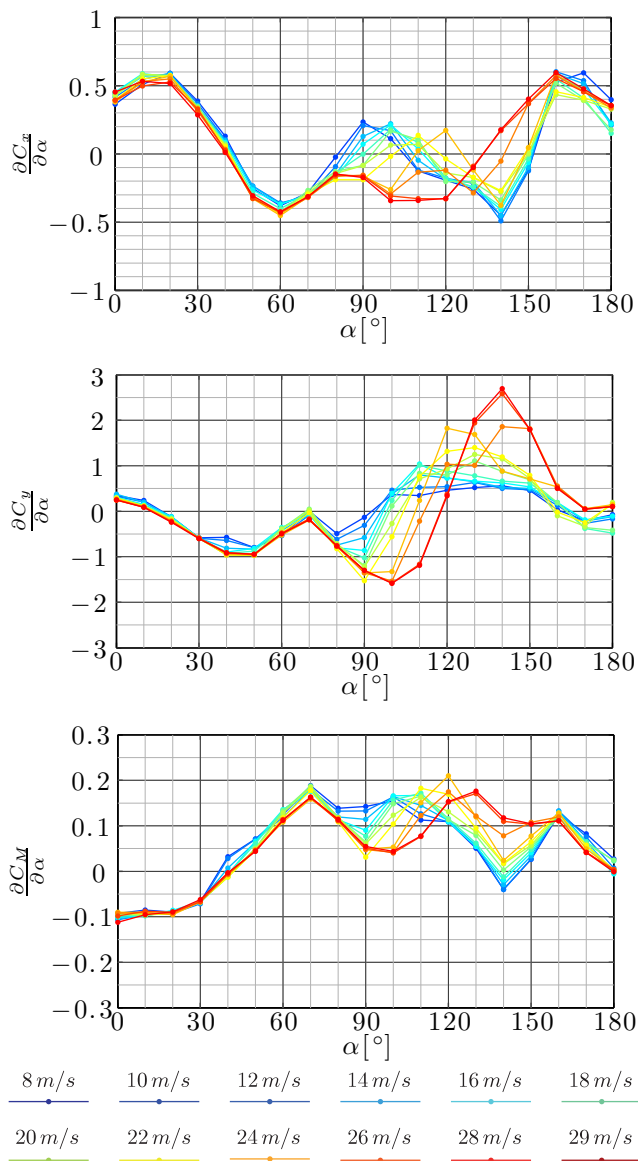


Figure A.7: Variation with the angle of attack of the derivative of the mean aerodynamic coefficients with respect to α for different wind speeds, in CC V4.

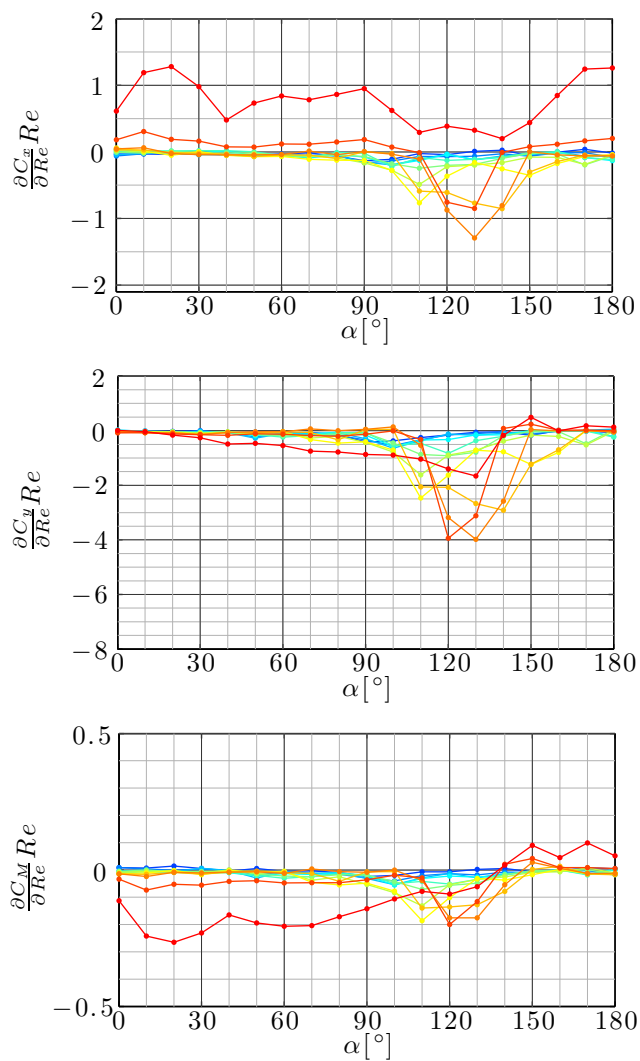


Figure A.8: Variation with the angle of attack of the derivative of the mean aerodynamic coefficients with respect to Re for different wind speeds, in CC V4.

A.2 Ice accreted stay cables

In this Section, the derivatives of the aerodynamic coefficients with respect to Φ and Re are given for the climatic conditions:

- CC I1 (dry case)
- CC I2
- CC I3
- CC I4
- CC I5
- CC I6
- CC I7a
- CC I7b
- CC I7c
- CC I8
- CC I9
- CC I10
- CC I11
- CC I12

The derivative with respect to α are given for:

- CC I7

The derivatives were evaluated in terms of Newton's difference quotient.

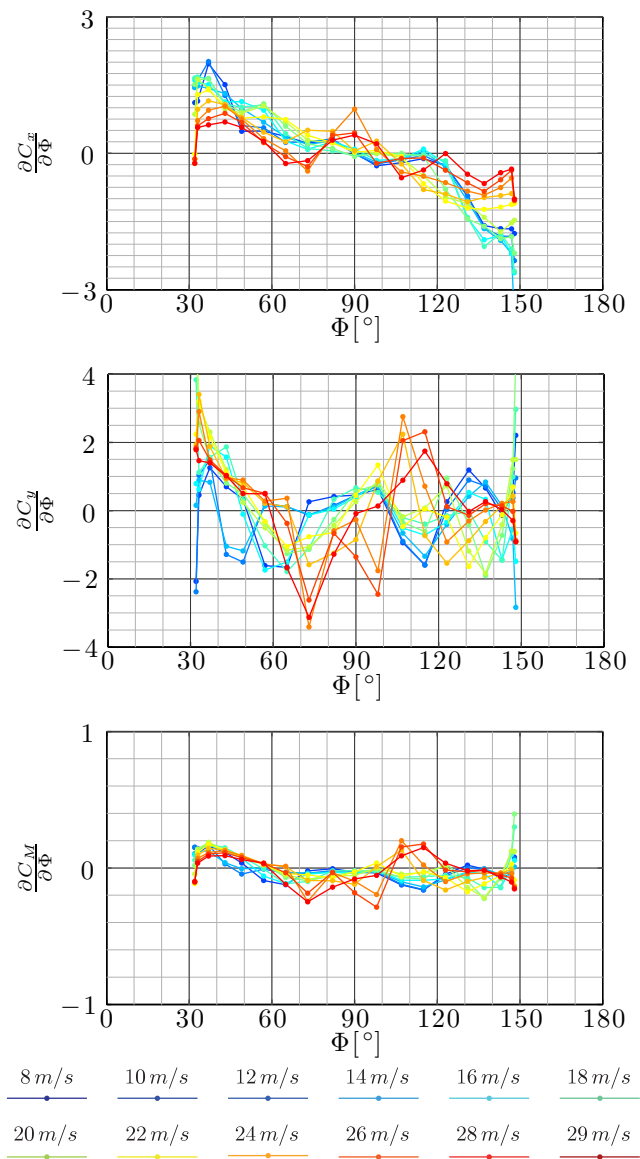


Figure A.9: Variation with the yaw angle of the derivative of the mean aerodynamic coefficients with respect to Φ for different wind speeds, in CC II.

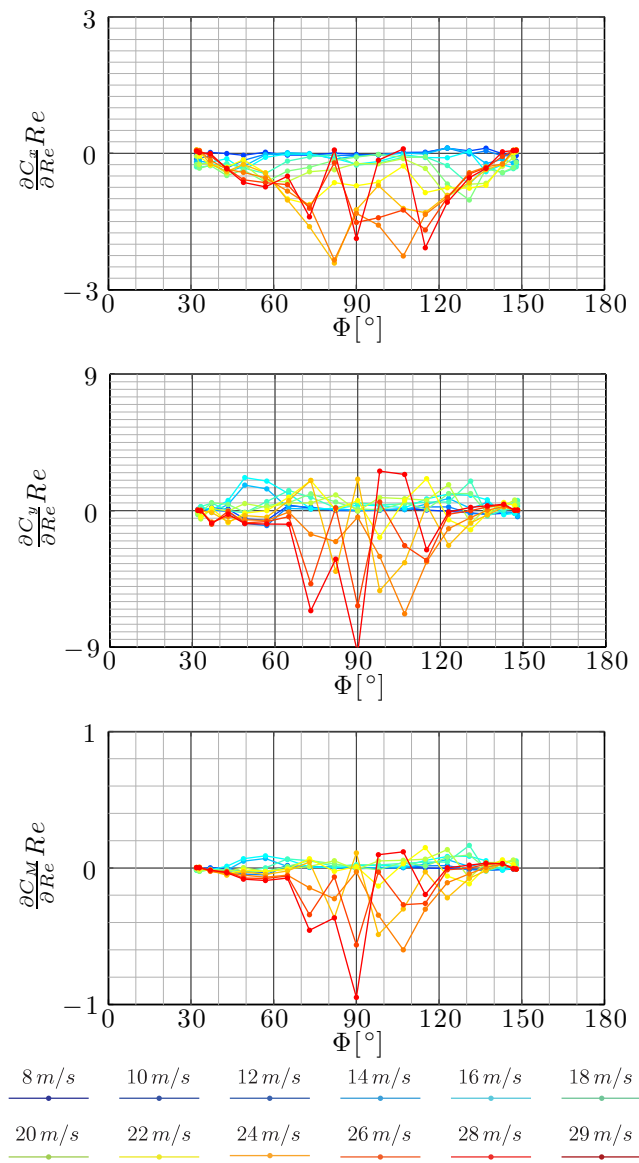


Figure A.10: Variation with the yaw angle of the derivative of the mean aerodynamic coefficients with respect to Re for different wind speeds, in CC I1. Plot scale is different from those of the other CCs.

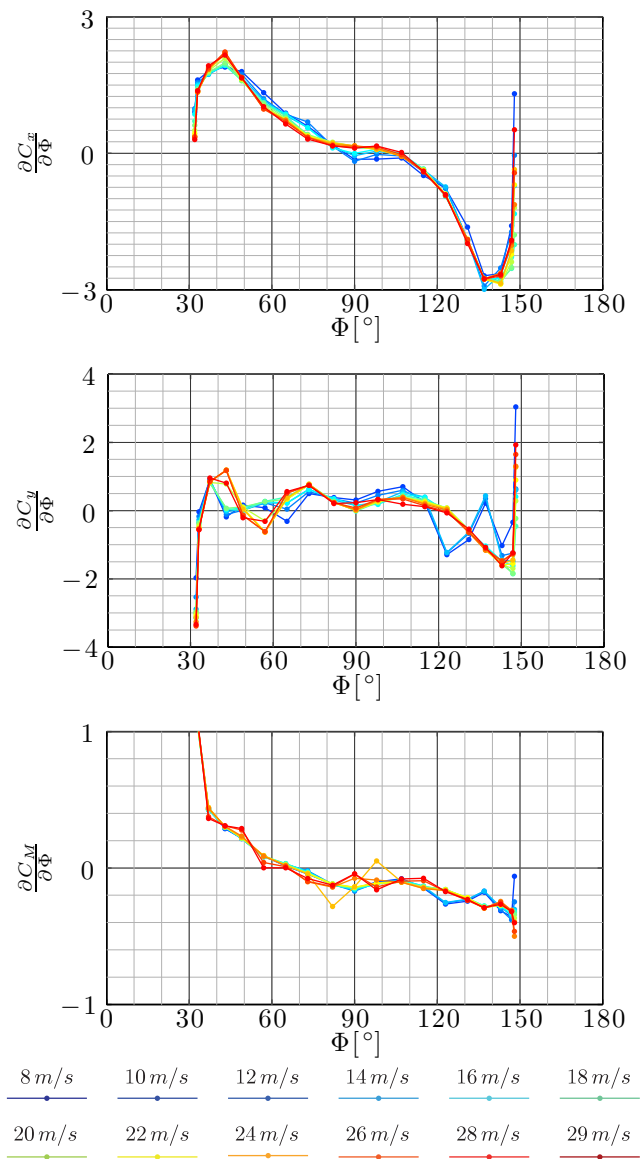


Figure A.11: Variation with the yaw angle of the derivative of the mean aerodynamic coefficients with respect to Φ for different wind speeds, in CC I2.

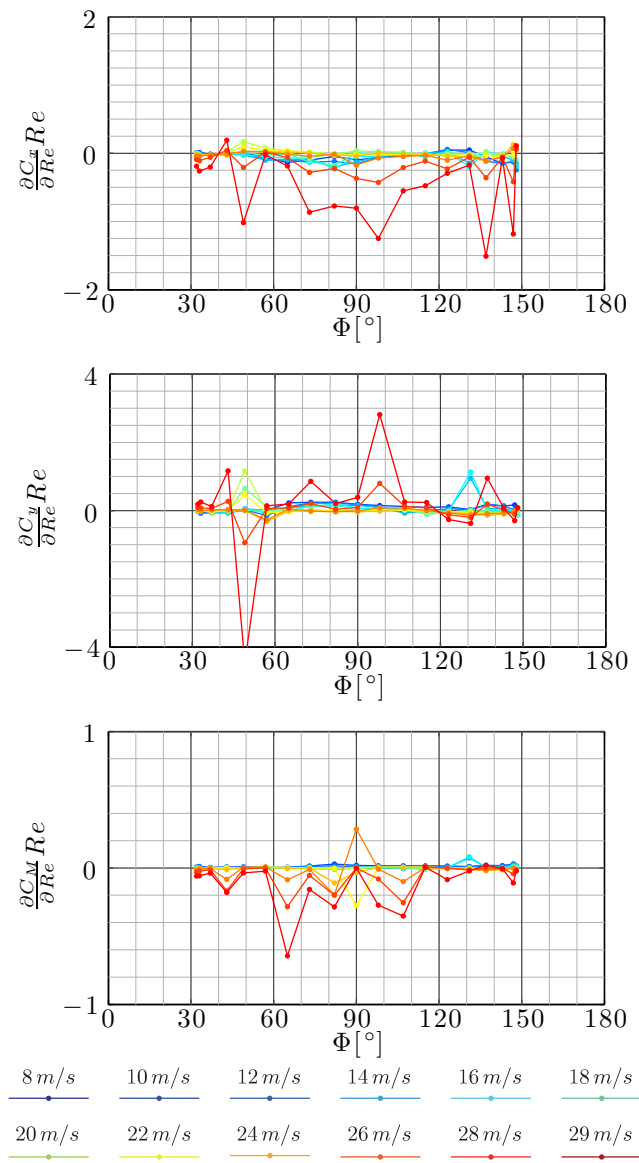


Figure A.12: Variation with the yaw angle of the derivative of the mean aerodynamic coefficients with respect to Re for different wind speeds, in CC I2.

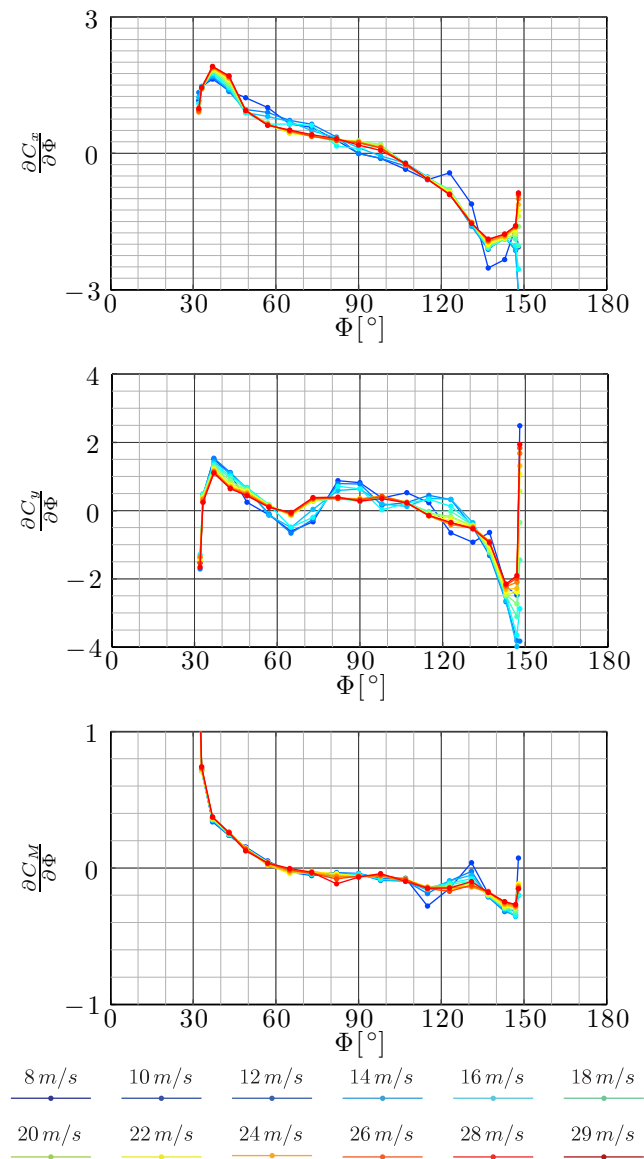


Figure A.13: Variation with the yaw angle of the derivative of the mean aerodynamic coefficients with respect to Φ for different wind speeds, in CC I3.

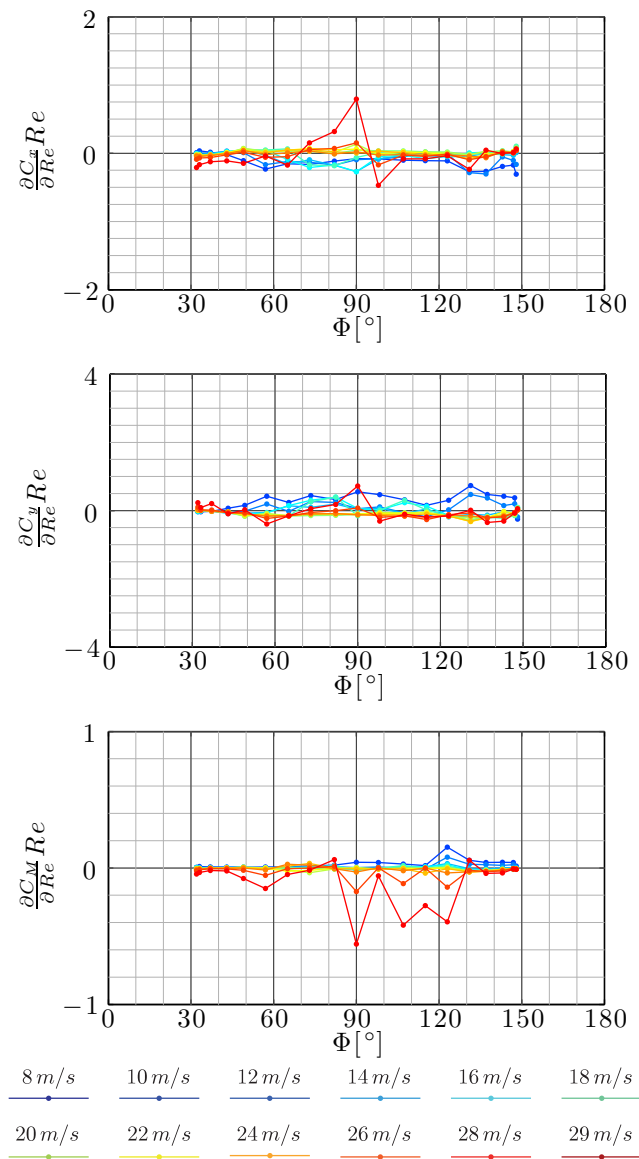


Figure A.14: Variation with the yaw angle of the derivative of the mean aerodynamic coefficients with respect to Re for different wind speeds, in CC I3.

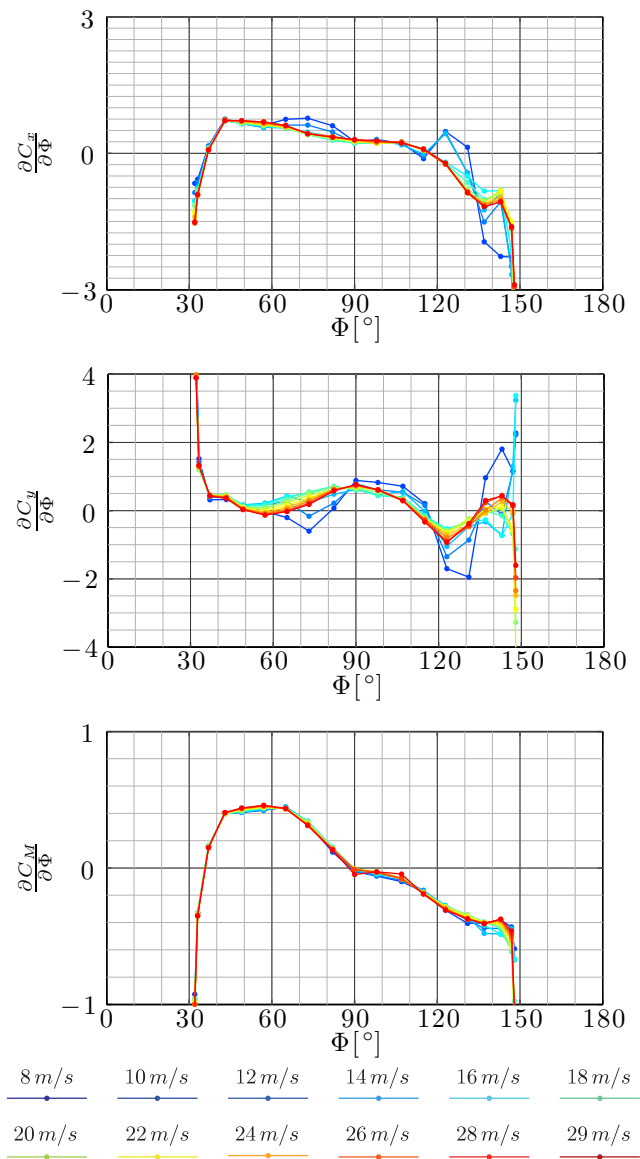


Figure A.15: Variation with the yaw angle of the derivative of the mean aerodynamic coefficients with respect to Φ for different wind speeds, in CC I4.

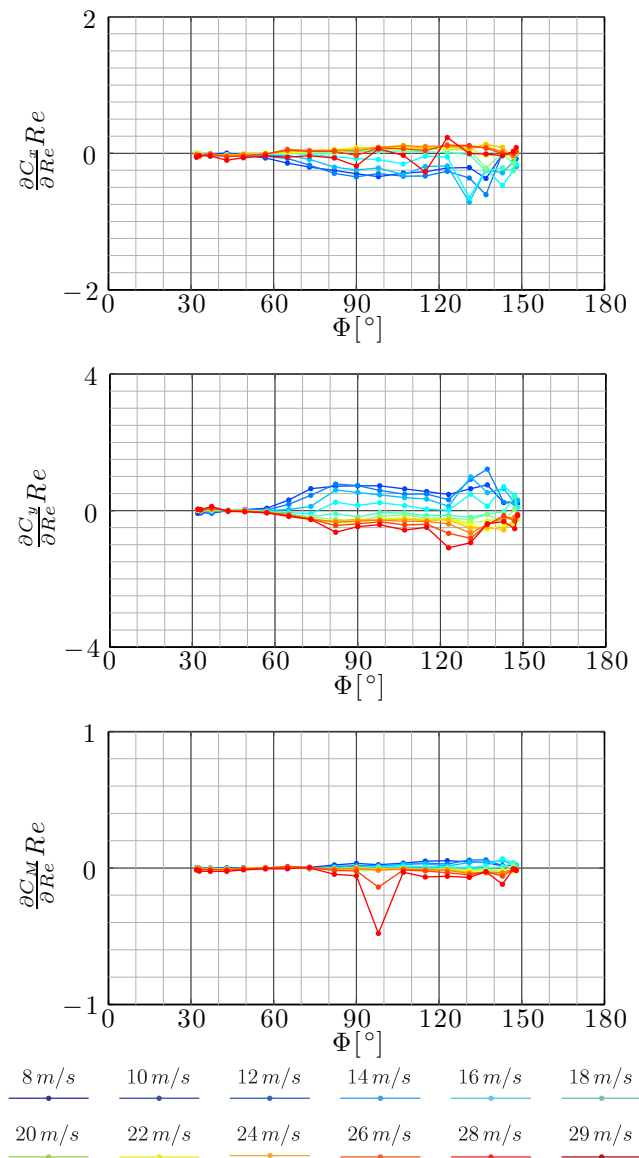


Figure A.16: Variation with the yaw angle of the derivative of the mean aerodynamic coefficients with respect to Re for different wind speeds, in CC I4.

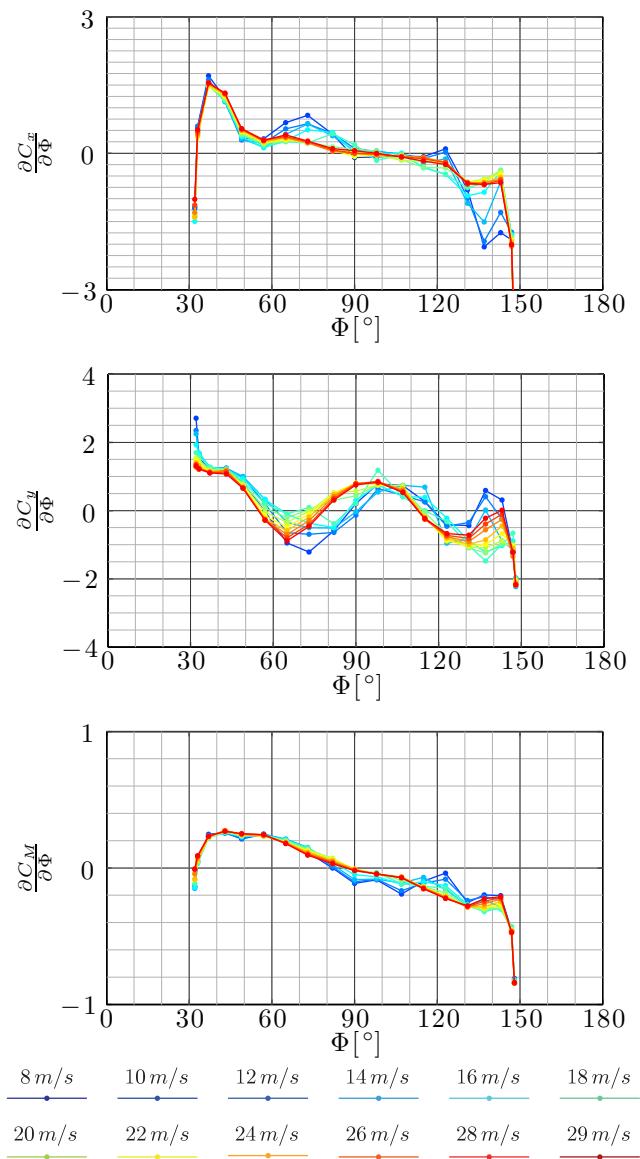


Figure A.17: Variation with the yaw angle of the derivative of the mean aerodynamic coefficients with respect to Φ for different wind speeds, in CC I5.

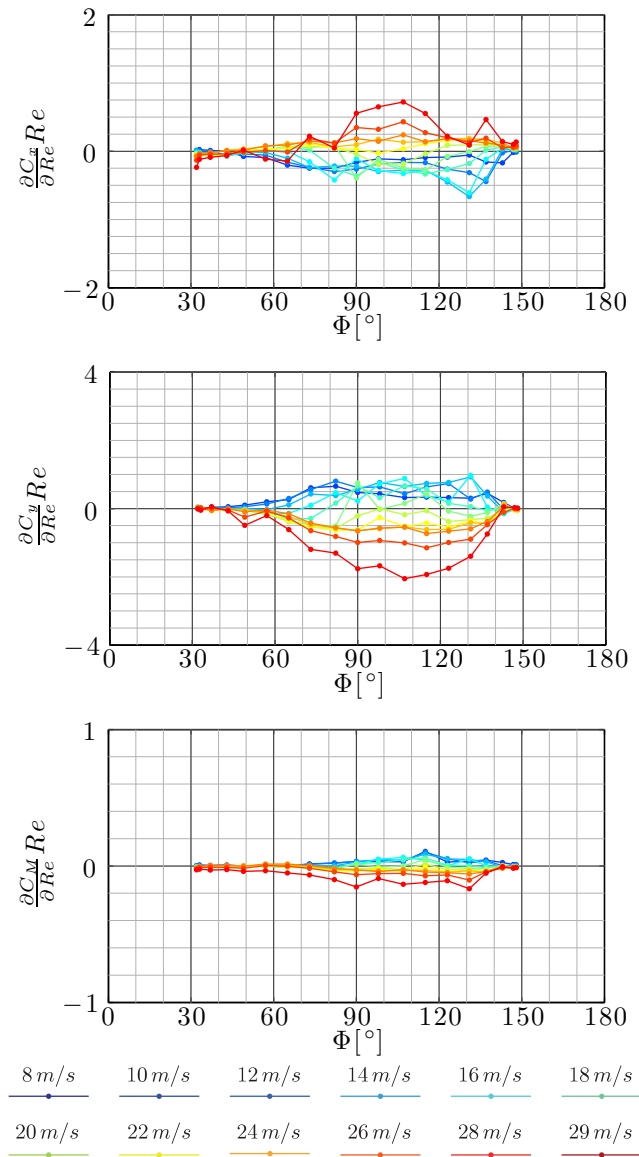


Figure A.18: Variation with the yaw angle of the derivative of the mean aerodynamic coefficients with respect to Re for different wind speeds, in CC I5.

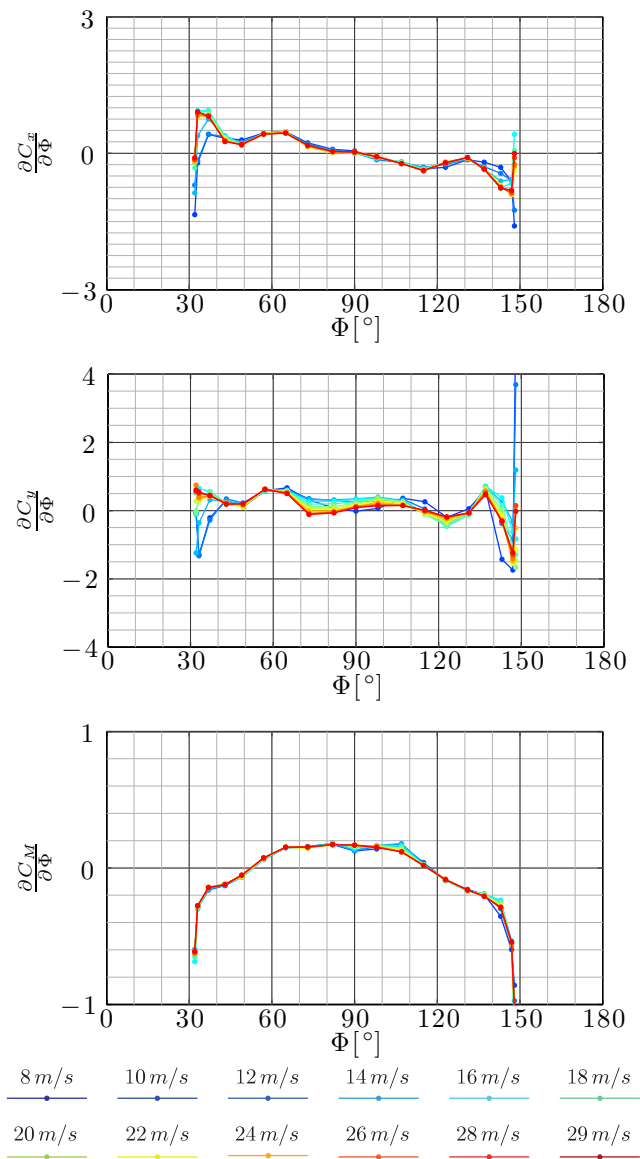


Figure A.19: Variation with the yaw angle of the derivative of the mean aerodynamic coefficients with respect to Φ for different wind speeds, in CC I6.

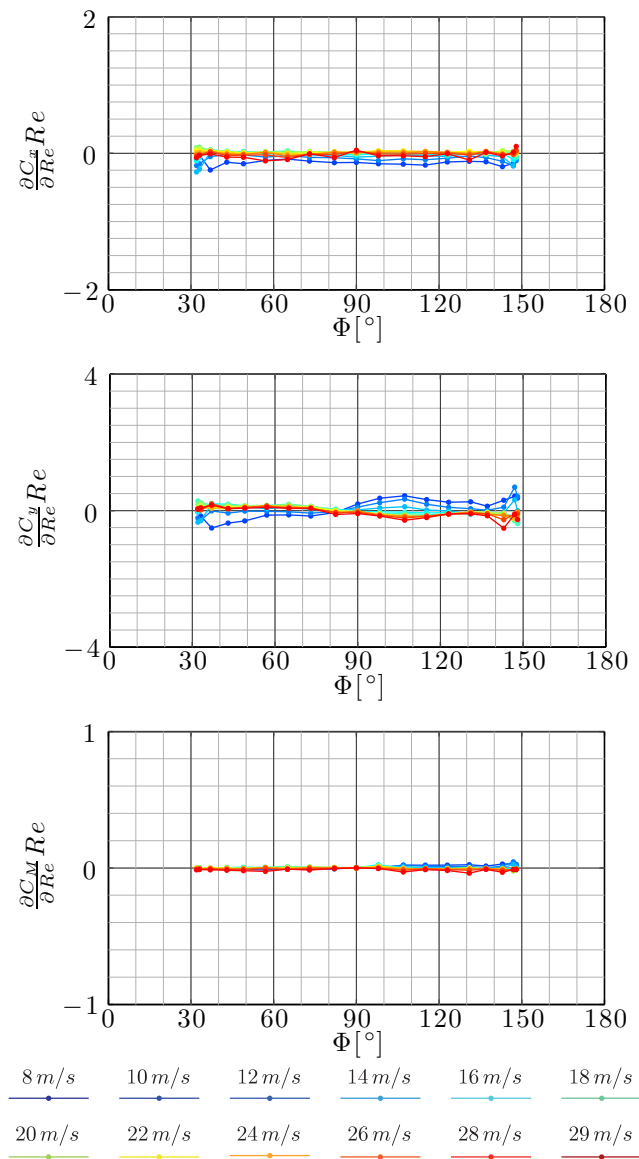


Figure A.20: Variation with the yaw angle of the derivative of the mean aerodynamic coefficients with respect to Re for different wind speeds, in CC I6.

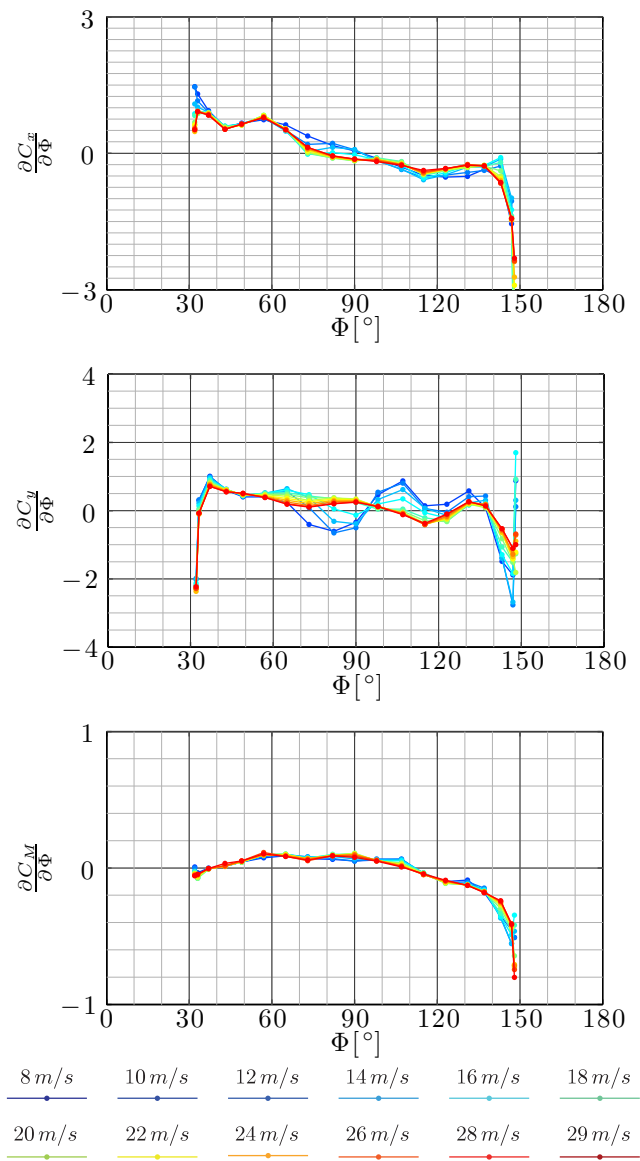


Figure A.21: Variation with the yaw angle of the derivative of the mean aerodynamic coefficients with respect to Φ for different wind speeds, in CC I7a.

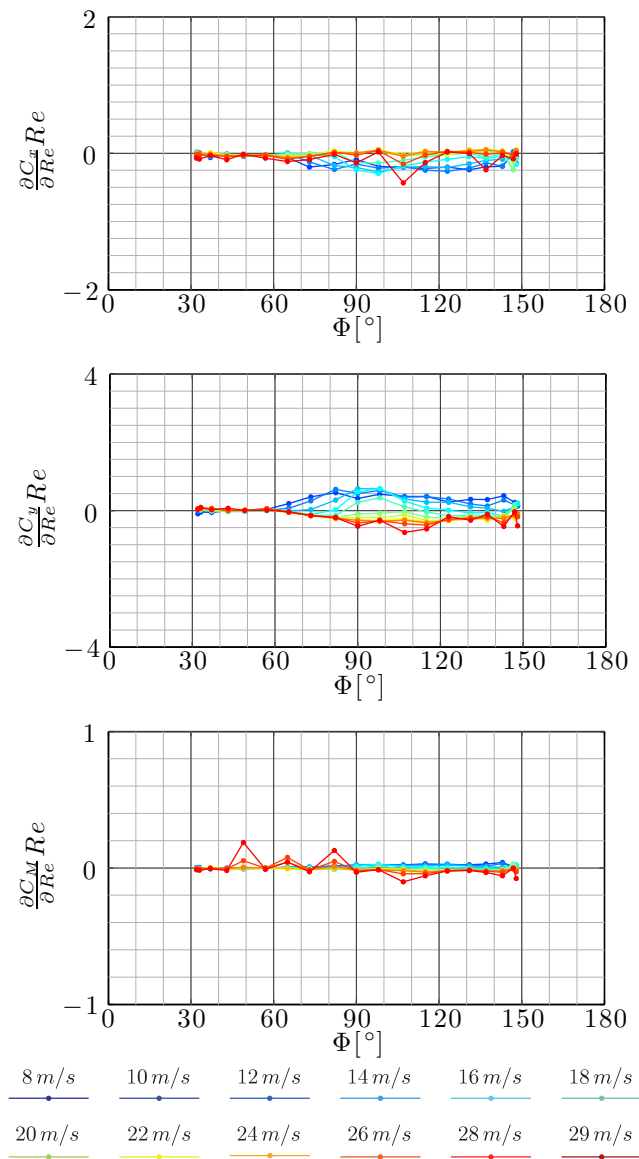


Figure A.22: Variation with the yaw angle of the derivative of the mean aerodynamic coefficients with respect to Re for different wind speeds, in CC I7a.

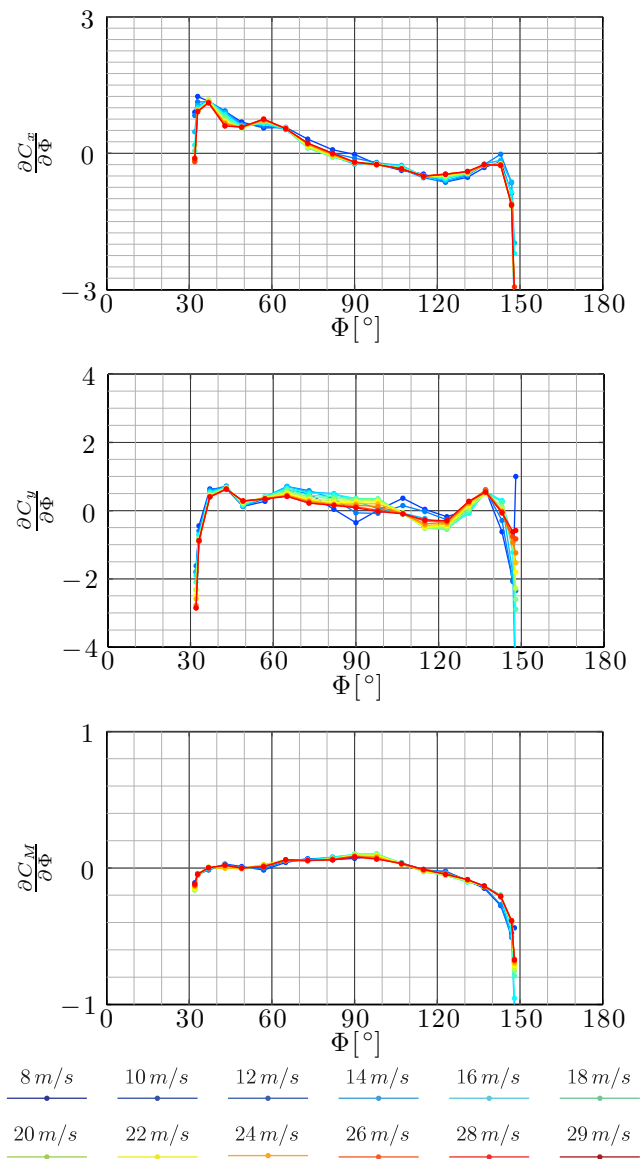


Figure A.23: Variation with the yaw angle of the derivative of the mean aerodynamic coefficients with respect to Φ for different wind speeds, in CC I7b.

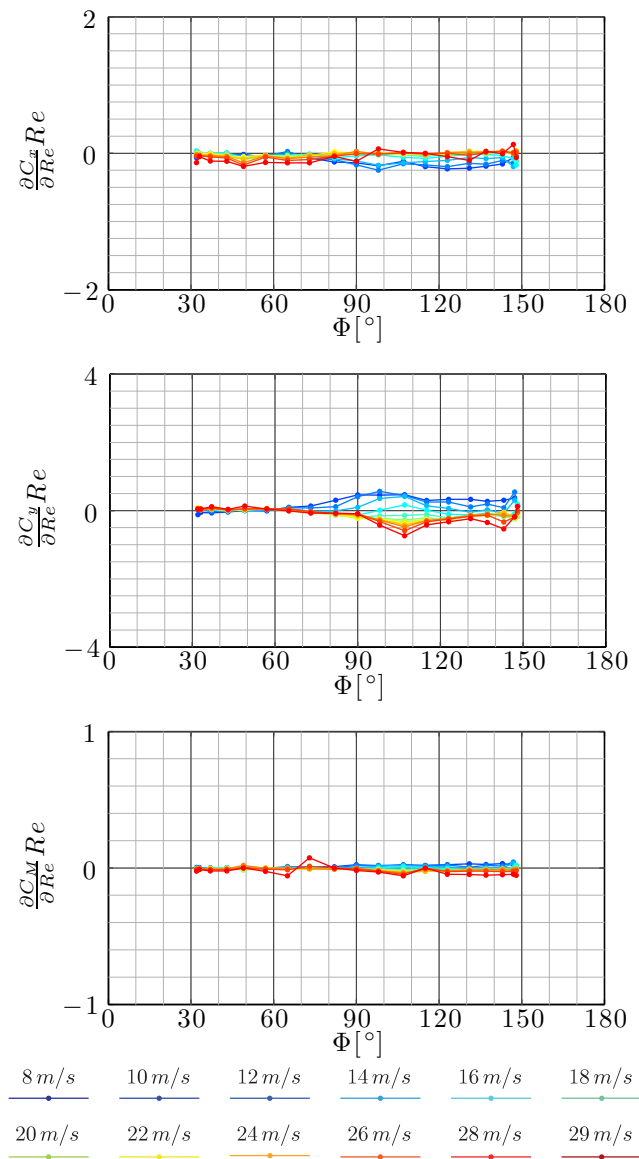


Figure A.24: Variation with the yaw angle of the derivative of the mean aerodynamic coefficients with respect to Re for different wind speeds, in CC I7b.

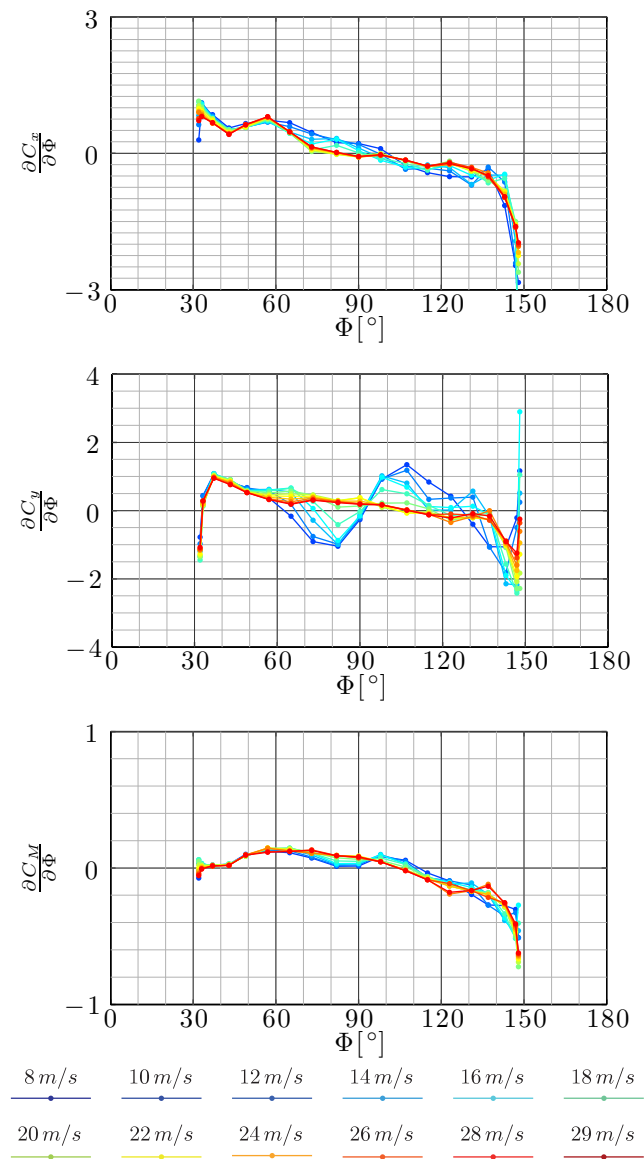


Figure A.25: Variation with the yaw angle of the derivative of the mean aerodynamic coefficients with respect to Φ for different wind speeds, in CC I7c.

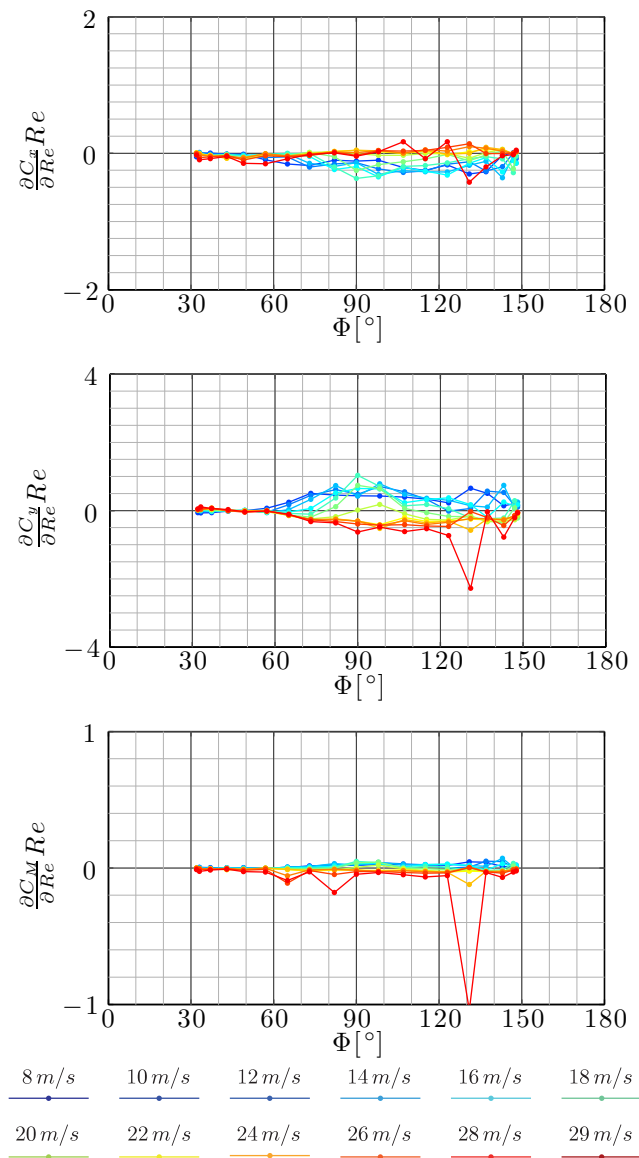


Figure A.26: Variation with the yaw angle of the derivative of the mean aerodynamic coefficients with respect to Re for different wind speeds, in CC I7c.

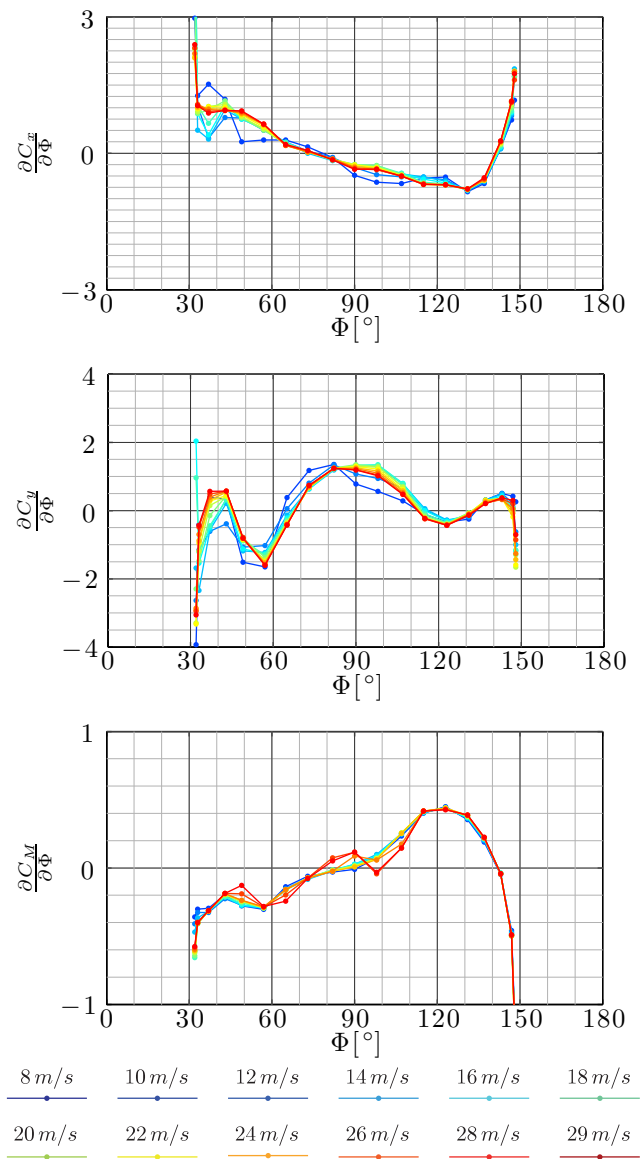


Figure A.27: Variation with the yaw angle of the derivative of the mean aerodynamic coefficients with respect to Φ for different wind speeds, in CC I8.

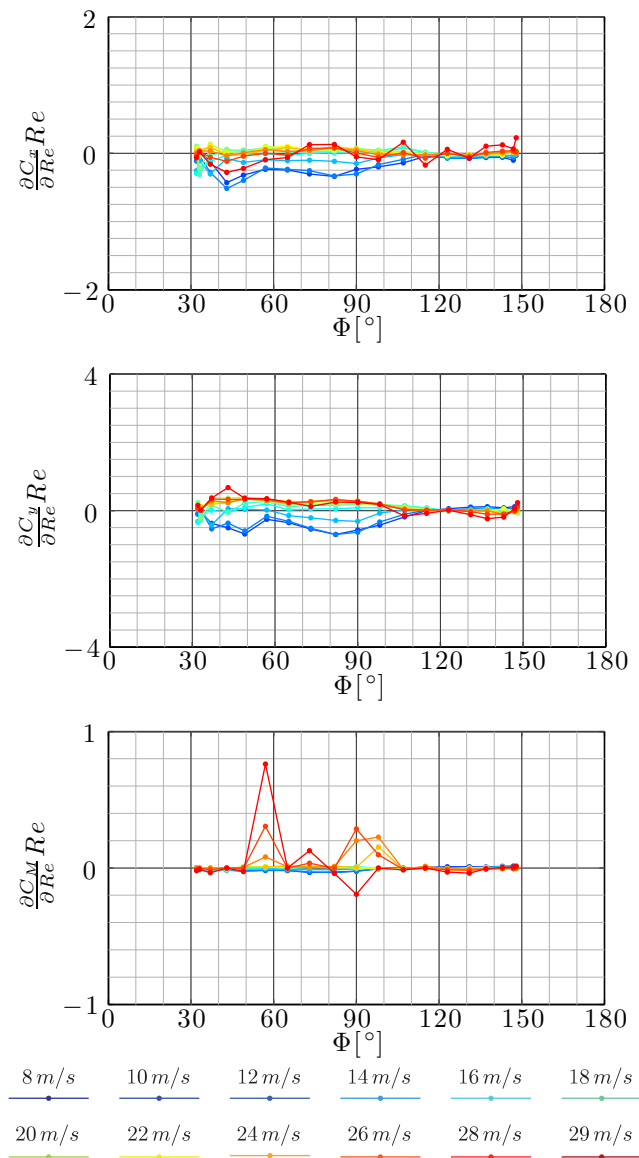


Figure A.28: Variation with the yaw angle of the derivative of the mean aerodynamic coefficients with respect to Re for different wind speeds, in CC I8.

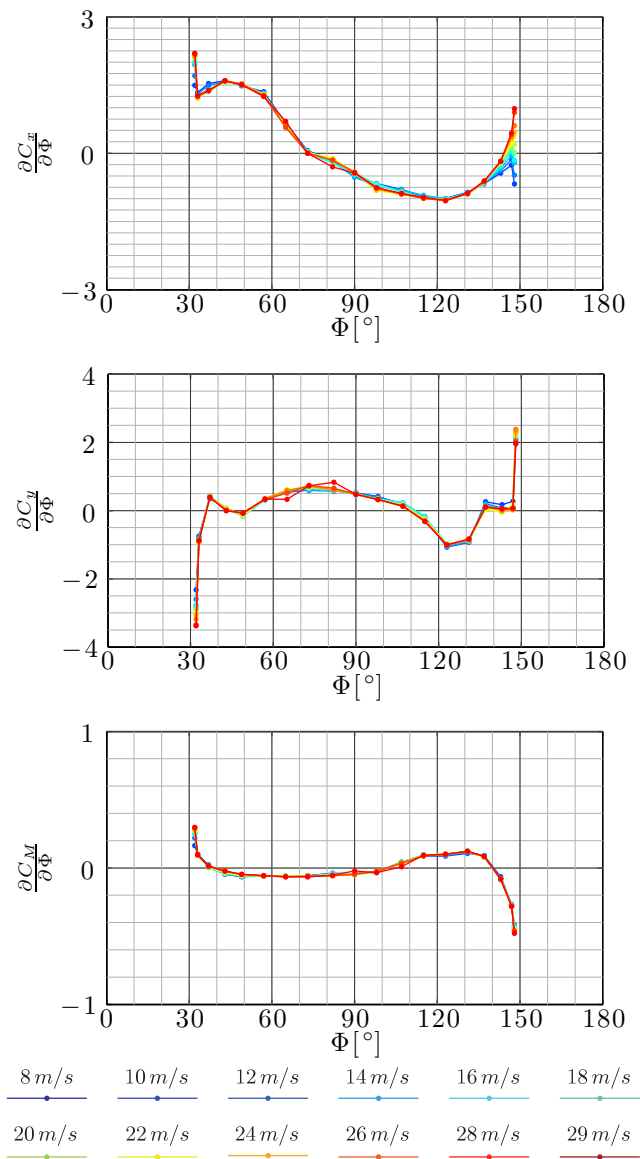


Figure A.29: Variation with the yaw angle of the derivative of the mean aerodynamic coefficients with respect to Φ for different wind speeds, in CC I9.

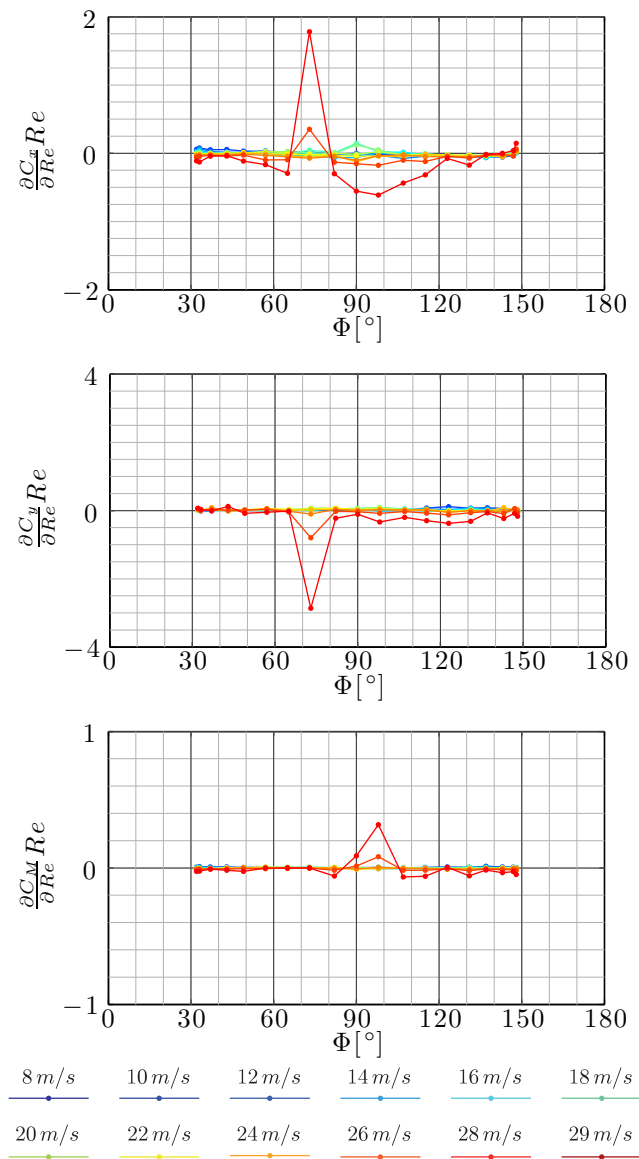


Figure A.30: Variation with the yaw angle of the derivative of the mean aerodynamic coefficients with respect to Re for different wind speeds, in CC I9.

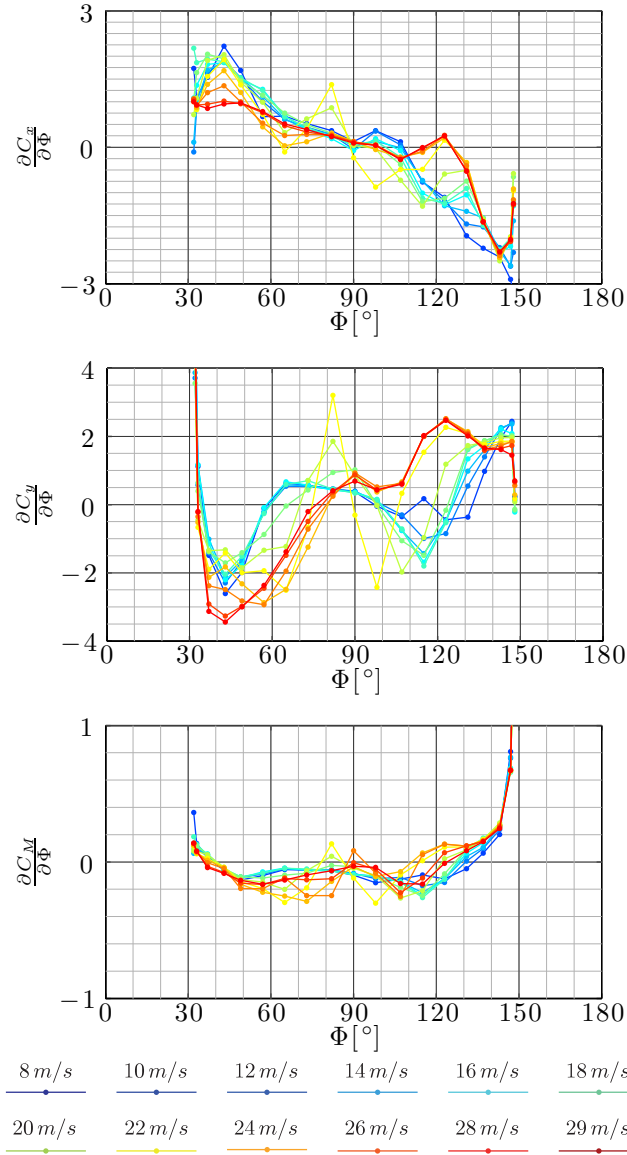


Figure A.31: Variation with the yaw angle of the derivative of the mean aerodynamic coefficients with respect to Φ for different wind speeds, in CC I10.

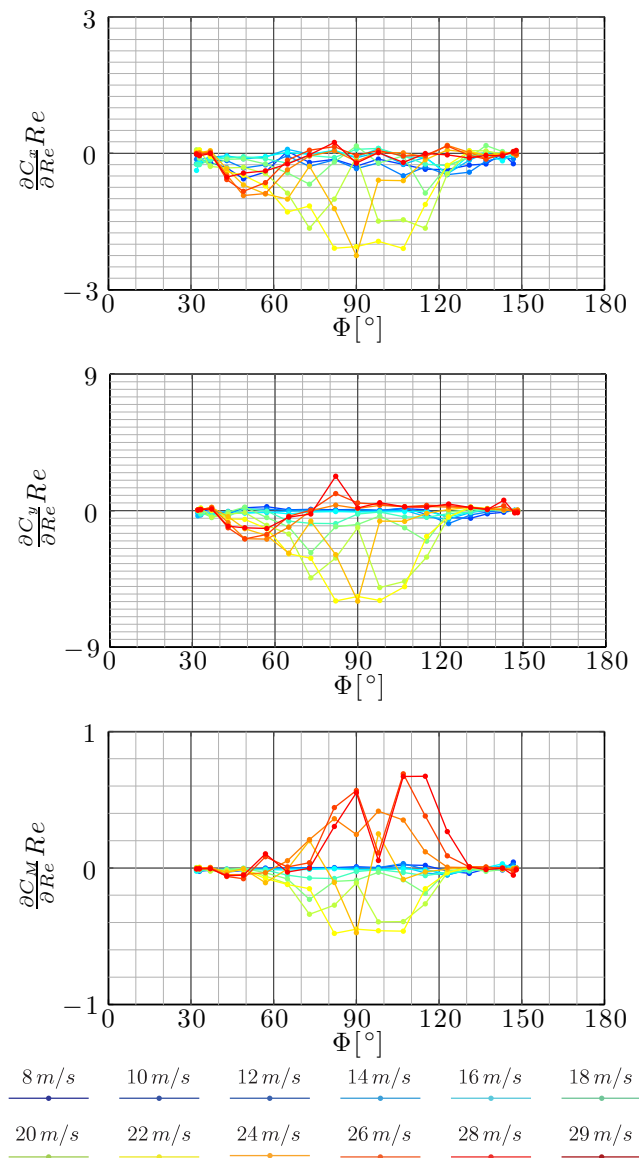


Figure A.32: Variation with the yaw angle of the derivative of the mean aerodynamic coefficients with respect to Re for different wind speeds, in CC I10. Plot scale is different from those of the other CCs.

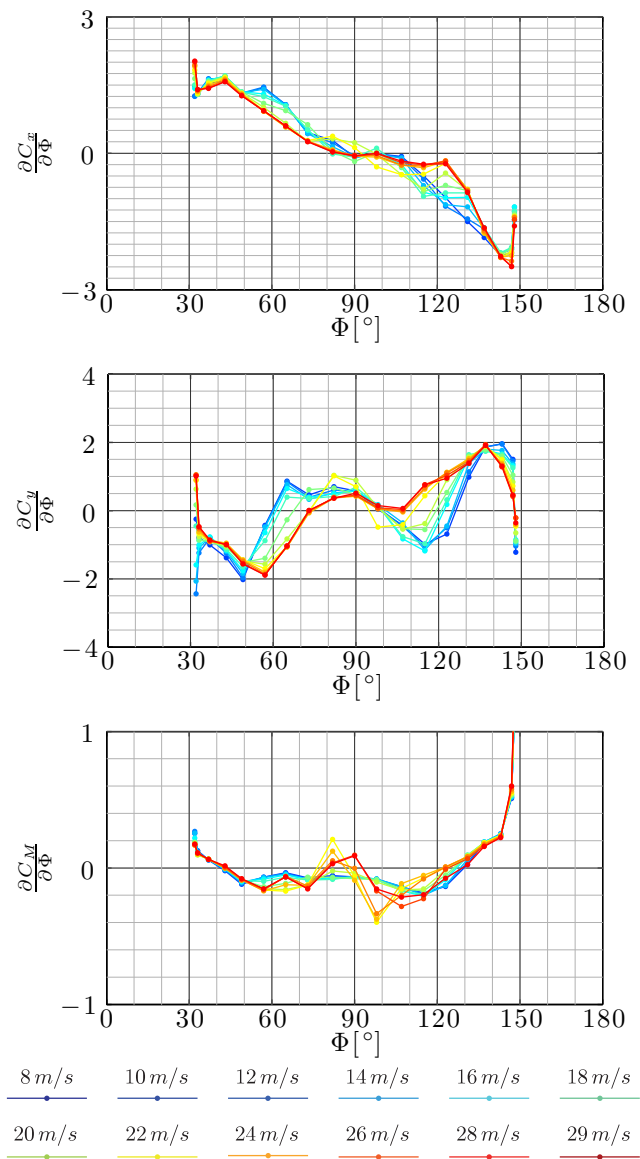


Figure A.33: Variation with the yaw angle of the derivative of the mean aerodynamic coefficients with respect to Φ for different wind speeds, in CC I11.

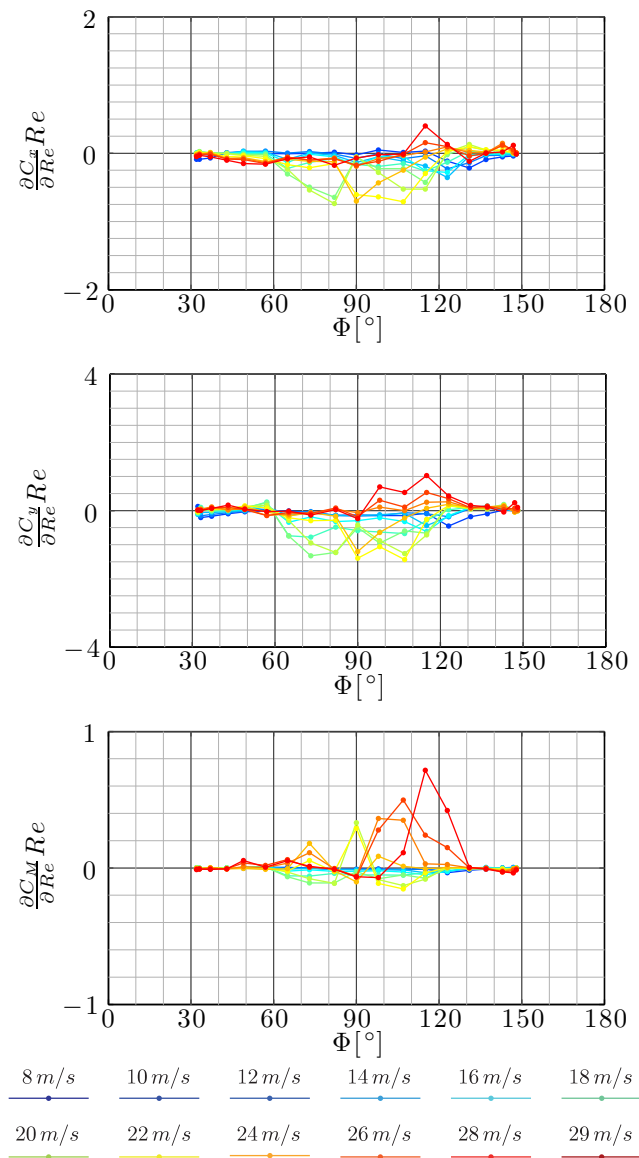


Figure A.34: Variation with the yaw angle of the derivative of the mean aerodynamic coefficients with respect to Re for different wind speeds, in CC I11.

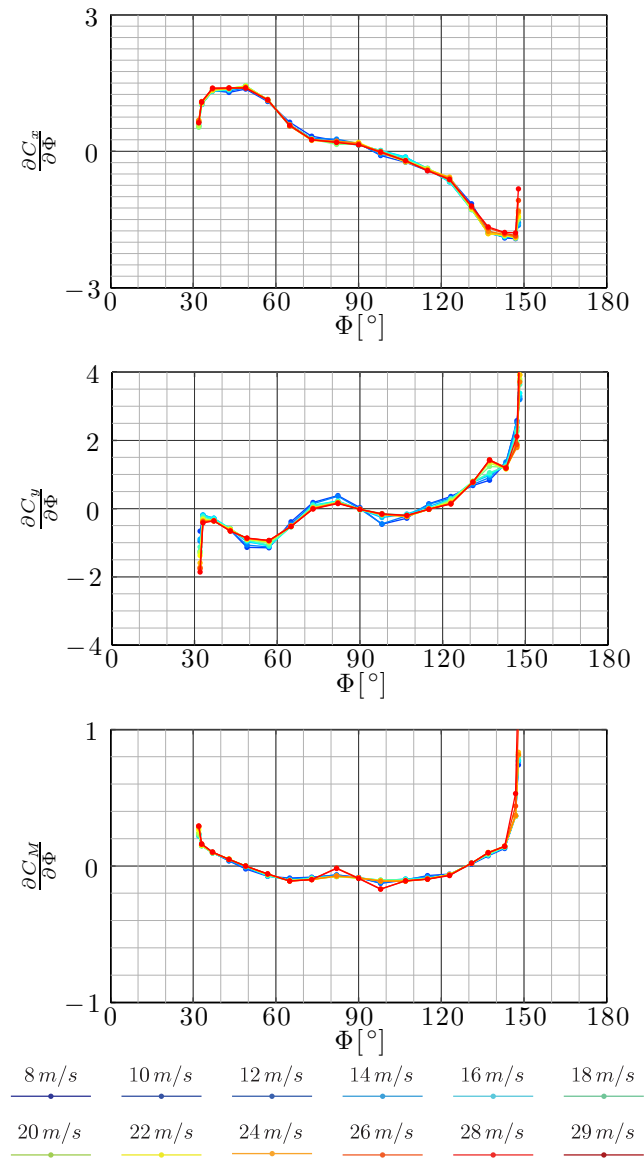


Figure A.35: Variation with the yaw angle of the derivative of the mean aerodynamic coefficients with respect to Φ for different wind speeds, in CC I12.

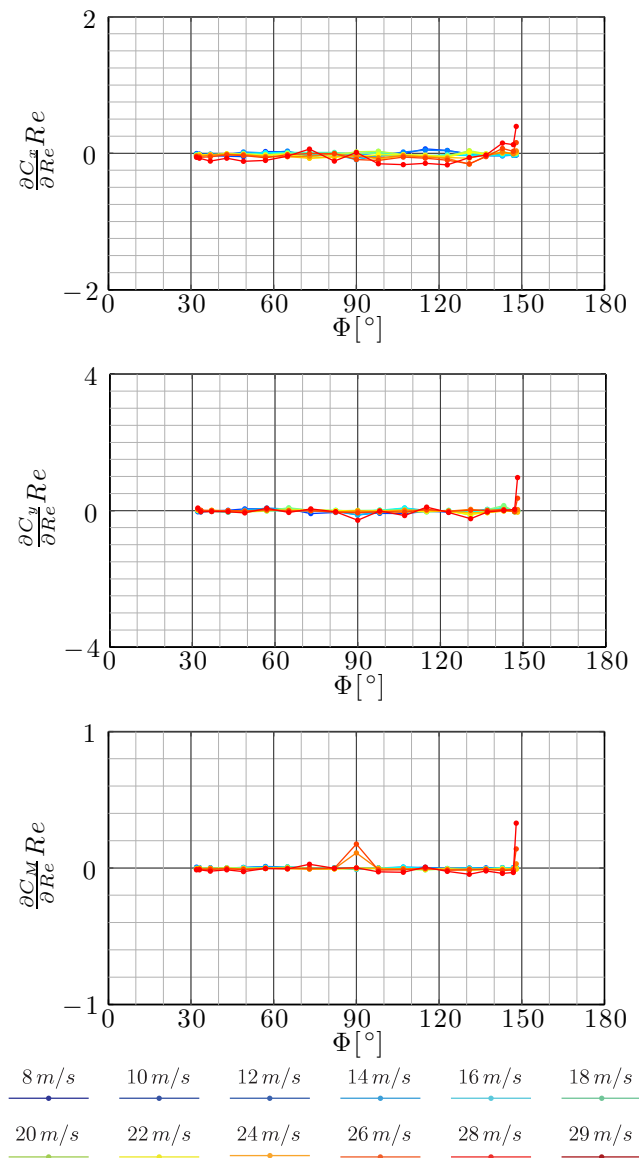


Figure A.36: Variation with the yaw angle of the derivative of the mean aerodynamic coefficients with respect to Re for different wind speeds, in CC I12.

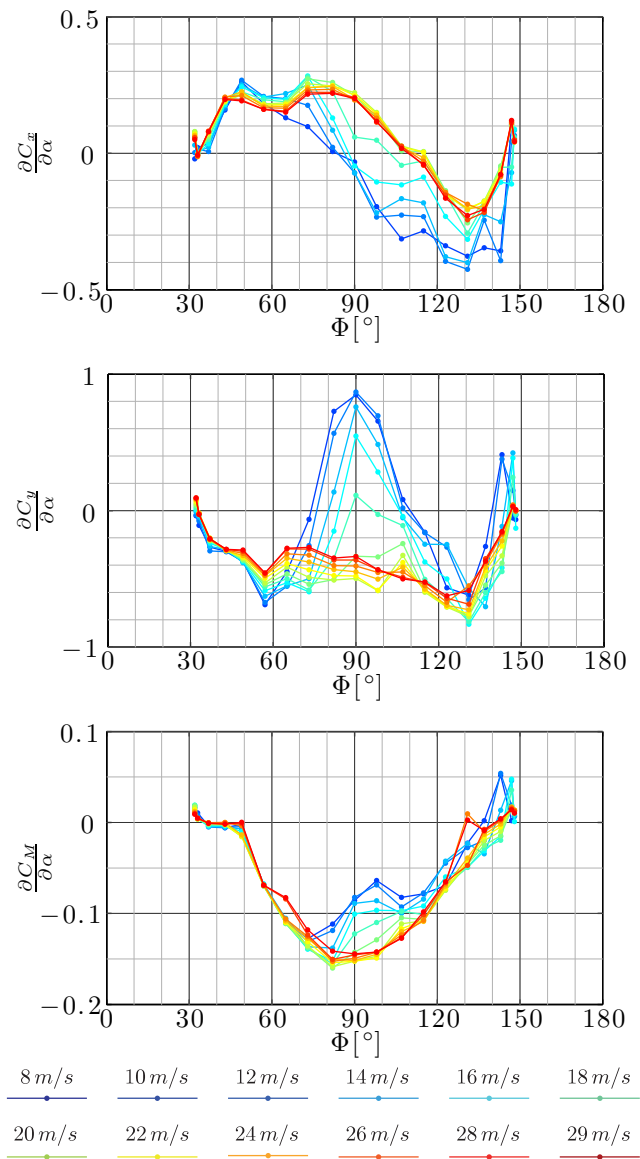


Figure A.37: Variation with the yaw angle of the derivative of the mean aerodynamic coefficients with respect to α for different wind speeds, in CC I7.

APPENDIX B

Fluctuating aerodynamic coefficients

B.1 Ice accreted bridge hangers

In this Section, the fluctuating aerodynamic coefficients are given for the climatic conditions:

- CC V1
- CC V2
- CC V3
- CC V4

Grey areas indicate the range of angles of attack where the dependency of the mean aerodynamic coefficients with wind speed is more pronounced.

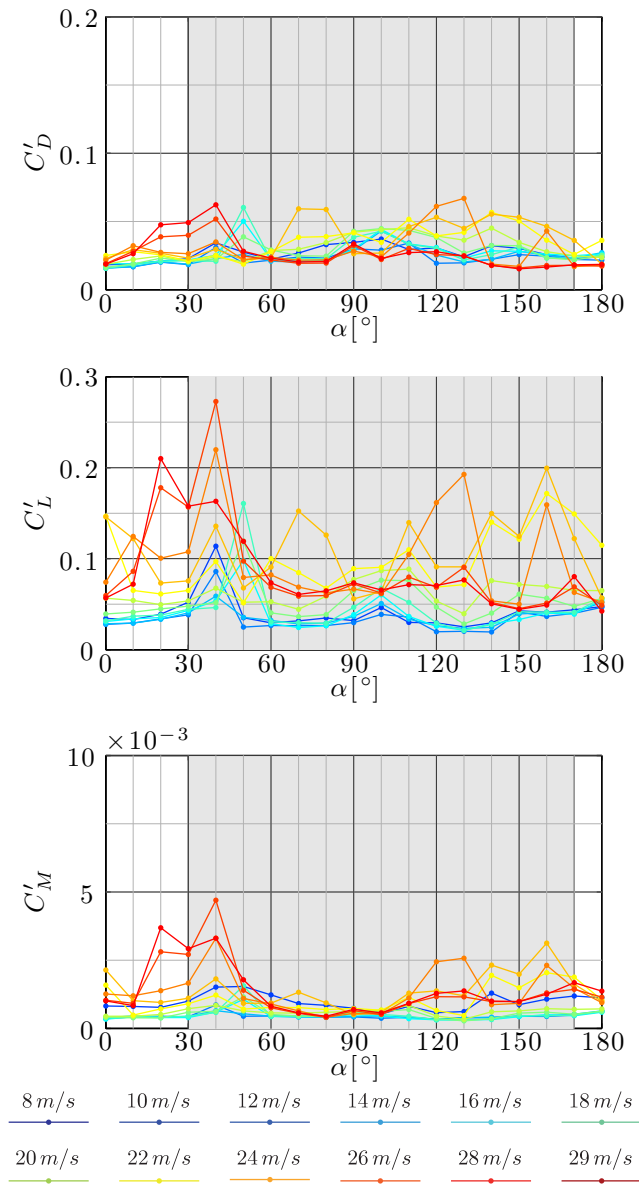


Figure B.1: Variation with the angle of attack of the fluctuating aerodynamic coefficients for different wind speeds, in CC V1.

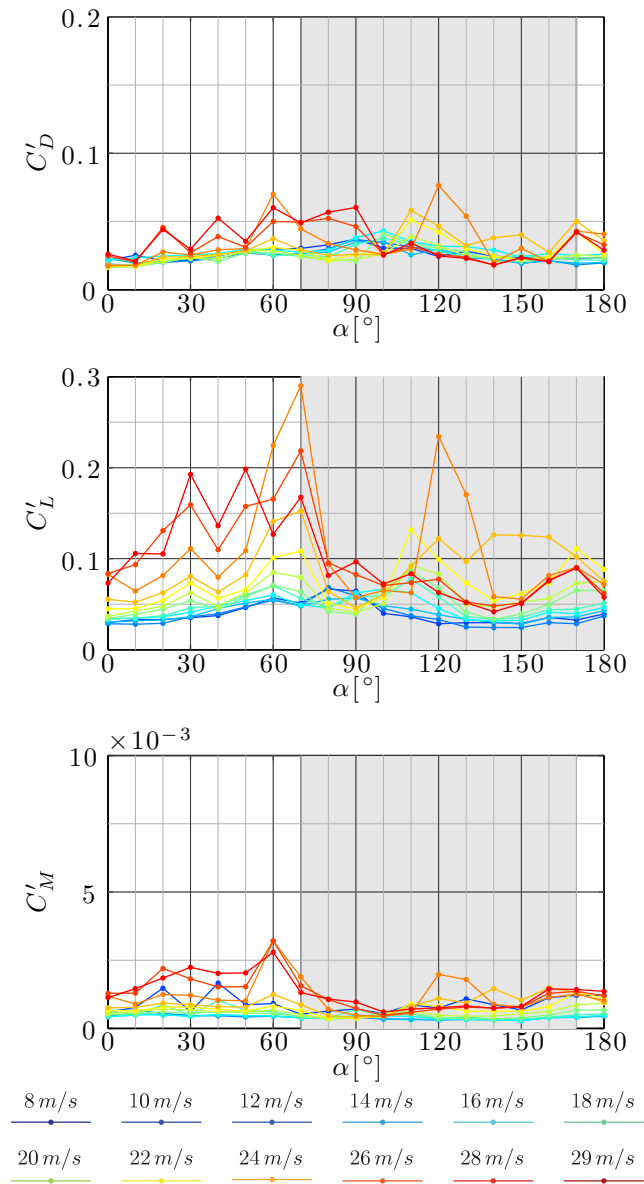


Figure B.2: Variation with the angle of attack of the fluctuating aerodynamic coefficients for different wind speeds, in CC V2.

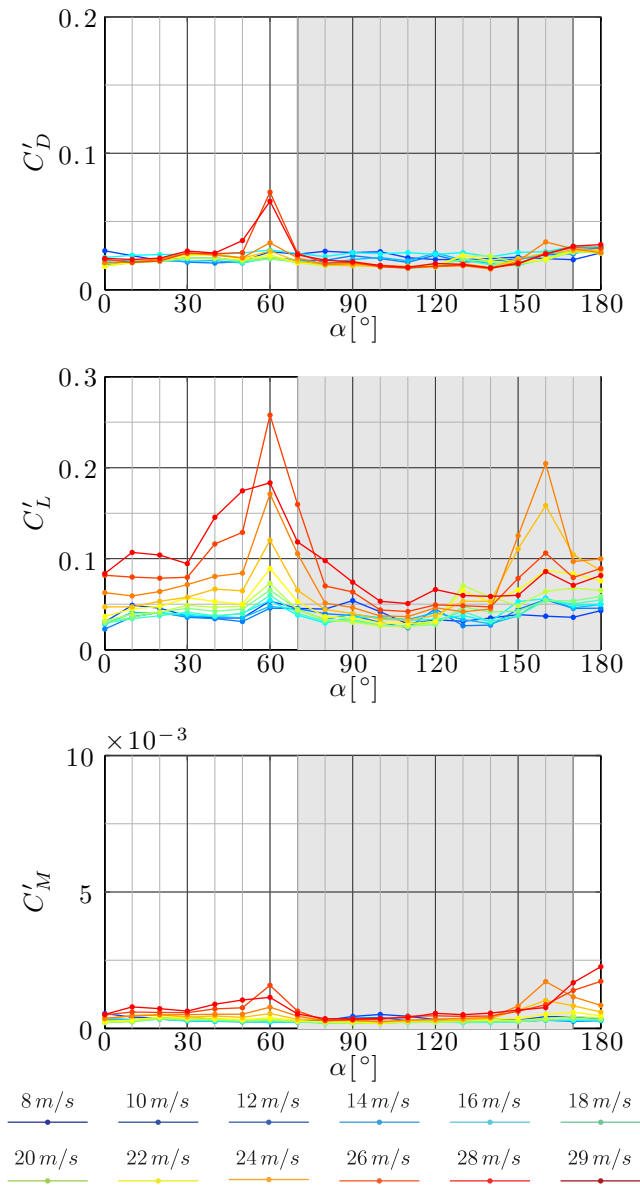


Figure B.3: Variation with the angle of attack of the fluctuating mean aerodynamic coefficients for different wind speeds, in CC V3.

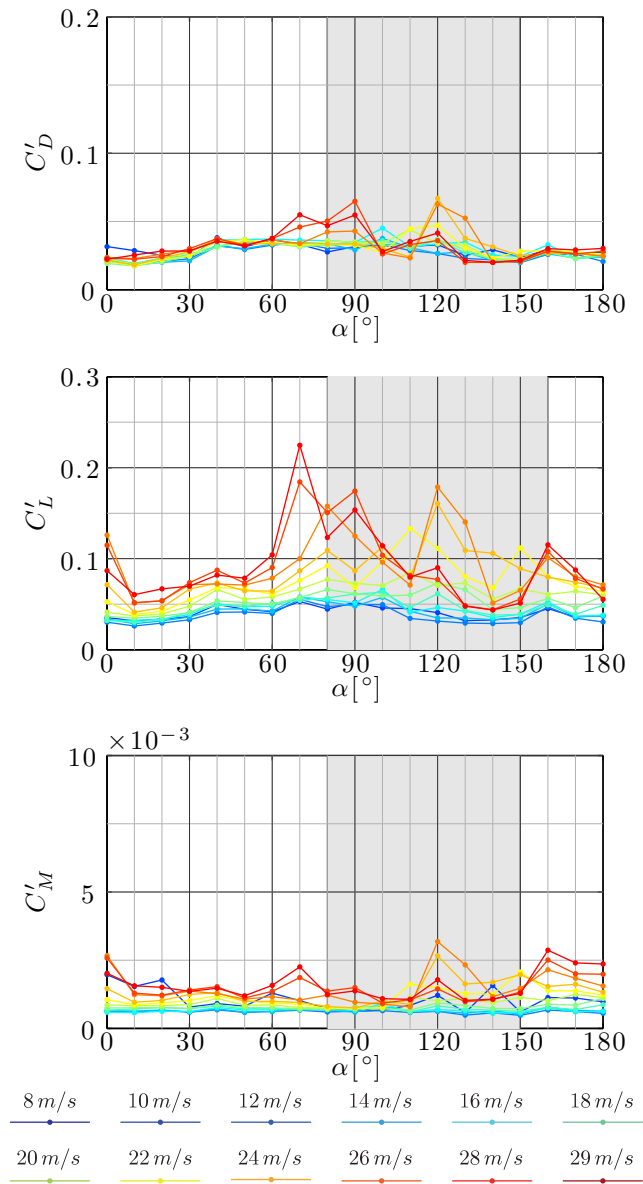


Figure B.4: Variation with the angle of attack of the fluctuating the mean aerodynamic coefficients for different wind speeds, in CC V4.

B.2 Ice accreted stay cables

In this Section, the fluctuating aerodynamic coefficients are given for the climatic conditions:

- CC I1 (dry case)
- CC I2
- CC I3
- CC I4
- CC I5
- CC I6
- CC I7a
- CC I7b
- CC I7c
- CC I8
- CC I9
- CC I10
- CC I11
- CC I12

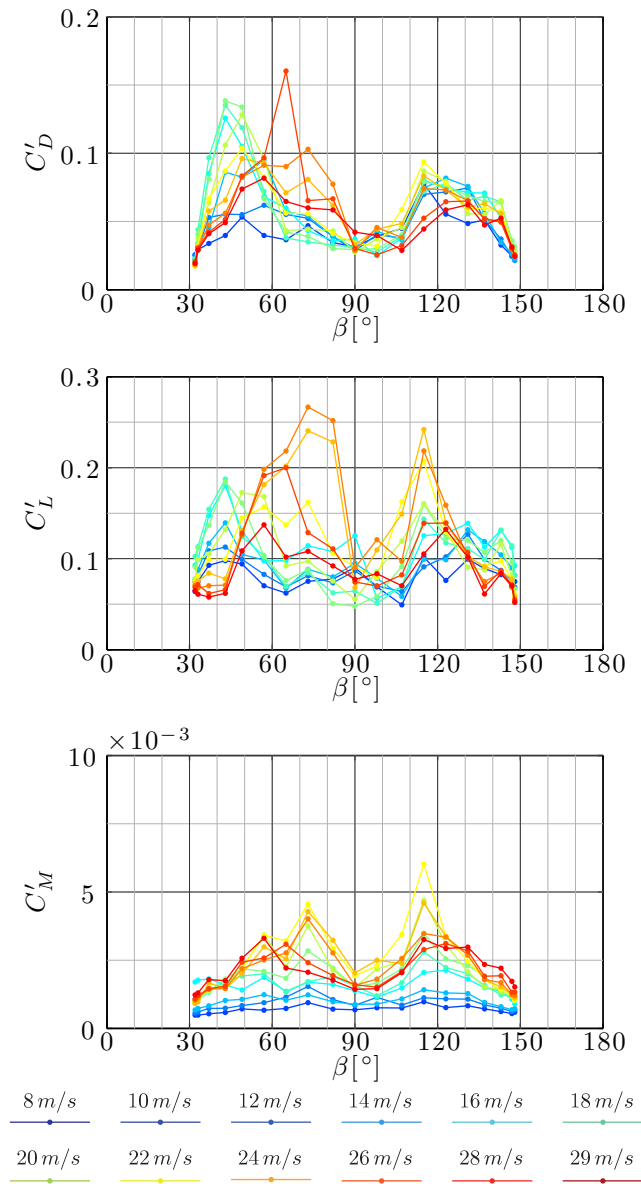


Figure B.5: Variation with the yaw angle of the fluctuating aerodynamic coefficients for different wind speeds, in CC I1.

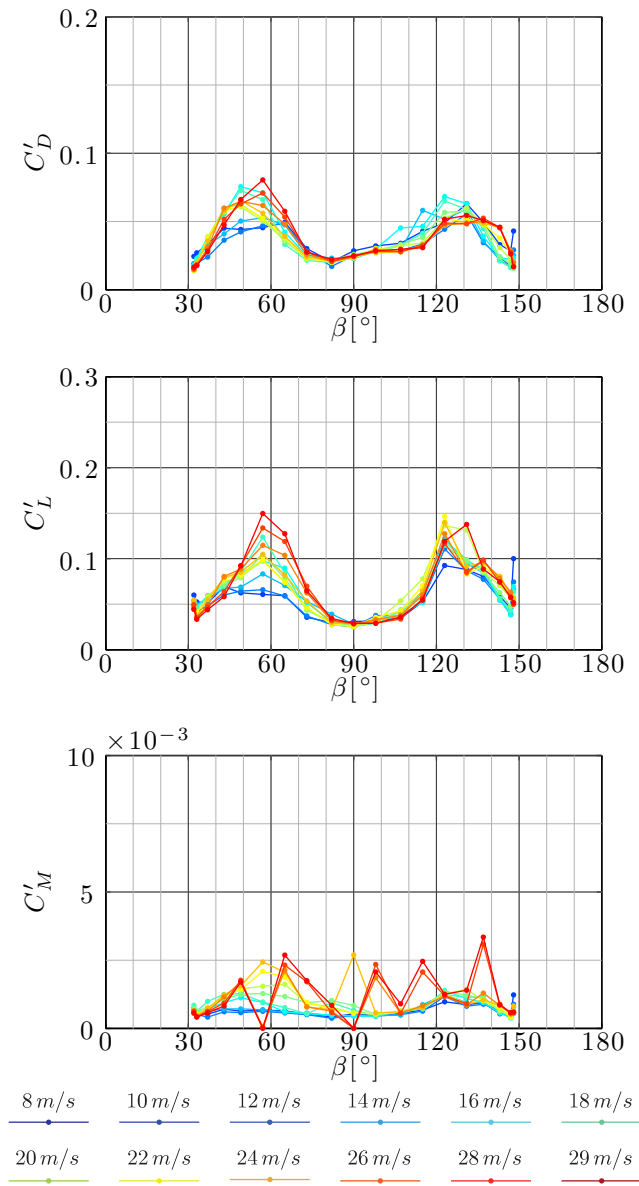


Figure B.6: Variation with the yaw angle of the fluctuating aerodynamic coefficients for different wind speeds, in CC I2.

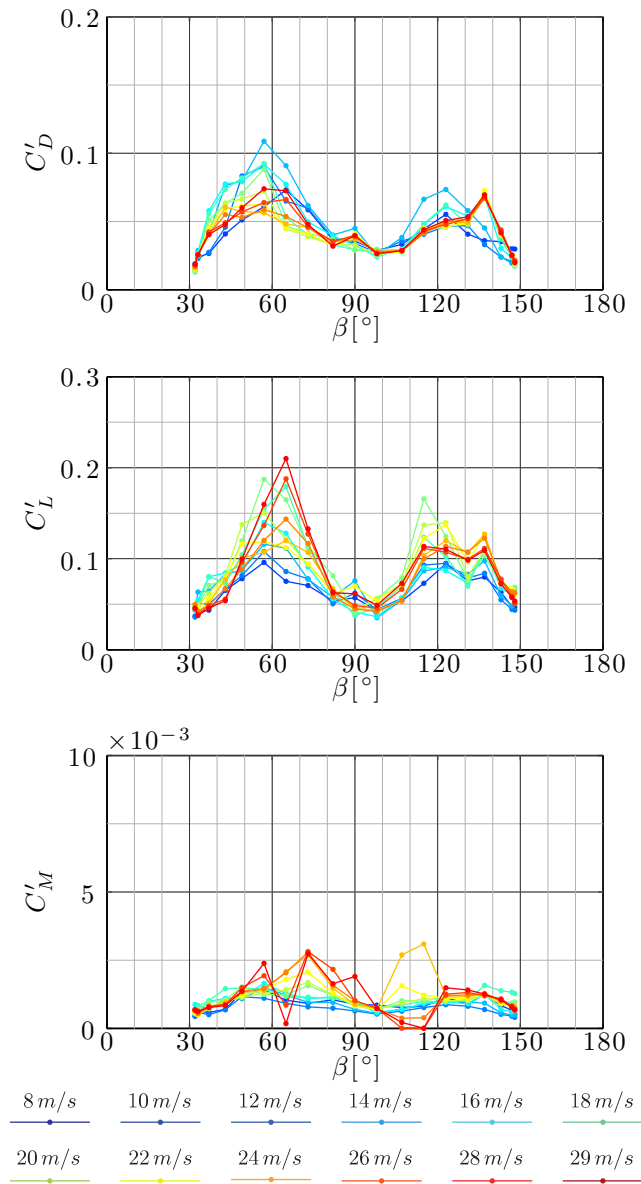


Figure B.7: Variation with the yaw angle of the fluctuating aerodynamic coefficients for different wind speeds, in CC I3.

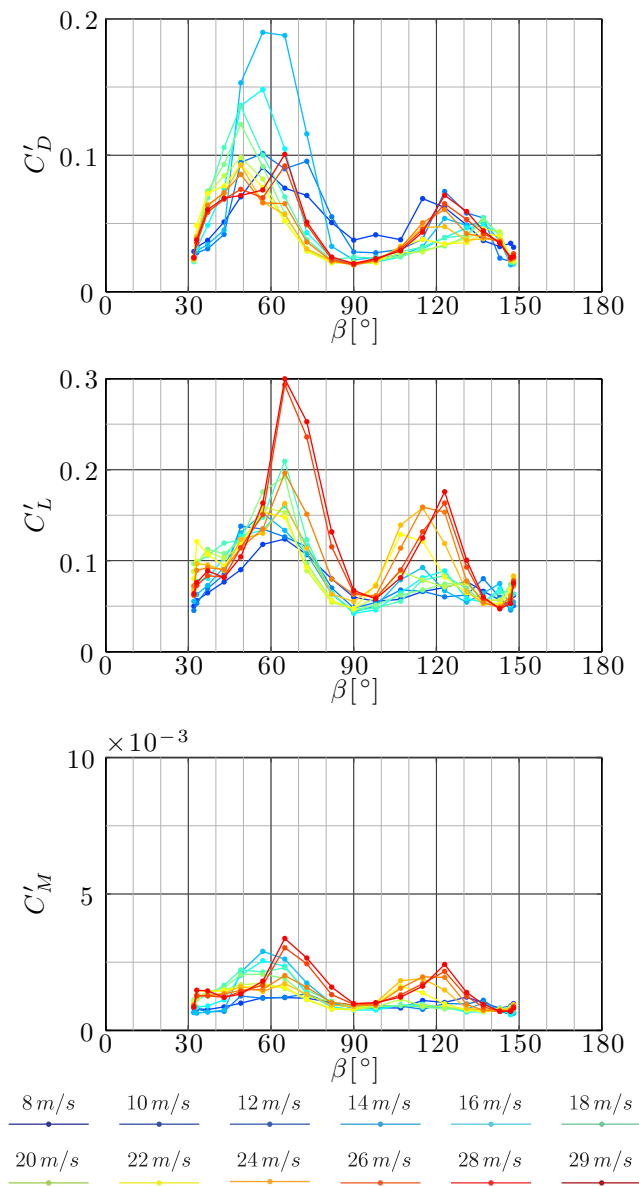


Figure B.8: Variation with the yaw angle of the fluctuating aerodynamic coefficients for different wind speeds, in CC I4.

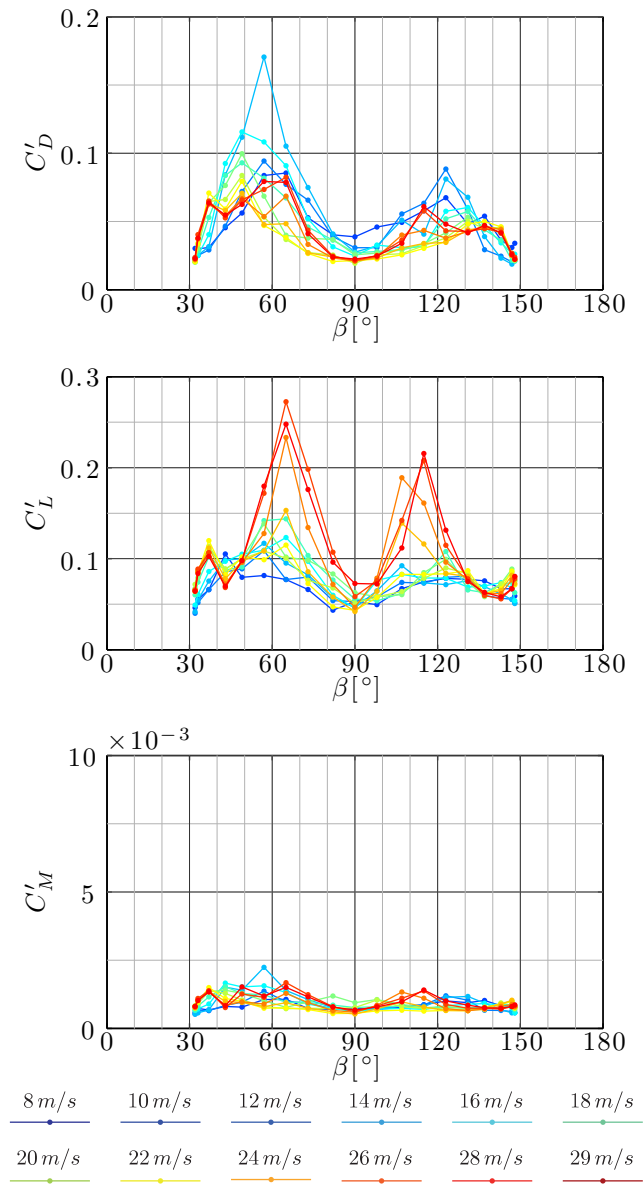


Figure B.9: Variation with the yaw angle of the fluctuating aerodynamic coefficients for different wind speeds, in CC 15.

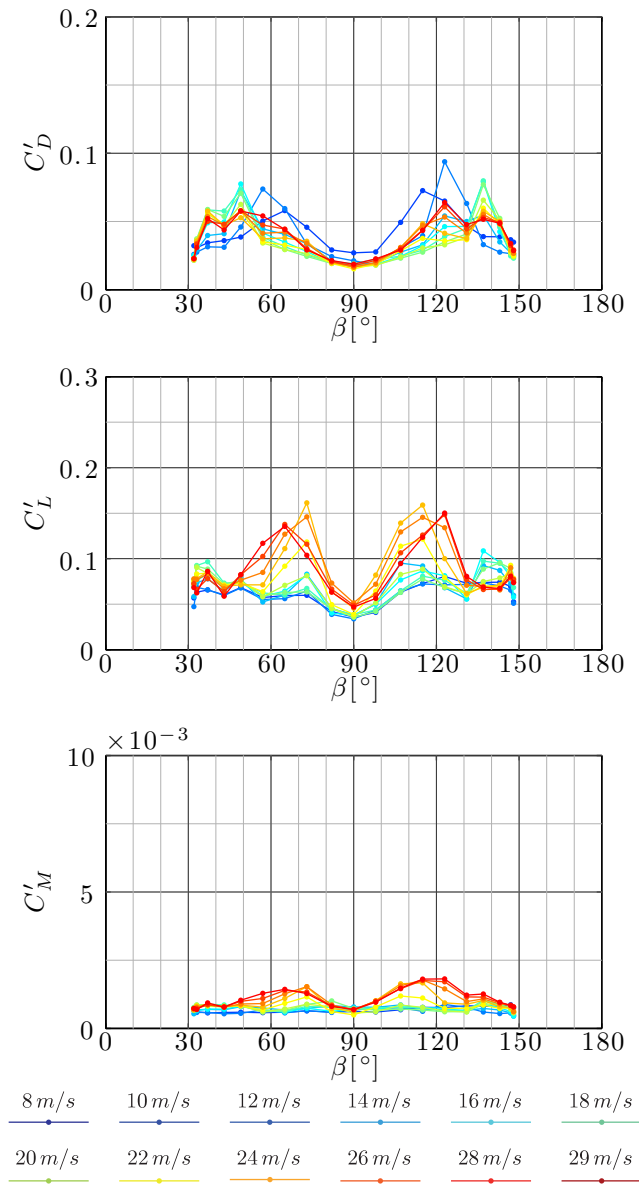


Figure B.10: Variation with the yaw angle of the fluctuating aerodynamic coefficients for different wind speeds, in CC I6.

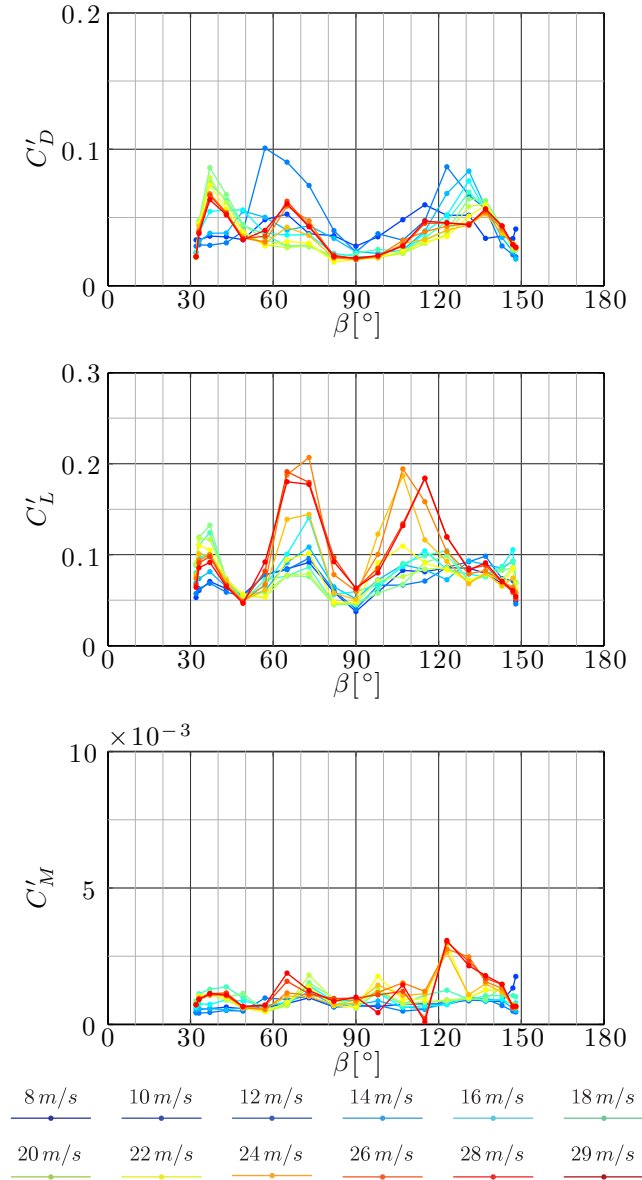


Figure B.11: Variation with the yaw angle of the fluctuating aerodynamic coefficients for different wind speeds, in CC I7a.

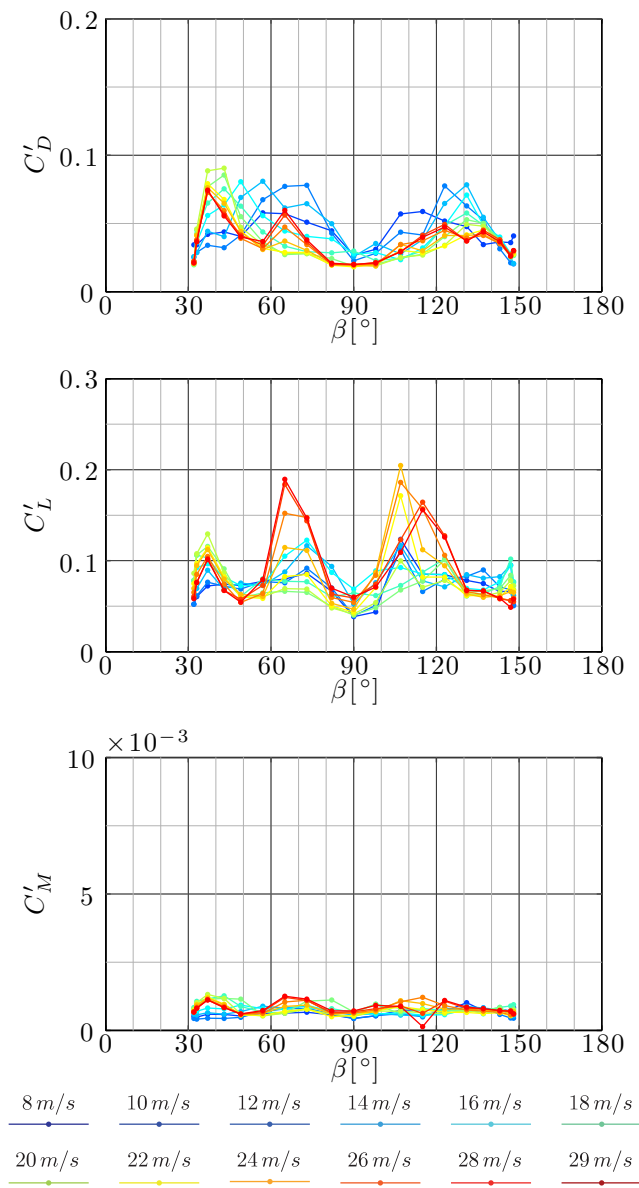


Figure B.12: Variation with the yaw angle of the fluctuating aerodynamic coefficients for different wind speeds, in CC I7b.

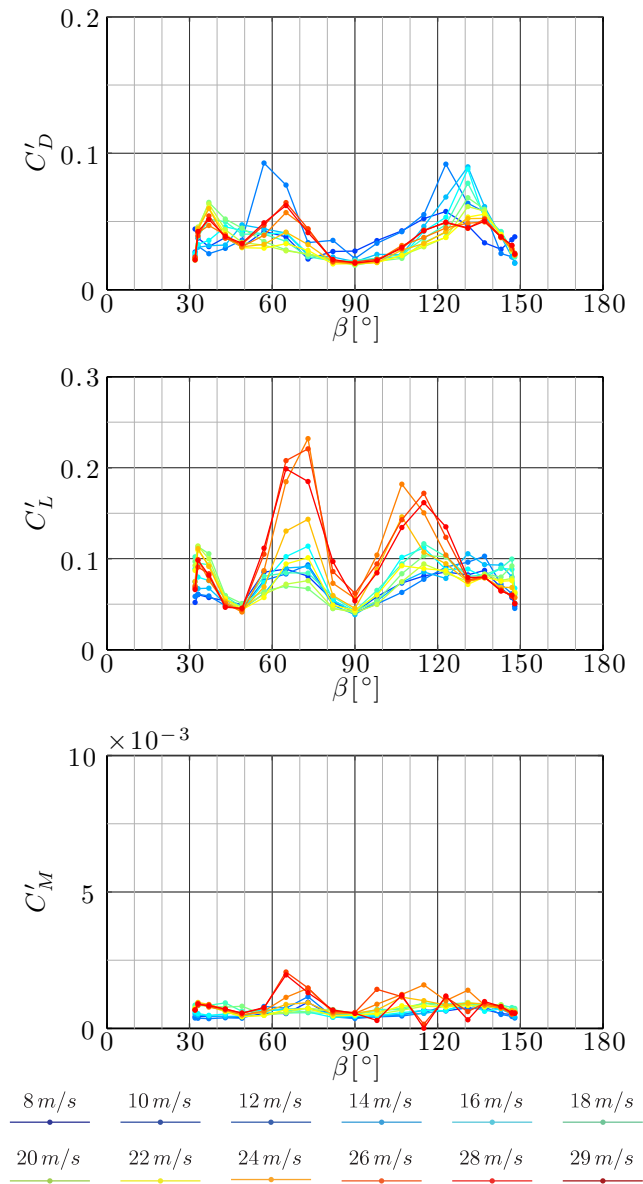


Figure B.13: Variation with the yaw angle of the fluctuating aerodynamic coefficients for different wind speeds, in CC I7c.

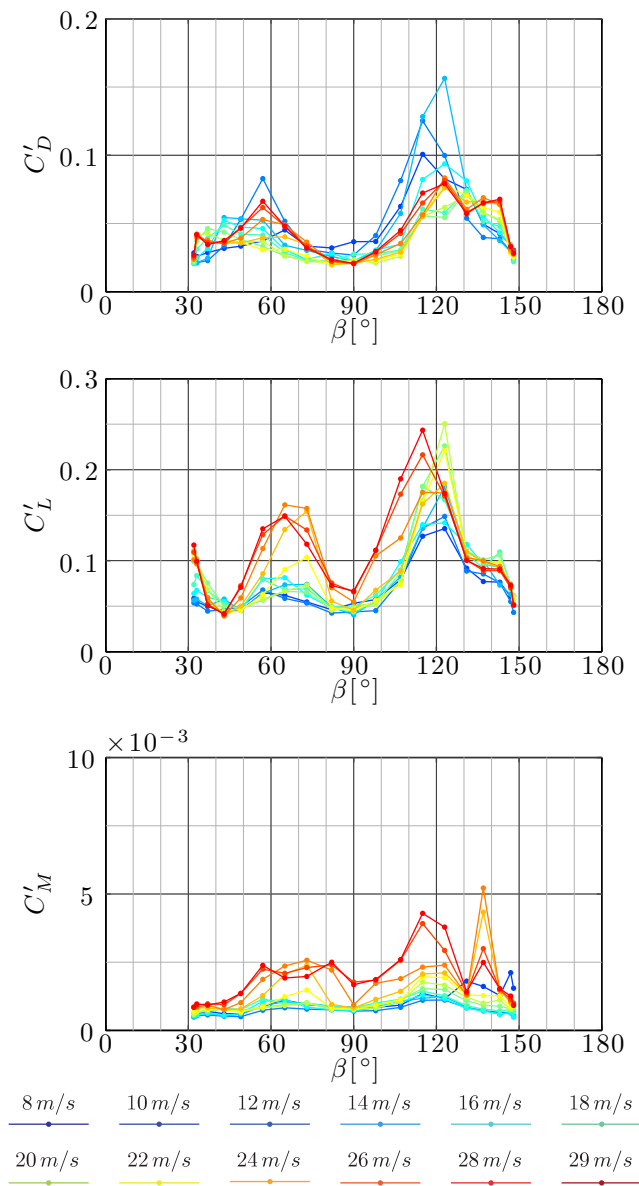


Figure B.14: Variation with the yaw angle of the fluctuating aerodynamic coefficients for different wind speeds, in CC I8.

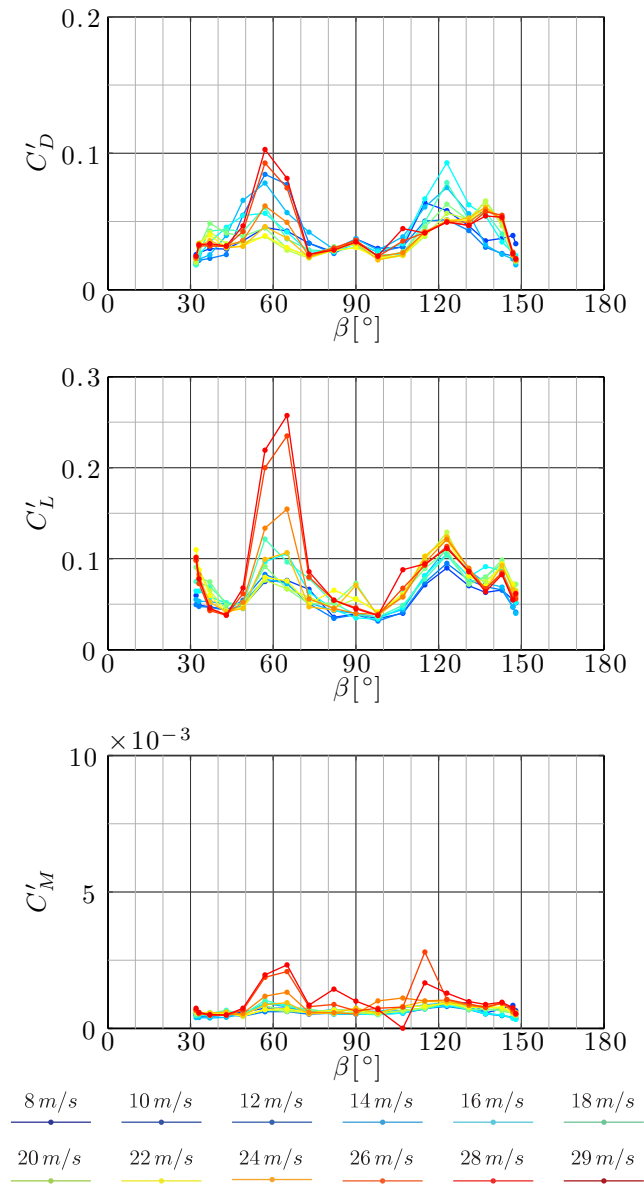


Figure B.15: Variation with the yaw angle of the fluctuating aerodynamic coefficients for different wind speeds, in CC 19.

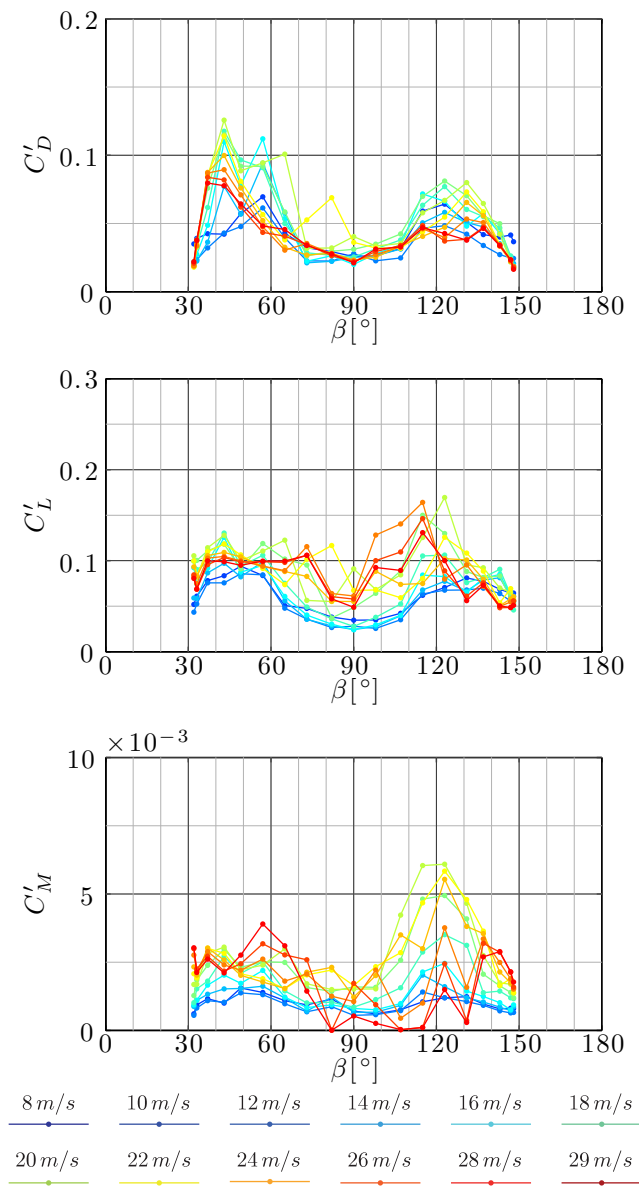


Figure B.16: Variation with the yaw angle of the fluctuating aerodynamic coefficients for different wind speeds, in CC I10.

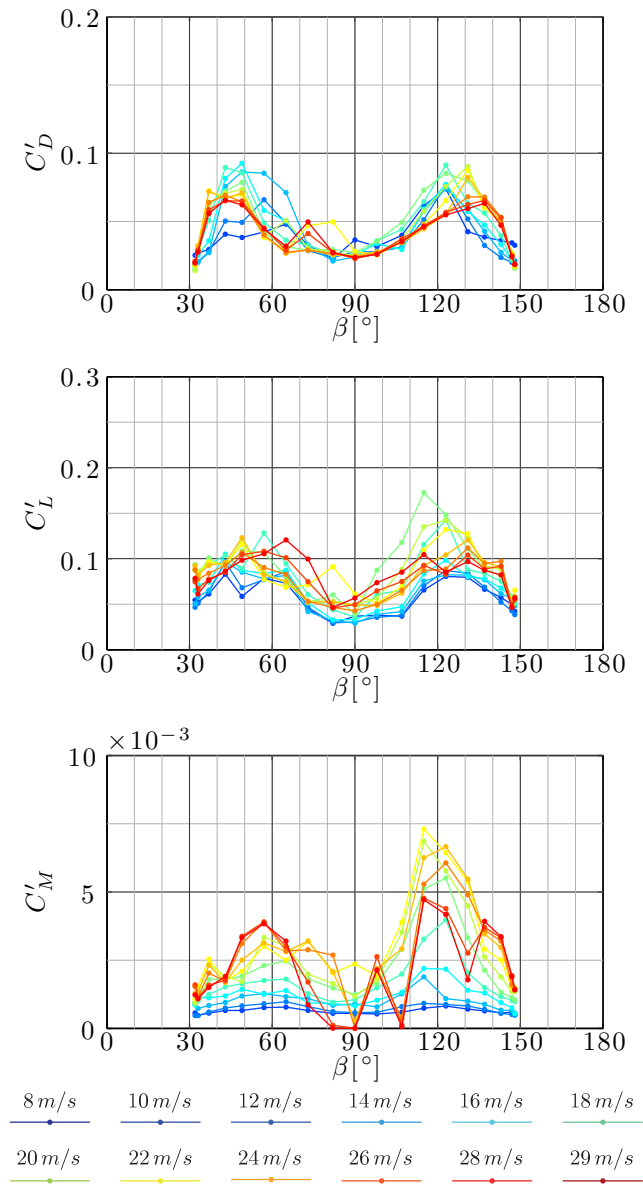


Figure B.17: Variation with the yaw angle of the fluctuating aerodynamic coefficients for different wind speeds, in CC I11.

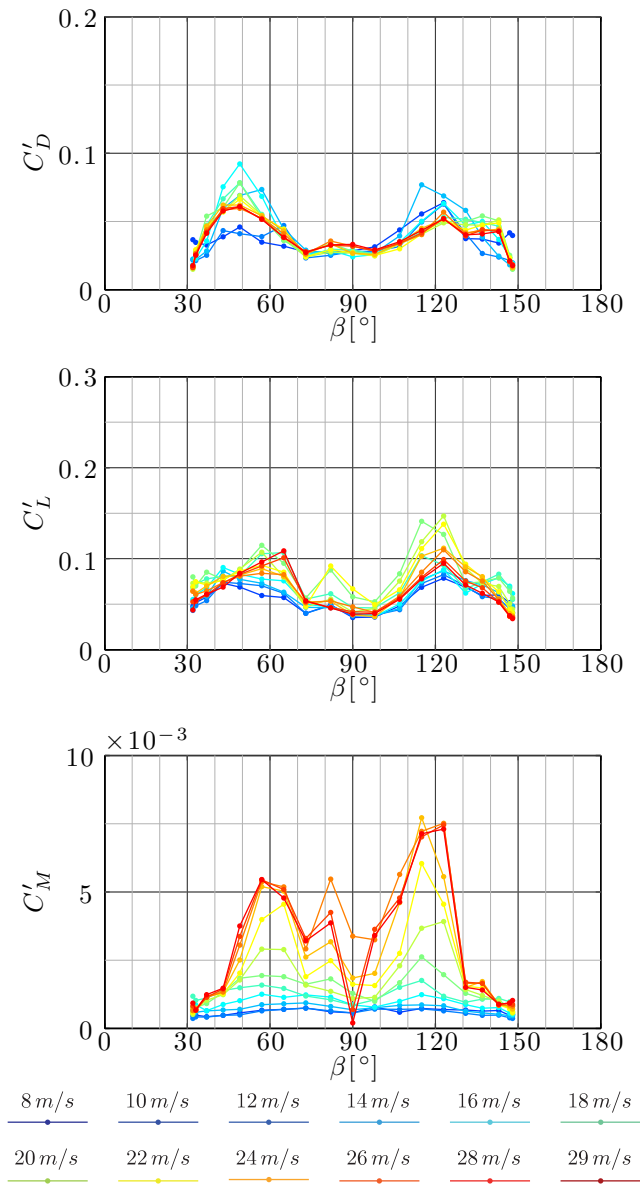


Figure B.18: Variation with the yaw angle of the fluctuating aerodynamic coefficients for different wind speeds, in CC I12.

Aerodynamic forces linearization

The detailed derivation of the last three terms of equation 7.38 is here given. For sake of simplicity, the point of evaluation of all the aerodynamic coefficients and their derivatives is omitted, i.e. $C_{x'}|_{(Re, \bar{\varphi}, \Phi)}$ is simply write as $C_{x'}$ and so forth.

C.1 Linearization of the aerodynamic damping matrix

The linearization of the aerodynamic damping matrix is:

$$\begin{aligned} \nabla_{\dot{\mathbf{q}}(t)} \mathbf{F}_a|_{(\mathbf{0}, \mathbf{0}, \mathbf{U})} = & \frac{\rho \nu^2}{2D} \left\{ \left[(\mathbf{R}_z(\alpha_R) \mathbf{C}) \otimes \left(\left(2Re \frac{D}{\nu} \right) \nabla_{\dot{\mathbf{q}}(t)} U_R \right) \right] \right. \\ & + Re_R^2 [(\mathbf{F} \mathbf{C} \otimes \nabla_{\dot{\mathbf{q}}(t)} \alpha_R) \\ & \left. + \mathbf{R}_z(\alpha_R) [(\nabla_{\mathbf{d}} \mathbf{C}) (\nabla_{\dot{\mathbf{q}}(t)} \mathbf{d})] \right] \Big|_{(\mathbf{0}, \mathbf{0}, \mathbf{U})} \end{aligned} \quad (\text{C.1})$$

The first term of the Equation C.1 is:

$$\frac{\rho \nu^2}{2D} (\mathbf{R}_z(\alpha_R) \mathbf{C}) \otimes \left(2Re \frac{D}{\nu} \nabla_{\dot{\mathbf{q}}(t)} U_R \right) \Big|_{(\mathbf{0}, \mathbf{0}, \mathbf{U})} = \rho \nu Re \sin \Phi \begin{bmatrix} f_1 & f_2 & f_3 \\ f_4 & f_5 & f_6 \\ f_7 & f_8 & f_9 \end{bmatrix} \quad (\text{C.2})$$

where:

$$f_1 = -\cos \bar{\varphi} (C_{x'} \cos \bar{\varphi} - C_{y'} \sin \bar{\varphi}) \quad (\text{C.3})$$

$$f_2 = -\sin \bar{\varphi} (C_{x'} \cos \bar{\varphi} - C_{y'} \sin \bar{\varphi}) \quad (\text{C.4})$$

$$f_3 = R_\delta \sin \delta [C_{x'} \cos \bar{\varphi} - C_{y'} \sin \bar{\varphi}] \quad (\text{C.5})$$

$$f_4 = -\cos \bar{\varphi} (C_{x'} \sin \bar{\varphi} + C_{y'} \cos \bar{\varphi}) \quad (\text{C.6})$$

$$f_5 = -\sin \bar{\varphi} (C_{x'} \sin \bar{\varphi} + C_{y'} \cos \bar{\varphi}) \quad (\text{C.7})$$

$$f_6 = R_\delta \sin \delta (C_{x'} \sin \bar{\varphi} + C_{y'} \cos \bar{\varphi}) \quad (\text{C.8})$$

$$f_7 = -DC_M \cos \bar{\varphi} \quad (\text{C.9})$$

$$f_8 = -DC_M \sin \bar{\varphi} \quad (\text{C.10})$$

$$f_9 = DC_M R_\delta \sin \delta \quad (\text{C.11})$$

The second term of the Equation C.1 is:

$$\frac{\rho \nu^2}{2D} Re_R^2 (\mathbf{FC} \otimes \nabla_{\dot{\mathbf{q}}(t)} \alpha_R) \Big|_{(\mathbf{0}, \mathbf{0}, \mathbf{U})} = \frac{\rho \nu Re}{2 \sin \Phi} \begin{bmatrix} g_1 & g_2 & g_3 \\ g_4 & g_5 & g_6 \\ 0 & 0 & 0 \end{bmatrix} \quad (\text{C.12})$$

where:

$$g_1 = -\sin \bar{\varphi} (C_{x'} \sin \bar{\varphi} + C_{y'} \cos \bar{\varphi}) \quad (\text{C.13})$$

$$g_2 = \cos \bar{\varphi} (C_{x'} \sin \bar{\varphi} + C_{y'} \cos \bar{\varphi}) \quad (\text{C.14})$$

$$g_3 = R_\delta \cos \delta (C_{x'} \sin \bar{\varphi} + C_{y'} \cos \bar{\varphi}) \quad (\text{C.15})$$

$$g_4 = \sin \bar{\varphi} (C_{x'} \cos \bar{\varphi} - C_{y'} \sin \bar{\varphi}) \quad (\text{C.16})$$

$$g_5 = -\cos \bar{\varphi} (C_{x'} \cos \bar{\varphi} - C_{y'} \sin \bar{\varphi}) \quad (\text{C.17})$$

$$g_6 = -R_\delta \cos \delta (C_{x'} \cos \bar{\varphi} - C_{y'} \sin \bar{\varphi}) \quad (\text{C.18})$$

The third term of the Equation C.1 is:

$$\frac{\rho \nu^2}{2D} Re_R^2 R_z(\alpha_R) [(\nabla_{\mathbf{d}} \mathbf{C}) (\nabla_{\dot{\mathbf{q}}(\mathbf{t})} \mathbf{d})] \Big|_{(\mathbf{0}, \mathbf{0}, \mathbf{U})} = \frac{\rho \nu Re}{2} \begin{bmatrix} h_1 & h_2 & h_3 \\ h_4 & h_5 & h_6 \\ h_7 & h_8 & h_9 \end{bmatrix} \quad (\text{C.19})$$

where:

$$h_1 = \left[\cos \bar{\varphi} \left(\frac{\sin \bar{\varphi}}{\sin \Phi} \frac{\partial C_{x'}}{\partial \alpha_R} - \cos \bar{\varphi} \left(\cos \Phi \frac{\partial C_{x'}}{\partial \Phi} + \sin \Phi \frac{\partial C_{x'}}{\partial Re} Re \right) \right) \right. \\ \left. + \sin \bar{\varphi} \left(-\frac{\sin \bar{\varphi}}{\sin \Phi} \frac{\partial C_{y'}}{\partial \alpha_R} + \cos \bar{\varphi} \left(\cos \Phi \frac{\partial C_{y'}}{\partial \Phi} + \sin \Phi \frac{\partial C_{y'}}{\partial Re} Re \right) \right) \right] \quad (\text{C.20})$$

$$h_2 = \left[\cos \bar{\varphi} \left(-\frac{\cos \bar{\varphi}}{\sin \Phi} \frac{\partial C_{x'}}{\partial \alpha_R} - \sin \bar{\varphi} \left(\cos \Phi \frac{\partial C_{x'}}{\partial \Phi} + \sin \Phi \frac{\partial C_{x'}}{\partial Re} Re \right) \right) \right. \\ \left. + \sin \bar{\varphi} \left(\frac{\cos \bar{\varphi}}{\sin \Phi} \frac{\partial C_{y'}}{\partial \alpha_R} + \sin \bar{\varphi} \left(\cos \Phi \frac{\partial C_{y'}}{\partial \Phi} + \sin \Phi \frac{\partial C_{y'}}{\partial Re} Re \right) \right) \right] \quad (\text{C.21})$$

$$h_3 = R_\delta \left[\cos \bar{\varphi} \left(-\frac{\cos \delta}{\sin \Phi} \frac{\partial C_{x'}}{\partial \alpha_R} + \sin \delta \left(\cos \Phi \frac{\partial C_{x'}}{\partial \Phi} + \sin \Phi \frac{\partial C_{x'}}{\partial Re} Re \right) \right) \right. \\ \left. + \sin \bar{\varphi} \left(\frac{\cos \delta}{\sin \Phi} \frac{\partial C_{y'}}{\partial \alpha_R} - \sin(\delta) \left(\cos \Phi \frac{\partial C_{y'}}{\partial \Phi} + \sin \Phi \frac{\partial C_{y'}}{\partial Re} Re \right) \right) \right] \quad (\text{C.22})$$

$$h_4 = \sin \bar{\varphi} \left[\frac{\sin \bar{\varphi}}{\sin \Phi} \frac{\partial C_{x'}}{\partial \alpha_R} - \cos \bar{\varphi} \left(\cos \Phi \frac{\partial C_{x'}}{\partial \Phi} + \sin \Phi \frac{\partial C_{x'}}{\partial Re} Re \right) \right] \\ + \cos \bar{\varphi} \left[\frac{\sin \bar{\varphi}}{\sin \Phi} \frac{\partial C_{y'}}{\partial \alpha_R} - \cos \bar{\varphi} \left(\cos \Phi \frac{\partial C_{y'}}{\partial \Phi} + \sin \Phi \frac{\partial C_{y'}}{\partial Re} Re \right) \right] \quad (\text{C.23})$$

$$h_5 = \sin \bar{\varphi} \left[-\frac{\cos \bar{\varphi}}{\sin \Phi} \frac{\partial C_{x'}}{\partial \alpha_R} - \sin \bar{\varphi} \left(\cos \Phi \frac{\partial C_{x'}}{\partial \Phi} + \sin \Phi \frac{\partial C_{x'}}{\partial Re} Re \right) \right] \\ + \cos \bar{\varphi} \left[-\frac{\cos \bar{\varphi}}{\sin \Phi} \frac{\partial C_{y'}}{\partial \alpha_R} - \sin \bar{\varphi} \left(\cos \Phi \frac{\partial C_{y'}}{\partial \Phi} + \sin \Phi \frac{\partial C_{y'}}{\partial Re} Re \right) \right] \quad (\text{C.24})$$

$$h_6 = R_\delta \left[\sin \bar{\varphi} \left(-\frac{\cos \delta}{\sin \Phi} \frac{\partial C_{x'}}{\partial \alpha_R} + \sin \delta \left(\cos \Phi \frac{\partial C_{x'}}{\partial \Phi} + \sin \Phi \frac{\partial C_{x'}}{\partial Re} Re \right) \right) \right. \\ \left. + \cos \bar{\varphi} \left(-\frac{\cos \delta}{\sin \Phi} \frac{\partial C_{y'}}{\partial \alpha_R} + \sin \delta \left(\cos \Phi \frac{\partial C_{y'}}{\partial \Phi} + \sin \Phi \frac{\partial C_{y'}}{\partial Re} Re \right) \right) \right] \quad (\text{C.25})$$

$$h_7 = D \left[\frac{\sin \bar{\varphi}}{\sin \Phi} \frac{\partial C_M}{\partial \alpha_R} - \cos \bar{\varphi} \left(\cos \Phi \frac{\partial C_M}{\partial \Phi} + \sin \Phi \frac{\partial C_M}{\partial Re} Re \right) \right] \quad (C.26)$$

$$h_8 = D \left[-\frac{\cos \bar{\varphi}}{\sin \Phi} \frac{\partial C_M}{\partial \alpha_R} - \sin \bar{\varphi} \left(\cos \Phi \frac{\partial C_M}{\partial \Phi} + \sin \Phi \frac{\partial C_M}{\partial Re} Re \right) \right] \quad (C.27)$$

$$h_9 = DR_\delta \left[-\frac{\cos \delta}{\sin \Phi} \frac{\partial C_M}{\partial \alpha_R} + \sin \delta \left(\cos \Phi \frac{\partial C_M}{\partial \Phi} + \sin \Phi \frac{\partial C_M}{\partial Re} Re \right) \right] \quad (C.28)$$

C.2 Linearization of the aerodynamic stiffness matrix

The linearization of the aerodynamic stiffness matrix is:

$$\begin{aligned} \nabla_{\mathbf{q}(t)} \mathbf{F}_a \Big|_{(\mathbf{0}, \mathbf{0}, \mathbf{U})} &= \frac{\rho \nu^2}{2D} \left\{ \left[(\mathbf{R}_z(\alpha_R) \mathbf{C}) \otimes \left(\left(2Re \frac{D}{\nu} \right) \nabla_{\mathbf{q}(t)} U_R \right) \right] \right. \\ &\quad + Re_R^2 [(\mathbf{F} \mathbf{C} \otimes \nabla_{\mathbf{q}(t)} \alpha_R) \\ &\quad \left. + \mathbf{R}_z(\alpha_R) [(\nabla_{\mathbf{d}} \mathbf{C}) (\nabla_{\mathbf{q}(t)} \mathbf{d})] \right] \Big|_{(\mathbf{0}, \mathbf{0}, \mathbf{U})} \end{aligned} \quad (C.29)$$

The first term of the Equation C.29 is:

$$\frac{\rho \nu^2}{2D} (\mathbf{R}_z(\alpha_R) \mathbf{C}) \otimes \left(2Re \frac{D}{\nu} \nabla_{\mathbf{q}(t)} U_R \right) \Big|_{(\mathbf{0}, \mathbf{0}, \mathbf{U})} = \mathbf{0} \quad (C.30)$$

The second term of the Equation C.29 is:

$$\frac{\rho \nu^2}{2D} Re_R^2 (\mathbf{F} \mathbf{C} \otimes \nabla_{\mathbf{q}(t)} \alpha_R) \Big|_{(\mathbf{0}, \mathbf{0}, \mathbf{U})} = \frac{\rho \nu^2}{2D} Re^2 \begin{bmatrix} 0 & 0 & C_{x'} \sin \bar{\varphi} + C_{y'} \cos \bar{\varphi} \\ 0 & 0 & -C_{x'} \cos \bar{\varphi} + C_{y'} \sin \bar{\varphi} \\ 0 & 0 & 0 \end{bmatrix} \quad (C.31)$$

The third term of the Equation C.29 is:

$$\begin{aligned} &\frac{\rho \nu^2}{2D} Re_R^2 \mathbf{R}_z(\alpha_R) [(\nabla_{\mathbf{d}} \mathbf{C}) (\nabla_{\mathbf{q}(t)} \mathbf{d})] \Big|_{(\mathbf{0}, \mathbf{0}, \mathbf{U})} \\ &= \frac{\rho \nu^2}{2D} Re^2 \begin{bmatrix} 0 & 0 & -\frac{\partial C_{x'}}{\partial \alpha} \cos \bar{\varphi} + \frac{\partial C_{y'}}{\partial \alpha} \sin \bar{\varphi} \\ 0 & 0 & -\frac{\partial C_{x'}}{\partial \alpha} \sin \bar{\varphi} - \frac{\partial C_{y'}}{\partial \alpha} \cos \bar{\varphi} \\ 0 & 0 & -D \frac{\partial C_M}{\partial \alpha} \end{bmatrix} \end{aligned} \quad (C.32)$$

C.3 Linearization of the buffeting matrix

The linearization of the buffeting matrix is:

$$\begin{aligned} \nabla_{\mathbf{U}(t)} \mathbf{F}_a|_{(\mathbf{0}, \mathbf{0}, \mathbf{U})} = & \frac{\rho \nu^2}{2D} \left\{ \left[(\mathbf{R}_z(\alpha_R) \mathbf{C}) \otimes \left(\left(2Re \frac{D}{\nu} \right) \nabla_{\mathbf{U}(t)} U_R \right) \right] \right. \\ & + Re_R^2 [(\mathbf{F} \mathbf{C} \otimes \nabla_{\mathbf{U}(t)} \alpha_R) \\ & \left. + \mathbf{R}_z(\alpha_R) [(\nabla_{\mathbf{d}} \mathbf{C}) (\nabla_{\mathbf{U}(t)} \mathbf{d})] \right] \Big|_{(\mathbf{0}, \mathbf{0}, \mathbf{U})} \end{aligned} \quad (\text{C.33})$$

The first term of the Equation C.33 is:

$$\begin{aligned} & \frac{\rho \nu^2}{2D} (\mathbf{R}_z(\alpha_R) \mathbf{C}) \otimes (2Re \frac{D}{\nu} \nabla_{\mathbf{U}(t)} U_R) \Big|_{(\mathbf{0}, \mathbf{0}, \mathbf{U})} \\ & = \rho \nu Re \begin{bmatrix} \cos \bar{\varphi} C_{x'} - \sin \bar{\varphi} C_{y'} & 0 & 0 \\ \sin \bar{\varphi} C_{x'} + \cos \bar{\varphi} C_{y'} & 0 & 0 \\ DC_M & 0 & 0 \end{bmatrix} \end{aligned} \quad (\text{C.34})$$

The second term of the Equation C.33 is:

$$\frac{\rho \nu^2}{2D} Re_R^2 (\mathbf{F} \mathbf{C} \otimes \nabla_{\mathbf{U}(t)} \alpha_R) \Big|_{(\mathbf{0}, \mathbf{0}, \mathbf{U})} = \frac{\rho \nu Re}{2} \begin{bmatrix} 0 & l_1 & l_2 \\ 0 & l_3 & l_4 \\ 0 & 0 & 0 \end{bmatrix} \quad (\text{C.35})$$

where:

$$l_1 = -(\sin \bar{\varphi} C_{x'} + \cos \bar{\varphi} C_{y'}) \frac{\sin \Theta (1 + \tan^2 \beta)}{(\sin^2 \Theta + \tan^2 \beta)} \quad (\text{C.36})$$

$$l_2 = -(\sin \bar{\varphi} C_{x'} + \cos \bar{\varphi} C_{y'}) \frac{\sin \beta \cos \Theta}{\cos^2 \beta (\sin^2 \Theta + \tan^2 \beta)} \quad (\text{C.37})$$

$$l_3 = (\cos \bar{\varphi} C_{x'} - \sin \bar{\varphi} C_{y'}) \frac{\sin \Theta (1 + \tan^2 \beta)}{(\sin^2 \Theta + \tan^2 \beta)} \quad (\text{C.38})$$

$$l_4 = (\cos \bar{\varphi} C_{x'} - \sin \bar{\varphi} C_{y'}) \frac{\sin \beta \cos \Theta}{\cos^2 \beta (\sin^2 \Theta + \tan^2 \beta)} \quad (\text{C.39})$$

The third term of the Equation C.33 is:

$$\frac{\rho \nu^2}{2D} Re_R^2 \mathbf{R}_z(\alpha_R) [(\nabla_{\mathbf{d}} \mathbf{C}) (\nabla_{\mathbf{U}(t)} \mathbf{d})] \Big|_{(\mathbf{0}, \mathbf{0}, \mathbf{U})} = \frac{\rho \nu Re}{2} \begin{bmatrix} m_1 & m_2 & m_3 \\ m_4 & m_5 & m_6 \\ m_7 & m_8 & m_9 \end{bmatrix} \quad (\text{C.40})$$

where:

$$m_1 = \frac{\partial C_{x'}}{\partial Re} Re \cos \bar{\varphi} - \frac{\partial C_{y'}}{\partial Re} Re \sin \bar{\varphi} \quad (C.41)$$

$$\begin{aligned} m_2 = \cos \bar{\varphi} & \left(-\frac{\partial C_{x'}}{\partial \Phi} \frac{\cos \Theta \sin \beta}{\sin \Phi} + \frac{\partial C_{x'}}{\partial \alpha} \frac{\sin \Theta (1 + \tan^2 \beta)}{(\sin^2 \Theta + \tan^2 \beta)} \right) \\ & - \sin \bar{\varphi} \left(-\frac{\partial C_{y'}}{\partial \Phi} \frac{\cos \Theta \sin \beta}{\sin \Phi} + \frac{\partial C_{y'}}{\partial \alpha} \frac{\sin \Theta (1 + \tan^2 \beta)}{(\sin^2 \Theta + \tan^2 \beta)} \right) \end{aligned} \quad (C.42)$$

$$\begin{aligned} m_3 = \cos \bar{\varphi} & \left(\frac{\partial C_{x'}}{\partial \Phi} \frac{\sin \Theta}{\sin \Phi} + \frac{\partial C_{x'}}{\partial \alpha} \frac{\cos \Theta \sin \beta}{\cos^2 \beta (\sin^2 \Theta + \tan^2 \beta)} \right) \\ & - \sin \bar{\varphi} \left(\frac{\partial C_{y'}}{\partial \Phi} \frac{\sin \Theta}{\sin \Phi} + \frac{\partial C_{y'}}{\partial \alpha} \frac{\cos \Theta \sin \beta}{\cos^2 \beta (\sin^2 \Theta + \tan^2 \beta)} \right) \end{aligned} \quad (C.43)$$

$$m_4 = \frac{\partial C_{y'}}{\partial Re} Re \cos \bar{\varphi} + \frac{\partial C_{x'}}{\partial Re} Re \sin \bar{\varphi} \quad (C.44)$$

$$\begin{aligned} m_5 = \sin \bar{\varphi} & \left(-\frac{\partial C_{x'}}{\partial \Phi} \frac{\cos \Theta \sin \beta}{\sin \Phi} + \frac{\partial C_{x'}}{\partial \alpha} \frac{\sin \Theta (1 + \tan^2 \beta)}{(\sin^2 \Theta + \tan^2 \beta)} \right) + \\ & + \cos \bar{\varphi} \left(-\frac{\partial C_{y'}}{\partial \Phi} \frac{\cos \Theta \sin \beta}{\sin \Phi} + \frac{\partial C_{y'}}{\partial \alpha} \frac{\sin \Theta (1 + \tan^2 \beta)}{(\sin^2 \Theta + \tan^2 \beta)} \right) \end{aligned} \quad (C.45)$$

$$\begin{aligned} m_6 = \sin \bar{\varphi} & \left(\frac{\partial C_{x'}}{\partial \Phi} \frac{\sin \Theta}{\sin \Phi} + \frac{\partial C_{x'}}{\partial \alpha} \frac{\cos \Theta \sin \beta}{\cos^2 \beta (\sin^2 \Theta + \tan^2 \beta)} \right) + \\ & + \cos \bar{\varphi} \left(\frac{\partial C_{y'}}{\partial \Phi} \frac{\sin \Theta}{\sin \Phi} + \frac{\partial C_{y'}}{\partial \alpha} \frac{\cos \Theta \sin \beta}{\cos^2 \beta (\sin^2 \Theta + \tan^2 \beta)} \right) \end{aligned} \quad (C.46)$$

$$m_7 = \frac{D \partial C_M}{\partial Re} Re \quad (C.47)$$

$$m_8 = -\frac{D \partial C_M}{\partial \Phi} \frac{\cos \Theta \sin \beta}{\sin \Phi} + \frac{D \partial C_M}{\partial \alpha} \frac{\sin \Theta (1 + \tan^2 \beta)}{(\sin^2 \Theta + \tan^2 \beta)} \quad (C.48)$$

$$m_9 = \frac{D \partial C_M}{\partial \Phi} \frac{\sin \Theta}{\sin \Phi} + \frac{D \partial C_M}{\partial \alpha} \frac{\cos \Theta \sin \beta}{\cos^2 \beta (\sin^2 \Theta + \tan^2 \beta)} \quad (C.49)$$

APPENDIX D

Terms of the characteristics polynomial

The terms of the characteristic polynomial, Equation 7.71, are here reported. In the following, the terms of the structural damping matrix, \mathbf{C}_s , and of the structural stiffness matrix, \mathbf{K}_s , are expressed in the form of damping ratio and circular natural frequencies, respectively (See Eqs. 7.56 and 7.57). The terms of the aerodynamic damping matrix, ξ_a , are expressed as ξ_{aij} with $i, j \in \{x, y, \theta\}$. The terms of the aerodynamic frequency matrix, ω_a^2 , are expressed as ω_{aij} with $i \in \{x, y, \theta\}$ and $j = \theta$.

The terms $p_0 - p_6$ are:

$$p_0 = 1 \quad (\text{D.1})$$

$$\begin{aligned} p_1 = & \xi_x \omega_x \left(2 + \frac{2m \sin^2 \varsigma_0 \omega_x L_e^2}{J} \right) + \xi_y \omega_y \left(2 + \frac{2m \cos^2 \varsigma_0 L_e^2}{J} \right) + 2\xi_\theta \omega_\theta + \\ & + \omega_x \left(-2\xi_{\text{axx}} + \frac{2m L_e}{J} (-L_e \sin^2 \varsigma_0^2 \xi_{\text{axx}} + \sin(2\varsigma_0) L_e \xi_{\text{axy}} - \sin \varsigma_0 \xi_{\text{ax}\theta}) \right) + \\ & + \omega_y \left(-2\xi_{\text{ayy}} + \frac{2m L_e}{J} (\cos \varsigma_0 \sin \varsigma_0 L_e \xi_{\text{ayx}} - \cos \varsigma_0^2 L_e \xi_{\text{ayy}} + \cos \varsigma_0 \xi_{\text{ay}\theta}) \right) + \\ & + \omega_\theta (-2\xi_{\text{a}\theta\theta} + 2L_e (-\sin \varsigma_0 \xi_{\text{a}\theta x} + \cos \varsigma_0 \xi_{\text{a}\theta y})) \end{aligned} \quad (\text{D.2})$$

$$\begin{aligned}
p_2 = & \xi_x \omega_x \left[\left(-4\xi_{\text{ayy}} + \frac{4mL_e}{J} (-L_e \xi_{\text{ayy}} + \cos \varsigma_0 \xi_{\text{ay}\theta}) \right) \omega_y + \right. \\
& + (4 \cos \varsigma_0 L_e \xi_{\text{a}\theta y} - 4\xi_{\text{a}\theta\theta}) \omega_\theta \left. \right] + \\
& + \xi_y \left[\left(-4\xi_{\text{axx}} - \frac{4mL_e}{J} (L_e \xi_{\text{axx}} + \sin \varsigma_0 \xi_{\text{ax}\theta}) \right) \omega_x \omega_y + \right. \\
& - (4 \sin \varsigma_0 L_e \xi_{\text{a}\theta x} + 4\xi_{\text{a}\theta\theta}) \omega_y \omega_\theta \left. \right] + \\
& - \xi_\theta (4\xi_{\text{axx}} \omega_x + 4\xi_{\text{ayy}} \omega_y) \omega_\theta + \xi_x \xi_y \left(4 + \frac{4mL_e^2}{J} \right) \omega_x \omega_y + 4\xi_x \xi_\theta \omega_x \omega_\theta + \\
& + 4\xi_y \xi_\theta \omega_y \omega_\theta + \left(1 + \frac{m \sin^2 \varsigma_0 L_e^2}{J} \right) \omega_x^2 + \left(1 + \frac{m \cos^2 \varsigma_0 L_e^2}{J} \right) \omega_y^2 + \omega_\theta^2 + \quad (\text{D.3}) \\
& + (\xi_{\text{ayy}} (4 \sin \varsigma_0 L_e \xi_{\text{a}\theta x} + 4\xi_{\text{a}\theta\theta}) - \xi_{\text{a}\theta y} (4 \sin \varsigma_0 L_e \xi_{\text{ayx}} + \xi_{\text{ay}\theta})) \omega_y \omega_\theta + \\
& + \omega_x \left\{ \left[4 (\xi_{\text{axx}} \xi_{\text{ayy}} - \xi_{\text{axy}} \xi_{\text{ayx}}) + \frac{4mL_e}{J} \left(\xi_{\text{axx}} (L_e \xi_{\text{ayy}} - \cos \varsigma_0 \xi_{\text{ay}\theta}) + \right. \right. \right. \\
& - \xi_{\text{axy}} (L_e \xi_{\text{ayx}} + \sin \varsigma_0 \xi_{\text{ay}\theta}) + \xi_{\text{ax}\theta} (\cos \varsigma_0 \xi_{\text{ayx}} + \sin \varsigma_0 \xi_{\text{ayy}}) \left. \right] \omega_y + \\
& + (4\xi_{\text{a}\theta x} (\cos \varsigma_0 L_e \xi_{\text{axy}} - \xi_{\text{ax}\theta}) + 4\xi_{\text{axx}} (-\cos \varsigma_0 L_e \xi_{\text{a}\theta y} + \xi_{\text{a}\theta\theta})) \omega_\theta \left. \right\} + \\
& + \frac{mL_e}{J} (-\sin \varsigma_0 \omega_{\text{ax}\theta}^2 + \cos \varsigma_0 \omega_{\text{ay}\theta}^2) - \omega_{\text{a}\theta\theta}^2
\end{aligned}$$

$$\begin{aligned}
p_3 = & \xi_x \omega_x \left[\frac{2m \cos \varsigma_0 L_e \omega_{ay\theta}^2}{J} - 2\omega_{a\theta\theta}^2 + \left(2 + \frac{2mL_e^2}{J} \right) \omega_y^2 + \right. \\
& + (-8\xi_{ay\theta}\xi_{a\theta y} + 8\xi_{ayy}\xi_{a\theta\theta}) \omega_y \omega_\theta + 2\omega_\theta^2 \Big] + \\
& + \xi_y \left[\left(2 + \frac{2mL_e^2}{J} \right) \omega_x^2 \omega_y + (-8\xi_{ax\theta}\xi_{a\theta x} + 8\xi_{axx}\xi_{a\theta\theta}) \omega_x \omega_y \omega_\theta + \right. \\
& + \omega_y \left(-\frac{2m \sin \varsigma_0 L_e \omega_{ax\theta}^2}{J} - 2\omega_{a\theta\theta}^2 + 2\omega_\theta^2 \right) \Big] + \\
& + \xi_\theta (2\omega_x^2 \omega_\theta + (-8\xi_{axy}\xi_{ayx} + 8\xi_{axx}\xi_{a\theta y} + 8\xi_{x\theta y}) \omega_x \omega_y \omega_\theta + 2\omega_y^2 \omega_\theta) + \\
& - 8\xi_x \xi_y \xi_{a\theta\theta} \omega_x \omega_y \omega_\theta - 8\xi_x \xi_\theta \xi_{a\theta y} \omega_x \omega_y \omega_\theta - 8\xi_y \xi_\theta \xi_{axx} \omega_x \omega_y \omega_\theta + \\
& + \omega_x^2 \left[\left(-2\xi_{a\theta y} + \frac{2mL_e}{J} (-L_e \xi_{a\theta y} + \cos \varsigma_0 \xi_{ay\theta}) \right) \omega_y + \right. \\
& + 2(\cos \varsigma_0 L_e \xi_{a\theta y} - \xi_{a\theta\theta}) \omega_\theta \Big] + \tag{D.4} \\
& + \omega_x \left[-\frac{2mL_e}{J} (\cos \varsigma_0 \xi_{axx} + \sin \varsigma_0 \xi_{axy}) \omega_{ay\theta}^2 + 2\xi_{axx} \omega_{a\theta\theta}^2 \right. \\
& - 2 \left(\xi_{axx} + \frac{mL_e}{J} (L_e \xi_{axx} + \sin \varsigma_0 \xi_{ax\theta}) \right) \omega_y^2 + \\
& + 8 \left[\xi_{axx} (\xi_{ay\theta} \xi_{a\theta y} - \xi_{a\theta y} \xi_{a\theta\theta}) + 8\xi_{axy} (\xi_{ayx} \xi_{a\theta\theta} - \xi_{ay\theta} \xi_{a\theta x}) \right. \\
& + 8\xi_{ax\theta} (\xi_{a\theta y} \xi_{a\theta x} - \xi_{a\theta x} \xi_{a\theta y}) \Big] \omega_y \omega_\theta - 2\xi_{axx} \omega_\theta^2 \Big] + \\
& + \omega_y \left(\frac{2mL_e}{J} (\cos \varsigma_0 \xi_{ayx} \omega_{ax\theta}^2 + \sin \varsigma_0 \xi_{a\theta y} \omega_{ax\theta}^2) + 2\xi_{a\theta y} (\omega_{a\theta\theta}^2 - \omega_\theta^2) \right) + \\
& - 2\omega_\theta (\xi_{a\theta x} \omega_{ax\theta}^2 + \xi_{a\theta y} \omega_{ay\theta}^2) + \\
& - (2 \sin \varsigma_0 L_e \xi_{a\theta x} + 2\xi_{a\theta\theta}) \omega_y^2 \omega_\theta
\end{aligned}$$

$$\begin{aligned}
p_4 = & \xi_x \omega_x (-4\xi_{a\theta y} \omega_{ay\theta}^2 \omega_\theta - 4\xi_{a\theta\theta} \omega_y^2 \omega_\theta + \omega_y (4\xi_{a\theta y} \omega_{a\theta\theta}^2 - 4\xi_{a\theta y} \omega_\theta^2)) + \\
& + \xi_y (-4\omega_y \omega_\theta (\xi_{a\theta x} \omega_{ax\theta}^2 + \xi_{a\theta\theta} \omega_x^2) + 4\omega_x \omega_y (\xi_{axx} \omega_{a\theta\theta}^2 - \xi_{axx} \omega_\theta^2)) \\
& + \xi_\theta (-4\omega_x^2 \omega_y \omega_\theta (\xi_{a\theta y} + \xi_{axx})) + \xi_x \xi_y \omega_x \omega_y (-4\omega_{a\theta\theta}^2 + 4\omega_\theta^2) + \\
& + 4\xi_y \xi_\theta \omega_x^2 \omega_y \omega_\theta + 4\xi_x \xi_\theta \omega_x \omega_y^2 \omega_\theta + \\
& + \omega_x^2 \left(\frac{m \cos \zeta_0 L_e \omega_{ay\theta}^2}{J} - \omega_{a\theta\theta}^2 + \left(1 + \frac{m L_e^2}{J} \right) \omega_y^2 + \omega_\theta^2 \right) + \\
& + \omega_x^2 (-4\xi_{a\theta y} \xi_{a\theta y} + 4\xi_{a\theta y} \xi_{a\theta\theta}) \omega_y \omega_\theta + \\
& + \omega_y^2 \left(-\frac{m \sin \zeta_0 L_e \omega_{ax\theta}^2}{J} - \omega_{a\theta\theta}^2 + \omega_\theta^2 \right) + (-4\xi_{axy} \xi_{ayx} + 4\xi_{axx} \xi_{a\theta y}) \omega_\theta^2 + \\
& + \omega_x \left(4\omega_{ay\theta}^2 \omega_\theta (-\xi_{axy} \xi_{a\theta x} + \xi_{axx} \xi_{a\theta y}) + \omega_y (4\omega_{a\theta\theta}^2 (\xi_{axy} \xi_{ayx} - \xi_{axx} \xi_{a\theta y})) \right) + \\
& + 4\omega_y^2 \omega_\theta (-\xi_{ax\theta} \xi_{a\theta x} + \xi_{axx} \xi_{a\theta\theta}) + \omega_y \omega_\theta \omega_{ax\theta}^2 (4\xi_{a\theta y} \xi_{a\theta x} - 4\xi_{ayx} \xi_{a\theta y})
\end{aligned} \tag{D.5}$$

$$\begin{aligned}
p_5 = & \xi_x \omega_x \omega_y^2 (-2\omega_{a\theta\theta}^2 + 2\omega_\theta^2) + \xi_y \omega_x^2 \omega_y (-2\omega_{a\theta\theta}^2 + 2\omega_\theta^2) + 2\xi_\theta \omega_x^2 \omega_y^2 \omega_\theta + \\
& \omega_x^2 (-2\xi_{a\theta y} \omega_{ay\theta}^2 \omega_\theta - 2\xi_{a\theta\theta} \omega_y^2 \omega_\theta + \omega_y (2\xi_{a\theta y} \omega_{a\theta\theta}^2 - 2\xi_{a\theta y} \omega_\theta^2)) + \\
& + \omega_x \omega_y^2 (2\xi_{axx} \omega_{a\theta\theta}^2 - 2\xi_{axx} \omega_\theta^2) - 2\xi_{a\theta x} \omega_{ax\theta}^2 \omega_y^2 \omega_\theta
\end{aligned} \tag{D.6}$$

$$p_6 = \omega_x^2 \omega_y^2 (-\omega_{a\theta\theta}^2 + \omega_\theta^2) \tag{D.7}$$